

Xuzhu Dong
Li Cai *Editors*

The Proceedings of 2023
4th International
Symposium
on Insulation and
Discharge Computation
for Power Equipment
(IDCOMPU2023)

Volume I

Lecture Notes in Electrical Engineering

Volume 1100

Series Editors

Leopoldo Angrisani, Department of Electrical and Information Technologies Engineering, University of Napoli Federico II, Napoli, Italy
Marco Artega, Departament de Control y Robótica, Universidad Nacional Autónoma de México, Coyoacán, Mexico
Samarjit Chakraborty, Fakultät für Elektrotechnik und Informationstechnik, TU München, München, Germany
Jiming Chen, Zhejiang University, Hangzhou, Zhejiang, China
Shanben Chen, School of Materials Science and Engineering, Shanghai Jiao Tong University, Shanghai, China
Tan Kay Chen, Department of Electrical and Computer Engineering, National University of Singapore, Singapore, Singapore
Rüdiger Dillmann, University of Karlsruhe (TH) IAIM, Karlsruhe, Baden-Württemberg, Germany
Haibin Duan, Beijing University of Aeronautics and Astronautics, Beijing, China
Gianluigi Ferrari, Dipartimento di Ingegneria dell'Informazione, Sede Scientifica Università degli Studi di Parma, Parma, Italy
Manuel Ferre, Centre for Automation and Robotics CAR (UPM-CSIC), Universidad Politécnica de Madrid, Madrid, Spain
Faryar Jabbari, Department of Mechanical and Aerospace Engineering, University of California, Irvine, CA, USA
Limin Jia, State Key Laboratory of Rail Traffic Control and Safety, Beijing Jiaotong University, Beijing, China
Janusz Kacprzyk, Intelligent Systems Laboratory, Systems Research Institute, Polish Academy of Sciences, Warsaw, Poland
Alaa Khamis, Department of Mechatronics Engineering, German University in Egypt El Tagamoa El Khames, New Cairo City, Egypt
Torsten Kroeger, Intrinsic Innovation, Mountain View, CA, USA
Yong Li, College of Electrical and Information Engineering, Hunan University, Changsha, Hunan, China
Qilian Liang, Department of Electrical Engineering, University of Texas at Arlington, Arlington, TX, USA
Ferran Martín, Departament d'Enginyeria Electrònica, Universitat Autònoma de Barcelona, Bellaterra, Barcelona, Spain
Tan Cher Ming, College of Engineering, Nanyang Technological University, Singapore, Singapore
Wolfgang Minker, Institute of Information Technology, University of Ulm, Ulm, Germany
Pradeep Misra, Department of Electrical Engineering, Wright State University, Dayton, OH, USA
Subhas Mukhopadhyay, School of Engineering, Macquarie University, NSW, Australia
Cun-Zheng Ning, Department of Electrical Engineering, Arizona State University, Tempe, AZ, USA
Toyoaki Nishida, Department of Intelligence Science and Technology, Kyoto University, Kyoto, Japan
Luca Oneto, Department of Informatics, Bioengineering, Robotics and Systems Engineering, University of Genova, Genova, Italy
Bijaya Ketan Panigrahi, Department of Electrical Engineering, Indian Institute of Technology Delhi, New Delhi, Delhi, India
Federica Pascucci, Department di Ingegneria, Università degli Studi Roma Tre, Roma, Italy
Yong Qin, State Key Laboratory of Rail Traffic Control and Safety, Beijing Jiaotong University, Beijing, China
Gan Woon Seng, School of Electrical and Electronic Engineering, Nanyang Technological University, Singapore, Singapore
Jochaim Speidel, Institute of Telecommunications, University of Stuttgart, Stuttgart, Germany
Germano Veiga, FEUP Campus, INESC Porto, Porto, Portugal
Haitao Wu, Academy of Opto-electronics, Chinese Academy of Sciences, Haidian District Beijing, China
Walter Zamboni, Department of Computer Engineering, Electrical Engineering and Applied Mathematics, DIEM—Università degli studi di Salerno, Fisciano, Salerno, Italy
Junjie James Zhang, Charlotte, NC, USA
Kay Chen Tan, Department of Computing, Hong Kong Polytechnic University, Kowloon Tong, Hong Kong

The book series *Lecture Notes in Electrical Engineering* (LNEE) publishes the latest developments in Electrical Engineering—quickly, informally and in high quality. While original research reported in proceedings and monographs has traditionally formed the core of LNEE, we also encourage authors to submit books devoted to supporting student education and professional training in the various fields and applications areas of electrical engineering. The series cover classical and emerging topics concerning:

- Communication Engineering, Information Theory and Networks
- Electronics Engineering and Microelectronics
- Signal, Image and Speech Processing
- Wireless and Mobile Communication
- Circuits and Systems
- Energy Systems, Power Electronics and Electrical Machines
- Electro-optical Engineering
- Instrumentation Engineering
- Avionics Engineering
- Control Systems
- Internet-of-Things and Cybersecurity
- Biomedical Devices, MEMS and NEMS

For general information about this book series, comments or suggestions, please contact leontina.dicecco@springer.com.

To submit a proposal or request further information, please contact the Publishing Editor in your country:

China

Jasmine Dou, Editor (jasmine.dou@springer.com)

India, Japan, Rest of Asia

Swati Meherishi, Editorial Director (Swati.Meherishi@springer.com)

Southeast Asia, Australia, New Zealand

Ramesh Nath Premnath, Editor (ramesh.premnath@springernature.com)

USA, Canada

Michael Luby, Senior Editor (michael.luby@springer.com)

All other Countries

Leontina Di Cecco, Senior Editor (leontina.dicecco@springer.com)

**** This series is indexed by EI Compendex and Scopus databases. ****

Xuzhu Dong · Li Cai
Editors

The Proceedings of 2023 4th
International Symposium
on Insulation and Discharge
Computation for Power
Equipment (IDCOMP2023)

Volume I

 Springer

Editors

Xuzhu Dong
School of Electrical Engineering
and Automation
Wuhan University
Wuhan, China

Li Cai
School of Electrical Engineering
and Automation
Wuhan University
Wuhan, China

ISSN 1876-1100

ISSN 1876-1119 (electronic)

Lecture Notes in Electrical Engineering

ISBN 978-981-99-7392-7

ISBN 978-981-99-7393-4 (eBook)

<https://doi.org/10.1007/978-981-99-7393-4>

© Beijing Paiké Culture Commu. Co., Ltd. 2024

This work is subject to copyright. All rights are solely and exclusively licensed by the Publisher, whether the whole or part of the material is concerned, specifically the rights of translation, reprinting, reuse of illustrations, recitation, broadcasting, reproduction on microfilms or in any other physical way, and transmission or information storage and retrieval, electronic adaptation, computer software, or by similar or dissimilar methodology now known or hereafter developed.

The use of general descriptive names, registered names, trademarks, service marks, etc. in this publication does not imply, even in the absence of a specific statement, that such names are exempt from the relevant protective laws and regulations and therefore free for general use.

The publisher, the authors, and the editors are safe to assume that the advice and information in this book are believed to be true and accurate at the date of publication. Neither the publisher nor the authors or the editors give a warranty, expressed or implied, with respect to the material contained herein or for any errors or omissions that may have been made. The publisher remains neutral with regard to jurisdictional claims in published maps and institutional affiliations.

This Springer imprint is published by the registered company Springer Nature Singapore Pte Ltd.

The registered company address is: 152 Beach Road, #21-01/04 Gateway East, Singapore 189721, Singapore

Paper in this product is recyclable.

Contents

The Effect of Contact Structure on Electromagnetic Force	1
Min Li, Baochun Song, and Anthony Papillon	
Partial Discharge Characteristics of Millimeter Metal Particle on a GIS Insulator Surface Under Long-Term Constant Voltage	9
Yiping Ji, Shaojing Wang, Xing Li, Guliang Zhou, Kai Gao, and Haoyang Tian	
Ultrasound-Based Pressure Pipe Internal Water Ingress Defect Detection Technology	19
Wenhui Li, Haibo Li, Yian Fang, Huan Liu, Junzhe Liang, Fenggeng Jiang, Guang Liu, and Di Rao	
Optical Storage Emergency Power Supply Technology for Railway Locomotive	31
Hao Yang, Guosheng Huang, Kaixiang Ma, Meng Cui, and Shuo Zhang	
Condition Monitoring Technology for Temperature and Strain Status of Disconnecter Based on SAW	43
Dapeng Guo, Zhang Yan, Ruchuan Shi, and Chenrui Zhang	
Adsorption of SF₆/N₂ Decomposed Gas in NaA, MFI and NaZSM-5 Molecular Sieves	51
Fengxiang Ma, Hongpeng Zu, Demin Zhang, Xin Lin, Jianyuan Xu, Yue Zhao, and Feng Zhu	
Pre-sowing Treatment Using Plasma-Activated Water to Enhance the Germination of Cucumber Seeds Under Salt Stress	63
Tong Zhu, Di Zhang, Chongshan Zhong, Guangwei Guan, and Hongwei Tang	

Ultrasonic Image Recognition of Terminal Lead Seal Defects Based on Convolutional Neural Network	77
Linggang Zhou, Wenhui Li, Xin Lu, Xueyan Wang, Huan Liu, Junzhe Liang, Fenggeng Jiang, and Gu Zhou	
Temperature Distribution and Influencing Factors of 110 kV Single Core Cable Joint	89
Lei Zhang, Rui Li, Liangyuan Chen, Shaoming Pan, and Xiajin Rao	
Loss Calculation of GIS Disconnect Switches Considering Contact Resistance and Skin Effect	101
Lei Zhang, Rui Li, Liang-yuan Chen, Shao-ming Pan, and Xia-jin Rao	
A Novel Virtual Power Plant Model with Ito Integral Considering Random Noise of Renewable Energy	113
Li Kang, Zhao Yulin, Tong Weilin, Liu Zhongyi, Dong Jinzhe, Shao Zhenwei, Lv Yajuan, and Xie Jinghua	
Research on AlexNet Model-Based Partial Discharge Diagnosis of Cable Terminals	123
Hongliang Zou, Wenhui Li, Yiming Lu, Jie Sun, Xin Lu, Yijiong Jin, Huan Liu, and Yao Zhang	
Double-Ended Localization Method Based on Joint VMD and WVD Time–Frequency Analysis	135
Wenhui Li, Guang Liu, Jun Liu, Xin Lu, Haibo Li, Jie Sun, Wen Dai, and Yao Zhang	
Particle-In-Cell/Monte Carlo Collisional Simulation of Space Charge Layer Formation and Development in Nitrogen Negative Streamers	147
Jianxin Wang, Tiejun Li, Hua Zhang, Jiatao Zhang, Zhuo Chen, Dan Wang, and Lijun Wang	
Research on Switchgear Partial Discharge Signal Type Identification Based on Composite Neural Network	155
Renfeng Wang, Xiang Zheng, Jingjie Yang, and Zhihai Xu	
Research on Partial Discharge Noise Reduction Method of Motor Based on SVD-VMD	165
Zhihai Xu, Jingjie Yang, and Xiang Zheng	
Simulation of Seawater Orifice Intrusion of 500 kV Submarine Oil-Filled Cable	177
Qingshuai Wu, Kaiyu Zeng, Degao Zhu, Qiyuan Jiang, Lili Li, Junguo Gao, and Xiaofeng Xu	
3-D Segmentation and Surface Reconstruction of Gas Insulated Switchgear via PointNet-MLS Architecture	187
Chaowei Lv, Xiangyu Guan, Jiang Liu, and Jingwen Liao	

Optimization of Electromagnetic Vibration for FSPM Motor by NSGA-II Algorithm 195
 Shu Wang, You Bian, Wei Zhao, Zhenyu Liu, Xuelei Zhang, Zuxu Guo, and Chenhao Kou

Simulation and Analysis of Charge Distribution and Capacitance Effect on Uneven Surface of Dielectric with Leakage Current 207
 Ran Ding, Tianxin Zhuang, Yin Gu, Ke Zhao, Hongtao Li, Jin Miao, and Yujie Li

Thermal Simulation Model of Oil-Immersed Transformer and Analysis of Temperature Rise Characteristics Under Winding Fault 217
 Si Chen, Yadong Liu, Yingjie Yan, and Xiuchen Jiang

Nonlinear Vibration Model of Transformer Windings and Its Application in Short-Circuit Axial Strength Evaluation 229
 Lei Zhang, Rui Li, Liangyuan Chen, and Shaoming Pan

Study of Bidirectional Current Flow Controller for Multi-terminal DC Grid 243
 Mengyu Yao

A Current Flow Controller with Independent Regulation Capability for HVDC Grid 253
 Mengyu Yao and Xueao Qiu

Research on a New Type of Magnetically Controlled Distribution Transformer 263
 Long Di, Xiaoguo Chen, Dezhu You, Yongzhong Wu, Kai Liu, Jiawei Liu, and Yu Dong

The Study of Fire Spread Trend in Cable Tunnels with Different Wind Speeds 273
 Zhe Zhang, Ying Sun, Liang Zou, and Xiaolong Wang

Effects of Insulating Paper Thickness on Space Charge Characteristics in Oil-Impregnated Paper Insulation 283
 Si Fu, Jinzhao Miao, and Zhihui Ma

Preparation and Energy Storage Characteristics of Novel Poly(M-phenylene Isophthalamide) Dielectric Composites 293
 Guangyu Duan, Fengying Hu, Guiyuan Liu, Wenxuan Shao, and Zuming Hu

The Roof Cable Terminal Simulation Calculation Study Based on Electric-Thermal Coupling Physical Field 303
 Xuefei Li, Liankang Zhang, Jingbing Wang, Jiaxing Wang, and Guochang Li

Identification of Series Fault Arc Occurred in Motor with Inverter Circuits Under Vibration Conditions	315
Yanli Liu, Zhengyang Lv, Lingwei Zhang, Yiyang Liu, Hao Wang, and Huiyang Wang	
Electric Field Simulation and Defect Analysis of Transformer Oil-Paper Capacitive Bushing	325
Yu Rui, Lei Xu, Tao Jiang, Bowen Yao, Fanhua Zhang, Beibei Wang, and Binbin Wei	
Coupling Simulation Study on Dislocation Slip of Self-Elastic Arcing Contact Sets of SF6 Circuit Breaker	341
Yakui Liu, Fengchao Wang, and Hongyun Li	
Analysis of Aging Degree of Composite Insulators Based on Joint Relaxation Spectrum	351
Ding Zhang, Xinwen Hou, Yufei Zhang, Chuangang Zhu, Xiaonan Li, Xiong Ge, Ran Zhong, and Yu Lei	
Simulation for the Chain Formation of Cellulose Particles in Flowing Transformer Oil Under DC Voltage	361
Yuhang Yao, Mengyue Yu, Cheng Pan, Suyi Xia, and Ju Tang	
Calculation and Analysis of Induced Voltage in Overhead Ground Lines of UHVDC Transmission Lines After Ground Insulation Modification	375
Wei Li, Xinmin Li, Yanhua Han, Panfeng Hu, Lu Zhang, and Mingxi Zhu	
Numerical Modeling of the Arc in Switching-Type SPD	389
Yipeng Zhang, Qibin Zhou, Yijie Xiao, Xiaoyan Bian, and Zhenyu Pang	
Research on Relationship Between Aerodynamic Configuration and Ability to Extinguish Arc in Switching-Type SPD	399
Yijie Xiao, Qibin Zhou, Yipeng Zhang, and Xiaoyan Bian	
Study on Voltage Control Method of Energy Router Based on Common DC Voltage Bus	409
Shuxi Liu, Qin Luo, Jianhong Chen, and Yufei Qu	
Structural Parameters on the Performance of Magnetic Field Sensor Based on Faraday Effect	419
Meng Huang, Haomin Lv, Lei Zhang, and Bo Qi	
Study on the Effect of O₂ Content on the Decomposition Characteristics of C₅F₁₀O Under Different Buffer Gases	427
Long Li, Liangjun Dai, Baojia Deng, Qiang Yao, Ying Zhang, Huaxia Yang, Yifan Wang, and Yi Li	

Investigation of Gas Adsorption Properties Between CrB and SF₆ Decompositions: A Theoretical Study 435
 Xiangyu Tan, Fangrong Zhou, Zhimin Na, Dibo Wang, Ran Zhuo, Peng Wu, and Yi Li

Study About the Surface Charge Accumulation and Dissipation of Insulators Under Corona Condition 445
 Fan Yi, Wenli Xu, Xiaoshan Yao, Naifa Gong, Dazhao Zhang, Zhiye Du, Hao Meng, and Guohua Yue

Influence of Oxygen on Characteristic Law of C₅F₁₀O/N₂ Mixture Partial Discharge Statistical Characteristic 457
 Long Li, Qiang Yao, Baojia Deng, Liangjun Dai, Ying Zhang, Shiling Zhang, Ke Li, and Haoran Xia

Influence of Operating Environment on the Aging Characteristics of Composite Insulators 465
 Dong Yang, Chengjun Xu, Jian Zhang, Jianjun Yang, Shuaiwei Wang, Sile Chen, and Zhaoquan Chen

Self-Powered Insulating Oil Condition Monitoring System Based on Oil-Solid Contact Electrification 473
 Xiangyu Tan, Fangrong Zhou, Zhimin Na, Ran Zhuo, Dibo Wang, Haoying Wu, Song Xiao, and Yi Li

Research on Fast Calculation Method of Lightning Distribution in Mountainous Area Based on Conformal Mapping 481
 Nengxing Guo, Ruifang Li, Qian Lei, Jiayu Zhao, Chengzhi Li, Yujing Liang, and Xiaobin Cao

Research on Step Size Distribution in Lightning Path Simulation 491
 Qian Lei, Ruifang Li, Nengxing Guo, Ziyue Guo, Chengzhi Li, Lejia Liu, and Xiaobin Cao

Analysis and Optimization of Influencing Factors of DC Sheath Induced Voltage of AC/DC Trench Submarine Cable Based on Electrostatic Complementary Model 499
 Jingying Cao, Jie Chen, Xiao Tan, Kairui Li, Lixiang Wang, Chenjin Xu, and Wei Wang

Research on Typical Defects Electrical Performance of 1100 kV GIS Basin Insulator 517
 Xiangsong Zhan, Chun Xiao, Xixiu Wu, and Biao Zhang

Research on the Thermal Expansion and Contraction Characteristics of UHV AC GIL Expansion Joint 527
 Pengyang Li, Peipei Meng, Xixiu Wu, Hui Hou, Rongtai Wang, and Yiming Zhang

Improve the Toughness of Epoxy Resin Insulating Materials by Compounding Acid Anhydride Curing Agent	539
Yanning Zhao, Yushun Zhao, Zimin Luo, Xueping Li, and Shengtao Hu	
Fault Localization Method for Ring-Shaped DC Microgrids Based on Line Model and Euclidean Distance	549
Li Xinglong, Feng Bo, Yang Yi, Zhong Jiayong, and Zhao Hongwei	
Mechanical Structure Design and Strength Analysis of 750 kV High Voltage Test Platform	565
Ming Lei, Xinghui Jiang, and Yonggang Zhao	
Quality Improvement Method for Power Equipment Defect Record	573
Linghui Liu, Zehui Zhang, Hui Duan, Xiaojuan Qi, Xuliang Wang, and Qingquan Li	
Statistical Analysis of Electrothermal Damage Characteristics of Nanoelectrode Under High Electric Fields	583
Xinyu Gao, Fei Feng, Guofei Teng, Jun Zhao, Bing Xiao, and Yonghong Cheng	
Research on Online Monitoring of Submarine Cable Insulation Based on Two-Terminal Current Method	593
Huang Tao, Lei Zhicheng, Huang Xuancheng, and Zhou Xuwei	
Multi-physical Field Simulation of Permanent Arc Grounding Fault in 110 kV High Voltage Cable	603
Yisong Wang, Chaoqun Shi, and Yang Xu	
Review of Operation and Control of the New Energy Storage Isolated Network Systems	613
Xianqiang He, Weixing Zhao, Fei Cao, QinFeng Ma, Mingshun Liu, Hai Qin, Qingxin Pu, and Yudong Sun	
Design and Implementation of Passive Chip Temperature Measurement System for Primary Equipment	623
Kai Zhu, Fanglei Liu, Yaqing Li, Zhen Zheng, Zhaoyu Qin, and Zhaofan Wang	
A Multiphysics Computational Method for Thermal Field of Transformer Winding Using Finite Element Method	635
Xingxiang Yang, Yanpu Zhao, and Shucan Cheng	
Field Ionization Degree Influence on Discharge Streamer of Natural Ester Based on Ionization Energy Calculation Under Changing Electric Field	645
Jingwen Zhang, Junyi Zhang, Wenyu Ye, Hanting Zhang, Hongwei Li, and Jian Hao	

Research on the Energized Ice-Melting for the Ground Wire Optical Cable of ± 800 kV Ultra-High Voltage Direct Current Transmission Line 655
Wei Li, Xinmin Li, Yanhua Han, Songbo Chen, Lu Zhang, and Xiaoyue Chen

Analysis of Reactive Oxygen/Nitrogen Species in Cold Atmospheric Plasma Activated Water 671
Fan Bai and Yumin Xia

Study on Transient Electric Field Distribution of 40.5 kV Switchgear Vacuum Circuit Breaker Cut-Off Reactor 679
Wang Huaqing, Huang Daochun, Shuang Mingjing, Bi Jiayu, Li Huipeng, and Qiu Yiqun

Calculation of the Sensing Performance of SnO₂ Doped with Au Atom on C₄F₇N 689
Luoyu Li, Jie Yang, Lifeng Zhu, Sipeng Li, Chao Ma, Yang Zhao, Yifan Zhang, and Song Xiao

A Coordinated Control Method for Active Power Feedforward of Dual PWM Converter 697
Dapeng Cao and Jie Li

Optimal Design of Double-Fracture Disconnect Switchgears Based on BP Neural Network and NSGA-II Algorithm 707
Xueliang Liu, Jiangang Yin, Jiesshuai Ren, Jun Chen, Yaqin Wen, and Zhao Yuan

The Effect of Contact Structure on Electromagnetic Force



Min Li, Baochun Song, and Anthony Papillon

Abstract In order to improve the performance of vacuum interrupter, two types of radial magnetic field (RMF) contact structure were designed for electromagnetic force research. Electromagnetic force of arc and electric repulsion of move contact was simulated analysis by Ansys software at 25 kA. The electric repulsion of move contact can be decreased to 4% by improving contact structure at short time withstand current. It can improve the performance of short time withstand current (STC), peak withstand current and earthing switch making. The electromagnetic force direction of arc can be improved by improving contact structure. It can avoid arc erosion in a small area of contact and increase electric endurance performance. The electromagnetic force of arc can be increased by contact 15° dislocation assemble. It can increase the electric endurance performance of contact. The electric repulsion of move contact is about 190 N at 0.5 mm contact gap with arc for both contact structures.

Keywords Vacuum interrupter · Simulation · Electromagnetic force

1 Introduction

Vacuum circuit breaker (VCB) has been widely used in middle voltage electric network [1, 2]. Vacuum interrupter (VI) is the core part of VCB [3], which is used for current conduct, fault current breaking and shot time withstand. In order to reach these requirements, the VI contact need design to different shapes. But they can be classified to axial magnetic field (AMF) or RMF. Most of researchers focus on breaking performance of contact. Different contact structures have been designed and tested. The vacuum arc of RMF will rotate fast on the contact surface to avoid arc erosion in the small area [4]. In order to decrease the arc erosion of RMF, arc

M. Li (✉) · B. Song
Schneider Electric (Xiamen) Switchgear Equipment Co., Ltd, Xiamen 361000, China
e-mail: lim2013pg@126.com

A. Papillon
Schneider Electric Co., Ltd, Grenoble, France

© Beijing Paiké Culture Commu. Co., Ltd. 2024
X. Dong and L. Cai (eds.), *The Proceedings of 2023 4th International Symposium on Insulation and Discharge Computation for Power Equipment (IDCOMPU2023)*, Lecture Notes in Electrical Engineering 1100, https://doi.org/10.1007/978-981-99-7393-4_1

rotate speed need increase by increasing electromagnetic force of arc [5]. In order to pass shot time withstand current (STC) test for a period of time (1–4 s), the VCB must be able to open the contact after STC. Thus, the contact welding force must be minimized. The AMF VI has an additional attractive force due to the parallel current flowing in the fixed and moved AMF coils behind the contacts [6]. So, AMF is benefit for STC test. But RMF VI has a repulsive blow-off force due to the reverse current flowing in two electrodes.

In order to improve the performance of VI, some researchers combine AMF and RMF [7]. Many commercial simulation software was used for simulation, like Ansys [8], COMSOL [9] and et al. This paper researched the Electromagnetic force of arc and electric repulsion of move contact by Ansys software at 25 kA to improve the STC and breaking performance.

2 Contact Structures and Simulation Method

The contact structures are shown in Fig. 1. Two contact structures were designed. The diameter of contact is 44 mm, the thickness of contact is 8 mm. V1 is a simple, flat spiral contact. V2 is an improved spiral contact which has slope, contact surface and counterbore structure.

The electric repulsion simulation models of moved contact are shown in Fig. 2. A column was used to simulate the real contact area, its diameter is 1 mm and the height is 0.5 mm, its color is gray in the model. There are two real contact areas were designed in V1, one is near central hole, one is in the same position with that in V2. Because V2 has 4 contact area, 4 columns were designed in V2 model. The assemble method of moved contact and fixed contact is fully aligning.

The electromagnetic force simulation models of arc are shown in Fig. 3. The arc model was designed as a column, its diameter is 1 mm and height is 0.5 mm. The arc model color is gray. There are two arc model positions in V1 and one arc model position in V2.

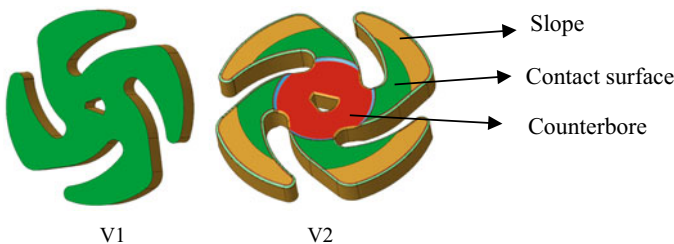


Fig. 1 Contact structures

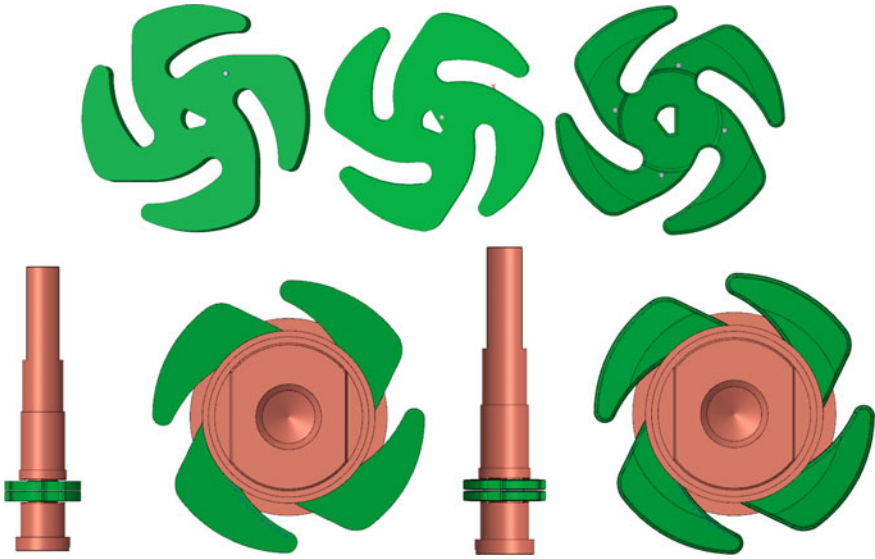


Fig. 2 Electric repulsion simulation models of moved contact



Fig. 3 Electromagnetic force simulation models of arc

In order to research the contact assemble effect on electromagnetic force of arc, two contact assemble models were designed as shown in Fig. 4. One is fully aligning assemble of fixed contact and moved contact, one is 15° dislocation assemble.

3 Simulation Results

The electric repulsion force of moved contact at closing with 25 kA STC is shown in Table 1. It shows that the electric repulsion force of V1 is about 23 times than that of V2. V2 is much benefit for STC to decrease contact welding. The contact area of V1 and the assemble method of V2 have some effect of electric repulsion force of moved contact, but it is little.

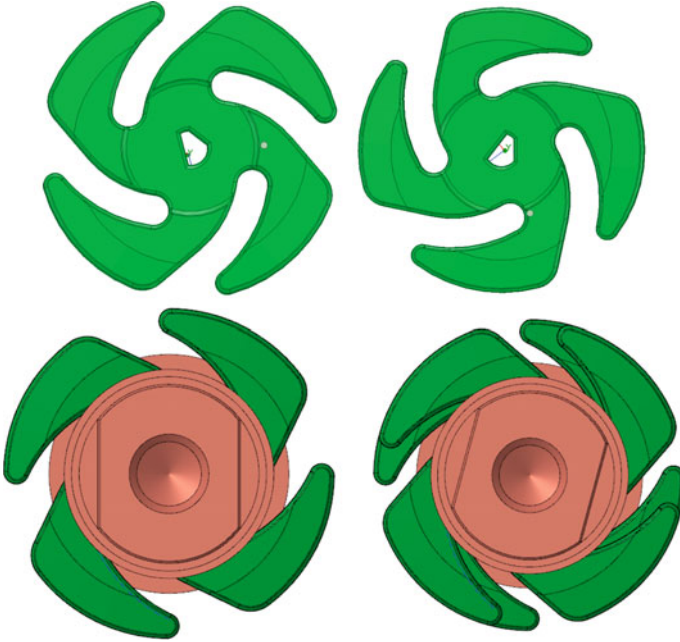


Fig. 4 Two contact assemble models

Table 1 Electric repulsion force of moved contact at closing with 25 kA STC (N)

Contact structure	Electric repulsion force
V1 with contact area like V2	192.7
V1 with contact area near central hole	182.5
V2 with fully aligning contact assemble	8.1
V2 with 15° dislocation assemble	7.3

The electric repulsion force of moved contact at 0.5 mm contact gap with 25 kA current is shown in Table 2. It shows that the electric repulsion force of V1 is similar than that of V2. The electric repulsion force of V2 with 15° dislocation assemble is 4.3 N higher than that with fully aligning contact assemble. Electric repulsion force of moved contact of RMF VI at small contact gap can help to increase open speed, so, it is benefit for VI breaking.

Magnetic strength of V2 at closing with 25 kA STC is shown in Fig. 5. The maximum value is 2.7 T which is around the column surface. There have radial and tangential magnetic field.

Magnetic strength of moved contact at 0.5 mm contact gap is shown in Fig. 6. The maximum value is little different from 10.5 to 11.4 T. The maximum value happened around the arc column surface. But the maximum value direction is different. Most of magnetic field is tangential.

Table 2 Electric repulsion force of moved contact at 0.5 mm contact gap with 25 kA current (N)

Contact structure	Electric repulsion force
V1 with contact area like V2	192.7
V1 with contact area near central hole	182.5
V2 with fully aligning contact assemble	191.7
V2 with 15° dislocation assemble	196.0

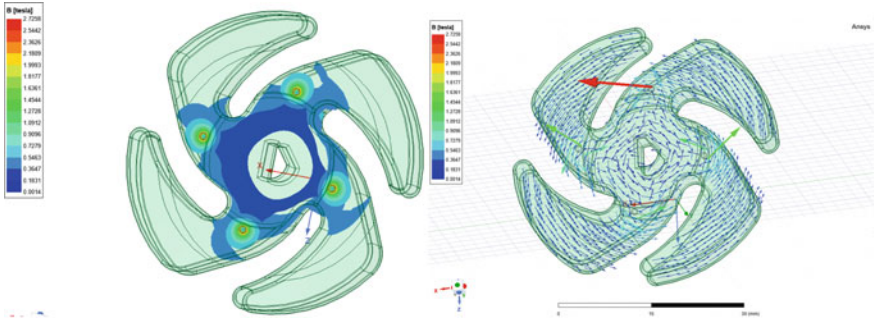


Fig. 5 Magnetic strength of V2 at closing with 25 kA STC

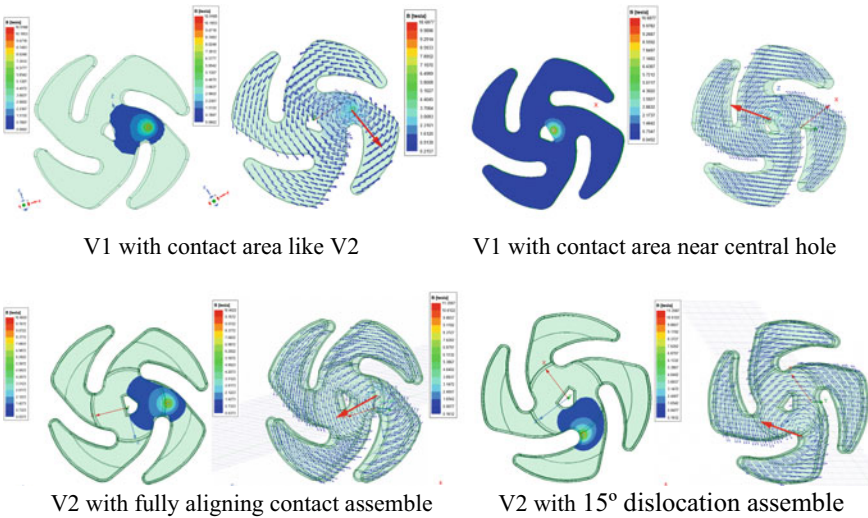


Fig. 6 Magnetic strength of moved contact at 0.5 mm contact gap

Volume force density of arc at 0.5 mm contact gap is shown in Fig. 7. The electromagnetic force of arc at 0.5 mm contact gap is shown in Table 3. It shows that the maximum electromagnetic force of arc is 13.1 N at V1 with contact area near central hole, but the force direction is $-x$. This force will push the arc go to the center of contact, which will make a high erosion at contact center area. The force direction of V1 with contact area like V2 is x , which will push the arc go to the contact edge and erosion the edge. The force direction of V2 is $-x$ and z , it will push arc rotate around the petal. The force value of V2 with 15° dislocation assemble is higher than that of V2 with fully aligning contact assemble. It can decrease the arc erosion on contact.

Magnetic strength of arc at 0.5 mm contact gap is shown in Fig. 8. The maximum value of magnetic strength of arc is from 10.7 to 11.4 T at different situation, it is not much different. But the magnetic strength distribution is different.

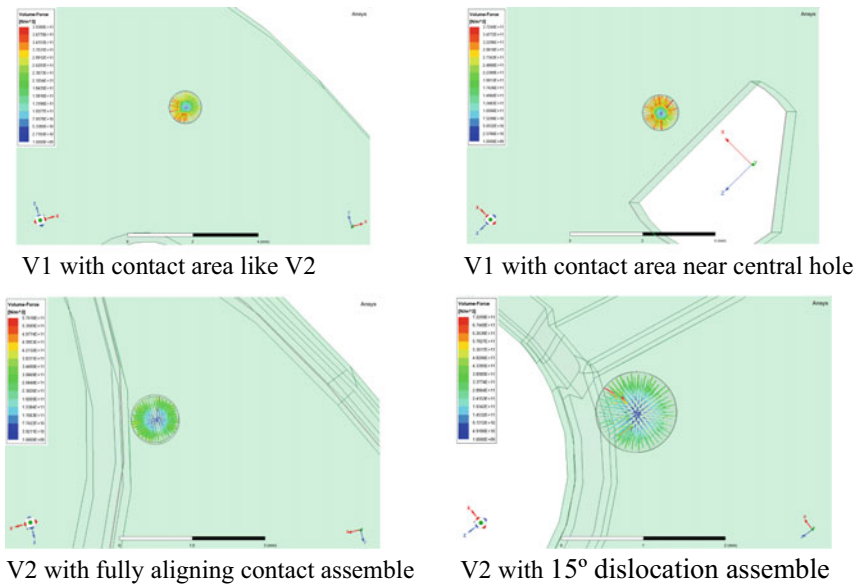


Fig. 7 Volume force density of arc at 0.5 mm contact gap

Table 3 Electromagnetic force of arc at 0.5 mm contact gap (N)

Contact structure	F(x)	F(y)	F(z)	Mag(F)
V1 with contact area like V2	7.9	-1.4	0.9	8.1
V1 with contact area near central hole	-13.1	0.2	-0.2	13.1
V2 with fully aligning contact assemble	-4.3	0.2	3.8	5.7
V2 with 15° dislocation assemble	-6.2	-2.1	3.8	7.6

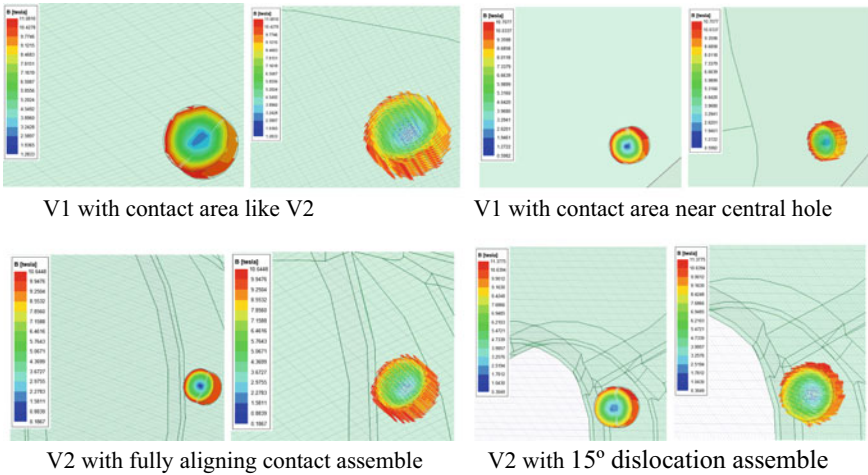


Fig. 8 Magnetic strength of arc at 0.5 mm contact gap

4 Conclusion

The electric repulsion of move contact can be decreased to 4% by improving contact structure at STC. It can improve the performance of short time withstand current (STC), peak withstand current and earthing switch making. The electromagnetic force direction of arc can be improved by improving contact structure. It can avoid arc erosion in a small area of contact and increase electric endurance performance. The electromagnetic force of arc can be increased by contact 15° dislocation assemble. It can increase the electric endurance performance of contact. The electric repulsion of move contact is about 190 N at 0.5 mm contact gap with arc for both contact structures. It can increase open speed at small contact gap. The maximum value of magnetic strength of arc is from 10.7 to 11.4 T at different situation, it is not much different. But the magnetic strength distribution is different.

References

1. Kojima H, Donen T, Kimura T, Kokura K, Hayakawa N (2020) Discrimination of discharge pattern in cut model of vacuum interrupter. In: XXIX international symposium on discharges and electrical insulation in vacuum, pp 323–326, Padova
2. Ge G, Cheng X, Liao M, Duan X, Zou J (2018) Vacuum arcs and postarc characteristic of vacuum interrupters with external AMF at current zero. *IEEE Trans Plasma Sci* 46(4):1003–1008
3. Falkingham LT (2017) The future of vacuum switchgear. In: 4th international conference on electric power equipment—switching technology. IEEE, China, pp 80–84
4. Li Y, Wang Z, Li Q, Geng Y, Wang J, Liu Z, Zhao X, Bi Y (2019) Vacuum arc characteristics of a novel contact consists of arcing contact and main contact. In: 5th international conference on electric power equipment—switching technology. IEEE, Japan, pp 174–178

5. Xiu S, Liu Z, Li R, Cui J, Liu T (2021) The influence of TMF and AMF components on arc movement characteristics in spiral-slot contacts. *IEEE Trans Plasma Sci* 49(4):1440–1447
6. Slade PG (2021) *The vacuum interrupter: theory, design, and application*, 2nd edn. CRC Press, Boca Raton
7. Li M, Wang X, Li W, Sun S (2015) Magnetic field and vacuum arc of new TMF-AMF contact. In: 3rd international conference on electric power equipment—switching technology (ICEPE-ST). IEEE, Korea, pp 270–273
8. Fan S, Yao X, Zhang J, Chen X, Liu Z, Wang J, Geng Y (2021) Fatigue failure of vacuum interrupter bellows in vacuum-type metal-enclosed gas-insulated switchgear. In: 2021 IEEE international conference on electrical engineering and mechatronics technology (ICEEMT 2021). IEEE, China, pp 254–257
9. Bhat R, Kulkarni SV (2018) Influence of contact plate parameters and eddy currents on residual flux decay in AMF-type vacuum interrupters. *IEEE Trans Power Deliv* 33(6):2812–2821

Partial Discharge Characteristics of Millimeter Metal Particle on a GIS Insulator Surface Under Long-Term Constant Voltage



Yiping Ji, Shaojing Wang, Xing Li, Guliang Zhou, Kai Gao,
and Haoyang Tian

Abstract It is unavoidable for metal particle to be brought in gas-insulated switchgears (GISs) during the production, installation, and operation of the equipment. Currently, the metal particle is considered as one of the critical factors in insulation failures. In this paper, the partial discharge (PD) test of metal particle on the surface of an actual 220-kV insulator is performed under operation electric field of 1100 kV GIS insulators. Then the discharge characteristics of millimeter particle under a long-term constant voltage are investigated. The experiment result indicates that the PDs of metal particles is intermittent under working condition. In the initial period of the experiment, the discharge level can attain 9 pC, and a maximum of 150 discharges occur per second. Subsequently, when the test voltage keeps unchanged, the discharge level and repetition rate of PDs gradually decrease. Finally, the discharge tends to disappear within 60 min after the voltage application, and then suddenly become intense again briefly when $t = 210$ min and $t = 270$ min. The results in this paper gives an important basis for knowing the discharge characteristics of small metal particle well and can help to improve the reliability of GISs.

Keywords Gas-insulated switchgear (GIS) · Long-term constant voltage · Metal particle · Insulator surface · Partial discharge (PD)

Y. Ji · S. Wang · G. Zhou · K. Gao · H. Tian
Electric Power Research Institute of Shanghai Power Grid Corporation, Shanghai, China

X. Li (✉)
Sichuan Energy Internet Research Institute, Tsinghua University, Chengdu, Sichuan, China
e-mail: lx1230716@163.com

© Beijing Paiké Culture Commu. Co., Ltd. 2024
X. Dong and L. Cai (eds.), *The Proceedings of 2023 4th International Symposium on Insulation and Discharge Computation for Power Equipment (IDCOMPU2023)*, Lecture Notes in Electrical Engineering 1100, https://doi.org/10.1007/978-981-99-7393-4_2

1 Introduction

With the development of the power grid, ultra-high voltage (UHV) technique has become an important solution for large capacity and long-distance power transmission. Due to its excellent performance, the gas-insulated switchgears (GISs) are widely used in the power system [1, 2]. All the UHV substations in China have adopted GIS equipment. The reliability of the GIS equipment is crucial, which directly determines the security and stability of the grid. Considerable GIS insulation failures have occurred in field, causing huge economic losses and adverse social impact [3, 4].

During the manufacturing, installation and operation of a GIS, conductive particle may be brought into the equipment, greatly reducing the insulation performance of GIS [5]. At present, the metal particle is still regarded as a critical factor in insulation failures [6]. Hence, it is urgent to investigate the surface discharge characteristics of particles on the insulation surface in a GIS.

Extensive research has been carried out to investigate the insulator surface insulation performance with metal particles in the GIS [7, 8]. However, in previous studies, particles longer than 1 cm are usually used to study the PD characteristics [9, 10], and the research on shorter particles (<1 cm) are mainly performed on a scaled model [11, 12]. Obviously, these are inconsistent with the actual conditions in an actual GIS. The metal particles in an actual GIS equipment are usually millimeter or even micrometer in length [13], and the GIS insulator, especially the ultra-high voltage GIS insulator, is much larger than the metal particles. The previous research focusing on the centimeter particle and scaled models seems to have limited guidance on engineering applications, and the results cannot explain the fault phenomenon in field well.

An experimental platform for PD test is established in this study, which can be employed for long-term continuous PD test for GIS insulators. Then, the PD test for 4-mm long metal particles on a GIS insulation surface is performed under operation electric field of the UHV GIS insulator. The discharge characteristics under a long-term constant voltage are obtained, and the PRPS patterns at different times are investigated. The results of this paper give an important basis for knowing the discharge characteristics of metal particle and is also helpful for improving the reliability of the GIS.

2 Experiment Arrangement

2.1 Experiment Platform

In this paper, an experiment platform is established for long-term PD test, which can realize the PD measurement of multiple insulators. The platform mainly includes an armored test transformer, three test units and a PD detection system as shown

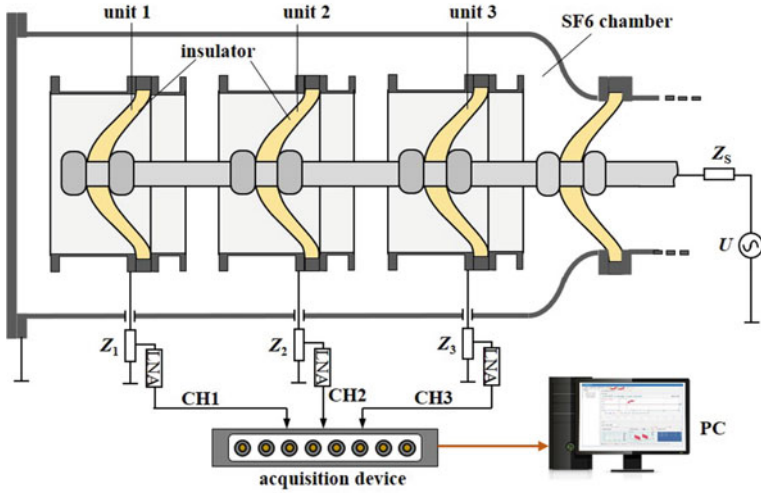


Fig. 1 Experimental platform

in Fig. 1. Each test unit is composed of a 220-kV insulator. The enclosures of the three units are insulated from each other and three detection impedances Z_1 – Z_3 are connected to the enclosure of the three units respectively. The center electrode of the three test GIS insulators is connected to the power supply (U) via the protection resistance (Z_s). During the test, the test units are placed in the chamber filled with SF_6 gas (0.4 MPa).

2.2 PD Detection System

The PD detection system shown in Fig. 1 consists of three detection impedances Z_1 – Z_3 , which are used to measure PDs of the three test insulators respectively. A low-noise amplifier (LNA, bandwidth: 100–500 kHz, gain: 50 dB) is applied to pre-amplify the PD signals. The analog bandwidth and maximum sampling rate of the data acquisition device are 200 MHz and 1 GS/s respectively.

According to the method proposed in our previous study [14], the interference and discharge pulse can be identified reliably. The channels 1–3 represent the outputs of detection impedance Z_1 – Z_3 , respectively. As shown in Fig. 2a, when obvious pulse appears in the channel CH1, and the pulse appearing in channels CH2 and CH3 is very small. In this case, the pulse can be considered to be generated by discharge in unit 1. Similarly, as displayed in Fig. 2b and c, when the amplitude detected by Z_2 and Z_3 is far greater than that of others, the signals can be determined as discharges generated by the insulator in test unit 2 and 3 respectively. As indicated in Fig. 2d, the

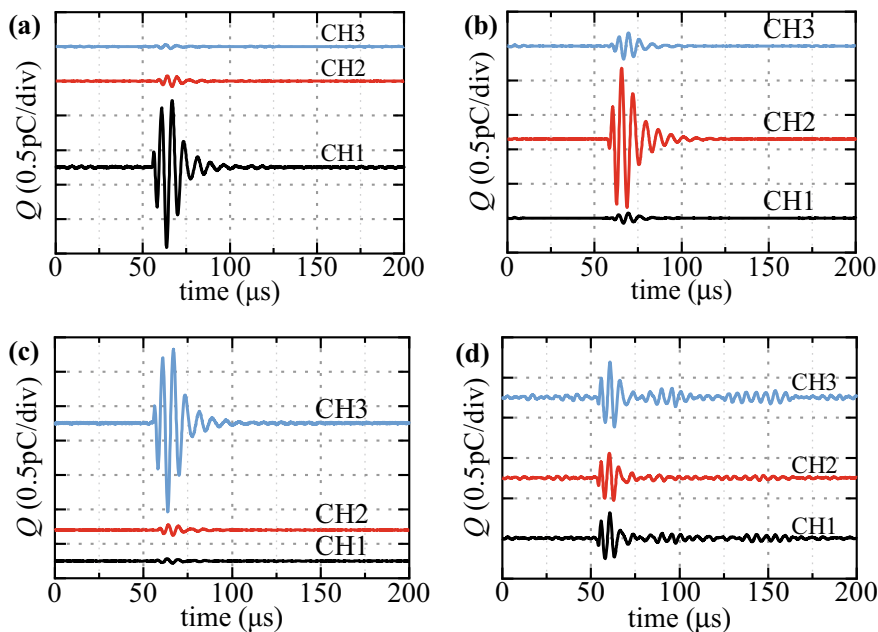


Fig. 2 PD and interference pulse identification: **a** PD occurs in unit 1, **b** PD occurs in unit 2, **c** PD occurs in unit 3, **d** external interference occurs

signal amplitude of CH1–CH3 is close to each other, so the signals can be considered to be caused by interference.

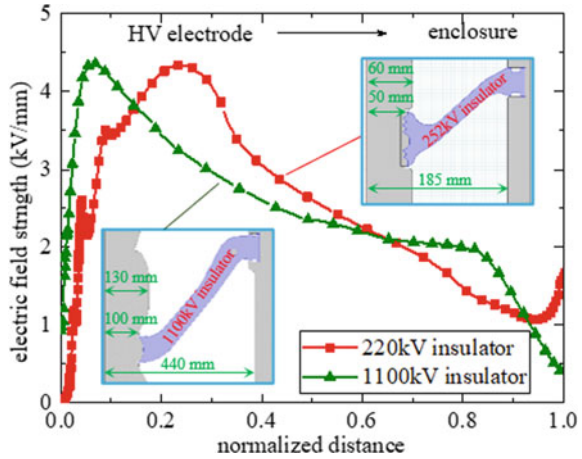
The calibration result based on IEC method [15] indicates that the detection sensitivity of the PD system is 0.2 pC.

2.3 Experimental Model

In order to obtain the real operation condition of a 1100 kV GIS insulator, factors such as electric field intensity and distribution, and surface insulation distance should be considered when selecting the experimental model. Firstly, the surface insulation distance of the test insulator should be far greater than particle length. Secondly, the electric field (including the intensity and distribution) on the test insulator surface should be closed to that on the UHV insulator surface under working conditions ($U_{\text{rms}} = 635$ kV for 1100 kV insulators).

For above considerations, an actual 220-kV insulator is selected as the experimental model in this paper. The surface insulation distance of the 220-kV insulator is approximately 170 mm, which is dozens of times the metal particle length. Moreover, as illustrated in Fig. 3, when the test voltage of 270 kV (effective value) is

Fig. 3 Electric field on the actual 220-kV and 1100-kV GIS insulator surface



applied, the electric field on the test insulator surface is closed to that on a UHV insulator surface under working conditions.

2.4 Defect Setting

In our previous research, it has been found that the critical length of metal particles that cause surface flashover of 1100 kV insulators under operating conditions is approximately 5 mm [16]. Consequently, in this study, cylindrical aluminum metal particles with a diameter of 0.5 mm and a length of 4 mm are selected as defect to investigate long-term discharge characteristics. As shown in Fig. 4, the defect is set at the position where the electric field intensity is the largest on the concave surface (4.5 cm away from the high-voltage electrode).

Fig. 4 Defect setting



2.5 Voltage Application

To obtain the operation condition of a 1100 kV GIS insulator, the test voltage of 270 kV should be applied to a 220-kV insulator. Hence, during the test, the voltage is applied as: 127 kV for 3 min, then 175 kV and 200 kV for 5 min, and 270 kV for 6 h.

3 Experiment Results

3.1 PD Characteristics

When no defects are set, the test voltage of 270 kV is applied for 10 min. The discharge level under this voltage is lower than 0.2 pC (lower than the detection sensitivity).

Then the metal particle is set on the concave surface of all three insulators, and the voltage is applied according to the above-mentioned method. The PD measurement is performed continuously during the experiment. It is found that the PD characteristics of the three insulators are similar. Here is an example of the insulator in test unit 3.

Figure 5 shows the PD characteristics under step voltage. It can be seen that there is no discharge under only 127 kV. Then, the PD occurs under 175 kV. However, the discharges are weak and intermittent. The discharge level is lower than 1 pC, and only approximately 10 discharges appear within a second. Under 200 kV, the discharge level and discharge number increase slightly. Under 270 kV, the discharge level and repetition rate of PDs both increase significantly. The discharge level can exceed 5 pC, and a maximum of 150 discharges occur per second.

Figure 6 shows the PD characteristics under long-term constant voltage. It can be seen that under the voltage of 270 kV, the PDs are intense in the initial period. Subsequently, the discharge level and discharge repetition rate both begin to decrease. The

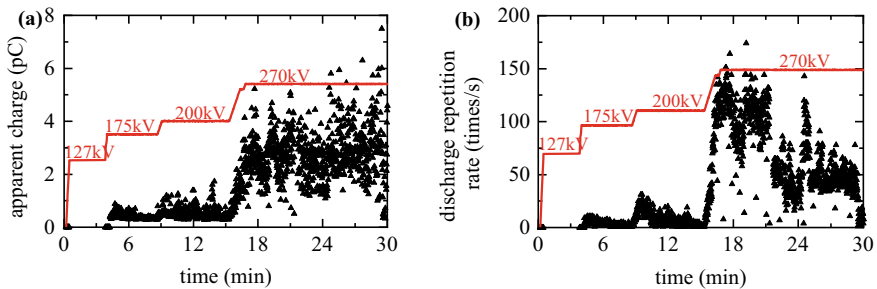


Fig. 5 PD characteristics under step voltage: **a** maximum discharge level per second, **b** discharge number per second

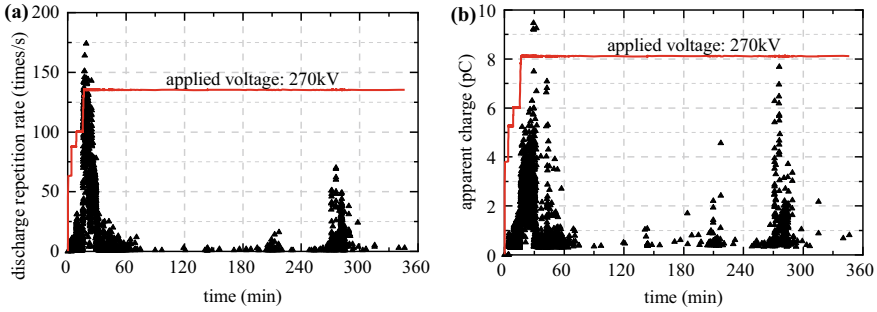


Fig. 6 PD characteristics under long-term constant voltage: **a** discharge number per second, **b** maximum discharge level per second

discharges became weak and intermittent. Approximately 60 min after the voltage is increased to 270 kV, the discharge tends to disappear. Then when $t = 210$ min and $t = 270$ min, the PD becomes intense again temporarily. Especially when $t = 270$ min, more than 70 discharges occur in one second at most, and the maximum discharge level can attain approximately 8 pC.

Figure 7 shows the PRPS patterns at different moments during the test. When the voltage is low, discharges only occur in the negative half cycle, as displayed in Fig. 7a. With the increase of the test voltage, the discharges begin to appear in the positive half cycle. However, the discharge level (Q) is still very low, as illustrated in Fig. 7b and c. When the voltage is maintained at 270 kV, the discharge becomes intense, and the discharges in the negative half cycle is significantly stronger than that in the positive half cycle, as displayed in Fig. 7d. Then under constant voltage, the PDs gradually weakens. After about 30 min, the discharge becomes sporadic, as shown in Fig. 7e and f. When $t = 270$ min, the discharges become severe again, and the discharge in the negative half cycle is stronger than that in the positive half cycle, as shown in Fig. 7h.

The above results show that under long-term constant voltage, the discharge of meal particle on a GIS insulator surface is intermittent, which is consistent with some fault phenomenon in the field. Although the discharge is relatively weak and sporadic, with the development of surface discharge and surface charge accumulation, the insulator flashover will eventually occur [16]. Therefore, in field detection, the sensitivity and anti-interference ability of PD detection method need to be further improved to capture the weak and intermittent discharge pulses. Meanwhile, in online detection and monitoring, those weak and intermittent signals, as well as the signals that disappear and then appear again briefly, need to be given more attention. Moreover, it is also a feasible method to comprehensively monitor and analyses the PD signals in a longer period, which can help to avoid the misjudgment caused by the intermittent discharge.

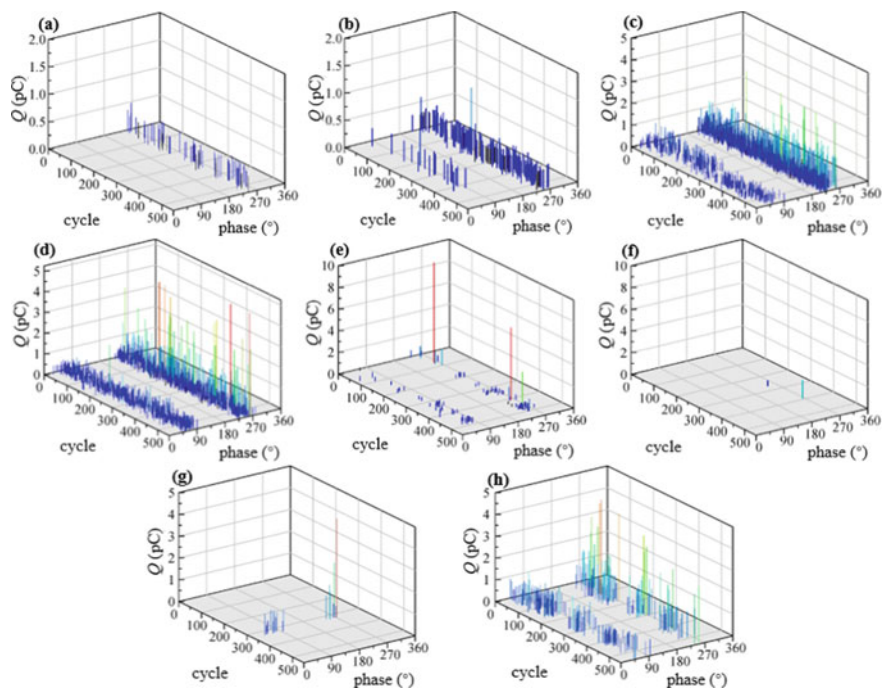


Fig. 7 PRPS patterns of the particles during the test: **a** $t = 5$ min 10 s–5 min 20 s, **b** $t = 10$ min 50 s–11 min 0 s, **c** $t = 16$ min 30 s–16 min 40 s, **d** $t = 20$ min 50 s–21 min 0 s, **e** $t = 31$ min 50 s–32 min 0 s, **f** $t = 60$ min 0 s–60 min 10 s, **g** $t = 231$ min 30 s–231 min 40 s, **h** $t = 270$ min 0 s–270 min 10 s

4 Conclusion

In this study, the PD test of 4-mm long particle on an actual 220-kV basin insulator surface under long-term constant voltage is conducted, and the discharge characteristics are obtained.

- (1) The PD increases with the increase of test voltage. When the test voltage is lower than 200 kV, the discharge level is smaller than 2 pC, and there are less than 30 discharges in one second. Under 270 kV (the operation condition of a UHV GIS insulator), the discharge is enhanced markedly, and the discharge level can exceed 9 pC.
- (2) Under working condition, the discharge is intermittent. When the voltage is kept at 270 kV, the discharge level and repetition rate of PDs firstly increase and then gradually decrease within 60 min. Then, under long-term constant voltage, the PD tends to disappear and suddenly become intense again in a period.

- (3) It is necessary to promote the sensitivity and anti-interference performance of PD detection method to capture and identify the weak and intermittent PDs. Through PD detection and diagnosis during a longer period, the misjudgment and missed judgment can be avoided.

Acknowledgements The authors gratefully acknowledge the support of the Scientific and Technological Project of State Grid Corporation of China (program 52094022004A).

References

1. Okubo H, Beroual A (2011) Recent trend and future perspectives in electrical insulation techniques in relation to sulfur hexafluoride (SF₆) substitutes for high voltage electric power equipment. *IEEE Electr Insul Mag* 27(2):34–42
2. Riechert U, Halaus W (2011) Ultra high-voltage gas-insulated switchgear—a technology milestone. *Eur Trans Electr Power* 22(1):60–82
3. Dreisbusch K, Kranz H, Schnettler A (2008) Determination of a failure probability prognosis based on PD—diagnostics in GIS. *IEEE Trans Dielectric Electr Insul* 15(6):1707–1714
4. Schichler U, Koltunowicz W, Endo F et al (2013) Risk assessment on defects in GIS based on PD diagnostics. *IEEE Trans Dielectric Electr Insul* 20(6):2165–2172
5. Wang H, Xue JY, Chen JH et al (2019) Effects of metal particle material on surface flashover performance of alumina-filled epoxy resin spacers in SF₆/N₂ mixtures under DC voltage. *AIP Adv* 9(8):085212
6. Okabe S, Yamagiwa T, Okubo H (2008) Detection of harmful metallic particles inside gas insulated switchgear using UHF sensor. *IEEE Trans Dielectric Electr Insul* 15(3):701–709
7. Wang J, Hu Q, Chang YN et al (2021) Metal particle contamination in gas-insulated switchgears/gas-insulated transmission lines. *CSEE J Power Energy Syst* 7(5):1011–1025
8. Liang RX, Hu Q, Liu H et al (2022) Research on discharge phenomenon caused by cross-adsorption of linear insulating fibre and metal dust under DC voltage. *High Voltage* 7(2):269–278
9. Zhao CH, Tang ZG, Zhang LG et al (2020) Entire process of surface discharge of GIS disc-spacers under constant AC voltage. *High Voltage* 5(5):591–597
10. Qi B, Li CR, Hao Z et al (2011) Surface discharge initiated by immobilized metallic particles attached to gas insulated substation insulators: process and features. *IEEE Trans Dielectric Electr Insul* 18(3):792–800
11. Wu ZC, Lyu B, Zhang QG et al (2020) Phase-space joint resolved PD characteristics of defects on insulator surface in GIS. *IEEE Trans Dielectric Electr Insul* 27(1):156–163
12. Budiman FN, Khan Y, Malik NH et al (2013) Utilization of artificial neural network for the estimation of size and position of metallic particle adhering to spacer in GIS. *IEEE Trans Dielectric Electr Insul* 20(6):2143–2151
13. You H, Zhang QG, Guo C et al (2017) Motion and discharge characteristics of metal particles existing in GIS under DC voltage. *IEEE Trans Dielectric Electr Insul* 24(2):876–885
14. Li X, Liu WD, Xu Y et al (2022) Discharge characteristics and detectability of metal particles on the spacer surface in gas-insulated switchgears. *IEEE Trans Power Delivery* 37(1):187–196
15. High-voltage test techniques—partial discharge measurements, 60270, Standard of International Electro-technical Commission (IEC) (2001)
16. Li X, Liu WD, Xu Y et al (2020) Surface charge accumulation and pre-flashover characteristics induced by metal particles on the insulator surfaces of 1100 kV GILs under AC voltage. *High Voltage* 5(2):134–142

Ultrasound-Based Pressure Pipe Internal Water Ingress Defect Detection Technology



Wenhui Li, Haibo Li, Yian Fang, Huan Liu, Junzhe Liang, Fenggeng Jiang, Guang Liu, and Di Rao

Abstract Long-term operation in the harsh environment of the tension clamp aluminum tube unpressured area, easy to produce water ingress defects. Based on the reflection characteristics of ultrasound, the optimal detection position, the best detection frequency and the echo characteristics of the internal water inlet in the unpressurized area were studied, and a method for ultrasonic detection of the internal water ingress of the tension-resistant clamp was proposed. The results show that observing the reception time of the primary echo at the water–air interface can determine whether water ingress occurs in the unpressurized area and what the inlet depth is. This method provides a new idea for detecting water ingress inside the tension clamp.

Keywords Transmission lines · Tension clamp · Ultrasonic · Water ingress defects

1 Introduction

Tension clamp is one of the important fittings of transmission lines, which is used to fix the conductor or lightning protection wire on the tensile insulator string of the non-linear pole tower to play the role of anchoring and conduction [1, 2]. At present, the use of tensile clamps and connecting pipe crimping is the only means to realize long-distance uninterrupted transmission of ultra-high voltage transmission lines [3]. With the rapid development of the power grid, the voltage level is getting higher and higher, and the performance defects of tensile clamps have become an important factor

W. Li · Y. Fang · H. Liu · J. Liang · G. Liu
State Grid Zhejiang Electric Power Co., Ltd., Taizhou Power Supply Company, Zhejiang 318000, China

H. Li · D. Rao (✉)
Taizhou Hongchuang Power Group Co., Ltd., Technology Branch 17, Zhejiang 318000, China
e-mail: 978516547@qq.com

F. Jiang
State Grid Zhejiang Xinxing Technology Co., Ltd, Zhejiang 318000, China

© Beijing Paiké Culture Commu. Co., Ltd. 2024
X. Dong and L. Cai (eds.), *The Proceedings of 2023 4th International Symposium on Insulation and Discharge Computation for Power Equipment (IDCOMPU2023)*, Lecture Notes in Electrical Engineering 1100, https://doi.org/10.1007/978-981-99-7393-4_3

affecting the safe and stable operation of the power grid. On April 24, 2013, when the operation inspection branch of Anhui Power Transmission and Transformation Engineering Company treated the 1419#/1177# pole tower of the ± 500 kV Ge Nan and Lin Feng Yangtze River Great Cross Vietnam Shore Anchor Tower 1419#/1177# Anchor Tower, it was found that the aluminum pipe (unpressed area) of the wire was cracked or expanded. A total of 5 tensile clamp aluminum tubes were found to have cracking in the large span section, and the tensile clamp aluminum tubes without cracking had different degrees of expansion. In November 2015, the maintenance branch of State Grid Zhejiang Electric Power Company carried out a comprehensive maintenance of the 500 kV Fengyan 5832 line, and during the maintenance process, it was found that there were expansion cracks in the unpressed area of the 1# and 4# sub-conductor connection pipes at the third spacer rod on the small side of the 24# tower, and there were red rust spots, and there were expansion bulging phenomena in the unpressed areas of the 2# and 3# sub-conductor connection pipes. At 17:00 on July 7, 2017, the Xing'an Line Pole I failed, and it was found through UAV special inspection that the tension clamp of the upper right sub-conductor of the large side of the No. 1351 Pole I line was broken, and the discharged sub-conductor to the ground caused the line to trip, and at the same time caused damage to 5 wire spacer rods and 3 jumper spacer bars. The above defects are caused by the small gap between the wire strands after the wire crimping, forming a water seepage channel, long-term operation, rainwater along the water seepage channel to the line clamp cavity (unpressed area) water seepage, due to the steel anchor end is dense, the stagnant water can not flow out, resulting in the presence of water in the line clamp cavity, the temperature drops to the freezing point, the stagnant water freezes and expands, resulting in longitudinal cracks or bulges in the wire clamp aluminum pipe at the pressure pipe cavity. When galvanized steel wire electrochemical corrosion (rust) occurs in the pressure pipe cavity of stagnant water, it will gradually lose its mechanical properties, and eventually lead to the fracture of the steel core and aluminum tube, and the rust water will flow out [4–10].

At present, the research on the internal water inlet defects of the pressure pipe is mainly in the crimping area of the conductor, but the quantitative study of the internal water inlet in the unpressurized area of the pressure pipe by ultrasonic detection has not yet been carried out.

Therefore, in order to promote the application of ultrasonic nondestructive testing in the qualitative evaluation of the internal water inlet of the pressure pipe, combined with the actual detection needs, this paper establishes a two-dimensional model of the unpressed area of the aluminum tube for the pressure pipe of NY-630/45 model with the help of finite element simulation method, obtains the time domain echo signals of different detection positions, different ultrasonic detection frequencies and different water intake, analyzes the influence of different detection positions, ultrasonic frequencies and water inlet on the ultrasonic echo, and provides a new idea for the quantitative detection of the internal water inlet of the pressure pipe.

2 Model Building

2.1 Basic Principle

Ultrasonic pulse reflection at the monolayer interface, as shown in Fig. 1. When the incident sound wave is incident vertically from medium 1 to a plane interface composed of medium 1 and medium 2, reflection and transmission phenomena will occur, that is, part of the sound energy is reflected to form a reflected wave, which is conducted in the medium in the opposite direction to the incident wave; There is also a part of the sound energy that propagates through the interface in the same direction as the incident wave, forming a transmission wave. In the figure, S1 is the incident wave, S2 is the reflected wave, S3 is the transmitted wave, Z1 is the acoustic impedance of Dielectric 1, and Z2 is the acoustic impedance of Dielectric 2.

According to the propagation law of plane waves, the following reflection and transmission relationships can be derived for ideal elastic media. Sound pressure reflectivity R_p represents the ratio of reflected wave sound pressure to incident wave sound pressure, sound pressure transmittance T_p represents the ratio of transmitted wave sound pressure to incident wave sound pressure, and its formula is:

$$R_p = \frac{Z_2 - Z_1}{Z_2 + Z_1} \tag{1}$$

$$T_p = \frac{2Z_2}{Z_2 + Z_1} \tag{2}$$

Considering the acoustic impedance of aluminum tube $Z_{Al} = 16.7 \text{ Mkgm}^{-2}\text{s}^{-1}$, the sound impedance of water $Z_{Water} = 1.5 \text{ Mkgm}^{-2}\text{s}^{-1}$, the acoustic impedance of air $Z_{Air} = 0.0004 \text{ Mkgm}^{-2}\text{s}^{-1}$, calculated by formula (1), the sound pressure reflectivity of ultrasound in the aluminum tube-air interface and the water-air interface is 99%, and the sound pressure reflectivity in the aluminum tube-water interface is 83%. Therefore, in theory, the amplitude law at the aluminum tube-defect interface should be air > water.

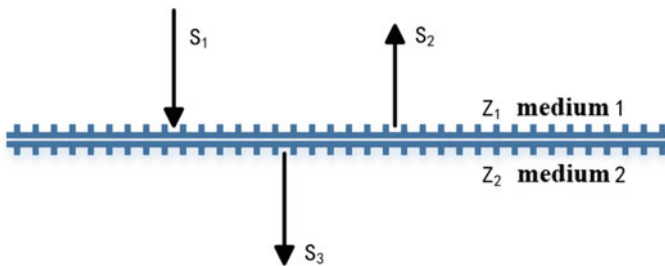


Fig. 1 Reflection and transmission of sound waves when they are incident perpendicular to a planar interface

Fig. 2 NY-630/45 crimp tube



2.2 Model Physics

Figure 2 is a well-crimped NY-630/45 crimp tube, Fig. 3 is a two-dimensional section inside the unpressed area of the compression pipe, the unpressed area is composed of a cavity aluminum tube immediately adjacent to the back end of the crimping area, and the detection position of the ultrasonic probe is set at the lowest point of the outer wall of the aluminum tube, followed by a counterclockwise deflection of 10° against the outer wall of the aluminum tube to set the detection position 2, and so on for a total of 5 ultrasonic probes. Add water to the cavity to ensure that the horizontal plane is horizontal, the probe is located at the detection position 1 The direction of ultrasonic transmission is perpendicular to the horizontal plane, and the depth value of the water inlet set below refers to the vertical distance from the horizontal plane to the lowest point of the inner wall of the aluminum tube.

2.3 Parameter Setting and Loading

The outer diameter of the hollow aluminum tube is set to 60 mm, the inner diameter is set to 35.5 mm, and the outer wall of the aluminum tube is set with a low reflection boundary so that the model boundary does not reflect ultrasound. The signal receiving point is set 0.1 mm above the ultrasonic excitation source. The mesh of the simulation model is divided by $1/8$ of the wavelength of the material, and the total simulation time is $60 \mu\text{s}$. The internal material parameters of the unpressed area are shown in Table 1, and the parameter settings of ultrasonic array elements are shown in Table 2.

3 Detect Echo Amplitude Characteristics at Different Locations

The unpressed area of the pressure pipe is ultrasonic detected, the probe is placed from position 1 (deflect 0°) to position 5 (deflect 40°), the deflection angle interval between each adjacent position is 10° , the primary echo time domain curve of the water–air

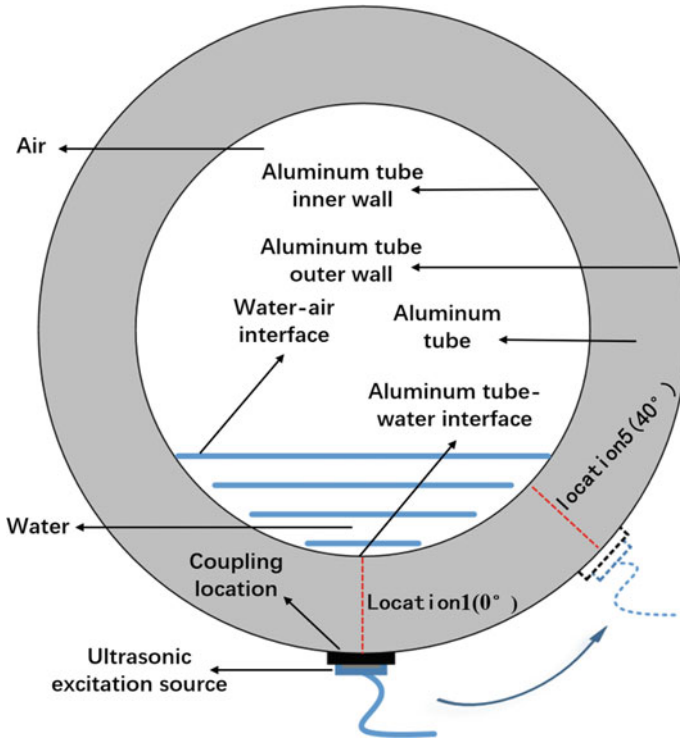


Fig. 3 Two-dimensional cross-section of water inlet inside the unpressed zone

Table 1 Material parameters

Medium	Density	Velocity/ ms^{-1}	Acoustic impedance/ $\text{Mkgm}^{-2}\text{s}^{-1}$
Al	2700	6200	16.7
Air	1.29	346	0.00045
Water	1000	1500	1.5

Table 2 Parameter settings for array elements

Parameter	Numerical
Number of elements	1
Element width/mm	6
Center frequency/MHz	3.5

interface is compared with the echo time domain curve under the condition of no water ingress, the change law of ultrasonic echo under different detection positions is studied, and the echo amplitude is normalized to obtain echo time domain curves at different detection positions, as shown in Fig. 4. The detection position in the

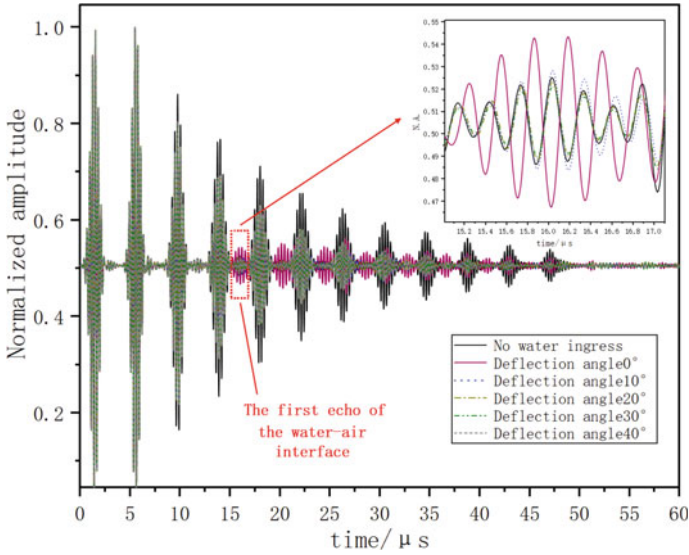


Fig. 4 Time domain curves of echoes at different detection locations

absence of water ingress is set at position 1; The water ingress depth in case of water ingress is set to 8 mm and detected in 5 different positions. According to the ratio of the size of the aluminum tube to the sound velocity of aluminum and water, the primary ultrasonic echo of the water–air interface appears at 15.2–17.0 μs .

Table 3 plots the maximum values of each echo in the time period during which the primary echo at the water–air interface occurs in Fig. 4. At position 1 and position 2, the ultrasonic echo amplitude received under water ingress is higher than the ultrasonic echo amplitude in the case of no water ingress, and the influent echo amplitude at position 1 is higher than that at position 2, and the echo amplitude received by the remaining three detection ultrasonic positions under water ingress is lower than the echo amplitude received in air condition. Because the ultrasonic wave propagation direction emitted at position 1 is vertical liquid level, when the ultrasonic wave reaches the liquid surface, almost no refractive waves are generated, so most of the energy is reflected back to the probe is received, when the detection position of the probe is moved, the ultrasonic wave propagation direction and the liquid level does not constitute a vertical relationship, when the ultrasonic wave reaches the liquid surface, there will be part of the sound wave refraction, resulting in the reflected wave energy received by the probe becomes smaller, reflected in the echo time domain curve is the sound pressure amplitude decreases. When the water ingress situation once occurs, the inner wall of the aluminum tube–air interface immediately into the inner wall of the aluminum tube–water interface, according to the transmitted wave sound pressure formula, ultrasonic in the inner wall of the aluminum tube–water interface transmittance is greater than the inner wall of the aluminum tube–air interface transmittance, in the water–air interface of a echo time

Table 3 Echo peaks at different detection locations

Different locations	Ultrasonic echo amplitude/MPa
(Not flooded) position 1	0.5252
(Depth of water intake: 8 mm) position 1	0.5434
(Depth of water intake: 8 mm) position 2	0.5281
(Depth of water intake: 8 mm) position 3	0.5237
(Depth of water intake: 8 mm) position 4	0.5216
(Depth of water intake: 8 mm) position 5	0.5226

period, reflected in the echo time domain curve is: the sound pressure amplitude in the case of water inlet is higher than the sound pressure amplitude in the case of air, the echo time domain curve obtained at position 1 and position 2 is more in line with the theory.

4 Optimal Detection of Ultrasonic Frequencies

4.1 Effect of Ultrasonic Frequency on Echo Morphology

In order to study the optimal ultrasonic frequency for detecting water ingress in the unpressurized area of the tension-resistant clamp, six different ultrasonic frequencies were set, the detection position was fixed at position 1, and the two situations of no ingress and water ingress depth of 5 mm were detected respectively, and the echo amplitude was normalized, and Fig. 5 showed the echo time domain curve of detecting the two inlet water ingress conditions at different ultrasonic detection frequencies. When the ultrasonic wave propagates to the interface of the inner wall of the aluminum tube, when the water ingress occurs, the transmittance of the ultrasonic wave will increase, that is, compared with the no water ingress, the ultrasonic energy entering the cavity inside the aluminum tube is enhanced, and the time domain echo curve is that the amplitude of the sound pressure of the sound wave will increase.

From Fig. 5, it is clear that as the ultrasonic detection frequency value increases, the period of a single waveform will be shortened, and the larger the time interval between primary echoes and multiple echoes at different interfaces, the more obvious the waveform of a single echo will be on the entire time domain echo plot, but the lower the amplitude of the primary echo at the water–air interface. When the ultrasonic frequency is increased to 5 MHz, the primary echo amplitude of the water–air interface under water ingress is lower than the echo amplitude when there is no water ingress.

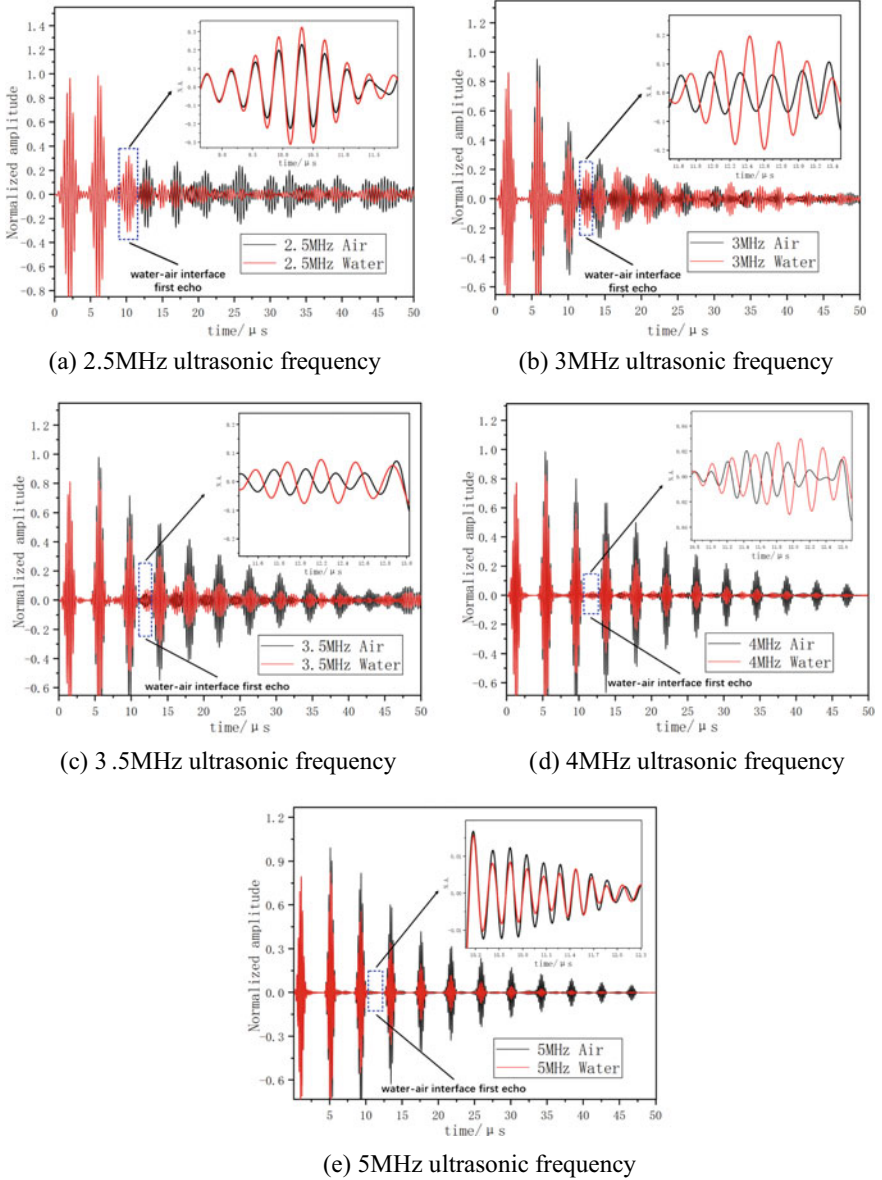


Fig. 5 Time domain curves for echoes at different UT frequencies

Table 4 Echo peaks at different frequencies

Frequency/MHz	The echo amplitude of ultrasound/ MPa		Increase the amount/%
	Water	Air	
2.5	0.3244	0.2291	41.6
3	0.1978	0.107	84.86
3.5	0.077	0.0428	79.91
4	0.03	0.0204	47.06
5	0.0085	0.0124	-31.5

4.2 The Effect of Ultrasonic Frequency on Echo Amplitude

From the time domain curves of different detection frequency echoes in Fig. 5, it can be seen that the ultrasonic echo amplitude is different in both cases in the primary echo time range of the water–air interface at different frequencies. In order to study the optimal detection frequency under the condition of water inlet depth of 5 mm, five groups of ultrasonic frequencies, 2.5 MHz, 3 MHz, 3.5 MHz, 4 MHz and 5 MHz, were selected, and the maximum value of each echo amplitude in the primary echo time range of the water–air interface was extracted for the influent and the ingress water ingress, and the increase of the echo amplitude in the ingress situation compared with the echo amplitude in the air case was calculated Table 4.

From Table 4, it can be seen that the echo amplitude increase at the two ultrasonic frequencies of 3 MHz and 3.5 MHz is similar, and both are higher than the echo amplitude increases at the remaining three ultrasonic frequencies, among which the echo amplitude increase at the 5 MHz frequency is negative.

4.3 Selection of the Optimal Ultrasonic Testing Frequency

By observing the morphology of each echo in the time domain curve of each group of echoes under five sets of frequencies and the degree of interval between each echo, It can be seen that the echoes at the two sets of ultrasonic frequencies of 3.5 MHz and 4 MHz are easier to observe the waveform of the primary echo of the water–air interface.

By comparing the echo peak increase at different frequencies in Table 4, it can be seen that the difference between the echo amplitude of the water inlet and the echo amplitude of the air condition in the primary echo time range of the water–air interface is relatively large under the two sets of frequencies of 3 MHz and 3.5 MHz, and it can better analyze whether water ingress occurs in the uncrimped area through waveforms.

Based on the above two situations, it is considered that 3.5 MHz is considered to be the appropriate ultrasonic detection frequency.

5 Simulation Study of Different Inlet Depths

5.1 The Depth of the Water Influent Affects the Echo Time

In order to study the influence of different inlet depths on the ultrasonic test results, five groups of inlet depth values, 5 mm, 11 mm, 17 mm, 23 mm, and 29 mm, were selected, and the 3.5 MHz ultrasonic frequency was selected at the detection position 1, and the amplitude of ultrasonic sound pressure obtained by the final detection was normalized to obtain the ultrasonic echo time domain curve at different inlet depths as shown in Fig. 6.

In Fig. 6, the first ultrasonic echo curve of ultrasonic waves at the water–air interface under the five groups of inlet depths is marked, because the propagation speed of ultrasonic waves in the medium is unchanged, so the time it takes for sound waves to propagate at the same distance is unchanged, and it can be seen in Fig. 6 that when the interval values of the five groups of inlet depths are 6 mm, the primary echo time interval of the water–air interface obtained at different inlet depths is the same.

By observing the time point at which the primary echo of the water–air interface appears, the depth value of the water influent in the unpressurized area can be judged.

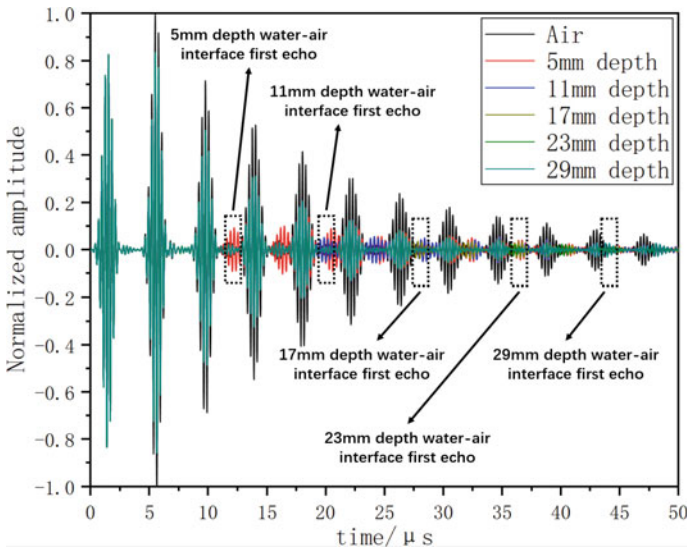
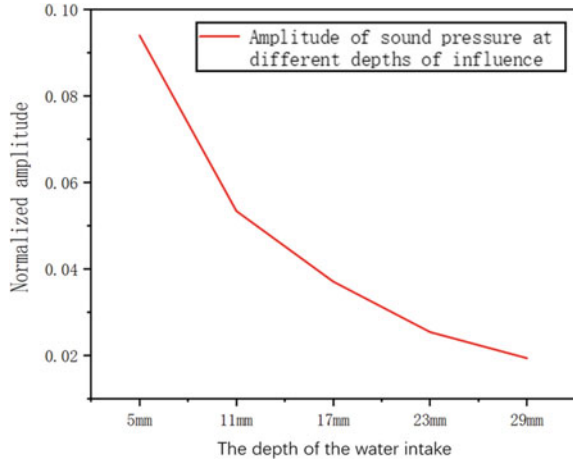


Fig. 6 Ultrasonic echo time domain curves at different inlet depths

Fig. 7 Ultrasonic echo time domain curves at different water inlet depths



5.2 The Effect of the Depth of the Incoming Water on the Echo Amplitude

The maximum value of the primary echo of the water–air interface at each inlet depth in Fig. 6 was extracted and the maximum value of the primary echo of the water–air interface at different water inlet depths in Fig. 7 was drawn. As can be seen from Fig. 7, as the amount of water intake increases, the lower the maximum value of the primary echo amplitude of the water–air interface, the overall downward trend, because with the increase of water intake, the distance of ultrasonic propagation in the water becomes longer, the more energy is lost, the energy reaching the water–air interface is also reduced, and finally the lower the energy received by the ultrasonic instrument.

6 Conclusion

- (1) Placing the ultrasonic probe in the detection position 1, that is, the lowest point of the outer wall of the aluminum tube, is conducive to detecting internal water ingress defects.
- (2) For the NY-630/45 model tensile clamp, the ultrasonic detection frequency of 3.5 MHz is conducive to obtaining an ultrasonic echo curve to observe whether water ingress occurs in the unpressed area.
- (3) The time point of the first echo of the water–air interface in the ultrasonic echo time domain curve can be observed, and the depth value of the water inlet in the unpressurized area can be quantitatively judged.

Acknowledgements This research was partially Supported by Open Fund of State Key Laboratory of Power Grid Environmental Protection (No. GYW5120221415).

References

1. Jie D (2010) Power fittings manual, 3 edn. China Electric Power Press, Beijing, 150–194 (in Chinese)
2. Hu J, Xie Y, Liu C et al (2013) Analysis of typical defects of tensile clamps in transmission lines. *North China Electr Power Technol* 4:34–37 (in Chinese)
3. Zhu D, Li B, Sun B (2016) Expansion cracking analysis of unpressurized area of 500 kV transmission line conductor connection. *Sci Technol Innov Appl* 9:166–167 (in Chinese)
4. Zhou L, Sun T, Gu J (2020) Evaluation of crimping performance of tension-resistant wire clamps for large-section conductors. *Chin J Electr Eng* 40(S1):149–154 (in Chinese)
5. Yan T, Li X, Wang YH et al (2021) Analysis of typical faults in overhead line tension-resistant wire clips. *Electr Eng Technol* 01:32–35 (in Chinese)
6. Wang D, Miu C, Fang Z (2021) Statistics of tensile clamp defects of three-span transmission line based on radiographic inspection. *Nondestructive Testing* 43(7):71–73 (in Chinese)
7. Kang T, Wang B et al (2022) Review of deep learning detection methods for transmission line fittings and their defects. *Power Inf Commun Technol* 20(11):1–12 (in Chinese)
8. Zhang W, Liu Y, Li S, Tang J (2022) Analysis on the crimping quality of overhead transmission line conductors considering equivalent cross-sectional stiffness. *AIP Adv* 12(105321):1–9
9. Mozer J, Wood W, Hribar J (1981) Broken wire tests on a model transmission line system. *IEEE Trans Power Appar Syst PAS* 100(3):938–947
10. McGill PB, Ramey GE (1986) Effect of suspension clamp geometry on transmission line fatigue. *J Energy Eng* 112(3):168–184

Optical Storage Emergency Power Supply Technology for Railway Locomotive



Hao Yang, Guosheng Huang, Kaixiang Ma, Meng Cui, and Shuo Zhang

Abstract Railway locomotive is the core equipment of the railway transportation system, which undertakes the transportation function of the whole railway system, and is a veritable core device of transportation capacity. It plays an important role in the whole transportation system. The safety and reliability of railway locomotives is very important. It is necessary to add emergency devices in the power supply system other than the main power supply to ensure the power supply at emergency time. In this paper, the photovoltaic array is used as the main power supply, and the Boost + SIV circuit topology is connected at the back. The Boost and SIV are the intermediate DC bus voltage stabilizing link. The link is connected in parallel with a battery pack, which can realize emergency power supply when the light intensity is weak. The system adds a voltage sensor to achieve stable voltage output by control method, and adds a photosensitive sensor to achieve different working conditions of the power system under different light intensity, The experimental prototype is designed and verified.

Keywords Emergency power supply · Inversion · Battery · Railway locomotive

H. Yang · M. Cui

China Railway 14th Bureau Group, The Electrification Engineering Co., Ltd., Beijing 100043, China

G. Huang · S. Zhang (✉)

Beijing China Railway Construction Electrification Design and Research Institute Co., Ltd, Beijing 100043, China

e-mail: zhangshuo.dqh@crcc.cn

K. Ma

Jinan Rail Transit Group Co., Ltd., Jinan 250101, Shandong, China

© Beijing Paiké Culture Commu. Co., Ltd. 2024

X. Dong and L. Cai (eds.), *The Proceedings of 2023 4th International Symposium on Insulation and Discharge Computation for Power Equipment (IDCOMPU2023)*, Lecture Notes in Electrical Engineering 1100, https://doi.org/10.1007/978-981-99-7393-4_4

1 Introduction

The railway locomotive power supply system plays a key role in the safe and reliable operation of the whole railway locomotive, and with the rapid development of China's railway industry, such importance has gradually increased [1]. The reliability of the power supply system is also a very important indicator to measure the railway power distribution, which is related to the final safety and economic benefits of the railway system [2]. Generally, the locomotive is powered by pantograph. In case of failure, the system can continue to operate reliably [3]. The quality of power supply is related to the safety of equipment, which is a major indicator that needs to be paid attention to. Therefore, how to improve the high-quality electric energy for the communication, lighting and other equipment in the locomotive and how to design a stable and reliable power supply system have attracted more and more attention.

2 Emergency Power Supply Device System Design

The circuit topology of the power supply system adopts the composition structure of the former Boost + the latter SIV [4]. The front boost is responsible for stabilizing the output voltage of the photovoltaic array, so as to stabilize the unstable voltage of the photovoltaic array and adapt to the wide range of voltage input of the system. The circuit topology is shown in Fig. 1. The front boost does not use an isolation structure, that is, does not add an isolation transformer [5]. The advantage of this is to reduce the loss of magnetic components and ensure the working efficiency of the system. The rear stage SIV is responsible for converting the DC output of the front stage Boost into three-phase AC, and incorporates a large-capacity battery in the middle DC link. The battery is designed to offset the impact of night light through the role of energy storage, thus achieving stable power supply to the load, so that the system can operate continuously, efficiently and stably.

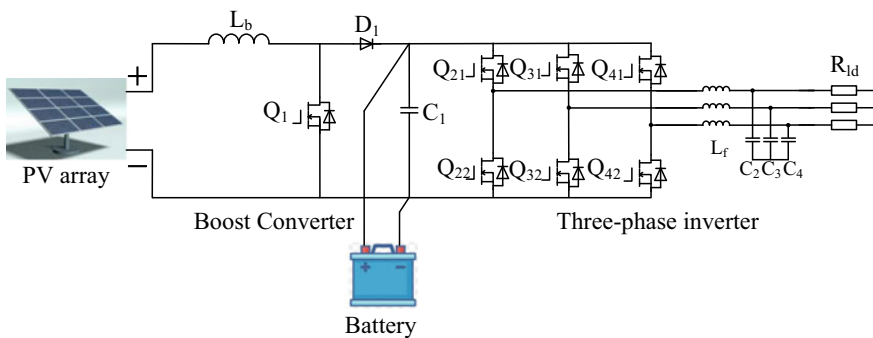


Fig. 1 Main circuit structure of power supply system

The power supply system controller selects DSP high-performance processor, which can enable accurate analog data acquisition and data conversion. In the control part, the double closed-loop algorithm of voltage outer loop + current inner loop is adopted to achieve output voltage stability and provide high-quality power to the equipment. In addition, voltage sensor and photosensitive sensor are added to the hardware, because the output voltage of the voltage array will vary with the light intensity, The voltage sensor is used to monitor the change of voltage, transmit the signal to the DSP controller, and then the DSP controller controls the voltage gain of BOOST converter to realize the stable voltage output of BOOST converter; When the light intensity is lower than a certain value, the photosensitive sensor transmits the signal to the controller to switch the power supply of the photovoltaic array to the battery pack.

3 Booster Circuit Design

Railway locomotives often use three-phase AC power supply for power supply, and a circuit solution of Boost + SIV is proposed. The voltage range of photovoltaic system in this paper is usually below 600 V, and the voltage is raised to a stable 600 V DC through boost converter. Due to the limitation of single battery voltage, multiple single batteries need to be connected in series and parallel to obtain DC voltage of higher voltage level. Connected to the input side of three-phase inverter circuit, the scheme is suitable for railway locomotive system with relatively compact space and high safety requirements.

Figure 2 shows the front BOOST circuit [6]. The main function of the circuit is to raise the low input voltage V_i of the photovoltaic array to the input voltage V_{C1} that meets the requirements of the inverter. In the figure, L_b is the main switch, L_b is the boost inductor, $D1$ is the diode, $C1$ is the capacitance, R_s is the secondary equivalent load, T_{sb} is the switching cycle of the switch $Q1$, and D is the duty cycle of the switch. Working principle under ideal condition: when $0 < t < D_y T$, the switch is on, the diode is off, the current i_L flows through the inductor, the inductance current increases linearly, and the energy is stored in the inductor in the form of magnetic energy; When $D_y T < t < T$, the switch tube is disconnected, the diode is on, and the energy in the inductor is transferred to the capacitor and load through the diode. Under ideal conditions, the steady-state voltage transfer equation of BOOST circuit is $V_0 = V_i / (1 - D_y)$. Because the duty cycle $0 < D_y < 1$, the output voltage is greater than the input voltage, so the purpose of boosting is realized.

Boost link adopts double closed-loop control mode of voltage outer loop and current inner loop to obtain stable DC voltage [7]. The control block diagram is shown in Fig. 3. The control principle of the control system is as follows: the output voltage reference value is compared with the actual value to obtain the output voltage difference, which is controlled by PI regulator. The output value is given to the current loop input and compared with the output current value. The difference value is adjusted by PI regulator. The output value is the duty cycle of the boost switch D_y ,

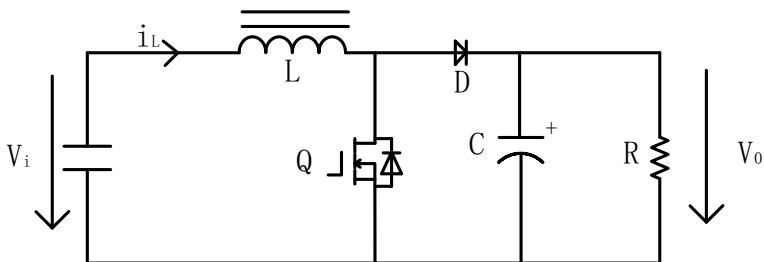


Fig. 2 BOOST circuit

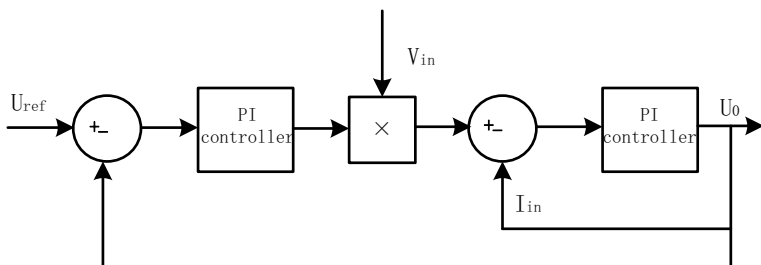


Fig. 3 Voltage and current double closed-loop control block diagram

and the stable output voltage U_0 is obtained. In addition, the reference value U_{ref} is converted according to the output voltage. The output voltage of the circuit can be flexibly changed by changing the reference value U_{ref} .

The pulsation of boost inductor current is

$$\Delta I_{Lb_L} = D_y \left(\frac{1}{2} - D_y \right) \frac{V_{cb} T_{sb}}{L_b} \quad (1)$$

Generally, the pulsating current of the step-up inductor shall not exceed 20% of the average current, i.e.

$$\Delta I_{Lb} \leq 0.2 \frac{P_o}{V_i} = 0.2 \frac{P_o}{2(1 - D_y) V_{cb}} \quad (2)$$

The calculation formula of boost inductance is as follows

$$L_b \geq \frac{D_y (2D_y^2 - 3D_y + 1) T_{sb}^2 V_{cb}^2}{0.2 P_o} \quad (3)$$

The size of filter capacitance is related to duty cycle, switching period, output power and voltage pulse momentum. The calculation formula of filter capacitance is as follows.

Voltage pulse momentum of filter capacitor

$$\Delta V_{cb} = \frac{D_y T_{sb} P_o}{2C_1 V_{cb}} \quad (4)$$

It is generally required that the capacitance ripple voltage pulse momentum shall not exceed 1% of the average value V_{cb} , i.e.

$$\frac{\Delta V_{c1}}{V_{c1}} = \frac{D_y T_{sb} P_o}{2C_1 V_{c1}^2} \leq 0.01 \quad (5)$$

where, D_y is the duty cycle, C_1 is the filter capacitance, P_o is the output power, T_{sb} is the switching cycle, and V_{c1} is the BOOST output voltage.

4 Inverter Circuit Design

4.1 Principle of Three-Phase Inverter Circuit

Three-phase bridge inverter circuit is used in the inverter part to invert the DC power after BOOST, and then transmit it to the load for power supply after AC filter [8]. The circuit structure is shown in Fig. 4. U_{DC} is the voltage of the intermediate DC bus, that is, the output voltage of the front step boost link. The main circuit is composed of six main power switches from S1 to S6, which form the upper and lower three bridge arms. The midpoint of each bridge arm is connected to the power grid through the inductors L1, L2, L3 respectively, and plays the role of filtering. C_{DC} is the DC bus support capacitor, which plays the role of energy storage, and also serves as the output filter capacitor of the front BOOST circuit. The control part adopts advanced DSP digital control. The PWM control signal sent by DSP drives the opening and closing of six switches to control the mid-point voltage of the bridge arm. To ensure the normal operation of the circuit, the DC side voltage shall be higher than the peak value of the inverter output AC voltage.

The emergency power supply system studied in this paper adopts space vector pulse width modulation (SVPWM) technology [9]. This technology can make the output current waveform closer to the ideal sine wave by controlling six switches to generate pulse width modulation wave [10]. SVPWM is slightly different from the traditional SPWM. It starts from the overall effect of the output voltage, and hopes to output the magnetic linkage track drawn by the ideal circle. SVPWM technology can achieve a closer selection of rotating magnetic field, and greatly improve the utilization of DC bus voltage, and greatly reduce the difficulty of digital realization [11]. The basic principle of SVPWM is as follows: the combined voltage is equivalent by superposition of voltage vectors in a cycle.

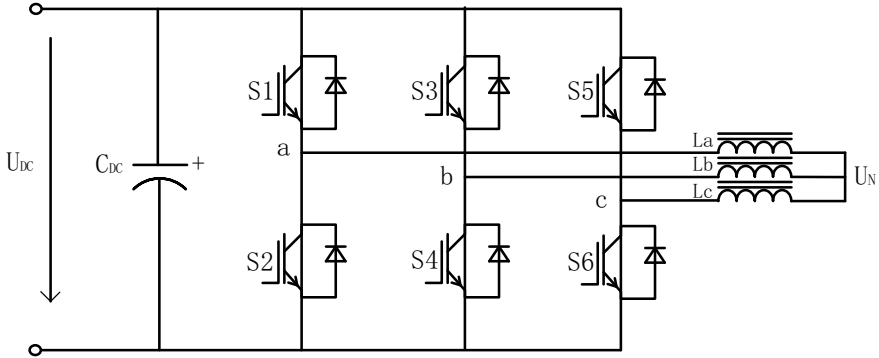


Fig. 4 Three-phase bridge inverter circuit

The intermediate bus voltage is used as the input of the voltage outer loop, and its difference is used as the input of the current inner loop through the PI regulator. The current inner loop is controlled by the deadbeat current theory, and the parameters are relatively easy to set and adjust. The main function of the outer loop voltage control is to make the voltage U_{DC} at both ends of the DC bus support capacitor C_{DC} constant; The main function of the inner loop current control is to make the output current change in a sinusoidal manner to ensure the output power quality.

4.2 Voltage Vector of Three-Phase Inverter Circuit

The DC bus voltage is U_{C1} , and the three-phase voltage output by the inverter is U_a, U_b, U_c ; The switch tubes of three-phase bridge arm are S_A, S_B and S_C . Now we specify that S_i ($i = A, B, C$) = 1 means the upper arm switch of the phase is on, and S_i ($i = A, B, C$) = 0 means the upper arm switch of the phase is off, and the upper and lower arm switch states are complementary. Therefore, there are 8 switch combinations in this circuit.

$$s_i = \begin{cases} 1 & \text{Upper bridge arm conduction Output high level} \\ 0 & \text{Lower bridge arm conduction Output low level} \end{cases}$$

There are eight switch states: 100, 110, 010, 010, 011, 011, 000. Where V0 (000) V7 (111) is the zero vector with modulus 0 (that is, the upper bridge arm is fully connected and the lower bridge arm is fully connected, and the inverter does not output voltage at this time).

The relationship between line voltage of three-phase inverter and switching function is obtained:

Table 1 Voltage vector table of three-phase inverter

S_A	S_B	S_C	U_A	U_B	U_C	U_{AB}	U_{BC}	U_{CA}
0	0	0	0	0	0	0	0	0
0	0	1	$-U_d/3$	$-U_d/3$	$2U_d/3$	0	$-U_d$	U_d
0	1	0	$-U_d/3$	$2U_d/3$	$-U_d/3$	$-U_d$	U_d	0
0	1	1	$-2U_d/3$	$U_d/3$	$U_d/3$	$-U_d$	0	U_d
1	0	0	$2U_d/3$	$-U_d/3$	$-U_d/3$	U_d	0	$-U_d$
1	0	1	$U_d/3$	$-2U_d/3$	$U_d/3$	U_d	$-U_d$	0
1	1	0	$U_d/3$	$U_d/3$	$-2U_d/3$	0	U_d	$-U_d$
1	1	1	0	0	0	0	0	0

$$\begin{bmatrix} U_{AB} \\ U_{BC} \\ U_{CA} \end{bmatrix} = U_d \begin{bmatrix} 1 & -1 & 0 \\ 0 & 1 & -1 \\ -1 & 0 & 1 \end{bmatrix} \begin{bmatrix} S_A \\ S_B \\ S_C \end{bmatrix} \quad (6)$$

Relation between three-phase inverter phase voltage and switching function:

$$\begin{bmatrix} U_A \\ U_B \\ U_C \end{bmatrix} = \frac{U_d}{3} \begin{bmatrix} 2 & -1 & -1 \\ -1 & 2 & -1 \\ -1 & -1 & 2 \end{bmatrix} \begin{bmatrix} S_A \\ S_B \\ S_C \end{bmatrix} \quad (7)$$

(U_d is the DC bus voltage)

The above two expressions are replaced by Table 1.

4.3 Three-Phase Inverter Filter Design

The harmonics in the voltage and current output by the inverter will lead to the deterioration of the power quality, so the selection and design of the filter is very important. In this paper, LC low-pass filter is used in three-phase inverter to eliminate the high order harmonics near the switching frequency, so as to obtain a good sinusoidal voltage and current waveform.

In the design of the filter, the filter inductance is determined first, and then the value of the filter capacitance is obtained by combining the cut-off frequency.

After determining the cut-off frequency, the values of L_f and C_f need to be determined separately. The calculation formula of filter inductance is as follows.

$$L_f = \sqrt{\frac{\left(\frac{\omega_1 V_{o1N}^2}{\omega_L^2} + \frac{\omega_1^3 V_{o1N}^2}{\omega_L^4}\right)}{\omega_1 I_{o1}^2}} \quad (8)$$

In which, ω_1 is the output voltage angular frequency, ω_L is the cut-off angle frequency, V_{o1N} is the output phase voltage, I_{o1} is the output phase current.

The filter inductor is designed by combining engineering experience calculation and simulation results. In order to better ensure the filtering effect, the cut-off frequency should be initially determined. The relationship between cut-off frequency f_c and filtering parameters is as follows:

$$f_c = \frac{1}{2\pi\sqrt{L_f C_s}} \tag{9}$$

where, L_f is the filter inductance and C_s is the filter capacitance. From this, the size of the filter capacitance is determined.

5 Simulation and Experimental Waveforms

Use MATLAB software to simulate the device. In the circuit, the BOOST input voltage is DC 500 V, the photovoltaic array is abstracted as a DC power supply, and the output voltage is DC 500 V. The circuit built with Simulink is shown in Fig. 5.

The waveforms of inductive current, inductive voltage, output voltage and input voltage of the front BOOST circuit are shown in Fig. 6. After the duty cycle is configured and the input voltage is 500 V, the BOOST circuit outputs a stable 600 V voltage.

The input and output voltage waveform of three-phase inverter circuit is shown in Fig. 7. When the input voltage is 600 V, a stable 380 V three-phase power frequency AC is obtained (Table 2).

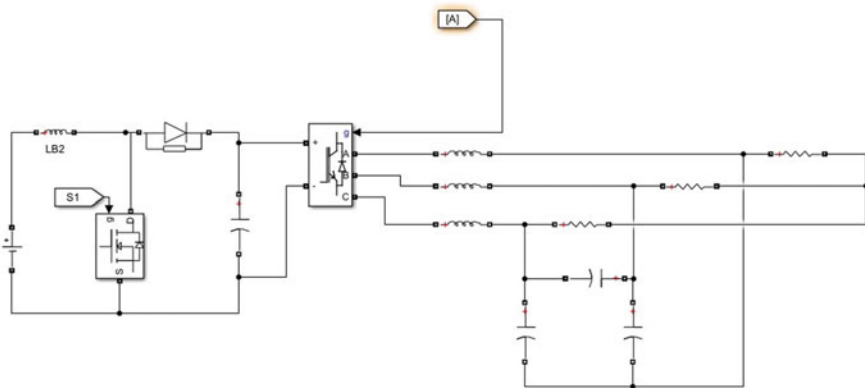


Fig. 5 Simulink simulation circuit

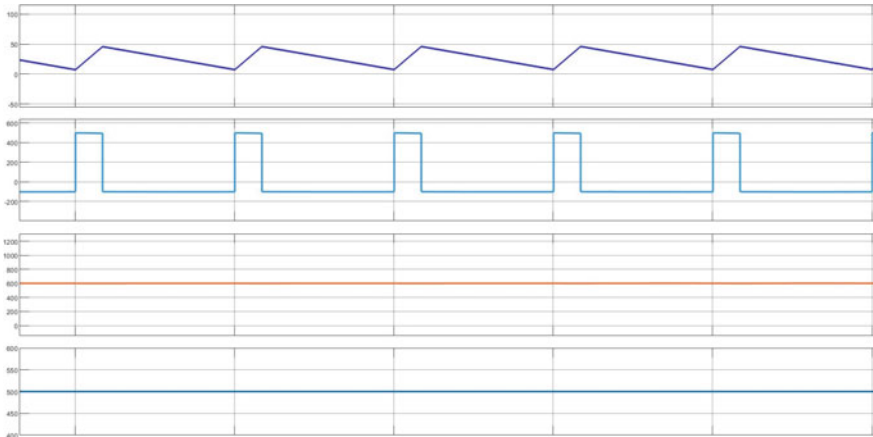


Fig. 6 BOOST circuit waveform

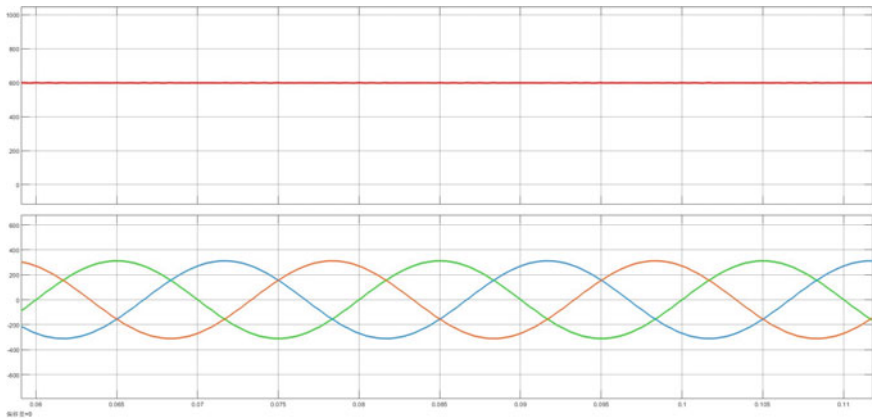


Fig. 7 Inverter input and output voltage waveform

Table 2 Parameters of railway locomotive emergency power supply system

Characteristics of emergency power supply system	Design value
Rated output power (kW)	60
Rated output voltage (V)	380 AC
Rated output frequency (Hz)	50

The oscilloscope experimental waveform is shown in Fig. 8. They are the output voltage of the front BOOST circuit, the system input voltage, the system output current, and the system output voltage.

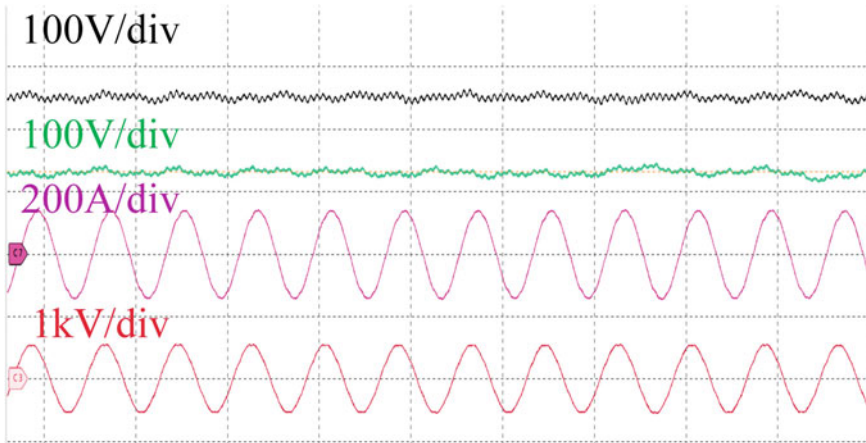


Fig. 8 Oscilloscope test waveform

6 Conclusion

This paper briefly analyzes the function of emergency power supply for railway locomotive and the overall structure of emergency power supply system. This paper focuses on the detailed design and analysis of the emergency power supply device with photovoltaic array as the main power supply and battery pack as the standby power supply. The emergency power supply device adopts the circuit topology of the front Boost + the rear SIV to realize the voltage stabilization and inversion output of the photovoltaic array output voltage, and the inversion of the battery output, so that the final output voltage is the same frequency and phase as the AC bus voltage of the railway locomotive. When the main power supply encounters a fault and stops power supply, the battery emergency power supply device based on inverter technology can replace the main power supply to supply power for the emergency load, ensuring the normal operation of the locomotive and the safety of railway operation.

Acknowledgements This research is supported by the Research project of Study on Development of Lithium Iron Phosphate Safety Battery and Intelligent Monitoring and Management System (No. CRSSJLSDSG-1-QT-001).

References

1. Gokhale KP, Kawamura A, Hoft RG (1987) Dead beat microprocessor control of PWM inverter for sinusoidal output waveform synthesis. *IEEE Trans Ind Appl* 23(5):901–910
2. Liu F, Wu Z, Wang H, Cui Z (2022) A new three-phase L-type double-active bridge Buck-Boost converter. *Power Electron Technol* 56(09):119–121 (in Chinese)

3. Deng H, Oruganti R, Srinivasan D (2007) Analysis and design of iterative learning control strategies for UPS inverters. *IEEE Trans Ind Electron* 54(3):1739–1751
4. Chen J-F, Chu C-L (1995) Combination voltage-controlled and current-controlled PWM inverters for UPS parallel operation. *IEEE Trans Power Electron* 10(5):547–558
5. Li M, Peng J, Sun S (2022) Buck-Boost converter with high gain and low output current ripple. *J Liaoning Univ Eng Technol (Nat Sci Ed)* 41(04):372–378 (in Chinese)
6. Wang L, Liu L, Li Z (2021) A new single-stage non-insulated Buck-Boost photovoltaic inverter. *J Solar Energy* 42(03):338–346 (in Chinese)
7. Dong Q, Zou Z, Hao X, Jiang F, Zhang Q (2010) Design of data center power supply and distribution system. *Build Electr* 29(07):11–23 (in Chinese)
8. Ovalle A, Hernandez ME, Ramos GA et al (2017) A Flexible nonorthogonal-reference-frame-based SVPWM framework for multilevel inverters. *IEEE Trans Power Electron* 32(6):4925–4938
9. Tong L (2022) Scheme design and cost analysis of new energy shunting locomotive. *Railway Locomotive Motor Train* 09:5–8+32+61 (in Chinese)
10. Xiao J, Mei Q, Huang X, Jiang L, Zhang J (2022) Current situation and development trend of China's photovoltaic power generation technology under the “double carbon” goal. *Nat Gas Technol Econ* 16(05):64–69 (in Chinese)
11. Ye L (2022) On the in-depth optimization and application of automatic pantograph lowering system test. *Railway Locomotive and Motor Train* 08:34–38+6 (in Chinese)

Condition Monitoring Technology for Temperature and Strain Status of Disconnecter Based on SAW



Dapeng Guo, Zhang Yan, Ruchuan Shi, and Chenrui Zhang

Abstract Disconnecter is an important equipment for power transmission and distribution in the power system, and its working state has an important impact on the safety and reliability of the power system. However, due to the complex and changeable environment of the Disconnecter, its working state is often affected by uncontrollable factors, and it is urgent to monitor its working state in real time. In this paper, based on the theory of SAW sensing, strain and temperature will cause the frequency shift of SAW devices, and a scheme of on-line monitoring system for disconnectors based on wireless passive SAW (SAW) sensors is proposed. Through the finite element simulation and test of the stress and strain of the disconnecter, a SAW sensor suitable for the temperature composite detection of the disconnecter's finger strain gauge is developed. Practical tests show that the stress measurement sensitivity of the contact finger strain is 220 Hz/ $\mu\epsilon$, and the temperature measurement sensitivity is 10 kHz/ $\mu\epsilon$, which can effectively discriminate the working state of the disconnecter. It has important application prospects on the online detection of power system equipment.

Keywords Surface acoustic wave · Frequency shift · Temperature · Strain

Foundation: Henan Province Science and Technology Research Project.
Project No: 222102210206.

D. Guo (✉) · R. Shi
Shanghai Jiao Tong University, Shanghai 200240, China
e-mail: yunnanguodapeng@163.com

Z. Yan
School of Information Engineering, Nanyang Institute of Technology, Nanyang 473004, China

R. Shi · C. Zhang
OFWelt(Suzhou)Technologies Co. Ltd, Shanghai 200241, China

© Beijing Paiké Culture Commu. Co., Ltd. 2024
X. Dong and L. Cai (eds.), *The Proceedings of 2023 4th International Symposium on Insulation and Discharge Computation for Power Equipment (IDCOMPU2023)*, Lecture Notes in Electrical Engineering 1100, https://doi.org/10.1007/978-981-99-7393-4_5

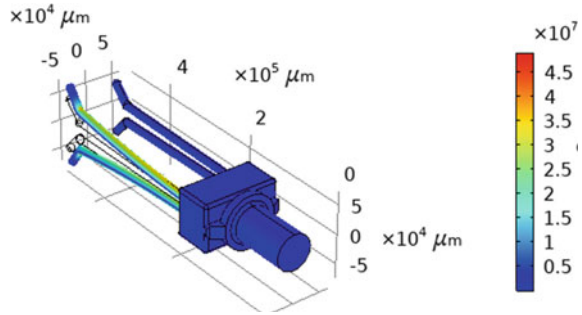
1 Introduction

The disconnecter is a commonly used general power equipment in the power system, mainly installed on both sides of the substation circuit breaker, playing an isolation role. Compared with other power equipment, Disconnecter operate outdoors and are subject to uncontrollable factors such as atmospheric corrosion and temperature changes for a long time. Therefore, establishing a real-time online status monitoring system for Disconnecter is of great significance for the reliability of power systems.

Isolation state detection technology mainly includes current detection, contact finger pressure detection, vibration signal detection, operating rod rotation angle signal detection, and temperature detection. Among them, current detection is highly susceptible to interference in the complex strong electromagnetic environment on site, while vibration signal detection can only detect a single state of isolation and cannot make effective response to complex disconnecter changes [2, 3]. During the operation of Disconnecter, the open circuit and open circuit of the switch mainly cause changes in temperature and stress–strain variables. Therefore, the current method of detecting the status of Disconnecter that has received more attention from researchers is the composite detection of contact finger or contact pressure and temperature. This article proposes a composite detection of the temperature and stress of the contact finger of the disconnecter based on SAW sensing technology, and can achieve wireless passive online detection, which has great applicability.

This article designs an disconnecter temperature and stress–strain sensor composed of SAW resonators based on the principle that temperature and stress–strain can cause the resonance frequency of SAW resonators to shift in the acoustic surface theory. The temperature and stress–strain changes can be represented based on the frequency shift of the sensor, and a detection system as shown in Fig. 1 is constructed. Using the GW4 type disconnecter as the experimental object, the SAW sensor is attached to the surface of the contact finger, and the antenna on the sensor can accept a certain range of RF signals. The reader sends an RF signal and generates a SAW through a resonator finger transducer. The SAW propagates within the waveguide of the resonator to the reflective grating, and the resonant signal reflected by the reflective grating is then returned to the reader through the finger transducer to generate an RF signal. The reader can determine whether the temperature or stress–strain of the contact finger has changed by the frequency offset of the two resonant signals returned before and after, Thus achieving status monitoring of the disconnecter. The temperature, stress, and strain sensor and detection system designed in this article based on acoustic surface wireless passive disconnecter have shown good performance in both experimental and on-site testing after continuous improvement, and have broad application prospects.

Fig. 1 Finite element analysis of stress field of isolation knife switch finger switch



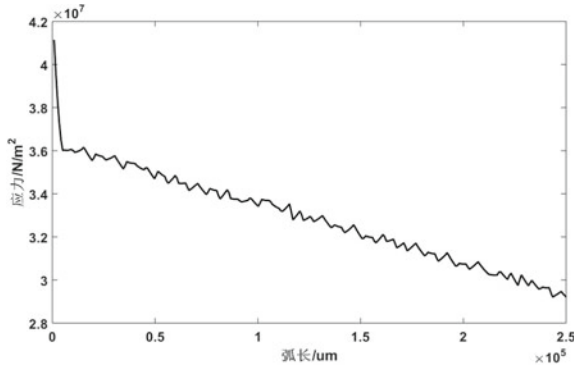
2 Force-Field Analysis of Disconnecter Finger

The GW4 disconnecter is shown in Fig. 1. The key to the connection of the switch is the contact finger. During the operation of the disconnecter, the stress at the connection point of the contact finger will cause strain changes in the contact finger. Therefore, it can be determined that the knife switch is in place by detecting the changes in stress and strain on the contact finger of the knife switch.

In order to analyze the strain distribution on the contact finger when the disconnecter is closed, COMSOL software was used to conduct finite element analysis of stress and strain on the contact finger. Firstly, import the 3D model of the disconnecter into COMSOL; Then the disconnecter is meshed, and the mesh subdivision is needed in the stress and strain concentration area; Secondly, add initial stress at the connection end of the disconnecter to simulate the load received under the closed state of the disconnecter; Finally, a steady-state analysis is conducted on the set disconnecter to simulate the stress and strain of the disconnecter under load. The finite element simulation results of the stress-strain field of the disconnecter are shown in Fig. 1. From the simulation results, it can be seen that when the disconnecter is closed, the surface strain of the contact finger of the disconnecter will change. After global calculation of the changes in the contact finger of the disconnecter, the stress distribution on the surface of the switch contact finger can be obtained. The results of the stress distribution are shown in Fig. 2. From the figure, it can be seen that the stress on the surface of the switch contact finger will gradually decrease with the distance from the fixed end of the contact finger, and the closer it is to the fixed end, the greater the surface stress. Therefore, in order to obtain more stress information from the contact finger of the stress-strain sensor, the best fixed position for the sensor is near the fixed end of the disconnecter contact finger.

By conducting finite element analysis of the stress field distribution of the disconnecter, the stress-strain distribution of the contact finger of the disconnecter was determined, thereby determining the optimal fixed position of the sensor on the disconnecter. In addition, it is also necessary to test the stress-strain range of fixed points to provide guidance for sensor selection. In this paper, a four wire bridges Strain gauge is used to test the strain of the contact finger in the closing state, and the stress and strain of the contact finger in the closing state of the disconnecter is

Fig. 2 The relationship between the surface stress of the contact finger and the position from the fixed end



about 400 $\mu\epsilon$ through test and calculation. The range of SAW stress–strain sensors is 0–1000 $\mu\epsilon$. It precisely includes the stress and strain of the knife switch contact finger, so using SAW stress and strain sensors is feasible.

3 Design and Development of SAW Sensors

SAW is an elastic wave that propagates along the surface of an object, with energy mainly concentrated on the surface of the object within a single wavelength during the propagation process. During the propagation process of surface acoustic waves, their propagation rate is influenced by the surface characteristics of the object, which are mainly influenced by temperature and stress–strain. Therefore, changes in SAW propagation characteristic parameters can be used to characterize changes in surface temperature and stress–strain of the object. The influence of temperature and pressure on the propagation of surface acoustic waves is mainly reflected in the propagation speed of surface acoustic waves. By monitoring the wave speed of surface acoustic waves, their changes are one-to-one corresponding to the changes in temperature and pressure [4]. Generally speaking, the influence of temperature and pressure on the propagation speed of surface acoustic waves can be shown by the following formula

$$\Delta v = \frac{\partial v}{\partial T} \Delta T + \frac{\partial v}{\partial \epsilon} \Delta \epsilon \tag{1}$$

The resonant frequency of SAWR is:

$$f_{saw} = \frac{v}{\lambda_{saw}} \tag{2}$$

Bring (1) into (2) to obtain:

$$\Delta f_{saw} = \frac{1}{\lambda_{saw}} \left(\frac{\partial v}{\partial T} \Delta T + \frac{\partial v}{\partial \epsilon} \Delta \epsilon \right) \tag{3}$$

From the above equation, it can be concluded that the influence of object temperature and strain on the velocity of acoustic surface waves will be fed back to the acoustic surface resonator, causing changes in the resonant frequency of the resonator. Therefore, the detection of object surface temperature and strain can be achieved by detecting changes in the resonant frequency of the SAW resonator.

The SAW sensor is composed of resonators, and the measurement results obtained by different combination structures are also different. In order to understand the dual effects of coupled temperature and stress-strain on acoustic surface resonators, this paper designs a differential compensation structure for temperature and stress-strain as shown in Fig. 3. Two AT cut resonators have similar sensitivity to temperature, and the influence of temperature is eliminated after differentiation, thus decoupling the stress-strain measurement results that are not affected by temperature changes; The resonators of the AT and XY cut resonators in the same direction, due to being perpendicular to the stress-strain direction, are subjected to similar stress-strain effects. After differentiation, the influence of stress-strain can be eliminated, and temperature measurement results that are not affected by stress-strain changes can be decoupled [3]. The differential structure is developed on the sensor as shown in the physical image, and the resonator and packaging structure are bound with gold wire.

The SAW sensor needs to receive the radio frequency signal through the antenna. The radio frequency signal is connected to the resonator through the gold wire. The inserted finger transducer on the resonator excites the SAW through the inverse Piezoelectricity. The reflected SAW signal carries the detection information, and then converts the SAW signal into an electrical signal through the inserted finger transducer, which is transmitted to the receiving end through the antenna. Sensors receive signals, transmit signals, and transmit signals through a packaging structure. The conceptual design of the packaging structure is shown in Fig. 4, where the sensor chip is composed of the aforementioned resonator differential combination structure. The overall structure of the sensor developed based on this structure is

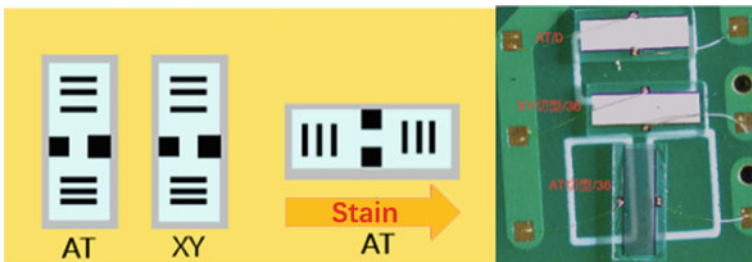
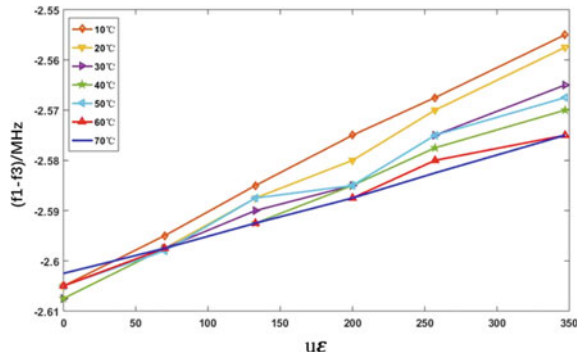


Fig. 3 Sensor chip design structure and sensor chip physical map

Fig. 4 Sensor strain calibration test results



shown in Fig. 4, where the matching circuit and peripheral packaging material are PCBs.

The SAW sensor characterizes the temperature and strain on the surface of an object through changes in the resonant frequency of the resonator. It needs to be calibrated with standard temperature and stress–strain sensors to correspond the compensated sensor resonant frequency offset with temperature and stress–strain one by one. In actual measurement, changes in temperature and stress–strain can be accurately detected through the resonant frequency offset.

This article uses standard thermocouple thermometers and cantilever beams to calibrate SAW sensors. The calibration method is to place a cantilever beam with a SAW sensor inside a temperature box, with a temperature range of 0–70 °C. Measure a set of data every 10 °C and record the resonant frequency corresponding to different loads at a constant temperature. The stress and strain calibration test results at different temperatures are shown in Fig. 5. From the figure, it can be concluded that the resonance frequency offset of the SAW sensor at different temperatures after compensation shows a clear linear relationship with stress and strain. Therefore, the change in stress and strain can be characterized by the resonance frequency offset. The temperature calibration test results of the SAW sensor are shown in Fig. 5. From the figure, it can be concluded that the resonance frequency offset of the SAW sensor shows a good linear relationship with temperature change under different stress and strain after compensation. Therefore, the temperature change can be characterized by the resonance frequency offset.

4 Testing of Wireless Monitoring System for Disconnecter

Cut the contact finger of the disconnecter into a plane of about 5 * 30 mm, as shown in Fig. 5, with a cutting depth of about 1 mm. Stick the sensor onto the cutting plane with special aerospace grade strong structural adhesive, and start debugging the testing system after the adhesive is fully cured. The installation position of the sensor and the entire testing system are shown in Fig. 5.

Table 1 Measurement data of the sensor (ambient temperature $-2\text{ }^{\circ}\text{C}$)

Experiment#	Text#	Open		Close	
		T/ $^{\circ}\text{C}$	s/ $\mu\epsilon$	T/ $^{\circ}\text{C}$	s/ $\mu\epsilon$
E#1	1	-1.5	19	-2.1	229
	2	-2.2	16	-2.3	274
	3	-2.1	6	-2.3	266
	4	-2.2	17	-2.3	244
E#2	1	-1.4	24	-1.4	251
	2	-1.4	9	-1.4	277
	3	-2.1	34	-1.7	202
	4	-1.7	22	-1.7	252
E#3	1	-1.4	15	-1.4	301
	2	-2.1	25	-2.1	293
	3	-2.3	17	-2.3	278
	4	-1.8	29	-2.4	245

During the testing process, first record the test data of the four sets of Disconnector in the open circuit state of the sensors. Then, close the Disconnector and record the test data of the four sets of Disconnector in the open circuit state of the sensors. Then repeat the open circuit and open circuit processes three times to measure the stability and repeatability of the sensors. Finally, replace other sensors and repeat the above testing process. Due to being an on-site test, temperature variation testing cannot be conducted, so the temperatures measured by the sensors are all ambient temperatures (Table 1).

5 Conclusion

- (1) During the closing process of the GW5 type disconnector, the stress, strain, and temperature on the contact finger will change. By using acoustic surface sensing technology to composite detect the strain and temperature of the contact finger switch, effective discrimination of the disconnector can be achieved.
- (2) Through finite element simulation and testing of the stress field of the contact finger of the disconnector, a SAW sensor suitable for composite detection of contact finger strain and temperature was designed and developed. Field testing showed that the sensitivity of the SAW sensor for stress measurement was $220\text{ Hz}/\mu\epsilon$, The sensitivity of temperature measurement is $10\text{ kHz}/^{\circ}\text{C}$. In practical applications, it can effectively distinguish the working status of Disconnector.

- (3) Compared with other sensors, the composite SAW sensor for contact finger strain and temperature of Disconnector has the advantage of wireless passivity. The disconnector online monitoring system constructed based on this sensor can not only achieve wireless passive measurement of contact finger stress and temperature of Disconnector, but also real-time online monitoring. It has strong applicability in future online monitoring of power equipment.

References

1. Yuan H, Sun Z, Wang L, Yang A, Wang X, Rong M (2022) Disconnector fault diagnosis based on attitude sensing system. *High Voltage Technol* 48(01)
2. Liu Y, Yang J, Jia Y, Song S, Wu B, Li J (2019) Contact state detection technology for GIS disconnector based on vibration principle 45(05)
3. Ma H, Zhou T, Peng S, Qiu Z, Zhu L, Simulation and diagnosis technology for mechanical faults of GW4 disconnector. *J Electr Technol* 20
4. Zhang Q (2018) Research on SAW devices with layered structure of aluminum nitride thin films based on finite element method. Shanghai Jiaotong University. LNCS Homepage, <http://www.springer.com/lncs>. Last accessed 21 Nov 2016
5. Fu Y (2014) Optimization design of SAW wireless passive temperature sensing system. Shanghai Jiao Tong University
6. Hu F, Cheng L, Fan S, He X, Xue X, Liang Y, Lu M, Wang W (2021) Enhanced sensitivity of wireless and passive SAW based strain sensor with a differential structure. *IEEE Sens J*, 1–1
7. Sinha BK, Tiersten HF (1979) First temperature derivatives of the fundamental elastic constants of quartz. *J Appl Phys* 50(4):2732–2739
8. Bulst WE, Fischerauer G, Reindl L (2001) State of the art in wireless sensing with surface acoustic waves. *IEEE Trans Industr Electron* 48(2):265–271
9. Yang J (2005) Free vibrations of an electroelastic body under biasing fields. *IEEE Trans Ultrason Ferroelectr Freq Control* 52(3):358–364

Adsorption of SF₆/N₂ Decomposed Gas in NaA, MFI and NaZSM-5 Molecular Sieves



Fengxiang Ma, Hongpeng Zu, Demin Zhang, Xin Lin, Jianyuan Xu, Yue Zhao, and Feng Zhu

Abstract The adsorption behavior of NaA, MFI and NaZSM-5 molecular sieves on SF₆/N₂ decomposition gases SO₂, NF₃, SO₂F₂ and CS₂ was studied. The adsorption isotherms and adsorption heat of four gas molecules at different temperatures on three molecular sieves were calculated by software. It is found that the adsorption capacity of NaA molecular sieve for four gases is more than that of MFI and NaZSM-5 molecular sieve. Except for a few cases, the adsorption capacity of NaZSM-5 molecular sieve for four gases is also slightly more than that of MFI molecular sieve. This is related to the presence of Na⁺ metal cations in NaA and NaZSM-5 molecular sieves. The presence of metal cations increases the active sites in the molecular sieve, which is beneficial to the adsorption of adsorbate on the molecular sieve. Compared with MFI and NaZSM-5 molecular sieves, NaA molecular sieves are more suitable for adsorption of four decomposition products of SF₆/N₂ mixture. In SF₆/N₂ electrical equipment containing NaA molecular sieve, if you want to monitor the operation status of insulated electrical equipment through the change of decomposition gas content, you must consider the influence of NaA molecular sieve on the adsorption behavior of decomposition gas.

Keywords SF₆/N₂ decomposition gas · Molecular sieve · Adsorption isotherm · Heat of adsorption

1 Introduction

SF₆ is a colorless, odorless, and non-toxic gas widely used in gas insulated electrical equipment due to its excellent insulation and arc extinguishing performance. However, the greenhouse effect potential (GWP) of SF₆ is approximately 23,900

F. Ma · Y. Zhao · F. Zhu

State Grid Anhui Electric Power Company Limited Research Institute, Hefei 230601, China

H. Zu (✉) · D. Zhang · X. Lin · J. Xu

School of Electrical Engineering, Shenyang University of Technology, Shenyang 110870, China
e-mail: iamzuhp@163.com

© Beijing Paiké Culture Commu. Co., Ltd. 2024

X. Dong and L. Cai (eds.), *The Proceedings of 2023 4th International Symposium on Insulation and Discharge Computation for Power Equipment (IDCOMPU2023)*, Lecture Notes in Electrical Engineering 1100, https://doi.org/10.1007/978-981-99-7393-4_6

times that of CO_2 , and its atmospheric lifespan is about 3200 years, making it a strong greenhouse gas. In 1997, it was listed as one of the six greenhouse gases prohibited for emissions under the Kyoto Protocol [1]. In order to reduce the use and emissions of SF_6 , SF_6/N_2 mixed gas has been widely used as insulation gas in the electrical field.

The 240 kV grade GIL developed by Alstom with 20% $\text{SF}_6/80\%$ N_2 mixed gas as insulation medium has been applied at Swiss airports; Siemens has also developed a GIL with a voltage level of 550 kV and a transmission capacity of 300 MW for 20% $\text{SF}_6/80\%$ N_2 [2]; In December 2017, the 30% $\text{SF}_6/70\%$ N_2 mixed gas pilot bus of the 220 kV Puqing substation in Wuhu, Anhui Province successfully passed the monitoring one week after dizziness [1].

It is inevitable to have trace amounts of water in GIS or GIL. When the trace water content is too high, it not only reduces the electrical performance of SF_6/N_2 gas mixture, but also causes chemical corrosion to the equipment [3]. At the same time, electrical equipment inevitably has insulation defects inside during the manufacturing, assembly, and operation processes. With the increase of equipment operation time, it can lead to discharge or overheating faults at the insulation defects [4]. Both discharge and overheating faults can cause the decomposition of the mixed insulation gas SF_6/N_2 , thereby affecting the insulation performance of the mixed gas. So corresponding adsorbents will be equipped in both GIS and GIL, which can adsorb water and ensure that the water content in the equipment meets the standard. On the other hand, it can adsorb various components decomposed by insulation gas due to discharge or overheating faults. Therefore, in order to diagnose insulation faults in GIS or GIL by monitoring the changes in SF_6/N_2 decomposition gas content, it is necessary to consider the influence of adsorbents on the changes in SF_6/N_2 decomposition gas content, find suitable gas component changes to characterize insulation degradation, and understand the characteristics and severity of insulation defects to ensure the normal operation of electrical equipment [4].

In this paper, based on Monte Carlo simulation method, the adsorption characteristics of four characteristic gases SO_2 , SO_2F_2 , NF_3 and CS_2 decomposed from SF_6/N_2 on three molecular sieves, NaA, MFI and NaZSM-5, were studied. The adsorption isotherm and adsorption heat of four decomposition gases in three molecular sieves at 298 K, 473 K, 573 K and 673 K were obtained by software simulation [5]. Analyzed and compared the differences in adsorption behavior of three types of molecular sieves on four types of decomposed gases at different temperatures. This provides a certain foundation for the treatment of SF_6/N_2 mixed gas waste gas and the study of how to use SF_6/N_2 decomposition characteristic components to diagnose faults generated inside gas insulated electrical equipment in the presence of adsorbents.

2 Method of Calculation

This article selected three types of molecular sieves, NaA, NaZSM-5, and MFI, to simulate the adsorption of four decomposition gases. The molecular formula of the single cell structure of NaA molecular sieve is Na₉₆Al₁₉₆Si₉₆O₃₈₄, and each single cell structure contains 8 α Cage (diameter 1.14 nm) and 8 pieces β Cage (diameter 0.66 nm) [6]. The pore size of NaA is 0.4 nm, and its framework structure is LTA type. 96 Na⁺ ions are introduced into LTA to balance the system charge, and geometric optimization is performed to obtain it. The molecular formula of the single cell structure of NaZSM-5 molecular sieve is Na₂Si₉₄Al₂O₁₉₂, and its framework structure is consistent with that of MFI molecular sieve. The Si/Al ratio is 47, and the pore size is 0.55 nm. After replacing two Si atoms with Al atoms in MFI, two Na⁺ ion equilibrium system charges are introduced and geometrically optimized. The molecular formula of the MFI molecular sieve unit cell structure is Si₉₆O₁₉₂, consisting of a Z-shaped channel with a diameter of approximately 0.53 nm and a linear channel with a diameter of approximately 0.55 nm. Figure 1 shows three types of molecular sieve models. The amount of charge carried by atoms in NaA molecular sieve is referred to in Ref. [7].

The four decomposition gases SO₂, NF₃, SO₂F₂ and CS₂ of the SF₆/N₂ gas mixture are geometrically optimized using the Dmol³ module in the Materials Studio simulation software. The GGA-PBE functional is used for the electron exchange correlation. The electronic eigen wave function is expanded by the DNP basis group. The four decomposition gas models are shown in Fig. 2.

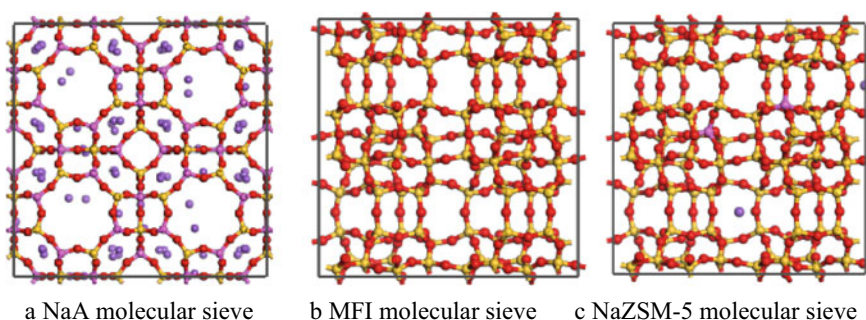


Fig. 1 Three molecular sieve models

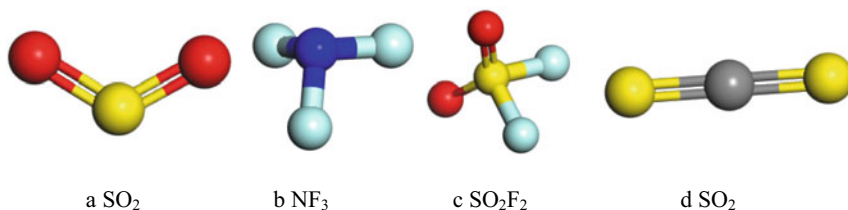


Fig. 2 Four gas molecular models

3 Calculation Results and Analysis

3.1 Adsorption Isotherm of SO₂, NF₃, SO₂F₂ and CS₂ on Molecular Sieve

Monte Carlo calculation method was applied to simulate the adsorption behavior [8] of three types of molecular sieves for SO₂, NF₃, SO₂F₂, and CS₂ at 298 K, 473 K, 573 K, and 673 K. The adsorption isotherm of SO₂, NF₃, SO₂F₂ and CS₂ on NaA, MFI and NaZSM-5 molecular sieves at different temperatures are shown in Figs. 3, 4, 5 and 6. From Figs. 3, 4, 5 and 6, it can be seen that at a constant temperature, the adsorption capacity of SO₂, NF₃, SO₂F₂, and CS₂ [9] on the molecular sieve increases with increasing pressure, and the final adsorption capacity tends to saturation with increasing pressure. But the adsorption capacity of the four gas molecules on the molecular sieve will decrease with the increase of temperature, mainly because the kinetic energy of the gas molecules will increase as the temperature increases. When the kinetic energy of the gas molecules exceeds the adsorption capacity of the molecular sieve, they will escape from the molecular sieve framework, thereby reducing the adsorption capacity. At the same temperature and pressure, the adsorption capacity of four gas molecules on NaA is higher than that on MFI and NaZSM-5 molecular sieves. The pore size of NaA molecular sieve is smaller than that of MFI and NaZSM-5 molecular sieves, but NaA molecular sieve contains 96 Na⁺ cations. When the molecular sieve adsorbs gas, Na⁺ metal cation sites will have electrostatic attraction to gas molecules, preferentially adsorbing gas molecules, improving adsorption capacity. Therefore, under the same conditions, the four types of gas molecules have the highest adsorption capacity on NaA molecular sieve. The average adsorption capacity of SO₂F₂ at 298 K in NaZSM-5 molecular sieve is slightly lower than that of MFI. Under other conditions, the average adsorption capacity of NaZSM-5 molecular sieve for four gas molecules is greater than or close to the average adsorption capacity of MFI molecular sieve. NaZSM-5 molecular sieve only has two more Na⁺ metal cations than MFI molecular sieve, so the adsorption capacity of the two molecular sieves for the four gas molecules is not significantly different.

At room temperature, the average adsorption capacity of NaA molecular sieve for NF₃ and SO₂ molecules is close to 6 mol/kg, with the order of adsorption capacity being NF₃ > SO₂ > CS₂ > SO₂F₂. The average adsorption capacity of SO₂ molecules

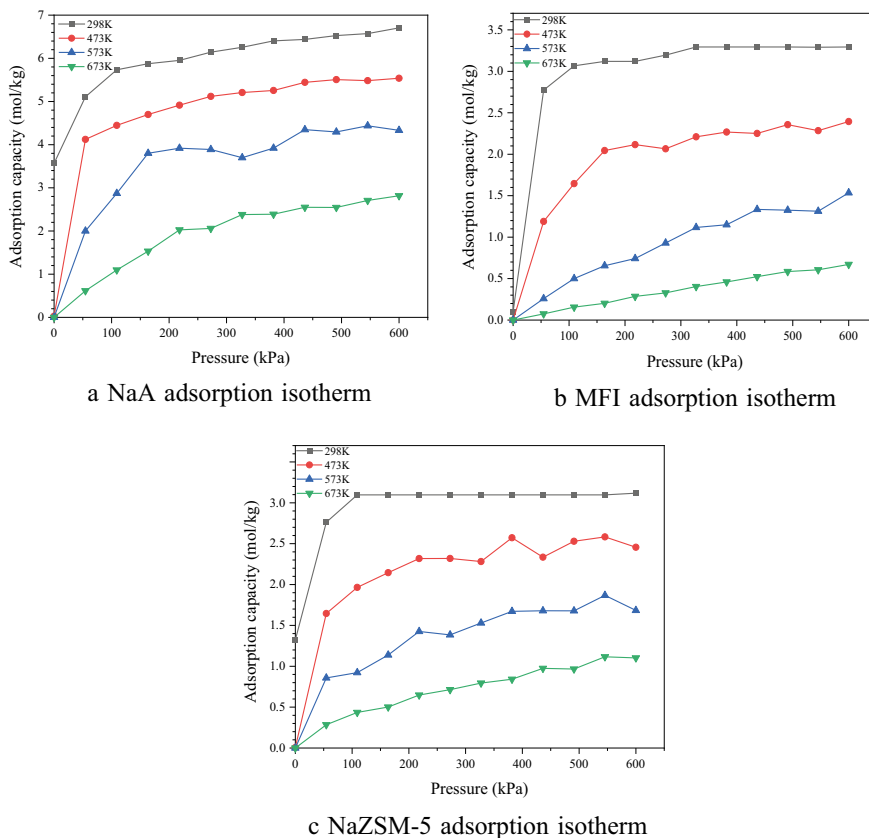


Fig. 3 Adsorption isotherm of SO₂ on three molecular sieves

in MFI and NaZSM-5 molecular sieves is slightly higher than that of NF₃ molecules. The order of adsorption capacity in MFI is SO₂ > NF₃ > SO₂F₂ > CS₂, while in NaZSM-5, the order of adsorption capacity is SO₂ > NF₃ > CS₂ > SO₂F₂. In NaZSM-5, the adsorption capacity of CS₂ is slightly higher than that of SO₂F₂, which is opposite to the adsorption behavior of MFI molecular sieve and consistent with the adsorption behavior of NaA molecular sieve. This may be related to the presence of Na⁺ metal cations in NaZSM-5, which have a better adsorption capacity for CS₂ than for SO₂F₂.

From the adsorption isotherm diagram of three molecular sieves for four decomposition gases, it can be seen that the adsorption capacity of NaA for four gases is relatively large. Therefore, if NaA molecular sieves are placed in SF₆/N₂ electrical equipment, if you want to monitor equipment failure through the decomposition gas content, you must consider the influence of NaA molecular sieves on the adsorption behavior of four gases. However, MFI and NaZSM-5 molecular sieves have relatively low adsorption capacity for the four types of decomposition gases, and have

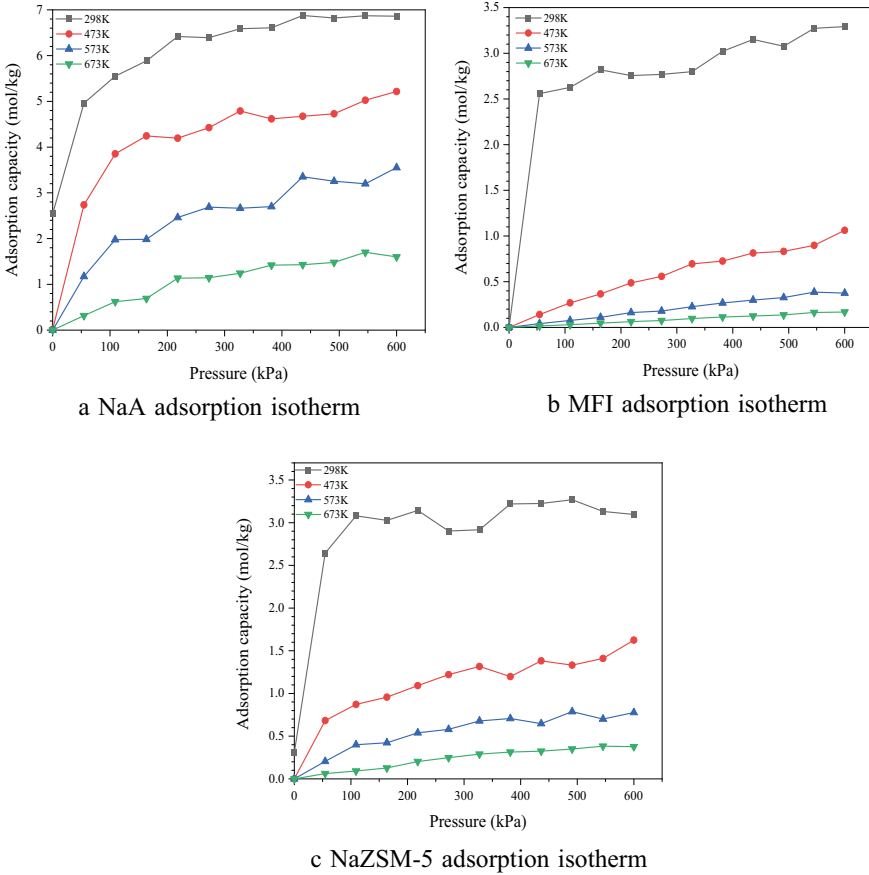


Fig. 4 Adsorption isotherm of NF₃ on three molecular sieves

little impact on the gas production law of SF₆/N₂ electrical equipment decomposition gases [10]. Similarly, when using molecular sieves to remove the four decomposition gases generated by SF₆/N₂ electrical equipment, NaA molecular sieves have advantages over MFI and NaZSM-5 molecular sieves.

3.2 Adsorption Heat of SO₂, NF₃, SO₂F₂, and CS₂ on Molecular Sieves

When the molecular sieve adsorbs the adsorbate during adsorption heat, the adsorbate moves towards the surface of the molecular sieve, and its movement speed greatly decreases, thereby releasing heat [11]. The value of adsorption heat depends on the nature of adsorption force, the type and strength of adsorption bonds, and

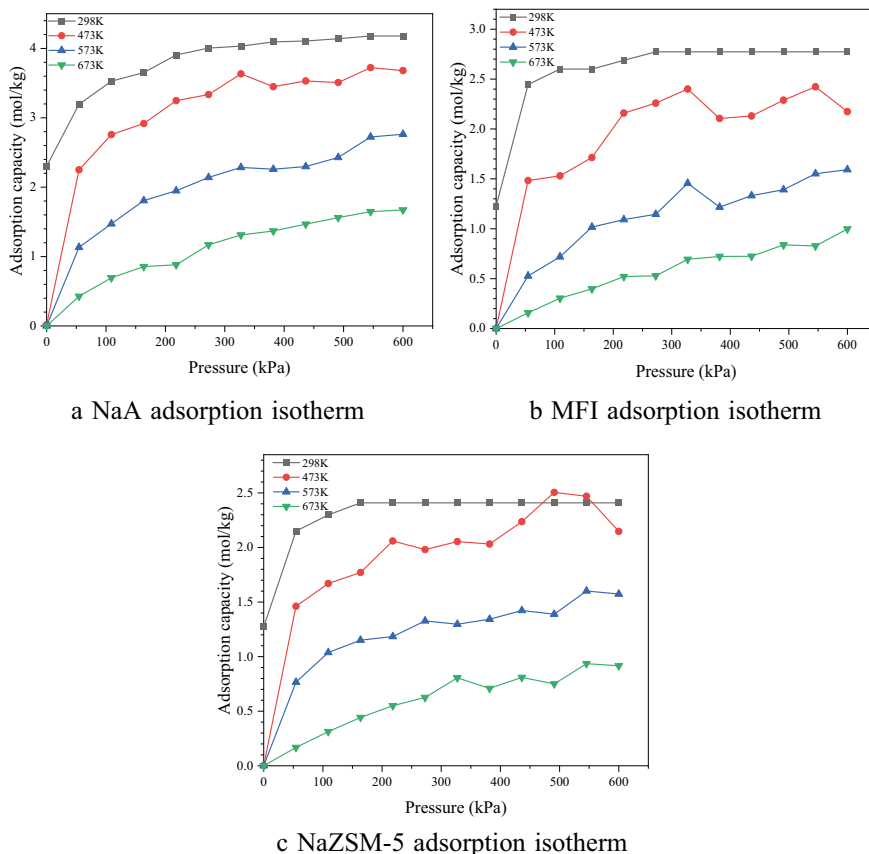


Fig. 5 Adsorption isotherm of SO₂F₂ on three molecular sieves

the temperature of the system also affects the value of adsorption heat [8]. In the actual adsorption process, the release of a large amount of heat from the adsorbate will lead to a decrease in the activity of the adsorbent, thereby reducing the adsorption capacity of the adsorbent on the adsorbate. When molecular sieves adsorb four types of gas molecules, the adsorbate first approaches the strong adsorption sites (such as Na⁺ cation sites) of the molecular sieve [12]. As gas molecules increase, gas molecules also occupy the weak adsorption sites of the molecular sieve, and finally the adsorption heat tends to stabilize. When there are many gas molecules adsorbed by molecular sieves, the large amount of heat released by gas molecules during the adsorption process will lead to an increase in temperature. The increase in temperature will affect the activity of molecular sieves, leading to a decrease in their adsorption capacity for gas molecules. However, the final adsorption capacity will also tend to stabilize. Figures 7, 8, 9, and 10 show the adsorption heats of SO₂, NF₃, SO₂F₂, and CS₂ on three types of molecular sieves, respectively. It can be seen that as the temperature increases, the adsorption heat of the same type of molecular sieve

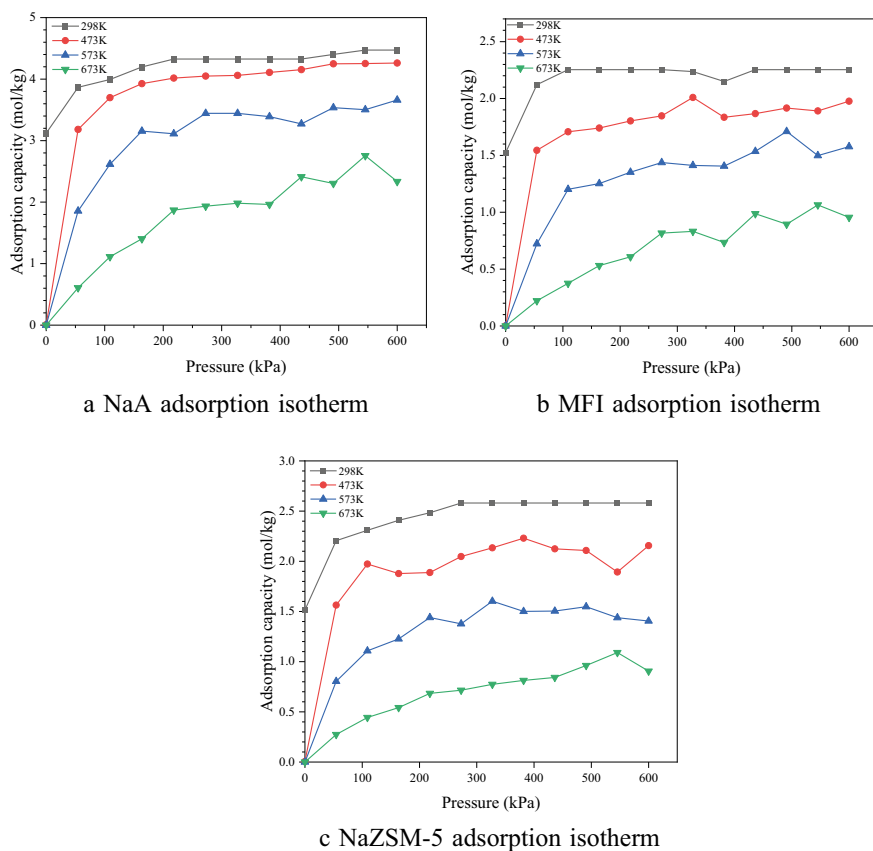


Fig. 6 Adsorption isotherm of CS_2 on three molecular sieves

on the same gas molecule will slightly decrease, with the maximum difference being about 5.23 kJ/mol in the adsorption heat of NaA molecular sieve on the SO_2F_2 gas molecule. This is because as the temperature increases, on the one hand, the activity of the molecular sieve decreases, leading to a decrease in its adsorption capacity for gas molecules. On the other hand, as the temperature increases, the kinetic energy of gas molecules increases, making it easier for the molecular sieve to bind to gas molecules, resulting in a decrease in adsorption heat. From the change of adsorption heat, it can also be seen that the ability of NaA molecular sieve to adsorb SO_2 , NF_3 , SO_2F_2 and CS_2 is stronger than MFI and NaZSM-5 molecular sieve, which has a certain relationship with the fact that NaA molecular sieve contains 96 Na^+ metal cations. The presence of metal cations increases the active site of the molecular sieve, and its electrostatic interaction force on the adsorbate will increase, thus enhancing the adsorption capacity of the molecular sieve. So in SF_6/N_2 gas electrical equipment, NaA molecular sieves are suitable for adsorbing SO_2 , NF_3 , SO_2F_2 , and CS_2 produced by the decomposition of SF_6/N_2 mixed gas

Fig. 7 Adsorption heat of SO₂ on three types of molecular sieves

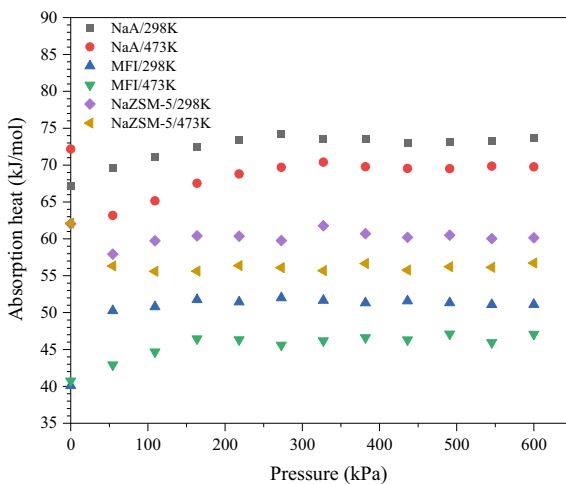


Fig. 8 Adsorption heat of NF₃ on three types of molecular sieves

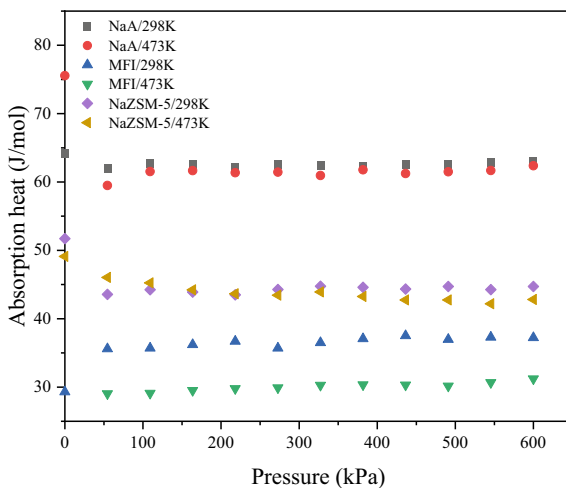


Fig. 9 Adsorption heat of SO_2F_2 on three types of molecular sieves

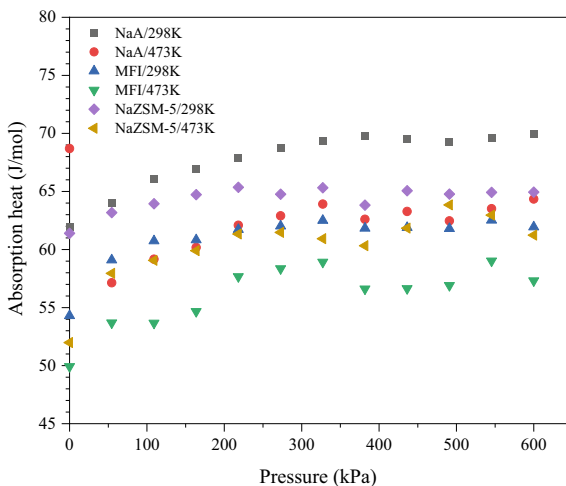
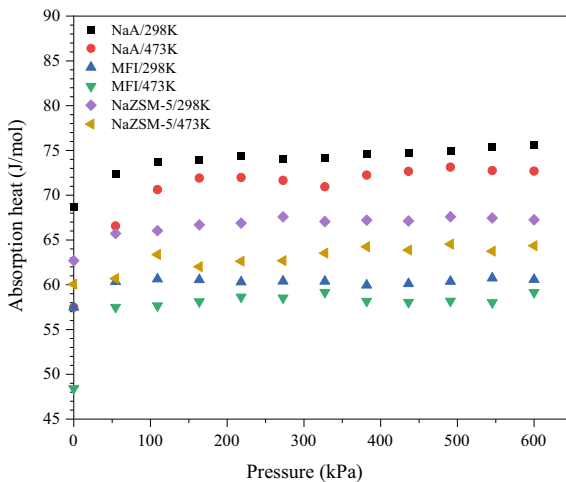


Fig. 10 Adsorption heat of CS_2 on three types of molecular sieves



4 Conclusion

By studying the adsorption behavior of three types of molecular sieves for SO_2 , NF_3 , SO_2F_2 , and CS_2 , it can be found that NaA molecular sieves have better adsorption capacity compared to MFI and NaZSM-5 molecular sieves, and are more suitable for adsorbing the four decomposition gas products of SF_6/N_2 decomposition. This is related to the fact that NaA molecular sieve has multiple active adsorption sites. NaZSM-5 only has two more Na^+ metal cations than MFI. Except for the average adsorption capacity of SO_2F_2 at 298 K, which is slightly lower than the average

adsorption capacity of MFI, the average adsorption capacity of NaZSM-5 molecular sieve for four gas molecules under other conditions is greater than or close to the average adsorption capacity of MFI molecular sieve. It can be seen that after the molecular sieve contains metal cations, the active adsorption sites will increase, which is beneficial for improving the adsorption capacity of the molecular sieve. Therefore, the treatment of waste gas in SF₆/N₂ electrical equipment and the removal of toxic decomposition gas in SF₆/N₂ electrical equipment to protect the safety of maintenance personnel can be completed by selecting molecular sieves with many active site. In SF₆/N₂ electrical equipment containing NaA molecular sieves, in order to monitor the status of gas insulated equipment through the variation of decomposition gas content, it is necessary to consider the impact of NaA molecular sieves on the adsorption behavior of decomposition gas products of SF₆/N₂ mixed gas, and choose a reasonable plan to monitor the operation status of gas insulated electrical equipment.

References

1. Zhang X, Yang Z, Wen H, Wu Y, Hu G, Tang T (2020) Thermal decomposition of epoxy resin under SF₆/N₂ gas mixture. *High Voltage Technol* 46(07):2453–2459 (in Chinese)
2. Li X, Zhao Hu (2016) A review of the research progress of SF₆ replacement gas. *High Voltage Technol* 42(06):1695–1701 (in Chinese)
3. Qiao SY, Zhou WJ, Wang Y, Xiong J, Zheng Y (2018) Influence of typical adsorbents on the variation law of characteristic gas of GIS solid insulation medium discharge. *J Electr Eng Technol* 33(19):4627–4635 (in Chinese)
4. Tang T, Zeng F, Liang X, Qiu Y, Yuan J, Zhang X (2013) Experiment and analysis of two adsorbents for the adsorption of SF₆ decomposition characteristic components. *Chin J Electr Eng* 33(31):211–219+26 (in Chinese)
5. Zhai D, Zhao L, Pan H, Zhao Z, Duan A, Gao J, Chen Y (2011) Monte Carlo study on the adsorption of C₄ hydrocarbons in FAU, BEA and LTL type molecular sieves. *J Phys Chem* 27(06):1400–1406 (in Chinese)
6. Hou H, Yan X, Yu X, Liu W, Liu Z, Wang B (2019) Theoretical study on the adsorption of C₄F₇N/CO₂ mixed insulating gas and its decomposition products by molecular sieve. *High Voltage Technol* 45(04):1040–1047 (in Chinese)
7. Ramin, Ekhteiri, Salmas et al (2013) Silver–sodium ion exchange dynamics in LTA zeolite membranes. *J Phys Chem B*
8. Filippova NL (1998) Adsorption and heat of adsorption onto polymer particular surface by inverse gas chromatography. *J Colloid Interface Sci* 197(1):170–176
9. Ji Y, Zhang M, Wang C, Bi J, Mei K, Feng Y, Gong Y, Huang Y, Wang H (2020) SF₆/N₂ mixed gas decomposition products detection method and experimental research. *High Voltage Electr* 56(12):97–102 (in Chinese)
10. Cao J, Yuan X, Ma F, Liu Z, Song Y, Li J (2022) Study on the detection technology of characteristic decomposition products in SF₆/N₂ gas mixture. *Low Temp Special Gas* 40(03):26–30 (in Chinese)
11. Hirotani A, Mizukami K, Miura R et al (1997) Grand canonical Monte Carlo simulation of the adsorption of CO₂ on silicalite and NaZSM-5. *Appl Surf Sci* 120(s1–2):81–84
12. Tian S, Yuan Z, Zhang X et al (2022) Adsorption properties of environmentally friendly insulating medium C₄F₇N and its common decomposition products in NaA, NaZSM-5, and NaX molecular sieves. *High Voltage*

Pre-sowing Treatment Using Plasma-Activated Water to Enhance the Germination of Cucumber Seeds Under Salt Stress



Tong Zhu, Di Zhang, Chongshan Zhong, Guangwei Guan, and Hongwei Tang

Abstract The present work is focused on the effects on the germination of cucumber seeds by plasma activated water (PAW) treatment in simulated saline environment, to evaluate the improvement on the saline tolerance of cucumber seeds from PAW treatment. PAW was prepared by self-made gas–liquid two-phase underwater pulsed spark discharge plasma reactor, which was driven by self-made microsecond bipolar pulse power at constant frequency of 100 Hz. The processing durations of PAW was set as 0, 10, 20, and 30 min, respectively. The detection indicators were chosen as physical characteristics including oxidation reduction potential, pH and electrical conductivity and chemical parameters including nitrates and hydrogen peroxide. The germination experiment of cucumber seeds was performed after immersing in PAW processed for different durations, and during the experiment the seeds were kept wet by PAW processed for the same duration. The saline environments were simulated by different concentrations of NaCl solution. The germination of cucumber seeds was recorded every 12 h. The images of surface morphology was captured by scanning electron microscope to observe the changes of seeds due to immersing in PAW. The result showed that the improvement of germination of seeds treated by PAW processed for 10 min was most significantly, of which the germination rate and the mean germination time in various simulated salt environment were improved quite a lot. This work provides a new direction of a promising seed pretreatment research and application in saline environments.

Keywords Plasma activated water (PAW) · Seed germination · Saline tolerance

T. Zhu · D. Zhang · C. Zhong · G. Guan · H. Tang (✉)
College of Information and Electrical Engineering, China Agricultural University,
Beijing 100083, People's Republic of China
e-mail: tang7643@163.com

© Beijing Paiké Culture Commu. Co., Ltd. 2024
X. Dong and L. Cai (eds.), *The Proceedings of 2023 4th International Symposium on Insulation and Discharge Computation for Power Equipment (IDCOMPU2023)*, Lecture Notes in Electrical Engineering 1100, https://doi.org/10.1007/978-981-99-7393-4_7

1 Introduction

Soil salinization has become one of the world's most severe problems for agriculture, resulting in the inhibition of crop growth and the decrease of agricultural comprehensive production [1]. Therefore, strengthening the anti-adversity of plants under salt stress will be helpful to solve the challenge of growing demand of food supply. Referring to the salt concentration in the soil, the saline land can be classified into three levels: slightly saline soil, moderately saline soil and severe saline soil [2].

The primary measures to enhance the salt tolerance of plants include breeding, strain crossing, genetic engineering, pre-sowing seed treatment, etc., among which pre-sowing seed treatment has been widely utilized in practice. The conventional methods of pre-sowing treatment include water immersing, mechanical injuries, and chemical processing, however, there are still some problems with them [3]. For instance, chemical treatment leads to potential water and soil pollution; and in terms of anti-adversity, another two methods display little effect to improve the salt tolerance of seeds.

Low-temperature plasma has been recognized as a novel seed treatment technology which demonstrates significant efficacy [4]. Numerous investigations indicate low temperature plasma may create positive effects on germination rate, the anti-adversity, and the growth of plants. According to whether seeds are contacted with plasma directly, the low-temperature plasma technique can be classified into two types: direct and indirect treatment [5]. For direct plasma treatment, there are still challenges to achieve large-scale or homogeneous processing [6]. In recent years, soaking large amounts of seeds in plasma activated water (PAW) as an indirect method has shown good promise for improving seed treatment yield and uniformity [7].

Various seeds have been reported to be treated by PAW, e.g., carrot [8], tomato [9], potato [10], rape [11], soybean [12], etc. The investigations showed that PAW treatment could regulate the concentrations of endogenous hormones and therefore the expression of genes and the activity of some enzymes, which could improve some indicators of seeds, such as chlorophyll synthesis, total soluble protein, and sugar concentration [13]. Finally, the seeds treated by PAW would germinate better than untreated [14]. Apart from this, some studies have found that PAW can also significantly increase the germination rate of these seeds, and the effect is closely related to the concentration of NO_3^- and H_2O_2 in PAW.

However, to the authors' best knowledge, there are no reports on whether PAW could strengthen the anti-adversity of seeds under salt stress. In this work, cucumber seed was selected to be treated by PAW, which is highly sensitive to salt stress during the germination stage and planted widely in the world. A reactor to produce PAW was designed to treat cucumber seeds. Positive effects were observed in the results, which implies potential for future applications.

2 Material and Method

2.1 Reactor to Produce PAW

The PAW was prepared by a gas–liquid two-phase underwater pulsed discharge plasma reactor, shown in Fig. 1. The high voltage electrode comprises five hollow needles of stainless steel (inner radius 0.61 mm, outer radius 0.91 mm) which were arranged in parallel from top to bottom. Each needle was wrapped in industrial-grade silica gel, while only the tip of needle was exposed. The five needles were fixed on an acrylic plate every 7.9 mm in a row. Each needle was also set parallel in a gas path connected by a plastic pipeline driven by a pump. The working gas is air, of which the flux was measured and adjusted by a flow meter. A stainless-steel plate was fixed at another side against the needles to act as the ground electrode, and the distance between the needle points to the ground electrode was 23 mm. The reactor created discharge at the interface between gas and liquid, which made air participate in the formation of radicals in PAW.

A power supply was designed to generate high-voltage pulses (0–20 kV, 100 Hz). The voltage and the current across the reactor were recorded by the digital oscilloscope (TDS 2012C, Tektronix, USA) using a 1000:1 high-voltage probe (P6015A, Tektronix, USA) and a current viewing resistor of 0.01 Ω (SDN-414-01, T&M Research Products, USA), respectively. The energy cost of a single pulse was calculated by the integration of instantaneous voltage (U) and current (I) over time. The images of plasma discharge were captured by a digital camera (Canon 5DII). It is worth mentioning that the width of pulses is referred to as the duration from the original ascending point to the zero-crossing point of one single pulse.

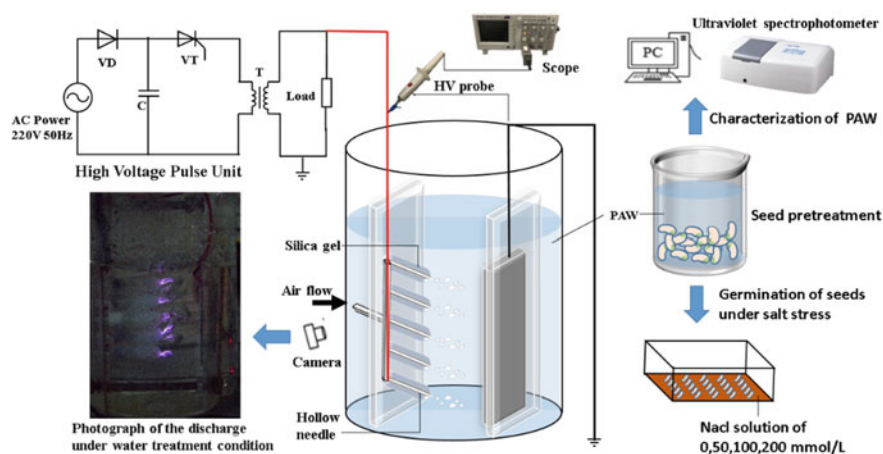


Fig. 1 Preparation of PAW and treatment of cucumber seeds

2.2 Production of PAW

Deionized water was processed for 10, 20, and 30 min, respectively, marked as PAW10, PAW20, and PAW30, correspondingly. The yield of each PAW generation was 800 mL. The control group untreated was marked as PAW0. The input voltage of the plasma source was set to 190 V, and the peak voltage of the output will vary with the state of the workload. The flow rate of working gas was 2 L/min, and the feed water temperature was 27 °C.

2.3 Characterization of PAW

The following physical and chemical properties of PAW were measured: pH (measured by pH-100, precision ± 0.02 , Lichen, Co., China), electrical conductivity (EC, measured by SW301, Suwei Co., China), oxidation–reduction potential (ORP, measured by CT-8022, Kedida Co., China). It is widely accepted that the effects that PAW takes on seeds mainly thanks to radicals of oxygen and nitrogen species (RONS). Therefore H_2O_2 and NO_3^- were selected as the indicators for the RONS in PAW, of which the concentrations were measured by an Ultraviolet spectrophotometer (UV2900, Shimadzu, Japan). The energy efficiency was calculated by Eq. (1). All the properties were sampled and detected in 5 min.

$$\eta (\%) = \frac{c_i V_0}{P_s} \quad (1)$$

where c_i was concentrations of the detection indicators in mg/L units, and V_0 (mL) was the total volume of PAW treated; η ($\mu\text{g}/\text{kWh}$) was the energy efficiency, the higher, the better; P_s (kWh) was the energy cost.

2.4 Seed Germination Statistics and Morphological Indicators

2.4.1 Seed Pretreatment

Cucumber seeds were purchased from the Chinese Academy of Agricultural Sciences in Beijing, China. Healthy and full cucumber seeds of similar size and uniform appearance were selected for the following experiment. Seeds were washed with fresh water three times first and immersed in 3% NaClO solution for 10 min to disinfect. After disinfection, the seeds were rewashed with deionized water five times and dried in the air overnight, and then put in centrifuge tubes with 6 mL PAW0,

PAW10, PAW20, and PAW30 for 5 h, respectively. After immersion, the seeds were dried in air for 10 h again.

2.4.2 Germination of Seeds Under Salt Stress

The normal, slight, moderate, and severe saline land was simulated by NaCl solution of 0, 50, 100, and 200 mmol/L, respectively. The seeds treated were put in groups of 30 in germinating boxes coated with double layers of dry germination paper. Then 4 mL NaCl solution of different concentrations and 1.5 mL PAW treated for the same durations were put into each group. Each group was repeated for three times. All the seeds were cultivated under the controlled surrounding condition of 25 °C and 60–70% relative humidity without light. Every 24 h, the seeds were fed with 1.5 mL PAW treated for the same durations to keep them wet. Statistics of germination were recorded every 12 h.

2.4.3 Morphological Indicators of Seeds

The average weights of the seeds in the same group were recorded before and after the treatment. The water uptake of seeds was defined as the additional weight of seeds treated compared to when untreated. And the water absorption rate (W_a) in the average weight of seeds was calculated by Eq. (2):

$$W_a (\%) = \frac{W_1 - W_0}{W_0} \times 100 \quad (2)$$

where W_0 was the average weight of untreated seeds, and W_1 as the average weight immersed in PAW of different concentrations and dried. Each group contained 30 seeds and was repeated for 5 times.

The surface morphology of seeds that were treated and dried in the air was analyzed. The images were captured by scanning electron microscope (SEM) (S4800, Hitachi, Japan) at 15 kV accelerating voltage with 200× or 500× magnification.

2.4.4 Seed Germination

Germination rate (GR), germination potential (GP), germination index (GI), mean germination time (MGT), and mean germination rate (MGR) of seeds treated were studied. The seed of which the radicle reached 2 mm and more would be counted as germinated. N_n represented the total number of germinated seeds till n th recording, which the maximum n were 7. Specifically, N_0 represented the total number of seeds, whether germinated or not. E_y is the number of seeds germinated on day y . Table 1 shows the relevant calculation formulas.

Table 1 Some formulas about seed germination

Index	Formula	Introduction	Number
<i>GR</i>	$GR = \frac{N_7}{N_0} \times 100\%$	A measure of the germ inability of seeds	(3)
<i>GP</i>	$GP = \frac{N_4}{N_0} \times 100\%$	A measure to reflect the germination of seeds	(4)
<i>GI</i>	$GI = \frac{N_0}{N_0} \times 100\%$	A measure to evaluate the viability of seeds	(5)
<i>MGT</i>	$MGT = \frac{\sum E_y}{\sum E}$	A measure of the average time cost of germination	(6)
<i>MGR</i>	$MGR = \frac{1}{MGT}$	A measure of the average time cost of germination	(7)

3 Results

3.1 Electrical Characters Diagnosis

The voltage and current waveforms across the generator are shown in Fig. 2, which varied with reaction time and were driven by the same input voltage of 190 V (AC). The peak voltage, the pulse width, the average energy cost of a single pulse, and the Electrical conductivity (EC) of the PAW were listed in Table 2.

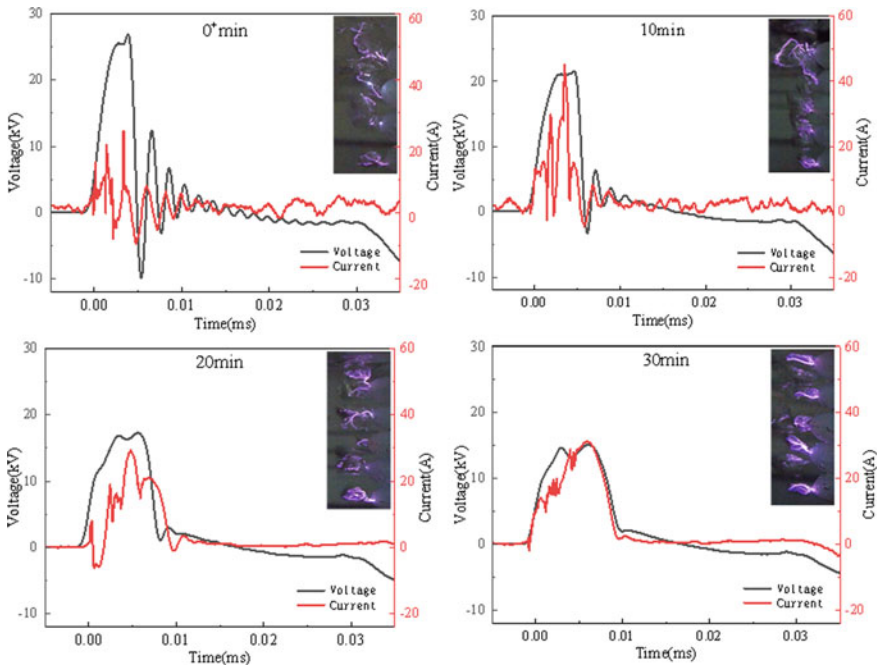


Fig. 2 Waveforms of current and voltage of a single pulse and images of underwater discharges of the related pulse when PAW was treated for various durations

Table 2 Main characters of discharge pulses when PAW was treated (EC was attached)

Time (min)	Voltage (kV)	Pulse width (μ s)	Power of Single Pulse (J)	EC (μ s/cm)
0+	26.85 \pm 0.15	5.97 \pm 0.23	0.19 \pm 0.32	10
10	23.48 \pm 0.37	6.59 \pm 0.06	0.91 \pm 0.34	40
20	18.18 \pm 1.43	8.48 \pm 0.44	2.14 \pm 0.21	80
30	15.94 \pm 0.92	17.23 \pm 0.02	2.41 \pm 0.13	132

It was observed that the peak value of pulsed voltage decreased with the increase of discharge time (in Fig. 2). The reason for this phenomenon could be the increase of EC of treated water with the process durations extending and the decrease of the impedance of the reactor. As a result, the water between the electrodes changed from capacitive-dominated to resistive-dominated. It can be seen in Fig. 2 that the phase differences between the current and voltage within each pulse were getting smaller with time. Meanwhile, energy cost of a single pulse listed in Table 2 was calculated by Eq. (1), showing an ascending trend.

3.2 Chemical Composition Detection of PAW

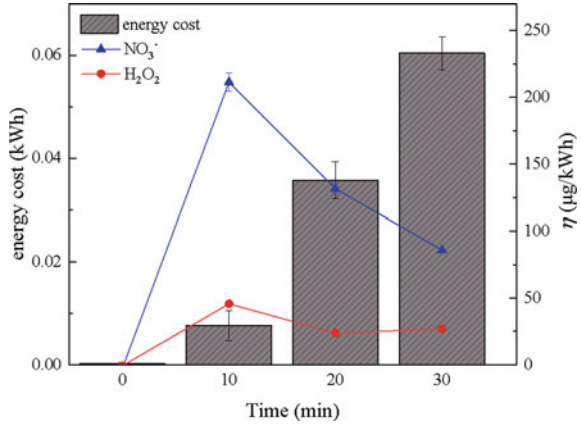
The PAW was characterized by measuring the pH scale, EC, oxidation–reduction potential (ORP), and the concentrations of NO_3^- and H_2O_2 , as shown in Table 3. It is indicated that with the increase of treating time, the pH of the water descends with the PAW processing, while the value of EC, ORP and the concentrations of NO_3^- and H_2O_2 were all increasing, as the PAW was treated longer.

The mass of NO_3^- and H_2O_2 generated in PAW costing per kWh, also energy efficiency was shown in Fig. 3. It could be seen that content of NO_3^- and H_2O_2 in PAW increased as treatment durations increased, while the energy efficiency rose first when the duration was 10 min and then declined. The leakage current increased as the EC ascended with process durations, which cause the actual voltage between the electrodes to decrease and the discharge intensity to weaken.

Table 3 Physical and chemical properties of PAW treated for various durations

Properties	Treatment duration (min)			
	0	10	20	30
pH	7.02	5.98	4.02	3.39
EC (μ s/cm)	10	40	80	132
ORP (mV)	337	421	446	458
c(NO_3^-) (mg/L)	0	2.02 \pm 0.07	5.87 \pm 0.16	6.48 \pm 0.04
c(H_2O_2) (mg/L)	0	0.43 \pm 0.00	1.05 \pm 0.01	2.03 \pm 0.01

Fig. 3 The energy cost of NO_3^- and H_2O_2 and the energy efficiency of both of them



3.3 Characterization of Seeds

3.3.1 Seed Germination

Compared with CK, PAW treatment can not only improve the GR and the GP of the seeds in common environment, but also relieve the negative influences of the salt stress. As shown in Fig. 4, the GR of CK is 87.78%, and the GP is 70.00%. After treated by PAW, including PAW10, PAW20, and PAW30, the GR and the GP of the cucumber seeds had increased, and seeds treated by PAW10 germinated best, which could reach to 95.56% of GR and 81.11% of GP, both improving around 10% compared to the CK.

Under the salt stress, the more the environment contained salt, the worse the germination of cucumber seeds was inhibited. Under the simulated severe salt stress, the GR of cucumber seeds was only 76.67%, and the GP was only 4.44%. The result

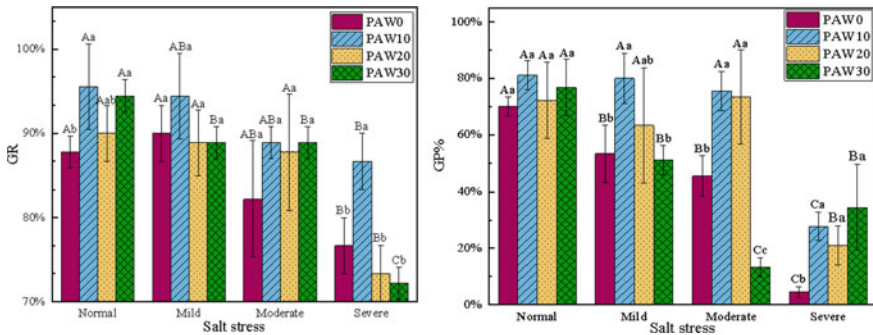


Fig. 4 GR and GP under various treatments and simulated saline environment

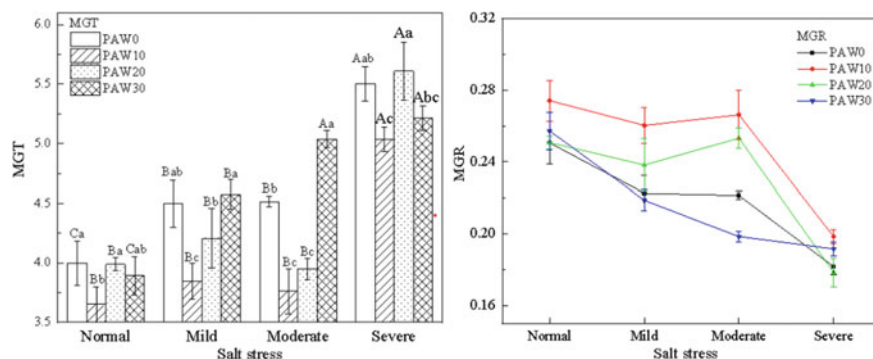


Fig. 5 MGT and MGR of seeds treated in various PAW with different processing durations

of experiment was shown in the Fig. 4 that PAW treatment can strengthen the anti-adversity of salt stress significantly. After treated by PAW10, the GR and the GP of cucumber seeds had increased significantly. Treating seeds with PAW20 could improve the GR of seeds under simulated moderate salt stress and the GP under simulated slight and moderate salt stress.

Figure 5 showed that the MGT and MGR of cucumber seeds treated by various PAW under different simulated salt stress. It was figured out that the salt stress would affect the MGR negatively. Compared to the CK, the MGT had decreased to some degrees after PAW treatment, especially PAW10.

The germination of seeds was recorded every 12 h, and the GI changing curve was given in Fig. 6. It was showed that the effects that PAW took on seeds existed throughout the germination of seeds, especially significantly within 24–60 h. Among the PAW processed for different durations, PAW10 behaved best. The treatment of PAW10 to seeds had shown an acceptable positive contribution for all the simulated salt stress; while PAW20 had shown a better effect in the treatment to seeds in slight and simulated moderate salt stress, and unstable effects on seeds under simulated severe salt stress environment. And PAW30 had shown insignificant effects or even negative effects on seeds in whichever the simulated salt content is in the environment.

3.3.2 Water Absorption of Seeds and Surface Morphology

The reason why PAW treatment could strengthen the salt tolerance of seeds was charming. Limited by the experiment condition, the water absorption and the surface morphology of treated seeds were chosen and measured to investigate and evaluate the effects that PAW took on seeds briefly.

The weight of water absorbed in seeds treated by various PAW was recorded and compared, as shown in Fig. 7. It could be seen that the W_a of all the seeds treated by PAW was higher than the control group. It could be speculated that immersing in

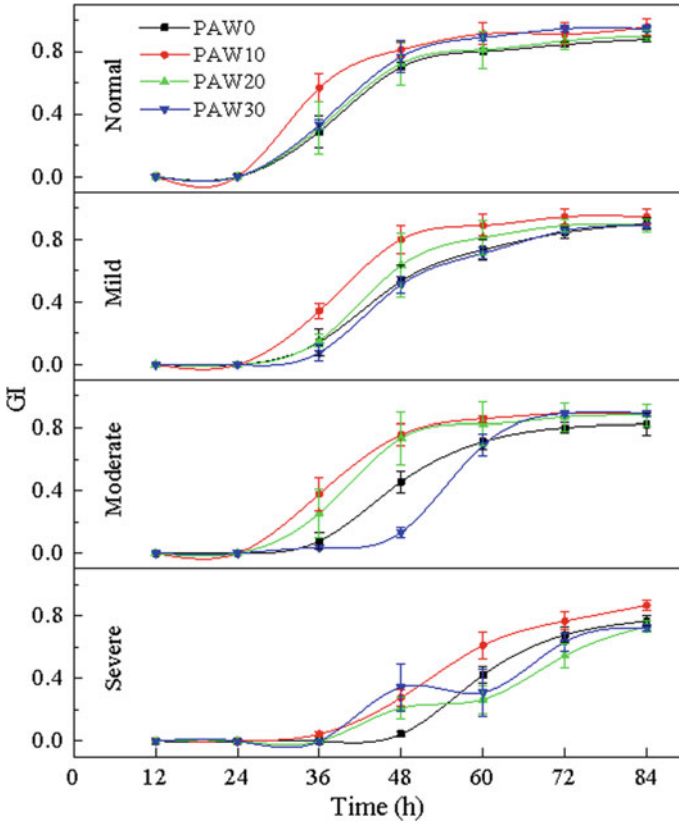


Fig. 6 GI in various simulated saline environments treated by PAW

PAW could significantly strengthen the capability of seeds to absorb water, and the processing durations of PAW affected the final W_a little.

SEM images of cucumber seeds were captured to investigate the surface morphology changes due to PAW treatment. Figure 8a–d showed the surface morphology of seeds treated by PAW0, PAW10, PAW20, and PAW30, respectively. Compared to seeds treated with deionized water, those treated with PAW showed a much clearer surface grid structure. To the best of our knowledge, this grid structure was the cell walls of the seed coat of the cucumber seeds. It could be speculated that the more water the seeds absorbed, the larger the cells of cucumber seeds would become. Thus, the cell walls were significantly highlighted. It could also be seen that the more extended PAW was treated, the more water the seeds absorbed, and the more apparent cell walls were seen. The possible reason was that, in the process of absorbing water, the radicals in PAW, such as NO_3^- and H_2O_2 , would influence the various reactions happening in the surface and inner cells of seeds, which was considered as a reason that PAW processed longer had a more substantial effect on the cells of seeds.

Fig. 7 Water absorption rate treated by various PAW with different processing durations

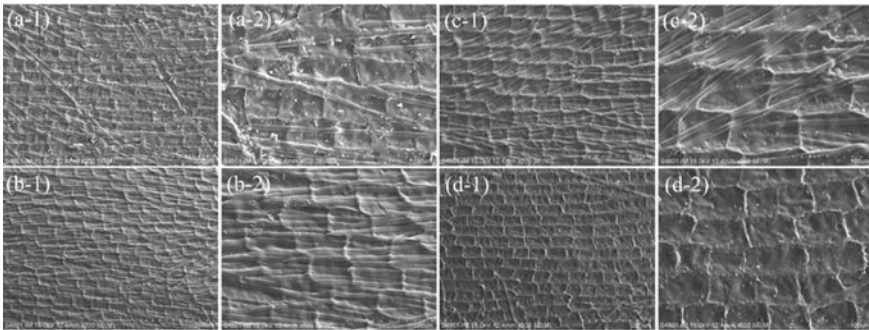
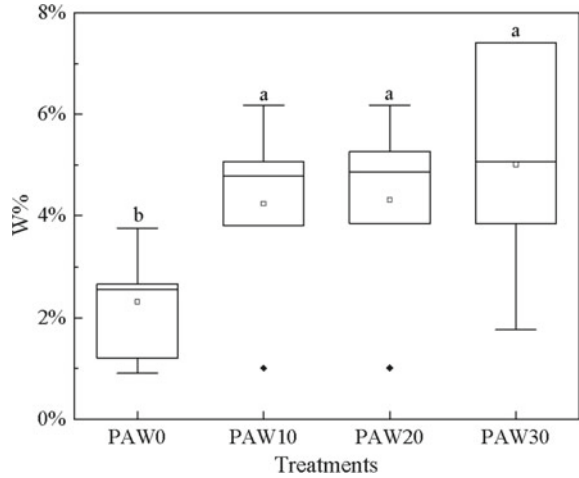


Fig. 8 SEM images of cucumber seeds surface. **a–d** were seeds treated by PAW0, PAW10, PAW20, and PAW30, respectively. And the first image and the second one in the same group were images captured with 200× and 500× magnification, respectively

4 Discussion

The seed germination process is related to metabolisms in cells and molecular behaviors, which will be affected by various genetic, endogenous, and environmental factors. As one of the significant problems in agricultural production, salt stress is one of the main abiotic stress factors. The negative influences of salt stress on seed germination are mainly reflected in the potent inhibition of enzyme activity. The internal metabolism system of reactive oxygen species (ROS) of seeds under salt stress would lose balance, causing a substantial gathering of free radicals, which resulted in the injuries of the membrane structures and abnormal states of selective permeability furthermore. It can be speculated that improving endogenous metabolism could have improved the germination of seeds under abiotic stress, for example, salt stress.

In this paper, PAW processed for different durations was used to treat cucumber seeds by immersing before and during seed germination to investigate the influences of PAW on seed germination. It is generally considered that the effective substance acting in the treatment is RONS. RONS can participate in the metabolism, acting as signal molecules. As a kind of ROS, the half-lives of H_2O_2 are relatively long and can be transported across membranes. Thus, H_2O_2 can be a kind of ideal signal molecule to act as an exogenous regulator. The current studies indicated that a proper concentration of exogenous H_2O_2 can relieve the inhibition of cucumber seed germination due to salt stress by mediating the synthesis of ABA and GA and increasing the activity of ant oxidase. As for reactive nitrogen radicals (RNS), the nitrogen in RNS is essential for the growth of plants. In addition, RNS in PAW, including NO_3^- , NO_2^- , and some other particles that contain nitrogen, can also act as the signal molecules to regulate gene expression, similar to ROS. Nevertheless, too many RONS will also bring metabolic disorders and, consequently, a decrease in germination.

To sum up, RONS in PAW were absorbed in seeds and accumulated, and then participated in the various metabolic procedure acting as a kind of signal molecule. Proper concentrations of RONS would lighten the inhibition of kinds of enzymes and consequently increase the germination of seeds treated by PAW. It is worth noting that, except for various radicals generated by underwater discharges, the overall physical and chemical characters, such as a slightly acidic environment and specific values of OPR, also make contributions to the increase of seed germination.

The mechanism how PAW treatment affected cucumber seed germination under salt stress was investigated briefly. Further investigation into definite mechanisms still needs to be combined with methods such as genomics.

5 Conclusions

In this paper, the effect of PAW treatment on seeds under salt stress was investigated, and several germination characters were chosen to evaluate this effect comprehensively. The following conclusions have been drawn:

- (1) PAW treatment can improve cucumber seed germination rate, shorten the mean germination time of cucumber seeds in salt-free environments, and relieve the inhibition of cucumber seed germination due to salt stress. However, not all the PAW processed by additional time could bring better germination. In this paper, PAW processed for 10 min was much better than PAW processed for 20 min or 30 min.
- (2) The proposed mechanism of how PAW treatment improved the germination of cucumber seeds was RONS generated in PAW. PAW treatment modified the surface morphology of seeds so that the capacity of seeds to absorb water could be better. The RONS accumulated in seeds affected the metabolism in seed cells, and the macro performance of seeds treated would be increases in germination rate, potential, and velocity of cucumber seeds.

- (3) PAW in this paper was prepared by gas–liquid two-phase plasma discharge driven by a self-made microsecond pulse power source. PAW was prepared for different durations. As the durations extended, the pH of PAW descended, the electrical conductivity and the oxidation–reduction potential ascended, and the concentrations of NO_3^- and H_2O_2 were higher. The energy efficiency of PAW was highest when PAW was processed for 10 min according to the duration gradient set in this paper. The gradient in this paper was few, and the best efficiency point still needed to be deeply investigated.

References

1. Hossain S (2019) Present Scenario of global salt affected soils, its management and importance of salinity research. *Int Res J Biol Sci* 1
2. Liu L, Wang B (2021) Protection of halophytes and their uses for cultivation of saline-alkali soil in China. *Biology* 10:353
3. Pańka D, Jeske M, Łukanowski A (2022) Can Cold plasma be used for boosting plant growth and plant protection in sustainable plant production? *Agronomy* 12:841
4. Attri P, Ishikawa K, Okumura T (2006) Plasma agriculture from laboratory to farm: a review. *Processes* 8:1002; Finch-Savage WE, Leubner-Metzger G (2006) Seed dormancy and the control of germination. *New Phytol* 171:501–523
5. Darmanin M, Kozak D (2020) Generation of plasma functionalized water: antimicrobial assessment and impact on seed germination. *Food Control* 113:107168
6. Fan L, Liu X, Ma Y (2020) Effects of plasma-activated water treatment on seed germination and growth of mung bean sprouts. *J Taibah Univ Sci* 14:823–830
7. Guragain RP, Pradhan SP, Baniya HB (2021) Impact of plasma-activated water (PAW) on seed germination of soybean. *J Chem* 2021:1–12
8. Iranbakhsh A, Ardebili NO, Ardebili ZO (2018) Non-thermal plasma induced expression of heat shock factor A4A and improved wheat (*Triticum aestivum* L.) growth and resistance against salt stress. *Plasma Chem Plasma Process* 38:29–44
9. Lo Porto C, Ziuzina D, Los A (2018) Plasma activated water and airborne ultrasound treatments for enhanced germination and growth of soybean. *Innov Food Sci Emerg Technol* 49:13–19
10. Rezaei F (2019) Applications of plasma-liquid systems: a review. *Materials* 12:2751
11. Sajib SA, Billah M, Mahmud S (2020) Plasma activated water: the next generation eco-friendly stimulant for enhancing plant seed germination, vigor and increased enzyme activity, a study on black gram (*Vigna mungo* L.). *Plasma Chem Plasma Process* 40:119–143
12. Sivachandiran L (2017) Enhanced seed germination and plant growth by atmospheric pressure cold air plasma: combined effect of seed and water treatment. *RSC Adv* 7:1822–1832
13. Anpilov AM, Barkhudarov EM, Kossyi IA (2021) High-voltage pulsed discharge at the gas-liquid interface in a multiphase system. *Tech Phys* 66:675–680
14. Zhou R, Zhou R, Wang P (2020) Plasma-activated water: generation, origin of reactive species and biological applications. *J Phys D: Appl Phys* 53:303001

Ultrasonic Image Recognition of Terminal Lead Seal Defects Based on Convolutional Neural Network



Linggang Zhou, Wenhui Li, Xin Lu, Xueyan Wang, Huan Liu, Junzhe Liang, Fenggeng Jiang, and Gu Zhou

Abstract At present, high-voltage cables are widely used in urban power grid transmission projects. As an important part of high-voltage cable terminal accessories, lead seals at high-voltage cable terminals will have defects such as holes, cracks or debonding due to unqualified installation quality or external forces during operation, affecting the safe and stable operation of power systems. The traditional ultrasonic phased array detection method for lead seal defects is to process the ultrasonic defect image and observe it manually, which has low efficiency and accuracy. Traditional machine learning methods need to manually select the detection object features, lack of adaptability and robustness, and have low accuracy of target detection. In order to improve the intelligent level of lead seal defect detection, an ultrasonic image recognition method of lead seal defect based on convolutional neural network is proposed, which can automatically learn features from the ultrasonic image of lead seal defect and complete defect classification and recognition. The ultrasonic image sample library of four typical lead seal defects was established, and the ultrasonic image recognition model of lead seal defects was built. The model was trained and tested by using standardized ultrasonic image data. The results show that by adjusting the convolution neural network test parameters, different types of defects in lead seal can be quickly and accurately identified, and the accuracy rate can reach 100%. It shows that the method has good robustness, strong anti-interference ability and good detection performance for lead seal defects, and has a good application prospect in the actual terminal lead seal defect detection.

Keywords Cable terminal · Lead seal · Image recognition · Convolutional neural network · Defect detection

L. Zhou · W. Li · X. Lu · H. Liu · J. Liang · G. Zhou (✉)

State Grid Zhejiang Electric Power Co., Ltd. Taizhou Power Supply Company, Zhejiang 318000, China

e-mail: 3141279874@qq.com

X. Wang

Taizhou Hongchuang Power Group Co., Ltd. Technology Branch, Zhejiang 318000, China

F. Jiang

State Grid Zhejiang Xinxing Technology Co., Ltd, Zhejiang 318000, China

© Beijing Paiké Culture Commu. Co., Ltd. 2024

X. Dong and L. Cai (eds.), *The Proceedings of 2023 4th International Symposium on Insulation and Discharge Computation for Power Equipment (IDCOMPU2023)*, Lecture Notes in Electrical Engineering 1100, https://doi.org/10.1007/978-981-99-7393-4_8

1 Introduction

With the continuous improvement of urban modernization level in China, the development of urban power systems is also changing with each passing day. In order to solve the electricity demand of urban load centers, the main way is to develop efficient and stable large-capacity power transmission and transformation projects. High-voltage cross-linked polyethylene single-core power cable is more and more widely used in urban transmission projects because of its excellent electrical performance, heat resistance, high safety, small land occupation and easy installation [1]. The high-voltage cable terminal can connect the cable with other power equipment. It is an indispensable part of long-distance transmission and plays a vital role in the safe and stable operation of the power system. As one of the key processes for the manufacture of high-voltage cable terminal accessories, lead seals can connect metal sheaths and other electrical equipment into a good grounding system and play an important role in sealing and waterproofing [2–4].

Due to the unqualified installation quality of manual field operation or the influence of uncontrollable factors such as external force damage and poor environment in actual operation, the lead seal of high voltage cable terminal will have defects such as holes, cracking or debonding [5–7]. After loosening, the lead seal will induce a high floating potential. At this time, the potential of the copper tail pipe is low, and there will be a potential difference between the two, forming air breakdown discharge. During the process of air ionization, high temperatures of thousands of degrees will be generated. Under the action of high temperatures, the main insulation of the cable will gradually carbonize, and the insulation performance will rapidly decline, ultimately leading to serious high-voltage cable breakdown faults, affecting the safe and stable operation of the power system [8–10]. The ultrasonic phased array detection method has been widely used in non-destructive testing of high-voltage post insulators and composite insulators due to its outstanding advantages such as wide scanning range, clear defect images, high detection efficiency, obvious defect echoes, and accurate defect positioning [11–13]. Applying the ultrasonic phased array detection method to the detection of lead seal defects in cable terminals requires on-site experienced technicians to effectively observe and determine the type of lead seal defects now. It requires a lot of manual support. In addition to wasting a lot of time and increasing unnecessary costs, the detection efficiency and accuracy cannot be guaranteed [14].

Traditional machine learning requires manual selection of detection object features, which lacks adaptability and robustness. In recent years, intelligent inspection technology and deep learning technology have been widely used in industrial defect recognition with strong target detection ability and image processing ability. Masci J et al. studied the defect detection and recognition of industrial steel surface by using convolutional neural network, and compared the accuracy of defect detection and recognition between convolutional neural network and feature filter, which fully proved the effectiveness and superiority of convolutional neural network for defect detection and recognition [15].

In this paper, convolutional neural network is applied to the detection of lead seal defects in cable terminals. By studying the influence of different convolution kernel sizes of convolutional neural network on the detection effect, the best detection model parameters are found. Through the constructed CNN network, the automatic feature learning and pattern recognition of ultrasonic image samples of lead seal defects can be realized, which avoids the problems of misjudgment and low efficiency caused by manual diagnosis and recognition of lead seal defects in traditional methods, and provides a new method for lead seal defect detection in high voltage cable terminals.

2 Basic Theory of Convolutional Neural Network

Convolutional neural network is a two-dimensional network model, which can directly perform convolution operations on two-dimensional data. It can effectively reduce the complexity of the feedback neural network and make image data processing more convenient and faster. It has been widely used in the field of natural speech analysis and image detection and recognition [16, 17].

2.1 Convolutional Neural Network Structure

The convolutional neural network structure is shown in Fig. 1, which is mainly composed of five parts: input layer, convolution layer, pooling layer, fully connected layer and output layer. In the convolutional neural network, the convolutional layer and the pooling layer are alternately connected by one layer, and one or more full-link layers are usually connected behind the pooling layer.

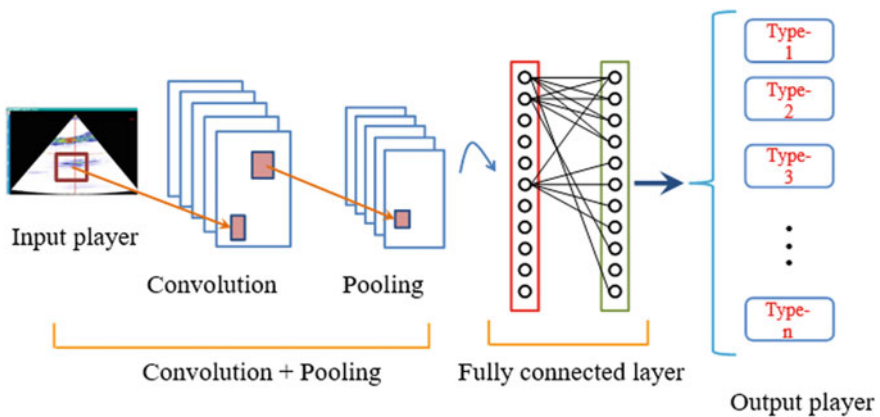


Fig. 1 Convolutional neural network structure

The convolutional layer is an important component of the convolutional neural network. It contains several feature maps. Neurons can form a feature map through a certain rectangular arrangement. The neurons of the same feature map share weights, and the convolution kernel is the shared weight. The convolution operation is a linear operation. The convolution operation can be described as:

$$y_m^l = f\left(\sum_n x_n^{l-1} \otimes \omega_m^l + b_m^l\right) \quad (1)$$

In the formula: y_m^l is the output of the n filter in the l layer of the convolution operation; $f(\cdot)$ represents the activation function used by the convolutional layer; x_n^{l-1} denotes the m feature map in the $l - 1$ layer; \otimes for convolution operation; b_m^l represents bias.

The pooling layer, also known as the sampling layer, generally follows the convolution layer. According to a certain pooling rule, a sampling operation is performed after feature extraction, which is to combine the similar regional features extracted after convolution. Through the pooling operation, the number of training parameters can be significantly reduced and the network training speed can be accelerated. It can also prevent overfitting. The common pooling methods are maximum pooling, average pooling and random pooling. If the sampling width of the pooling process is $q \times 1$, the output result when the sampling layer S matches the k th convolution kernel is:

$$a_{S,j,k} = \frac{\sum_{i=jq-q+1}^{jq} a_{C,i,k}}{q} \quad (2)$$

In the formula: $a_{C,i,k}$ represent the i element of the output of the k convolution kernel; $a_{S,j,k}$ represents the j output of the layer corresponding to the k th convolution kernel.

In the ultrasonic image classification model of lead seal defects, the fully connected layer is connected after the convolution layer and the pooling layer, and the soft max layer is added as the output layer. The fully connected layer and the soft max layer are applied to the end of the network to automatically classify the lead seal defects. The output of the fully connected layer can be expressed as:

$$f_x^{l+1} = \delta(W_{f_x}^l \alpha^l + n_{f_x}^l) \quad (3)$$

In the formula: f_x^{l+1} is the network $l + 1$ layer output; $n_{f_x}^l$ and $W_{f_x}^l$ represent the bias matrix and weight matrix of the first layer of the network respectively; and represent the l th layer bias matrix and weight matrix of the network respectively; α^l is the input of the network.

2.2 Convolutional Neural Training Method

The feature information of the lead seal ultrasonic image can be extracted by a series of operations such as convolution, pooling, and activation function in the convolutional neural network. Finally, the image category information is classified by the fully connected layer. The training model uses the back propagation algorithm to optimize the network structure and solve the network parameters. The error can be fed forward from the last layer by layer, and the objective function can be converged to the preset range, so that the error of each layer is reduced and the image recognition accuracy is improved.

3 Lead Seal Defect Recognition Based on Convolutional Neural Network

3.1 Image Recognition Process

The lead seal defect recognition process based on convolutional neural network is shown in Fig. 2, which mainly includes four stages: lead seal ultrasonic image acquisition, ultrasonic image preprocessing, model training and defect image recognition.

3.2 Lead Seal Defect Detection Platform

The ultrasonic phased array flexible coupling detection cable terminal lead seal defect test platform is shown in Fig. 3. It is mainly composed of cable terminal lead seal sample, ultrasonic probe, flexible coupling device, power supply, digital controller and display system. The ultrasonic phased array detection equipment used in this test is provided by Wuhan Zhong Ke Innovation Technology Co. L. and the model of the equipment is Hanwei HS PA20-A. The model of ultrasonic phased array probe is ZKCX3210.

In this paper, a large number of lead seal image samples of high-voltage cable terminal are collected through experiments. According to the characteristics of ultrasonic images, whether the lead seal has defects and their defect types are judged. The collected lead seal ultrasonic images are mainly classified into four types: lead seal without defects, lead seal internal defects, lead seal interlayer defects and lead seal internal and interlayer defects. A total of 144 lead seal ultrasonic image samples of cable terminals were collected after preliminary collection and screening. Some samples of lead seal defect images are shown in Fig. 4. In order to improve the generalization ability of the lead seal defect recognition model, random flipping and random rotation are used to enhance the data. The expanded database has a

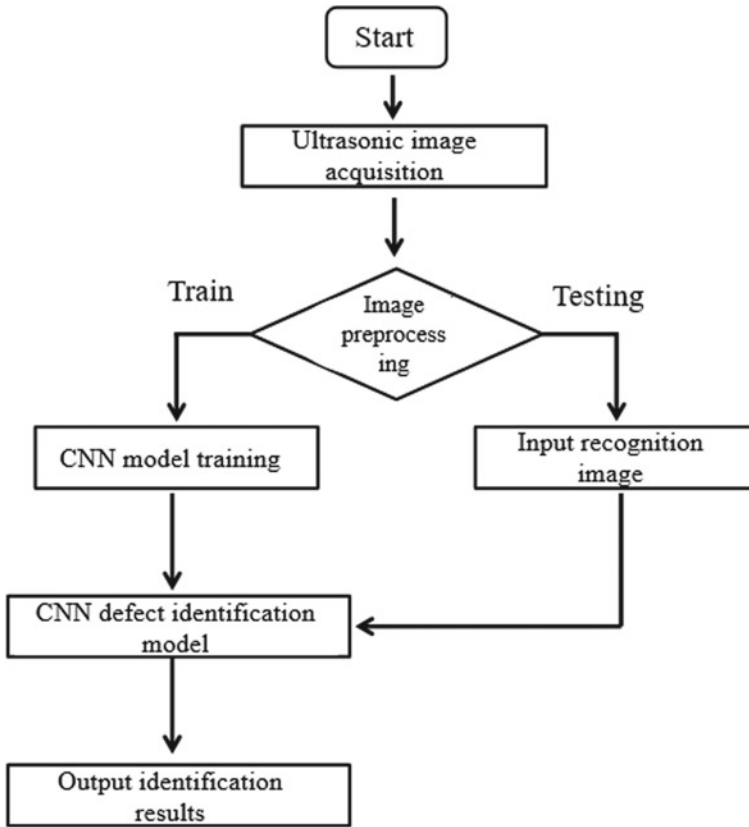


Fig. 2 Sealing defect identification flow chart

total of 1728 cable terminal lead seal defect image samples, including 276 defect-free samples, 492 internal defect samples, 552 interlayer defect samples, and 408 samples with both internal and interlayer defects.

3.3 CNN Network Model Establishment

The lead seal automatic recognition platform based on convolutional neural network mainly consists of hardware, software, and deep learning framework.

The hardware environment of the experiment is: Intel (R) Core (TM) i5-8500 CPU, Intel (R) UHD Graphics 630 GPU;

The software environment is: deep learning open source framework GoogLeNet, Windows10 operating system, MATLAB 2021a and sample image library to be tested.

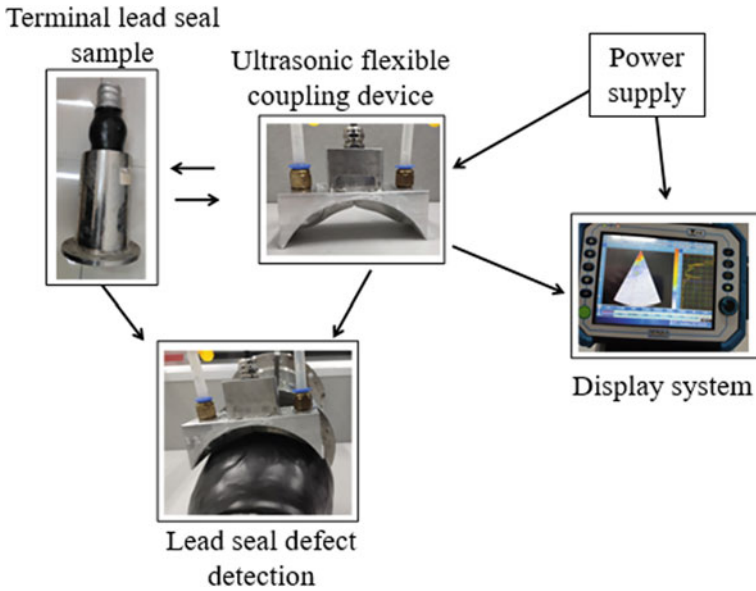


Fig. 3 Ultrasonic flexible coupling lead seal defect detection platform

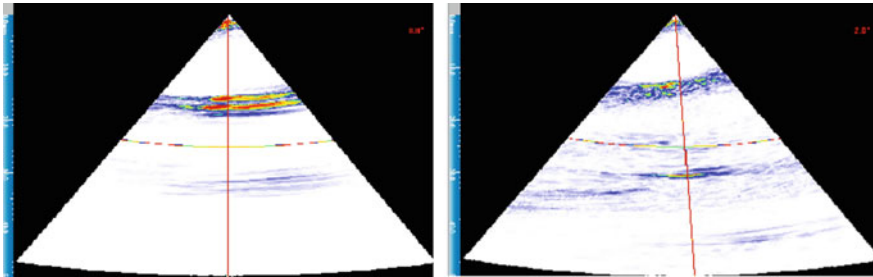


Fig. 4 Lead seal ultrasonic test image

A total of 1380 samples were randomly selected from the data-enhanced samples as training samples, and the remaining 348 samples were used as validation set test sets. The distribution of four sample sets of cable terminal lead seal is shown in Table 1.

The ultrasonic images of lead seal defects are uniformly planned into an image of 224×224 pixels as the input sample set. Finally, the input terminal lead seal samples are trained and tested.

Table 1 Distribution of lead seal sample sets in various states

Classification	No defect	Internal defect	Interlaminar defect	Internal and interlayer defects
Training set	216	396	444	324
Validation set	30	48	54	42
Test set	30	48	54	42

4 Experimental Result Analysis

4.1 A Subsection Sample

In the study of recognition and classification of lead seal defect images, it can be found that the number of convolution kernels in the convolution layer will affect the types of features extracted, which will change the performance of the convolution neural network, thus affecting the accuracy of defect recognition. Therefore, several experiments were carried out on convolution kernels of different sizes. The number of training iterations was 2300 times, 100 times per iteration, and the training results were tested once. The recognition results of different convolution kernels were compared and analyzed. The model loss value changes with the number of iterations during the training process as shown in Fig. 5, and the accuracy rate changes with the number of iterations during the training process as shown in Fig. 6, the training results after the training is stable are shown in Table 2.

The experimental results show that the loss value of the lead seal defect recognition model decreases rapidly and the accuracy increases rapidly before 800 training iterations. When the training iteration is about 1000 times, the lead seal defect recognition model begins to converge, and the model loss value and accuracy have stabilized. When the convolution kernels are 11×11 and 13×13 respectively, during the training process of the model, the change curves of the loss value and the accuracy rate fluctuate obviously. The whole process is not smooth enough, and the accuracy of the trained model does not reach 100%, only about 95% and 96%. When the size of the convolution kernel is 7×7 and 9×9 respectively, the accuracy of the trained model for lead seal defect detection is 100%, and the loss values are only 0.003921 and 0.008435, indicating that the model has reached the highest value of detection learning for lead seal defect recognition training, and can identify and test the actual lead seal defect image. Through comparison, it is found that when the convolution kernel is 9×9 , the change process of loss value and accuracy in the training process is smoother, the loss value is reduced from the initial 1.4 to about 0.008, and the accuracy is increased from 27 to 100%. The whole process fluctuates less and the overall effect of training is better. Therefore, the size of the convolution kernel is set to 9×9 to train the model, and then the actual test experiment is carried out.

As shown in Fig. 7, the confusion matrix is obtained when the convolution kernel size is 9×9 . The horizontal axis represents the actual classification of the input,

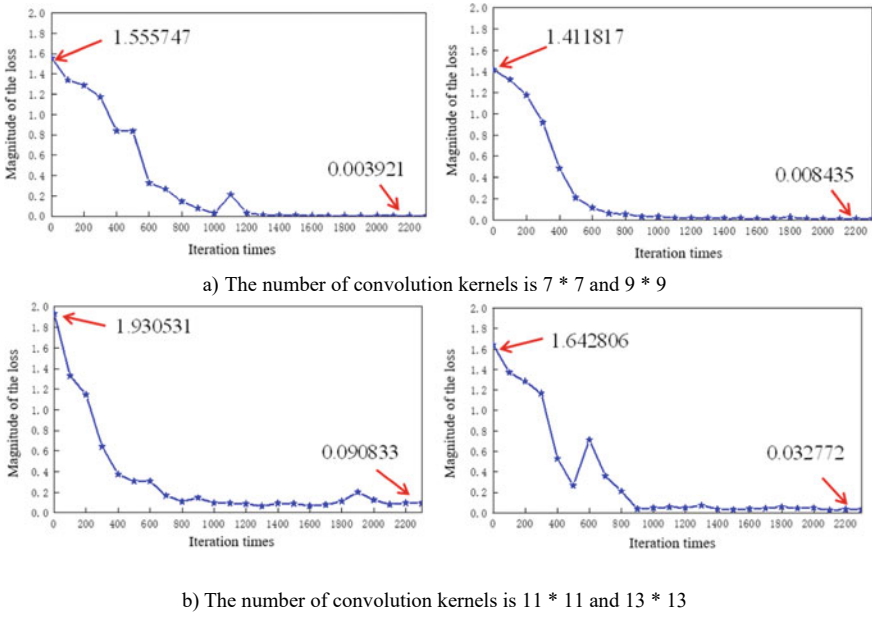


Fig. 5 The change curve of the loss value of different convolution kernel numbers

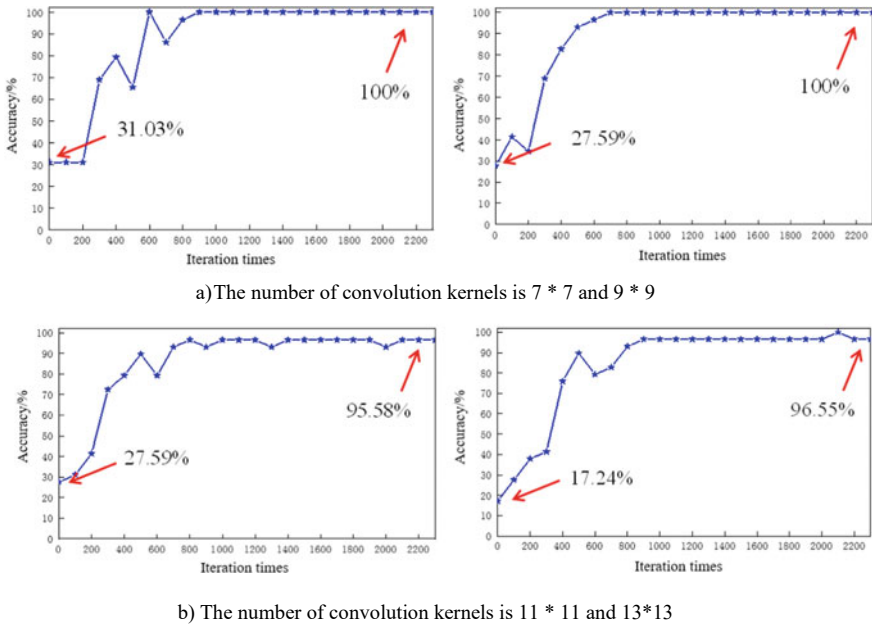


Fig. 6 The change curve of the accuracy rate of different convolution kernel numbers

Table 2 Training results with different number of convolution kernels

Number of convolution kernels	Magnitude of the loss	Accuracy/%
7×7	0.003921	100
9×9	0.008435	100
11×11	0.090833	95.58172
13×13	0.032772	96.55172

and the vertical axis represents the predictive classification of the output. It can be found that the ultrasonic images of different types of high-voltage cable terminal lead seal defects are input into the trained model. The coincidence between the predicted classification and the actual classification is 100%, indicating that the lead seal image defect type of each input can be accurately predicted 100%. The experimental results show that the model has high accuracy in detecting different types of lead seal defects.



Fig. 7 Confusion matrix with kernel size 9×9

5 Conclusion

In this paper, the feasibility and effectiveness of lead seal defect detection of high voltage cable terminal based on convolutional neural network are verified by combining ultrasonic detection method with deep learning algorithm. Different types of lead seal defect images were obtained by using the ultrasonic phased array flexible coupling lead seal defect detection platform. After the ultrasonic image was pre-processed, the ultrasonic image was trained by the constructed convolutional neural network. The most suitable parameters were selected through multiple trainings to obtain the optimal network model and realize the automatic identification of lead seal defects. For the sample library in this paper, the model can accurately identify the ultrasonic image of the terminal lead seal defect, and the recognition rate can reach 100%, which has a good recognition effect and verifies the effectiveness of the method. The next work will further expand the lead seal ultrasonic image data set, expand the application scope of convolutional neural network in terminal lead seal defect detection, and use it in actual field defect detection.

References

1. Wang G (2019) Research on power cable laying technology in power engineering construction. *China High-tech* 02:86–88 (in Chinese)
2. Shao S, Ma X, Feng R et al (2021) Review of domestic and foreign research on power cables. *Wire and Cable* 03:1–6+10 (in Chinese)
3. Zhou C, Zhao H, Ren P (2021) Improvement of lead sealing process for high-voltage cable accessories. *Northeast Electr Power Technol* 42(02):23–26+29 (in Chinese)
4. Cao J, Zha X, Chen J et al (2018) 220 kV cable line terminal fault and simulation analysis. *Power Eng Technol* 37(06):151–155 (in Chinese)
5. Yang J, Liu X, Yu L (2021) Research on the detection method of high voltage cable lead seal crack defect. *Dazhong Electric Power* 36(08):41–42 (in Chinese)
6. Tan Y (2018) 110 kV cable terminal fault analysis and preventive measures. *China High-tech* 15:105–107 (in Chinese)
7. Chen H, Li L, Xia Z et al (2019) Ultrasonic phased array flexible coupling detection of internal defects in composite insulators. *High Voltage Technol* 45(04):1274–1280 (in Chinese)
8. Ma J, Sun X, Li S et al (2019) Defect detection and location of basin-type insulators based on ultrasonic guided waves. *High Voltage Technology* 45(12):3941–3948 (in Chinese)
9. Deng H, He Z, Chen L (2019) Ultrasonic guided wave detection of debonding defects in composite insulators. *High Voltage Technol* 45(01):196–202 (in Chinese)
10. Fang C, Hu D, Guo K et al (2022) Research on ultrasonic testing method for lead seal defects of high voltage cable terminals. *China Test* 48(03):118–123 (in Chinese)
11. Ma H, Yu X, Lv Q et al (2022) Application of one-dimensional convolutional neural network in fault diagnosis of reciprocating compressor valve. *J Xi'an Jiaotong Univ* 56(04):101–108 (in Chinese)
12. Chang H, Gou J, Li X (2018) Application of faster R-CNN in industrial CT image defect detection. *Chin J Image Graph* 23(07):1061–1071 (in Chinese)
13. Chang L, Deng X, Zhou M et al (2016) Convolutional neural networks in image understanding. *J Autom* 42(9):1300–1312 (in Chinese)

14. Faghih-Roohi S, Siamak H, Núez A et al (2016) Deep convolutional neural networks for detection of rail surface defects. In: International joint conference on neural networks (IJCNN 2016). IEEE
15. Yuan C, Xie C, Li L et al (2016) Ultrasonic phased array detection of internal defects in composite insulators. *IEEE Trans Dielectr Electr Insul* 23(1):525–531
16. Simes RJ, Pedrosa A, Pereira W et al (2016) A complete COMSOL and MATLAB finite element medical ultrasound imaging simulation. In: ICA 2016
17. Jing L, Zhao M, Li P et al (2017) A convolutional neural network based feature learning and fault diagnosis method for the condition monitoring of gearbox. *Measurement* 111:1–10

Temperature Distribution and Influencing Factors of 110 kV Single Core Cable Joint



Lei Zhang, Rui Li, Liangyuan Chen, Shaoming Pan, and Xiajin Rao

Abstract To realize the dynamic capacity increase of power cable and accurately grasp the temperature distribution in the weakest cable joint area, a two-dimensional axisymmetric model of 110 kV cable joint is established. The temperature field of cable joint is calculated by finite element method in this paper. The conclusion is: when the ambient temperature is 25 °C and the load current is 1000 A, the hottest spot temperature of cable joint is 80.93 °C, the shell temperature is about 26.37 °C, and the cable core temperature of cable body is about 56.68 °C. The temperature of the cable core inside the cable joint has an approximate exponential relationship with the load current and a linear relationship with the ambient temperature. When the load current is 1100 A, the cable core temperature exceeds 90 °C specified in GB/T 11017.2. Excessive temperature will lead to accelerated aging of the insulation and affect the normal operation life of the cable. This provides a reference for the implementation of power cable dynamic capacity increase measures.

Keywords Cable joints · Temperature field · Influencing factors · Dynamic capacity increase

1 Introduction

Power cables have the advantages of smaller floor area, higher power supply reliability and less affected by environmental factors than overhead lines. They are suitable for urban power systems and high-voltage transmission. As a cable accessory, the

L. Zhang (✉) · R. Li · L. Chen · S. Pan · X. Rao
Guangxi Key Laboratory of Intelligent Control and Maintenance of Power Equipment, Electric Power Research Institute of Guangxi Power Grid Co., Ltd., Nanning 530023, Guangxi, China
e-mail: 464873459@qq.com

L. Chen
e-mail: chen_jy.sy@gx.csg.cn

X. Rao
e-mail: rao_xj.sy@gx.csg.cn

© Beijing Paiké Culture Commu. Co., Ltd. 2024
X. Dong and L. Cai (eds.), *The Proceedings of 2023 4th International Symposium on Insulation and Discharge Computation for Power Equipment (IDCOMPU2023)*, Lecture Notes in Electrical Engineering 1100, https://doi.org/10.1007/978-981-99-7393-4_9

cable joint is a part prone to insulation accidents in the process of electric energy transmission, and is easily affected by factors such as production process and on-site installation level. Once partial discharge or high temperature rise occurs, it will lead to serious insulation deterioration of cable joints and affect the carrying capacity of transmission lines. After a certain period of operation, insulation breakdown and even explosion accidents often occur, which has become one of the important problems endangering the power supply safety of urban distribution networks. Therefore, the research on the temperature rise of cable joints has important engineering value and practical significance [1–3].

Foreign research on the temperature rise of cables and cable joints started early, and the early research methods were mainly analytical methods [4, 5]. At the end of the twentieth century, scholars formulated relevant standards for cable temperature rise and Ampacity [6, 7]. At present, the research methods mainly include direct temperature measurement method [8, 9] and indirect temperature measurement method. The latter includes thermal path model method [10], numerical calculation method [11–13], data mining method [14, 15], etc. Direct temperature measurement method is built-in temperature measurement module to monitor the joint temperature in real time. It is intuitive but affects temperature transmission, and its reliability is low. Thermal circuit modeling method is to establish a model including thermal resistance, heat capacity and other parameters, and establish the heat flow, thermal resistance and heat capacity analogous to current, resistance and capacitance with reference to the concept of circuit. The disadvantage is that it cannot reflect the axial temperature rise process. Numerical mining method uses intelligent algorithm to establish the relationship between eigenvalues and internal joint temperature, and realize temperature inversion. The disadvantage is that it cannot reflect the real physical process and does not involve the study of heat transfer mechanism. Numerical methods, including finite element method, can better reflect the physical heat transfer process and calculate the temperature distribution.

The structure of single core cable joint is complex. Considering its symmetry, this paper establishes a two-dimensional axisymmetric model of 110 kV cable joint, calculates its temperature field by finite element method, and explores the influence of ambient temperature and load current on the temperature distribution of cable joint.

2 Single Core Cable Joint Model

2.1 Cable Joint Model Parameters

The calculation model refers to the cable model YJLW03-Z 64/110 kV 630 mm². The cable body structure is composed of cable core, cross-linked polyethylene (XLPE), waterstop, aluminum sheath, EPDM prefabricated parts and outer sheath from inside to outside. The cable joint structure is composed of joint resistance, crimping pipe,

shielding cover, EPDM prefabricated parts, copper shell, waterproof sealant and FRP shell from inside to outside. The total length of the cable is set at 10 m, The cable body and joint structure are shown in Fig. 1, and the outer diameter, thermal conductivity, density, specific heat capacity and other parameters of each material are shown in Table 1.

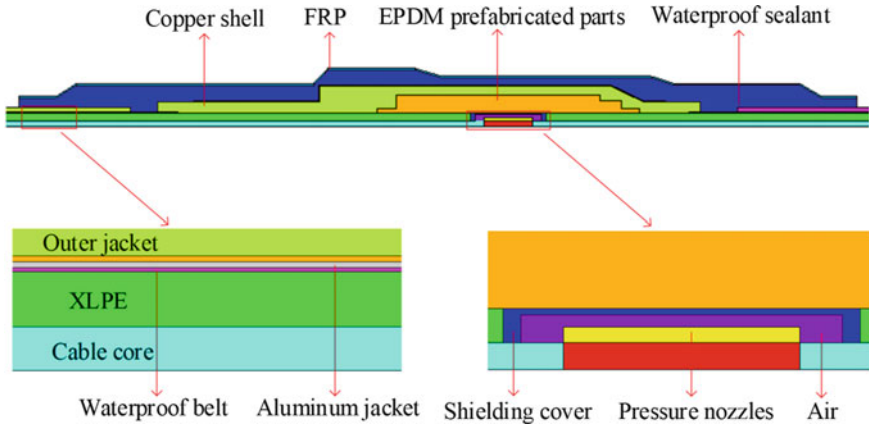


Fig. 1 Structure diagram of 110 kV cable joint

Table 1 Cable and connector parameters

Components	Parameters			
	Outer diameter (mm)	Thermal conductivity ($W m^{-1} K^{-1}$)	Density ($kg m^{-3}$)	Specific heat capacity ($J kg^{-1} K^{-1}$)
Cable core	30	383	8889	390
XLPE	68	0.4	920	2500
Waterproof belt	70.5	0.6	600	2000
Aluminum jacket	78.5	218	2780	883
Outer jacket	98	0.5	950	1842
Shielding cover/ pressure nozzles/ copper shell	–	383	8889	390
EPDM prefabricated parts	–	0.45	1030	2219
Waterproof sealant	–	0.04	1050	1750
FRP	–	1.85	1850	535

2.2 Governing Equation of Temperature Field

The thermal conductivity of the material is set as a constant, and the temperature field control equation is divided into transient thermal analysis and steady-state thermal analysis, as shown in the following formula:

$$\begin{cases} \frac{\partial^2 t}{\partial x^2} + \frac{\partial^2 t}{\partial y^2} + \frac{\partial^2 t}{\partial z^2} + \frac{\Phi}{\lambda} = 0 \\ \rho c \frac{\partial t}{\partial \tau} = \lambda \frac{\partial^2 t}{\partial x^2} + \lambda \frac{\partial^2 t}{\partial y^2} + \lambda \frac{\partial^2 t}{\partial z^2} + \Phi \end{cases} \quad (1)$$

where, t is the temperature, K; c is the specific heat capacity, J/(kg K); τ is time, s; ρ is the density, kg/m³; λ is the thermal conductivity of the thermal conductive material, W/(m K); Φ is the heat generation, W/m³.

There are three types of boundaries related to heat transfer. The first type of boundary conditions is a known boundary temperature function, which can be expressed as:

$$T|_{\Gamma} = T_w \quad (2)$$

where, Γ is the integral boundary; T_w is the known temperature boundary, K.

The second kind of boundary condition is the known boundary normal heat flux, which is expressed as:

$$-\lambda \left. \frac{\partial T}{\partial n} \right|_{\Gamma} = q \quad (3)$$

where, λ is the thermal conductivity, W/(m K); q is the known heat flux, W/m².

The third type of boundary condition is the convective boundary condition, which is expressed as:

$$-\lambda \left. \frac{\partial T}{\partial n} \right|_{\Gamma} = \alpha(T - T_f)|_{\Gamma} \quad (4)$$

where, α is the convective heat transfer coefficient, W/(m² K); T_f is the fluid temperature, K.

For cable joints and adjacent areas, since the test cable is exposed to the air, the cable surface and air are the third kind of boundary conditions; For the end of the cable body, it belongs to the second kind of boundary conditions. Because it is far away from the cable joint, it is little affected by its temperature. There is only radial heat flow in the cable body, and there is no axial heat flow, that is, the normal heat flow density is 0.

2.3 Heat Source Analysis

The heat source comes from two parts, namely, the conductor heating at the cable core and crimping pipe of the cable body, which are Joule heat generated by current, as shown in Fig. 2.

The two heat sources are calculated by the following formula:

$$G_1 = \frac{W_1}{V} = \frac{I^2 \times R_1}{3.14 \times r_1^2} = \frac{I^2}{3.14 \times r_1^2} \times \frac{\rho}{3.14 \times r_1^2} = \frac{I^2 \times \rho}{3.14 \times r_1^4} \tag{5}$$

$$G_2 = \frac{W_2}{V} = \frac{I^2 \times R_j}{3.14 \times r_2^2 \times l} \tag{6}$$

where, ρ is the resistivity of copper conductor, $\rho = 1.75 \times 10^{-8} \Omega \text{ m}$; l is the total length of crimping pipe, $l = 0.133 \text{ m}$; r_1 and r_2 are the radius of copper and crimping pipe respectively, $r_2 = 0.0237 \text{ m}$; $G_1 = I^2 \times 0.035$; $G_2 = I^2 \times 0.0217$; the measured resistance R_j is $5.1 \mu\Omega$.

3 Temperature Field Distribution of Single Core Cable Joint

The cable length is 10 m, and the third type of boundary conditions are loaded on the cable surface. The temperature of the initial cable and connector should be consistent with the ambient temperature, both of which are $25 \text{ }^\circ\text{C}$, and the convection heat transfer coefficient is $8 \text{ W}/(\text{m}^2 \text{ K})$. The end of the cable body is the second kind of boundary condition, and the cable core current is 1000 A. The temperature distribution is shown in Fig. 3.

The hottest spot temperature appears at the cable core inside the cable joint, where the temperature reaches $80.93 \text{ }^\circ\text{C}$. This is because the contact resistance at the crimping pipe is large, resulting in the highest temperature. The lowest temperature occurs at the FRP shell, where the temperature is $26.37 \text{ }^\circ\text{C}$, close to the ambient temperature of $25 \text{ }^\circ\text{C}$. The temperature of the cable body gradually decreases from

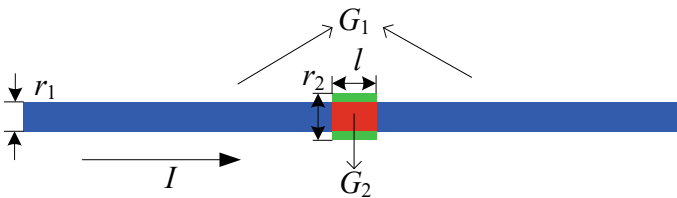
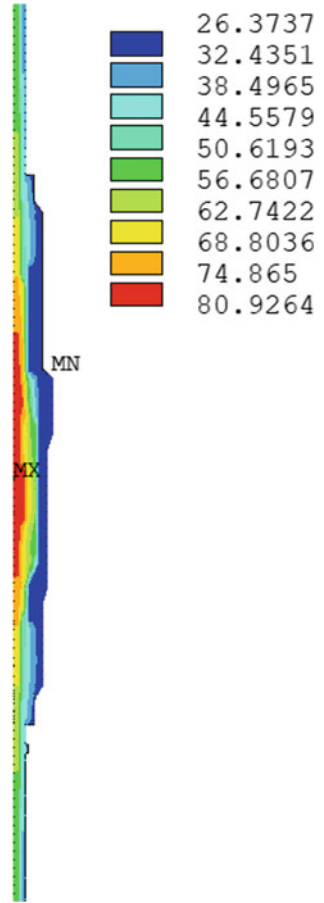


Fig. 2 Schematic diagram of cable heat source loading

Fig. 3 Temperature field distribution of 110 kV cable joint (°C)



the cable joint to both sides, and the temperature of the cable body is about 56.68 °C. From the internal cable core to the FRP shell, the temperature gradually decreases and the distribution is uneven, which is because, compared with the cable body, the structure at the joint is more complex, the distribution of various materials is more uneven, and the thermal conductivity is also different.

4 Influencing Factors of Cable Joint Temperature

4.1 Load Current

Keep the parameters and initial ambient temperature of each structure of the cable model unchanged, and change the load current to 600 A, 700 A, 800 A, 900 A, 1000 A and 1100 A respectively, recalculate the temperature field, and explore the impact of load current on the joint temperature. The temperature distribution under different load currents is shown in Fig. 4, the change curve is shown in Fig. 5.

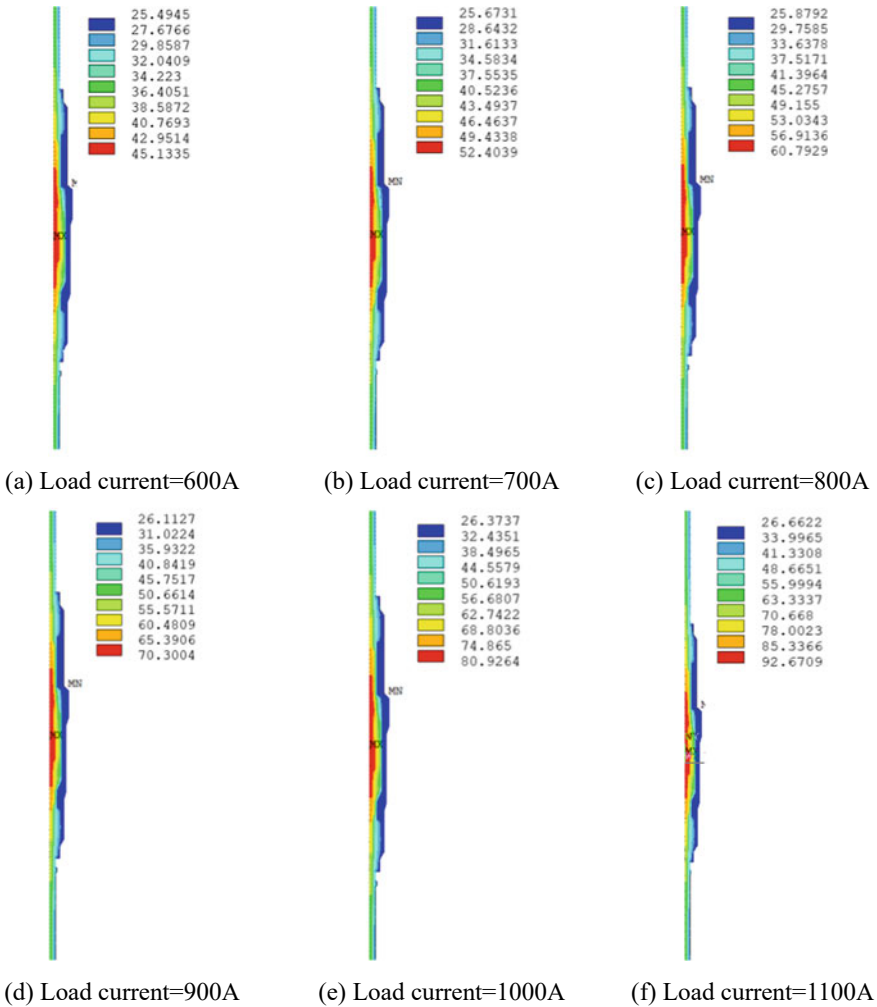


Fig. 4 Temperature field distribution of cable joint under different load currents (°C)

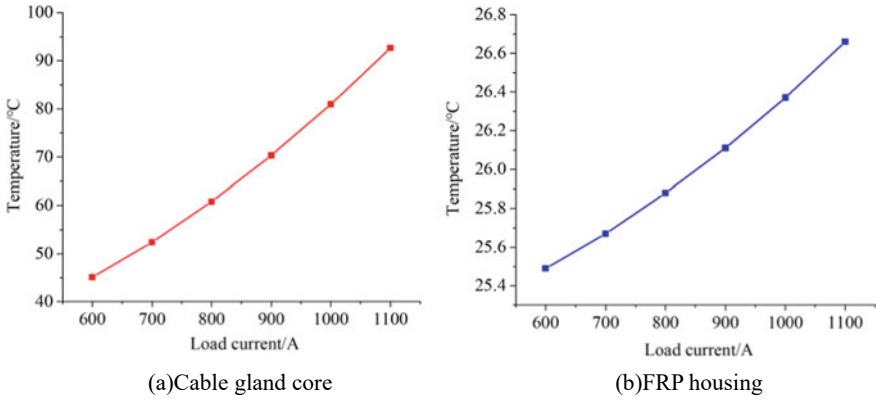


Fig. 5 Temperature variation curve of cable core and FRP shell of cable joint with load currents (°C)

The results show that as the load current increases, the temperature of the cable joint increases exponentially. The temperature of FRP shell is approximately equal to the ambient temperature, and the change with load current is relatively small.

4.2 Ambient Temperature

Keep the parameters and load current of each structure of the cable model unchanged, change the ambient temperature to 5 °C, 10 °C, 15 °C, 20 °C, 25 °C and 30 °C respectively, recalculate the temperature field, and explore the impact of ambient temperature on the joint temperature. The temperature field distribution of the corresponding cable joint is shown in Fig. 6, the change curve is shown in Fig. 7.

When the load current is 1000 A, the results show that as the ambient temperature increases, the temperature of the FRP shell increases linearly. The temperature change of both is about the change of ambient temperature.

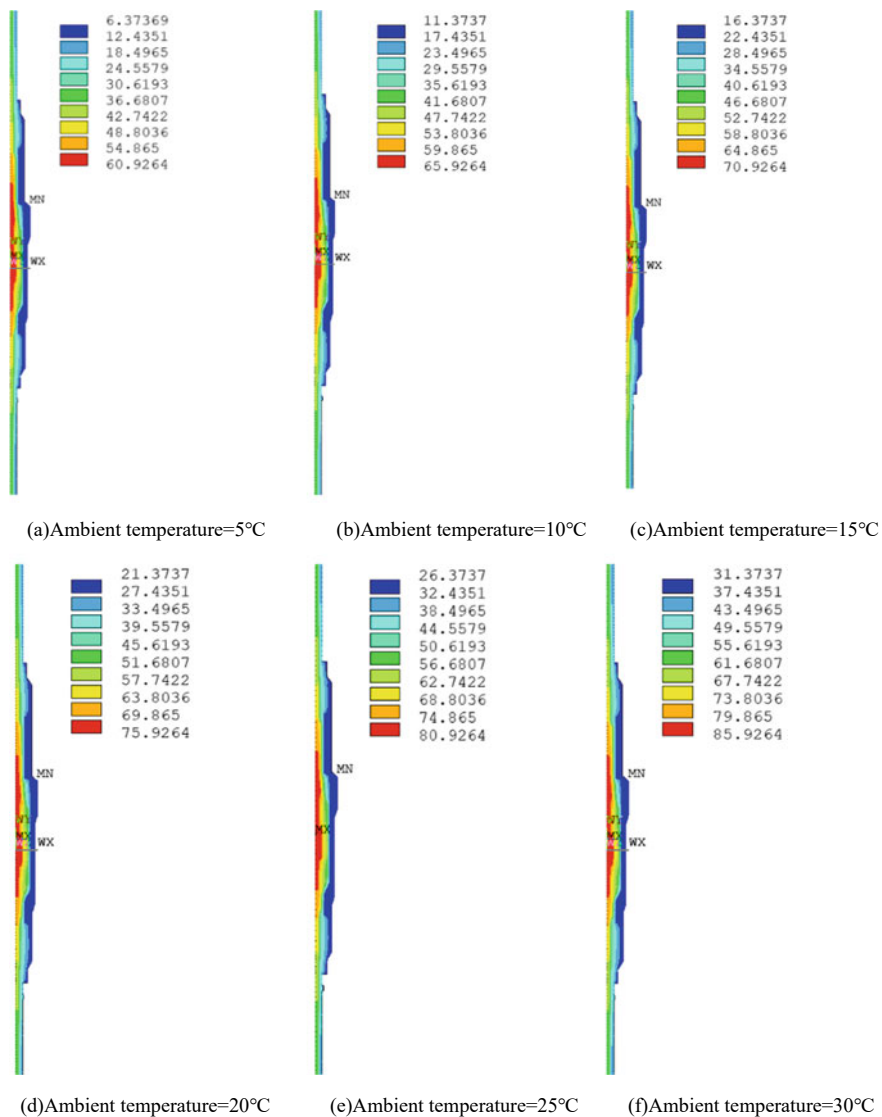


Fig. 6 Temperature field distribution of cable joint under different ambient temperatures (°C)

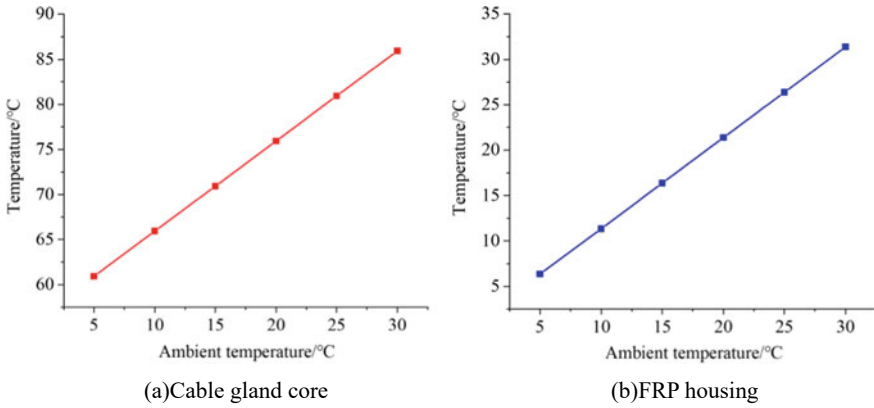


Fig. 7 Temperature change curve of cable core and FRP shell of cable joint with ambient temperature (°C)

5 Conclusion

In this paper, a two-dimensional axisymmetric model of 110 kV cable joint is established, and the temperature field of cable joint is calculated by finite element method, and the following conclusions are obtained:

- When the load current is 1000 A and the ambient temperature is 25 °C, the hottest spot temperature at the cable core inside the cable joint is about 80.93 °C, the shell temperature is about 26.37 °C, and the cable core temperature of the cable body is about 56.68 °C.
- When the boundary conditions remain unchanged, as the load current increases, the temperature of the cable joint increases exponentially. The temperature of FRP shell is approximately equal to the ambient temperature, and the change with load current is relatively small. When the load current remains unchanged, the temperature of glass steel shell is approximately equal to the ambient temperature, but relatively high. The temperature of the cable core inside the cable joint and the temperature of the FRP shell have an obvious linear relationship with the ambient temperature, and the change of the two temperatures is about the change of the ambient temperature.
- When the load current is 1100 A and the ambient temperature is 25 °C, the temperature of the cable core inside the cable joint exceeds 90 °C specified in the regulations. If the temperature is too high, insulation accelerated aging will occur, affecting the normal operation life of the cable and increasing the operation risk.

Acknowledgements Thanks for the support of science and technology project of Guangxi Power Grid Co., Ltd (Project number: GXKJXM20220072).

References

1. Tang K, Ruan J, Tang L, Zhan Q, Liu Y (2019) Calculation of temperature field of three-core cable joint. *High Voltage Technol* 45(11):3571–3578 (in Chinese)
2. Zong X, Han Y, Huang C (2022) Introduction of 35-kV kilometer-scale high-temperature superconducting cable demonstration project in shanghai. *Superconductivity* 2:100008
3. Wang L, Niu L, He X (2022) Cable temperature alarm threshold setting method based on convolutional neural network. *J Phys Conf Ser* 2160(1):012076
4. Atkinson RW, Fisher HW (1913) Current rating of electric cables. *Proc Am Inst Electr Eng* 32(2):565–573
5. Church EA (1931) Temperatures in electric power cables under variable loading. *Trans Am Inst Electr Eng* 50(3):982–991
6. Calculation of the current rating of electric cables, part1: current rating equations (100% load factor) and calculation of losses, In: section 1: general: IEC 60287-1-1:1994 (1994)
7. Calculation of the current rating of electric cables, part 2: thermal resistance, In: section 1: calculation of thermal resistance: IEC 60287-2-1:1994 (1994)
8. Singh RS, Cobben J, Cuk V (2020) PMU-based cable temperature monitoring and thermal assessment for dynamic line rating. *IEEE Trans Power Deliv* 36(3):1859–1868
9. Sanches DS, Sanches TS, Mariano G et al (2021) The evaluation of twisted pair cable performance in circuits with DS18B20 temperature sensors. *Int J Innov Educ Res* 9(6):286–297
10. Fang J, Zhang M, Mo W (2021) Simulation analysis of current in metal sheath of power cable considering temperature characteristics. *J Phys Conf Ser* 2108(1):012015
11. Lü A, Li J, Zhang Z, Song H, Lin X (2022) Finite element analysis for the influence of clamp on the thermal characteristics of high voltage insulated power cable. *Trans China Electrotech Soc* 37(1):283–290 (in Chinese)
12. Tang K, Wen W, Ruan J, Zhan Q, Xiao W, Liu C (2018) Simulation study on temperature field of single-core cable based on finite element method. *J Wuhan Univ (Eng Sci)* 51(09):811–816 (in Chinese)
13. Chen X, Wang Q, Yu J, Yao G (2021) Simulation study of DC ampacity of 10 kV AC XLPE cable under different DC topologies and laying modes. *High Voltage Technol* 47(11):4044–4054 (in Chinese)
14. Chen Y, Wang J, Zeng Z, Zhou P (2022) Research on temperature prediction of high-voltage cable core based on data-driven model. *Hunan Electric Power* 42(02):59–63+67 (in Chinese)
15. Wang L, Niu L, He X et al (2022) Cable temperature alarm threshold setting method based on convolutional neural network. *J Phys Conf Ser* 2160(1):012076

Loss Calculation of GIS Disconnect Switches Considering Contact Resistance and Skin Effect



Lei Zhang, Rui Li, Liang-yuan Chen, Shao-ming Pan, and Xia-jin Rao

Abstract GIS is widely used in power systems because of its importance in power systems and. However, the device has a compact structure and electrical contact, which can easily cause internal overheating and pose a huge risk to the safe operation of the power grid. Therefore, it is necessary to study its temperature rise. The prerequisite for obtaining accurate temperature rise of GIS disconnect switches is to obtain accurate loss results. In this paper, we use the finite element method to calculate the eddy current field loss of 110 kV GIS disconnect switches, consider the effects of contact resistance, skin effect and proximity effect, and verify the validity of the mesh; we calculate that the conductor loss accounts for 60.75% of the total loss, the contact resistance loss accounts for 24.22%, and the structure loss such as the shell is small, which has little effect on the temperature rise. The research in this paper lays a solid foundation for the temperature rise calculation of GIS disconnect switches.

Keywords GIS disconnect switches · Temperature rise · Finite element numerical calculation · Loss distribution

1 Introduction

Gas Insulated Switchgear (GIS), as an important equipment in power systems, has the advantages of small footprint, stability and reliability, high interference resistance, and long maintenance intervals. However, its compact and sealed structure, and the

L. Zhang (✉) · R. Li · L. Chen · S. Pan · X. Rao
Guangxi Key Laboratory of Intelligent Control and Maintenance of Power Equipment, Electric Power Research Institute of Guangxi Power Grid Co., Ltd., Nanning 530023, Guangxi, China
e-mail: 464873459@qq.com

L. Chen
e-mail: chen_ly.sy@gx.csg.cn

X. Rao
e-mail: rao_xj.sy@gx.csg.cn

© Beijing Paiké Culture Commu. Co., Ltd. 2024
X. Dong and L. Cai (eds.), *The Proceedings of 2023 4th International Symposium on Insulation and Discharge Computation for Power Equipment (IDCOMPU2023)*, Lecture Notes in Electrical Engineering 1100, https://doi.org/10.1007/978-981-99-7393-4_10

fact that it is generally connected to high currents, usually causes severe internal heating of GIS equipment and major faults such as short circuits, which affect the safe and stable operation of the power grid [1]. For this reason, the majority of scholars have carried out research work on the temperature rise of GIS equipment [2], and the current methods [3–7] for studying the temperature rise of GIS equipment at home and abroad are mainly experimental methods and finite element numerical calculations [8]. The literature [9, 10] explored the factors affecting the temperature rise of contact resistance through experiments; Pawar et al. used the finite element method to calculate the eddy current field loss of SF₆ high-voltage circuit breakers, and then used the CFX platform to calculate the temperature rise of circuit breakers [11]; Song et al. [12] used the three-dimensional multi-physical field coupling method to calculate the temperature rise of three-phase common box GIS, and proposed that the current-carrying effect and tendency of the conductor should not be neglected in the temperature rise calculation. The additional losses generated by the proximity effect and skin effect of the conductor cannot be ignored in the temperature rise calculation; Wu et al. [13] considered the contact resistance, proximity effect and skin effect to carry out electromagnetic-thermal coupling simulation of the three-phase common box GIS equipment at 110 kV and obtained that the conductor loss density of the GIS disconnect switch is higher than that of the circuit breaker. For this reason, an accurate calculation of the loss of GIS equipment is a prerequisite for the temperature rise calculation of GIS equipment. In this paper, the influence of contact resistance is considered, the contact resistance is equated to a circle, the influence of proximity effect and skin effect is considered in the grid dissection, the method of grid validity verification is proposed, and the eddy current field loss calculation is carried out for the three-phase common box type GIS disconnecter of 110 kV, and the losses of each part of the GIS disconnecter switch.

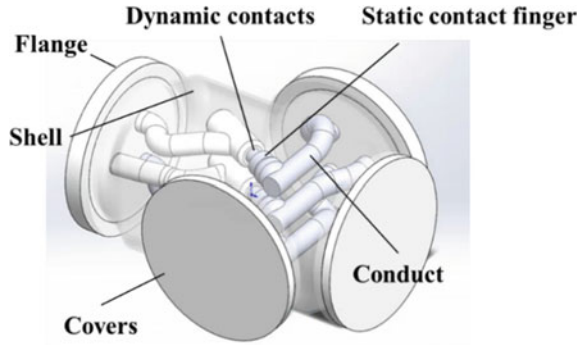
2 Model Simplification and Model Assumptions

2.1 Model Simplification

The research object of this article is a GIS three-phase isolation switch with model ZF12B-126. This article uses 3D modeling software to establish its 1:1 3D simulation model, as shown in Fig. 1. In order to achieve model simulation calculations, this article simplifies the 3D model reasonably. In the simplification process, the gear drive rods, gears and inter-phase insulator structures in the GIS disconnect switches are deleted, and a large number of sharp corners, chamfers and rounded corners in the model are simplified. In the static contacts, Since the plunger holding spring and the static contact shield have little effect on the final eddy current loss calculation results, they are removed The simplified simulation object is shown in Fig. 1.

The main electrical contact in the GIS disconnect switches exists between the dynamic contact and static contact finger position and static contact finger and static

Fig. 1 110 kV three-phase type GIS disconnect switch structure



contact base, in the eddy current field calculation, the contact resistance comes from the coating resistance of the contact surface and the contraction resistance of the current contraction effect caused by the current through the contact contacts. The contact finger and contact surface of this test object is silver plating, resistance is very small, can ignore the plating resistance [14–16], for this reason, in order to consider the contact resistance generated by the current contraction effect, this paper in the contact and contact finger, contact finger and base between the establishment of a rectangular circle to equivalent contact resistance, in order to ensure that the contact resistance can be simulated, the resistivity of the contact resistance can be back-calculated by the resistance calculation formula. The contact resistance equivalence is shown in Fig. 2.

The material parameters for each part of it are set in Table 1.

Under normal contact, the contact resistance is $6.5 \mu\Omega$, the resistivity of the contact resistance is converted by the formula: $\rho = \frac{R \cdot S}{l}$ The resistivity of the moving contact and the finger is $1.12323 \times 10^{-6} \Omega \text{ m}$, and the resistivity of the contact finger and the contact seat is $1.02221 \times 10^{-6} \Omega \text{ m}$.

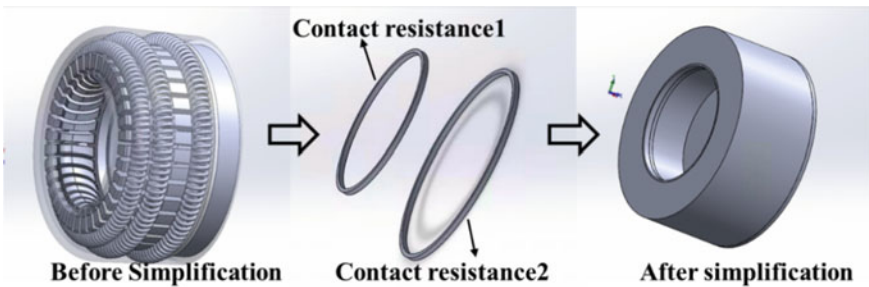


Fig. 2 Simplified diagram of static contacts

Table 1 Material parameters of each part of GIS disconnect switches

Part	Material	Relative magnetic permeability	Resistivity ($\times 10^{-8} \Omega \text{ m}$)
Cover	ZL101A	1	2.8
Housing	ZL101A	1	2.8
Conductor	ZL101A	1	2.8
Flange	ZL101A	1	2.8
Dynamic contacts	Copper	1	1.76
Static contact finger	Copper	1	1.76

2.2 Model Assumptions

- (1) The electromagnetic field is assumed to be plausibly steady and the effect of displacement currents is neglected in the calculation.
- (2) The relative permeability of each part of the equipment is constant at 1.
- (3) Current frequency is 50 Hz, and the three-phase currents are lagged 120° in sequence.
- (4) It is assumed that the resistance of the device is not affected by temperature and is constant.

3 Theoretical Analysis

3.1 Vortex Field Control Equation

In electromagnetic field calculations, a system of Maxwell's equations is usually used to describe the object of study. In this paper, it is assumed that the environment in which the GIS disconnect switches is located is the seemingly steady field of the industrial frequency AC, ignoring the influence of its displacement current, and also the seemingly steady field at this time is called the eddy current field. In solving the eddy current field, \mathbf{E} and \mathbf{H} cannot be found directly, for this reason, the vector magnetic potential \mathbf{A} is introduced, and its relation is as follows [17].

$$\mathbf{B} = \nabla \cdot \mathbf{A} \quad (1)$$

where \mathbf{B} is the magnetic induction intensity vector, from which the basic equation of the GIS disconnect switches eddy current field described by the vector magnetic potential \mathbf{A} can be obtained as follows:

$$\frac{1}{\mu} \nabla^2 \mathbf{A} - \sigma \frac{\partial \mathbf{A}}{\partial t} = -\mathbf{J}_x \quad (2)$$

where, μ is the magnetic permeability; σ is the electrical conductivity; t is the time; J_x is the original current vector density. In the three-dimensional eddy current field, this basic equation can be transformed into

$$\frac{1}{\mu} \left(\left(\frac{\partial^2 \mathbf{A}}{\partial x^2} \right) + \left(\frac{\partial^2 \mathbf{A}}{\partial y^2} \right) + \left(\frac{\partial^2 \mathbf{A}}{\partial z^2} \right) \right) - j\omega\sigma \mathbf{A}_z = -\mathbf{J}_x \quad (3)$$

The above equation is the control equation of three-dimensional eddy current field of GIS disconnect switch, where J_x is the sinusoidal excitation current source, for the research object of three-phase GIS disconnect switch, its three-phase current source is three-phase AC, each phase difference 120° , frequency is 50 Hz.

3.2 *Skinning Effect and Proximity Effect*

When the current-carrying conductor is energized with AC, its current distribution will be mainly concentrated on the conductor surface, when it is greater than the skinning depth, the current will be abruptly reduced, the higher the frequency The faster the frequency, the shorter the skin depth. In the meantime, for the three-phase common box GIS disconnect switches in this paper, the internal three-phase conductors are not completely distributed symmetrically in three phases, and most of the structures are distributed in parallel in three phases, and the current distribution will have proximity effect, which makes the current distribution of the conductors more uneven, and the skin effect and proximity effect are not negligible in the GIS disconnect switch eddy current field calculation. As a result, in the quasi-static field, the current-carrying conductor of the GIS disconnect switches will produce DC losses and additional losses caused by the skin effect and proximity effect caused by AC, and the shell will produce eddy current losses. Therefore, in the loss calculation of GIS disconnect switches, the skin effect and ohmic loss are calculated as:

$$d = \sqrt{\frac{2}{\omega\mu\gamma}} \quad (4)$$

$$P = \int_V \frac{\mathbf{J} \cdot \mathbf{J}^*}{2\gamma} dV \quad (5)$$

γ is electrical conductivity, μ is magnetic permeability, d is skinning depth, ω is angular frequency, \mathbf{J} is current density, \mathbf{J}^* is current density complex conjugate, and P is ohmic loss.

3.3 Boundary Conditions

Accurate boundary conditions in 3D vortex field calculations, is a prerequisite for accurate calculations. In vortex fields, the boundary conditions are generally divided into Dirichlet boundary, Neumann boundary, and mixed boundary, and the boundary conditions are as follows.

(1) Dirichlet boundary.

$$\Phi|_{\Gamma} = g(\Gamma) \quad (6)$$

The Dirichlet boundary is Γ , The position function is $g(\Gamma)$, when it is 0, said the condition for its Dirichlet boundary conditions.

(2) Neumann boundary.

$$\left. \frac{\partial \Phi}{\partial n} \right|_{\Gamma} + f(\Gamma) \Phi|_{\Gamma} = h(\Gamma) \quad (7)$$

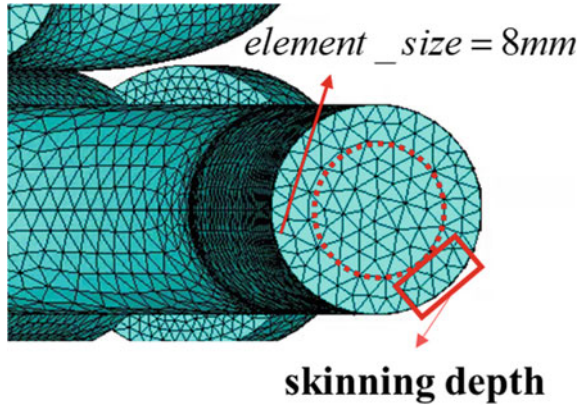
The Neumann boundary is Γ , n is the Neumann boundary of the outer normal vector, $h(\Gamma)$ and $f(\Gamma)$ is the general function. When it is 0, said that the condition for the Neumann boundary.

4 Numerical Calculation of Eddy Current Field

4.1 Mesh Dissection

In the numerical calculation, the control of the grid is related to the calculation volume, calculation results and calculation accuracy of the numerical calculation. In the grid division, the description of the shape of each object of the GIS disconnecting switch should be taken into account, and the grid density should be increased for the places with a greater influence on the results, and conversely, the grid density can be reduced appropriately, therefore, it is crucial for the reasonable allocation of the overall grid. In the loss calculation of the eddy current field of GIS disconnect switches, the contacts, conductors and shells have a greater impact on the loss calculation results, and a denser grid dissection is required for them. For the internal SF₆ gas, the insulation disc and the peripheral air package have little impact on the loss calculation, and the grid dissection density can be reduced to improve the efficiency of numerical calculation.

Fig. 3 Conductor meshing considering skinning depth verification



4.2 Verification of Grid Validity Considering Skinning Depth

For the contact resistance, its thickness is 0.975 mm, 1.635 mm respectively, so control its maximum grid size of 0.5 mm, the dissection results are shown in Fig. 4.

For metal structures with large size such as shell and conductor, the skin depth needs to be considered when the grid is dissected, according to $d = \sqrt{\frac{2}{\omega\mu\gamma}}$ which the skin depth of shell, conductor, cover and flange is 14.93 mm, and the skin depth of dynamic contact is 9.44 mm. In the grid dissection, it is necessary to satisfy that there are complete cell nodes within the skin depth to ensure the accuracy of loss calculation.

For this reason, the maximum cell size is 20 mm for the shell, which is 12 mm thick, and 30 mm for the flange and cover; for the conductor, which has a radius of 40 mm, the maximum cell size is 5 mm, as shown in Fig. 3, to meet the skin depth requirement, contact, control the maximum cell size of 5 mm.

For the SF₆ fluid domain and air domain, the maximum grid size is 20 mm and 30 mm respectively, as shown in Fig. 4.

4.3 Excitation and Boundary Condition Settings

After establishing the calculation model of the 3D vortex field, appropriate excitation and boundary conditions should be set to ensure that the final calculation results are accurate. In this paper, the boundary conditions for the 3D vortex field solution domain are set as follows, and as shown in Fig. 4.

- (1) Setting the four boundaries of the air package F1–F6 as the magnetic line parallel boundary ($A_z = 0$).
- (2) One end of the conductor is nodal voltage coupled, loaded with 1.1 times the rated current (3150 A), and the three phases are hysteresis 120°, frequency is

Fig. 4 Schematic diagram of air domain boundary

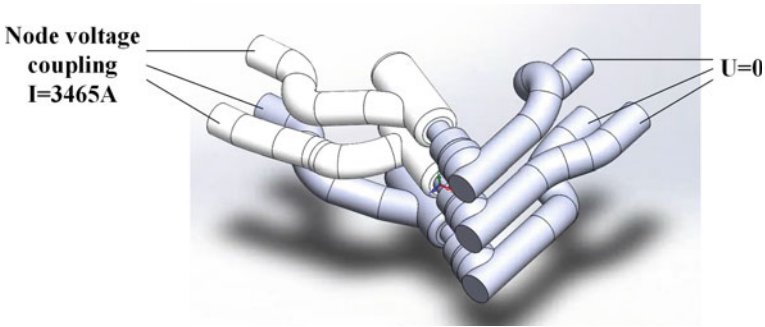
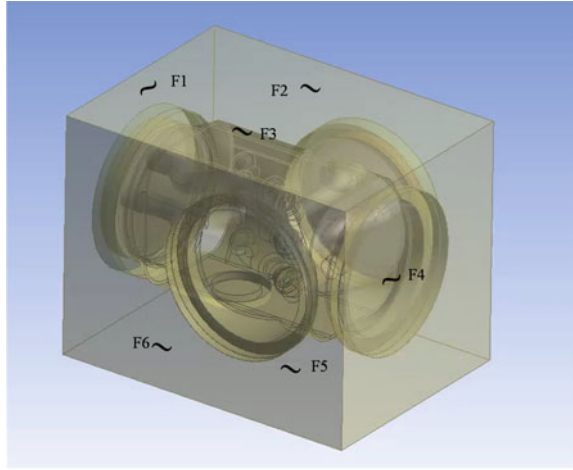


Fig. 5 Schematic diagram of conductor excitation loading

50 Hz, and the other end of the conductor is set to zero potential, as shown in Fig. 5.

4.4 Result Analysis

After carrying out grid dissection, boundary and excitation settings on the GIS disconnect switch 3D simulation model, its time-harmonic field simulation is calculated and its magnetic field intensity distribution is calculated as shown in Fig. 6. The closer to the conductor, the more obvious the magnetic induction effect is, the greater the magnetic field intensity is, so the magnetic field strength is greater where the shell is close to the conductor, making the top and bottom parts of the shell near the A-phase conductor and C-phase conductor magnetic field strength is significantly higher than the other parts.

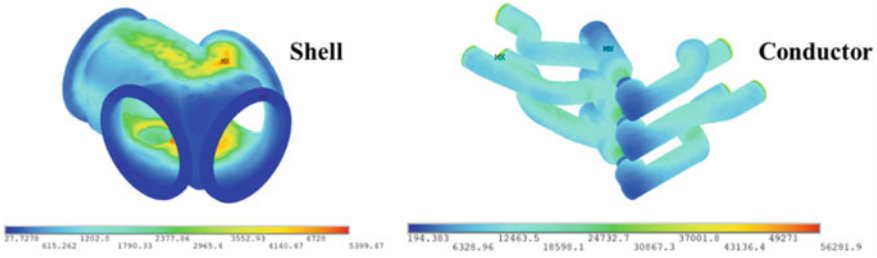


Fig. 6 Shell and conductor magnetic field strength distribution

Current density distribution of conductor, the current distribution shows obvious skin effect and proximity effect, while the current density at the contact resistance is the largest, which is due to the sudden reduction of the current channel at the contact resistance, producing a current contraction effect. The current on the shell is mainly due to the electromagnetic induction of the conductor generated eddy current, from the figure can be seen in the direction of its current and the direction of the conductive current opposite, and the formation of eddy current in the shell, while the closer to the conductor side of the eddy current density is greater, the reason for the same reason as the above magnetic field strength distribution, are closer to the conductor the greater the magnetic induction strength, as shown in Fig. 7.

The loss extraction of the eddy current field calculation results yielded the loss distribution of each part, as shown in Table 2. The conductor loss accounted for 60.75% of the total loss, the contact resistance loss accounted for 24.22%, and the induction eddy current loss of the shell, flange and cover accounted for 6.98%. Therefore, under the normal contact of the GIS disconnect switch, the conductor is affected by the skin effect and generates a large loss, while the contact resistance part has a large ratio of volume to loss, which is very easy to generate high temperature at the contact position, while the shell, flange and cover plate temperature rise is less affected by the loss.

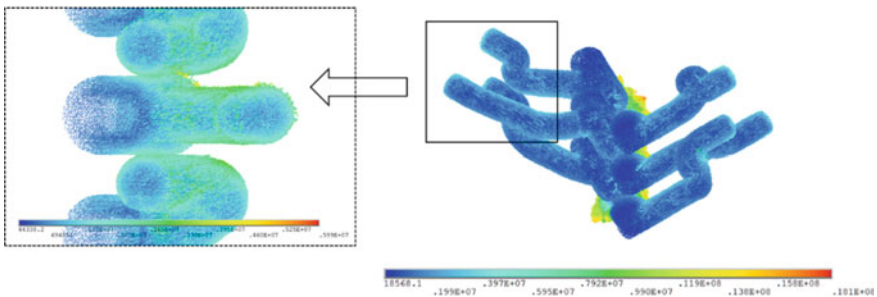


Fig. 7 Conductor current density distribution

Table 2 GIS disconnect switch parts loss settlement results

Part	Loss (W)
Conduct	578.78
Shell	41.59
Covers	0.35
Flange	24.61
Dynamic contact	44.86
Contact resistance	230.78

5 Conclusion

In this paper, the current density distribution of 110 kV GIS disconnect switch is obtained through electromagnetic field calculation using the finite element method, and the effects of contact resistance, skin effect and proximity effect were considered in the calculation, and the validity verification of the mesh was carried out to obtain the magnetic field strength distribution and current density distribution of each part of the GIS disconnect switch, and the loss calculation results of each part of the GIS disconnect switch were also extracted, and it can be seen that the GIS disconnect switch The conductor is influenced by the skin effect, which makes the loss larger, and the contact resistance loss accounts for a larger proportion, which is the main part of the hot spot temperature inside the GIS disconnect switch, and the eddy current loss generated by the GIS disconnect switch shell, flange and cover is less, i.e. the loss has less influence on its temperature rise. The calculation results of this paper provide a reference for the subsequent development of GIS disconnect switch temperature rise calculation.

Acknowledgements This paper is supported by Science and Technology Project of Guangxi Power Grid CO under project number **GXKJXM20220072**.

References

- Hou G, Deng X, Wu Y et al (2017) Overview of temperature rise simulation for power switchgear. *Electr Energy Manage Technol* 11:1–6 (in Chinese)
- Hang J, Zhang J, Li N et al (2017) Research on temperature field simulation of GIS circuit breakers based on finite element analysis. *Power Syst Clean Energy* 37(8):53–61 (in Chinese)
- Dhotre MT, Korbel J, Ye X et al (2017) CFD simulation of temperature rise in high voltage circuit breakers. *IEEE Trans Power Delivery* 32(6):2530–2536
- Rebzani N, Clavel E, Marty P et al (2016) Multi-physical numerical simulation of temperature rise in gas insulated busbars. *IEEE Trans Dielectr Electr Insul* 23(5):2579–2586
- Lindmayer M (2016) Simulation of switching arc under the action of transverse magnetic field when DC is disconnected. *IEEE Trans Plasma Sci* 44(2):187–194
- Niu C, Jiao L, Wang X et al (2020) Analysis of thermal characteristics of environmentally friendly GIS based on multifield coupling. *Trans China Electrotech Soc* 35(17):3765–3772 (in Chinese)

7. Huang M (2019) GIS equipment testing methods. Wuhan University of Technology (in Chinese)
8. Ma B, Wu X, Li X et al (2019) Finite element simulation of temperature field distribution characteristics and influencing factors in GIS. *Insul Mater* 52(3):69–73 (in Chinese)
9. Liu F, Liu G, Qin X et al (2020) Application of equivalent thermal circuit in temperature rise calculation of three phase closed isolation switch. *High Voltage Apparatus* 56(8):211–216 (in Chinese)
10. Luo C, Yang J, Li S et al (2021) Research on GIS temperature rise based on equivalent thermal circuit and finite element analysis. *High Voltage Apparatus* 57(5):67–76 (in Chinese)
11. Pawar S, Joshi K, Andrews L et al (2012) Application of computational fluid dynamics in shortening product development period of SF6 gas circuit breaker. *IEEE Trans Power Delivery* 27(1):156–163
12. Song H, Wang W, Huang Q et al (2019) The influence of proximity and skin effect of current carrying conductors and current frequency on the temperature rise of three phase integrated box GIS. *High Voltage Apparatus* 55(2):97–102 (in Chinese)
13. Wu J, Wang Z, Lv H et al (2020) GIS temperature rise calculation and experimental research considering the influence of airflow. *High Voltage Eng* 46(3):815–823 (in Chinese)
14. Timsit RS (1988) Electrical instability of fixed contacts: aluminum/aluminum and aluminum/brass connectors. *Electr Contacts* 11(1):12–16
15. Runde M, Hodne E, Tidal B (1989) Contact point aging caused by current. *Electr Contacts* 12(13):20–25
16. Lee KL, Hu CK, Tu KN (1995) In situ scanning electron microscope comparative study on electromigration of Cu and Cu (Sn) alloys for advanced chip interconnection. *J Appl Phys* 78(7):4428–4437
17. Rong M (2004) *Electrical contacts fundamentals*. China Machine Press (in Chinese)

A Novel Virtual Power Plant Model with Ito Integral Considering Random Noise of Renewable Energy



Li Kang, Zhao Yulin, Tong Weilin, Liu Zhongyi, Dong Jinzhe, Shao Zhenwei, Lv Yajuan, and Xie Jinghua

Abstract With the renewable energy connected to power grid, the virtual power plant (VPP) faces the uncertainty of new energy output in the dispatching process, which brings certain challenges to power system. Considering the continuous stochastic process of renewable energy, this paper proposes a novel VPP model based on stochastic differential equation. The model includes gas turbine, wind turbine, pumped storage power station and load. Based on the renewable energy grid, the random noise of renewable energy output is included, and the VPP model with Ito integral is constructed. The problem is solved by dividing, summing and seeking the limit of the time interval. The correctness and practicability of the proposed method are verified by real examples.

Keywords Virtual power plant · Ito integral · Stochastic differential equation · Renewable energy

1 Introduction

Traditional power generation methods will bring serious environmental pollution. With the proposal of the concept of sustainable development, renewable energy sources, such as wind power and photovoltaic power generation have developed rapidly [1–3]. However, the renewable energy power generation is highly random and uncontrollable. The increasing construction and grid integration of renewable energy generation in large scale will seriously affect the safe operation of power

L. Kang

State Grid Jiangsu Electric Power Co.,Ltd. Nanjing Branch, Nanjing, China

Z. Yulin

State Grid Jiangsu Electric Power Co, Ltd, Nanjing, China

T. Weilin (✉) · L. Zhongyi · D. Jinzhe · S. Zhenwei · L. Yajuan · X. Jinghua

State Grid Wuxi Electric Power Co, Ltd, Wuxi, China

e-mail: 21610067@zju.edu.cn

© Beijing Paiké Culture Commu. Co., Ltd. 2024

X. Dong and L. Cai (eds.), *The Proceedings of 2023 4th International Symposium on Insulation and Discharge Computation for Power Equipment (IDCOMPU2023)*, Lecture Notes in Electrical Engineering 1100, https://doi.org/10.1007/978-981-99-7393-4_11

system [4]. In order to overcome these shortcomings, domestic and foreign scholars put forward the concept of VPP [5–8].

VPP organically integrates various types of distributed generators (DG), controllable load and distributed energy storage (DES). VPP can not only reduce the impact of intermittent and randomness of renewable energy generation, but also obtain scale economies. The characteristics of VPP meet the development needs of the world and have broad application prospects. By the end of 2014, global VPP capacity had increased to 4.8 GW. VPPs are expected to grow to 28 GW by 2023, with annual revenues of \$ 5.3 billion.

In order to improve revenue, VPP operators need to consider the impact of renewable energy generation uncertainty in the process of optimal scheduling, and formulate the operation strategy with the largest profit. At present, the mathematical methods mainly used to deal with the uncertain output of renewable energy in VPP are stochastic programming (SP) and robust optimization (RO). References [9] used SP to deal with electricity price, wind power and photovoltaic output, and established the medium-term scheduling optimization model of VPP. They verified that the access of gas turbine and pumped storage power station can reduce the uncertainty of wind power output. SP can improve the adaptability of decision results, but this method has some problems such as difficult to accurately describe the probability distribution, large amount of calculation, and the accuracy and safety cannot be guaranteed. References [10, 11] used RO to deal with the uncertainty of wind power output, and established the bidding model of VPP in the hybrid electricity market. RO limits the uncertainty to a fixed interval, and the solution scale is relatively small, but it is conservative to some extent, and it is difficult to maximize profits.

On the basis of previous studies, considering the continuous stochastic process of renewable energy output, this paper proposes a VPP scheduling optimization model based on stochastic differential equations. The model aggregation unit includes gas turbine, wind turbine, pumped storage power station and load. Firstly, considering the continuity of renewable energy output, the VPP continuous scheduling optimization model is constructed. Secondly, the random noise of renewable energy is included, and the VPP scheduling optimization model with Ito integral is constructed. The problem is solved by dividing, summing and calculating the limit of the time interval. The correctness and practicability of the proposed method are verified by real examples. This model can support the correct decision-making of dispatchers and has certain engineering application value.

2 VPP Continuous Scheduling Optimization Model

2.1 Objective Function of VPP

The objective of VPP operators is to minimize the cost. Assuming that the optimization time interval is $[T_a, T_b]$, the objective function can be expressed as the following integral form.

$$\min \int_{T_a}^{T_b} [k_0 x(t) + k_j g(t) + \lambda_{su} y(t) + \lambda_{st} z(t)] dt \quad (1)$$

In (1), T_a, T_b are the starting and ending time of optimization respectively. k_0 is the fixed costs for gas turbines, and k_j is the slope of gas turbine generation cost. $g(t)$ is the gas turbine output, which is the decision variable. λ_{su} and λ_{st} are gas turbine start-up and stop costs respectively. Boolean variables $x(t), y(t), z(t)$ respectively indicate whether the gas turbine is working, starting, and stopping at time t . If yes, set to 1; otherwise set to 0. dt is a small time unit.

2.2 Constraint Conditions of VPP

VPP needs to meet its own constraints at runtime and the basic constraints are as follows.

- Gas turbine constraint conditions:

$$\begin{cases} x(t+dt) - x(t) \leq y(t) \\ x(t) - x(t+dt) \leq z(t) \\ g_{\min} x(t) \leq g(t) \leq g_{\max} x(t) \\ -r_d dt \leq g(t+dt) - g(t) \leq r_u dt \end{cases} \quad (2)$$

where g_{\max} and g_{\min} are gas turbine maximum, minimum output power. In (2), r_d and r_u are upward and downward climbing rates of gas turbine respectively.

- Constraint conditions of pumped storage power station:

The pumped-storage power station is composed of pumps and turbines. Most of the pumped-storage power stations currently used are reversible pumps and turbines. The water storage of the upstream reservoir is equivalent to the corresponding electricity storage, so the constraint conditions of the pumped-storage power station are as follows:

$$\begin{cases} g_t(t) \leq g_{t \max} \mu_t(t) \\ g_p(t) \leq g_{p \max} \mu_p(t) \\ 0 \leq s_c(t) \leq s_{c \max} \\ s_c(t+dt) = s_c(t) + g_p(t)dt - g_t(t)dt \end{cases} \quad (3)$$

where $s_c(t)$ is the equivalent storage capacity at t . $g_t(t)$ and $g_p(t)$ are the power of turbine and pump at t respectively, which are decision variables. $g_{t \max}$ and $g_{p \max}$ are the maximum output power of turbine and pump respectively. Boolean variables $\mu_t(t)$ and $\mu_p(t)$ indicate whether the turbine and pump work at t respectively. If yes, set to 1, and otherwise set to 0. $s_{c \max}$ is the maximum equivalent electricity storage.

- Internal power balance constraint of VPP:

$$g_w(t) + g(t) + \rho_t g_t(t) = \frac{g_p(t)}{\rho_p} + l(t) \quad (4)$$

In (4), $g_w(t)$ is the forecast value of wind power output at t . ρ_t and ρ_p are efficiency of hydraulic turbine and pump respectively. $l(t)$ is the load at t .

3 Novel Stochastic Differential Model of VPP

The VPP model in Sect. 2 does not consider the uncertainty of wind power output, and substitutes its predicted value into the solution of model directly. In fact, wind power output cannot be accurately predicted. This process is a Markov process and a steady independent increment process with continuous states. Wind power output can be expressed by predicted value and error.

$$\tilde{g}_w(t) = g_w(t) + W(t) \quad (5)$$

In (5), the uncertainty form of wind power output and $w(t)$ is a Gaussian white noise process. Considering the randomness of wind power output in (4), there are:

$$g_w(t) + g(t) + W(t) + \rho_t g_t(t) = \frac{g_p(t)}{\rho_p} + l(t) \quad (6)$$

Replace (6) with objective function (1) to:

$$\begin{aligned} & \min \int_{T_a}^{T_b} \left[k_0 x(t) + k_j \frac{g_p(t)}{\rho_p} + k_j l(t) - k_j g_w(t) \right. \\ & \quad \left. - k_j W(t) - k_j \rho_t g_t(t) + \lambda_{su} y(t) + \lambda_{st} z(t) \right] dt \\ & = \min \int_{T_a}^{T_b} \left[k_0 x(t) + k_j \frac{g_p(t)}{\rho_p} + k_j l(t) - k_j g_w(t) \right] dt \end{aligned}$$

$$\begin{aligned}
 & -k_j \rho_t g_t(t) + \lambda_{su} y(t) + \lambda_{st} z(t) \Big] dt \\
 & + \min \left[- \int_{T_a}^{T_b} k_j dB(t) \right] \tag{7}
 \end{aligned}$$

In (7), the objective function is equal to the sum of Riemann integral and Ito integral. In the way of adding Ito integral introduces random factors, the objective function considers the random process of wind power output. $B(t)$ in (7) is a Wiener process, assuming that $dB(t)/dt$ is a normal white noise. The one-dimensional probability density function $f[B(t)]$ of $B(t)$ is:

$$f[B(t)] = \frac{1}{\sqrt{2\pi t} \cdot \sigma} \exp \left[-\frac{B(t)^2}{2\sigma^2 t} \right] \tag{8}$$

In (8), the mean value of $B(t)$ equals 0. Variance $D[B(t)] = \sigma^2 t$, in which σ^2 is a constant depending on the degree of dispersion of $W(t)$.

In order to solve the above integral problem, the time interval $[T_a, T_b]$ is segmented. In this interval, a finite point sequence $T_a = t_0 < t_1 < t_2 < \dots < t_n = T_b$ is taken. Each closed interval $[t_m, t_{m+1}]$ is a subinterval, where $0 \leq m \leq n-1$. Define λ as the maximum subinterval length and $\lambda = \max(t_{m+1} - t_m)$. For each subinterval sum and limit, (7) can be expressed as:

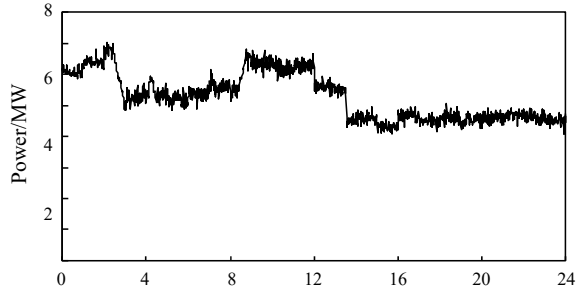
$$\begin{aligned}
 & \min \lim_{\lambda \rightarrow 0} \sum_{m=0}^{n-1} \left[k_0 x(t_m) + k_j \frac{g_p(t_m)}{\rho_p} + k_j l(t_m) - k_j g_w(t_m) \right. \\
 & \quad \left. - k_j \rho_t g_t(t_m) + \lambda_{su} y(t_m) + \lambda_{st} z(t_m) \right] (t_{m+1} - t_m) \\
 & \quad + \min \left[- \lim_{\lambda \rightarrow 0} \sum_{m=0}^{n-1} k_j (B(t_{m+1}) - B(t_m)) \right] \\
 & = \min \lim_{\lambda \rightarrow 0} \sum_{m=0}^{n-1} \left[k_0 x(t_m) + k_j \frac{g_p(t_m)}{\rho_p} + k_j l(t_m) - k_j g_w(t_m) \right. \\
 & \quad \left. - k_j \rho_t g_t(t_m) + \lambda_{su} y(t_m) + \lambda_{st} z(t_m) \right] (t_{m+1} - t_m) - k_j [B(t_n) - B(t_0)] \tag{9}
 \end{aligned}$$

Since $B(t)$ is independent of other variables, and independent of constraint conditions, the objective function is equal to the optimization result plus increment $-[B(t_n) - B(t_0)]$, without considering the random process of wind power output.

Constraints (2)–(4) are rewritten into the form of subintervals:

$$\begin{cases}
 x(t_{m+1}) - x(t_m) \leq y(t_m) \\
 x(t_m) - x(t_{m+1}) \leq z(t_m) \\
 g_{\min} x(t_m) \leq g(t_m) \leq g_{\max} x(t_m) \\
 -r_d(t_{m+1} - t_m) \leq g(t_{m+1}) - g(t_m) \leq r_u(t_{m+1} - t_m)
 \end{cases} \tag{10}$$

Fig. 1 Wind power output forecasting curve and daily load curve



$$\begin{cases} g_t(t_m) \leq g_{t \max} \mu_t(t_m) \\ g_p(t_m) \leq g_{p \max} \mu_p(t_m) \\ 0 \leq s_c(t_m) \leq s_{c \max} \\ s_c(t_{m+1}) = s_c(t_m) + g_p(t_m)(t_{m+1} - t_m) - g_t(t_m)(t_{m+1} - t_m) \end{cases} \quad (11)$$

$$\mu_t(t_m) + \mu_p(t_m) \leq 1 \quad (12)$$

So far, VPP continuous stochastic scheduling optimization model with Ito integral can be expressed by (9)–(12).

4 Case Analysis

4.1 Input Parameters

In this paper, a gas turbine, a small wind power station and a pumped storage power station are used to form VPP. The gas turbine adopts TAU5670 model, and the maximum output power is 5.67 MW. The upward and downward climbing rates are 17 MW/h, and the start and stop costs are 30. The predicted wind power output is shown in Fig. 1. It is assumed that the storage capacity of the upstream reservoir of the pumped storage power station is 0 at the initial time, the maximum equivalent storage capacity is 40 MW, the maximum output power of the turbine and the pump is 8 MW and 6 MW, respectively, and the efficiency is 75%. Wind power output is shown in Fig. 1.

4.2 Detailed Analysis

According to the set parameters and input data, the GAMS software CPLEX solver is used to solve the problem. The optimization results of pumped storage power station

and gas turbine are shown in Figs. 2 and 3 respectively. It can be seen that the power of turbine and pump and the output of gas turbine in pumped storage power station show fluctuation characteristics, indicating that pumped storage power station and gas turbine continuously adjust their own power to adapt to the change of wind power output and load. At about 0:00–4:00, the wind power output is greater than the load, and the water pump converts the electricity into water storage. During this period, the power of the pump is continuously adjusted according to the difference between the wind power output and the load. From around 4:00 to 8:00, the load is greater than the wind power output. The turbine uses the stored water to generate electricity. The higher the difference between the load and the wind power output is, the greater the power of the turbine is. It should be noted that the remaining equivalent storage capacity is insufficient to supply the difference between load and wind power output around 16:00, and VPP compensates for the power difference by calling gas turbines to generate electricity around 16:00–18:00. In summary, by optimizing the output of pumped storage power station and gas turbine, VPP balances the fluctuation of load and minimizes its own cost.

In order to verify the effectiveness of the VPP scheduling optimization model with Ito integration to calculate the objective function interval, the objective function boundary obtained from the Monte Carlo (MC) simulation results is used as the comparison standard. As a random simulation technology, the more Monte

Fig. 2 Water turbine and water pump power output, and equivalent storage capacity in pumped storage power station

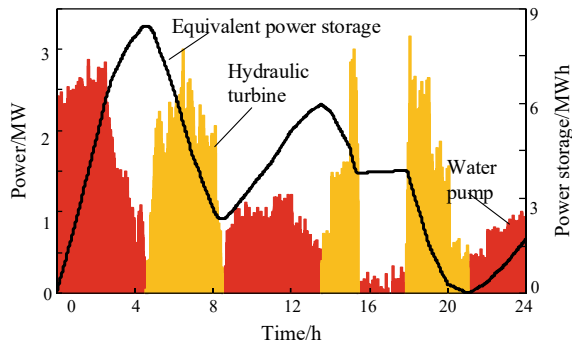


Fig. 3 Power output of the gas turbine

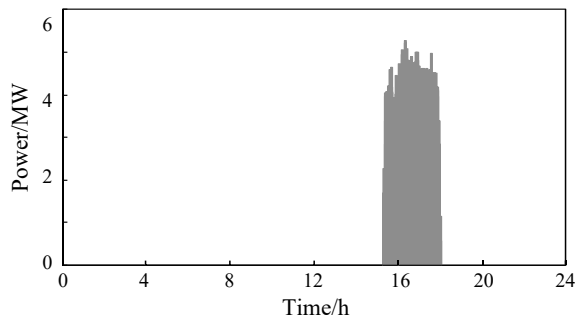


Table 1 Comparison of results of different methods

	Upper (\$)	Definite value (\$)	Lower (\$)	Computing time
MC10	388.99	359.12	338.426	1 min 8 s
MC100	416.65	359.12	331.56	13 min 15 s
MC500	422.818	359.12	324.13	1 h 5 min 49 s
Our method	429.12	359.12	289.12	6 s

Carlo simulation times, the more accurate the calculation results, but the more time-consuming. The maximum and minimum values in the calculation results are taken as the upper and lower boundaries of the objective function, which are compared with the method in this paper. The results are shown in Table 1.

It can be seen that the more the number of MC simulations, the closer the results are to the method in this paper, and the method in this paper contains the results of MC method. This is because: (1) The method in this paper is slightly conservative. When there is an interval variable with an average of 0, the Monte Carlo method is easy to underestimate the boundary of the interval variable, which has been proved in Reference. (2) The insufficient number of MC simulations leads to inaccurate calculation results.

In addition, compared with MC method, the proposed method greatly reduces the computational time and improves the computational efficiency.

5 Conclusion

In this paper, considering the randomness and continuity of renewable energy output, VPP continuous stochastic scheduling optimization model with Ito integral is proposed, and the model is simulated and analyzed. The conclusions are as follows:

The simulation results verify the effectiveness and practicability of the proposed method. By solving the VPP continuous stochastic scheduling optimization model, a set of determined optimal scheduling schemes can be obtained. The scheduling scheme shows that the power of turbine and pump in pumped storage power station and the output of gas unit follow the load change well, which can effectively support the decision of dispatchers and has certain practical value.

References

1. Merritt NR, Chakraborty C, Bajpai P (2022) An E-STATCOM based solution for smoothing photovoltaic and wind power fluctuations in a microgrid under unbalanced conditions [J]. IEEE Trans Power Syst 37. <https://doi.org/10.1109/TPWRS.2021.3106859>

2. Chishti F, Murshid S, Singh B (2021) Grid integration of renewable energy generating system using nonlinear harmonic observer under nonideal distribution system [J]. *IEEE Trans Ind Appl* 57(6). <https://doi.org/10.1109/TIA.2021.3103484>
3. Liu K, Meliopoulos APS, Xie B et al (2020) Dynamic state estimation-based protection of distribution systems with high penetration of DERs [C]. In: 2020 IEEE power and energy society general meeting (PESGM). IEEE. <https://doi.org/10.1109/PESGM41954.2020.9281574>
4. Dongliang W, Yang W, Chuangxin G et al (2012) An economic dispatching model considering wind power forecast errors in electricity market environment [J]. *Autom Electr Power Syst* 36(6):23–28 (in Chinese)
5. Zhang T, Hu Z (2022) Optimal scheduling strategy of virtual power plant with power-to-gas in dual energy markets [J]. *IEEE Trans Ind Appl* 2:58. <https://doi.org/10.1109/TIA.2021.3112641>
6. Wei Z, Yu S, Sun G et al (2013) Concept and development of virtual power plant [J]. *Autom Electr Power Syst* [J] 37(13):1–9 (in Chinese)
7. Chunwu C, Na L, Pengyuan Z et al (2013) Review of virtual power plant technology abroad and enlightenment to China [J]. *Power Syst Technol* 37(8):2258–2263 (in Chinese)
8. Morais H, Pinto T, Vale Z et al (2012) Multilevel negotiation in smart grids for VPP management of distributed resources [J]. *IEEE Intell Syst* 27(6):8–16
9. Pandzic H, Morales MJ, Conejo JA et al (2013) Offering model for a virtual power plant based on stochastic programming [J]. *Appl Energy* 105:282–292
10. Shuang Y, Zhinong W, Guoqiang S et al (2014) A bidding model for a virtual power plant considering uncertainties [J]. *Autom Electr Syst* 38(22):43–49 (in Chinese)
11. Rahimiyan M, Baringo L (2015) Strategic bidding for a virtual power plant in the day-ahead and real-time markets: price-taker robust optimization approach [J]. *IEEE Trans Power Syst* 28(5):1634–1655

Research on AlexNet Model-Based Partial Discharge Diagnosis of Cable Terminals



Hongliang Zou, Wenhui Li, Yiming Lu, Jie Sun, Xin Lu, Yijiong Jin, Huan Liu, and Yao Zhang

Abstract The main cause of cable accidents is the insulation degradation of cables or terminal joints, and the detection and identification of partial discharges in cables can effectively avoid the safety hazards caused by insulation degradation. In order to improve the speed and accuracy of recognition, this paper proposes an improved convolutional Neuronal Network (CNN) algorithm for partial discharge image recognition method based on variational mode decomposition and wigner-ville distribution (VMD-WVD) time–frequency spectrum gray image combined with AlexNet network model, which collects partial discharge signals by building a cable partial discharge test platform, determines the image size by bilinear interpolation after joint VMD-WVD analysis, and uses the grey-scale processed image as the network input to construct different defect time–frequency spectra. Finally, the feature samples were used to train the improved convolutional neural network to identify the three types of T-type terminal partial discharge defect types tested. The results show that the partial discharge image recognition method based on the AlexNet network model can extract image features at a deeper level than the traditional principal component analysis and support vector machine (PCA-SVM) recognition method, and has a better recognition effect and faster training speed in the recognition of partial discharge defect types.

Keywords Pattern recognition · Partial discharge · Power cables · Terminal joints

H. Zou · Y. Zhang (✉)

Science and Technology Branch of Taizhou, Hongchuang Power Group Co., Ltd.,
Taizhou 318000, Zhejiang, China
e-mail: 810795569@qq.com

W. Li · Y. Lu · J. Sun · X. Lu · Y. Jin · H. Liu

Taizhou Power Supply Company of State Grid Zhejiang Electric Power Co.Ltd., Taizhou 318000,
Zhejiang, China

© Beijing Paiké Culture Commu. Co., Ltd. 2024

X. Dong and L. Cai (eds.), *The Proceedings of 2023 4th International Symposium on Insulation and Discharge Computation for Power Equipment (IDCOMPU2023)*, Lecture Notes in Electrical Engineering 1100, https://doi.org/10.1007/978-981-99-7393-4_12

123

1 Introduction

Cables are widely used in various fields of the national economy due to their high reliability, small footprint, large capacity and burial underground, providing important support for industries, national defence construction and major construction projects. Power transmission is often lost due to cable failure problems, which seriously threaten the safety of the power supply [1–3]. The main cause of cable accidents is the insulation degradation of the cable or terminal joints, among them the T-type cable joint is easy to cause defects in the process of manufacture and installation because of its relatively complex structure [4, 5].

A large number of simulations and experimental studies have been carried out at home and abroad for terminal head partial discharge. In the articles [6], common insulation scratch defects were designed to analyse the trends of partial discharge initial voltage, partial discharge extinction voltage, partial discharge phase spectrum and partial discharge amount at 10 kV outdoor cold shrink terminal head under the operating impulse voltage degradation. The articles [7] analyzed the partial discharge signal found in the live detection of a substation in Beijing power grid, and used the ultrasonic method to locate the partial discharge source, and finally determined that the cable termination fabrication and installation process was the root cause of this defect.

Currently, the main methods of feature extraction for electrical signals include phase distribution-based feature parameter extraction, time-domain waveform-based feature parameter extraction and fractal theory-based feature parameter extraction. The articles [8] analyzed the differences between various defects based on the time–frequency waveform feature parameter extraction method and the three-dimensional discharge spectrum; The articles [9] analyzed the relationship between the ageing time and the phase distribution feature parameter extraction method based on the $q - n - \phi$ model.

In this paper, we build an AlexNet deep learning network, use the gray-scale processed image as the network input, construct different defect time–frequency spectrum gray image feature samples, identify the three types of T-type terminal partial discharge defect types tested, and finally analyse the recognition rate of different defects and Finally, the recognition rates of different defects are analyzed and compared with the traditional recognition method to verify the advantages of this method.

2 Cable Partial Discharge Test

The research work in this paper needs to be based on the physical experimental research, and the data collected mainly comes from the partial discharge signal of the 10 kV T-terminal. The schematic diagram of the partial discharge test principle is shown in Fig. 1.

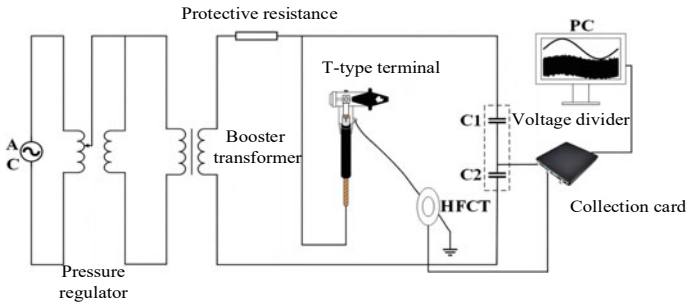


Fig. 1 Principle of the partial discharge test

2.1 Test Methods

This paper conducts experiments on three types of defects: insulation scratch, Casing fouling and joint looseness to study the characteristics of the partial discharge signal at different defects and to reproduce the process of cable partial discharge by stage boosting.

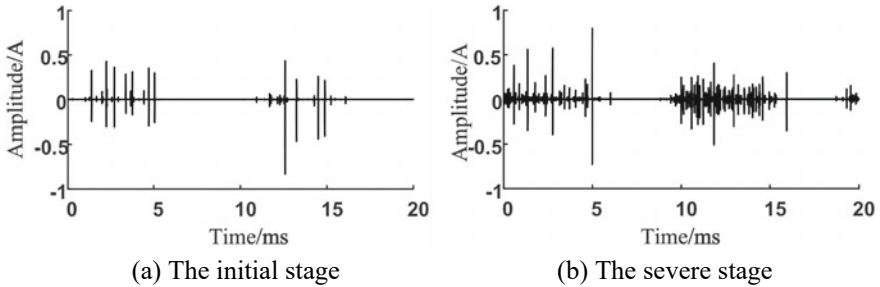
The specific work is: the three types of defect models produced are used as test pieces and are connected to the test system individually. Firstly, the initial discharge voltage of each defect is measured, and the voltage is rapidly increased to the rated working voltage of the joint $U_0 = 8.7 \text{ kV}$; the voltage is continued to be increased in small steps at an interval of 0.5 kV . By observing the waveform displayed on the oscilloscope, if at least one discharge exceeding 10pC is collected within 1 min , then the applied voltage is the initial discharge voltage; otherwise, continue to increase the voltage until at least one discharge of exceeding 10pC is collected within 1 min , then the initial discharge voltage is recorded. The initial discharge voltage is maintained for 30 min and data samples of the initial discharge stage are collected for various defects. Then the insulation deterioration is accelerated by a voltage ramp of approximately 5 kV per voltage gradient, each voltage gradient is maintained for 30 min and data samples are collected until the discharge is more severe (different types of defects are judged by different criteria, such as a large number of dense discharges, or a distinct discharge sound, or insulation breakdown, etc.). Repeat the above operation 5 times for the same test conditions.

2.2 Test Results

According to the variation rule of the number of partial discharge pulses, the test collected the partial discharge signals of insulation scratch, Casing fouling and joint looseness at the initial stage and the severe stage. Five sets of experimental data were randomly selected, and the initial discharge voltages of the three types of defects were extracted by WT filtering and shown in Table 1.

Table 1 Initial discharge voltage for each type of defect

Characteristic quantity	Insulation scratches	Casing fouling	Joint looseness
Voltage/kV	8.7	10.7	11.7
	9	10.9	12.1
	0.1	10.8	12.1
	9	11	12.4
	8.1	10.7	12.2
Average value/kV	8.8	10.8	12.1

**Fig. 2** Map of insulation scratch defects

The partial discharge test waveforms are shown in Fig. 2.

3 Partial Discharge Defect Type Recognition Based on AlexNet Model

To address the problems of subjectivity and insufficient feature extraction capability in traditional recognition methods, this paper uses the AlexNet model to identify the types of partial discharges and improve the recognition accuracy.

3.1 Principle of Convolutional Neural Networks

Convolutional Neural Network (CNN), as one of the most important deep learning network models, is widely used in image processing, image recognition, face recognition and other scenarios due to its excellent feature extraction ability and generalization ability. Figure 3 is a classic CNN structure, the standard CNN mainly consists of input layer, convolution layer, pooling layer, fully connected layer, and output layer [10, 11].

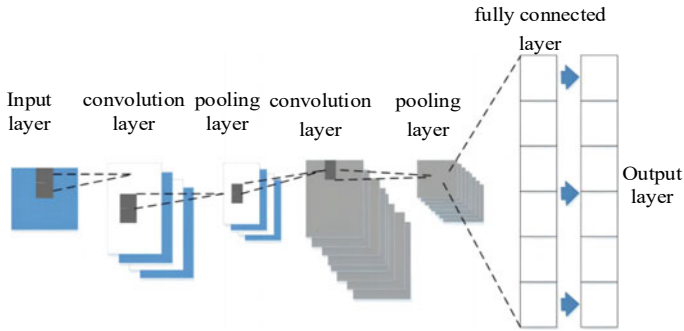


Fig. 3 Diagram of CNN network

Compared with traditional shallow artificial neural networks, CNN is a typical algorithm of deep learning, which takes raw data as input and automatically extracts deep and shallow features of the data layer by layer without human intervention by stacking layers of convolutional and pooling operations, and finally identifies data types based on features. Compared with traditional recognition methods, which require manual construction of feature parameters through feature engineering before the classification task, CNN avoids the subjectivity of feature extraction and the limitation of feature selection to a certain extent.

3.2 AlexNet Model

CNN, the most classical deep learning networks, share the weights of the convolution layers during training so that fewer parameters can be trained in the network, reducing the complexity of the network model and thus obtaining a better generalization capability [12]. At the same time, the pooling operations in the CNN structure reduces the number of neurons in the model and is more robust to the translation invariance of the input space. Moreover, the CNN structure is highly scalable and it can employ a very deep number of layers. Deeper models are more expressive and can handle more complex classification problems. However, with a normal CNN, the overfitting phenomenon becomes more serious as the number of layers increases, and the multi-layer back-propagation of the error signal triggers the phenomenon of gradient dispersion and explosion, leading to a reduction in the recognition rate of the network.

AlexNet is a modified version of the traditional CNN, with more layers than the traditional CNN, the same choice of ReLU as the activation function, the design of a local response normalization layer, the use of neighbouring data for normalization, and the addition of a Dropout layer using the Dropout technique [13]. The basic structure is shown in Fig. 4.



Fig. 4 AlexNet network basic structure

In Fig. 8, Block is the AlexNet network module, Cov is the convolution layer; Fulc1 and Fulc2 are the first and second fully connected layers respectively; LRN is the local response normalization layer; ReLU is the linear rectification function; and Maxpool is the pooling layer, whose activation function is the maximum function. Compared to the traditional CNN, the AlexNet network has an additional LRN layer and a Dropout layer. The LRN layer mainly normalizes the neighbouring data, while the Dropout layer uses a dropout technique to randomly discard individual neurons with a certain probability and replaces the mean value function with a more effective maximum function as the pooling layer activation function. AlexNet can effectively avoid or suppress the phenomenon of gradient disappearance during network training, and the convergence rate of the network model is stable and the model training speed is faster, which ultimately improves the recognition rate.

3.3 Construction of Recognition Network Model

As the partial discharge signal used in practice is not a single frequency component, after WVD time–frequency analysis, the time–frequency distribution of the multi-component signal will interact with each other and generate spurious cross-interference terms. Therefore, the joint VMD–WVD analysis is used in this paper, where the image size is determined by bilinear interpolation and the grey-scale processed image is used as the network input. For effective comparison, the VMD–WVD time–frequency profiles were unified using maximum normalization prior to transformation. The normalized VMD–WVD time–frequency profile of any one partial discharge signal for each type of defect is shown in Fig. 5.

In addition, the choice of image size is crucial, as zooming in and out of an image will result in pixel changes. Too large an image will result in too much useless information and increase unnecessary computation, while too small an image will result in missing graphical features, resulting in insufficient training and reduced

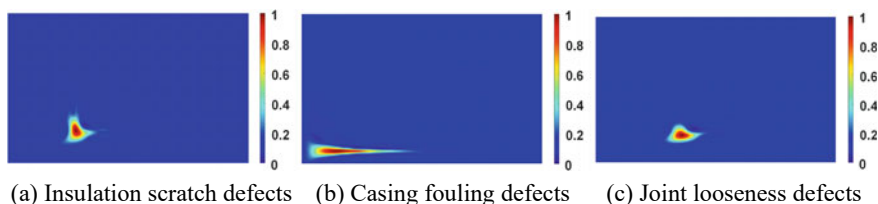


Fig. 5 Normalised VMD–WVD time–frequency mapping

recognition rates [14]. The bilinear interpolation method has been tested to obtain the optimal image size. The pixel values of four points adjacent to any point $R(a_0, b_0)$ in the image are calculated by interpolating the pixel values $P(a, b)$ twice, and then calculating the distance d_1 and d_2 between the interpolated point $P(a, b)$ and the point $R(a_0, b_0)$.

$$\begin{cases} d_1 = a_0 - a \\ d_2 = b_0 - b \end{cases} \quad (1)$$

Interpolate $P(a_0, b)$ according to $P(a, b)$, $P(a + 1, b)$.

$$P(a_0, b) = P(a, b) + d_1[P(a + 1, b) - P(a, b)] \quad (2)$$

Then find $P(a_0, b + 1)$ according to $P(a, b + 1)$, $P(a + 1, b + 1)$.

$$P(a_0, b_0) = P(a_0, b) + d_2[P(a_0, b + 1) - P(a_0, b)] \quad (3)$$

After bilinear interpolation, the size of the VMD-WVD time–frequency map is 650×370 in uniform use. In order to facilitate the network to use the image partial discharge signal for direct recognition and reduce the computation in the model training process, the VMD-WVD time–frequency map of the partial discharge signal is grayed out using the weighted average method, and the image graying formula is shown in the equation [15]:

$$I_{\text{gray}}(i, j) = 0.299R(i, j) + 0.578G(i, j) + 0.114B(i, j) \quad (4)$$

where $I_{\text{gray}}(i, j)$ is the grey scale value of image I at pixel (i, j) , and $R(i, j)$, $G(i, j)$ and $B(i, j)$ are the red, green and blue components at pixel (i, j) respectively.

Using the AlexNet deep learning network to automatically extract the intrinsic features of the grey-scale images of the time–frequency mapping, the final identification of the 3 types of defective discharges, based on the VMD-WVD with improved CNN, its specific steps are as follows.

- (1) The VMD-WVD algorithm is used to decompose the original partial discharge signal to obtain the VMD-WVD time–frequency map, and finally the VMD-WVD time–frequency map is output as an image.
- (2) The resulting VMD-WVD time–frequency profiles were greyed out and divided into training sample S_{train} , validation sample S_{valid} and test sample S_{test} .
- (3) Build an AlexNet deep learning network model, and train the network model with training sample S_{train} and validation sample S_{valid} .
- (4) The cross-entropy loss function is used to derive the training loss values, and the stochastic gradient descent algorithm is used to update the optimization model parameters and optimize the network parameter settings.
- (5) Using the optimal AlexNet deep learning network, we identified the partial discharge type of the test sample S_{test} and obtained the identification results.

4 Analysis of the Recognition Effect

This paper compares the recognition effects of the network at learning rates of 0.01, 0.001, 0.0001 and 0.00001 respectively, as shown in Fig. 6.

In Fig. 6, when the learning rate is 0.01, the recognition accuracy remains almost constant and the recognition rate is lower than the other three learning rates. The analysis shows that the higher learning rate results in incomplete image feature information due to the faster extraction of effective features, thus increasing the loss in the learning process. When the learning rate is less than 0.001, the training speed becomes slower due to the slower learning rate, and it will take more time to achieve the same recognition accuracy if the learning rate is reduced.

In order to analyse the effect of the number of iterations on the recognition rate, the learning rate was set to 0.001 and the number of iterations was 480, the network training results are shown in Fig. 7.

The training loss value of the network gradually decreases and stabilizes with the number of iterations, and the recognition rate curve gradually increases and stabilizes at around 95% with the number of iterations. At the same time, the figure also shows that the recognition rate and the loss value basically level off after the number of iterations reaches 320, and it will take a lot of running time if we continue

Fig. 6 Recognition rate of the network with different learning rates

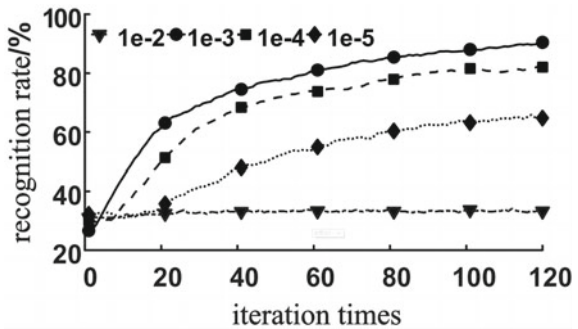
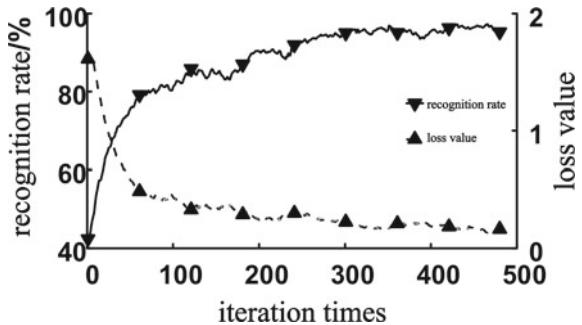


Fig. 7 Effect of the number of iterations on the network



to increase the number of iterations. Therefore, based on the above analysis, the number of iterations is 320 and the learning rate is 0.001.

To further illustrate the advantages of this method over conventional methods in terms of feature depth extraction and identification of partial discharge defect types, this method is compared with the most commonly used SVM method for identifying partial discharge signal waveform features. A total of 300 test samples from each of the three types of defects were substituted into the identification network, and the confusion matrices of the two methods are shown in Tables 2 and 3 respectively.

From Tables 2 and 3, it can be seen that the VMD-WVD time–frequency mapping grayscale images and improved CNN identification method proposed in this paper can identify the three types of defects better, and the average identification rate can reach 95%. For the casing fouling defects, the recognition rate of VMD-WVD temporal spectral grey map combined with AlexNet network model is as high as 98%, while the recognition rates of the other two types of defects are lower than that of the casing fouling defects. The average recognition rate of the traditional PCA-SVM method for the three types of defects was 84.3%, which was 10.7% lower than that of the VMD-WVD time–frequency mapping grayscale images and improved CNN method, and the recognition rate of the VMD-WVD time–frequency mapping grayscale images and improved CNN method was higher than that of the PCA-SVM for each type of defects.

Table 2 VMD-WVD combined with AlexNet pattern recognition

Type of identification	Actual defect category			Recognition rate (%)
	Insulation scratches	Casing fouling	Joint looseness	
Insulation scratches	93	0	7	93.0
Casing fouling	2	98	0	98.0
Joint looseness	0	6	94	94.0
Average value/kV				95.0

Table 3 PCA-SVM pattern recognition

Type of identification	Actual defect category			Recognition rate (%)
	Insulation scratches	Casing fouling	Joint looseness	
Insulation scratches	86	4	10	86.0
Casing fouling	7	85	8	85.0
Joint looseness	12	6	82	82.0
Average value/kV				84.3

5 Conclusion

In this paper, an AlexNet deep learning network is built to construct VMD-WVD time–frequency mapping grayscale images of the original signal of T-type terminal partial discharge as the input for autonomous extraction of image features to identify the three types of T-type terminal partial discharge defect types tested. Meanwhile, the results of the method in this chapter and the traditional SVM recognition method were compared and analysed, and the following conclusions were obtained.

- (1) The AlexNet network used in this paper is an improved CNN network model that can extract image features at a deeper level and has better recognition results and faster training speed in the recognition of partial discharge defect types than traditional CNN models.
- (2) Compared with RGB images, the VMD-WVD time–frequency mapping grayscale images can effectively retain the image feature information, reduce the computation and training time, and increase the recognition rate of the network.
- (3) The average recognition rate of the VMD-WVD spectral grey-scale map combined with the AlexNet network model method can reach 95%, while the average recognition rate of the traditional PCA-SVM method for the three types of defects is only 84.3%, and the recognition rate for each defect type was higher than that of PCA-SVM.

References

1. Stan A, Costinaş S, Ion G (2022) Overview and assessment of HVDC current applications and future trends. *Energies* 15(3):1
2. Winkelmann E, Shevchenko I, Steiner C, Kleiner C, Kaltenborn U, Birkholz P, Steiner T (2022) Monitoring of partial discharges in HVDC power cables 38(1)7–18
3. Chang CK, Chang HH, Boyanapalli BK (2022) Application of pulse sequence partial discharge based convolutional neural network in pattern recognition for underground cable joints. *IEEE Trans Dielectr Electr Insul* 29(3):1070–1078
4. Liu Y, Zhang BJ, Gao X (2022) Establishment and application of a comprehensive system for condition assessment of HV XLPE cable lines. *High Voltage Eng* 48(11):4437–4444 (in Chinese)
5. Guo L, Cao WD, Bai LL et al (2021) Fault diagnosis based on multiscale texture features of cable terminal on EMU of high-speed railway. *IEEE Trans Instrum Measur* 70:1–12
6. Xu L, Zhao AX, Li JM et al (2020) Influence of multiple operating shocks on the partial discharge characteristics of 10 kV cable terminals with knife mark defects. *High Voltage Technol* 46(2):673–681 (in Chinese)
7. Cheng X, Tao SY, Wang W (2013) An example of 110 kV XLPE cable termination discharge detection and disassembly analysis. *Chin J Electr Eng* 33(z1):226–230. (in Chinese)
8. Tang J, Gong NT, Li W et al (2009) Analysis of partial discharge characteristics of high-voltage cross-linked polyethylene cable accessories. *J Chongqing Univ* 32(5):528–534 (in Chinese)
9. Arief YZ, Ahmad H, Hikita M (2008) Partial discharge characteristics of XLPE cable joint and interfacial phenomena with artificial defects. *IEEE Int Power Energy Conf* 1518–1523

10. Kollias D, Zafeiriou S (2021) Exploiting multi-CNN features in CNN-RNN based dimensional emotion recognition on the OMG in-the-wild dataset. *IEEE Trans Affect Comput* 12(03):595–606
11. Kitani R, Iwata S (2023) Verification of interpretability of phase-resolved partial discharge using a CNN with SHAP. *IEEE Access* 11:4752–4762
12. Cortés E, Sánchez S (2021) Deep learning transfer with AlexNet for chest X-ray COVID-19 recognition. *IEEE Lat Am Trans* 19(06):944–951
13. Shi X et al (2021) An improved bearing fault diagnosis scheme based on hierarchical fuzzy entropy and AlexNet network. *IEEE Access* 9:61710–61720
14. Wei Z, Qi B, Zuo J et al (2015) Diagnosis method of oil-paper insulation defects in converter transformers based on partial discharge image features. *Power Grid Technol* 39(4):1160–1166 (in Chinese)
15. Gao AR, Zhu YL, Zhang Y et al (2021) Transformer partial discharge pattern recognition based on marginal spectrum images and deep residual networks. *Power Grid Technol* 45(06):2433–2442 (in Chinese)

Double-Ended Localization Method Based on Joint VMD and WVD Time–Frequency Analysis



Wenhui Li, Guang Liu, Jun Liu, Xin Lu, Haibo Li, Jie Sun, Wen Dai,
and Yao Zhang

Abstract The double-end traveling wave method has been increasingly applied and studied for locating cable defects in operation, but the problem of difficulty in accurately matching and synchronizing the pulse signals in long cables has an impact on the accuracy as well as the accuracy of locating cable defects. This paper proposes an improved double-end traveling wave fault location method based on the joint variational mode decomposition (VMD) and wigner-ville distribution (WVD) time–frequency analysis. By installing sensors at both ends of the cable to collect the partial discharge signals, the phase spectra of the first and last partial discharge pulses are obtained and the phase of the wave head moment and amplitude moment are extracted through the joint analysis of VMD and WVD, and the improved double-end traveling wave fault location method is used to The improved double-ended traveling wave fault location method was used to locate the partial discharge defects in the cable. The improved double-ended travelling wave fault location method uses phase instead of wave speed to avoid the difficulties of matching incoming and reflected signals and the over-dependence on data synchronisation and the accuracy of line parameters. Simulations using PSCAD software for cable lines with a double-ended configuration show that the improved method has higher localisation accuracy and is better than the traditional double-ended traveling wave method for any fault point location.

Keywords Partial discharge · Fault location · Power cable · Double end location

W. Li · G. Liu · J. Liu · X. Lu · J. Sun · W. Dai

Taizhou Power Supply Company of State Grid Zhejiang Electric Power Co. Ltd., Taizhou 318000, Zhejiang, China

H. Li · Y. Zhang (✉)

Science and Technology Branch of Taizhou, Hongchuang Power Group Co., Ltd., Taizhou 318000, Zhejiang, China

e-mail: 810795569@qq.com

© Beijing Paiké Culture Commu. Co., Ltd. 2024

X. Dong and L. Cai (eds.), *The Proceedings of 2023 4th International Symposium on Insulation and Discharge Computation for Power Equipment (IDCOMPU2023)*, Lecture Notes in Electrical Engineering 1100, https://doi.org/10.1007/978-981-99-7393-4_13

135

1 Introduction

Cables are an integral part of life and production. Ensuring their normal operation is an important prerequisite for the operation of power systems [1]. The cable joint is the location with the highest fault rate and it is necessary to strengthen the monitoring of cable joints. At present, there are various means of diagnosing cable joint faults, such as partial discharge detection, dielectric loss detection and insulation resistance detection [2]. Partial discharge detection is an effective way of visually monitoring the degree of insulation deterioration and thus avoiding further safety incidents.

The main methods used to locate partial discharge faults in cables are injection, impedance and travelling wave methods. The most widely used method is Time Domain Reflectometry (TDR), also known as the single-ended travelling wave method, which is widely used in geological exploration, line ranging and localisation of partial discharges [3]. Due to the long cable systems in operation, typically several kilometres or even tens of kilometres, the longest reflected signal can travel up to twice the length of the cable and is severely affected by attenuation and dispersion, resulting in distortion of the reflected signal and affecting the accuracy of TDR positioning [4]. In [5], Zhang Roubing et al. proposed a single-ended traveling wave method based on oscillatory wave testing, in which the localisation accuracy was improved by splitting the different pulse signals with a floating threshold. In the literature [6], Zhang Ruobing et al. proposed a method extraction based on EMD and Teager energy operator for high noise, signal decay and other problems, and identification matching based on DTW algorithm, which can locate the partial discharge point with high accuracy under high accuracy.

Accurate matching of incoming and reflected signals in fault location is the key to TDR. The presence of a large amount of noise during propagation and the susceptibility of the signal to attenuation distortion over the field distance will inevitably have a serious impact on the accuracy of location. The traditional double-terminal method relies on data synchronisation and the accuracy of the localisation is affected by the accuracy of the line parameters. To address these problems, the literature [7] increases the arrival time of the reflected wave from the arrival point of the fault and proposes a formula independent of the propagation speed of the travelling wave. In the literature [8], the accuracy of data synchronisation is ensured by compensating the communication delays through the local fault locator clock.

This paper proposes an improved method for locating double-ended traveling wave short circuit faults to overcome the problem of data synchronization in the double-ended traveling wave method. Due to the longer signal propagation time in long cables, the positioning accuracy is more affected by time. By combining VMD and WVD time–frequency analysis, the wavehead moment of the double-ended partial discharge signal is accurately marked, and phase positioning is used to achieve double-ended synchronisation of the partial discharge signal in the cable, effectively avoiding the problems of difficult matching of incoming and reflected signals and over-dependence on data synchronisation and accuracy of line parameters.

2 Based on Joint VMD and WVD Time–Frequency Analysis

2.1 Shortcomings of Conventional WVD Time–Frequency Analysis

The Wigner-Ville Distribution (WVD) is defined as the Fourier transform of the signal transient autocorrelation function. Compared with the wavelet transform, this method is a time–frequency distribution with a bilinear form, which has excellent time–frequency resolution and mathematical properties, and can better describe the edge characteristics of the signal, transient frequency, etc., and determine the time, frequency and energy of the signal mutation. It can also determine the time, frequency and energy of sudden changes in the signal [9].

However, the cross terms of the WVD become a bottleneck in the application, as the partial discharge signal used in practice is not a single frequency component and different frequency components interact with each other during the calculation process, resulting in cross terms [9]. This can have a significant impact on the results when performing time–frequency analysis of the partial discharge signal. The presence of cross-terms can lead to inaccurate and ineffective extraction and analysis of the partial discharge signal.

Variational Mode Decomposition (VMD) is a new non-recursive decomposition model, which can reflect the signal singularity characteristics well and has the advantages of good stability, high operational efficiency and good robustness. The decomposed IMF contains a large amount of fault information [10–13]. The decomposed IMF contains a large amount of fault information. Therefore, this paper adopts the joint analysis of VMD and WVD for the time–frequency analysis of the partial discharge signal.

2.2 Joint VMD and WVD Time–Frequency Analysis

The WVD for the partial discharge signal $f(t)$ is [14].

$$W_X(t, \omega) = \frac{1}{2\pi} \int f\left(t + \frac{\tau}{2}\right) f^*\left(t + \frac{\tau}{2}\right) e^{-j\omega\tau} d\tau \quad (1)$$

Assume that the partial discharge signal $f(t)$ consists of two signals with different frequency components $f_1(t)$, $f_2(t)$, i.e.

$$f(t) = f_1(t) + f_2(t) \quad (2)$$

Substituting Eq. (2) into Eq. (1) gives the following derivation

$$W_x(t, \omega) = \frac{1}{2\pi} \int \left[f_1\left(t + \frac{\tau}{2}\right) + f_2\left(t + \frac{\tau}{2}\right) \right] \left[f_1^*\left(t + \frac{\tau}{2}\right) + f_2^*\left(t + \frac{\tau}{2}\right) \right] e^{-j\omega\tau} d\tau = W_{f_1}(t, \omega) + W_{f_2}(t, \omega) + 2\text{Re}[W_{f_1 f_2}(t, \omega)] \quad (3)$$

The $2\text{Re}[W_{f_1 f_2}(t, \omega)]$ in Eq. (3) is the cross term.

The theoretical analysis of VMD shows that VMD can decompose the partial discharge signal into multiple IMFs with a single frequency component, i.e. [15–17]

$$f(t) = \sum_{k=1}^K f_{\text{IMF-k}}(t) \quad (4)$$

In Eq. (4), $f_{\text{IMF-k}}$ is the k IMF components obtained from the WMD decomposition of the partial discharge signal. Therefore, in order to avoid the influence of the cross term of WVD, the joint time–frequency analysis method of VMD and WVD [13, 16] is used, i.e., first VMD decomposes the original partial discharge signal to obtain k IMF components, then WVD is performed on the k IMFs separately, and finally the results are linearly superimposed to obtain the WVD of the original partial discharge signal, whose expression is as follows

$$W_x(t, \omega) = \frac{1}{2\pi} \sum_{k=1}^K \int f_{\text{IMF-k}}\left(t + \frac{\tau}{2}\right) f_{\text{IMF-k}}^*\left(t - \frac{\tau}{2}\right) e^{-j\omega\tau} d\tau \quad (5)$$

In this paper, an adaptive variational modal decomposition algorithm based on energy difference [21] is used to improve the VMD. The flow of VMD combined with WVD for time–frequency analysis is shown in Fig. 1, and its main steps are as follows.

- (1) Initialize the number of decomposition layers $k = 2$ and set the maximum number of decomposition layers $k = 10$.
- (2) The k -layer VMD decomposition of the partial discharge signal and the calculation of the energy of the partial discharge signal and the energy of each IMF layer.
- (3) Calculation of the energy difference parameter ρ layer by layer starting from $k = 2$ up to a preset maximum number of modes.
- (4) Define the absolute rate of change of energy difference β , select the k corresponding to the maximum value of β as the final decomposition layer, and obtain the $f_{\text{IMF-k}}$ feature component of the partial discharge signal.
- (5) WVD analysis for each of the k $f_{\text{IMF-k}}$

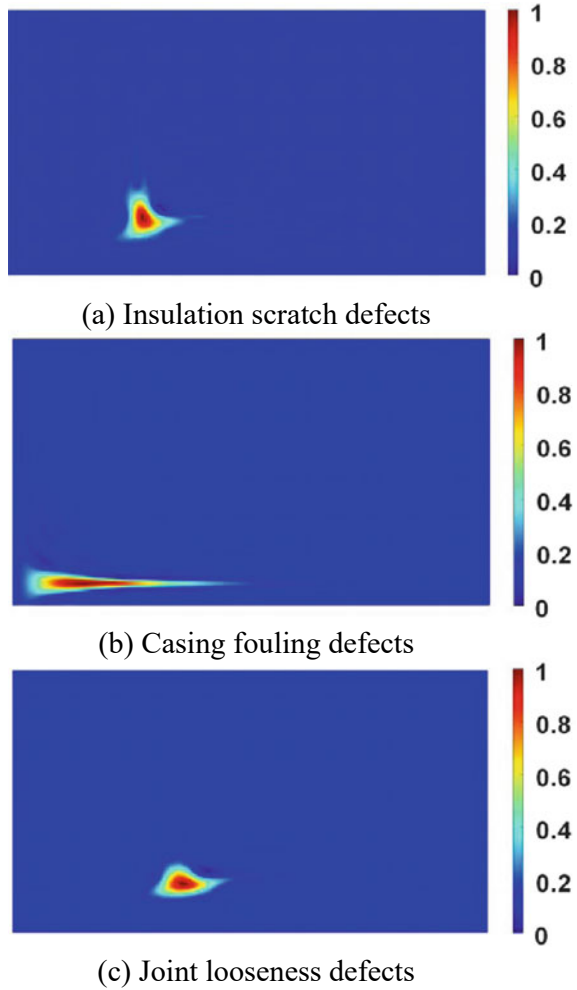


Fig. 1 Joint time–frequency analysis process of VMD and WVD

- (6) The results of the WVD analysis of each f_{IMF-k} are linearly superimposed to finally obtain the time–frequency analysis of the original partial discharge signal $f(t)$.

The joint VMD and WVD time–frequency diagram is shown in Fig. 2.

Fig. 2 VMD-WVD time–frequency mapping



3 Based on Joint VMD and WVD Time–frequency Analysis

3.1 Traditional Double-Ended Traveling Wave Method

The traditional double-ended travelling wave method locates the fault point by determining the time difference between the arrival of the travelling wave at each end of the line separately, calculated as Eq. (6).

$$\begin{cases} L_{MF} = \frac{L-(t_{n1}-t_{m1})v}{2} \\ L_{NF} = \frac{L-(t_{m1}-t_{n1})v}{2} \end{cases} \quad (6)$$

where L_{MF} is the distance from fault point F to endpoint M; L_{NF} is the distance from fault point F to endpoint N; t_{n1} and t_{n2} are the time for the traveling wave to reach the two endpoints respectively; L is the distance between the two endpoints M and N, and v is the propagation speed of the traveling wave.

The double-ended travelling wave method is more reliable and accurate than the single-ended travelling wave method. However, the traditional double-ended method relies on data synchronisation and its positioning accuracy is strongly influenced by the accuracy of the line parameters.

3.2 Improved Double-Ended Positioning Combining VMD and WVD

The steps are shown below.

Sensors are installed at the first and last ends of the cable, the signals are collected and de-noised to extract and split the first and last partial discharge signals. The partial discharge signal is transformed into a frequency domain signal according to Eq. (7).

$$f_{fft}(n) = \text{Re}[f_{fft}(n)] + j\text{Im}[f_{fft}(n)] \quad (7)$$

The phase spectrum of the first and last partial discharge pulses is calculated by substituting the frequency domain signal into Eq. (8) in turn.

$$\varphi(n) = \arctan\left(\frac{\text{Re}[f_{fft}(n)]}{\text{Im}[f_{fft}(n)]}\right) \quad (8)$$

Initialize the number of decomposition layers $k = 2$, set the maximum number of decomposition layers $k = 10$; decompose the partial discharge signal into k VMD layers, calculate the energy of the partial discharge signal and the energy of each IMF layer.

The energy difference parameter ρ is calculated layer by layer starting from $k = 2$ up to a preset maximum number of modes, the absolute rate of change of energy difference β is defined, the k corresponding to the maximum value of β is selected as the final decomposition layer, and IMF1 is selected as the characteristic component of the partial discharge signal.

The WVD instantaneous energy distribution of the IMF is found using the WVD, and the moment of amplitude of the WVD instantaneous energy distribution is the moment of the wavehead of the partial discharge signal.

The wavehead moment and amplitude moment phases are extracted from the phase spectrum and substituted into Eq. (9) to calculate the fault location, which can be obtained from the average value of $d(\omega)$ for the partial discharge fault.

$$d(\omega) = \frac{\varphi_1}{\varphi_1 + \varphi_2 g(\omega)} l \quad (9)$$

Due to the complex structure of the distribution network and the influence of environmental noise in the field, it is difficult to detect the wavehead of the partial discharge signal [18]. VMD and WVD jointly can adaptively decompose the partial discharge signal into IMF with a large amount of fault characteristic information, accurately describe the energy change of the signal over time, detect the sudden change point of the partial discharge signal to determine the wavehead moment of the partial discharge signal, and synchronize the signal at both ends. The partial discharge signal collected by the test is used for verification, and a set of partial discharge signals of three types of defects in two discharge stages are selected to determine the number of VMD decomposition layers of the signal, and the specific results are shown in Table 1, where β_a and β_b are the absolute rates of change of energy difference between the starting stage of insulation scratch and the severe stage, β_c and β_d are the absolute rates of change of energy difference between the starting stage of casing accumulation and the severe stage, β_e and β_f are the absolute rates of change of energy difference at the beginning and severe stages of casing staining.

From Table 2, $\beta_a, \beta_b, \beta_e, \beta_f$ have the maximum value when $k = 9$, and β_c and β_d have the maximum value when $k = 10$. Therefore, $k = 8$ is selected as the decomposition layer of the partial discharge signal of insulation scratch and joint loosening, and $k = 9$ is the decomposition layer of the partial discharge signal of casing accumulation.

4 Analysis of Positioning Effects

In order to further verify the applicability of the above double-end location method based on the joint VMD and WVD time–frequency analysis in long cable lines, the proposed joint VMD and WVD double-end location was verified by simulating the long cable lines using PSCAD software.

Table 1 Absolute change rate of VMD decomposition energy difference

Decomposition layers	Absolute change rate					
	β_a	β_b	β_c	β_d	β_e	β_f
2	0.0474	0.0386	0.0215	0.0045	0.0408	0.0134
3	0.0643	0.0466	0.0355	0.1126	0.0542	0.0268
4	0.0829	0.0316	0.0248	0.0248	0.0447	0.0579
5	0.0621	0.0285	0.0135	0.1260	0.0163	0.1424
6	0.1728	0.3566	0.0128	0.1740	0.1887	0.4983
7	0.6178	0.9354	0.4431	0.3962	0.6845	0.7212
8	1.7437	7.1710	0.4498	0.1406	2.1310	3.5916
9	0.3095	1.9686	1.1727	0.4168	0.2407	0.8174
10	0.0474	0.0386	0.0215	0.0045	0.0408	0.0134

Table 2 VMD and WVD joint double-ended positioning error

Fault distance (m)	Ranging results (m)	Error (m)	Error rate (%)
1700	1689.5	10.5	0.62
2400	2387.3	12.7	0.53
3100	3085.1	14.9	0.48
3800	3782.1	17.9	0.47
4500	4473.9	26.1	0.58
Equal error rate			0.54

According to the measured partial discharge signal waveforms, it is shown that the adoption of double exponential oscillation attenuation pulses can simulate the partial discharge signal well, and the measured signal can be expressed as Eq. (10)

$$S(t) = A \left[\exp\left(-\frac{1.3t}{\tau}\right) - \exp\left(-\frac{2.2t}{\tau}\right) \right] \sin(2\pi f_c t) \quad (10)$$

where A is the pulse amplitude constant, set to 5 mA; τ is the attenuation constant, set to 100 ns; f_c is the oscillation frequency, set to 5 MHz; and the sampling rate f_s is set to 500 MHz.

The simulation model line built is shown in Fig. 3. By setting different fault locations, cable lengths and sampling frequencies, the single-ended traveling wave method, the double-ended traveling wave method and the combined VMD and WVD double-ended localisation method were tested and compared to analyse the localisation effect of the double-ended localisation method based on the combined VMD and WVD time–frequency analysis.

Firstly, the cable length $l = 1500 \sim 3000$ m was set in steps of 100m, and the pulse was recorded from the end to the first end at each length, and the final average value was taken as the wave velocity.

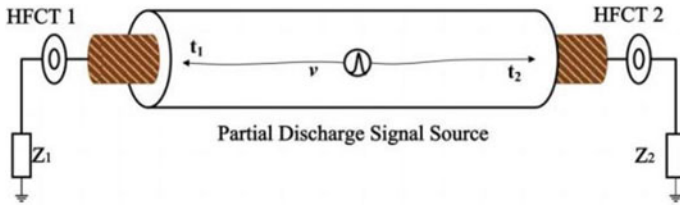
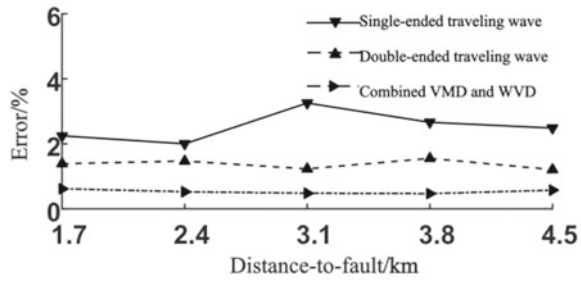


Fig. 3 Combined analysis of VMD and WVD

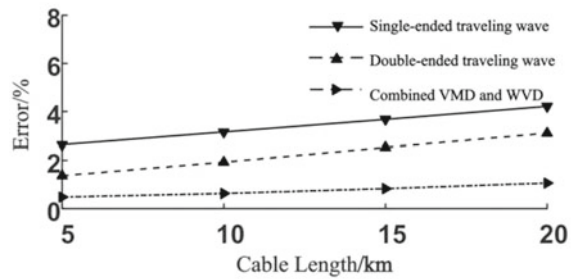
For different fault locations: set cable length $l = 6000$ m, distance between fault and first end $d = 1700$ m, 2400 m, 3100 m, 3800 m, 4500 m; for different cable lengths: change cable length $l = 5000$ m, 10000 m, 15000 m, 20000 m, keep fault distance $d = 3/5l$, locate set cable length $l = 6000$ m, distance between fault and first end $d = 3/5l$. length $l = 6000$ m, fault and first end distance $d = 1700$ m, 2400 m, 3100 m, 3800 m, 4500 m; for different sampling frequencies: set cable length $l = 5000$ m, fault distance $d = 1/2l$. The three positioning algorithm errors are shown in Fig. 4.

The results show that, keeping the cable length constant, the change of the local position has a small effect on the error of the three localisation methods, and the errors of the combined VMD and WVD phase methods are 0.62% , 0.53% , 0.48% , 0.47% and 0.58% respectively, with an average error of 0.54% ; the localisation error of the three methods increases with the increase of the cable length and decreases with the increase of the sampling rate. For different fault locations, cable lengths and sampling frequencies, the combined VMD and WVD time–frequency analysis outperforms the single-ended traveling wave method and the double-ended traveling wave method in terms of localisation accuracy.

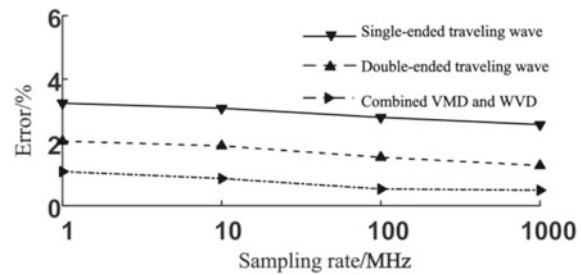
Fig. 4 Error comparison of different fault location methods



(a) Positioning error of different partial discharge positions



(b) Positioning error of different cable lengths



(c) Positioning error of different sampling rate

5 Conclusion

In this paper, the traditional double-ended traveling wave method is improved for the time synchronization problem, using VMD and WVD joint time–frequency analysis, and using phase positioning to achieve double-ended synchronization of the incoming and outgoing signals in the cable local area, effectively avoiding the problem of difficult matching of incoming and outgoing signals and excessive dependence on data synchronization. In this paper, phase is used instead of wave speed, effectively reducing the dependence of fault location on line parameters. In the case of long cable signal propagation times where synchronisation is difficult, the localisation error

based on the combined VMD and WVD time–frequency analysis is significantly lower than that of the conventional double-ended traveling wave method.

References

1. Winkelmann E, Shevchenko I, Steiner C, Kleiner C, Kaltenborn U, Birkholz P, Steiner T (2022) Monitoring of partial discharges in HVDC power cables 38(1):7–18
2. Li SY et al (2022) Partial discharge detection and defect location method in GIS cable terminal. *Energies* 16(1):413–413
3. Muhammad S et al (2019) Identification and location of PD defects in medium voltage underground power cables using high frequency current transformer. *IEEE Access* 7:103608–103618
4. YII CC et al (2017) Multi-end PD location algorithm using segmented correlation and trimmed mean data filtering techniques for MV underground cable. *IEEE Trans Dielectr Electr Insul* 24(1):92–98
5. Zhang RB, Chen ZH, Du G (2019) Automatic localization algorithm of cable partial discharge under oscillating wave voltage based on traveling wave method. *High Voltage Technol* 45(04):1289–1296 (in Chinese)
6. Zhang RB, Jin S, Du G (2020) Localization method of partial discharge in cables under oscillation waves based on EMD and DTW algorithms. *High Voltage Technol* 46(01):273–281 (in Chinese)
7. Gilany M, Ibrahim DK et al (2017) Traveling-wave-based fault-location scheme for multi-ended underground cable system. *IEEE Trans Power Delivery* 22(1):82–89
8. Lopes FV, Silva KM, Costa FB et al (2015) Real-time traveling-wave-based fault location using two-terminal unsynchronized data. *IEEE Trans Power Delivery* 30(3):1067–1076
9. Gao JC, Zhu, Li Y, Zheng YY et al (2019) Partial discharge type identification based on joint VMD and WVD distribution with stacked sparse self-coding networks. *Chin J Electr Eng* 39(14): 4118–4129
10. Wang YW et al (2022) A denoising method for mining cable PD signal based on genetic algorithm optimization of VMD and wavelet threshold. *Sensors* 22(23):9386–9386
11. Yang JJ et al (2022) A novel denoising method for partial discharge signal based on improved variational mode decomposition. *Energies* 15(21):8167–8167
12. Deng Y et al (2022) Efficient partial discharge signal denoising method via adaptive variational modal decomposition for infrared detectors. *Infrared Phys Technol* 125
13. Chen X et al (2022) Feature extraction of partial discharge in low-temperature composite insulation based on VMD-MSE-IF. *CAAI Trans Intell Technol* 7(2):301–312
14. Jin YH, Wei MF, Li QX (2023) An RF fingerprint extraction method based on time-frequency domain feature fusion. *J Phys, Conf Ser* 2424(1)
15. Dhandapani R et al (2021) Enhanced partial discharge signal denoising using dispersion entropy optimized variational mode decomposition. *Entropy* 23(12):1567–1567
16. Liang YF et al (2023) A VMD-PE-SG denoising method based on K–L divergence for satellite atomic clock [J]. *Meas Sci Technol* 34(5)
17. Zhao ZN et al (2023) Hybrid VMD-CNN-GRU-based model for short-term forecasting of wind power considering spatio-temporal features. *Eng Appl Artif Intell* 121
18. Zhang M et al (2021) A double-terminal traveling-wave-based method using novel noncontact sensors for fault location in transmission cable lines. *IEEE Access* 9:80797–80805

Particle-In-Cell/Monte Carlo Collisional Simulation of Space Charge Layer Formation and Development in Nitrogen Negative Streamers



Jianxin Wang, Tiejun Li, Hua Zhang, Jiatao Zhang, Zhuo Chen, Dan Wang, and Lijun Wang

Abstract In this paper, the space charge layer formation and development in negative streamers is simulated using a one-dimensional particle-in-cell/Monte Carlo collisional model. The effects of the space charge layer on the negative streamer discharge are investigated. The space charge layer reduces the effect of the external field on the discharge. During the streamer propagation, the thickness of the space charge layer decreases; the average electron energy in the plasma is as low as 2 eV, which is proved to be the result of rotational and vibrational excitations; and because of the electric field shielding of the space charge layer, the electron energy distribution shifts toward low energy.

Keywords Vacuum breakdown · Particle-in-cell · Monte Carlo collisional simulation · Plasma

J. Wang · T. Li · H. Zhang · J. Zhang
Langfang Power Supply Company of State Grid Jibei Electric Power Co., Ltd., Hebei
Langfang 100054, China
e-mail: 13722660325@139.com

J. Zhang
e-mail: zhangjia888222@sina.com

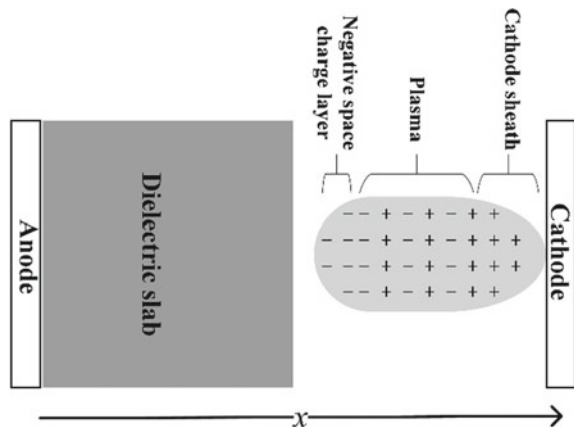
Z. Chen (✉) · D. Wang · L. Wang
State Key Laboratory of Electrical Insulation and Power Equipment, Xi'an Jiaotong University,
Shaanxi Xi'an 710049, China
e-mail: cz18191523193@163.com

L. Wang
e-mail: lijunwang@mail.xjtu.edu.cn

1 Introduction

The streamer is the foundation of some industrial applications, for examples, plasma helped ignition [1], material surface treatment [2], polluted air cleaning [3], and breakdown in power switches [4]. Since Raether [5], Loeb and Meek [6] first reported on the streamer mechanism, the topic has been popular. Positive streamers can emerge at a lower electric field, so in experiments, positive streamers are easy to form and become popular [7]. Apart from this, negative streamers has many usages in industry, for examples, C-GIS and trigatrons [4], so it is indispensable to research on negative streamers. Negative streamers can initiate from several seed electrons. During the propagation of electron avalanches, electrons are accelerated efficiently and accumulate at the front, while ions are left behind. As a result, a negative space charge layer and a cathode sheath form at the head and tail respectively of the streamer as shown in Fig. 1. The space charge layer plays an important role during the streamer propagation. In ref. [8], it was shown that the space charge layer can act like an electron accelerator and may be a possible source for X-rays. In ref. [9], the author believes that due to the instability of the space charge layer at the tip of the negative streamer, the streamer branches in a uniform electric field above the threshold. Therefore, a deep understanding of the space charge layer formation and development in negative streamers is very important and necessary. In ref. [10], the authors developed a one-dimensional fluid model in local field approximation to investigate the negative streamer ionization front and compared results with those from particle models. The difference between the results of the particle model and the fluid model is mainly in the front, and this effect cannot be reflected in the velocity, but is seen in the ionization level behind the front. In ref. [11], a high order fluid model was developed and used to study the propagation of negative fronts in nitrogen. Electron density, electric field, average energy and propagation velocity were given by this high order fluid model. In ref. [12], the particle model was applied to reproduce the ionization front formation and development in argon and nitrogen.

Fig. 1 The schematic diagram of the simulation physical model



Although the space charge layer can also be studied through fluid models, a particular particle model is indispensable considering some non-equilibrium characteristics. So in this paper, a one-dimensional (1D) particle-in-cell/Monte Carlo collisional (PIC/MCC) model is developed, and a detailed process of the space charge layer formation and development during the negative streamer propagation in nitrogen is given. The rotational excitation between electrons and nitrogen molecules is included in the simulations.

2 Model Description

Following the configuration chosen in ref. [12], the similar configuration used in this study includes two parallel planar electrodes, a gas gap and a dielectric slab (the relative dielectric constant is 3.5) to avoid the transition to the arc. As shown in Fig. 1, the anode grounded is located at $x = 0$, and the cathode with a nanosecond pulsed voltage is located at $x = 1$ cm. The length of the gas gap is 5 mm. The nanosecond pulsed voltage applied to the cathode has a rise time of 10 ns. A typical voltage with amplitude of 100 kV is plotted in Fig. 2.

The PIC/MCC model is 1 dimensional in space and 3 dimensional in velocity (1D3V). Using the XOOPIC code which has been validated in previous works [13], the charged particles are followed by the Newton's second law; we get the electric field through solving the Poisson equation in 1D Cartesian coordinates; collisions between charged particles and neutrals are handled with the Monte Carlo collision

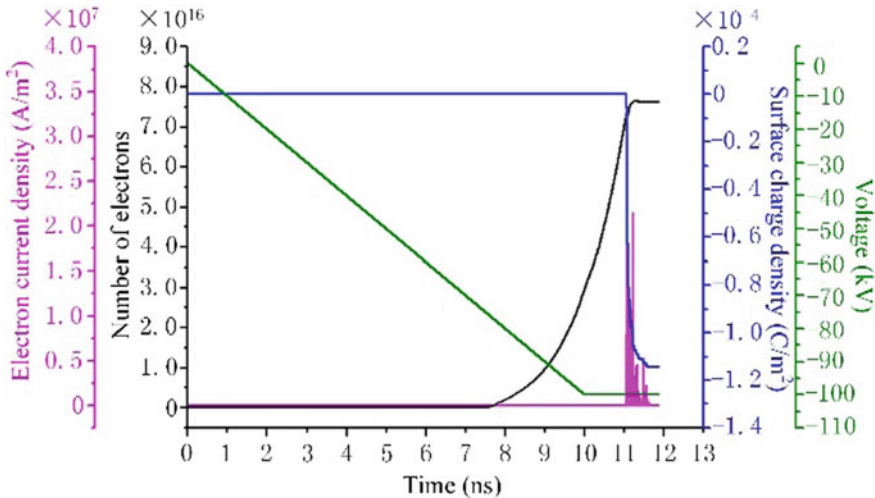


Fig. 2 The voltage, the number of electrons in the calculation domain, the electron current density and the charge density on the dielectric slab surface as the function of time. The background gas is nitrogen; the voltage amplitude is 100 kV; the gas temperature is 300 K

method. Elastic scattering collision [14], impact ionization [14], rotational excitation [15], vibrational excitation [14] and electronic excitation [14] between electrons and nitrogen are included in simulations and listed in Table 1. Besides reactions involving electrons, momentum exchange and charge exchange between ions and molecules are also included. At the beginning of the simulation, 100 electrons are placed near the cathode. The weight of the macro particle is 1 at the beginning and adapted during the simulation. A dynamic weight managing method is applied, which can product a reasonable distribution of weights as discussed in ref. [16]. The simulations are performed on an Intel (R) Xeon (R) CPU E5-2650 v2 @2.60 GHz with four cores. The maximum weight of the macro particles is about 5×10^9 , and 43 h are taken to run single operating condition in this work.

3 Results and Discussion

In the baseline simulation, we use nitrogen as background gas; the gas density is $2.5 \times 10^{25} \text{ m}^{-3}$; we set the gas temperature at 300 K; and the voltage amplitude applied on the cathode is 100 kV. For stable and reliable results, the space interval $\Delta x = 5 \times 10^{-7} \text{ m}$ and time interval $\Delta t = 1 \times 10^{-13} \text{ s}$ are used. The time evolution of the applied voltage, the number of electrons in the calculation domain, the electron current density and the surface charge density deposited on the dielectric slab is shown in Fig. 2. It can be seen that the increasing rate of electron number changes at about 7.5 ns. The change of the electron increasing rate indicates the transition in the discharge from the avalanche regime to the space charge affected regime. So 7.5 ns can be regarded as the time when the negative space charge layer forms in this simulation at the streamer front. We can see that the electron current density and the surface charge density deposited increase suddenly at about 11 ns, which indicates the streamer front arrives at the dielectric slab.

Figure 3 shows the density of electrons and ions at different times. The density before 7 ns is low and not plotted here. At 7 ns, the electron density and the ion density are at a similarly low level, about 10^{14} m^{-3} . Note that at this time, the space charge layer has not formed. As the voltage increases with time, electrons are accelerated efficiently, and ionizations occur frequently. So the streamer front moves forward, and the density of charged particles increases. At 8 ns, the maximum density of electrons in the streamer front comes up to $9 \times 10^{18} \text{ m}^{-3}$, while the ion density is obviously lower than the electron density. As a result, a noticeable negative space charge layer forms at the streamer head as shown in Fig. 3b. At 9 ns, the thickness of the negative space charge layer is about 2 mm as shown in Fig. 3c, while at 11 ns, the time before the streamer arrives at the dielectric slab, the negative space charge layer is so thin that is difficult to be distinguished in Fig. 3e. During the development of the space charge layer, the thickness decreases. At 12 ns, the streamer arrives at the dielectric slab as shown in Fig. 3f. The negative space charge layer disappears because the negative space charge deposits on the dielectric slab, which results in the suddenly increases of electron current density and surface charge density in Fig. 2

Table 1 Considered reactions involving electrons

Reaction	Equation	Threshold energy (eV)	References
Total scattering	$e + N_2 \rightarrow e + N_2$	0	[17]
Ionization	$e + N_2 \rightarrow 2e + N_2^+$	15.6	[17]
Rotational excitation	$e + N_2 \rightarrow e + N_2(rot)$	0.02	[18]
Vibrational excitation	$e + N_2 \rightarrow e + N_2(v = 1)$	0.29	[17]
Vibrational excitation	$e + N_2 \rightarrow e + N_2(v = 2)$	0.59	[17]
Vibrational excitation	$e + N_2 \rightarrow e + N_2(v = 3)$	0.88	[17]
Vibrational excitation	$e + N_2 \rightarrow e + N_2(v = 4)$	1.17	[17]
Vibrational excitation	$e + N_2 \rightarrow e + N_2(v = 5)$	1.47	[17]
Vibrational excitation	$e + N_2 \rightarrow e + N_2(v = 6)$	1.76	[17]
Vibrational excitation	$e + N_2 \rightarrow e + N_2(v = 7)$	2.06	[17]
Vibrational excitation	$e + N_2 \rightarrow e + N_2(v = 8)$	2.35	[17]
Electronic excitation	$e + N_2 \rightarrow$ $e + N_2(A^3\Sigma_u^+, v = 0 - 4)$	6.17	[17]
Electronic excitation	$e + N_2 \rightarrow$ $e + N_2(A^3\Sigma_u^+, v = 5 - 9)$	7.00	[17]
Electronic excitation	$e + N_2 \rightarrow e + N_2(B^3\Pi_g)$	7.35	[17]
Electronic excitation	$e + N_2 \rightarrow e + N_2(W^3\Delta_u)$	7.36	[17]
Electronic excitation	$e + N_2 \rightarrow$ $e + N_2(A^3\Sigma_u^+, v > 10)$	7.80	[18]
Electronic excitation	$e + N_2 \rightarrow e + N_2(B^3\Sigma_u^-)$	8.16	[17]
Electronic excitation	$e + N_2 \rightarrow e + N_2(a^1\Sigma_u^-)$	8.40	[17]
Electronic excitation	$e + N_2 \rightarrow e + N_2(a^1\Pi_g)$	8.55	[17]
Electronic excitation	$e + N_2 \rightarrow e + N_2(w^1\Delta_u)$	8.89	[17]
Electronic excitation	$e + N_2 \rightarrow e + N_2(C'^3\Pi_u)$	11.03	[17]
Electronic excitation	$e + N_2 \rightarrow e + N_2(E^3\Sigma_g^+)$	11.88	[17]
Electronic excitation	$e + N_2 \rightarrow e + N_2(a''^1\Sigma_g^+)$	12.25	[17]

Figure 4 shows the distributions of the electron velocity and the ion velocity in x-direction. At 8 ns, the electron velocity in the negative streamer front is up to 3×10^6 m/s, while it is below 1×10^6 m/s in the plasma as shown in Fig. 4a. The increase of the velocity in the streamer front is resulted from the electric field enhanced by the negative space charge at the streamer front. It also can be seen in Fig. 4a that besides the streamer front, the electron velocity in the cathode sheath is also enhanced. This phenomenon can be explained by the distorted electric field resulted from the positive space charge which located in the cathode sheath. However, at the next moment as shown in Fig. 4b, the electrons in the cathode sheath are accelerated into the plasma, and the velocity decreases. As time goes by, the electron velocity in the

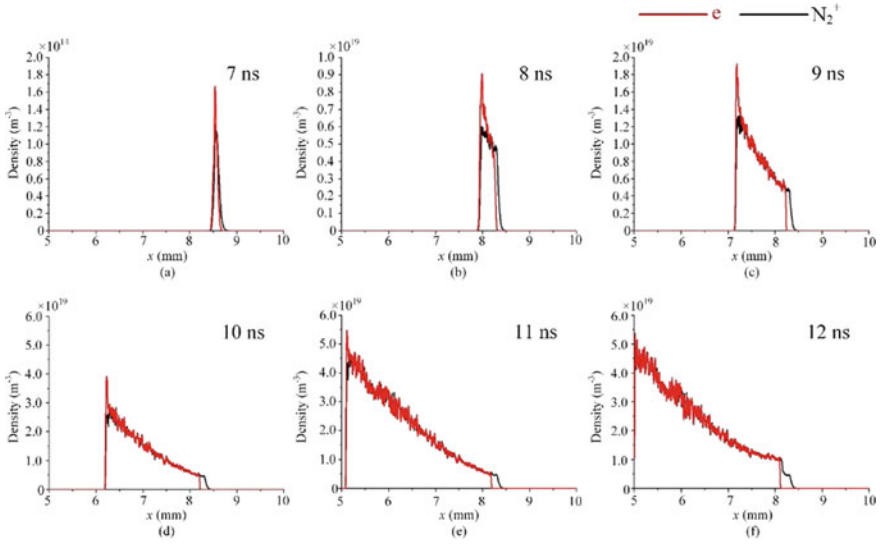


Fig. 3 The density of electrons and ions. The background gas is nitrogen; the voltage amplitude is 100 kV; and the gas temperature is 300 K

negative space charge layer and the ion velocity in the cathode sheath increase. The maximum electron velocity and ion velocity come up to 4×10^6 m/s and 7500 m/s respectively as shown in Fig. 4d and h. It should be noted that velocities in positive x -direction and opposite x -direction are not equilibrium for both electrons and ions because electrons at the streamer front are accelerated toward the anode, while ions in the cathode sheath are accelerated toward the cathode.

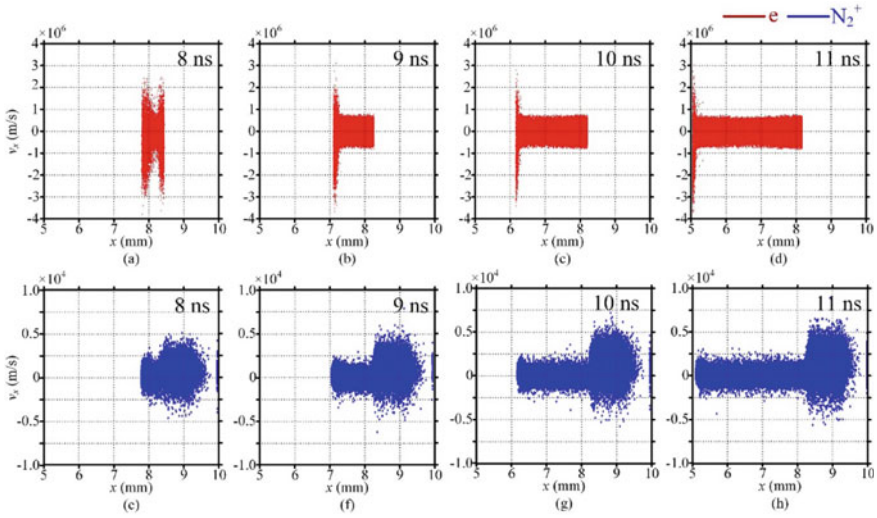


Fig. 4 The distributions of the electron velocity and the ion velocity in x -direction. The back

4 Conclusion

The formation and development of space charge layers under pulse voltage were studied using a one-dimensional PIC/MCC model. A complete negative current structure has been proposed, including a negative space charge layer, plasma body, and cathode sheath. During the formation and propagation of negative current, a negative space charge layer is formed at the front of the current. The space charge layer reduces the influence of external fields on discharge. With the development of the space charge layer, the electron energy increases while the thickness decreases, which may increase the stability of the streamer front. After the formation of the space charge layer, the energy distribution of electrons shifts towards low energy due to the increase in plasma, where the electric field is shielded by space charges, and electrons quickly lose energy through excitation collisions.

Acknowledgements This work is supported by National Natural Science Foundation of China (U1630135) and National Key Basic Research Program of China (2015CB251002).

References

1. Starikovskiy A, Aleksandrov N (2013) Plasma-assisted ignition and combustion. *Prog Energy Combust Sci* 39(1):61–110
2. Stoffels E, Kieft IE, Sladek REJ (2003) Superficial treatment of mammalian cells using plasma needle. *J Phys D: Appl Phys* 36(23):2908

3. Kozák T, Bogaerts A (2014) Splitting of CO₂ by vibrational excitation in non-equilibrium plasmas: a reaction kinetics model. *Plasma Sources Sci Technol* 23(4):045004
4. Wang L, Huang X, Jia S et al (2014) Experimental investigation of electrode erosion of trigatron in microsecond arc discharge process. *IEEE Trans Plasma Sci* 42(5):1393–1399
5. Raether H (1939) Die Entwicklung der Elektronenlawine in den Funkenkanal: Nach Beobachtungen in der Nebelkammer. *Z Phys* 112(7–8):464–489
6. Loeb LB, Meek JM (1940) The mechanism of spark discharge in air at atmospheric pressure. II. *J Appl Phys* 11(7):459–474
7. Luque A, Ratushnaya V, Ebert U (2008) Positive and negative streamers in ambient air: modelling evolution and velocities. *J Phys D: Appl Phys* 41(23):234005
8. Köhn C, Chanrion O, Babich LP et al (2018) Streamer properties and associated x-rays in perturbed air. *Plasma Sources Sci Technol* 27(1):015017
9. Arrayás M, Ebert U, Hundsdorfer W (2002) Spontaneous branching of anode-directed streamers between planar electrodes. *Phys Rev Lett* 88(17):174502
10. Li C, Brok WJM, Ebert U et al (2007) Deviations from the local field approximation in negative streamer heads. *J Appl Phys* 101(12):123305
11. Markosyan AH, Dujko S, Ebert U (2013) High-order fluid model for streamer discharges: II. Numerical solution and investigation of planar fronts. *J Phys D: Appl Phys* 46(47):475203
12. Taccogna F, Pellegrini F (2018) Kinetics of a plasma streamer ionization front. *J Phys D: Appl Phys* 51(6):064001
13. Messmer P, Bruhwiler DL (2014) A parallel electrostatic solver for the VORPAL code. *Comput Phys Commun* 164(1–3):118–121
14. LXCAT Homepage. <http://www.lxcat.net> for more information on Biagi database. Accessed 3 July 2021
15. LXCAT Homepage. <http://www.lxcat.net> for more information on Phelps database. Accessed 3 July 2021
16. Wang D, Wang L, Zheng Y (2018) Particle-in-cell/Monte Carlo collisional simulation of negative streamer formation and branching between planar electrodes. *J Appl Phys* 124(20):203301
17. See <http://www.lxcat.net> for more information on Biagi database (last accessed on July 26, 2023)
18. See <http://www.lxcat.net> for more information on Phelps database (last accessed on July 26, 2023)

Research on Switchgear Partial Discharge Signal Type Identification Based on Composite Neural Network



Renfeng Wang, Xiang Zheng, Jingjie Yang, and Zhihai Xu

Abstract Due to the low accuracy of traditional machine learning algorithm to identify the local discharge signal type, this paper proposes a BP neural network (BPNN) identification method based on improved whale optimization algorithm (WOA)—Cubic Improved Whale Optimization Algorithm Back Propagation Neural Network (CIWOA-BP) to achieve the purpose of improving the accuracy of local discharge signal type identification in switchgear. The method improves the algorithm ability and convergence accuracy of the traditional WOA by combining adaptive inertia weights with improved convergence factors through Cubic chaotic mapping of the initial population, and the improved algorithm gives the optimal weights and thresholds to the BPNN to enhance the recognition accuracy of the model, while maintaining the generalization capability and fault tolerance of the BPNN. In this paper, three types of TEV partial discharge (PD) models of switchgear are established, the feature quantities are downscaled using wavelet soft threshold denoising and principal component analysis (PCA), and the CIWOA-BP algorithm is used to classify the discharge defect types. The results show that the recognition rates of CIWOA-BP are all above 93.3%, which is better than WOA-BP and BPNN models, proving the practicality of this recognition method.

Keywords PD · Pattern recognition · CIWOA-BP · Chaotic mapping · Adaptive inertia weight

1 Introduction

Switchgear failure is mainly caused by insulation defects, and partial discharge of switchgear is the main cause of insulation defects. After partial discharge occurs, if not handled in time, it will change from weak to strong and finally lead to insulation breakdown, further losing the insulation capacity of the switchgear and eventually

R. Wang (✉) · X. Zheng · J. Yang · Z. Xu
College of Automation and Electrical Engineering, Dalian Jiaotong University, Dalian, China
e-mail: wangrenfeng666@163.com

© Beijing Paiké Culture Commu. Co., Ltd. 2024
X. Dong and L. Cai (eds.), *The Proceedings of 2023 4th International Symposium on Insulation and Discharge Computation for Power Equipment (IDCOMPU2023)*, Lecture Notes in Electrical Engineering 1100, https://doi.org/10.1007/978-981-99-7393-4_15

leading to power outage, which brings serious losses to the national economy. Therefore, detection equipment is required to provide accurate partial discharge information to avoid losses to the maximum extent, and the identification of partial discharge patterns and defect types is particularly important.

Among the commonly used detection methods, the transient earth voltage method (TEV) [1] can greatly improve the sensitivity of PD detection of electrical equipment, especially online detection, and has obvious advantages for online monitoring of high-voltage switchgear because of its small attenuation of electromagnetic signal during transmission and rapid induction of pulse change rate, etc. Therefore, this paper takes partial discharge TEV signal as the basis for pattern recognition research.

At present, neural network classification has become one of the main means of partial discharge pattern recognition, and various models have emerged, such as Random Forest (RF) [2], Convolutional Neural Networks (CNN) [3], SVM [4], BPNN method and other fusion algorithms [5–8], etc. As the most widely used among all network models, BP [9] has good robustness and fault tolerance. However, the traditional BPNN is greatly influenced by the initial values of thresholds and weights, and different initial values tend to converge to different local minima and fall into the defect of local optimum. Therefore, selecting appropriate weights and thresholds plays a vital role in the algorithm.

In summary, CIWOA-BP was proposed in paper for partial discharge pattern recognition, which can optimize the shortcomings of each part of the algorithm to achieve more accurate and favorable classification and identification of partial discharges. Firstly, wavelet noise reduction and feature extraction are performed on the simulated partial discharge signal, followed by dimensionality reduction of the feature parameters using PCA, and finally the input data are trained to CIWOA-BP neural network for classification and recognition.

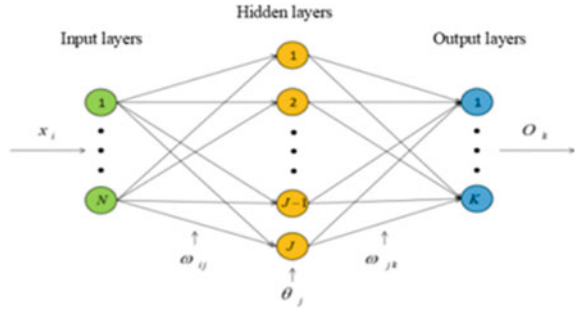
2 Theoretical Foundation

2.1 BPNN

BPNN is a network model with three layers, which the core algorithm is the gradient descent method. The connection status of neurons between layers is reflected by weights, which can be used to handle complex mapping relations of nonlinear functions, as shown in Fig. 1:

In Fig. 1, let there be i nodes in the input layer ($i = 1, 2 \cdots N$), j nodes in the hidden layer ($j = 1, 2 \cdots J$), k nodes in the output layer ($k = 1, 2 \cdots K$). The data is input from the input node i and its value is x_i . ω_{ij} indicates the weight. Then, the x_j of the node j is shown in Eq. (1), and its actual output O_j is shown in Eq. (2). The S-type activation function is used by $f(x)$, and the non-linear change function Sigmoid function is chosen for the hidden layer.

Fig. 1 BPNN



$$x_j = \sum_{i=1}^n \omega_{ij}x_i - \theta_j \tag{1}$$

$$O_j = f(x_j) \tag{2}$$

2.2 Whale Optimization Algorithm (WOA)

Whale optimization algorithm is a population intelligence algorithm proposed by Mirjalili and Lewis, A in 2016. The optimization algorithm is relatively simple, with few computational formulas and non-empirical parameters, which improves the efficiency of the algorithm and reduces the difficulty of application [10, 11], and the WOA algorithm has a novel structure and simpler parameter settings compared with other traditional single algorithms.

- (1) Prey hunting mechanism: when a whale is identified as the best position, other whales target its position to update their own position as follows:

$$P(t + 1) = P^*(t) - C_1 \cdot S \tag{3}$$

$$S = |C_2 \cdot P^*(t) - P(t)| \tag{4}$$

where t denotes the current iterations; C_1 C_2 are coefficient variables; $P^*(t)$ is the current best whale position; $P(t)$ denotes the current whale position; $| \cdot |$ denotes the absolute value; \cdot denotes element-by-element multiplication.

Calculate the coefficient variables C_1 and C_2 :

$$C_1 = 2f \times r_1 - f \tag{5}$$

$$C_2 = 2 \times r_2 \tag{6}$$

- where f decreases linearly from 2 to 0; r_1 r_2 are taken at random on $[0, 1]$.
- (2) Spiral bubble net attack: the process trace of the whale rounding up its prey is similar to the logarithmic spiral equation, with the position update process as follows:

$$P(t + 1) = S' \cdot e^{sr_3} \cdot \cos(2\pi r_3) + P^*(t) \quad (7)$$

$$S' = |P^*(t) - P(t)| \quad (8)$$

where S' indicates the distance to the current optimal position; s represents the logarithmic spiral shape parameter; r_3 is taken at random on $[-1, 1]$.

The mathematical model for obtaining the best solution through the two modes of hunting described above and continuously approaching the prey with a probability of 50% each is as follows:

$$P(t + 1) = \begin{cases} P^*(t) - C_1 \cdot S, & p < 0.5 \\ S' \cdot e^{sr_3} \cdot \cos(2\pi r_3) + P^*(t), & p \geq 0.5 \end{cases} \quad (9)$$

where p is the size of p determines which mode the whale chooses.

3 Improved Whale Optimization Algorithm (CIWOA)

3.1 Cubic Mapping

The traditional whale optimization algorithm uses a random distribution for the initialization process, which in turn guarantees the quality of the unawareness. To improve the quality of the initial solution, a first-generation whale population is generated from a random chaotic sequence generated by a Cubic chaotic map as shown in Eq. (10):

$$x_{n+1} = \rho x_n (1 - x_n^2) \quad (10)$$

where $x_n \in (0,1)$; ρ is the control parameter.

3.2 Adaptive Inertia Weights

To enhance local search capabilities, this paper introduces inertia weights to improve the algorithm [12], the idea of inertia weights in particle swarm algorithm (PSO) [13] is introduced into WOA algorithm, adaptive weights are added to the leader whale, so

the cloud improvement of Eqs. (3) and (7), the improved individual position update equation is:

$$P(t + 1) = P^*(t) - \omega \cdot C_1 \cdot S \tag{11}$$

$$P(t + 1) = \omega \cdot S' \cdot e^{sr^3} \cdot \cos(2\pi r_3) + P^*(t) \tag{12}$$

where the inertia weight expression is:

$$\omega = \omega_{\min} + (\omega_{\max} - \omega_{\min}) \times c \times e^{(\frac{-t}{t_{\max}})} \tag{13}$$

where ω_{\max} ω_{\min} is the maximum/minimum value of the given weights; c is the empirical constant.

3.3 Convergence Factor Improvement

In WOA, f affects the global foraging range and local exploration ability, there will be problems such as easy to fall into local optimality [14], which is improved in this paper so that it converges nonlinearly with the number of iterations as follows:

$$f = 2 \times \left(1 - \sqrt{\frac{t}{t_{\max}}} \right)^2 \tag{14}$$

3.4 Algorithm Process

- Step 1** Define population size, location information, maximum iterations, maximum and minimum of inertial weights.
- Step 2** Initialize location of the whale population using Cubic mapping and transform the initial variables to the value interval of the initial variables of the objective function.
- Step 3** The whale at the current best position is determined by the fitness function and considered as the current optimal solution.
- Step 4** Calculate the coefficient vectors C_1 and C_2 , introduce the improved convergence factor calculation, and determine if the p is less than 50%, then go directly to step 5; Otherwise, use formula (12) to update the position.
- Step 5** If $p < 0.5$ and $C_1 < 1$, the whale update the current position of the individual by formula (11); Otherwise, use formula (9) to update the position.

- Step 6** After each position update, the fitness function is recalculated and the current optimal solution is selected, and replaced if it is better than the previous optimal solution.
- Step 7** Calculate the current number of iterations and return to step 4 if the maximum number of iterations has not been reached, otherwise stop the calculation.

Finally, the optimal value is sent to BPNN for subsequent classification operations.

4 Signal Simulation and Feature Extraction

4.1 Partial Discharge Signal Establishment

In this paper, the mathematical model is established for three types of faults: air gap discharge, suspended defect discharge and high-voltage conductor spike discharge model of switchgear typical partial discharge types, and the sampling frequency of the signal model is set to 10 MHz. In order to simulate the real field acquisition of the partial discharge signal, add white noise and narrowband interference noise to the PD signals.

4.2 Signal Denoising and Feature Extraction

In this paper, the wavelet soft threshold denoising method is used to take the high-voltage conductor spike discharge as an example, and the corresponding signal waveform after denoising is shown in Fig. 2. The time domain features, frequency domain features and wavelet decomposition features of the partial discharge signal are extracted, and the dimensionality of the signal is reduced by using PCA.

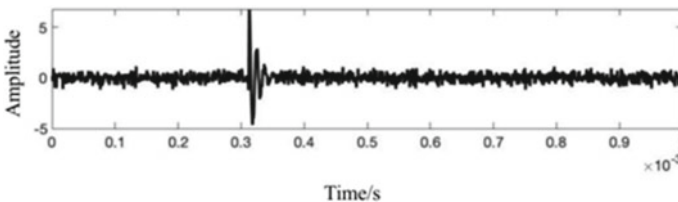
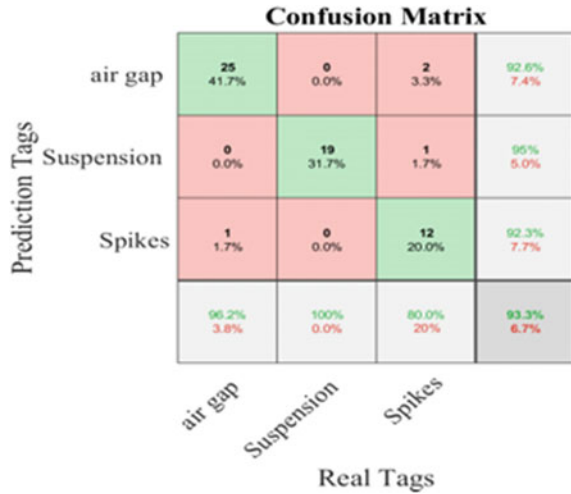


Fig. 2 Partial discharge signal denoising waveform

Fig. 3 Identification result chart



5 CIWOA-BP Partial Discharge Pattern Recognition

5.1 Algorithm Performance Test

In this paper, 200 samples of each of the three categories are selected and randomly disordered as input training samples for training, where the number of whale populations is 20, the maximum number of iterations is 50, the chaos mapping control parameter is 2.595, the input layer is set to 25, the output layer is set to 3, and the training is completed 1000 times with a target minimum error of 0.0001 and a maximum number of failures of 6. The model is trained until the optimal parameters, and save and use the model parameters during testing.

Twenty samples were taken for each of the three types of partial discharge data in the test data to test the accuracy of partial discharge pattern recognition for each type of sample, the results are as follows (Fig. 3).

As seen from the figure, the recognition rates of CIWOA-BP neural network for air gap discharge, suspended defect discharge and high-voltage conductor spike discharge reached 92.6%, 95% and 92.3%, respectively, and the overall recognition rate reached 93.3%.

5.2 Comparison of Recognition Results

The partial discharge identification method in this paper is compared with the traditional BPNN and WOA-BP, and the experimental results are shown in Table 1.

Table 1 Recognition rate comparison table

Partial discharge signal type	Correct recognition rate/%		
	BPNN	WOA-BP	CIWOA-BP
Air gap discharge	89.3	86.3	92.6
Suspended defect discharge	85.4	90.0	95.0
High-voltage conductor spike discharge	87.9	89.1	92.3

6 Conclusion

This paper achieved the following:

- (1) Generating the initial whale population using chaotic mapping to improve the quality of the initial solution and reduce randomness; introducing adaptive weights to improve the local search capability of the algorithm by improving the convergence coefficient;
- (2) Using the optimized WOA algorithm to define initial thresholds and weights of BPNN, which solves the drawback that the BPNN model easily falls into local optimum and enhances model computational capabilities;
- (3) By establishing the switchgear PD signal, performing wavelet denoising and PCA dimensionality reduction, and composing the feature volume into training and test samples for recognition and classification, the results show that the recognition rate of CIWOA-BP for all three types of partial discharge defects reaches more than 93.3%, indicating that the model can achieve accurate and effective discharge type recognition, which can provide reference for subsequent partial discharge recognition.

References

1. Heli NI, Weiqiang YAO, Chenzhao FU et al (2022) Review of the status of technical standards for partial discharge of power equipment. *High Voltage Apparatus* 58(03):1–15 (in Chinese)
2. Pan W, Chen X, Zhao K (2022) Cable-partial-discharge recognition based on a data-driven approach with optical-fiber vibration-monitoring signals. *Energies* 15(15):5686–5686
3. Jianfeng Z et al (2022) GIS partial discharge pattern recognition based on time-frequency features and improved convolutional neural network. *Energies* 15(19):7372–7372
4. He J, Tian T, Song X et al (2020) Research on the identification method of partial discharge in switchgear based on UHF method. *High Voltage Apparatus* 56(11):90–95+101. (in Chinese)
5. Xi C et al (2022) Feature extraction of partial discharge in low-temperature composite insulation based on VMD-MSE-IF. *CAAI Trans Intell Technol* 7(2):301–312
6. Yanxin W et al (2021) GAN and CNN for imbalanced partial discharge pattern recognition in GIS. *High Voltage* 7(3):452–460
7. Gu FC (2020) Identification of partial discharge defects in gas-insulated switchgears by using a deep learning method. *IEEE Access* 8:163894–163902
8. Mitiche I et al (2018) Classification of partial discharge signals by combining adaptive local iterative filtering and entropy features. *Sensors* 18(2):406–406

9. Feng XY et al (2015) Partial discharge pattern recognition method for GIS based on GA-BPNN. *Appl Mech Mater* 3785(738–739):397–400.
10. Mirjalili S, Lewis A (2016) The whale optimization algorithm. *Adv Eng Softw* 95:51–67
11. Feng W, Deng B (2021) Study on global convergence analysis and parameter selection of whale optimization algorithm. *Control Theory Appl* 38(05):641–651. (in Chinese)
12. Sha J (2018) Application of improved whale algorithm in multi-objective water resources optimization allocation. *Water Resour Hydropower Eng* 49(04):18–26. (in Chinese)
13. Bangyal WH et al (2022) An improved particle swarm optimization algorithm for data classification. *Appl Sci* 13(1):283–283
14. Chen X (2020) Research on new adaptive whale algorithm. *IEEE Access* 8:90165–90201

Research on Partial Discharge Noise Reduction Method of Motor Based on SVD-VMD



Zhihai Xu, Jingjie Yang, and Xiang Zheng

Abstract Online monitoring of Partial discharge (PD) is an ordinary technology for condition monitoring of high-voltage motor. However, it is difficult because of noise interference on site. Therefore, to solve the problem that the signal of high voltage motor PD is swamped by white Gaussian noise and narrowband periodic interference, a new denoising method combining Singular value decomposition (SVD) and Variational Mode Decomposition (VMD) is proposed. First, the original PD signal is decomposed by SVD. After the Kurtosis of the singular value sequence is calculated, periodic narrowband noise is removed by adaptively selecting the singular value to be reconstructed; Then, the starting position of PD signal is determined by calculating the variance of the signal in the sliding window; The signal after noise removal is obtained by zeroing the no PD location finally. The obtained PD signals are denoised and compared with VMD and EMD-WT. Simulation results show that compared with other denoising methods, SVD-VMD improves signal-to-noise ratio by 30% and has good performance. Simulation results show that compared with other denoising methods, SVD-VMD improves signal-to-noise ratio by 30% and has good performance.

Keywords High-voltage motor · Partial discharge · SVD · VMD

1 Introduction

With the wide use of large frequency conversion motor, the field of insulation predictive maintenance of high-voltage motor is rising gradually. The use of frequency converters exacerbates insulation failures, which can lead to high maintenance costs

Z. Xu (✉) · J. Yang · X. Zheng
School of Automation and Electrical Engineering, Dalian Jiaotong University, Dalian 116028,
China
e-mail: zxyh2001@163.com

J. Yang
e-mail: luoxueqianqian@foxmail.com

© Beijing Paiké Culture Commu. Co., Ltd. 2024
X. Dong and L. Cai (eds.), *The Proceedings of 2023 4th International Symposium on Insulation and Discharge Computation for Power Equipment (IDCOMPU2023)*, Lecture Notes in Electrical Engineering 1100, https://doi.org/10.1007/978-981-99-7393-4_16

and unplanned production shutdowns. The state of the stator winding will directly affect the operation of the motor. Usually, the reason for stator winding failure is the aging of insulation materials [1]. PD signal is one of the important references to reflect the insulation defects of stator windings. However, the PD signals detected in the field are always interfered by noises. Effectively restraining the noise in signals is an important problem in monitoring the insulation condition of stator windings [2].

At present, noise interference is a major problem limiting online PD monitoring. Especially in the motor device driven by inverter, PWM voltage contains similar components with the frequency of the PD to be measured, which greatly affects the accuracy of PD monitoring. To eliminate the influence of noise interference, there are two main methods: one is to install multiple sensors and judge whether the signal belongs to noise or PD signal according to the different time when the signal reaches each measuring point, the second is to judge by pulse waveform (Fig. 1).

At present, scholars have proposed many methods to denoise partial discharge signals. Such as WT [3], EMD [4], SVD [5], VMD [6, 7] and so on. WT has an excellent time analysis performance, however it can't separate noise effectively when the noise is complex. EMD is able to adaptively resolve the signal into different modes, but the aliasing of the modal components is easy to occur. SVD can be used to reconstruct the narrowband noise and eliminate it in the local emission electric signal, but the residual white noise cannot be effectively removed. VMD can overcome mode aliasing and end point effects, but its decomposition parameters need to be set artificially. When the parameters are not reasonable, it is difficult to obtain ideal results.

To eliminate the noise and harmonic interference in the PD signal as much as possible and retain the features, A new denoising method is presented by combining SVD and VMD.

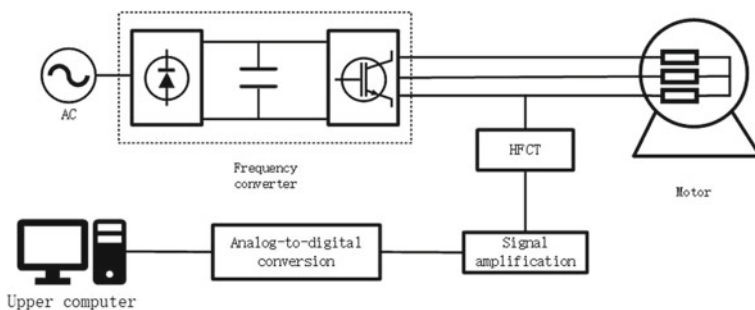


Fig. 1 PD on-line monitoring system of variable frequency motor

2 Basic Theory

2.1 Singular Value Decomposition

The signal was constructed as a Hankel matrix F with the following construction formula [8].

$$F = \begin{bmatrix} f(a) & f(b) & \cdots & f(P) \\ f(b) & f(c) & \cdots & f(P+1) \\ \vdots & \vdots & & \vdots \\ f(Q) & f(Q+1) & \cdots & f(R) \end{bmatrix} \tag{1}$$

where Q is an integer, $P = R - Q + 1$ and $Q = R/3$, F is decomposed by SVD, and the decomposition formula is as follows:

$$F = U_{L \times L} \cdot S_{L \times K} \cdot V_{K \times K}^T \tag{2}$$

According to the selected singular values, the reconstruction formula is as follows:

$$F_s = U_{L \times r} \cdot S_{r \times r} \cdot V_{K \times r}^T \tag{3}$$

2.2 Variational Mode Decomposition

As a method of completely non-recursive signal process, VMD is able to decompose modes into diverse center frequencies with good stability, effectively avoid the problems of aliasing and boundary effect of different modes, and has relatively good resolution accuracy and strong noise filtering ability.

It calculates these modes and estimates bandwidth of center frequencies under the constraint of minimum bandwidth sum. The formula can be expressed as:

$$\begin{aligned} & \min_{\{u_k\}, \{\omega_k\}} \left\{ \sum_{k=1}^K \|\partial_t \left[\left(\delta(t) + \frac{j}{\pi t} \right) \cdot u_k(t) \right] e^{-j\omega_k t} \|_2^2 \right\} \\ & s.t. \sum_{k=1}^K u_k(t) = x(t) \end{aligned} \tag{4}$$

where $\{u_k\}$ is IMFs set, $\{\omega_k\}$ is central frequencies set, K is predetermined number of modes for mode decomposition.

Equation (4) can be unconstrained with the Lagrangian multiplication operator λ and α , the extended Lagrangian formula can be obtained:

$$L(\{u_k\}, \{\omega_k\}, \lambda) = \alpha \sum_{k=1}^K \|\partial(t) \left[\left(\delta(t) + \frac{j}{\pi t} \right) \cdot u_k(t) \right] e^{-j\omega_k t}\|_2^2 + \|f(t) - \sum_{k=1}^K u_k(t)\|_2^2 + \lambda(t), f(t) - \sum_{k=1}^K u_k(t) \quad (5)$$

With alternate direction multiplier method, obtain IMF mode and center frequency:

$$\hat{u}_k^{n+1} = \frac{\hat{f}(\omega) - \sum_{i \neq k} \hat{u}_i(\omega) + \frac{\hat{\lambda}(\omega)}{2}}{1 + 2\alpha(\omega - \omega_k)^2} \quad (6)$$

$$\omega_k^{n+1} = \frac{\int_0^\infty \omega |\hat{u}_k(\omega)|^2 d\omega}{\int_0^\infty |\hat{u}_k(\omega)|^2 d\omega} \quad (7)$$

2.3 Kurtosis

Kurtosis is a numerical statistic of the distribution properties of reactive random variables and the normalized 4th central moment of the data [9]. The formula is as follow:

$$Ku = \frac{E[(x - \mu)^4]}{(E[(x - \mu)^2])^2} \quad (8)$$

3 Simulation Analysis

3.1 Simulation PD

The PD can be expressed by single and double exponential decay oscillations:

$$x_1(t) = A \cdot e^{-\frac{t}{\tau}} \cdot \sin 2\pi f_c t \quad (9)$$

$$x_2(t) = B \cdot \left(e^{-\frac{1.3t}{\tau}} - e^{-\frac{2.2t}{\tau}} \right) \cdot \sin 2\pi f_c t \quad (10)$$

where f_c is oscillation frequency, τ is attenuation coefficient, A and B are amplitude [10].

Four PD signals are simulated by Eqs. (9) and (10), whose parameters are shown in Table 1. Frequency is 10 MHz (Fig. 2).

Because the actual detection of common PD signal strength is -2dB , -2dB white noise, periodic narrowband noise and 1 MHz frequency Harmonic wave should be added to the real signal. The periodic narrowband noise mathematical expression is as follows:

$$S = A * \sum_{i=1}^3 \sin(2\pi f_i t) \tag{11}$$

A is 0.2 mV, f_i is 0.5 MHz, 0.7 MHz, 2 MHz (Fig. 3).

Table 1 PD signal parameters

Pulse	1	2	3	4
A/mV	0.5	0.5	2	2
f_c/MHz	1	1	1	1
τ/ns	15	15	15	15

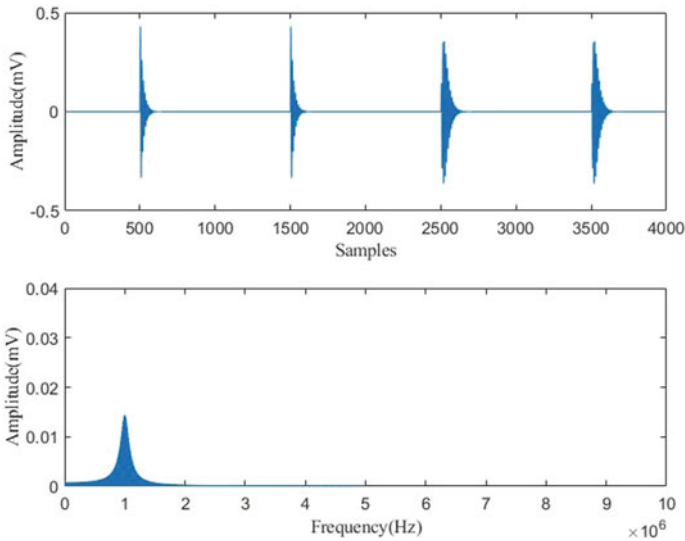


Fig. 2 Pure PD signal

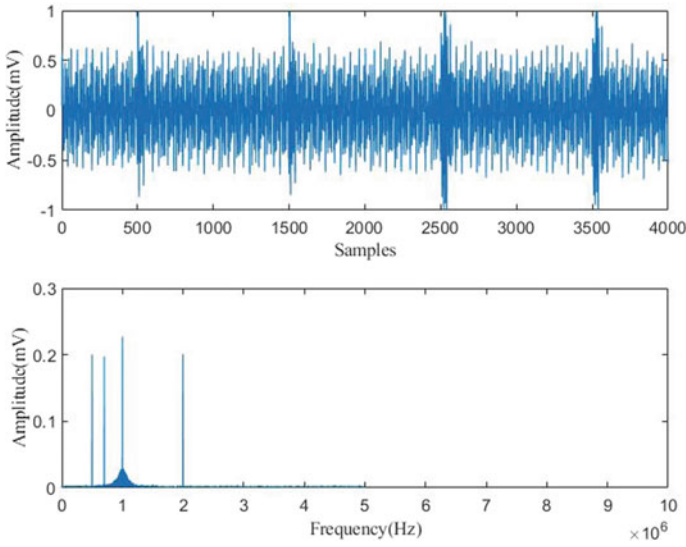


Fig. 3 PD signal with noise

3.2 Denoising Process

The proposed steps of SVD-VMD to suppress PD signal noises:

Step1: Decompose PD with noise F using the SVD, get the sequences of singular values $\{s_1, s_2, \dots, s_L\}$.

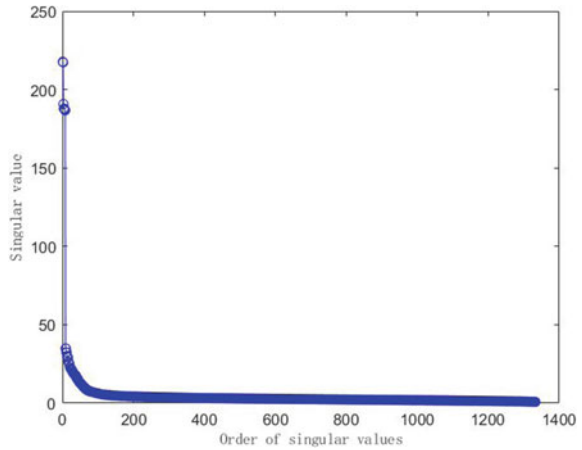
Step2: Calculate the Kurtosis of $\{s_1, s_2, \dots, s_L\}$, $\{s_2, s_3, \dots, s_L\} \dots \{s_{L-2}, s_{L-1}, s_L\}, \{s_{L-1}, s_L\}$ separately. Make the highest cliff point as the critical point, reconstruct the critical point and its previous singular values to obtain the signal F_1 . The signal after removing periodic narrowband noise is calculated by formula $F_2 = F - F_1$.

Step3: Denoise the signal F_2 using the VMD, get the signal F_3 contained residual white noise.

Step4: Add a sliding window of length 10, calculate the variance value of the signal F_3 in the sliding window, determine PD starting position according to change in the variance values, obtain the final denoising signal after the residual white noise removal.

The SVD decomposition was performed on the stained-noise PD signal, the resulting singular values are shown in Fig. 4. The 8th and 9th singular value gaps are obvious, therefore, the values of the first 8 singular values correspond to periodic narrow band noise.

Fig. 4 Signal values of noise PD



3.3 Denoising Analysis

After removing the reconstructed narrowband interference from the stained PD signal, PD is denoised by VMD, set k to 4, get PD shown in Fig. 5.

Then, a sliding window of length 10 is added, the variance value of the signal in the sliding window was calculated, and the starting position of the PD signal was determined according to the change of the variance value, as shown in Fig. 6. Residual white noise was removed to obtain the final denoising signal, as shown in Fig. 7. It shows that the noise in the PD signal at this time has been completely removed with well preserved PD signal characteristics.

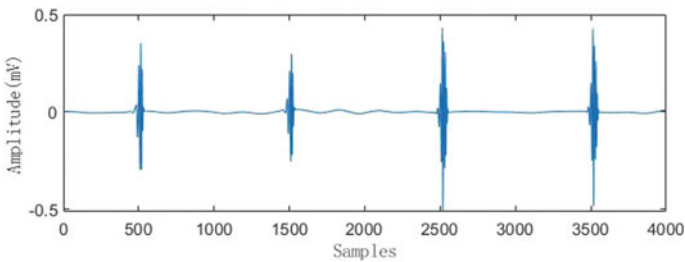


Fig. 5 PD signal after noise reduction by SVD-VMD

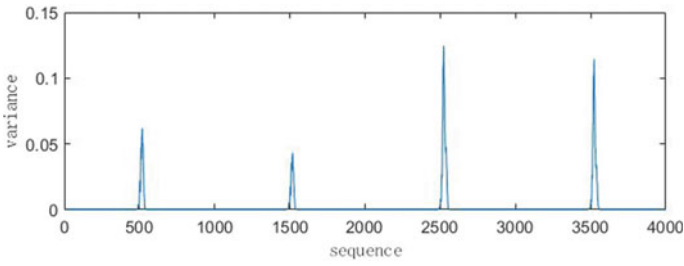


Fig. 6 The starting position of PD

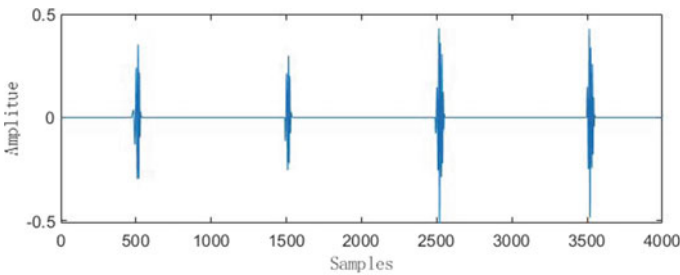


Fig. 7 PD after final denoising

3.4 Denoising Contrast

To prove the advantages of the method proposed, VMD and EMD-WT [11] denoising of simulated PD signals were carried out at the same time. In Figs. 8, 9 and 10, the SVD-VMD has better denoising ability.

In this paper, SNR, NCC, RMSE are introduced to better evaluate three methods denoising performance. In Table 2, SVD-VMD has a relatively high SNR and NCC and a lower RMSR.

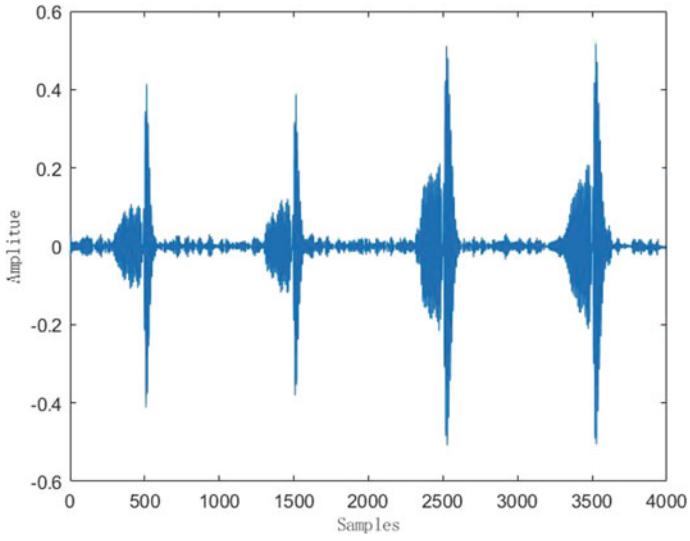


Fig. 8 VMD denoising

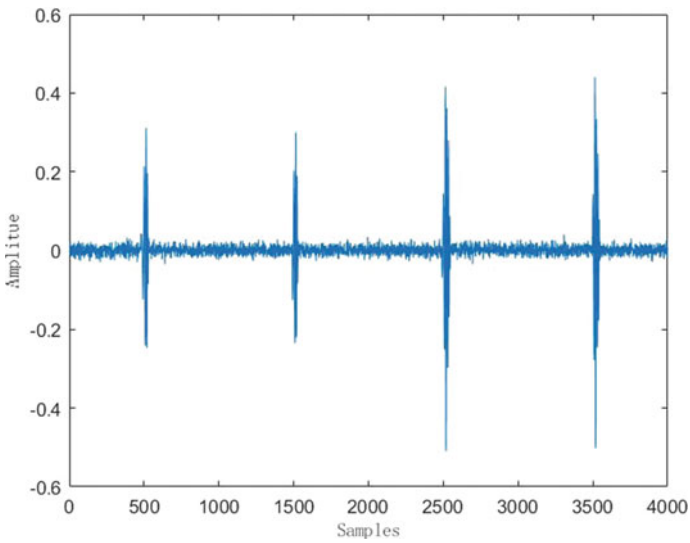


Fig. 9 EMD-WT denoising

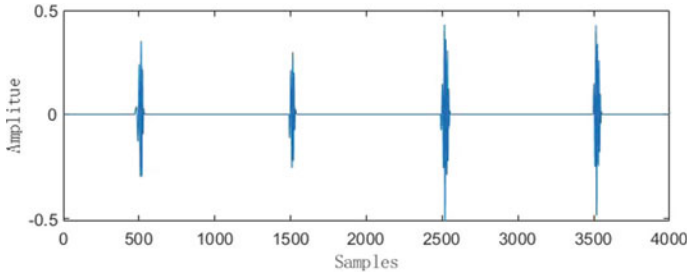


Fig. 10 SVD-VMD denoising

Table 2 The index of the three denoising methods

	SNR	NCC	RMSE
VMD	3.3594	0.6581	0.1015
EMD-WT	5.3796	0.7103	0.0971
SVD-VMD	6.6723	0.8028	0.0875

4 Conclusion

Based on PD and noise characteristics:

- (1) A new method to suppress white noise, harmonic wave and narrow band noise in PD is presented by combining SVD and VMD.
- (2) An adaptive selective reconstruction singular value based on kurtosis of singular value sequences is proposed.
- (3) A method is proposed to calculate the sequence variance based on sliding window to determine the PD signal starting position.
- (4) Compared with VMD and EMD-WT, the proposed method has better effect, which facilitates the subsequent processing of local emission electrical signals.

References

1. Song H, Dai J, Sheng G et al (2018) GIS partial discharge pattern recognition via deep convolutional neural network under complex data source[J]. *IEEE Trans Dielectr Electr Insul* 25(2):678–685
2. Zheng X, Tian W, Guan P (2020) Denoising method of partial discharge signal of motor based on improved VMD algorithm [J]. *Electr Mach Control Appl* 47(11):117–121. (in Chinese)
3. Tang J, Zhou S, Pan C (2019) A denoising algorithm for partial discharge measurement based on the combination of wavelet threshold and total variation theory[J]. *IEEE Trans Instrum Meas* 69(6):3428–3441
4. Chen X, Yang Y (2018) Analysis of the partial discharge of ultrasonic signals in large motor based on Hilbert-Huang transform[J]. *Appl Acoust* 131:165–173

5. Jiang Y, Zhu Y, Yang X et al (2022) Hankel-SVD-CEEMDAN improved threshold partial discharge feature extraction method [J]. *Power Syst Technol* 1–11. (in Chinese)
6. Jin Z, He D, Wei Z (2022) Intelligent fault diagnosis of train axle box bearing based on parameter optimization VMD and improved DBN[J]. *Eng Appl Artif Intell* 110:104713
7. Yang J, Yan K, Wang Z et al (2022) A novel denoising method for partial discharge signal based on improved variational mode decomposition [J]. *Energies* 15(21):8167
8. Zhong J, Bi X, Shu Q et al (2020) Partial discharge signal denoising based on singular value decomposition and empirical wavelet transform[J]. *IEEE Trans Instrum Meas* 69(11):8866–8873
9. Yin Y, Wen Z (2022) A joint method for electrostatic signal denoising based on mode functions optimized reconstruction and sparse representation [J]. *Chin J Sci Instrum* 43(02):196–204. (in Chinese)
10. Li S, Sun S, Shu Q et al (2020) Partial discharge signal denoising method based on frequency spectrum clustering and local mean decomposition[J]. *IET Sci Meas Technol* 14(10):853–861
11. Yang X, Huang H, Shu Q et al (2021) Partial discharge signal extraction method based on EDSSV and low rank RBF neural network[J]. *IEEE Access* 9:9744–9752

Simulation of Seawater Orifice Intrusion of 500 kV Submarine Oil-Filled Cable



Qingshuai Wu, Kaiyu Zeng, Degao Zhu, Qiyuan Jiang, Lili Li, Junguo Gao, and Xiaofeng Xu

Abstract After the submarine oil-filled cable is damaged, it is necessary to cut off the water entry part of the cable and then connect the spare cable. So it is significant to know the exact length of seawater entry into the cable. Based on the 500 kV submarine oil-filled cable of the Hainan interconnection system, the length of seawater entering the cable when the orifice is at different depths and locations of the same depth is modeled and simulated. The results show that: when the orifice is close to the Guangdong side, the length of water entering both sides of the orifice increases first and then decreases, with the maximum increase of 6.32% on the left side of the orifice and 83.37% on the right side of the orifice; when the orifice is close to the Hainan side, the length of seawater entering both sides of the orifice increases as the depth of the orifice increases, and the length of water entering the left side of the orifice increases significantly; when the orifice is close to the Guangdong side, at the same depth, the more the orifice is closer to the middle of the cable, the length of water entry on both sides of the orifice decreases.

Keywords Oil-filled cable · Inflow length · Two-phase flow · Numerical simulation

Q. Wu · K. Zeng · D. Zhu
Guangzhou Bureau of EHV Power Transmission Company, China Southern Power Grid Co., Ltd.,
Guangzhou 510000, China

Q. Jiang · L. Li · J. Gao (✉)
Harbin University of Science and Technology, Harbin 150000, China
e-mail: gaojunguo@hrbust.edu.cn

X. Xu
State Key Lab of Special Cable Technology, Shanghai Electrical Cable Research Institute Co.
Ltd., Shanghai 200093, China

1 Introduction

Hainan interconnection is China's first long-distance, ultra-high voltage, high-capacity trans-sea interconnection transmission system [1, 2]. This project uses oil-filled cables with oil-impregnated paper insulation, which can adapt to various laying conditions. Since the electrical performance of oil-filled cables is stable [3], the chance of their electrical breakdown is minimal, so more failures are due to external damage that leads to oil leakage from the cables. When a submarine oil-filled cable breaks down, there is a risk of seawater entering inside the cable, which will seriously affect the operation and service life of the submarine cable, so when repairing the submarine cable, it is necessary to cut off the water part of the cable and then connect the cable [4–6]. Therefore, when repairing submarine cables, it is necessary to cut off the water part of the cable and then connect the cable. Thus, knowing the exact length of seawater in the cable is essential for the submarine cable connection.

Submarine cables are generally modeled and analyzed by finite element simulation for submarine oil-filled cables due to the limitations of physical experiment cost and specific working environment [7]. Zhou Fengzheng and others studied cable failures caused by typical defects in high-voltage cable terminals and proposed targeted technical measures through simulation analysis [8]. Weng Yawei builds a simulation model of a pulse current ranging system based on cable fault ranging work, providing more accurate data for cable fault maintenance [9]. Bangle summarized the characteristics of grounding current changes under different sheath faults through simulation to provide a theoretical basis for fault detection in cable crossover transposition systems [10]. In summary, the current simulation on submarine cable faults mainly focuses on anchor damage research and electrical simulation research of cable faults, while simulation research to support cable maintenance is rare.

This paper uses the Hainan interconnection system's 500 kV AC submarine oil-filled cable as the research object and model. It analyzes the seawater entering the cable at different hole depths and locations at the same depth, which can provide a reference for determining the cut-off length for cable maintenance.

2 Mathematical Model

The flow of insulating oil in a pipe satisfies the Reynolds average Navier–Stokes equation (hereinafter referred to as the “RANS equation”),

$$\rho \frac{\partial u}{\partial t} + \rho u \cdot \nabla(u) = -\nabla p + \nabla \cdot (\mu(\nabla u + \nabla u^T)) + F \quad (1)$$

where: ρ is the fluid density, kg/m^3 ; u is the fluid velocity, m/s ; t is the time, s ; p is the fluid pressure, Pa ; T is the temperature, K ; μ is the dynamic fluid viscosity, Pa s ; F is the external force acting on the fluid, N .

The above equation is always solved simultaneously with the continuity equation, which for insulating oil yields:

$$\nabla \cdot u = 0 \tag{2}$$

3 Simulation Model

3.1 Geometric Model

The flow velocity of insulating oil in the whole pipeline was firstly simulated using the pipeline flow module. Then the area of 100m each near the orifice was simulated by the two-phase flow module to derive the situation of seawater entering inside the cable. Construct the pipe flow model according to the cross-sectional schematic diagram of the Hainan Power Grid Project, as shown in Fig. 1.

The length of the cable model is 31 km, and the maximum depth is 100 m. When the orifice is close to the Guangdong side, there are cases with multiple locations at the same depth due to the change in the seafloor topography, as shown in Table 1.

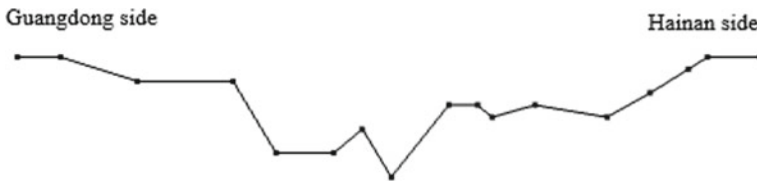


Fig. 1 Simplified geometric model of pipeline flow

Table 1 Position of the notch at different depths

Depth/m	Guangdong side position/m			Hainan side position/m
10	3400			28,000
20	5000	9000		27,200
30	9300			26,400
40	9600			25,500
50	9900			24,600
60	10,200	14,400		17,200
70	10,500	13,800	14,700	16,800
80	10,800	13,200	15,000	16,400
90	15,300			16,000
100	15,600			15,600

Fig. 2 Geometric model at the notch



The two-phase flow model is shown in Fig. 2, the orifice size is $0.03 * 0.055$ m, and the oil channel size is $0.03 * 200$ m.

3.2 Simulation Conditions

The pipeline flow simulation is a pressure boundary condition, the pressure at both ends is determined by whether the oil pump is started or not, and the pressure at the orifice is the pressure of seawater. For the two-phase flow simulation, the velocity boundary condition is at both ends, and the pressure boundary condition is at the orifice [11].

According to literature [12], the height of the oil pumping station on the Guangdong side is 11 m, and the height on the Hainan side is 25 m. The density of insulating oil is 855 kg/m^3 , so when the oil pump is not started, the pressure at sea level on the Guangdong side is 0.92 bar, and the pressure on the Hainan side is 2.10 bar. When the oil pump pressurization reaches the set value, the pressure at the sea level is 5 bar.

4 Results and Analysis

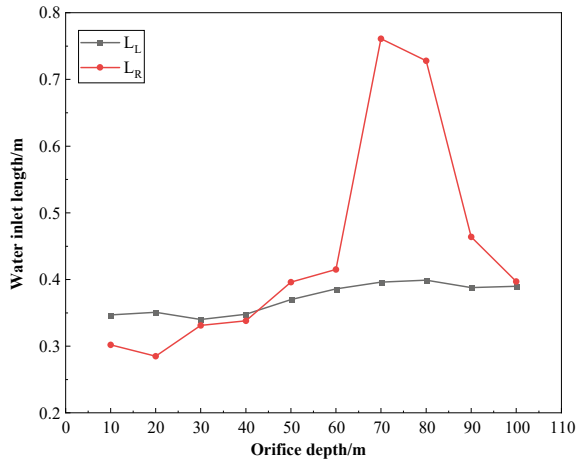
4.1 Effect of Different Depths on the Length of Seawater Entering the Cable

(1)(1) The inlet length on the Guangdong side.

When the orifice is located at a depth of 10–100 m, the length of seawater entering both sides of the orifice is shown in Fig. 3, where L_L indicates the length of seawater entering the left side of the orifice, and L_R indicates the length of seawater entering the right side of the orifice. The location of the orifice is 5000 m at 20 m, 10,200 m at 60 m, 10,500 m at 70 m, and 10,800 m at 80 m.

From Fig. 3, the left side inlet length is within the range of 0.35–0.4 m. The left inlet length shows a trend of increasing and then decreasing with increasing depth, reaching the maximum at a depth of 40 m, which is 0.399 m; the maximum change from 40 to 50 m, which is 6.32%, so it can be considered that the overall change in the left side inlet length is small. The right inlet length first increases and then decreases, reaching a maximum of 0.761 m at a depth of 70 m, with a maximum

Fig. 3 Length of water inlet on the guangdong side



change of 83.37% from 60 to 70 m, a significant change compared to the left inlet length.

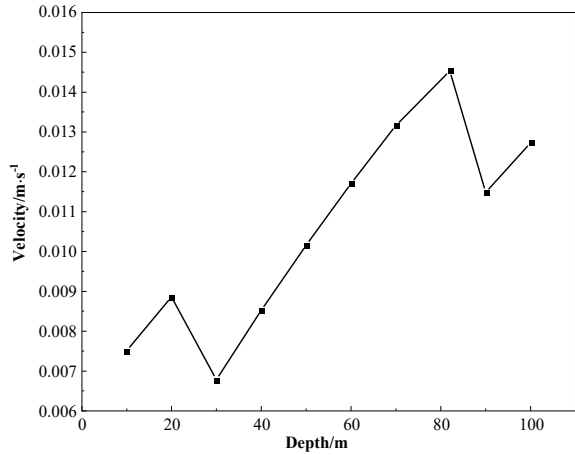
After analysis, when the orifice is close to the Guangdong side, the pressure at the orifice increases as the depth of seawater where the orifice is located increases, and the orifice gradually approaches the middle of the cable (15,500 m), according to Eq. (3):

$$\Delta P = \frac{32\mu lv}{d^2} \rightarrow v = \frac{\Delta P d^2}{32\mu l} \tag{3}$$

When the pipe diameter d and the insulating oil viscosity μ are constant, and the pressure difference ΔP increases simultaneously with the length l , the velocity change cannot be accurately judged, so the length of seawater entering the left side of the orifice cannot be accurately analyzed. According to the cable flow velocity results, seawater’s speed entering the left side of the orifice under different depths is obtained, as shown in Fig. 4. From Fig. 4, it can be seen that the overall size of the seawater inflow velocity increases as the depth increases but decreases from 20 to 30 m and from 80 to 90 m. The seawater inflow velocity is maximum at a depth of 80m, roughly the same as the change rule of seawater length entering the cable’s left side in Fig. 3. This shows that the cable inlet length is proportional to the inflow rate of the orifice.

When seawater flows to the right side of the orifice, due to the high altitude and pressure of the pumping station on the south side of the right end of the sea, at 10 m ~ 60 m, seawater and insulating oil form a relatively stable mixing interface at the orifice, resulting in a small amount of seawater diffusing into the interior of the cable, and at 70 m ~ 100 m seawater begins to flow slowly into the interior of the cable. When the depth is 70 m or more, the oil–water mixture on the left side of the orifice flows to the right side of the empty mouth under the action of the oil pump on the

Fig. 4 Velocity to the left of the orifice



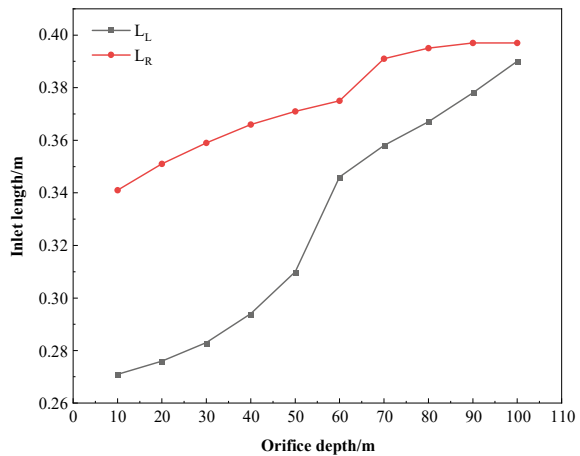
left side, so the length of the incoming water increases significantly. As the empty mouth is located in the middle of the cable at 90 m and 100 m, the oil pump starts at roughly the same time on both sides; therefore, the length of the incoming water starts to decrease at this time.

(2)(2) The inlet length on the Hainan side.

When the orifice is close to the south side of the sea, the results of the length of seawater entering both sides of the cable orifice at different orifice depths are shown in Fig. 5.

From Fig. 5, it can be obtained that when the orifice is close to the Hainan side, the length of seawater entering both sides of the orifice increases with the depth of the orifice. The left inlet length increases the most from 50 to 60 m, which is 10.40%, and the left inlet length changes significantly compared with the right side; the right

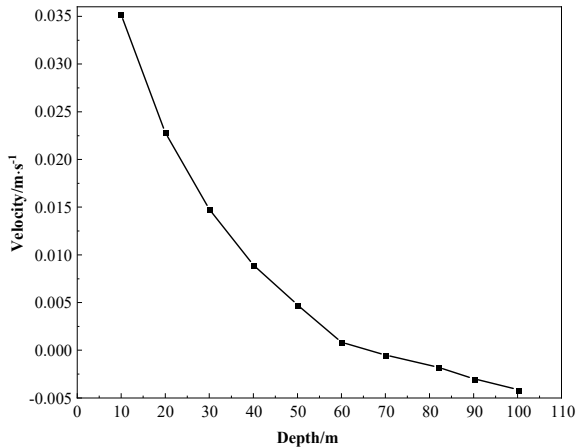
Fig. 5 Length of water inlet on the hainan side



inlet length increases the most from 60 to 70 m, which is 5.33%, and the overall change of the right inlet length is not apparent.

As the depth of the orifice increases, the orifice is close to the middle of the cable, the cable length on the left side of the orifice decreases, the orifice pressure increases, so the velocity of seawater inflow increases, and in turn, the length of seawater entering the left side of the orifice increases. When the orifice is close to the middle of the cable, the length of the cable on the right side of the orifice increases, and the pressure at the orifice also increases, and according to Eq. (3), it is known that the velocity change is uncertain at this time. The velocity image of the right side of the orifice can be seen as shown in Fig. 6. With the increase in depth, the velocity decreases, and when the depth is greater than 60 m, the velocity is negative, indicating that seawater flows into the orifice. After analysis, when the depth is 10 m ~ 60 m, the seawater pressure at the orifice is slightly less than the internal pressure of the cable. At this time, the insulating oil flows out slowly, but due to the entry of seawater on the left side of the orifice, resulting in an oil–water mixture near the orifice. The right side of the orifice is mixed with a shorter distance of seawater, and as the speed of the insulating oil flows out gradually decreases, the distance of the oil–water mixture into the right side of the orifice also increases. When the depth of the orifice is 70 m ~ 100 m, the seawater pressure is greater than the internal pressure of the cable, seawater flows into the cable internal. With the increase of depth, the inflow speed increases, so the length of seawater into the right side of the orifice also increases.

Fig. 6 Velocity on the right side of the orifice



4.2 Effect of Different Locations at the Same Depth on the Length of Seawater Entering the Cable Interior

Figure 7 shows the results of the lengths of seawater entering both sides of the orifice at different positions of 20 m and 60 m for the depth of the orifice. Figure 8 shows the results of the length of seawater entering both sides of the orifice when the depth of the orifice is at different positions of 70 m and 80 m.

From Fig. 7, it can be obtained that at the same depth, with the location of the orifice near the middle of the cable, the length of water entry on both sides of the orifice decreases, and the decrease is in the range of 2.28–4.56%, and the overall

Fig. 7 Inlet lengths of 20 m and 60 m

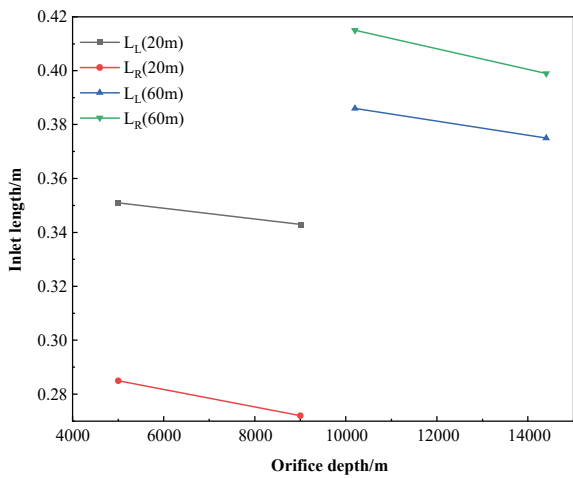
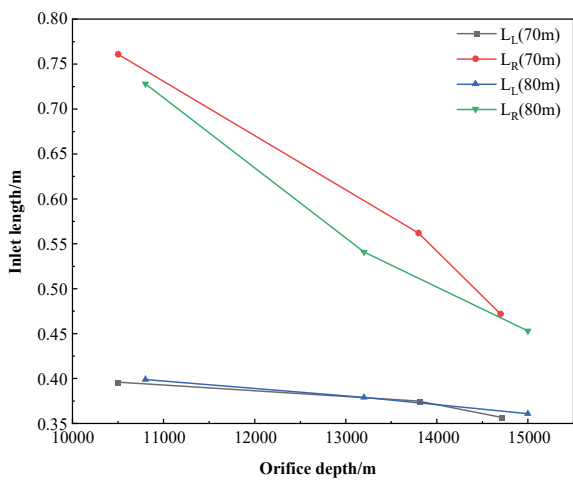


Fig. 8 Inlet lengths of 70 m and 80 m



decrease is not apparent. From Fig. 8, it can be obtained that at the same depth, the length of seawater entering both sides of the orifice decreases as the location of the orifice approaches the middle of the cable. The length of seawater entering the left side of the orifice decreases slowly, with an average decrease of 4.97%; the length of seawater entering the right side decreases rapidly, with an average decrease of 21.03%.

Under the same depth, when the orifice is close to the middle of the cable, the length of the left side of the orifice increases, and the pressure loss caused by the liquid flow in the pipe increases, but the pressure at the orifice remains unchanged. The speed of liquid flow decreases at this time, so the length of the water inlet on the left side of the orifice at each depth is reduced. When the depth of the orifice is between 20 and 60 m, although the insulating oil on the right side of the orifice slowly flows out from the orifice, when seawater enters the cable from the left side of orifice, seawater also appears on the right side of the orifice due to the diffusion movement of the insulating oil and the collision with the pipe wall. The volume fraction of seawater is tiny compared to the left side, and the entry length is also concise. When the depth is constant, and the location of the orifice is close to the middle of the cable, the cable length on the right side of the orifice becomes shorter, so the pressure loss caused by the liquid flow becomes smaller, at this time the speed of the insulating oil outflow increases, and the length of the oil–water mixture near the orifice into the right side of the orifice decreases.

When the depth of the orifice is 70 m and 80 m, the seawater enters the cable from the right side of the orifice. The location of the orifice is gradually close to the middle of the cable, the time difference between the two sides of the oil pump starts gradually shortened, so the distance of the oil–water mixture flowing to the right side under the action of the oil pump on the Guangdong side is shortened.

5 Conclusion

In this paper, the following conclusions were obtained by simulating the length of seawater entering the cable from the orifice at different depths and locations at the same depth.

- (1) When the orifice is close to the Guangdong side, with the increase of orifice depth, the overall length of seawater entering both sides of the orifice increases first and then decreases due to the change of terrain, and at a depth of 80 m, the maximum length of water entering the left side of the orifice is 0.399 m; at 70 m depth, the maximum length of water entering the right side of the orifice is 0.761 m.
- (2) When the orifice is close to the south side of the sea, the length of seawater entering both sides of the orifice increases with the depth of the orifice, and the left inlet length increases the most from 50 to 60 m, 10.40%, and the left inlet length changes significantly compared with the right side; the right inlet length

increases the most from 60 to 70 m, 5.33%, and the overall change of the correct inlet length is not significant.

- (3) When the orifice is close to the Guangdong side, the length of seawater entering both sides of the orifice decreases at the same depth as the location of the orifice gradually approaches the middle of the cable. At 20 m and 60 m, the length of seawater entering both sides of the orifice decreases by 2.28–4.56%. At 70 m and 80 m, the length of seawater entering the left side of the orifice decreases by 4.97% on average, and the length of seawater.

Acknowledgements This research was partially funded by the Postdoctoral Research Startup Fund Project of Heilongjiang Province of China under Grant LBH-Q19106.

References

1. Wu QH, Ma L, Yue H et al (2021) 500 kV submarine cable line design for Hainan interconnection project [J]. *Shanghai Electr Technol* 14(03):5–9+43. (in Chinese)
2. Gaobo W, Hao Y, Jian L et al (2022) Study on the impact induced voltage of metal sheath of 500 kV AC submarine cable[J]. *Sichuan Electr Power Technol* 45(02):43–47. <https://doi.org/10.16527/j.issn.1003-6954.20220209>. (in Chinese)
3. Liao J, Chu J, Gao F et al (2021) Alkyl benzene pyrolysis gas production law and DGA-based fault diagnosis of oil-filled cables [J]. *Insul Mater* 54(08):109–114. <https://doi.org/10.16790/j.cnki.1009-9239.im.2021.08.017>. (in Chinese)
4. Youzhi G, Linpeng R (2021) Introduction to the application of submarine cable fault detection and repair technology [J]. *China Petrol Chem Stan Qual* 41(06):58–62 (in Chinese)
5. Ke L, Wei C (2021) Analysis of DC withstands voltage problems in cable maintenance [J]. *China Equipment Eng* 01:82–84 (in Chinese)
6. Zhou Q et al (2020) Effect of nano-composite repair fluid on electrical tree growth under different conditions in cables. In: 2020 IEEE International conference on high voltage engineering and application (ICHVE). Beijing, China, pp 1–4
7. He S (2020) Finite element analysis of electrothermal characteristics of XLPE insulation in high-voltage cables [D]. North China Electric Power University. (in Chinese)
8. Zhou F, Meng ZZ, Song P et al (2020) Simulation and fault analysis of typical defects in GIS terminal epoxy bushings of high-voltage cables [J]. *Synth Mater Aging Appl* 49(06):91–92. (in Chinese)
9. Yawei W (2022) Experimental cable fault-ranging simulation analysis based on pulse current method [J]. *Electr Transm Autom* 44(06):19–22 (in Chinese)
10. He B, Zhou Y, Li HT et al (2020) Fault identification of high-voltage cable sheath grounding system based on ground current analysis. In: 2020 IEEE 4th conference on energy internet and energy system integration (EI2), pp 3248–3251
11. Jafari R, Razvarz S, Gegov A et al (2020) Deep learning for pipeline damage detection: an overview of the concepts and a survey of the state-of-the-art. In: 2020 IEEE 10th international conference on intelligent systems (IS), pp 178–182
12. Nian C, Bailu Q (2005) Analysis and study on oil feeding system for submarine cable of Qiongzhou Strait [C]. In: 2005 IEEE/PES transmission and distribution conference and exposition: Asia and Pacific. IEEE, pp 1–6

3-D Segmentation and Surface Reconstruction of Gas Insulated Switchgear via PointNet-MLS Architecture



Chaowei Lv, Xiangyu Guan, Jiang Liu, and Jingwen Liao

Abstract High quality 3D reconstruction technique is essential for digital twin (DT) application of power equipment. This work presents a PointNet-MLS combined architecture to realize component segmentation and surface reconstruction of gas insulated switchgear (GIS) with complex background interference. In order to make the GIS ontology point cloud obtained continuous and smooth, greedy projection triangulation is then applied. Lastly, the local features of the GIS point cloud are enhanced, and the three-dimensional geometric properties of the GIS apparatus are better restored using the moving least squares approach. The results show that the mean intersection over union (mIoU) of PointNet++ algorithm for on-site GIS point cloud segmentation can reach 92.1%, which is higher than 32.8% and 13.7% of K-means and PointNet algorithms, respectively. The proposed MLS algorithm can effectively repair the defects of GIS point cloud after greedy projection triangulation, so that the repaired surface part can maintain the three-dimensional shape characteristics of the GIS point cloud.

Keywords GIS · Point cloud segmentation · PointNet · MLS

1 Introduction

Digital twin refers to the establishment and simulation of a physical entity, process or system in an information platform. With the help of digital twin, the state of physical entities can be understood on the information platform. By integrating physical feedback data, supplemented by artificial intelligence, machine learning and software analysis, a digital simulation can be established in the information platform

C. Lv (✉) · X. Guan · J. Liu · J. Liao
Fuzhou University, Fuzhou 350108, China
e-mail: 1035399432@qq.com

J. Liu
State Grid Ganzhou Power Supply Company, Jiangxi Ganzhou 341000, China

© Beijing Paiké Culture Commu. Co., Ltd. 2024
X. Dong and L. Cai (eds.), *The Proceedings of 2023 4th International Symposium on Insulation and Discharge Computation for Power Equipment (IDCOMPU2023)*, Lecture Notes in Electrical Engineering 1100, https://doi.org/10.1007/978-981-99-7393-4_18

[1]. In this study, a physical test platform for a GIS prototype is built in order to get the three-dimensional geometric properties of the field GIS equipment and reconstruct it in three dimensions. A variety of test-related instruments, including a power frequency high current generator, wiring copper bar, transformer, and other devices, cannot be avoided from being in the laser radar's field of view because the development of the field test necessitates their coordination [2]. This is due to the site's size limitations. The time of flight (TOF) approach is employed in this study to gather the point cloud data for the on-site GIS using Intel Realsense-L515 lidar [3]. Continuous emission light pulses, which are typically invisible light, are transmitted to the item to be measured, and the sensor then receives the light that is reflected from the surface of the object. To determine the depth of the item to be measured, the flight (round-trip) duration of the light pulse is detected. This information is used to determine the distance of the object to be measured. Owing to the significant background interference present in the gathered original GIS point cloud data, the noisy point cloud is dispersed and high in quantity, making it challenging for the current methods to eliminate [4].

This paper suggests a GIS point cloud segmentation algorithm based on PointNet++ [5] to realize the separation and extraction of the point cloud of GIS equipment under the background interference in order to obtain the three-dimensional geometric characteristics of GIS equipment under the background interference. Then the greedy projection triangulation algorithm [6] is used to reconstruct the surface, and finally the moving least squares method [7] is used to smooth the surface.

2 Raw Point Cloud Data Acquire and Preprocessing of GIS

2.1 GIS Point Cloud Data Set Construction

In this paper, a GIS prototype physical test platform is built as shown in Fig. 1a. Laser radar is used to collect point cloud data from field GIS equipment, as shown in Fig. 1b. Firstly, the CloudCompare tool is used to frame the collected GIS original point cloud data. The GIS cavity and background are divided into two parts, marked with labels 0 and 1 respectively, and then the two parts of point cloud data with different labels are combined into a complete point cloud. Finally, the point cloud is subsampled to reduce the size of the data set, as shown in Fig. 1c, which is convenient for PointNet++ network training.

3 Component Segmentation and Surface Reconstruction Framework

The overall process framework of this article is shown in Fig. 2.

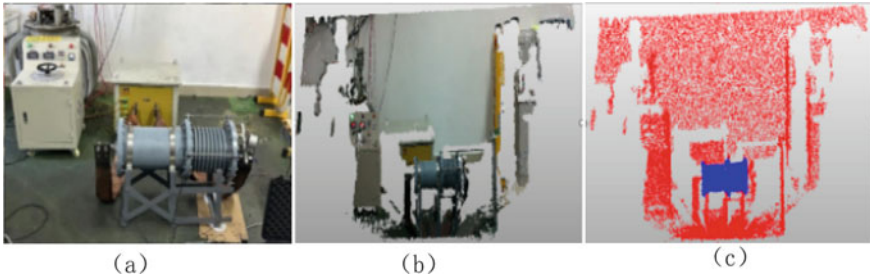


Fig. 1 On-site GIS and GIS point cloud and processed point cloud data

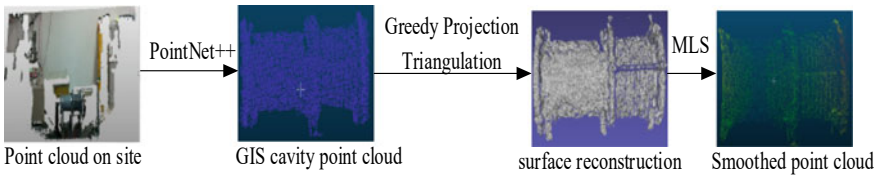


Fig. 2 Overall process framework

3.1 *PointNET-Based Component Segmentation*

This study processes the created GIS data set using the point-based PointNet++ neural network architecture to distinguish and separate the GIS point cloud from the complicated backdrop environment. Set abstraction, which comprises of the sample layer, grouping layer, and PointNet [8] layer, is the primary component of the PointNet++ network.

The convolution procedure on a two-dimensional picture is analogous to the design concept of set abstraction. The local operation is defined by the PointNet layer, which is determined by the sampling layer, the grouping layer, which specifies the neighborhood of the local operation. Specifically:

- (1) The sampling layer uses the Farthest Point Sampling (FPS) [9] to select local ‘key’ points for the point cloud.
- (2) The neighborhood surrounding the sample point is obtained by the grouping layer using the Ball query grouping technique.
- (3) The PointNet network is used to process the points in the neighborhood of all sampling points and extract the corresponding local features.

3.2 *MLS-Based Surface Reconstruction*

After point cloud segmentation and extraction, the GIS point cloud data is no longer surrounded by noise, but it is still disorganized. More surface reconstruction is

required because there isn't a clear relationship between the points and the shape of the GIS hollow cannot be properly stated.

The Greedy Projection Triangulation algorithm is a reconstruction technique based on triangulation. The local point cloud is projected onto the tangent plane of its central three-dimensional point, and Delaunay triangulation is performed on the obtained plane. Then the triangulation results on the plane are mapped back to the three-dimensional space to form a complete mesh surface in the three-dimensional space.

Because of the issue with non-smooth surfaces and gaps in point clouds following surface reconstruction. In order to considerably improve the local features of the GIS point cloud and more accurately recover the three-dimensional geometric properties of GIS equipment, we use the MLS algorithm to calculate the weighted least squares of any fixed point in the point set, then move the point on the whole parameter domain, and calculate each point separately. Finally, a weighted least squares fitting is determined to smooth the surface of the point cloud.

4 Results and Discussion

In this paper, 70% of the 360 sets of GIS point cloud data are randomly selected as the training set, 10% as the verification set, and 20% as the test set. The model is trained by 100 iterations, the Batch size is set to 10, the initial learning rate is set to 0.001, and the Adam optimizer is used to optimize the model.

4.1 Point Cloud Segmentation Results

The mAcc and mIoU of the model category are used as performance comparison indicators for various GIS point cloud segmentation models in order to further compare the performance indicators of the model and investigate the efficacy of the point cloud segmentation method [10].

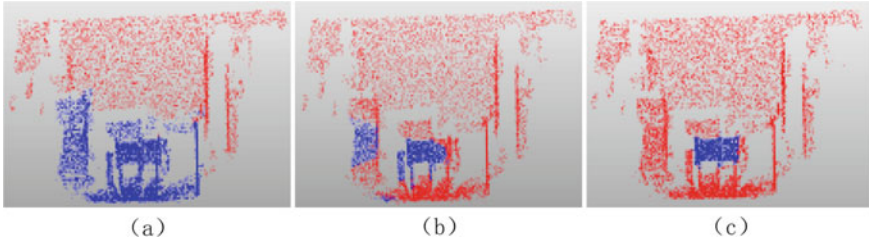
An essential metric to assess the precision of point cloud segmentation is the mIoU value, which is determined by averaging the IoU values for each category. The mAcc value is the ratio of the sum of the prediction accuracy of each class to the number of classes. The calculation formula is:

$$P_{mIoU} = \frac{1}{m+1} \sum_{g=0}^m \frac{P_{gg}}{\sum_{h=0}^m P_{gh} + \sum_{h=0}^m P_{hg} - P_{gg}} \quad (1)$$

$$mAcc = \frac{1}{m} \sum_{g=0}^{m-1} \frac{P_{gg}}{\sum_{h=0}^{m-1} P_{gh}} \quad (2)$$

Table 1 Comparison of segmentation results of GIS point cloud data set

Segmentation algorithm	mIoU (%)	mAcc (%)
PointNet++	92.1	94.7
PointNet	78.4	82.8
Kmeans	59.3	64.2

**Fig. 3** Comparison of GIS cavity segmentation results

where, m represents the number of categories, g represents the true value, h represents the predicted value, and p_{gh} represents the prediction of g as h .

The segmentation effects of three distinct algorithms—Kmeans clustering [11], PointNet and PointNet++—on GIS point cloud data sets are compared in this study. Table 1 presents the results.

Table 1 shows that PointNet++ enhances PointNet and adds the set abstraction module to maximize the model's ability to extract local and global features. Its mIoU is 13.7% higher than the PointNet point cloud segmentation algorithm and 32.8% higher than the Kmeans clustering method. Its mAcc is 11.9% higher than the PointNet point cloud segmentation algorithm and 30.5% higher than the Kmeans clustering method.

In order to evaluate the actual scene application effect of different models, the GIS field point cloud is randomly selected to test the recognition effect of different algorithms. The test results are shown in Fig. 3. The graphic shows that the incorrect categorization of points is a problem for both the PointNet method and the Kmeans algorithm, and that the recognition impact of the PointNet++ algorithm is clearly superior to that of these two algorithms.

4.2 Surface Reconstruction Results

The greedy projection triangulation reconstruction algorithm uses the local optimal greedy idea to make the reconstructed GIS surface point cloud continuous. The MLS algorithm further smooths the point cloud, thereby significantly improving the local details of the point cloud on the GIS surface and better restoring the three-dimensional

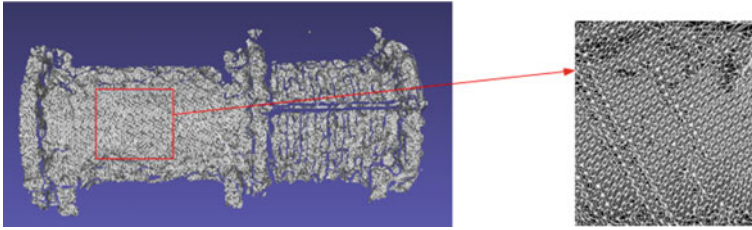


Fig. 4 Greedy projection triangulation reconstruction

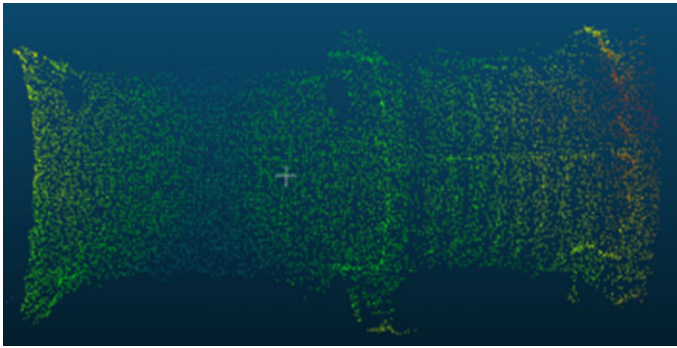


Fig. 5 GIS point cloud surface reconstruction

geometric features of the GIS equipment. The effect of GIS surface reconstruction is shown in Figs.4 and 5.

5 Conclusion

Based on the PointNet-MLS method, this paper obtains the point cloud data of GIS ontology under many background disturbances, and carries out surface repair and reconstruction to obtain a smooth and flat GIS surface point cloud. The conclusions are as follows:

- (1) Using the PointNet++ network, the GIS point cloud can be separated from other background interference, and the mIoU can reach 92.1%.
- (2) Using greedy projection triangulation algorithm and MLS can significantly improve the local details of GIS surface point cloud and make it smooth.
- (3) The PointNet-MLS method can extract the point cloud data of GIS ontology and reconstruct it under the interference of complex environment, which can provide data support for the construction of digital twin platform.

References

1. Liu S, Bao J, Lu Y et al (2020) Digital twin modeling method based on biomimicry for machining aerospace components [J]. *J Manuf Syst*
2. Qian J, Wei L, Li Y et al (2022) Research on transmission line classification denoising algorithm based on 3D point cloud [J]. *Appl Laser* 42(11):104–112. <https://doi.org/10.14128/j.cnki.al.20224211.104>. (in Chinese)
3. Park M, Yuan Y, Baek Y et al. Neuron-inspired time-of-flight sensing via spike-timing-dependent plasticity of artificial synapses [J]. *Adv Intell Syst*
4. Whebell RM, Moroney TJ, Turner IW et al (2021) Implicit reconstructions of thin leaf surfaces from large, noisy point clouds [J]. *Appl Math Model*
5. Qi CR, Li Y, Hao S et al (2017) PointNet++: deep hierarchical feature learning on point sets in a metric space [J]
6. Xu WU, Ling-Wen LU, Liang DD et al (2019) Comparison of surface reconstruction algorithms based on point cloud data [J]. *J Anhui Normal Univ (Nat Sci)*. (in Chinese)
7. Gross BJ, Kuberry P, Atzberger PJ (2022) First-passage time statistics on surfaces of general shape: surface PDE solvers using generalized moving least squares (GMLS) [J]. *J Comput Phys* 453
8. Qi CR, Su H, Mo K et al (2017) PointNet: deep learning on point sets for 3D classification and segmentation [J]. *IEEE*
9. Zhang Y, Hu Q, Xu G et al (2022) Not all points are equal: learning highly efficient point-based detectors for 3D LiDAR point clouds [J]
10. Jiang S, Guo W, Fan Y et al (2022) Fast semantic segmentation of 3D Lidar point cloud based on random forest method [J]
11. Yong AR, Kang CR, Kim KH et al (2022) A new method to determine cluster number without clustering for every K based on ratio of variance to range in K-means [J]. *Math Probl Eng*

Optimization of Electromagnetic Vibration for FSPM Motor by NSGA-II Algorithm



Shu Wang, You Bian, Wei Zhao, Zhenyu Liu, Xuelei Zhang, Zuxu Guo, and Chenhao Kou

Abstract As the theory of the air-gap field modulation, this paper calculates and analyzes the radial electromagnetic force of the motor from the perspective of the three elements. Thus the main sources of FSPM motors' vibration are found out. In this paper, a FSPM motor with 10-pole 12-slot is studied, and the rotor structure is optimized to weaken the radial force harmonics, which have great influence on electromagnetic vibration. The response surface curve CCD method is introduced to regress the sample data generated by the FEM, and then the radial force harmonics are to minimize and the electromagnetic torque is to maximize. Finally, the multi-objective optimization of the fitting model was carried out by using NSGA-II algorithm with the reduction of torque less than 5% as the constraint function, and the structure parameters of the optimal rotor were obtained. The simulation results show that with ensuring the electromagnetic performance, the optimized motor vibration can effectively be reduced.

Keywords FSPM motor · Electromagnetic vibration · Radial electromagnetic force · Response surface curve · NSGA-II algorithm

1 Introduction

Due to the restriction on the development of traditional rotor permanent magnet machine caused by heat dissipation, high-speed intensity load and other problems, the design of stator permanent magnet motor has received more and more attention

S. Wang (✉) · Z. Liu · X. Zhang · Z. Guo · C. Kou
Beijing Mechanical Equipment Research Institute, Beijing, China
e-mail: 1017234026@tju.edu.cn

Y. Bian
The First Military Representative Office for Air Force, Beijing, China

W. Zhao
The Sixth Military Representative Office for Air Force, Beijing, China

© Beijing Paiké Culture Commu. Co., Ltd. 2024
X. Dong and L. Cai (eds.), *The Proceedings of 2023 4th International Symposium on Insulation and Discharge Computation for Power Equipment (IDCOMPU2023)*, Lecture Notes in Electrical Engineering 1100, https://doi.org/10.1007/978-981-99-7393-4_19

from scholars [1]. Among them, the flux switching permanent magnet (FSPM) motor show the benefits of high efficiency, high torque density, low back EMF harmonics and so on, which has been widely used [2, 3]. Many papers have carried out a series of researches on FSPM motor from the aspects of electromagnetic performance calculation and optimization [4, 5], control algorithm optimization [6, 7] and new motor structure design [8, 9].

However, due to the structural characteristics of FSPM motor with double salient poles, the electromagnetic vibration response is relatively large. In [10], the rotor and stator topology are improved respectively to reduce the cogging torque. To some extent, this way can weakens the motor electromagnetic vibration. In [11], the cogging torque of a V-type FSPM motor with external rotor is reduced by multi-objective optimization method, and the motor electromagnetic vibration is suppressed. However, these literatures regard the cogging torque as the only excitation reason for the motor electromagnetic vibration. The radial electromagnetic force, which is the more important factors for motor electromagnetic vibration is ignored. To solve this problem, in [12], a fault tolerant FSPM motor was selected as study object, a new type of tooth structure of stator and rotor is proposed to make the low-order radial electromagnetic forces be decreased, and thus the level of motor vibration acceleration effectively decreases.

Currently, cogging torque of motor are mainly focused on to suppressed the FSPM motor electromagnetic vibration, neglecting the radial electromagnetic force that has a greater impact on motor vibration. A small number of papers have studied the radial electromagnetic force to suppress the motor vibration. But these studies only put forward some new topologies, rather than to optimize the structures' size.

This paper takes the FSPM motor as the research object. Suppress the motor electromagnetic vibration by weakening the radial electromagnetic force. Firstly, on account of the principle of magnetic field modulation, the theoretical formulas for the radial electromagnetic forces, which are the main causes of the motor vibration are derived. Through these formulas, the characteristics of the radial electromagnetic force with frequencies and orders are summarized. On this basis, a FSPM motor, whose pole-slot combination is 12/10 is taken as the prototype. The rotor structure is improved to weaken the harmonic components of the radial electromagnetic force. Finally, using the multi-objective optimization algorithm of the NSGA-II, and analyzing the preference relationship for the obtained Pareto optimal solution set, the optimal solution of the low electromagnetic vibration motor topology that meets the design requirements is selected.

2 Radial Electromagnetic Force Analysis

2.1 Characteristics of Radial Electromagnetic Force

The radial electromagnetic force generated by the FSPM motor acts on the stator teeth, causing periodic radial deformation of the motor yoke. The superposition of these deformations is the electromagnetic vibration generated by the motor. These electromagnetic force densities acting on the stator teeth can be derived from the Maxwell stress equation, as shown below [13]:

$$f_r = \frac{1}{2\mu_0}(B_r^2 - B_t^2) \approx \frac{1}{2\mu_0}B_r^2 \quad (1)$$

where B_r and B_t are radial and is the tangential component of the air gap magnetic flux density, respectively. Compared with the radial component B_r , the tangential component B_t is much smaller. Therefore, it can usually be ignored. μ_0 is the vacuum permeability.

The flux density B^{pm} and B^{S} in the air gap of FSPM motor is mainly produced by the source excitation F_{pm} and armature winding magneto-motive force F_s modulated by the rotor salient-pole air gap conductance Λ , then formula (1) can be rewritten as:

$$f_r = \frac{1}{2\mu_0}(B^{\text{pm}} + B^{\text{S}})^2 = \frac{1}{2\mu_0}[F_{\text{pm}}(\theta, t)\Lambda(\theta, t) + F_s(\theta, t)\Lambda(\theta, t)]^2 \quad (2)$$

According to the structure of FSPM motor, the expressions of F_{pm} , F_s and Λ are:

$$F_{\text{pm}}(\theta, t) = \sum_{\mu} F_{\mu} \cos\left(\mu \frac{N_s}{2} \theta + \frac{\pi}{2}\right) \quad (3)$$

$$F_s(\theta, t) = F_{\text{Av}}(\theta, t) + F_{\text{Bv}}(\theta, t) + F_{\text{Cv}}(\theta, t)$$

$$\begin{aligned} &= \sum_{\nu} F_{\phi\nu} \cos \nu\theta \sin \omega_e t + \sum_{\nu} F_{\phi\nu} \cos\left(\nu\theta - \frac{2}{3}\pi\right) \sin\left(\omega_e t - \frac{2}{3}\pi\right) \\ &+ \sum_{\nu} F_{\phi\nu} \cos\left(\nu\theta + \frac{2}{3}\pi\right) \sin\left(\omega_e t + \frac{2}{3}\pi\right) = \frac{3}{2} \sum_{\nu} F_{\phi\nu} \cos\left(-\nu\theta + \omega_e t + \frac{\pi}{2}\right) \end{aligned} \quad (4)$$

$$\Lambda(\theta, t) = \Lambda_0 + \sum_k \Lambda_k \cos(kN_r\theta - kN_r\omega_r t - kN_r\theta_0) \quad (5)$$

where N_s and N_r represent the stator slot number and rotor slot number for FSPM motor, respectively; F_{μ} is the amplitude of harmonic magneto-motive force of source excitation field; μ is the harmonic frequency of permanent magnetic field; $F_{\phi\nu}$ is the harmonic magnetomotive force amplitude produced by armature reaction magnetic field; ν is the harmonic frequency of the armature reaction magnetic field; ω_e is

the angular frequency of the fundamental current of the stator; ω_r is the rotational angular velocity of the rotor, $\omega_e = N_r \omega_r$; Λ_0 is the constant component of the air-gap conductance, and Λ_k is the harmonic component of the air-gap conductance.

By substituting (3)–(5) into (2) and simplifying, the characteristic parameters (spatial order r and time frequency f_r) and sources of radial electromagnetic force density produced by the interaction of various magnetic fields of FSPM motor are obtained. It shows that the spatial order r is related to the pole slot coordination, and the time frequency f_r is related to the number of rotor slots. This conclusion is different from that of the traditional rotor permanent magnet synchronous motor, that is, the time frequency of radial electromagnetic force is only related to the harmonic frequency [14].

2.2 FEM Simulation of Radial Electromagnetic Force

In this paper, a 12-slot 10-pole FSPM motor is studied. The parameters of the motor are shown in Table 1, and the cross section is shown in Fig. 1.

From above analysis, the main radial electromagnetic force harmonics which cause the vibration response of the motor with this pole-slot combination are summarized as follows: 2rd-order f , 4th-order $2f$, 6th-order $3f$, 8th-order $2f$, 10th-order f , 14th-order f , respectively. These force harmonics have smaller spatial orders and larger amplitudes, so they will cause more intense vibration of the motor.

This paper used Ansoft software to simulate the radial electromagnetic force density of the prototype under rated load by finite element method, so that the above force analysis can be verified. And the 2D FFT results of the force density is shown in Fig. 2.

It can be seen from Fig. 2, that:

- (1) Among the force harmonics, neglecting the harmonics that has no effect on the motor electromagnetic vibration (force harmonics with $0f$), the harmonics of 2rd-order f , 4th-order $2f$, the 6th-order $3f$, the 8th-order $2f$, the 10th-order f and

Table 1 Technical parameters of the FSPM motor

Parameter	Value	Parameter	Value
Slot/pole	12/10	Rotor yoke height/mm	7
Rated speed/(r/min)	400	PM radians/ $^\circ$	7.5
Rated current/A	10	Stator tooth radian/ $^\circ$	12
Rated torque/Nm	2	Rotor tooth radian/ $^\circ$	12/22
Outer diameter of stator/mm	45	Outer diameter of rotor/mm	27
Inner diameter of stator/mm	27.5	Inner diameter of rotor/mm	20
Stator yoke height/mm	3.5	Axial length/mm	30

Fig. 1 Cross section diagram of FSPM motor

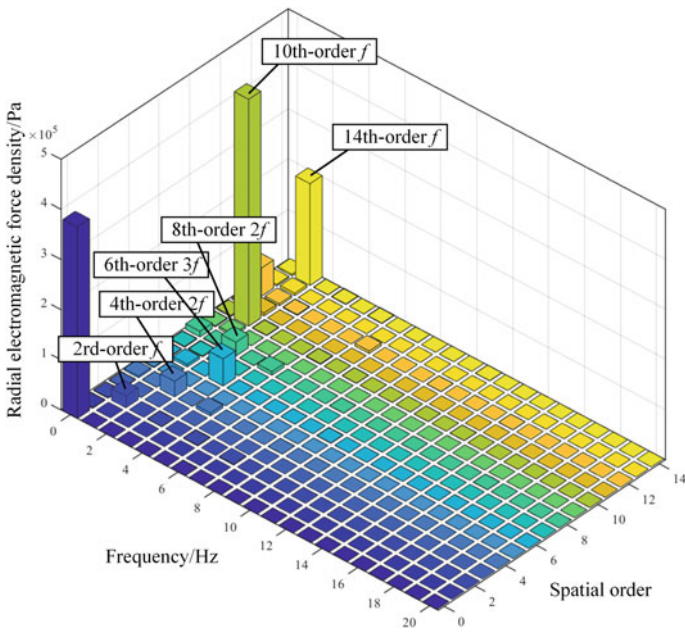
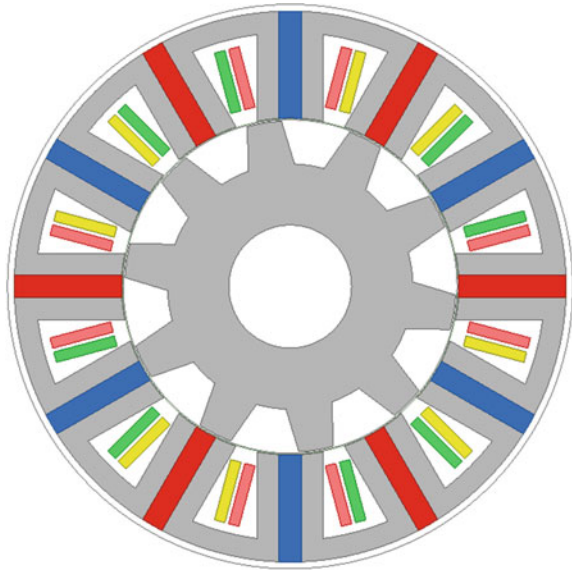


Fig. 2 2-D fft decomposition of radial electromagnetic force density

the 14th-order f have larger amplitude, which is consistent with the results of the previous theoretical analysis.

- (2) The amplitudes of the 10th- and 14th-order f components are relatively large with 452373Pa and 202770Pa respectively, which will cause more severe electromagnetic vibration response.
- (3) The amplitudes of the 2rd-order f and the 4th-order $2f$ harmonics are 23,555.1 Pa and 31,002.9 Pa, respectively, which are smaller than those of others. However, their orders are small. It has been demonstrated in [15], the magnitude of the deformation produced by the motor is inversely proportional to the fourth power of the order of the electromagnetic force acting on the motor. That is to say, the smaller the order of the force harmonic is, the more severe the motor vibration is.

2.3 Harmonic Response Analysis of Radial Electromagnetic Force

In order to restrain the motor vibration to the maximum extent, the first step is to sort the effects of different electromagnetic force harmonics on the electromagnetic vibration of the motor, in order to find the harmonic component that have a significant impact on the motor electromagnetic vibration. In this paper, the vibration responses are analyzed by applying the radial force harmonics with different spatial orders as the excitation sources to the crown of the stator. Set 2rd-, 4th-, 6th- and 8th- order radial forces as unit forces with amplitudes of 1Mpa. According to the above analysis, the amplitudes of the force harmonics with 10th- and 14th-order are larger, which are about 10 times that of the other force harmonics, therefore, the amplitudes of 10th- and 14th-order forces are set to 10Mpa. Select one point on the motor housing, and get the vibration acceleration responses under different force harmonics, as shown in Fig. 3. From Fig. 3, that:

- (1) When the unit radial force harmonics with 1 Mpa is applied, the vibrations of the 2rd-order force is larger than that of the 4th-order force and larger than that of the 6th-order force, which is in accordance with Jordan's formula [15].
- (2) The motor vibration under the action of the 8th-order unit force is exactly the same as that under the action of the 4th-order force. This is due to the presence of stator teeth, the concentrated force obtained by integrating the 8th- and 4th-order force densities on the stator crown is exactly the same.
- (3) Although the spatial order of the 10th- and 14th-order forces are relatively large, the amplitudes of these two order forces are also large, which are 10 Mpa respectively. So, the vibrations produced by these two order force harmonics are the most intense. And the influence of the 10th-order force on vibration is slightly larger than that of the 14th-order force.

In combination with the amplitudes of the radial force harmonics shown in Fig. 2 and the vibration response shown in Fig. 3, it can be seen that, after the amplitude

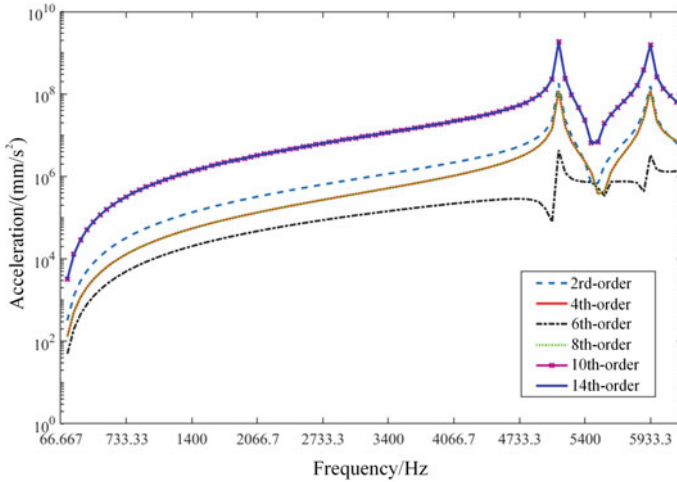


Fig. 3 Frequency response of electromagnetic force

weighting, the vibration caused by 10th-order f force harmonic is larger than that by 14th-order f force harmonic, and much larger than that of other force harmonics.

The influence of the unit 2rd-order force harmonic on the motor vibration is slightly larger than that of the 4th-order force harmonic, but the amplitude of 4th-order $2f$ force harmonic with 31,002.9 Pa is about twice that of the 2rd-order f force harmonic with 23,555.1 Pa, therefore, the vibration produced by the 4th-order $2f$ force harmonic is more severe than that produced by the 2rd-order f force harmonic.

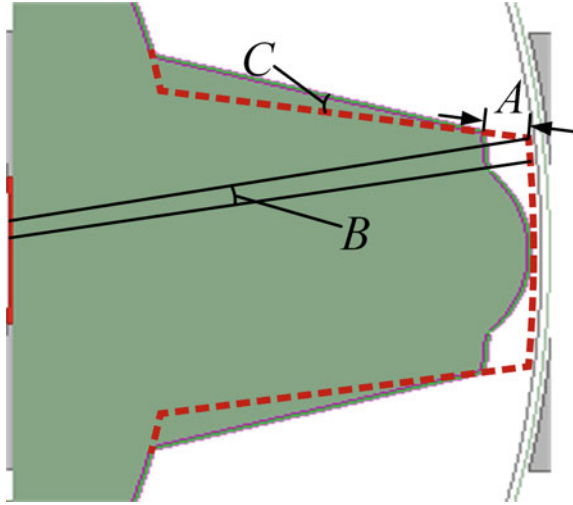
In summary, when the electromagnetic vibration of the prototype in this paper is restrained, the weight priority of these force harmonics to be weakened should be: 10th-order $f > 14$ th-order $f > 4$ th-order $2f > 2$ nd-order $f > 8$ th-order $2f > 6$ th-order $3f$.

3 Low Electromagnetic Vibration Optimization Design

On the basis of the modulation theory of air-gap field [1], optimizing the modulator structure can change the distribution of the air-gap flux density, so as to weaken the radial electromagnetic force and finally suppress the motor vibration. Therefore, this paper chooses to optimize the structure of the original saliency-pole rotor, as shown in Fig. 4, in which the red dotted line is the original rotor tooth structure. A, B and C are three optimization variables. A represents the distance between the optimized and original rotor tooth tip. B represents the rotor tooth cutting angle. C represents the angle between the optimized and the original rotor tooth edge.

The objective functions of this paper are the minimum of the harmonic components of the radial electromagnetic force density of 10-th order f , 14-th order f , 4-th order

Fig. 4 Schematic diagram of the rotor optimization



$2f$, 2- rd order f , 8-th order $2f$ and 6-th order $3f$, (expressed as $f_1 \sim f_6$, respectively), and the maximum of the torque T , the constraint condition is that the reduction of torque T is less than 5%. According to the structure parameters of the motor, the ranges of A , B and C are $0.2 \sim 1$ mm, $0.4 \sim 2^\circ$ and $2 \sim 10^\circ$ respectively. Design-expert software is used to design the response surface curve CCD method finite element simulation table, and Ansoft software is used to simulate and calculate the response surface curve regression sample library of $f_1 \sim f_6$ and T . According to the sample library, the response surface curve was fitted by CCD method in Design-Expert software, and the fitting model of $f_1 \sim f_6$ and T with A , B , C was obtained. The significance test $p < 0.05$, indicating that the model has statistical significance [16], which can be used to replace the real simulation results with regression equations for analysis.

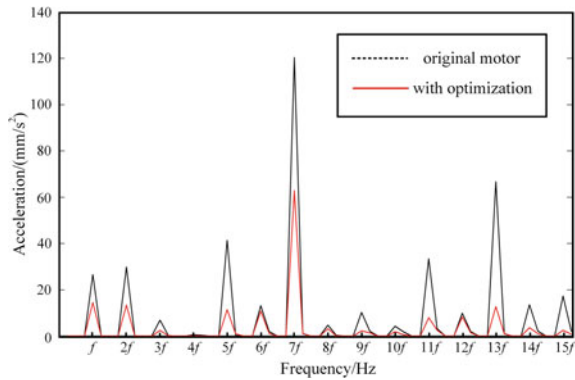
Motor vibration suppression is a multi-objective optimization problem, and there is no global optimal solution that makes all objectives optimal at the same time. Therefore, NSGA-II optimization algorithm is used in this paper to find the Pareto optimal solution set [17], and then, the Pareto optimal solution set is selected and sorted according to the priority of the electromagnetic force suppression analyzed above and the constraint condition: the reduction of the electromagnetic torque T of the motor is less than 5%, the final optimal solutions of A , B and C are 0.663248888, 1.740367704 and 6.409895657. Considering the actual processing situation, the final optimal solutions of A , B and C are 0.66mm, 1.74° and 6.4° , respectively.

4 Analysis of Optimization Results

Selecting the same point on the motor casing before and after optimization, and their vibration accelerations are shown in Fig. 5. It can be seen that the electromagnetic vibration is more intense in the frequencies with f , $2f$, $3f$, $4f$, etc., which accords with the frequency of the motor electromagnetic force analysis above. The overall vibration is obviously suppressed after optimization and the average vibration level has decreased by about 50% of the original motor. At the frequencies of $5f$, $9f$, $11f$ and $13f$, the vibration accelerations decrease more obviously, with a decrease of about 72%, 77%, 76% and 80%, which effectively suppressed the motor electromagnetic vibration.

The torques of the motors under rated operating conditions before and after the optimization are calculated, as shown in Fig. 6. From Fig. 6, the average torque of the motor before the optimization is 2 Nm, and after optimization, although the average

Fig. 5 Vibration acceleration spectrum contrast diagram of motor



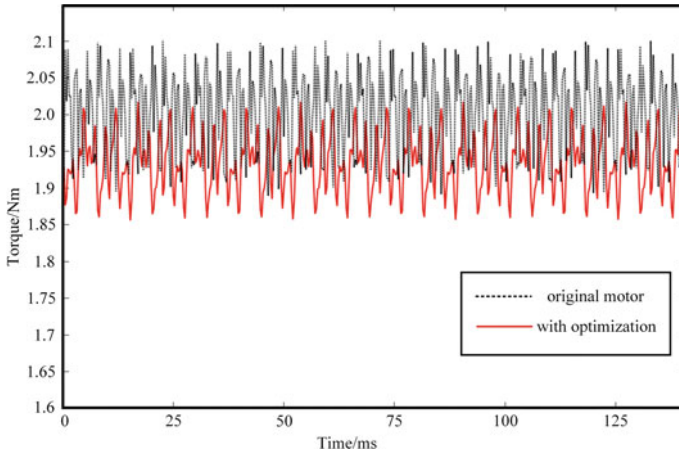


Fig. 6 Output torque waveform of the motor

torque decreases to 1.94 Nm, the reduction is about 3%, which meets the constraint: torque reduction not more than 5%. Therefore, the low electromagnetic vibration optimization scheme of the FSPM motor proposed in this paper is reasonable and feasible.

5 Conclusion

From the air-gap field modulation theory, the characteristics and the origins of the radial electromagnetic force harmonics (spatial order r and time frequency f) causing the electromagnetic vibration of FSPM are analyzed. Taking a 12-slot 10-pole FSPM motor as the research object, the structure of the rotor as the magnetic field modulator is improved, and the structural parameters are optimized by the NSGA-II algorithm, on the basis of guaranteeing the electromagnetic torque, the main radial electromagnetic force harmonics, which have great influences on the electromagnetic vibration of the motor, are reduced effectively. The motor electromagnetic vibration average level is nearly less 50% than before.

The optimization idea in this paper can be extended to the low electromagnetic vibration optimization design of the FSPM motors.

References

1. Cheng M, Gan Z, Wei H (2014) Overview of stator permanent magnet brushless machine systems and their key technologies. Proc CSEE 000(029):5204–5220. (in Chinese)

2. Du Y, Xiao F, Hua W et al (2016) Comparison of flux-switching PM motors with different winding configurations using magnetic gearing principle. *IEEE Trans Magn* 52(5):1–8
3. Shi Y, Jian L, Wei J et al (2016) A new perspective on the operating principle of flux-switching permanent-magnet machines. *IEEE Trans Indus Electron* 63(3):1425–1437
4. Zhu X, Hua W, Wu Z et al (2018) Analytical approach for cogging torque reduction in flux-switching permanent magnet machines based on magnetomotive force-permeance model. *IEEE Trans Indus Electron* 65(3):1965–1979
5. Zhao W, Pan X, Ji J et al (2020) Analysis of PM eddy current loss in four-phase fault-tolerant flux-switching permanent-magnet machines by air-gap magnetic field modulation theory. *IEEE Trans Indus Electron* 67(7):5369–5378
6. Xiao W, Wang Y, Geng L et al (2018) Comparative research of torque impulse balance control strategy under single-phase open circuit condition and multi-phase open circuit conditions. *Proc CSEE* 38(16):4873–4885. (in Chinese)
7. Chen Y, Zhou Y, Zhang J et al (2021) Rotor spatial position estimation and sensorless composite control of bearingless flux-switching permanent magnet motors 1–11. (in Chinese)
8. Cao L, Chau KT, Lee CHT et al (2021) A double-rotor flux-switching permanent-magnet motor for electric vehicles with magnetic differential. *IEEE Trans Indus Electron* 68(2):1004–1015
9. Li X, Shen F, Yu S et al (2021) Flux-regulation principle and performance analysis of a novel axial partitioned stator hybrid-excitation flux-switching machine using parallel magnetic circuit. *IEEE Trans Indus Electron* 68(8):6560–6573
10. Gan C, Wu J, Shen M et al (2018) Investigation of short permanent magnet and stator flux bridge effects on cogging torque mitigation in FSPM motors. *IEEE Trans Energy Convers* 33(2):845–855
11. Zhu X, Shu Z, Quan L et al (2016) Multi-objective optimization of an outer-rotor V-shaped permanent magnet flux switching motor based on multi-level design method. *IEEE Trans Magn* 52(10):1–8
12. Mao Y, Liu G, Zhao W et al (2018) Low-noise design of fault-tolerant flux-switching permanent-magnet machines. *IET Electr Power Appl* 12(6):747–756
13. Wang S, Li H (2020) Reduction of electromagnetic vibration and noise in permanent magnet motor for EVs by optimizing design of rotor based on GPR-PSO model. *J Electr Eng Technol* 15(3):1231–12430
14. Li X, Liu C, Mei B et al (2018) Vibration and noise sources analysis of IPMSM for electric vehicles in a wide-speed range 38(17):5219–5227. (in Chinese)
15. Jordan H (1950) *Electric motor silencer-formation and elimination of the noise in the electric motors*. Germany, W. Girardet
16. Tu H, Xin Y (2015) Analysis and experiments of buckling of precision products for automotive based on the response-surface methodology 34(4):565–569. (in Chinese)
17. Horn J, Nafpliotis N, Goldberg DE (1994) A niched Pareto genetic algorithm for multi-objective optimization. In: *The first IEEE conference on evolutionary computation*. Piscataway, NJ, pp 82–87

Simulation and Analysis of Charge Distribution and Capacitance Effect on Uneven Surface of Dielectric with Leakage Current



Ran Ding, Tianxin Zhuang, Yin Gu, Ke Zhao, Hongtao Li, Jin Miao, and Yujie Li

Abstract Insulation parts made of materials with the characteristics of dielectric and conductive media not only have capacitance and conductance effects between electrodes, but also have capacitance effects between adjacent surfaces on uneven surfaces. Positive and negative charges will accumulate on the surface, thereby affecting the surface electric field and insulating properties. This paper discusses the mechanism of the capacitance effect caused by the uneven surface, and gives the mathematical expression and solution method of the related electric field and charge distribution. Furthermore, this paper uses the finite element method to simulate and solve the electric field under AC excitation. The simulation results are demonstrated and discussed.

Keywords Surface charge · Electric field intensity · Capacitance effects · Simulation of uneven surface

R. Ding

State Grid Jiangsu Electric Power CO., LTD, Jiangsu, Nanjing 210024, China

T. Zhuang (✉) · Y. Li

State Grid Jiangsu Electric Power CO., LTD Electric Power Research Institute, Jiangsu, Nanjing 211102, China

e-mail: zkdkyjs@126.com

Y. Gu · J. Miao

State Grid Jiangsu Electric Power CO., LTD Wuxi Power Supply Company, Jiangsu, Wuxi 214062, China

K. Zhao · H. Li

State Grid Jiangsu Electric Power CO., LTD Research Institute, Jiangsu, Nanjing 211103, China

© Beijing Paiké Culture Commu. Co., Ltd. 2024

X. Dong and L. Cai (eds.), *The Proceedings of 2023 4th International Symposium on Insulation and Discharge Computation for Power Equipment (IDCOMPU2023)*, Lecture Notes in Electrical Engineering 1100, https://doi.org/10.1007/978-981-99-7393-4_20

1 Introduction

The problem of charge accumulation in dielectrics with leakage current is an important research topic in high-voltage insulation. It has been widely studied and many research results have been obtained. Under DC excitation, charge accumulation will show a monotonous increase trend, which has a significant impact on insulation [1–3]. Under AC excitation, charge accumulation and release will take place alternately, and the charge accumulation quantity is related to the time constant of the material. In general, when the resistivity of the material is large, then the time constant is also large, causing the increase of charge in one period cannot reach a steady state, so the charge accumulation quantity is small, but it also has a certain impact on insulation [4–6].

The calculation of charge accumulation in materials is a time-varying current field problem. Even for DC excitation, it is necessary to calculate the transition process of charge accumulation and development. The calculation of this problem is generally solved by the finite element method [7–9], and the calculation theory and method are relatively complete. However, this is a special type of problem in the electromagnetic field. Commercial software for general computing of electromagnetic fields generally does not focus on this type of problem, or in other words, general commercial software does not have the function of calculating charge distribution. Therefore, the special calculation software needs to be developed to solve this type of problem.

In addition to accumulating volume charges in inhomogeneous dielectrics, charges also accumulate on surfaces. This paper focuses on charge accumulation on material surfaces, especially on large uneven surfaces. This paper analyzes the characteristics of charge accumulation and electric field change of uneven surfaces, which results from such as the surface ageing of insulating parts including insulators.

2 Boundary Value Problem of Dielectric with Leakage Current

For the dielectric with leakage current, charges will accumulate in the dielectric when it is discontinuous, and charges will also accumulate on the medium interface perpendicular to the current density. This problem belongs to the time-varying current field problem, and it can also be seen as a coupling problem of the electrostatic field and the current field. In order to describe the current field and the electrostatic field of the dielectric, the charge is first divided into two states, that is, the charge in the moving state and the charge in the dynamic static state. The former is related to the current density J , and the latter is related to the electric displacement D . On this basis, the equation describing J , D and charge and the boundary value problem are given, and the method of applying the excitation source is given.

2.1 Charge Division Between the Two States

The charge in two states refers to: one is the charge of a single polarity in a moving state, called the moving charge, denoted by q_v and ρ_v ; the other is the charge after adding the charges of two polarities, that is, the net charge, denoted by q and ρ , and the electric field effect of the net charge is the same as that of the static charge. ρ_v is not the source of the Coulomb electric field, that is, its contribution to the electric field is not considered, in fact its contribution to the electric field is reflected in ρ .

The charge in the definition of electric current is the moving charge, while the charge in the definition of the law of conservation of charge is the net charge. As mentioned above, the current field is the flow velocity field of the charge, and the quantity describing the current field is the current density. If the moving charge density at a point is ρ_v , and the moving speed of the charge is \mathbf{v} , then the current density at this point is defined as:

$$\mathbf{J} = \rho_v \mathbf{v} \quad (1)$$

2.2 Extended Law of Conservation of Charge and Application of Excitation Source

For the problem of time-varying electromagnetic fields in the dielectric with leakage current, the constraint equations are based on the law of conservation of charge or known as continuity equation. The law of conservation of charge is defined as the area integral of the current density \mathbf{J} on the closed surface S is equal to the sum of all positive and negative charges in the volume V surrounded by the surface S , that is, the negative time-varying rate of the net charge q , as follows:

$$\oiint_S \mathbf{J} \cdot d\mathbf{S} = -\frac{dq}{dt} \quad (2)$$

where the normal direction of S is taken as the outer normal direction. The corresponding differential form of the above formula is:

$$\nabla \cdot \mathbf{J} = -\frac{\partial \rho}{\partial t} \quad (3)$$

which means the divergence of the current density \mathbf{J} is equal to the negative time-varying rate of the net charge volume density. In fact, the continuity equation or the law of conservation of charge just means that the conduction current may be discontinuous, and the current can start or end out of thin air in the field.

The charges in Eq. (2) and Eq. (3) are charges that conform to the characteristics that charges cannot be generated or disappeared alone. However, from the perspective of moving charges, at the source point, that is, the field area where the power source is applied, there will be charges injected into or flowed out of the field. From the standpoint of the field, these charges are generated or disappeared alone. At such a point, the above law of conservation of charge needs to be extended, and the extension form is:

$$\oiint_S \mathbf{J} \cdot d\mathbf{S} - \frac{dq_{vSc}}{dt} = -\frac{dq}{dt} \quad (4)$$

$$\nabla \cdot \mathbf{J} - \frac{\partial \rho_{vSc}}{\partial t} = -\frac{\partial \rho}{\partial t} \quad (5)$$

The meaning of the term added in Eq. (4) is the current $i_{Sc} = dq_{vSc}/dt$, which is actually the current injected into the field (if the charge is flowing out, the sign is opposite), and the subscript Sc represents Source.

The known source of the current field is the flow of charges injected into or extracted from the field, and the way the charges flow in and out has surface distribution and volume distribution. The surface distribution is to inject charges into a part of the boundary surface S_i of the field domain. The known quantity is generally the total current i_{Sc} of the surface S_i . This way of applying the excitation source is a common situation. This excitation source is reflected in the extended law of conservation of charge, that is, Eq. (4), and a known current is applied through the boundary conditions of the field. The specific application method is illustrated in the boundary value problem in the next section. For the source in the form of source charge volume density, which is the injection of charge into the field in a region, the known volume density ρ_{vSc} can be directly reflected in the equation.

2.3 Initial Boundary Value Problem of the Field

For the problem of the time-varying current field in the dielectric with leakage current, the initial condition must be given in addition to the boundary condition, and the initial boundary value problem is formed by combining the general equation of the field. The general equations, interface conditions, necessary and sufficient boundary conditions and initial conditions of the constrained field are given below, thus constituting the initial boundary value problem:

$$\left\{ \nabla \cdot \mathbf{J} + \frac{\partial \rho}{\partial t} = \frac{\partial \rho_{vSc}}{\partial t} \in V \right. \quad (6)$$

$$\{\nabla \cdot \mathbf{D} = \rho \in V \quad (7)$$

$$\{\nabla \times \mathbf{E} = 0 \quad \in \mathbf{V} \quad (8)$$

$$\{\mathbf{J} = \sigma \mathbf{E} \quad \in \mathbf{V} \quad (9)$$

$$\{\mathbf{D} = \varepsilon \mathbf{E} \quad \in \mathbf{V} \quad (10)$$

$$\{\mathbf{E}_{t=0} = 0 \quad \in \mathbf{V} \& \mathbf{S} \quad (11)$$

$$\left\{ \mathbf{n} \cdot \left(\mathbf{J}_1 + \varepsilon_1 \frac{\partial \mathbf{E}_1}{\partial t} \right) = \mathbf{n} \cdot \left(\mathbf{J}_2 + \varepsilon_2 \frac{\partial \mathbf{E}_2}{\partial t} \right) \quad \in \mathbf{S}_{\text{int}} \quad (12)$$

$$\{\mathbf{n} \cdot (\mathbf{D}_2 - \mathbf{D}_1) = \rho_S \quad \in \mathbf{S}_{\text{int}} \quad (13)$$

$$\{\mathbf{n} \times (\mathbf{E}_i - \mathbf{E}_j) = 0 \quad \in \mathbf{S}_{\text{int}} \quad (14)$$

$$\{\mathbf{n} \times \mathbf{E} = 0 \quad \in \mathbf{S}_1 \quad (15)$$

$$\left\{ \oint_S \left(\mathbf{J} + \varepsilon \frac{\partial \mathbf{E}}{\partial t} \right) \cdot d\mathbf{S} = i_{Sc} \quad \in \mathbf{S}_1 \quad (16)$$

$$\{\mathbf{n} \cdot \mathbf{E} = 0 \quad \in \mathbf{S}_2 \quad (17)$$

Equations (6)–(8) are general equations describing the current field and the Coulomb electric field. Note that the source charge density ρ_{vSc} in the equation does not generate the Coulomb electric field, so the charge is not included in Eq. (7); ρ_{vSc} is the source of the given current field, which is often given in the form of current i_{Sc} and ρ is the unknown quantity to be solved; Eq. (11) is the initial condition, Eqs. (12)–(14) are the interface conditions, and Eq. (15) is the boundary condition of the conductor electrode, it is considered that the electric field or current density on the surface of the conductor electrode is perpendicular to the surface, then the flux constraint is applied on the surface as Eq. (16), which is called the first-type boundary condition; Eq. (17) is the second-type boundary condition.

In order to solve the above equations, the equations can be merged to obtain an equation containing only one field quantity. After the variable is obtained, other variables can be calculated according to the known quantity. It can be combined into an equation with charge density ρ as the variable to be solved, but generally it is combined into an equation with electric field strength \mathbf{E} or current density \mathbf{J} as the variable to be solved, because it is easy to apply the current source excitation. Then the electric displacement \mathbf{D} is calculated, and finally the charge density is calculated using $\rho = \nabla \cdot \mathbf{D}$. For the surface charge density on the interface or surface, Eq. (13) can be used to solve it.

2.4 The Initial Boundary Value Problem of Potential and the Application of Excitation Source

If the given excitation source is the current source i_{sc} , the current excitation can be applied directly by using Eq. (16). But in many cases, the voltage source u_{sc} is the given excitation source. In this case, the potential φ should be solved first, and the voltage source is applied as the boundary condition of φ . Assuming that the relationship between potential and electric field strength is $\mathbf{E} = -\nabla \times \varphi$, then the equation that potential satisfies can be obtained by combining the above boundary value problem. Substituting $\mathbf{E} = -\nabla \times \varphi$ and $\mathbf{n} \cdot \mathbf{E} = E_n = -\partial\varphi/\partial n$ and the relationship between electric displacement and current density and electric potential into the above equations, the general equation, interface conditions and boundary conditions of electric potential can be obtained. The tangential continuity equation of electric field strength (Eq. 14) and the first-type boundary condition (Eq. 15) which only contain the electric field strength correspond to the interface condition of continuous potential $\varphi_i = \varphi_j$ and the boundary condition of known potential $\varphi = u_{sc}$, according to which the voltage excitation can be applied.

For the sinusoidal steady-state problem, the initial value condition is meaningless, and substituting $\partial/\partial t \rightarrow j\omega$ into the equations can form the boundary value problem of the potential in the form of phasor. The finite element method can be used to solve the boundary value problem [10, 11], and the finite element method will not be described here.

3 Volume Capacitance and Surface Capacitance Characteristics of the Dielectric with Leakage Current

For the dielectric with leakage current, charges will accumulate in the dielectric when it is discontinuous, and charges will also accumulate on the interface perpendicular to the current density. For the linear homogeneous dielectric, there is no charge accumulation in the material region, that is, although there is charge flowing in the material to form a current, the net charge at each point is zero. However, the charge will accumulate on the surface of the material, and the charge will generate the electric field in the material, causing the charge to move to form a current.

Figure 1 is a cylindrical dielectric material with leakage current, its relative permittivity is 2, conductivity is 2 S/m, and a time-varying voltage source is applied between the two ends. Figure 1a and b respectively show the distribution of the electric field strength \mathbf{E} and the electric displacement \mathbf{D} inside the material and outside the material. The electric field is perpendicular to the end surface of the material. This is because there are electrode plates with the same radius as the material on the upper and lower end surfaces, which are good conductors with the electrical conductivity much larger than the dielectric material. Therefore, the electrode plates are approximately equipotential conductors, where the electric field strength is approximately

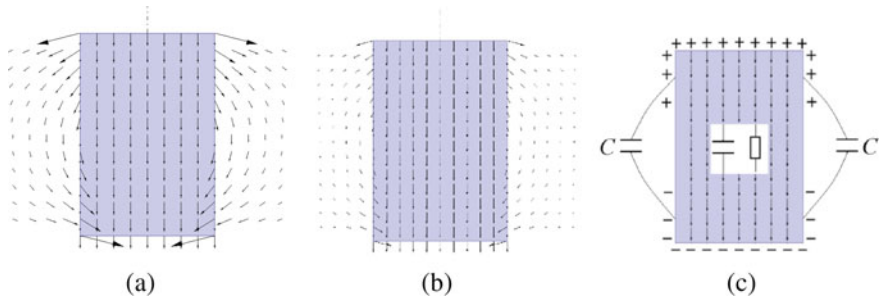


Fig. 1 Cylindrical dielectric with leakage current. **a** Distribution of the electric field strength E , **b** Distribution of the electric displacement D , **c** Schematic diagram of volume capacitance and surface capacitance

zero, and the electrodes are not drawn in the figure. The field in the material is uniform, which is caused by the uniform distribution of current density; while the field or electric force line in the air is emitted from the upper end and terminated at the lower end, and the normal component of D on the surface is the charge density distribution on the surface of the material, because the normal component of D inside the material must be zero; therefore, the charge distribution on the surface of the material is shown in Fig. 1c.

The distribution of charge is equivalent to the capacitive effect. Between the upper and lower end surfaces in Fig. 1, the total capacitance is composed of two parts connected in parallel, one part is the capacitance corresponding to the electric field or electric field energy in the material, which is connected in parallel with the conductance formed by the material, and the other part is the capacitance corresponding to the electric field energy in the air, as shown in Fig. 1c. The relationship between the two capacitances depends on the dielectric constant or permittivity of the material and the shape of the model. For a cylindrical structure, when the ratio of height to radius is 2.5:1, if the relative permittivity of the material is 4, the two capacitances values are nearly equal. It can be seen that the capacitance corresponding to the electric field in the air is relatively large. Generally, the relative permittivity of insulating materials is less than 4. At this time, the capacitance of the air will be greater than the capacitance of the material.

4 Simulation of the Charge Distribution and Capacitance Effect on Uneven Surface

When the surface of the dielectric with leakage current is uneven, positive and negative charges and capacitive effects will appear on the concave or convex surfaces. Figure 2a and b are the distribution of electric force lines. It can be seen that on the two opposite surfaces of the concave, the electric force lines start from one surface

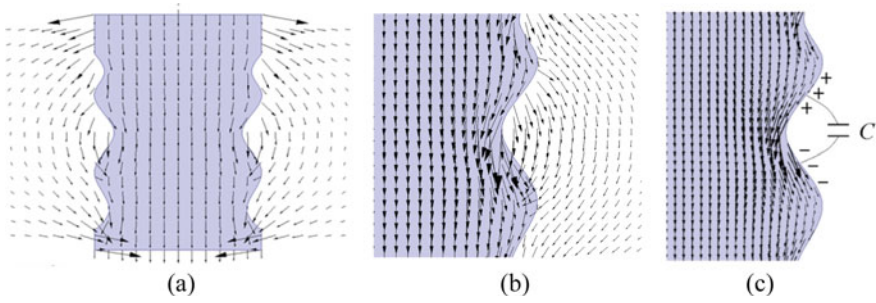


Fig. 2 Uneven surface of dielectric with electric leakage. **a** Distribution of the electric displacement D , **b** Partial enlarged detail of **a**, **c** Schematic diagram of the charge distribution and surface capacitance of the two opposite surfaces

and end on the other surface. It shows that the charge density is positive and negative respectively, and the positive and negative charges correspond to the capacitance effect, as shown in Fig. 2c.

The surface charge accumulation and capacitance effect will change the surface electric field strength. Since the electric field strength will also increase due to the convex, for the case of the uneven surface, the maximum field strength of the convex part is much larger than that of the regular surface given in the previous section. Especially in the middle part of the cylindrical, the electric field strength of the regular surface is zero at $1/2$ of the height, and it is small in the surrounding. While in the convex part of the uneven surface at $1/2$ of the height, the value of electric field strength or electric displacement is close to the value at the end. The total capacitance corresponding to the air region also increases, and the capacitance of the uneven surface is about 1.15 times that of the regular surface.

It can be seen that when analyzing the surface charge and electric field strength, the surface roughness and shape irregularities should be considered. Although it is not a new problem in terms of calculation methods, attention should be paid to this phenomenon and its influence on insulation characteristics in practice.

5 Conclusion

The equation describing the current field in the dielectric with leakage current is the law of conservation of charge, but when considering the current injected into the field by the source or the current flowing out of the field, the law of conservation of charge needs to be extended so that the excitation source can be included in the boundary value problem. The relationship between the net charge accumulated in the dielectric and the electric displacement satisfies Gauss's law. For a dielectric, the capacitance between its two ends is formed by the parallel connection of the volume capacitance and the equivalent capacitance in the surrounding air. The values of

the two capacitances are comparable, so the capacitance corresponding to the air region cannot be ignored. On the uneven surface, positive and negative charges will accumulate on the two opposite faces of the concave, thereby increasing the electric field strength, therefore the electric field effect of this charge accumulation should be considered when analyzing insulation characteristics.

Acknowledgements Funded by the Science and Technology Project of State Grid Jiangsu Electric Power CO., LTD (J2022005).

References

1. Bradwell A, Cooper R, Varlow B (1971) Conduction in polythene with strong electric fields and the effect of prestressing on the electric strength. *Proc Inst Electr Eng* 118:247–254
2. Wu J, Yin Y (2018) Application of space charge detection technology in dielectrics under periodic stress. *Proc CSEE* 38(05):1572–1581 (in Chinese)
3. Zhang Y, Pan J, Lei Q, Zheng F (2021) Space charge effect and application in solid insulation dielectrics. *Chin Sci Bull* 66:3695–3711 (in Chinese)
4. Hao J, Xu R, Chen G, Liao R, Fu J, Wu G, Wang Q (2013) Space charge characteristics difference of oil-impregnated paper insulation system under DC and power frequency voltage. *Power Syst Technol* 37(04):1166–1173 (in Chinese)
5. Li D, Wang T, Hou Y, Zhang G (2020) Charge accumulation on epoxy insulator surface in C4F7N/CO₂ mixtures under AC voltage. In: 2020 IEEE international conference on high voltage engineering and application (ICHVE), pp 1–4
6. Shen X, Sun G, Li W, Wu J, Yin Y (2022) The electric field threshold of charge accumulation in XLPE under AC field. In: 2022 IEEE international conference on high voltage engineering and applications (ICHVE), pp 1–4
7. Deng B, Zhang S, Zhang Z, Gan W, Luo X (2021) Dynamic analysis of DC GIL insulator surface charge accumulation based on COMSOL and MATLAB co-simulation. In: 22nd international symposium on high voltage engineering (ISH 2021), pp 853–858
8. Wang R, Xu Y, Jiang C, Peng X, Yu Z, Xie Y, Xie Y, Hu C (2021) Simulation and analysis of charge accumulation characteristics of post insulator of transmission line for the CRAFT NNBI system. *Fusion Eng Des* 173:112948
9. Shimakawa H, Sato M, Kumada A, Hidaka K, Yasuoka T, Hoshina Y, Shiiki M (2022) Temperature dependence of surface charge accumulation on DC-GIS insulating spacer. *IEEE Trans Power Delivery* 37(6):4539–4547
10. Jian J (2002) *The finite element method in electromagnetics*, 2nd edn. Wiley, New York, NY
11. Ida N, Bastos JPA (1997) *Electromagnetics and calculation of fields*, 2nd edn. Springer, New York, NY

Thermal Simulation Model of Oil-Immersed Transformer and Analysis of Temperature Rise Characteristics Under Winding Fault



Si Chen, Yadong Liu, Yingjie Yan, and Xiuchen Jiang

Abstract It is significant for safe operation and fault detection of transformers to know the temperature field distribution characteristics and the temperature variation rules accurately under fault conditions of oil-immersed transformer. In this paper, a thermal simulation model for oil-immersed transformer is established, and a faulty module is added to simulate the temperature field distribution under different fault parameters. Simulation results show that: compared to normal operating conditions, the overall temperature of transformer with winding fault increases, and a new winding hot spot appears at the location of the winding fault. As the heating power of the faulty coils increases, the new hot spot temperature increases, and the overall temperature of the oil-tank outer surface increases. With the rise of the fault coils' height, the position of the new hot spot increases, and the range of outer surface temperature increases. This study can provide guidance for condition detection and fault diagnosis of transformers.

Keywords Oil-immersed transformer · Thermal model · Winding fault · Temperature rise characteristic

S. Chen · Y. Liu (✉) · Y. Yan · X. Jiang
Department of Electrical Engineering, Shanghai Jiao Tong University, Shanghai 200240, China
e-mail: lyd@sjtu.edu.cn

S. Chen
e-mail: chensi_425@sjtu.edu.cn

Y. Yan
e-mail: yanyingjie@sjtu.edu.cn

X. Jiang
e-mail: xcjiang@sjtu.edu.cn

1 Introduction

As an important equipment in the power grid, the transformer's safety and stability is crucial. Due to poor manufacturing process, heat dissipation failure, long-term overload, lightning impact, insulation damage and other reasons, transformer operation failure rate is high. According to statistics, transformer failure rate in 10 kV distribution network in 2021 was 0.40 times per 100 sets per year, with a year-on-year growth of 30% [1]. Winding fault can cause more unplanned outages of transformers. One of the main phenomena is to cause local temperature rise. Therefore, it is necessary to research the temperature characteristics of the operating transformers.

At present, the temperature detection methods of transformer mainly include direct measurement method and guide calculation method [2, 3]. But only some large oil-immersed transformers in service have the installation conditions of optical fiber temperature measurement system inside. And the installation points are few, which cannot realize the monitoring of the internal overall temperature distribution. For small oil-immersed transformers, only top and bottom oil temperature are observed. So it is impossible to directly measure the overall temperature field distribution of transformer. The guideline calculation method usually has poor accuracy. It estimates hot spot temperature by the top oil temperature rise value. In order to accurately calculate the internal hot spot temperature and temperature field distribution, Susa et al. [4, 5] and Swift et al. [6, 7] conducted the research on the transient model of hot spot temperature and top oil temperature, and proposed the empirical thermal circuit model. But there are still some systematic errors. In order to accurately obtain the internal temperature field, finite element method(FEM) has gradually been applied to the calculation of the temperature fluid field in transformers. Cenk et al., used the FEM to calculate the hot spot temperature of a single-phase transformer [8]. Milad et al., used the FEM to conduct thermal simulation on transformer bushing, and studied the temperature characteristics of the casing under normal load rate conditions and short-term overload conditions [9]. Xie Yuqing et al. used the upwind finite element method to solve coupled equations of the flow field and temperature field of the transformer winding, effectively suppressing the non-physical oscillation of the solution, improving the stability of winding temperature calculation [10]. Deng Yongqing et al. established a transformer winding hot spot temperature inversion detection model based on the coupled numerical calculation of transformer temperature fluid field [11]. The above research has achieved the calculation of transformer hot spot temperature and temperature field distribution, but only studied the situation under normal operating conditions, without temperature characteristic analysis under fault operating conditions.

With regard to winding fault, domestic and foreign scholars have also conducted research on current harmonics [12], phase differences [13], main magnetic flux, and leakage magnetic flux before and after the fault [14]. However, the above research does not involve the study of the overall temperature field distribution characteristics after winding fault.

To sum up, aiming at the problem of unclear temperature rise characteristics of oil-immersed transformer winding fault, this paper establishes a transformer thermal simulation model including faulty module. The temperature field of transformer is simulated and calculated, and the distribution characteristics of the temperature field under winding fault are studied. The research results can provide guidance for transformer fault detection.

2 Simulation Model

2.1 Model Parameter

This paper simulates a transformer with rated parameters of $220\text{ kV} \cdot \text{A} - 10\text{ kV}/400\text{ V}$. The transformer structure is shown in Fig. 1.

The physical parameters of the simulation model are set as follows:

- (1) The inherent heat production of transformer mainly includes iron loss, copper loss, and eddy current loss. Eddy current loss is relatively small compared to iron loss and copper loss [15], and can be ignored. The heat sources in the model include windings and core. The heating power of core is 227 W . The heating power of winding is related to load rate η , as shown in Table 1.

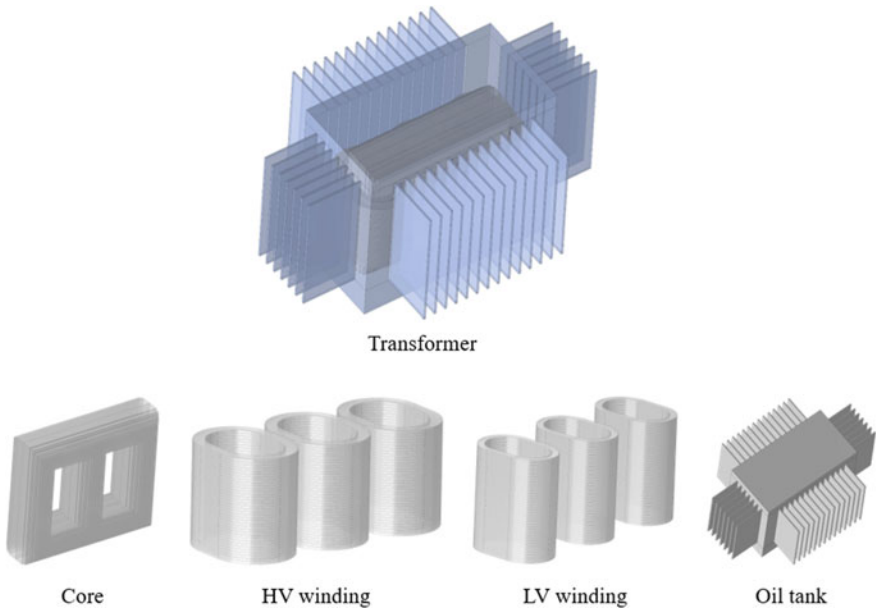
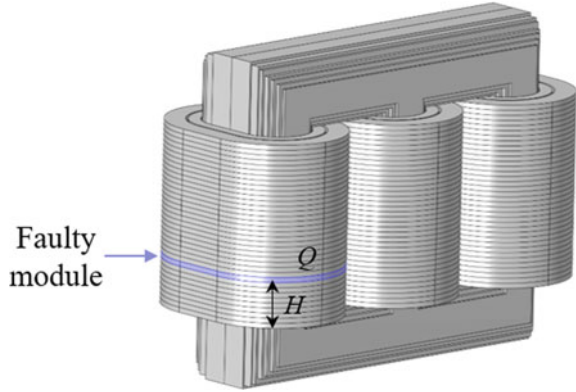


Fig. 1 Transformer structure diagram

Table 1 Relationship between basic heating power of winding and load rate η

η	0.2	0.4	0.6	0.8	1.0	1.2
Heating power of winding /W	430.8	861.6	1292.4	1723.2	2154.0	2584.8

Fig. 2 Schematic diagram of faulty module



(2) The heat dissipation of transformer is affected by various factors such as wind speed and ambient temperature. The research object of this article is indoor transformer. Due to small indoor air fluidity, the wind speed conditions are simplified. The wind speed is set to 0 m/s and the ambient temperature is 5 °C.

2.2 Faulty Module

In order to analyze the temperature characteristics of a transformer with winding fault, it is necessary to set a faulty module in the simulation model, as shown in Fig. 2.

Where, H represents the height from the location of the fault coils to the bottom of the winding, and Q represents the amount of heat generated by the faulty coils. By modifying the fault parameters H and Q , fault conditions with different heat occurring at different locations are simulated.

2.3 Heat Dissipation Process Analysis and Control Equation

Oil-immersed transformer contains solids such as core, windings, oil-tank, and fluids such as transformer oil. Inherent heat sources mainly include windings and core. The heat dissipation process is shown in Fig. 3.

When heat is generated in core and windings, it is first conducted from the inside of solid to the surface. Then, convective heat transfer occurs with the transformer

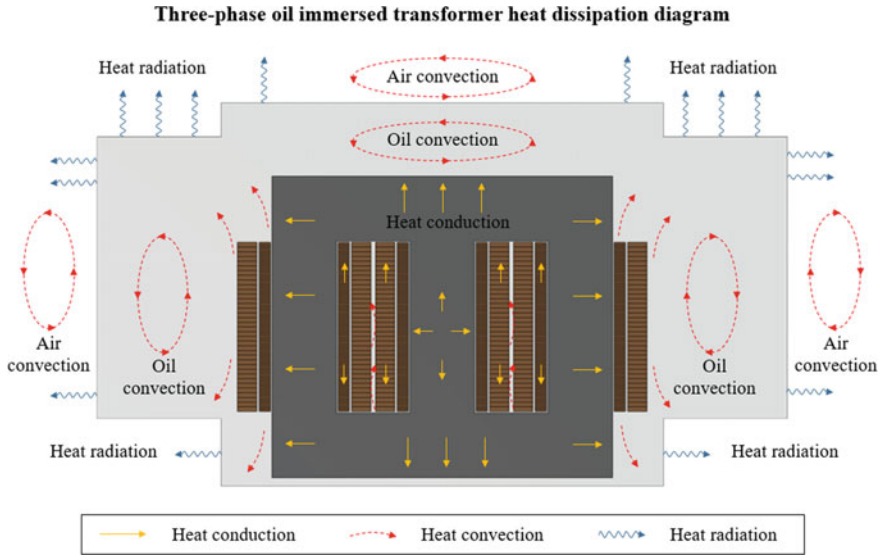


Fig. 3 Three-phase oil-immersed transformer heat dissipation diagram

oil at the solid surface, causing the temperature of oil around the surface of core and winding to rise, forming natural convection. And heat is transferred through thermal convection in transformer oil. As oil flows, heat is carried to the vicinity of oil-tank. Convective heat transfer occurs between oil and oil-tank, transferring heat from oil to the oil-tank inner surface, and through heat conduction to the oil-tank outer surface. The oil-tank outer surface and air are dissipated through thermal convection and radiation.

According to the principle of numerical heat transfer, the transfer process of heat in solids and fluids simultaneously follows the three laws of mass conservation, momentum conservation, and energy conservation.

The mass conservation equation is also known as the continuity equation, as shown in Formula (1).

$$\frac{\partial \rho}{\partial t} + \text{div}(\rho \mathbf{U}) = 0 \tag{1}$$

where, ρ Represents density, t represents time, and \mathbf{U} represents velocity vector.

The variable form of the momentum conservation equation applied to viscous incompressible fluids is Navier-Stokes equations, as shown in Eq. (2).

$$\frac{\partial \mathbf{U}}{\partial t} + (\mathbf{U} \cdot \nabla) \mathbf{U} = f - \frac{1}{\rho} \nabla p + \frac{\mu}{\rho} \nabla^2 \mathbf{U} \tag{2}$$

where, p is the pressure, f is the external force exerted on the fluid in the micro element, and μ is the dynamic viscosity.

The variation of the energy conservation equation in incompressible fluids is shown in Eq. (3).

$$\frac{\partial T}{\partial t} + \text{div}(\mathbf{UT}) = \text{div}\left(\frac{\lambda}{\rho c_p} \mathbf{grad}T\right) + \frac{S_T}{\rho} \quad (3)$$

where, T is the temperature, λ is the thermal conductivity of the fluid, c_p is a constant, S_T is a source term, which includes an internal heat source term and a dissipation term.

The above equations are applied to the transformer simulation model and solved by numerical methods to obtain the internal temperature field distribution results of the transformer.

3 Analysis of Temperature Rise Characteristics

In this paper, a transient solution method is used to calculate the temperature field distribution of transformer. The simulation time is set to 10 h, at which time the temperature rise of transformer reaches a stable state.

3.1 Effect of H on Temperature Rise Characteristics

In order to study the impact of load rate η changes on the temperature field distribution of transformer, simulations were conducted for normal and fault operating conditions under different load rates. Under different load rates, the temperature comparison of the C-phase high-voltage winding under normal and fault operating conditions (C-phase high-voltage winding, $Q = 1000\text{W}$, $H = 75 \text{ mm}$) is shown in Fig. 4, and the outer surface temperature comparison is shown in Fig. 5.

By observing Figs. 4 and 5, it can be found that:

- (1) As the load rate η increases, the temperature of winding and the oil-tank outer surface increases under normal operating condition.
- (2) Under the same load rate η , compared to normal operating condition, the winding temperature increases and new winding hot spot temperatures appear at the location of faulty coils under fault operating conditions. The overall temperature of the oil-tank outer surface also increases.

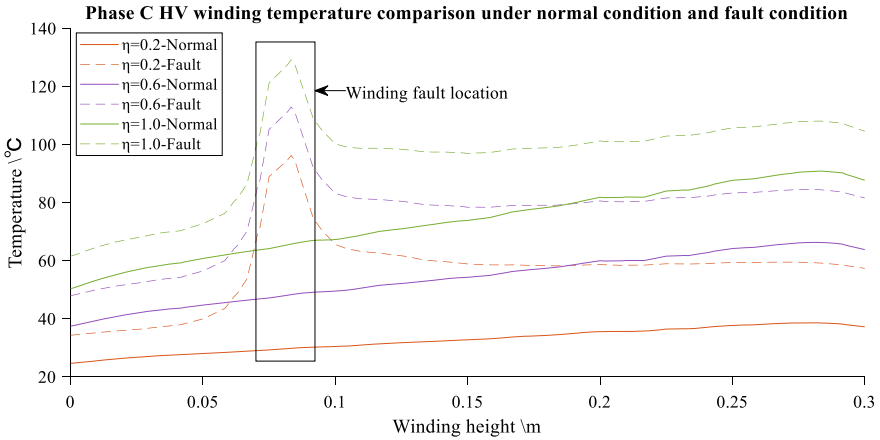


Fig. 4 Phase C HV winding temperature comparison under normal and fault condition

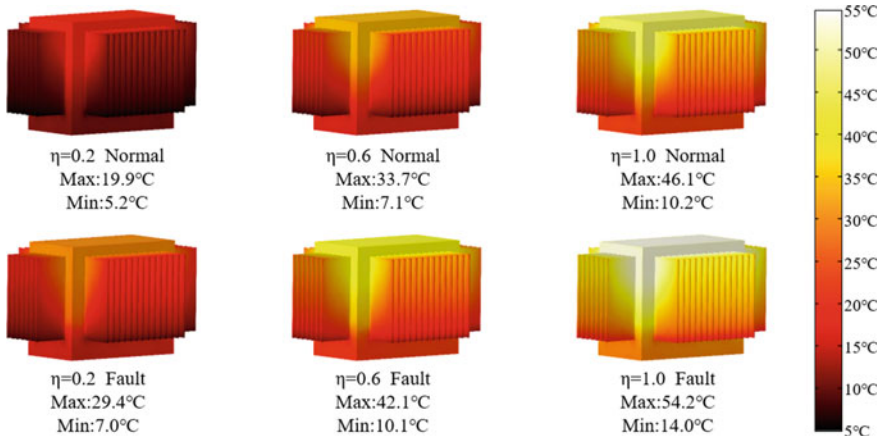


Fig. 5 Oil-tank outer surface temperature comparison under normal and fault condition

3.2 Effect of Q on Temperature Rise Characteristics

In order to study the effect of Q on the temperature field of transformer, the temperature fields generated by different Q of the C-phase high-voltage winding are calculated at the same load rate η ($\eta = 1.0$) and H ($H = 75$ mm). The temperature comparison of the C-phase high-voltage winding under normal operating condition and fault operating conditions with different Q is shown in Fig. 6, and the surface temperature comparison is shown in Fig. 7.

By observing Figs. 6 and 7, it can be found that:

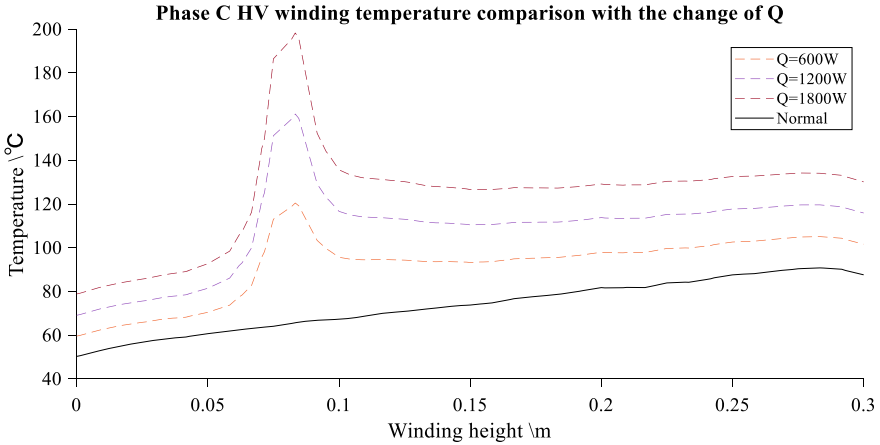


Fig. 6 Phase C HV winding temperature comparison with the change of Q

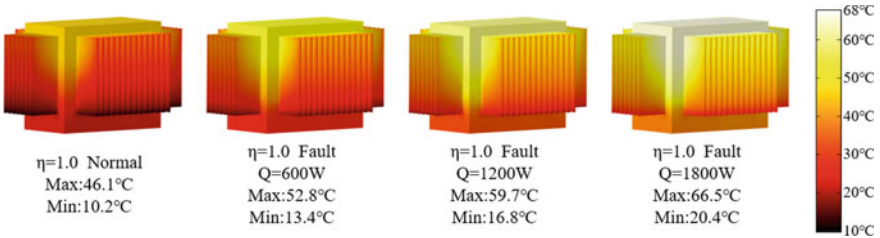


Fig. 7 Oil-tank outer surface temperature comparison of oil-tank with the change of Q

- (1) With the increase of Q , the winding temperature increases, and the temperature at the faulty point also increases with the change of Q .
- (2) The oil-tank outer surface temperature rises as Q increases under fault operating conditions.

3.3 Effect of H on Temperature Rise Characteristics

In order to study the influence of H on the temperature field of the transformer, it is calculated at the same load rate η ($\eta = 1.0$) and the same Q ($Q = 1000W$), the temperature fields corresponding to different H of the C-phase high-voltage winding. The temperature comparison of phase C high-voltage winding under normal working condition and different fault operating conditions with different H is shown in Fig. 8, and the outer surface temperature comparison is shown in Fig. 9.

By observing Figs. 8 and 9, it can be found that:

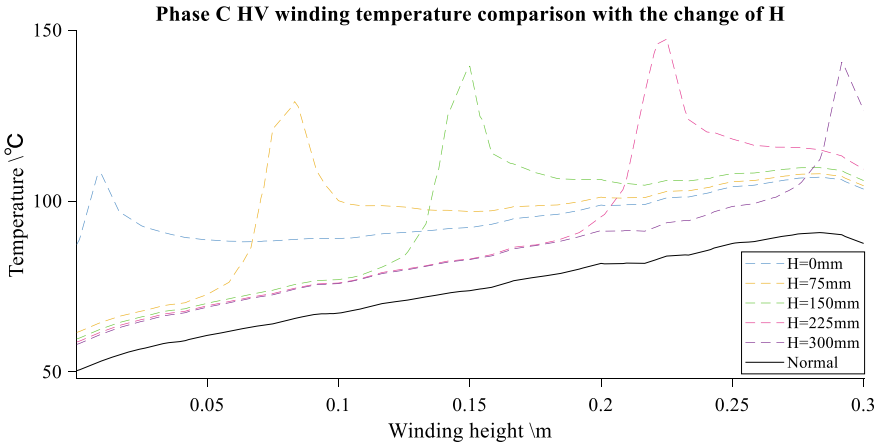


Fig. 8 Phase C HV winding temperature comparison with the change of H

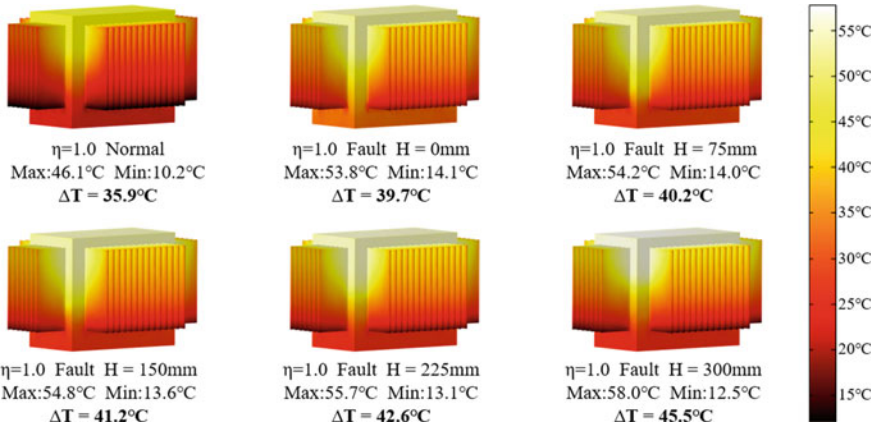


Fig. 9 Oil-tank outer surface temperature comparison with the change of H

- (1) With the change of H , the overall temperature of the winding does not increase, but the new hot spot temperature caused by the winding fault becomes higher and higher, which is positively correlated with H .
- (2) With the rise of H , the overall temperature of the oil-tank outer surface does not change much, but the range of temperature gradually increases.

4 Conclusion

In this paper, the temperature field of oil-immersed transformer is modeled, and a winding faulty module is added to analyze the temperature rise characteristics of the transformer under fault operating conditions. The analysis results are as follows:

- (1) As the load rate η increases, both the winding temperature and the temperature of outer surface under normal operating conditions increase overall;
- (2) Compared to normal operating condition, the winding temperature increases and new winding hot spot appears at the location of the winding fault under fault operating conditions;
- (3) As Q scales up, the new hot spot temperature ascends, and the tank shell temperature increases;
- (4) With the rise of H , the position of the new winding hot spot rises, and the range of temperature of the outer surface enlarges.

This research provides a guiding basis for transformer fault detection.

References

1. China Electric Power Enterprise Federation (2021) National electric power reliability annual report. <http://prpq.nea.gov.cn/ndbg/8540.html>. Last accessed 20 Mar 2023 (in Chinese)
2. GB/T 109.7–1993 Power transformers—Part 7: Loading guide for oil-immersed power transformers. In Chinese. (in Chinese)
3. IEC 60076–7:2018 Power transformers—Part 7: Loading guide for mineral-oil-immersed power transformers; Susa D, Lehtonen M, Nordman H (2005) Dynamic thermal modeling of distribution transformers. *IEEE Trans Power Delivery* 20(3):1919–1929
4. Susa D, Lehtonen M, Nordman H (2005) Dynamic thermal modeling of distribution transformers. *IEEE Trans Power Delivery* 20(3):1919–1929
5. Susa D, Lehtonen M, Nordman H (2005) Dynamic thermal modelling of power transformers. *IEEE Trans Power Delivery* 20(1):197–204
6. Swift G, Molinski TS, Lehn W (2001) A fundamental approach to transformer thermal modeling. I. Theory and equivalent circuit. *IEEE Trans Power Delivery* 16(2):171–175
7. Swift G, Molinski TS, Bray R, Menzies R (2001) A fundamental approach to transformer thermal modeling. II. Field verification. *IEEE Trans Power Delivery* 16(2):176–180
8. Gezegin C, Ozgonenel O, Dirik H (2021) A monitoring method for average winding and hot-spot temperatures of single-phase, oil-immersed transformers. *IEEE Trans Power Delivery* 36(5):3196–3203
9. Akbari M, Rezaei-Zare A (2021) Transformer bushing thermal model for calculation of hot-spot temperature considering oil flow dynamics. *IEEE Trans Power Delivery* 36(3):1726–1734
10. Xie Y, Li L, Song Y et al (2016) Multi-physical field coupled method for temperature rise of winding in oil-immersed power transformer. *Proc CSEE* 36(21):5957–5965+6040 (in Chinese)
11. Deng Y, Ruan J, Ddpng X et al (2022) Establishment and verification of 10kV oil immersed transformer winding hot spot temperature inversion model based on streamline analysis. *Proc CSEE* 1–13 (in Chinese)
12. Venikar PA, Ballal MS, Umre BS et al (2016) A novel offline to online approach to detect transformer interturn fault. *IEEE Trans Power Delivery* 31(2):482–492
13. Asadi N, Kelk HM (2015) Modeling, analysis, and detection of internal winding faults in power transformers. *IEEE Trans Power Delivery* 30(6):2419–2426

14. Pan C, Shi W, Meng T (2020) Study on electromagnetic characteristics of interturn short circuit of single-phase transformer. *High Voltage Eng* 46(05):1839–1856 (in Chinese)
15. Wang L, Qin N, Du X et al (2010) WSN 3D localization algorithm based on Tikhonov regularization method. *Chinese J Sci Instrument* 31(04):770–775 (in Chinese)

Nonlinear Vibration Model of Transformer Windings and Its Application in Short-Circuit Axial Strength Evaluation



Lei Zhang, Rui Li, Liangyuan Chen, and Shaoming Pan

Abstract The transformer winding produces strong axial vibration under the short-circuit condition, which affects the strength. In order to deeply study the short circuit nonlinear vibration characteristics of the winding and its influence on the axial strength, the nonlinear vibration model of the winding is established first and the calculation method of dynamic compression force of windings, spacers, and clamping rings as well as axial bending stress of conductor is proposed; Then the axial strength of a SZ-50,000/110 kV transformer is evaluated and compared with the traditional static calculation results; The results show that the calculated compressive forces, the stresses on clamping rings and axial bending stress from the dynamic assessment are little bit higher than that of the static assessment. The model and calculation method proposed in this paper are of great significance for improving the evaluation level of transformer short-circuit strength.

Keywords Power transformer · Windings · Short-circuit strength · Non-linear vibration first section

1 Introduction

Power transformer is an expensive and important equipment in the power system. Which is related to the security and stability of the entire power system. CIGRE statistical results show that the proportion of transformer damage caused by external

L. Zhang (✉) · R. Li · L. Chen · S. Pan
Electric Power Research Institute of Guangxi Power Grid Co. Ltd, Nanning 530023, China
e-mail: 920858776@qq.com

L. Zhang · R. Li · S. Pan
Guangxi Power Grid Equipment Monitoring and Diagnosis Engineering Technology Research Center, Nanning 530023, China

L. Chen
Guangxi Key Laboratory of Intelligent Control and Maintenance of Power Equipment, Nanning 530023, China

© Beijing Paiké Culture Commu. Co., Ltd. 2024
X. Dong and L. Cai (eds.), *The Proceedings of 2023 4th International Symposium on Insulation and Discharge Computation for Power Equipment (IDCOMPU2023)*, Lecture Notes in Electrical Engineering 1100, https://doi.org/10.1007/978-981-99-7393-4_22

short circuit in China is about 40% [1, 2]. Therefore, the evaluation of winding mechanical strength is of great significance to improve the ability to withstand short-circuit of power transformers.

A lot of research has been carried out on the condition monitoring and short-circuit resistance evaluation of transformers at home and abroad [3]. Foreign scholars established and improved the mass-spring-damping model of winding vibration in the 1960s [4]. Zhang Fan et al. considered the nonlinear effect of winding short circuit and calculated the electrodynamic force and vibration signals under short circuit impact, providing a basis for evaluating the mechanical state and short circuit withstand capacity of the winding under short circuit impact [5]. In terms of mechanical strength evaluation, Bakshi considers the structure of transformer spacers, braces, and other structures, constructs a winding buckling equation, and uses analytical methods to calculate the critical buckling load of the transformer, providing a theoretical basis for transformer stability evaluation [6, 7]; The transformer is composed of coils and spacers in the axial direction and the vibration of the coil itself transmits dynamic force to the spacers and coils adjacent to it, which is different from the transmission of static force [8]. And this difference increases with the increase of resonance degree. Although the above documents have evaluated the axial strength of the transformer from different angles, they lack the dynamic evaluation method that considers the coil vibration.

This paper firstly establishes a nonlinear axial vibration model and put forward methodologies to calculate dynamic compressive forces of windings, spacers, clamping rings, and the axial bending stresses in conductors. Then the model is used to calculate the axial strength of a Z-50,000/110kV machine and compared with the static strength. The proposed model and methodology are meaningful to improve the assessment of windings' mechanical strength.

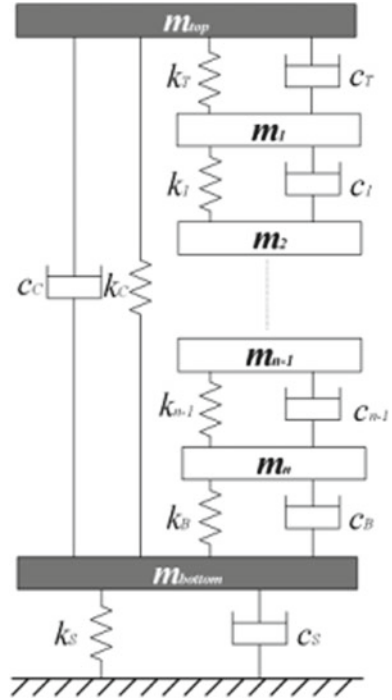
2 Nonlinear Vibration Model of Winding

2.1 Multi-degree-of-freedom Dynamic Model of Winding

The spiral and disk type windings are divided by oil passages and spacers in the axial direction. The winding axial vibration model shown in Fig. 1 can be obtained by equating the conductor to a lumped mass block, and the stiffness and damping of insulating materials such as clamping rings, and spacers are equivalent to springs and dashpots respectively[9].

With the gravity direction as the negative axis, the dynamic equation is established as follows:

Fig. 1 The axial vibration model of transformer winding



$$\begin{cases} m_T \ddot{x}_T + (c_T + c_C) \dot{x}_T - c_T \dot{x}_1 - c_C \dot{x}_B + (k_T + k_C)x_T - k_T x_1 - k_C x_B \\ \quad = F_c + m_T g \\ m_1 \ddot{x}_1 + (c_T + c_1) \dot{x}_1 - c_T \dot{x}_T - c_1 \dot{x}_2 + (k_T + k_1)x_1 - k_T x_T - k_1 x_1 \\ \quad \quad \quad \quad = m_1 g + f \\ m_2 \ddot{x}_2 + (c_1 + c_2) \dot{x}_2 - c_1 \dot{x}_1 - c_2 \dot{x}_3 + (k_1 + k_2)x_2 - k_1 x_1 - k_2 x_3 \\ \quad \quad \quad \quad = m_2 g + f_2 \\ \quad \quad \quad \quad \dots \\ m_n \ddot{x}_n + (c_{n-1} + c_B) \dot{x}_n - c_{n-1} \dot{x}_{n-1} - c_B \dot{x}_B + (k_{n-1} + k_B)x_n - k_{n-1} x_{n-1} \\ \quad \quad \quad \quad - k_B x_B = m_n g + f_n \\ m_B \ddot{x}_B + (c_B + c_C + c_S) \dot{x}_B - c_B \dot{x}_n - c_C \dot{x}_T + (k_B + k_C + k_S)x_B - k_B x_n \\ \quad \quad \quad \quad - k_C x_T = m_B g \end{cases} \tag{1}$$

where, M is the mass matrix of the winding coil, C is the damping coefficient matrix, K is the stiffness coefficient matrix. \ddot{x} , \dot{x} and x are the acceleration, velocity and displacement matrices of the coil; F is the electromagnetic force matrix; g is the acceleration of gravity; F_c is the clamping force matrix of the winding.

Due to the large rigidity of the winding, the equivalent rigidity of the group of spacers and windings can be regarded as the series connection of the springs formed by the spacers and the insulating paper. So, N spacers in the circumferential direction in the same height of the winding are equivalent to N parallel springs. According

to the stiffness equivalence principle of parallel spring, the equivalent stiffness of spring between mass blocks in the model is:

$$k = N \times k_e = N \times A \times \frac{E_s E_p}{E_p L_s + L_p E_s} \tag{2}$$

where, N is the number of spacers, A is the area of spacers, μ is the Poisson’s ratio of spacers, E_s and E_p are the elastic modulus of spacers and insulating paper respectively, L_s and L_p are the thickness of spacers and insulating paper respectively.

2.2 Nonlinear Mechanical Properties of Paperboard in Out-of-plane Direction

The pressboard which presents nonlinear mechanical characteristics in the out-of-plane direction have significant visco-elastic-plasticity due to the porous fiber structure. In order to obtain the mechanical properties of paperboard in the out-of-plane direction, the 0MPa-5MPa-0MPa, 2Hz triangular wave load was applied on the dry laminated paperboard, and the obtained stress–strain curve is shown in Fig. 2.

The average value of stress corresponding to the same strain in the loading and unloading curves is calculated in Fig. 2, and the nonlinear stress–strain relationship and elastic modulus of spacers and paper can be expressed as:

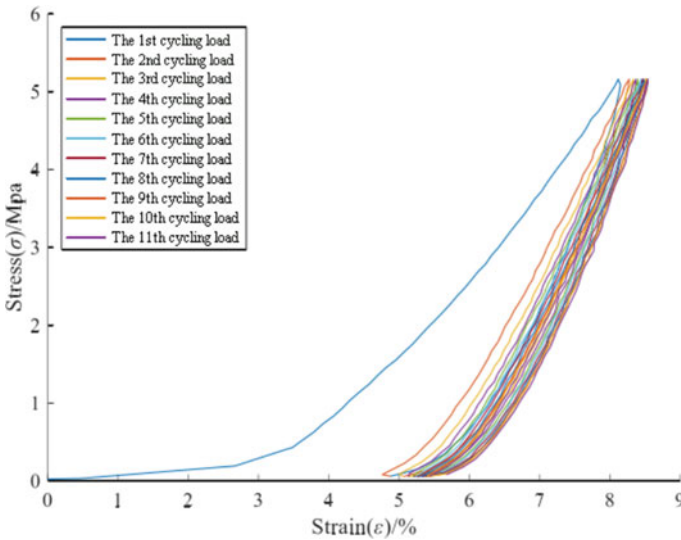


Fig. 2 Stress and strain characteristics of pressboards

$$\sigma = a\varepsilon^b (\varepsilon \geq 0) \tag{3}$$

$$E = a\varepsilon^{b-1} = a((x_{i+1} - x_i)/L_0 + \varepsilon_0)^{b-1} \\ ((x_{i+1} - x_i)/L_0 + \varepsilon_0 \geq 0) \tag{4}$$

Here, a is the amplitude scale coefficient, its value is 830MPa, b is the nonlinear coefficient, its value is 1.432, x_i and x_{i+1} is the displacement of the i and $i + 1$ winding disk respectively; L_0 is the original thickness of the spacers, and ε_0 is the static strain generated by the spacer under the action of gravity and compression force.

2.3 Nonlinear Response of Winding Under Short Circuit

The established model was used to calculate the axial vibration of SZ-50000/110($\pm 8 \times 1.25\%$)/10.5kV YNd11 transformer, and the corresponding model parameters are shown in Tables 1 and 2 respectively.

Two-dimensional axisymmetric model of the leakage magnetic field of the winding was established by taking a single disk as the basic unit, and the electrodynamic force is as shown in Fig. 3. The amplitude of the electrodynamic force at the end of the low-voltage winding is 105.7kN, and the amplitude of the electrodynamic force at the end of the high-voltage winding is 86.3kN.

The electric force borne by each coil of the winding is brought into (1). The rigid differential equation solver ode23t in MATLAB is selected to calculate the vibration response of the winding within 1s after the short circuit impact with a time step of 10-4s. The winding electrodynamic spectrum and vibration signal under short-circuit current are calculated as shown in Fig. 4. As can be seen from Fig. 4a, the frequency band of electric power is mainly 0-600Hz, and mainly concentrated around 0Hz, 50Hz and 100Hz. It can be seen from Fig. 4b that the vibration acceleration of the first coil calculated by the nonlinear vibration model of the winding is significantly

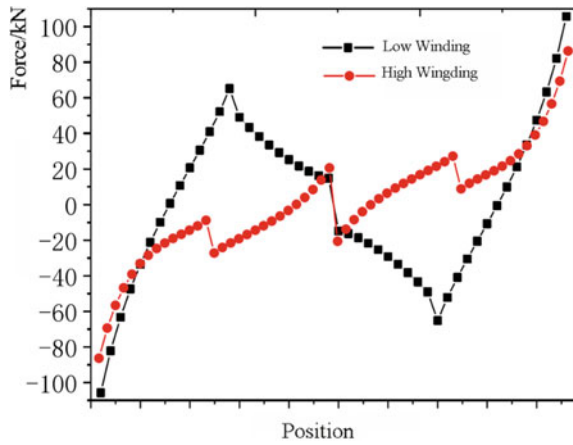
Table 1 Parameters of the 110kV Transformer

Parameter	Value	Parameter	Value
Short-circuit impedance	17.2	Short-circuit capacity	9000
Short-circuit current multiple	1.8	Weight of high and low windings	808/1318
Winding type	Continuous	$R_{p0.2}$	220/160
High-voltage inner/outer diameter	487.5/582	Low-voltage inner/outer diameter	340/418.5
High/low voltage disks	48/58	High/low voltage turns	85/514
Spacer width	40/30	Winding clamping force	25
Number of spacers	20	Thickness of clamping ring	40

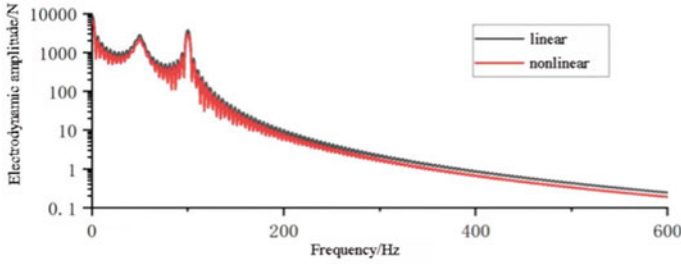
Table2 Parameters of the vibration model

High-voltage winding		Low-voltage winding	
Parameter	Value	Parameter	Value
$m_T.m_B$	33.34kg	$m_T.m_B$	33.64kg
$m_1 - m_{58}$	22.72kg	$m_1 - m_{58}$	16.83kg
k_T	$4.06 \times 10^8 N/m$	k_T	$2.81 \times 10^8 N/m$
$k_1 - k_{14}$	$3.63 \times 10^9 N/m$	$k_1 - k_{13}$	$2.26 \times 10^9 N/m$
$k_{16} - k_{28}$		$k_{15} - k_{23}$	
$k_{30} - k_{43}$		$k_{25} - k_{33}$	
$k_{45} - k_{57}$		$k_{35} - k_{47}$	
$k_{15}.k_{44}$	$1.08 \times 10^9 N/m$	$k_{14}.k_{34}$	$5.86 \times 10^8 N/m$
k_{29}	$5.01 \times 10^8 N/m$	k_{24}	$3.72 \times 10^8 N/m$
k_B	$3.25 \times 10^8 N/m$	k_B	$2.25 \times 10^8 N/m$
k_s	$3.48 \times 10^{11} N/m$	k_s	$2.15 \times 10^{11} N/m$
k_c	$3.48 \times 10^{11} N/m$	k_c	$2.15 \times 10^{11} N/m$

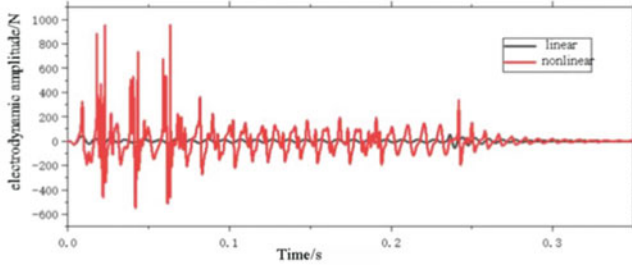
Fig. 3 Axial electromagnetic forces at the peak of short circuit current



higher than the linear calculation result, and the vibration amplitude of the nonlinear model gradually increases with the increase of time.



(a) Electrodynamic spectrum



(b) First disk winding acceleration

Fig. 4 The excitation and response vibration signals of top rings

3 Dynamic Evaluation of Axial Mechanical Strength of Winding

3.1 Dynamic Model of Axial Force

The compression force on the winding derived from the extrusion of adjacent winding and the axial electric force and compression force borne by itself. ΔF_i is:

$$\Delta F_i = -m_i a_i - F_c - mg + f_i \tag{5}$$

where, $m_i a_i$ is the force of adjacent winding during coil vibration, F_c and mg are fixed values, and f_i is proportional to the square of current. When the acceleration of winding is large, the axial compression force increases significantly.

Under the action of short-circuit electrodynamic force, the distance between winding continuously changes, and the stress of spacer is:

$$\begin{aligned} \sigma &= a\varepsilon^b = a((x_{i+1} - x_i)/L_0 + \varepsilon_0)^b \\ ((x_{i+1} - x_i)/L_0 + \varepsilon_0 &\geq 0) \end{aligned} \tag{6}$$

where, $(x_{i+1} - x_i)$ indicates that the distance between winding decreases, the spacer is compressed, and the stress increases; On the contrary, the distance between windings increases, and the stress decreases.

The clamping rings and ending disk are connected by spring k_T (k_B) and damping c_T (c_B), so the sum of forces acting on the upper and lower clamping rings by spacers is:

$$F_T = N \times A \times \sigma + c_T \times (\dot{x}_T - \dot{x}_1) \quad (7)$$

$$F_B = -N \times A \times \sigma - c_B \times (\dot{x}_B - \dot{x}_n) \quad (8)$$

where, σ is the compression force of the spacer.

Under the action of axial force, the conductor between the circumferential spacers will bend, and the maximum bending stress of the contact surface between the spacers is calculated according to the fixed support straight beam.

$$\sigma_{axial_bending} = \frac{q \times l^2}{2 \times w} \quad (9)$$

$$l = \frac{2\pi R}{N} - W \quad (10)$$

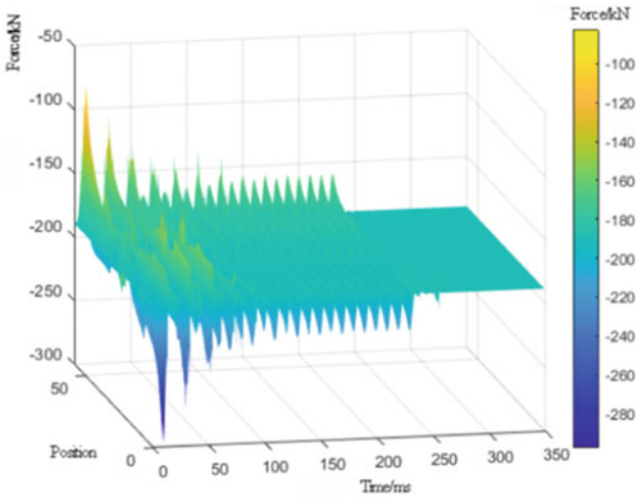
where, q is the axial electrodynamic mass density of the conductor, l is the span of conductor between spacers; W is the width of spacers.

3.2 The Compression Force of Windings

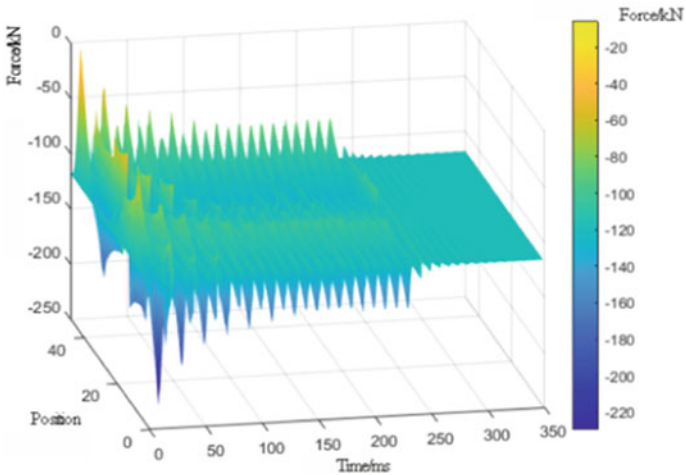
The above transformer parameters are used for calculation. According to the winding structure, the compression force coefficients of high and low voltage windings are 75.6kN/MPa and 47.1kN/MPa respectively, and the corresponding compression force of 2.5 MPa is 189.2kN and 117.8kN respectively. The axial compression forces at the top and bottom of the high-voltage coil calculated by the static method are 275.5kN and 102.9kN respectively, and the axial compression forces at the top and bottom of the low-voltage coil are 223.5kN and 12.1kN respectively.

According to formula (5), the axial dynamic compression force borne by different disk of high and low voltage windings is shown in Fig. 5. With the reduction of short-circuit current and electrodynamic force, the axial compression force of the winding attenuates. The maximum compression force of the first disk during the short-circuit of the high-voltage winding is 297.6kN, which is 108% of the static calculation result (275.5kN); The minimum compressive force amplitude of the 58th disk is 82.2kN, which is about 80% of the static calculation result (102.9kN); The maximum axial compression force at the end of low-voltage winding is 236.2kN

and 18.9kN respectively, which are about 105% and 156% of the static calculation results.



(a)High voltage

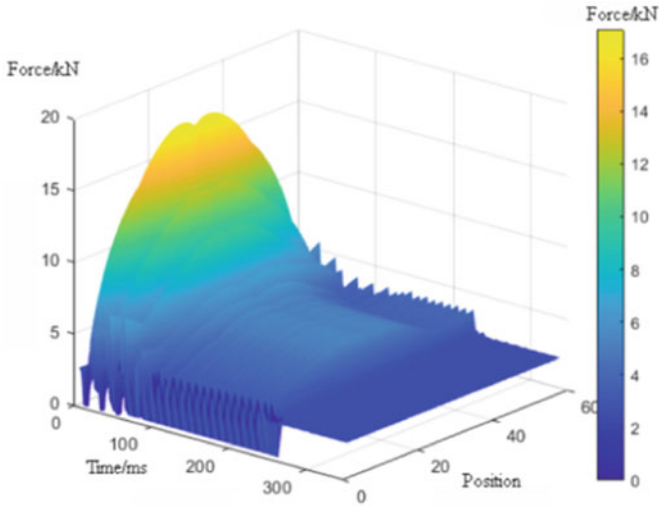


(b)Low voltage

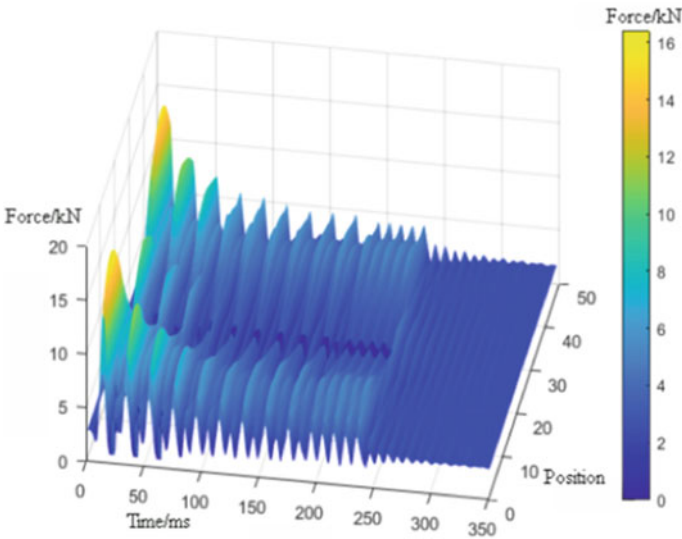
Fig. 5 Axial dynamic force of the HV winding

3.3 The Compression Force of Spacers and Clamping Rings

The stress of spacers at different positions of high and low voltage windings calculated by (6) is shown in Fig. 6.



(a) High voltage



(b) Low voltage

Fig. 6 Dynamic compression force of spacers in windings

It can be seen from the winding displacement that the high-voltage winding is compressed towards the middle as a whole, so the spacers in the middle of the winding are subject to extrusion, and the maximum compression force of the winding 15th–45th disks is about 16.58 MPa; Low-voltage winding is stretched towards both ends, with the maximum compression force of 5–15 disks and 37th–47th disks. In addition, at 25th disk of low voltage winding and 1st–2nd disks of high voltage winding, the pressure near the maximum moment of short circuit electrodynamic force is 0, which means that the coil separated with the spacers and lost the axial support of the spacers.

In the short-circuit process, the thickness of spacers and the force of clamping rings change continuously. The high-voltage winding reaches the maximum value 30 ms after the short circuit, which is 3.5 MPa and 3.3 MPa respectively, and the minimum pressure during the period is 0, indicating that the ending winding is separated from the spacer; The pressure of the low-voltage winding on the clamping rings decreases first and then increases to 4.2 MPa within 0–5 ms after the short circuit. The minimum pressure in the whole process is 0.8 MPa. Compared with the static results, the calculated maximum dynamic compression force of the high and low voltage winding on the clamping rings and spacers is 1.8 MPa (100%) and 0.9 MPa (27%) respectively.

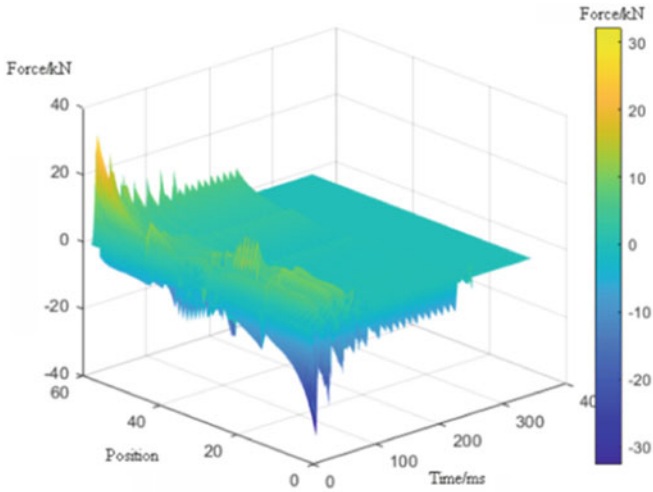
3.4 Axial Bending Stress

The maximum axial bending stress of HV and LV windings calculated by static method is 32.14 MPa and 26.36 MPa respectively. The dynamic axial bending stress distribution of high and low voltage winding conductors calculated from (9) and (10) is shown in Fig. 7. The maximum axial bending stress of high and low voltage windings is about 33 MPa, which is about 103% and 125% of the results calculated by static method.

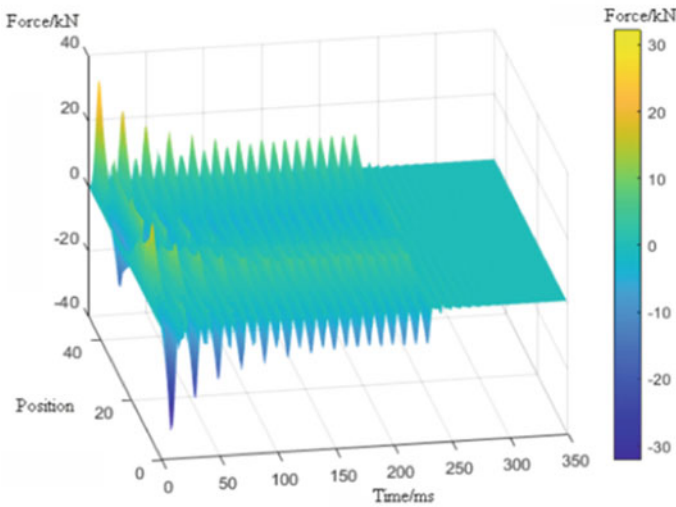
The comparison between the calculation results of the static method and the dynamic method proposed in this paper is shown in Table 3. It can be seen from the results that the compression force and bending stress calculated by the dynamic method are greater than those calculated by the static method, in which the compression force of the high-voltage winding spacers is 88% higher, and the compression force of the high-voltage and low-voltage winding clamping rings is 106% and 27% higher, respectively, indicating that the dynamic method is more rigorous in evaluating the short-circuit strength.

4 Conclusion

Based on the nonlinear dynamic model of winding axial vibration, this paper proposes the calculation method of dynamic compression force of windings, spacers, clamping rings and axial bending stress of conductor. The main conclusions are as follows:



(a)High voltage



(b)Low voltage

Fig. 7 Axial bending stresses in conductors

- (1) Short-circuit electrodynamic force is a broadband signal of 0-600Hz, mainly concentrated in the vicinity of 50Hz and 100Hz. The winding short-circuit vibration signal has harmonics of 50 Hz and 100 Hz with the same excitation frequency and higher than 100 Hz due to the nonlinear mechanical characteristics.

Table3 Comparison of the calculated results

	HV winding	LV winding
<i>Compression force of windings/kN</i>		
Static method	275.5	223.5
Dynamic method	297.6	236.2
<i>Compression force of spacers/MPa</i>		
Static method	8.8	15.21
Dynamic method	16.58	16.44
<i>Compression force of clamping rings /MPa</i>		
Static method	1.7	3.3
Dynamic method	3.5	4.2
<i>Axial bending stress/MPa</i>		
Static method	32.14	32.14
Dynamic method	32.23	32.23

- (2) In the short-circuit process, a single winding disk oscillates in the equilibrium position, and its displacement direction depends on the overall short-circuit electric power distribution. The electric power at the end changes rapidly with the height, while the displacement amplitude changes gradually saturation.
- (3) Compared with the static evaluation method, the the compression force of windings, spacers, clamping rings and axial bending stress calculated by the dynamic evaluation method are all higher in varying degrees. The compression force of the pad of high voltage winding is 88% larger, and the compression force of the platen of high and low voltage winding is 106% and 27% larger, respectively.

References

1. Working Group A2.37 (2015) Transformer reliability survey[R].Paris: CIGRE
2. Mengyun W (2006) Statistical analysis of 110kV and higher voltage transformer accident in 2005[J]. Power Supply 23(1):1–4 (in Chinese)
3. Ji S, Zhang F, Shi Y et al (2020) Review on vibration-based mechanical condition monitoring in power transformers[J]. High Voltage Eng 46(01):257–272 (in Chinese)
4. Tournier Y, Ebersohl G, Ciniero A et al (1962) A study of the dynamic behavior of transformer windings under short-circuit conditions[C]. Cigré Conférence Internationale des Grands Réseaux Electriquesa Haute Tension, Paris
5. Zhang F, Wu S, Xu Z et al (2022) Research on nonlinear vibration characteristics of transformers’ windings during short circuits [J]. High Voltage Eng 48(12):4882–4892 (in Chinese)
6. Kumar, Bakshi A (2022) Effects of axial sticks and proof stress of conductor material on the buckling strength of transformer inner winding. Trans Power Delivery 37(6):5465–5468
7. Kumar I, Bakshi A (2022) Effect of flexibility of axial supporting spacers on the buckling strength of transformer inner winding. In: 2022 7th international advanced research workshop on transformers (ARWtr), Baiona, Spain, pp 87–91

8. Working Group A12.19 (2002) The short-circuit performance of power transformers[R]. Paris, CIGRE
9. Zhang F, Ji S, Ma H et al (2020) Operational modal analysis of transformer windings[J]. IEEE Trans Power Delivery 35(03):1285–1298 (in Chinese)

Study of Bidirectional Current Flow Controller for Multi-terminal DC Grid



Mengyu Yao

Abstract This paper studies the need for DC current flow controllers (DCCFCs) in multi-terminal DC power grids. The DCCFC can regulate power flow and prevent overloading of DC lines, promoting the utilization of renewable and regenerative energies. The proposed DCCFC topology is presented with independent ability. It can achieve bidirectional power flow regulation. The operation principles and control strategy of the DCCFC are analyzed. Computer simulated results of steady-state and dynamic-response are provided to validate the entire study. This paper provides a comprehensive overview of the demands for DCCFCs in multi-terminal DC grids which can regulate power flow efficiently and effectively, with the results retrieved from simulation demonstrating the operation and performance of the proposed DCCFC.

Keywords DC power flow controller · Multi-terminal DC grids · Independent · Bidirectional

1 Introduction

It is crucial to address the pressing issues of power transmission and grid connection. In comparison to AC transmission systems, DC transmission systems offer a range of advantages, including lower losses and no need for synchronization or reactive power compensation. The widespread adoption of voltage source converters (VSC) has created a solid foundation for the development of DC power grids. As a result, high voltage direct current (HVDC) transmission technology has become a top priority for large-scale clean energy transmission and integration [1–3].

The development trend of DC power grids is moving towards multi-terminal or meshed configurations that are larger in scale, more reliable, and offering greater flexibility of operation [4, 5]. However, this evolution not only brings corresponding

M. Yao (✉)

Xi'an High Voltage Apparatus Research Institute Co. Ltd, Xi'an 710077, China

e-mail: 1124400243@qq.com

© Beijing Paiké Culture Commu. Co., Ltd. 2024

X. Dong and L. Cai (eds.), *The Proceedings of 2023 4th International Symposium on Insulation and Discharge Computation for Power Equipment (IDCOMPU2023)*, Lecture Notes in Electrical Engineering 1100, https://doi.org/10.1007/978-981-99-7393-4_23

243

advantages, but also poses certain challenges to existing technologies. Power flow control is an important issue that needs to be researched and addressed in multi-terminal DC grids. In AC grids, flexible AC transmission systems (FACTS) are used to control reactive power and regulate line power flow, but this is not possible in DC grids [6]. Therefore, special devices for DC power flow control, called DC current flow controllers (DCCFCs), are being studied and deployed to regulate power flow in meshed DC grids.

After conducting a comprehensive study on DC power regulation, four main types of DCCFC have been identified: variable series resistor, series voltage source, inter-line DC current flow controller (IDCCFC), and DC transformer. The series resistor type DCCFC has a simple control system but results in high loss and cannot achieve bidirectional regulation [7, 8]. Although the series voltage source type DCCFC requires relatively fewer devices and has lower losses, it has challenges with insulation design and high cost [9]. The IDCCFC has a straightforward topology and lower losses, but it can only be applied to multiple lines simultaneously and cannot achieve independent regulation for each controlled line [10–12]. The DC transformer type DCCFC generally necessitates AC transformers and numerous power electronic devices, resulting in a complex structure. It is better suited for connecting DC power grids with varying voltage levels [13, 14].

This paper studies the DCCFC with bidirectional power flow control ability. The device is capable of adjusting the power flow by controlling the voltage difference between terminals. Simulation results of a three-terminal DCCFC device are compared to the analysis for validate the study.

2 Topology and Operation Principles

This section presents the topology of the proposed DCCFC and analyzes its operation principles based on the equivalent circuit.

2.1 Basic Circuit Topology

The schematic diagram of the proposed DCCFC applied to a multi-terminal DC grid is shown in Fig. 1. The DCCFC consists of one auxiliary terminal and n controlled transmission lines connected by the proposed device. It includes one stack with N series-connected half-bridge sub-modules (SMs), a large inductor L_T , a resonant tank composed of inductor L_r and capacitor C_r , a full-bridge rectifier composed of controlled semiconductor switches, rectifier capacitor C_o , magnitude control switches S_t and S'_t , and LC filters applied on each controlled line. The auxiliary terminal supplies energy to the stack through the large inductor, and the output of the stack is used as the input of the rectifier through the resonant tank together with the auxiliary terminal. The current magnitude control switches are

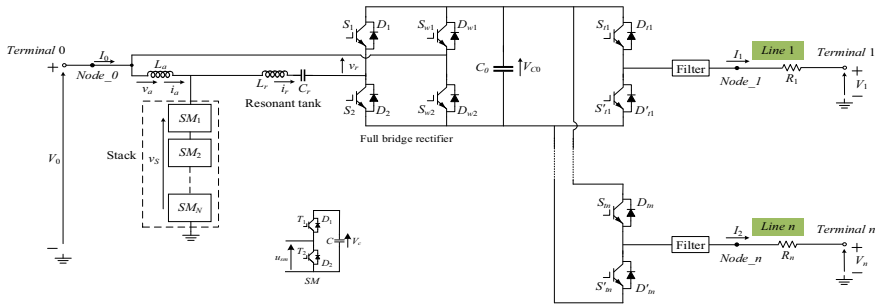


Fig. 1 Topology of the proposed DCCFC in multi-terminal DC grid

connected in parallel with the rectifier capacitor C_o , which is used as the output of the rectifier. Each midpoint of the magnitude control switches is connected to the LC filter as a DCCFC output terminal and is connected to the corresponding controlled transmission line.

The terminal voltages of the DC grid are denoted by V_j ($j = 1, 2, \dots, n$), while V_0 represents the auxiliary terminal voltage. The resistance of the j th transmission line is represented by R_j , and the current flowing through the j th line is represented by I_j . The voltage at the j th DCCFC output terminal is denoted by V_{outj} . The capacitor voltage and output voltage of the i th sub-module are represented by v_{Ci} and v_{SMi} ($i = 1, 2, \dots, N$), respectively. The voltage across the stack and large inductor are represented by v_S and v . The input voltage of the rectifier and the current flowing through the resonant tank are v_r and i_r , respectively. The rectifier capacitor voltage is represented as V_{Co} .

2.2 Operation Principles

The stack operates using phase-shift modulation to generate a two-level square wave by periodically inserting N and M SMs. The stack voltage, represented as v_S , will alternate between NV_{SM} and MV_{SM} at a fixed frequency, where V_{SM} is the average balanced value of all capacitor voltages. As a result, the stack converts the DC power grid into AC power, and the voltage across the large inductor, represented as v_a , is a square wave.

The resonant tank is designed with a series resonant frequency that is the same as the frequency of v_a and v_S , which makes its AC impedance almost zero during normal operation. This provides a path for transferring AC power from the stack to the rectifier. By correctly controlling the switches in the full bridge rectifier, the voltage of the rectifier capacitor can be almost equal to the peak value of v_a .

The proposed DCCFC is capable of regulating power flow by adjusting the output terminal voltages, which is achieved by modifying the polarity and magnitude of the equivalent voltage inserted in each transmission line using two groups of controlled

switches and the capacitor C_o . One of the groups consists of the previously mentioned magnitude control switches, while the other group comprises two switches connected to the auxiliary terminal in the full bridge rectifier. These two switches, marked as S_{w1} and S_{w2} in Fig. 1, also function as polarity control switches and carry out rectification. Their duty cycle is fixed at 0.5, leaving only the duty cycle of magnitude control switches adjustable for power flow regulation.

To provide a clear explanation of how the two groups of switches work, a single controlled transmission line is used as an example, and equivalent circuits in different states are shown in Figs. 2 and 3. The directions indicated in the figures are considered as positive reference directions, and the amplitude of the input voltage of the full bridge rectifier, marked as V_r , is used. When $v_r \geq 00$, as shown in Fig. 2, switches S_{w1} and S_2 are turned on, and v_r is rectified by diodes D_{w1} and D_2 . In Fig. 2a, when switch S_{ij} is turned on and S'_{ij} is turned off, capacitor C_o is bypassed, and the line power flows through S_{w1} and S_{ij} Fig. 2b, when switch S'_{ij} is turned on and S_{ij} is turned off, capacitor C_o is inserted into the line with positive polarity, resulting in a decrease in the output voltage of the DCCFC and a reduction in the line power flow. Therefore, the output voltage V_{outj} can be regulated by changing the duty cycle α_j of the switch S_{ij} , where V_{outj} is equal to $V_0 - (1 - \alpha_j)V_{C_o}$ in this state. It is important to note that the two switches of each group are complementary.

When $v_r < 0$, as shown in Fig. 3, the switches S_{w2} and S_1 are turned on and v_r is rectified by the diodes D_{w2} and D_1 . In Fig. 3a, when switch S'_{ij} is turned on and S_{ij} is turned off, capacitor C_o is bypassed and the line power flows through S_{w2} and S'_{ij} . In Fig. 3b, when the switch S_{ij} is turned on and S'_{ij} is turned off, the capacitor C_o is inserted into the line with negative polarity so that the output voltage of the DCCFC will increase, resulting in an increase in line power flow. Therefore, in this state, the output voltage V_{outj} is equal to $V_0 + \alpha_j V_{C_o}$.

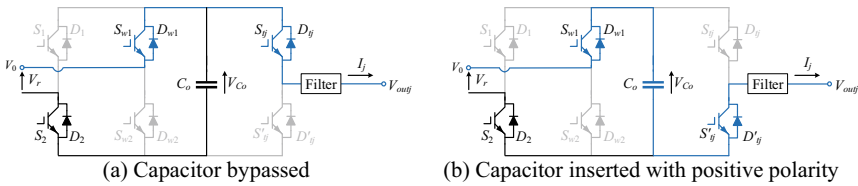


Fig. 2 Equivalent circuits of DCCFC when $v_r \geq 0$

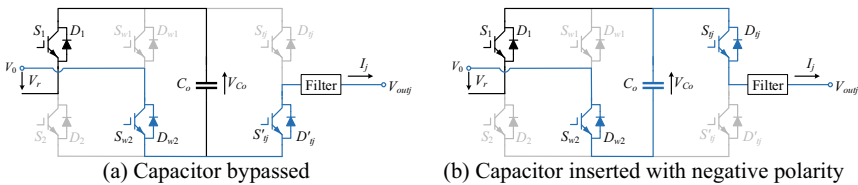


Fig. 3 Equivalent circuits of DCCFC when $v_r < 0$

3 Control Strategy

The proposed control strategy includes two parts: stack voltage control and voltage inserted control. The controlled stack voltage sets the maximum regulating range of the DCCFC. Within this range, power flow control is achieved by adjusting the inserted voltage.

3.1 Stack Voltage Control

The two-level phase-shift modulation proposed in [15] is utilized for controlling the stack voltage due to its ability to achieve high operating frequency with low switching frequency, and the advantages of self-balanced SM capacitor voltages. This modulation determines the voltage of capacitor C_o by calculating the difference between the number of sub-modules inserted at different times. As analyzed in the previous section, when the number of inserted sub-modules is N and M respectively, the stack voltage v_S takes the form of a square wave with amplitudes of NV_{SM} and MV_{SM} . The auxiliary DC terminal voltage V_0 is equivalent to the average voltage of the stack.

$$V_0 = \frac{N + M}{2} V_{SM} \quad (1)$$

The average voltage across the large inductor is

$$\begin{cases} V_a = NV_{SM} - V_0, \text{ the number of inserted SMs is } N \\ V_a = MV_{SM} - V_0, \text{ the number of inserted SMs is } M \end{cases} \quad (2)$$

Because the voltage of the C_o is almost equal to the peak value of the large inductor voltage, it can be derived from (1) and (2) that

$$V_{C0} = \frac{N - M}{N + M} V_0 \quad (3)$$

Therefore, by adjusting the parameters of phase-shift modulation, the value of the rectifier capacitor voltage V_{C0} can be changed, which in turn changes the range of equivalent inserted voltage, allowing for adjustment of the power flow regulation range.

3.2 Voltage Inserted Control

Based on the analysis in section II, the equivalent inserted voltage control is essentially controlling the duty cycle of switches S_{ij} and S'_{ij} . As an example, let's consider a single controlled line, where the relationship between the output voltage of the DCCFC and the duty cycle of S_{ij} is given by:

$$\begin{cases} V_{outj} = V_0 - (1 - \alpha_j)V_{Co}, & v_t \geq 0 \\ V_{outj} = V_0 + \alpha_j V_{Co}, & v_t < 0 \end{cases} \quad (4)$$

Since v_t half cycle is positive and half cycle is negative, the average voltage of output voltage is

$$V_{outj} = 0.5\Delta V_{outj(t \geq 0)} + 0.5\Delta V_{outj(t < 0)} = V_0 + (\alpha_j - 0.5)V_{Co} \quad (5)$$

Then the power flowing through DC terminal j on j th line is

$$P_j = \frac{V_{outj} - V_j}{R_j} V_j = \frac{V_0 - V_j + (\alpha_j - 0.5)V_{Co}}{R_j} V_j \quad (6)$$

Hence, the maximum adjustment range of power flow and the power flow changed by the DCCFC are

$$P_{j \max} = \frac{V_0 - V_j + 0.5V_{Co}}{R_j} V_j \quad (7)$$

$$P_{j \min} = \frac{V_0 - V_j - 0.5V_{Co}}{R_j} V_j \quad (8)$$

$$\Delta P_j = \frac{(\alpha_j - 0.5)V_{Co}}{R_j} V_j \quad (9)$$

From Eq. (5), the inserted voltage can be expressed as $(\alpha_j - 0.5)V_{Co}$. Therefore, the line current can be controlled by manipulating the duty cycle α_j . Let P_{refj} be the desired power of the j th transmission line, and I_{origj} be the current without DCCFC. From Eq. (6), we can obtain the duty cycle as:

$$P_{refj} = \frac{V_0 - V_j + (\alpha_j - 0.5)V_{Co}}{R_j} V_j = I_{origj} V_j + \frac{(\alpha_j - 0.5)V_{Co}}{R_j} V_j \quad (10)$$

From (3) and (10), the duty cycle α_j can be calculated as

$$\alpha_j = \left(\frac{P_{refj}}{V_j} - I_{origj} \right) \frac{N + M}{N - M} \frac{R_j}{V_0} + 0.5 \quad (11)$$

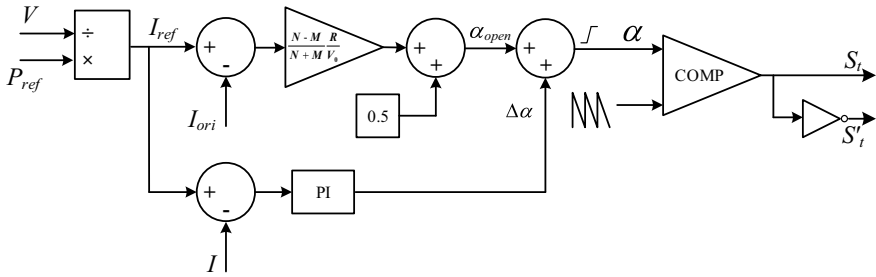


Fig. 4 The closed loop diagram of inserted voltage control

To ensure control reliability, closed-loop control is employed to adjust the open-loop duty cycle. Figure 4 shows the closed-loop control diagram for a single line. The sum of α_{open} , calculated from (7), and $\Delta\alpha$, the output of the PI controller, is restricted to the range of 0 to 1. The switching signals for switches S_t and S_t' can be generated through pulse-width modulation (PWM) control.

4 Simulation Result

To validate the effectiveness of the proposed DCCFC in regulating the current of transmission lines, a MATLAB/SIMULINK model of the DCCFC in a three-terminal DC grid was developed. In this section, we present a set of simulation results using the model. The simulation parameters are listed in Table 1, and the stack control parameters are set as $N = 5$ and $M = 2$. Based on the given parameters, the line currents without DCCFC are expected to be -500A and 400A, respectively. The simulation results, which include steady-state and dynamic operation, are shown in Fig. 5.

Table 1 Simulation parameters

Parameter	Description	Value
V_0	Auxiliary terminal voltage	10 kV
V_1	Voltage of DC terminal 1	10.5 kV
V_2	Voltage of DC terminal 2	9.6 kV
R_1, R_2	Line resistance	0.6 Ω
L_r	Inductor of resonant tank	280 μ H
C_r	Capacitor of resonant tank	22.874 μ F
f_r	Resonant frequency	2 kHz
f_t	Switching frequency of magnitude control switches	2 kHz

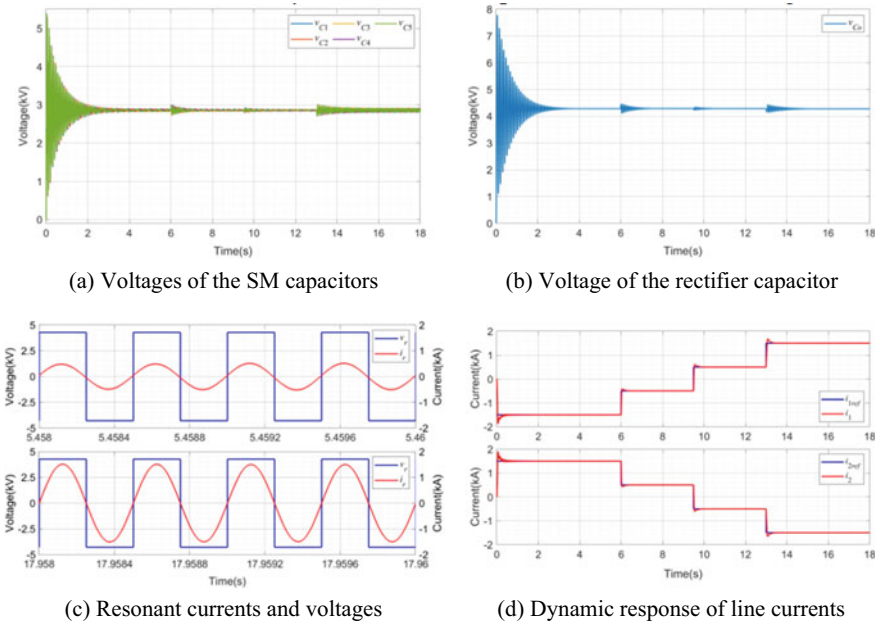


Fig. 5 Simulation results of operation performance of the DCCFC

Figure 5a illustrates the waveforms of the SM capacitor voltage v_{Cj} ($j = 1, 2, \dots, 5$), which are well balanced around the theoretical value of 2.86kV calculated from (3) due to the self-balanced control strategy. The switching frequency of each SM is 1200Hz, while the phase-shift modulation enables an equivalent operating frequency of 2kHz, thus reducing the operating frequency of each switch. Figure 5b presents the voltage waveforms of the rectifier capacitor voltage V_{CO} , which stabilizes at the theoretical value of 4.286kV through the power conversion of the stack and full bridge rectifier. The capacitor voltage fluctuates when the line currents change, but it quickly stabilizes. Figure 5c shows the waveforms of the rectifier input voltage and resonant tank current. In the resonant operation mode, the voltage and current of the rectifier maintain the same phase, effectively reducing the switching loss. Figure 5d displays the dynamic response of line currents in both directions, as the given power flow has both positive and negative directions. The simulation results indicate that the proposed DCCFC can regulate the current of each line in either direction to follow the given current.

5 Conclusion

This paper studies a bidirectional and independent power flow regulation scheme using DCCFC. The DCCFC scheme is able to adjust the power flow of the transmission line by controlling the voltage difference between the two terminals. The rectifier capacitor voltage is maintained as stable as the regulated current is almost constant with negligible ripple. The power is transferred from the stack and exchanged through the resonant tank at the auxiliary terminal. By controlling the duty cycle of the magnitude control switches, the DCCFC can independently insert any voltage values with either directions into transmission line, enabling independent and bidirectional power flow regulation. The simulation results have validated the operation principles and power flow control analysis presented in this paper.

References

1. Dragicevic T, Lu X, Vasquez JC et al (2016) Dc microgrids-part ii: a review of power architectures, applications, and standardization issues. *IEEE Trans Power Electron* 31(5):3528–3549
2. Solas E, Abad G, Barrena JA et al (2013) Modular multilevel converter with different submodule concepts-part ii: Experimental validation and comparison for hvdc application. *IEEE Trans Industr Electron* 60(10):4536–4545
3. Gomis BO, Sau BJ, Prieto AE et al (2020) Flexible converters for meshed hvdc grids: from flexible ac transmission systems (FACTS) to flexible dc grids. *IEEE Trans Power Delivery* 35(1):2–15
4. Lagier T, Ladoux P (2015) A comparison of insulated DC–DC converters for HVDC off-shore wind farms. In: *International conference on clean electrical power*, pp 33–39
5. Kish GJ (2019) On the emerging class of non-isolated modular multilevel DC–DC converters for DC and hybrid AC–DC systems. *IEEE Trans Smart Grid* 10(2):1762–1771
6. Li N, Xu Y, Chen H (2000) FACTS-based power flow control in interconnected power system. *IEEE Trans Power Syst* 15(1):257–262
7. Adam GP, Vrana TK, Li R, Li P, Burt G, Finney S (2019) Review of technologies for DC grids–power conversion, flow control and protection. *IET Power Electron* 12(8):1851–1867
8. Jovicic D, Hajian M, Zhang H et al (2012) Power flow control in dc transmission grids using mechanical and semiconductor based dc/dc devices. In: *10th IET international conference on AC and DC power transmission (ACDC 2012)*, pp 1–6
9. Veilleux E, Ooi B (2012) Multiterminal hvdc with thyristor power flow controller. *IEEE Trans Power Delivery* 27(3):1205–1212
10. Sau-Bassols J, Prieto-Araujo E, Gomis-Bellmunt O (2017) Modelling and control of an interline current flow controller for meshed hvdc grids. *IEEE Trans Power Delivery* 32(1):11–22
11. Barker CD, Whitehouse RS (2012) A current flow controller for use in hvdc grids. In: *10th IET international conference on AC and DC power transmission*, pp 1–5
12. Hofmann V, Bakran M (2018) A dc current flow controller for meshed hvdc grids. In: *2018 international power electronics conference*, pp 2476–2483
13. Rouzbehi K, Miranian A, Candela JI, Luna A, Rodriguez P (2014) Proposals for flexible operation of multi-terminal DC grids: Introducing flexible DC transmission system (FDCTS). In: *2014 international conference on renewable energy research and application (ICRERA)*, pp 180–184
14. Kish GJ, Lehn PW (2013) A modular bidirectional dc power flow controller with fault blocking capability for dc networks. In: *2013 IEEE 14th workshop on control and modeling for power electronics (COMPEL)*, pp 1–7

15. Qiao Y, Zhang X, Xiang X, Yang X, Green TC (2020) Trapezoidal current modulation for bidirectional high-step-ratio modular DC–DC converters. *IEEE Trans Power Electron* 35(4):3402–3415

A Current Flow Controller with Independent Regulation Capability for HVDC Grid



Mengyu Yao and Xueao Qiu

Abstract With the increasing significance of renewable energy and demand for long-distance power transmission and large-scale grid interconnection, developing and expanding high voltage direct current (HVDC) grids have become essential. However, in multi-terminal or meshed DC grids, controlling the current flow of each line through converter stations is not completely feasible. The line current flow regulation devices used in AC grids cannot be applied in DC grids straightforwardly. Therefore, in order to implement complete power flow control in HVDC grids, DC current flow controller (DCCFC) becomes indispensable. As the state-of-the-art interline DCCFCs need to exchange power between multiple lines, this paper presents a DCCFC topology that can be used in multi-terminal DC grids and which can achieve independent control and bidirectional regulation. The operation principle and control strategy of the proposed DCCFC are studied, with simulation results of steady-state and dynamic response presented to validate the theoretic analysis.

Keywords HVDC grids · DC current flow controller · Multi-terminal DC grids · Independent regulation

1 Introduction

With the growing concern over energy issues, many countries and regions are investing in research and implementing projects to develop renewable energy and ensure energy security [1]. However, the traditional AC transmission system faces limitations in accommodating the distribution of renewable energy. Whereas the DC transmission systems offer more advantages in power transmission, including

M. Yao (✉)

Xi'an High Voltage Apparatus Research Institute Co. Ltd, Xi'an 710077, China

e-mail: 1124400243@qq.com

X. Qiu

Xi'an Jiaotong University, Xi'an 710049, China

© Beijing Paiké Culture Commu. Co., Ltd. 2024

X. Dong and L. Cai (eds.), *The Proceedings of 2023 4th International Symposium on Insulation and Discharge Computation for Power Equipment (IDCOMPU2023)*, Lecture Notes in Electrical Engineering 1100, https://doi.org/10.1007/978-981-99-7393-4_24

253

lower losses and no need for synchronization or reactive power compensation. Therefore, high voltage direct current (HVDC) transmission technology is a priority for large-scale renewable energy transmission and integration [2–4].

In DC power grids, the line currents can only be regulated by changing the line resistance or voltage across the line, as stated by Ohm's law. This means that the traditional power flow regulation technology used in AC power grids is not suitable for HVDC power grids [5]. As a result, it is essential to apply new devices that can regulate line currents in HVDC grids, known as the DC current flow controllers (DCCFCs) due to their function. These devices are specifically designed for use in HVDC systems.

Most research on DCCFC focuses on the variable voltage source type due to its advantages, including low power losses and high regulation flexibility [6, 7]. Specifically, the series–parallel-connected DCCFC, which is a type of variable voltage source DCCFC, is of particular interest because it allows for independent regulation of the current of each line. This type of DCCFC typically consists of a series-connected circuit that exchanges power with the line [7–9] and a parallel-connected circuit that transfers power between the DC terminals and lines [10, 11].

This paper proposes a series–parallel-connected DCCFC with the ability to regulate the voltage on each output terminal independently, thereby changing the inserted voltage between lines to achieve current regulation. Simulation of a three-terminal device applied in DC grids is conducted to verify the feasibility of this topology.

2 Topology and Operation Principle

This section illustrates the function and operation process of the proposed DCCFC topology when installed on multi-terminal DC grids. To explain the operation principle, an example of a single line is used.

2.1 Basic Circuit Topology

Figure 1 illustrates the schematic of the proposed DCCFC installed on multi-terminal DC grids. The system includes $n + 1$ DC terminals represented by V_0 and V_j ($j = 1, 2, \dots, n$), with the proposed DCCFC installed at terminal V_0 . The DCCFC has a total of n output ports connected to n DC lines through filters. The proposed DCCFC can be divided into three main parts: the energy supply DC-DC converter, the Boost converter, and the regulation switches.

The energy supply DC-DC converter utilizes a DC transformer consisting of two symmetrical arms, two symmetrical resonant tanks, and a full bridge rectifier with the output capacitor C_p . It absorbs energy from terminal V_0 and generates a stable DC voltage across the output capacitor C_p . Each arm is comprised of a stack of N series-connected half-bridge submodules (SMs) and an inductor L_S (or L'_S). The

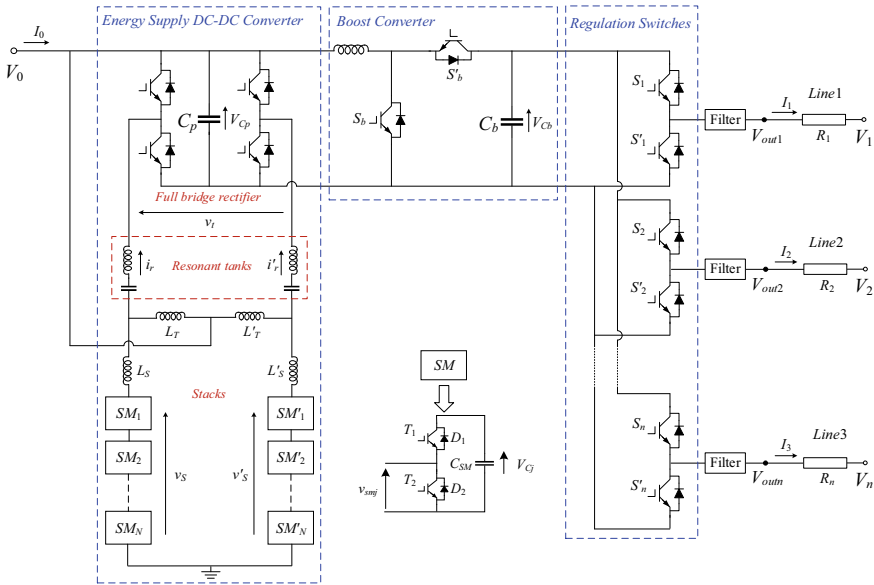


Fig. 1 Topology of the proposed DCCFC in multi-terminal DC grids

SM capacitor is denoted by C_{SM} , and the SM capacitor voltages in two stacks are represented by v_{SMi} and v_{SMi}' ($i = 1, 2, \dots, N$), respectively. DC Terminal V_0 inputs DC power to the arms through two large inductors L_T and L_T' , which suppress AC current components flowing into the DC terminal. Each resonant tank consists of an inductor and a capacitor in series, operating in resonant mode. The resonant tanks block DC current and allow AC power to be transmitted. The full bridge rectifier, composed of controllable semiconductor switches, stabilizes the voltage on the output capacitor C_p and enables bidirectional power exchange. The average voltage across the capacitor C_p is denoted by V_{Cp} .

The diode in the classic boost circuit is replaced by a controllable semiconductor switch in the boost converter of the proposed topology, which ensures the bidirectional transmission of power. The output capacitor of the boost converter and the average voltage across it is represented by and respectively.

The boost converter in the proposed topology replaces the diode in the classic boost circuit with a controllable semiconductor switch, enabling bidirectional power transmission. The output capacitor of the boost converter is represented by C_b , and the average voltage across it is denoted by V_{Cb} .

There are n groups of regulation switches, each consisting of two controllable semiconductor switches for n output ports. The midpoint of each group of switches is connected to a filter as the output port of the DCCFC, represented by V_{outj} , respectively. The n output ports of the DCCFC are connected to n controlled lines, respectively, to control the power flowing through the DC terminal V_j .

2.2 Operation Principle

The energy supply DC-DC converter applies a phase-shift modulation introduced in [12, 13]. In each stack, the X and Y ($N \geq X > Y \geq 1$) SM capacitors are deployed in series in different half cycles, generating a voltage of two levels. As a result, the terminal voltage V_0 can be expressed as:

$$V_0 = |v_S| = |v'_S| = \frac{X V_{CSM} + Y V_{CSM}}{2} = \frac{X + Y}{2} V_{CSM} \quad (1)$$

Here, V_{CSM} represents the average voltage of the SM capacitor. As a result, the voltage across the two large inductors is a square wave voltage with an average amplitude of V_T , which can be calculated as follows:

$$V_T = |v_S - v'_S| = (X - Y) V_{CSM} = \frac{2(X - Y)}{X + Y} V_0 \quad (2)$$

Due to the resonant mode, the AC impedance of each resonant tank is almost zero. As a result, the input voltage v_t of the full bridge rectifier is also a square wave voltage with an average amplitude of V_T . Consequently, the average value of the rectifier output voltage V_{Cp} is V_T .

To analyze the principle of current regulation, we have chosen the operation of line1 as an example. The simplified equivalent circuit is shown in Fig. 2, and the directions indicated in the figures are taken as the positive reference directions. The two regulation switches of each group are complementary. When S_1 is turned on and S_1' is turned off, as shown in Fig. 2a, the output port voltage V_{out1} of the DCCFC can be calculated as follows:

$$V_{out1} = V_0 - V_{Cp} + V_{Cb} \quad (3)$$

Similarly, When S_1' is turned on and S_1 is turned off as shown in Fig. 2b, the output port voltage V_{out1} can be calculated as

$$V_{out1} = V_0 - V_{Cp} \quad (4)$$

Hence, the voltage variation ΔV_1 caused by the DCCFC can be derived as

$$\Delta V_1 = V_{out1} - V_0 = \begin{cases} V_{Cb} - V_{Cp}, & S_1 \text{ turned on} \\ -V_{Cp}, & S_1' \text{ turned on} \end{cases} \quad (5)$$

Because V_{Cp} and V_{Cb} are the input and output voltages of the boost converter respectively, the relationship between the two voltages must be $V_{Cb} > V_{Cp}$. Therefore, when S_1 is turned on, $\Delta V_1 > 0$, and when S_1' is turned on, $\Delta V_1 < 0$. In other words, the proposed DCCFC is capable of not only increasing the DC terminal voltage but also decreasing it equivalently, thereby regulating the line current.

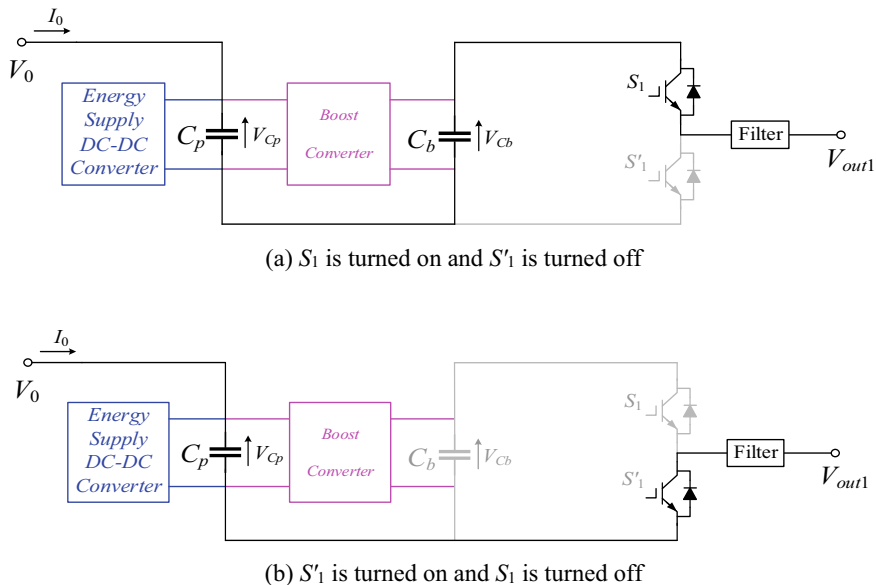


Fig. 2 Simplified equivalent circuits

3 Control Strategy

For illustration purposes, let us consider the current flowing through line1 denoted as I_1 , with the positive direction flowing into terminal 1. Assuming that the duty cycle of S_1 is D_1 , we can calculate the average value of V_{out1} as:

$$\begin{aligned}
 V_{out1} &= D_1(V_0 - V_{Cp} + V_{Cb}) + (1 - D_1)(V_0 - V_{Cp}) \\
 &= V_0 - V_{Cp} + D_1 V_{Cb}
 \end{aligned}
 \tag{6}$$

Assuming the duty cycle of S_b in boost converter (as shown in Fig. 1) is α , it can be derived that

$$\begin{aligned}
 V_{out1} &= V_0 - V_{Cp} + D_1 V_{Cb} \\
 &= V_0 + \frac{(D_1 + \alpha) - 1}{1 - \alpha} V_T
 \end{aligned}
 \tag{7}$$

Therefore, the current flowing through line1 is

$$\begin{aligned}
 I_1 &= \frac{V_{out1} - V_1}{R_1} \\
 &= I_{ori1} + \frac{(D_1 + \alpha) - 1}{1 - \alpha} \frac{V_T}{R_1}
 \end{aligned}
 \tag{8}$$

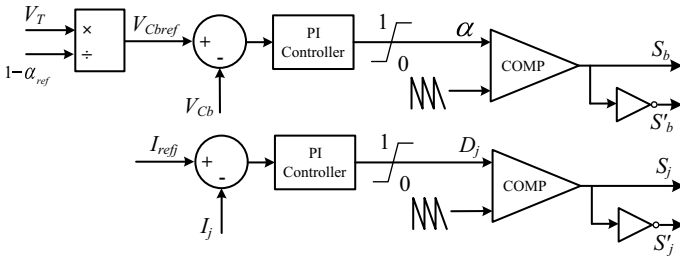


Fig. 3 Control strategy diagram

where I_{ori1} is the original current of line1 without DCCFC installed and R_1 is the resistance of line1.

From Eq. (8), it is apparent that the duty cycles of the proposed DCCFC can be adjusted to regulate the line current. Although the boost converter is shared by all the lines, each group of regulation switches can be controlled independently. Therefore, the duty cycle α , together with V_T determined by the modulation parameters of the stack, determines the current regulation range of the DCCFC. Meanwhile, the duty cycle D_j determines the specific value of current in the corresponding line.

The control strategy of the proposed DCCFC utilizes a traditional PI controller to regulate the regulation switches. Additionally, to ensure stability of the output capacitor voltage V_{Cb} of the boost converter, the PI controller is also utilized to correct the switching duty cycle of the boost converter. The control strategy is illustrated in Fig. 3.

4 Simulation Result

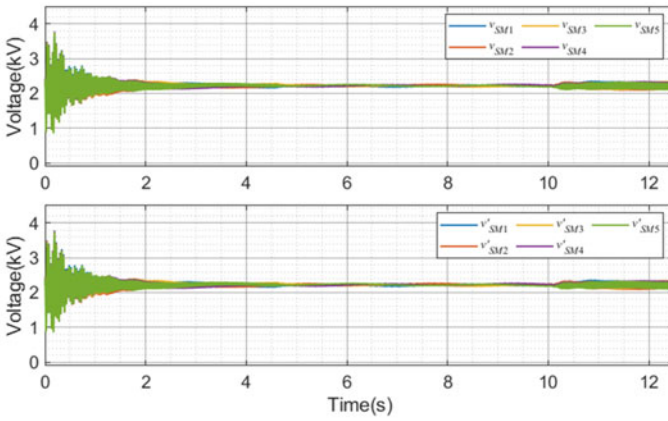
To verify the feasibility of the proposed DCCFC, a simulation in a three-terminal DC grid using MATLAB/SIMULINK was conducted. This section presents a set of simulation results. The simulation parameters used are presented in Table 1, where $X = 5$ and $Y = 4$ are the modulation parameters of the stacks.

Table 1 Simulation parameters

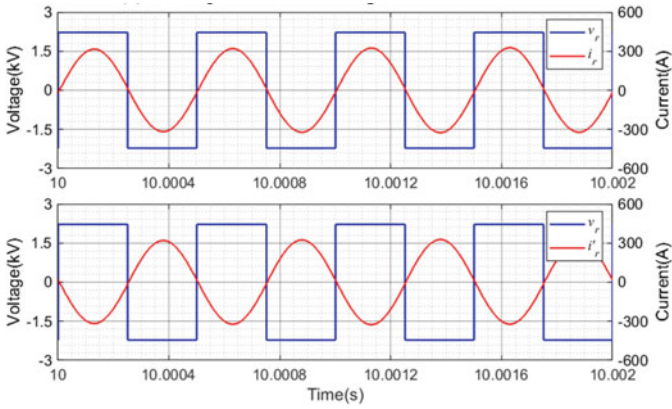
Parameter	Description	Value
V_0	Voltage of terminal which DCCFC installed on	10 kV
V_1	Voltage of DC terminal 1	9.8 kV
V_2	Voltage of DC terminal 2	10.3 kV
R_1, R_2	Line resistance	1 Ω
L_r	Inductor of resonant tank	500 μH
C_r	Capacitor of resonant tank	12.713 μF
f_r	Resonant frequency	2 kHz
α	Switching duty cycle of the boost converter	0.5

The simulation was set up as follows: initially, the DC grid system operated without the DCCFC, and the currents in lines 1 and 2 were 200A and -300A , respectively, which were uncontrollable. At 1s, the DCCFC was activated with I_{ref1} set at 1kA and I_{ref2} set at -900A . At 4.5s, I_{ref1} dropped to 500A and I_{ref2} dropped to -600A . At 7s, the target currents were reversed, with I_{ref1} set at -500A and I_{ref2} set at 200A. At 10s, I_{ref1} increased to -1000A and I_{ref2} increased to 1100A. The simulation results are presented and discussed in the following sections. The simulation parameters used in the study are presented in Table 1, with the stacks modulation parameters set to $X = 5$ and $Y = 4$.

Figure 4a displays the waveforms of the SMs capacitors, which are well-balanced around the theoretical value of 2.22kV. Figure 4b depicts the waveforms of the rectifier input voltage and the currents of the resonant tanks. Under the resonant operation mode, the voltage and current of the rectifier are in the same phase, i.e., the zero-crossing points of the voltage and current coincide, thus effectively reducing the switching loss. Figure 5 illustrates the dynamic response of line currents, which are given in both positive and negative directions. The simulation results demonstrate that each line current can follow the given current in any direction under the control of the proposed DCCFC.



(a) Voltages of the SM capacitors in the stack



(b) Resonant currents and full bridge voltages

Fig. 4 Simulation results of steady state

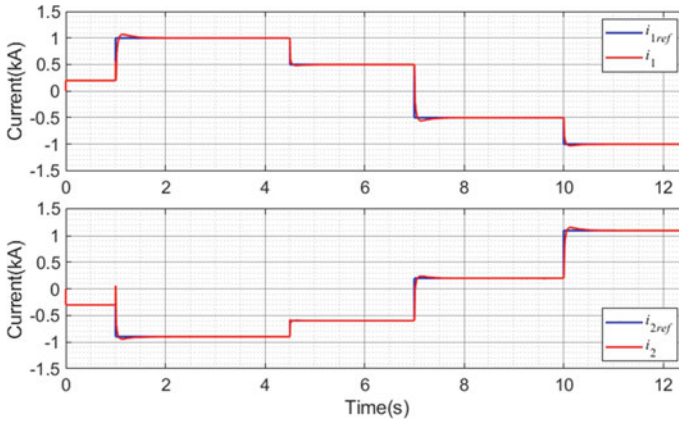


Fig. 5 Dynamic response of line currents under the operation of the DCCFC

5 Conclusion

This paper proposed a bidirectional DCCFC with independent power flow regulation ability, which can be utilized in HVDC grids to regulate the line current. The proposed DCCFC can change the voltage of each output port independently, thereby altering the inserted voltage between DC lines. The energy supply DC-DC converter maintains the rectifier capacitor voltage. By controlling the duty cycle of the boost converter, the regulating range of the DCCFC can be adjusted. By controlling the duty cycle of each group of regulation switches, the DCCFC can independently adjust each output terminal voltage to regulate the current flow of each line. Simulation results are presented to validate the proposed DCCFC's operation principle and power flow control analysis.

References

1. Gomis-Bellmunt O, Sau-Bassols J, Prieto-Araujo E et al (2020) Flexible converters for meshed hvdc grids: From flexible ac transmission systems (FACTS) to flexible dc grids. *IEEE Trans Power Delivery* 35(1):2–15
2. Liangzhong YAO, Jing WU et al (2014) Pattern analysis of future HVDC grid development [JJ. *Proc CSEE* 34(34):6007–6020
3. Solas E, Abad G, Barrena JA et al (2013) Modular multilevel converter with different submodule concepts-part ii: experimental validation and comparison for hvdc application. *IEEE Trans Industr Electron* 60(10):4536–4545
4. Bucher MK, Wiget R, Andersson G et al (2014) Multiterminal hvdc networks-what is the preferred topology. *IEEE Trans Power Delivery* 29(1):406–413
5. Li N, Xu Y, Chen H (2000) FACTS-based power flow control in interconnected power system. *IEEE Trans Power Syst* 15(1):257–262
6. Adam GP, Vrana TK et al (2019) Review of technologies for DC grids–power conversion, flow control and protection. *IET Power Electron.* 12(8):1851–1867

7. Zhang X, Jin J, Ye Y, Yang X (2022) Analysis of a series-parallel-connected type dc power flow controller in multiterminal grids. *IEEE Trans Power Electron* 37(6):7400–7410
8. Rouzbehi K, Yazdi SSH et al (2018) Power flow control in multi-terminal HVDC grids using a serial-parallel DC power flow controller. *IEEE Access* 6:56934–56944
9. Wu W, Wu X, Zhao Y, Wang L, Zhao T, Jing L (2020) An improved multiport DC power flow controller for VSC-MTDC grids. *IEEE Access* 8:7573–7586
10. Sau-Bassols J, Ferrer-San-José R, Prieto-Araujo E, Gomis-Bellmunt O (2020) Multiport interline current flow controller for meshed HVDC grids. *IEEE Trans Industr Electron* 67(7):5467–5478
11. Sau-Bassols J, Prieto-Araujo E, Gomis-Bellmunt O, Hassan F (2018) Series interline DC/Dc Current flow controller for meshed HVDC grids. *IEEE Trans Power Delivery* 33(2):881–891
12. Zhang X, Xiang X, Green TC, Yang X, Wang F (2019) A push-pull modular-multilevel-converter-based low step-up ratio DC transformer. *IEEE Trans Industr Electron* 66(3):2247–2256
13. Qiao Y, Zhang X, Xiang X, Yang X, Green TC (2020) Trapezoidal current modulation for bidirectional high-step-ratio modular DC–DC converters. *IEEE Trans Power Electron* 35(4):3402–3415

Research on a New Type of Magnetically Controlled Distribution Transformer



Long Di, Xiaoguo Chen, Dezhu You, Yongzhong Wu, Kai Liu, Jiawei Liu, and Yu Dong

Abstract This paper proposes a compact magnetically controlled distribution transformer topology, which combines a controllable reactor with a distribution transformer to make a conventional distribution transformer with the ability to flexibly regulate reactive voltage in addition to the basic function of voltage transformation. Firstly, the structure of a new magnetically controlled distribution transformer is proposed in this paper. The equivalent circuit of the magnetically controlled distribution transformer is obtained through the analysis of its basic electromagnetic relationship. Then, the formula for calculating the permeability of the core and the air gap in the magnetic valve section under saturation condition is analyzed theoretically by using Schwartz—Christopher transformation. The leakage flux is included in the calculation of excitation inductance, and the influence of the air gap beside the magnetic valve on the excitation reactance is fully considered. Finally, the inductance characteristics of the magnetically controlled distribution transformer are studied, and the finite element electromagnetic simulation is also carried out.

Keywords Magnetically controlled distribution transformer · Equivalent circuit · Magnetic valve · Finite element analysis

L. Di · D. You · Y. Wu
Zhaoqing Power Supply Company, China Southern Power Grid, Zhaoqing 526040, China

X. Chen (✉) · K. Liu
China Southern Power Grid Research Institute, Guangzhou 510700, China
e-mail: chenxg@csg.cn

J. Liu · Y. Dong
School of Electrical Engineering and Automation, Wuhan University, Wuhan 430072, China

1 Introduction

With the progress and development of productivity, electric energy has been widely used in all aspects of social life because of its advantages of simple production, easy control, convenient transmission, green and clean, and has gradually become indispensable energy in modern life. How to improve the quality of electric energy has also become a research hotspot. Most of the loads in low-voltage distribution network are single-phase loads, and the fluctuation and randomness of loads are easy to cause the problem of three-phase unbalance. This phenomenon will increase the loss of power system, affect the reliability of power supply, and is not conducive to the safe and stable operation of power system [1].

The controllable reactor can adjust the magnetic saturation of the iron core by changing the size of the DC excitation, so as to realize the function of smoothly adjusting the reactive power output of the reactor. Its development is based on the research of magnetic amplifier. A series of controllable magnetic valve reactors with different voltage levels have been successfully developed, but there are still shortcomings in harmonics and loss. In the 1990s, Wuhan University took the lead in conducting research on magneto-controlled reactor [2], and carried out research on response speed, harmonics, loss and other aspects, and achieved a series of innovative achievements [3–5]. At present, the developed products are in the international leading level, hundreds of sets of products have been put into operation. In September 2007, the UHV magneto-controlled reactor jointly developed by TbeA Shenyang Transformer Group was successfully put into operation in Jiangling. Subsequently, more and more magneto-controlled reactors with different voltage levels and capacities were successfully put into operation in various places [6–8].

To solve the above problems, this paper proposes a new type of magneto reactance transformer, which combines the core and winding of the common power transformer and magneto reactance transformer into one. The inductance characteristics of the magnetically controlled distribution transformer are studied, and the finite element electromagnetic simulation is also carried out.

2 Model Mechanism Analysis

2.1 The Topology of the New Magneto-Controlled Distribution Transformer

Based on the optimization of the existing single-phase magnetic transformer topology, a compact three-dimensional three-phase magnetically controlled transformer topology is proposed. Since there are both DC and AC magnetic fluxes in the core, it is necessary to obtain an equivalent magnetic circuit model by studying the magnetic circuit topology of the transformer, so as to provide theoretical basis for the optimization of the topology structure. It is shown in Fig. 1.

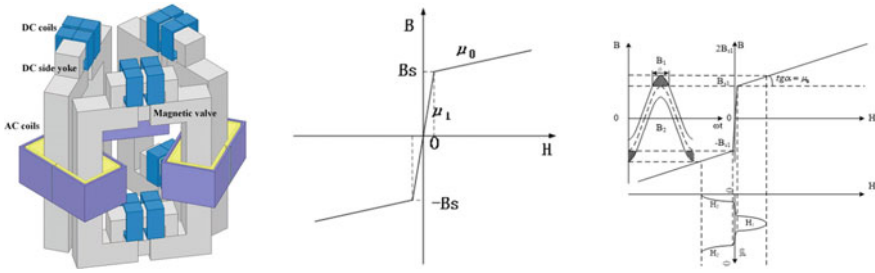


Fig. 1 The topology and B-H curve of magnetically controlled distribution transformers

2.2 The Working Mechanism of the New Magneto-Controlled Reactance Transformer

In order to simulate the magnetization characteristics of the new magnetically controlled transformer core, a segmented ideal B-H magnetization curve model is adopted in this paper. Ignoring complex factors such as hysteresis and anisotropy of ferromagnetic materials, the magnetization curve is divided into two sections, as shown in Fig. 2. Among them, the permeability of the core is μ_1 when unsaturated, μ_0 when saturated, and $\mu_1 \approx 1000\mu_0$. The critical saturation magnetic induction intensity of the core is B_s . At this time, the mathematical model of the ideal magnetization curve is shown in Eq. (1):

$$H_t = \begin{cases} \frac{B}{\mu_1} & |B| < B_s \\ \frac{\mu_0}{\mu_1} \frac{B}{B_s} + \frac{B_s}{\mu_1} & B > B_s \\ \frac{\mu_0}{\mu_1} \frac{B}{B_s} - \frac{B_s}{\mu_1} & B < -B_s \end{cases} \quad (1)$$

Ignoring the resistance of the working winding, the basic equation of the magneto reactance transformer is shown in Eq. (2):

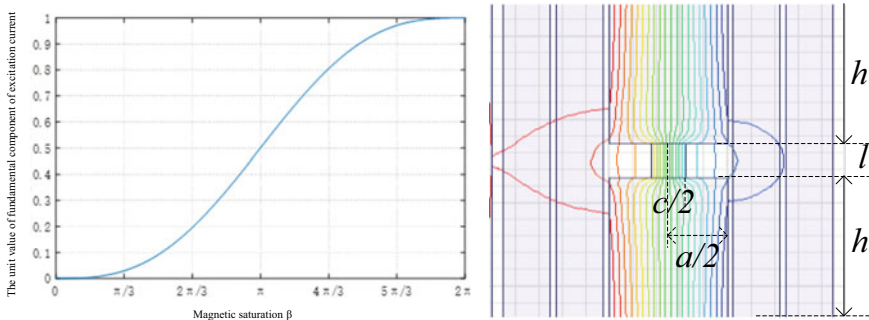


Fig. 2 The unit value of fundamental component and the magnetic valve field line diagram

$$\begin{cases} F_1 = N_1 i_1 + N_2 i_2 + N_k i_k = f(B_1)(l - l_t) + f(B_{t1})l_t \\ F_2 = N_1 i_1 + N_2 i_2 - N_k i_k = f(B_2)(l - l_t) + f(B_{t2})l_t \\ N_1 \frac{d(\Phi_1 + \Phi_2)}{dt} = U_1 \\ N_k \left(\frac{d\Phi_1}{dt} - \frac{d\Phi_2}{dt} \right) + i_k R_k = U_k \end{cases} \quad (2)$$

In the formula, F_1 and F_2 refer to the magnetic motive force of core I and II, B_1 and B_2 refer to the magnetic induction intensity of the non-magnetic valve segment of core I and II, B_{t1} and B_{t2} refer to the magnetic induction intensity of the magnetic valve segment of core I and II, $f(B)$ is the corresponding magnetic field intensity. N_1 , N_2 and N_k are the turns of primary side winding, secondary side winding and DC excitation control side winding, respectively.

It can be seen from the state of the iron core I and II of the magneto-controlled reactance transformer and the working state of the winding that they have symmetry. Therefore, they have the following relation is shown in Eq. (3):

$$\begin{cases} B_1(\omega t) = -B_2(\omega t + \pi) \\ B_2(\omega t) = -B_1(\omega t + \pi) \end{cases} \quad (3)$$

Suppose the expression of B_1 and B_2 is shown in Eq. (4):

$$\begin{aligned} B_1(\omega t) = & B_d + B_{1m} \sin(\omega t - \phi_1) + B_{2m} \sin(2\omega t - \phi_2) \\ & + B_{3m} \sin(3\omega t - \phi_3) + \dots \end{aligned} \quad (4)$$

$$\begin{aligned} B_2(\omega t) = & -B_d + B_{1m} \sin(\omega t - \phi_1) - B_{2m} \sin(2\omega t - \phi_2) \\ & + B_{3m} \sin(3\omega t - \phi_3) - \dots \end{aligned} \quad (5)$$

It can be seen from is as Eqs. (6 and 7) that the odd harmonics in the magnetic induction intensity of core I and core II at any time are in phase, and the even harmonics are in reverse phase, which can be obtained

$$\begin{aligned} e_k = e_{k1} + e_{k2} = & N_k A_b \left(\frac{dB_1}{dt} - \frac{dB_2}{dt} \right) \\ = & \omega N_k A_b [4B_{2m} \cos(2\omega t - \phi_2) + 8B_{4m} \cos(4\omega t - \phi_4) + \dots] \end{aligned} \quad (6)$$

$$U_1 = \omega N A_b [B_m \cos(\omega t - \phi_1) + 3B_{3m} \cos(3\omega t - \phi_3) + \dots] \quad (7)$$

According to the principle of harmonic balance, it is shown in Eq. (8):

$$\begin{cases} B_1(\omega t) = B_d - B_{1m} \cos \omega t \\ B_2(\omega t) = -B_d - B_{1m} \cos \omega t \end{cases} \quad (8)$$

It is noted that the DC component B_d is not equal to the initial DC magnetic induction B_0 ($f(B_0) = E_k N_k / R_k l_{11}$) when the primary winding is not connected to AC power supply and only DC excitation voltage is applied in the DC excitation control winding. The size of B_d is controlled by the DC excitation voltage E_k .

According to the magnetically controlled transformer excitation current and primary current, secondary current relationship is shown in Eq. (9):

$$N_1 i_0 = N_1 i_1 + N_2 i_2 \tag{9}$$

Since the magnetization curve $f(B)$ is an odd function, it is shown in Eq. (10):

$$f[B_1(\omega t)] = f[-B_2(\omega t + \pi)] = -f[B_2(\omega t + \pi)] \tag{10}$$

Current $i_0(t)$ contains only odd harmonic components, which can be expressed by the following relation is shown in Eq. (11):

$$i_0(t) = \sum_{k=0}^{\infty} i_{0(2k+1)m} \cos[(2k + 1)\omega t] \tag{11}$$

The amplitude of each harmonic component is as Eq. (12):

$$i_{0(2k+1)m} = \frac{2}{\pi} \int_0^{\pi} \frac{I_t}{2N_1} \{f[B_1(\theta)] + f[B_2(\theta)]\} \cos(2k + 1)\theta d\theta \tag{12}$$

Among them, $\theta = \omega t$. It is shown in Fig. 2.

When the DC excitation control current is 0, $B_d = 0$, the magnetic induction intensity B_1 and B_2 of core I and core II varies in the range from $-B_s$ to B_s , with the amplitude $B_{1m} = B_{s1}$. When the DC excitation control current increases, the DC component in B_1 and B_2 will also increase, which will make part of the curve of B_1 and B_2 in the figure go beyond the range of $-B_s$ to B_s . The shaded section of the curve corresponds to the horizontal axis, which is represented by magnetic saturation, and represents the time that core I or Core II reaches saturation in one power frequency cycle.

$$\beta = 2 \arccos \frac{B_{s1} - B_d}{B_{s1}} \tag{13}$$

When DC excitation is 0, $B_d = 0$, the core does not reach saturation state within a period, so $\beta = 0$. With the increase of DC excitation control current, the saturation time of the core also increases. When the core is saturated throughout the whole power frequency cycle, $\beta = 2\pi$, magnetic saturation reaches the limit value. Therefore, the magnetic saturation β reflects the magnetic saturation degree of the core with a range of 0 to 2π . It can be deduced that the expression of magnetic saturation β is shown

in Eq. (13). $f[B_1(t)], f[B_2(t)]$ is as in Eqs. (14)–(17).

$$f[B_1(t)] = \begin{cases} \frac{B_s(1-\cos\frac{\beta}{2}-\cos\omega t)}{\mu_1} & 0 \leq \omega t < \pi - \frac{\beta}{2} \\ \frac{B_s(-\cos\frac{\beta}{2}-\cos\omega t)}{\mu_0} + \frac{B_s}{\mu_1} & \pi - \frac{\beta}{2} \leq \omega t < \pi + \frac{\beta}{2} \\ \frac{B_s(1-\cos\frac{\beta}{2}-\cos\omega t)}{\mu_1} & \pi + \frac{\beta}{2} \leq \omega t \leq 2\pi \end{cases}$$

$$f[B_2(t)] = \begin{cases} \frac{B_s(\cos\frac{\beta}{2}-\cos\omega t)}{\mu_0} - \frac{B_s}{\mu_1} & 0 \leq \omega t < \frac{\beta}{2} \\ \frac{B_s(-1+\cos\frac{\beta}{2}-\cos\omega t)}{\mu_1} & \frac{\beta}{2} \leq \omega t < 2\pi - \frac{\beta}{2} \\ \frac{B_s(\cos\frac{\beta}{2}-\cos\omega t)}{\mu_0} - \frac{B_s}{\mu_1} & 2\pi - \frac{\beta}{2} \leq \omega t \leq 2\pi \end{cases} \tag{14}$$

$$i_{0(1)}^* = \frac{1}{2\pi}(\beta - \sin\beta) \tag{15}$$

$$i_{0(2k+1)}^* = i_{0(2k+1)} / \left(\frac{1}{\mu_0} - \frac{1}{\mu_1} \right) \frac{B_s l_{t1}}{N_1} \tag{16}$$

$$i_{0(2k+1)}^* = \frac{1}{(2k+1)\pi} \left[\frac{\sin k\beta}{2k} - \frac{\sin(k+1)\beta}{2(k+1)} \right] \quad k = 1, 2, 3, \dots \tag{17}$$

2.3 Working Mechanism of the New Magneto-Controlled Reactance Transformer

When $\beta = 2\pi$, the per unit value of the fundamental wave of the excitation current is equal to 1, which indicates that the current reference value is exactly the amplitude of the fundamental wave component of the excitation current when the limit saturation of the magnetically controlled transformer is $\beta = 2\pi$. The curve of fundamental current per unit value changing with magnetic saturation can be drawn, as shown in Fig. 2. As can be seen from the figure, with the increase of the magnetic saturation β of the iron core, the per unit value of the fundamental wave component of the excitation current also increases, that is, the equivalent excitation inductance of the magnetically controlled transformer decreases. The equivalent excitation inductance of the transformer can be smoothly adjusted by changing the value of magnetic saturation β .

Considering that the structure of the magnetic valve is of polygonal irregular shape, and the magnetic flux distribution of the air gap edge and the magnetic valve have a great influence on the excitation inductance when the core is saturated, the Schwarz-Christoffel transformation will be used in this paper to calculate the air gap permeability and the magnetic valve segment permeability respectively when the magnetic valve is saturated. It is shown in Eqs. (18)–(23)

$$\Lambda'_{GH} = \frac{\mu}{\frac{l}{c} + \frac{1}{k\pi} \ln\left(\frac{(1+k)^{(1+k)}}{(1-k)^{(1-k)}}\right) - \frac{\ln 4}{\pi}} \tag{18}$$

$$\sigma_{fa} = \frac{\Lambda_{GH}}{\mu c/l} = \frac{1}{1 + \frac{c}{\pi l} \left(\frac{1}{k} \ln\left(\frac{(1+k)^{(1+k)}}{(1-k)^{(1-k)}}\right) - \ln 4 \right)} \tag{19}$$

$$\Lambda_{fa} = \mu \sigma_{fa} \frac{\pi bc}{l} \tag{20}$$

$$\Lambda_{all} = \Lambda_g + \Lambda_{fa} = \mu \sigma_{fa} \frac{bc}{l} + \mu_0 b \frac{\sigma_a a - c}{l} \tag{21}$$

$$\sigma_{fa} = \frac{1}{1 + \frac{c}{\pi l} \left(\frac{1}{k} \ln\left(\frac{(1+k)^{(1+k)}}{(1-k)^{(1-k)}}\right) - \ln 4 \right)} \tag{22}$$

$$\sigma_a = 1 + \frac{2l}{\pi a} \left(1 + \ln \frac{\pi h}{2l} \right) \tag{23}$$

3 Model Mechanism Analysis

A simulation model of single-phase MCT is constructed. Figure 3 shows the simulation model of the MCT, and the voltage ratio is 400 V/64 V (Table 1).

Set the DC power supply voltage to 60 V, and MCT reaches the rated reactive output state. As shown in Fig. 4, MCT can output reactive power of 30% of active power capacity while transmitting active power.

From the simulation, MCT in this paper can realize the function of buck-boosting voltage of traditional transformers, and can also output reactive power stably. The single-phase magnetic control reactor is of three column structure, and the single-phase transformer is of two column structure, so they have five columns in total.

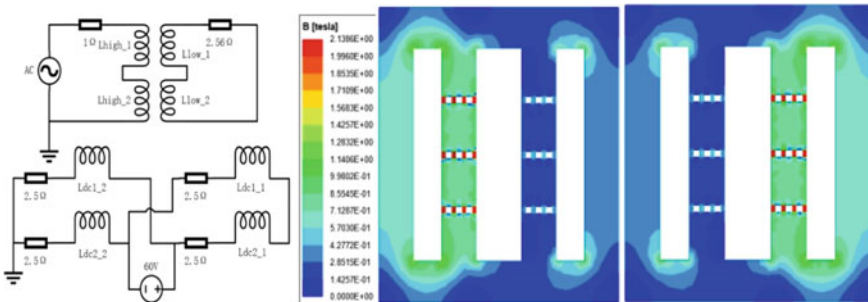


Fig. 3 The flux density distribution of MCT in one current cycle (Add 60 V DC excitation)

Table 1 Design parameters

Parameter type	Numerical value
Rated capacity	1.8(kVA)
Primary side/secondary side rated voltage	400 V/64 V
Primary side/secondary side rated current	4.5A/28A
Length and Diameter of magnetic valve	30 mm and 40mm
Core diameter	60 mm
Number of turns on primary side/secondary side	624 turns/100 turns

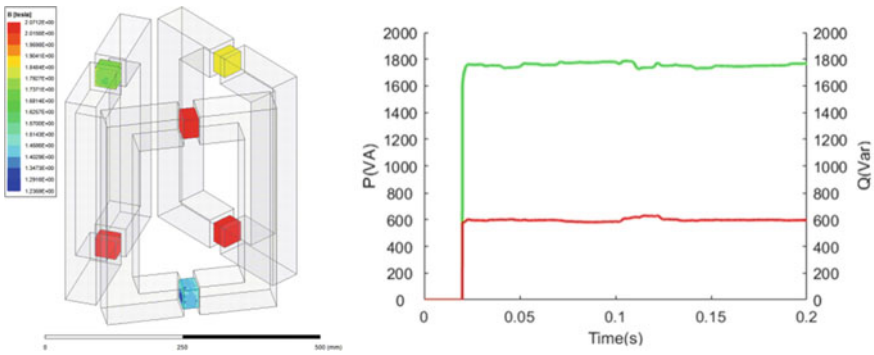


Fig. 4 The active power and reactive power (Add 60 V DC excitation)

Single phase MCT has only 4 columns, so its volume is 25% less than that of the original transformer and reactor.

4 Conclusion

This paper proposes a compact magnetically controlled distribution transformer topology, which combines a controllable reactor with a distribution transformer to make the traditional distribution transformer have the ability to flexibly regulate the reactive voltage in addition to the basic function of raising and lowering the voltage, and only adds part of the floor space to the original distribution transformer volume, which is especially suitable for urban distribution stations with a high proportion of renewable energy sources.

References

1. Tian M, Li Q, Wang S (2002) An equivalent physical model and a mathematical model of the controlled saturable reactor[J]. *Trans China Electrotech Soc* 17(4):18–21
2. Chen B, Chen W (1997) Analyses of harmonics and overvoltage limitation characteristics of EHV controlled reactor[J]. *Proc CSEE* 17(2):122–125 (in Chinese)
3. Dong Y, Zhou H, Chen B, Tian C, Yuan J, Muramatsu K (2022) Compact type of magnetic control transformer[C]. In: 2022 IEEE 20th Biennial conference on electromagnetic field computation (CEFC). Denver, CO, USA, pp 1–2
4. Wu Y, Tian C, Zhang Z, Chen B, Liu S, Chen Y (2023) A novel current transformer based on virtual air gap and its basic measuring characteristics[J]. *IEEE Trans Power Delivery* 38(1):13–25
5. Yu M, Chen B, Cao Z et al (2008) A novel 110kV shunt controllable reactor and its application[J]. *Autom Electric Power Syst* 32(3):87–91 (in Chinese)
6. Lei X, Deng Z, Xu G et al (2014) Research and practice of magnetically controlled shunt reactor[J]. *Proc CSEE* 34(S1):225–231 (in Chinese)
7. Ben T, Hou L, Chen L, Zhang P, Kong Y, Yan R (2022) The vector electromagnetic vibration of magnetically controlled reactor considering the vector hysteretic magnetostriction effect[J]. *IEEE Trans Magn* 58(9):1–5, Art no. 2501805
8. Gai X, Shu S (2022) Energy harvesting method of insulated ground wire based on self-excited magnetically controlled reactor[C]. In: 2022 IEEE international conference on high voltage engineering and applications (ICHVE). Chongqing, China, pp 1–4

The Study of Fire Spread Trend in Cable Tunnels with Different Wind Speeds



Zhe Zhang, Ying Sun, Liang Zou, and Xiaolong Wang

Abstract Recently, power grid fire accidents happen frequently, the cable fire is an important part. To address this issue, it is advisable to conduct effective simulation tests to investigate the impact of various factors on cable fires. Therefore, a simulation model for cable tunnel fires was established based on the typical design of cable tunnels and cable layout schemes, in order to investigate the distribution of temperature and generated gases under different wind speed conditions. According to the simulation results, the higher wind speed condition is more likely to accelerate the fire combustion process and to increase the concentration of harmful gas generation than those obtained for lower wind speed condition. However, higher wind speed potentially reduces the temperature of the upper tuyere more effectively, and then decreases the fire disaster area, avoiding further spread of fire. The high wind speed condition has been found to significantly decrease the amount of harmful gas produced at the air inlet and prevent the multi-directional diffusion of noxious gas. These findings provide some reference for the prevention of cable tunnel fires and the post-disaster handling work.

Keywords Cable tunnel · Fire spread · Temperature distribution · Gas distribution

Z. Zhang · Y. Sun (✉) · L. Zou · X. Wang
School of Electrical Engineering, Shandong University, Jinan 250000, China
e-mail: ys2018@sdu.edu.cn

Z. Zhang
e-mail: 202134728@mail.sdu.edu.cn

L. Zou
e-mail: zouliang@sdu.edu.cn

X. Wang
e-mail: wangxiaolong@sdu.edu.cn

1 Introduction

With the rapid economic development, the usage of cable increases rapidly in our country. The fire caused by non-flame retardant cable also increases [1]. The fires caused by electrical failures accounted for 52% of the identified fires, among which fires caused by cable line breakage are particularly prominent [2]. During the operation of the cable, due to the dense and narrow space of the underground cable tunnel, the heat is easy to accumulate near heat sources. The overheating will burn through the insulation layer and generate arc, which is easy to cause fire [3]. Burning cables will again generate a lot of heat and release a lot of toxic and harmful smoke, which is likely to cause casualties and property losses [4].

Currently, several studies investigating the hazards and developmental characteristics of underground cable fires have been conducted [5–12]. Lv et al. [5] summarized the ignition mechanism of cable fires under the action of multiple factors. It summarized the combustion characteristics and tests of wires and cables. Huang et al. [6] established a full-size fire HRR estimation model for vertical cable bridge, which can accurately estimate the heat release rate of vertical cable bridge fire. Zhang et al. [7] used conical calorimeter for radiation ignition experiment, and measured combustion parameters such as heat release rate (HRR) and mass loss rate (MLR) of crosslinked polyethylene cable under three radiation intensification conditions. Bai et al. [8] analyzed the law of smoke propagation in cable trench under traditional firewall and new firewall. Xie et al. [9] proposed a new fire area map containing surface temperature and critical mass flux to quantify the fire risk of cables. Zeng et al. [10] investigated the flammability of cable coatings and developed a fire test method to assess the fire propagation tendency of groups of cables protected by cable coatings. Chen et al. [11] proposed a hybrid Bayesian network (BN)-based fire risk analysis model, to investigate the evolution of overload-induced early cable fire risks. Li et al. [12] carried out the fire spread dynamic simulation of the power cabin of the pipe corridor by building a corresponding simulation platform of the pipe corridor. It analyzed the effectiveness, reliability and adaptability of the temperature sensing detector, the point-type smoke sensing detector, the distributed fiber temperature sensing detector and the photo type fire detector. These above contents mainly focused on fire temperature changes or fire products. However, they do not involve the analysis of the overall development law of fire in underground cable tunnel. In particular, it is impossible to know the temperature distribution and the various gases distribution. Moreover, there is no analysis and research on the fire spread in the relatively closed space of underground cable tunnel of substations.

Cable combustion simulation test is the basis of fire risk prediction and an effective means to evaluate cable combustion characteristics [13]. This paper is based on the previous research and simulation work, in consideration of the common substation cable tunnel design. The cable simplification model is optimized. The simulation model of cable trench fire is constructed. The temperature and gas distribution under different wind speed conditions are studied. The influence of different wind speed conditions on the development of cable fire under typical substation cable

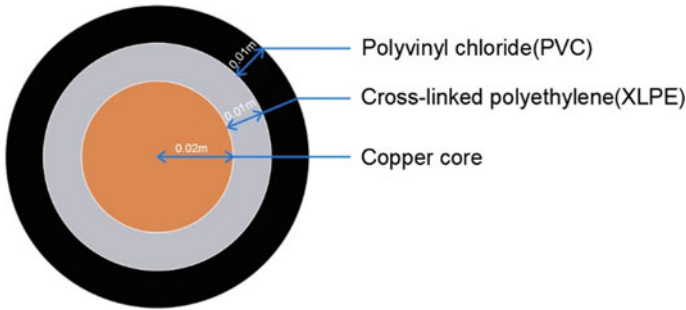


Fig. 1 Cable simplification model

tunnel design is summarized. The findings offer a theoretical reference for preventing underground cable fires and post-disaster treatment in the future.

2 Fire Simulation Model Setting

2.1 Cable Simplification Model

The prevailing type of cable used today is the three-layer structured cable, which comprises of a metal conductor layer, an insulating layer, and a oversheath layer. These layers are arranged in the following order: an inner copper core with a thickness of 0.02 m, a middle crosslinked polyethylene layer with a thickness of 0.01 m, and an outer polyvinyl chloride layer with a thickness of 0.01 m. To simplify the design of the cable structure model, a concentric structure was adopted. The structure of this simplified cable model is illustrated in Fig. 1.

2.2 Simulation Model Parameter Setting

A simulation model of a cable tunnel fire was constructed based on typical cable settings for 110 kV substations and common designs for underground cable tunnels. The cable tunnel has a rectangular shape, measuring 10 m in length, 1.4 m in width, and 1.5 m in height, with concrete walls and a concrete top. A layer of 0.1 m-thick fireproof bricks is laid at the bottom of the cable trench. Fireproof bricks of 0.1 m thickness are laid at the bottom of the cable trench. The cables inside the cable tunnel are three-layer cable as shown in Fig. 1. These three-layer cables are fixed by steel structural supports. Each layer comprises six cables, distributed evenly on both sides of the tunnel. The spacings between these three-layer cables from the ground are 0.1 m, 0.6 m and 1.1 m respectively.

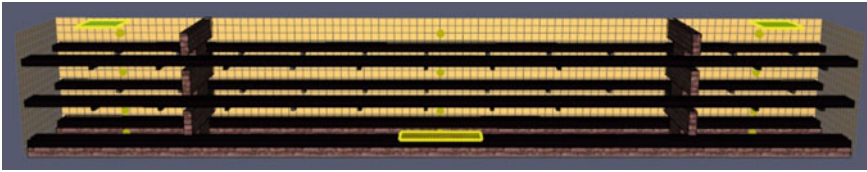


Fig. 2 Schematic diagram of fire simulation model

Based on the structure and size of the above cable tunnel, the center of the bottom surface is taken as the coordinate reference. The fire source, firewall, monitoring sensor, ventilation hole and other equipment are set in the model. The fire source is a rectangular surface with dimensions of 1 m in length and 0.4 m in width, and a heat release rate of 2500 kW/m^2 . Two firewalls composed of fireproof bricks are installed in the cable tunnel and symmetrically placed on both sides of the fire source. The distance between these two firewalls is 6 m. There is a small gap between the firewall and the cable. In the cable tunnel, three sets of sensors are installed to monitor gas and temperature. Set 1 is positioned in close proximity to the fire source. Set 2 is located at the upwind inlet. Set 3 is located at the downwind inlet. In this simulation, three sets of sensors were designed, including temperature sensors and gas sensors. The gas sensors mainly measured the content of CO , CO_2 , O_2 , and HCl . These sensors were installed at four different heights (1.4 m, 0.9 m, 0.4 m, and 0.1 m) in order to capture data on the distribution of temperature and gas concentrations. The height was denoted as h . The fire source, the firewall location and the monitoring sensor positions were kept constant throughout the experiments. Two ventilation holes were installed on both sides of the cable tunnel, with dimensions of 0.55 m square. The ventilation hole on the right side served as the inlet, while the other served as the outlet. The wind speed was denoted as v . Two sets of wind speed, $v = 1.0 \text{ m/s}$ and $v = 2.0 \text{ m/s}$, are used respectively. Cable tunnel simulation model settings are shown in Fig. 2 to study the effect of different firewall distance on cable fire spread characteristics.

3 Analysis of Fire Simulation Spread Results

By establishing underground cable trench fire model. The development of fire under two different wind speeds was simulated. The temperature variation and gas concentration distribution in the cable tunnel during cable fires were analyzed.

3.1 Temperature Variation Situation Analysis

In the cable tunnel, three sets of temperature sensors are utilized to achieve comprehensive temperature monitoring for various positions during the simulation process. The temporal behavior of temperature in monitoring Set 2 and monitoring Set 3 is analyzed under different wind speed conditions. The corresponding outcomes are presented in Fig. 3.

The temperature distribution information was obtained by collecting sensor data with longitudinal heights of 1.4 m, 0.9 m, 0.4 m and 0.1 m. Analysis of the temperature distribution in the cable tunnel showed clear stratification in the temperature distribution of the cable trench fire located at the upwind outlet. The temperature basically increases with the increase of longitudinal height. This is because hot air is less dense than cold air. The hot flue gas generated by the fire source to rise to the upper cable tunnel, which was the primary cause of the thermal stratification. However, under the condition of low wind speed, there is no stratification of the temperature at the downwind inlet. This is due to the mixing of temperature distribution by the air flow caused by the action of wind. Furthermore, as the fire spread, the burning part gradually spread from down to up. The flame also affected the temperature stratification inside the tunnel. Moreover, under the action of wind, the temperature distribution on both sides of the firewall is uneven. The temperature of the upper tuyere is lower than that of the lower tuyere. When the wind speed increases, this temperature difference also shows an increasing trend. Under the condition of low wind speed, the temperature of tunnel increases rapidly with the increase of time at first 100 s. The larger the vertical height, the faster the temperature rises. Then, the temperature of tunnel gradually becomes stable and fluctuates. It can be seen from Fig. 3a that the monitored temperature reaches its maximum value when it is close to 100 s and then it drops slowly and becomes a relatively stable state after 100 s. The reason is that the fire spreading trend is rapid during the early burning of the cable. The quantity of heat accumulates rapidly as well. Finally, the fire stabilized and stopped spreading. With the help of the wind cooling effect, the temperature

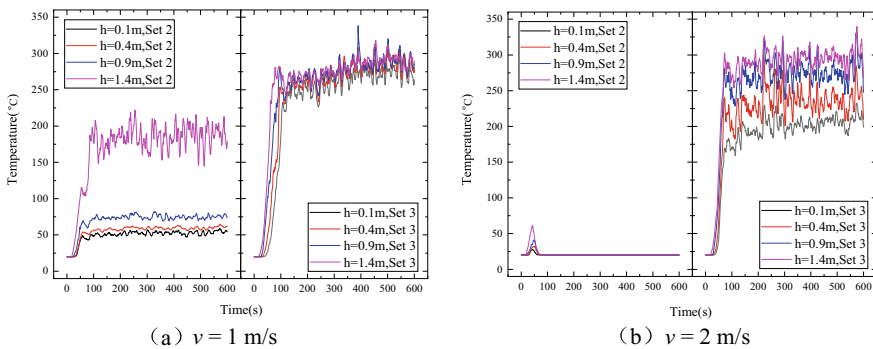


Fig. 3 Temperature change curve in cable tunnel

inside the tunnel decreased slightly. It can be seen from Fig. 3b that under the action of rapid fire in the early stage, the temperature at the upper air outlet reaches the maximum in 50 s. The temperature gradually decreases to normal temperature under the action of wind.

Comparing Fig. 3a, b, it can be observed that the wind speed has a significant impact on temperature. The temperature at the upper air inlet at high wind speed is much lower than that at low wind speed, with a maximum temperature difference of about 60 °C. Furthermore, the maximum temperature at the upper air inlet is only 60 °C under high wind speed, which effectively reduce the loss caused by the spread of fire.

3.2 Gas Variation Situation Analysis

The cable tunnel is equipped with three sets of gas sensors to monitor different gases, which can realize whole-process monitoring of gas cylinder concentration at different positions in the simulation process. Gas concentrations in monitoring Set 1 and monitoring Set 2 at a height of 1.4 m under different wind speeds were analyzed, and the results were shown in Fig. 4.

It can be found that the concentrations of CO and HCl produced under high wind speed conditions are significantly higher than those produced under low wind speed conditions, regardless of whether they are near the fire source. The reason for this phenomenon is that when a fire occurs in the cable tunnel, the high wind speed condition has better ventilation conditions, which leads to better combustion. This leads to more generation of noxious gases in the fire space, leading to higher CO and HCl contents being released. In the case of high wind speed, both gas generation and O₂ consumption at the upwind inlet have little change. The concentration of gas at the upwind inlet differs greatly from that near the fire source. This is because good ventilation conditions under the condition of high wind speed keep the gas concentration at the air inlet relatively stable. At the same time, the firewall has a certain sealing function. Two firewalls can inhibit the diffusion of gas to a certain extent. This makes it difficult for high concentrations of gas to reach the upper tuyere area with low concentrations.

Based on the analysis of Fig. 4c, d, it can be observed that the concentration of CO₂ generated by cable combustion is higher at low wind speed compared to high wind speed, regardless of whether near the fire source or not. The concentration of residual O₂ at low wind speed is lower than that at high wind speed. This is because the good ventilation capacity at high wind speed promotes the gas exchange near the fire source. Even at high wind speeds, more gas is produced and consumed by combustion. However, the residual content of gas in the air during combustion is opposite to the situation of production and consumption. Under the condition of low wind speed at the upwind inlet, the wind cannot completely block the gas exchange inside and outside the firewall. Meanwhile, it can be judged that a complete gas path

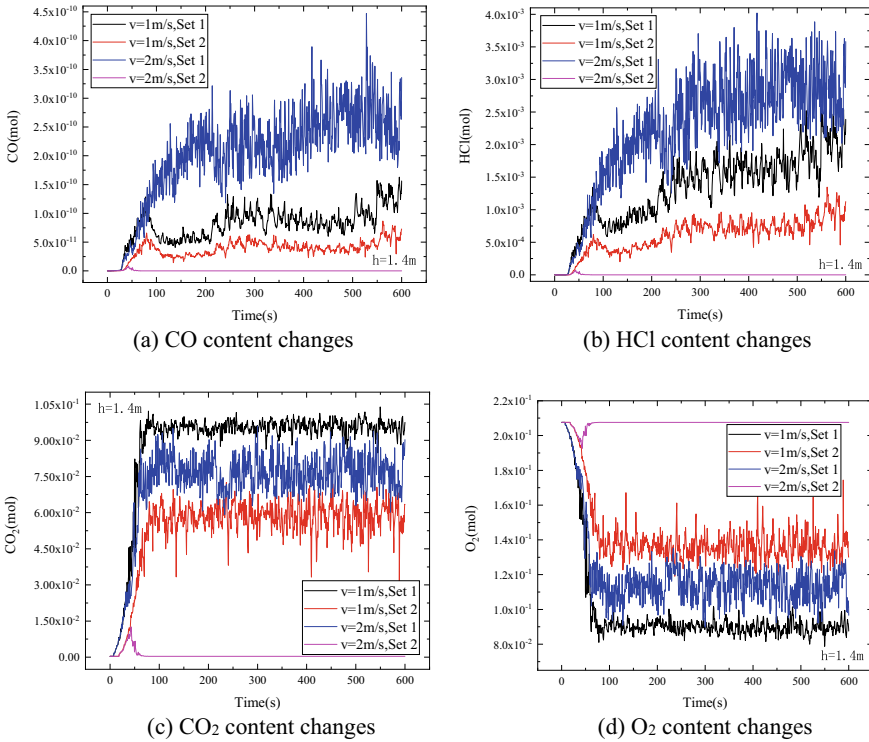


Fig. 4 Change of gas concentration at $h = 1.4$ m

is formed under the condition of high wind speed, so as to ensure the stability of each gas concentration.

After analyzing the gas at different positions, it is evident that there is a clear stratification of noxious gas content in tunnel. The CO concentration at different positions and heights under the condition of low wind speed is taken as an example, and the result is shown in Fig. 5. During the cable combustion process, the concentration of noxious gases such as CO and HCl increases significantly with increasing height, particularly in the vicinity of the upwind opening and the fire source. At the downdraft, the noxious gas concentration is similar. Furthermore, the concentration of CO gas at the downdraft outlet is significantly higher than other locations. This finding has important implications for post-disaster rescue operations in the cable tunnel.

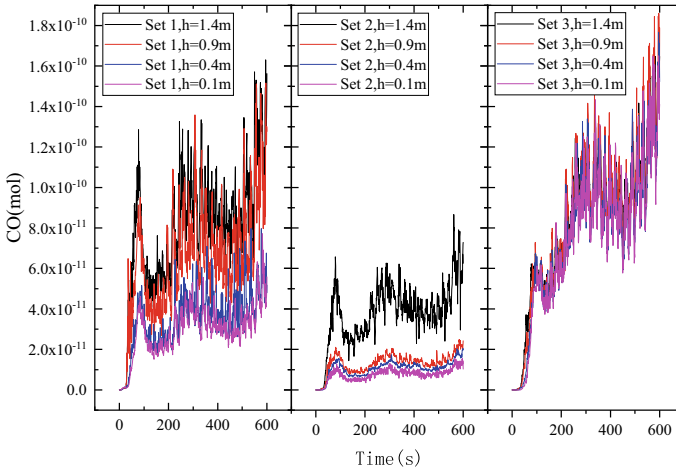


Fig. 5 CO content at $v = 1$ m/s

4 Conclusion

Based on the finite element simulation software, the fire simulation model is established in this paper. The fire spreading in two different wind speed conditions was studied. The distribution of temperature and concentration of CO, HCL, CO₂ and O₂ at different positions in the cable tunnel was obtained. The distribution of gas concentration under two different conditions was compared. The following conclusions were drawn: Wind speed conditions have a significant impact on the development of the fire, with high wind speed promoting its spread. Temperature changes are greatly influenced by wind speed conditions, with high wind speed effectively reducing the temperature of updraft outlet and preventing the fire spreading, thereby minimizing its impact. Different wind speed conditions have influence on the noxious gases content. High wind speed conditions will increase the concentration of harmful gas generation. However, the high wind speed condition can greatly reduce the harmful gas content at the upper air inlet. It can prevent noxious gas from spreading in multiple directions.

References

1. Feng J, Bao GH, Hu LM (2022) Horizontal combustion test apparatus for wire and cable. *Modern Arch Electric* 13(2):15–18+47 (in Chinese)
2. Hu KZ (2021) Comparison and analysis of bundle burning test methods of wire and cable. *Fujian Construct Sci Technol* 178(3):85–87 (in Chinese)
3. Li Y, Wang XH, Wang J (2022) Experimental study on the effect of ZR-KVV cable arrangement number on combustion characteristics. *Fire Safety Sci* 31(2):67–75 (in Chinese)

4. Gao Y, Feng ZL, Xi TP et al (2022) Emission of smoke and its associated PAHs and chloride ion from YJV cable sheath based on Ignition scenarios. *Safety Environ Eng* 29(6):230–239 (in Chinese)
5. Lv L, Duan C, Ji SC et al (2021) Overview of ignition mechanism and combustion characteristic of wire and cable. *High Voltage Eng* 48(2):612–625 (in Chinese)
6. Huang XJ, Wang JK, Zhu H et al (2022) A global model for heat release rate prediction of cable burning on vertical cable tray in different fire scenarios. *Fire Technol* 58(5):3119–3138
7. Zhang H, Yao JX, Zhu H et al (2022) Study on combustion characteristics of cable based on cone calorimeter. *Energies* 15(5):1904
8. Bai Y, Ren XF, Gou RJ (2018) Study on fire prevention of the new fire resisting wall on cable trench. *J Test Measure Technol* 32(1):76–80
9. Xie QY, Gong T, Huang XY (2021) Fire zone diagram of flame-retardant cables: ignition and upward flame spread. *Fire Technol* 57(5):2643–2659
10. Zeng D, Wang Y, Boardman D (2020) Effect of passive protection on fire propagation of electrical cables. *Fire Mater* 45(3):345–354
11. Chen XL, Huang GZ, Gao XH et al (2021) BN-RA: a hybrid model for risk analysis of overload-induced early cable fires. *Appl Sci-Basel* 11(19):8922
12. Li CY, Chen J, Li HZ et al (2019) Experimental research on fire spreading and detection method of underground utility pipe tunnel. *Fire Sci Technol* 38(9):1258–1261 (in Chinese)
13. Li CY, Chen J, Tan X et al (2021) A review of typical fire source simulation methods for cable combustion. *Fire Sci Technol* 40(3):345–351 (in Chinese)

Effects of Insulating Paper Thickness on Space Charge Characteristics in Oil-Impregnated Paper Insulation



Si Fu, Jinzhao Miao, and Zhihui Ma

Abstract Oil-paper insulation is the main form for converter transformers insulation. The space charge characteristics under the action of direct current electric field is obvious in voltage conversion. In order to reveal the physical mechanism of the effect of insulating paper thickness on the space charge characteristics, a bipolar charge transport model is introduced. Three charge transfer processes of trapping, de-trapping and recombination are fully considered in this paper. The effect of insulating paper thickness on space charge characteristics is investigated. The results show the thickness of the insulating paper has a decisive effect on the width of the low-density trap region within the dielectric. Electric field distortion within the dielectric deepens as the thickness of the insulating paper decreases.

Keywords Oil-paper insulation · Space charge characteristics · Bipolar charge transport model · Electric field distortion

1 Introduction

The supply and demand of electric energy show the characteristics of reverse distribution. In recent years, our country has been vigorously developing high-voltage direct current transmission projects, and thus realizing large-scale, long-distance and high-efficiency power transmission [1]. In high-voltage DC transmission projects, high-voltage converter transformers are irreplaceable equipment. Its internal insulation form is a combination of oil and paper composite insulation. Since the degradation of insulation paper causes irreversible performance degradation, insulation paper is the main factor affecting the service life of converter transformers. Space charge characteristics is one of the key issues facing the development of insulating paper and other polymers. It is closely related to the thickness of the insulating paper. The

S. Fu · J. Miao (✉) · Z. Ma
Shenyang University of Technology, Liaoning, China
e-mail: miaojinzhao@smail.sut.edu.cn

© Beijing Paiké Culture Commu. Co., Ltd. 2024
X. Dong and L. Cai (eds.), *The Proceedings of 2023 4th International Symposium on Insulation and Discharge Computation for Power Equipment (IDCOMPU2023)*, Lecture Notes in Electrical Engineering 1100, https://doi.org/10.1007/978-981-99-7393-4_27

existence of space charges will cause serious distortion of the electric field distribution and partial discharge or breakdown of the insulating paper in the transformer [2]. Thus, the existence of space charge makes the characteristics of the insulating paper destroyed and affects the service life of the converter transformer.

Space charge refers to the fact that under the action of DC voltage for a long time, positive and negative charges will be injected from the electrode into the solid dielectric interior. If the positive and negative charges somewhere inside the dielectric cannot completely cancel each other out, the part of the charges are called the space charge at the corresponding position. The space charges of insulating paper and other polymers have two main sources. One is traps formed by impurities inherent and aging in the insulating dielectric. The electrode injected charges under electric field, the traps result in charge accumulation. The other one is positive and negative ions generated by thermal ionization decomposition of impurities in the insulating dielectric, resulting in charge accumulation [3]. The number of space charges formed by thermal ionization of the insulating dielectric is much smaller than the number of charges injected by the electrode, so the space charges formed by thermal ionization are ignored in the simulation.

Existing methods for studying insulating paper with respect to space charge distribution can be divided into two categories: physical experimental methods [4] and numerical simulation methods. The method of physical experiment has some deficiencies. For instance, the aging experiment of insulating paper demands a prolonged experimental period, as well as the accuracy of measurement data cannot be guaranteed. Moreover, it cannot reveal the charge movement process inside the insulating medium directly, and the interaction between various microscopic particles inside the medium cannot be obtained. The numerical simulation method considers the physical processes of charge movement, which includes charge injection, trapping, de-trapping, recombination and migration. It provides an insight into the internal charge transport mechanism of insulating dielectric. Also, it is simpler to change the relevant structures and parameters. It is more intuitive to get the impact regulation of various experimental conditions and dielectric parameters on the space charge characteristics. The numerical simulation results obtained by using software to model bipolar charge transport are in high agreement with the measured results obtained through experiments [5, 6].

In order to investigate the effect of insulating paper thickness on the space charge characteristics of oil paper insulation, it adopts numerical simulation method and bipolar transport model with carriers in this paper. Under the conditions of different thicknesses of insulating paper, it obtains the internal electric field intensity curves and the polarity distribution range characteristics of the internal net space charge density curves of the insulating paper under different pressurization times, respectively.

2 Simulation Method

2.1 Carrier Model

The bipolar carriers transfer process under DC voltage [7, 8] is shown in Fig. 1. It is assumed that the space charges of the insulating paper are all from electrode injection, then the cathode injects mobile electrons and the anode injects mobile holes. The current density of the electrode injected charges can be expressed by Schottky law [6]:

$$J_{e,h}(x, t) = AT^2 \exp\left(-\frac{\varphi_{e,h}}{kT}\right) \exp\left(\frac{q}{kT} \sqrt{\frac{qE_{e,h}(x, t)}{4\pi\epsilon_0\epsilon_r}}\right) \quad (1)$$

With for the Eq. (1), $J_{e,h}(x, t)[A.m^{-2}]$ is the current density of electrons and holes, A is the Richardson constant, $T[K]$ is the temperature, $\varphi_{e,h}[eV]$ is the injection barriers for electrons and holes, q is the elementary charge, $E_{e,h}(x, t)[V.m^{-1}]$ is the electric field, k is the Boltzmann's constant ϵ_0 and ϵ_r are the vacuum permittivity and relative permittivity, respectively.

Where S_0, S_1, S_2 and S_3 are the recombination coefficient of trapped electrons and trapped holes, mobile electrons and trapped holes, trapped electrons and mobile holes, mobile electrons and mobile holes, respectively; B_e and B_h are the coefficients of mobile electrons and mobile holes trapped by deep traps, respectively; D_e and D_h are the de-trapping coefficients of trapped electrons and trapped holes, respectively.

When the numerical simulation method is used to calculate the space charge characteristics, the sum of the changes in the concentration of the various types of carriers inside the insulating paper caused by non-charge conduction transport is considered as the source term and is denoted as S_{ik} ($i = e, h$ is electrons or holes, $k = \mu, t$ is mobile or trapped).The source terms for the four types of carriers are given as follows [9]:

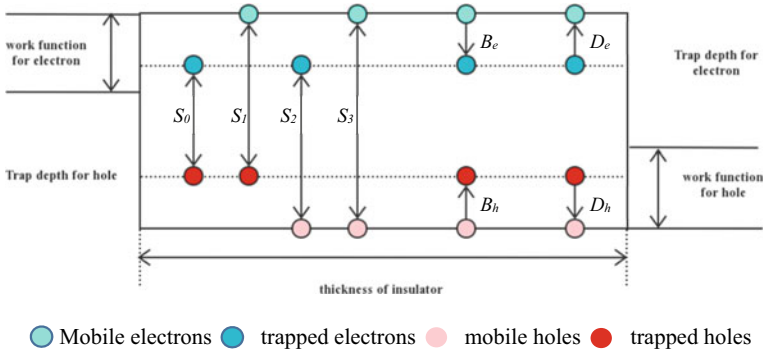


Fig. 1 Movement process of internal carriers

$$S_{e\mu} = \frac{\partial n_{e\mu}}{\partial t} = -B_e n_{e\mu} \left(1 - \frac{n_{et}}{n_{et,0}}\right) + D_e n_{et} - S_1 n_{ht} n_{e\mu} - S_3 n_{h\mu} n_{e\mu} \quad (2)$$

$$S_{et} = \frac{\partial n_{et}}{\partial t} = B_e n_{e\mu} \left(1 - \frac{n_{et}}{n_{et,0}}\right) - D_e n_{et} - S_2 n_{h\mu} n_{et} - S_0 n_{ht} n_{et} \quad (3)$$

$$S_{h\mu} = \frac{\partial n_{h\mu}}{\partial t} = -B_h n_{h\mu} \left(1 - \frac{n_{ht}}{n_{ht,0}}\right) + D_h n_{ht} - S_2 n_{et} n_{h\mu} - S_3 n_{h\mu} n_{e\mu} \quad (4)$$

$$S_{ht} = \frac{\partial n_{ht}}{\partial t} = -B_h n_{h\mu} \left(1 - \frac{n_{ht}}{n_{ht,0}}\right) + D_h n_{ht} - S_2 n_{et} n_{h\mu} - S_3 n_{h\mu} n_{e\mu} \quad (5)$$

With for the Eqs. (2–5), $n_{e\mu}$ is the density of mobile electrons, $n_{h\mu}$ is the density of mobile holes, n_{et} is the density of trapped electrons, n_{ht} is the density of trapped holes; $n_{et,0}$ and $n_{ht,0}$ are the maximum density of electron and hole traps, respectively.

According to the physical process of charge transport, the set of control equations of the bipolar charge transport model can be obtained [10]. Gauss's Law (Poisson's Equation) is used to solve for the overall electric field distribution; Ohm's Law (Transport Equation) is used to solve for the instantaneous current density of carriers when the diffusion process is neglected; and Charge Conservation Law (Conservation Equation) is used to solve for the density of various carriers. The three equations are given as follows:

$$\frac{\partial E(x, t)}{\partial x} = - \frac{(n_{h\mu} + n_{ht} - n_{e\mu} - n_{et})(x, t)}{\varepsilon_0 \varepsilon_r} \quad (6)$$

$$j_{e,h}(x, t) = n_{e,h}(x, t) \mu_{e,h} E(x, t) \quad (7)$$

$$\frac{\partial n_{e,h}(x, t)}{\partial t} + \frac{\partial j_{e,h}(x, t)}{\partial x} = S_{ik}(x, t) \quad (8)$$

With for the Eqs. (6–8), $E[V.m^{-1}]$ is the electric field, $n_{e,h}[C.m^{-3}]$ is the charge density of carriers, $\mu_{e,h}[m^2.V^{-1}.s^{-1}]$ is the mobility of mobile charge, $S_{ik}(x, t)[A.m^{-3}]$ is the source items which contain all the physical processes such as charge trapping, de-trapping and recombination.

2.2 Simulation Setup

This paper studies the space charge distribution in the thickness direction of the insulating paper. Since the insulating paper is a thin film sample, the insulating paper can be simplified to a 1-D spatial structure in the thickness direction. The finite element method is used to solve the bipolar charge transfer model. In this paper, the sample thickness is 1 mm, the maximum cell of the grid is 0.5 μm and the dissection cell is 200. The grid is partially shown in Fig. 2. According to the statistical ranges

of parameters such as charge mobility, complex coefficient, trap density, injection potential barrier, and decoupling rate given in the literature [11], the parameters are shown in Table 1. Since the sample thickness is thin and the DC field effect is more likely to cause the accumulation of space charge inside the sample, the potential at 0 mm is 0 V, the current voltage at 1 mm is 3000 V, and the temperature T is taken as 293 K.

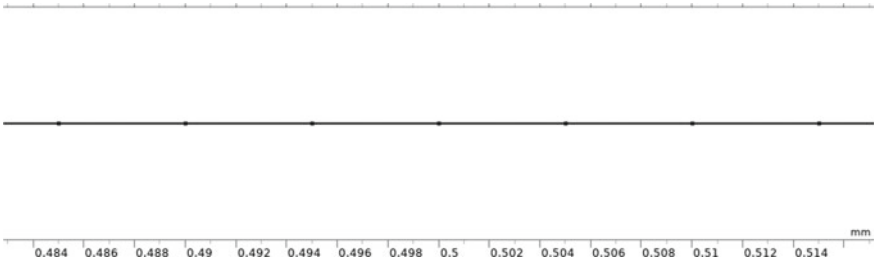


Fig. 2 Partial schematic diagram of grid section

Table 1 Main parameters of the simulation

Name	Expression	Description
U	3[kV]	Direct current voltage
ϵ_r	2.7	Relative dielectric constant
ϵ_0	8.854E-12[F/m]	Vacuum dielectric constant
B_e	0.1[1/s]	Trapping coefficient for electron
B_h	0.1[1/s]	Trapping coefficient for hole
D_e	0.91[eV]	De-trapping coefficient for electron
D_h	0.92[eV]	De-trapping coefficient for hole
Φ_e	1.126[eV]	Injection barriers for electron
Φ_h	1.13[eV]	Injection barriers for hole
μ_e	8E-13[m ² /(V*s)]	Effective mobility for electron
μ_h	4E-13[m ² /(V*s)]	Effective mobility for hole
$n_{et,0}$	100[C/m ³]	Deep trap densities for electron
$n_{ht,0}$	100[C/m ³]	Deep trap densities for hole
S_0	1E-5[m ³ /(s*C)]	Recombination coefficients
S_1	1E-5[m ³ /(s*C)]	Recombination coefficients
S_2	1E-5[m ³ /(s*C)]	Recombination coefficients
S_3	0	Recombination coefficients
F_0	96458[C/mol]	Faraday constant

3 Simulation Result

3.1 Space Charge Characteristics

The parameters in Table 1 and the 1-D model shown in Fig. 2 are used for numerical simulation. The transient potential and internal net charge density of insulating paper at pressure time of 0 min, 10 min, 30 min, 50 min and 60 min are shown in Figs. 3 and 4, respectively.

According to Fig. 3, the space charge characteristic causes polarity and distribution range shift of the potential in the insulating paper at the same time. The polarity offset means that the potential on the cathode side decreases and the potential on the anode side increases. The longer the pressurization time, the more obvious the polarity offset. The distribution range offset means that the potential offset on the cathode side is distributed in the thickness range of about 0~0.73 mm, while the potential offset on the anode side is only distributed in the thickness range of about 0.74~1 mm. The reason is that the potential polarity offset is caused by the pole plate injection into the charges, while the distribution range offset is caused by the different mobility of mobile electrons and mobile holes. Specifically, the decrease of potential near-cathode is caused by the accumulation of mobile electrons in electrode injection, while the increase of potential near-anode is caused by the accumulation of mobile holes in electrode injection. With the increase of pressurization time, the amount of charge injected by the electrode increases, which is expressed as an increase of potential offset. For example, when d is 0.26 mm and the pressurization time is

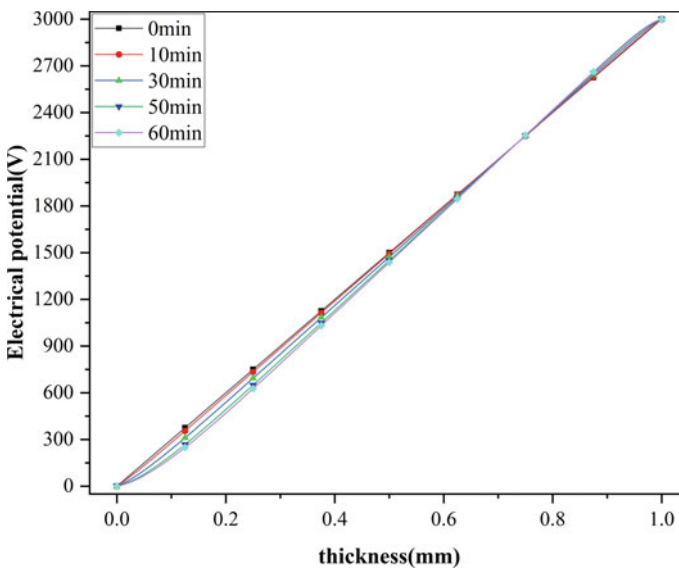


Fig. 3 Electrical potential transient distribution

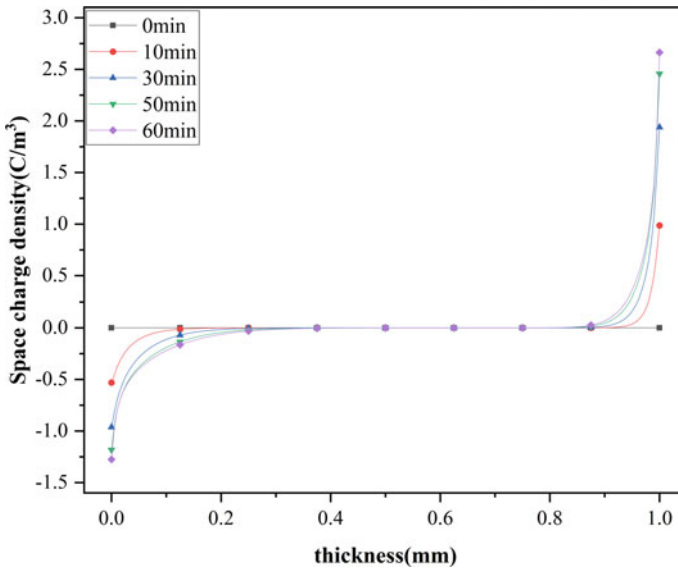


Fig. 4 Distribution of net charge density

increased from 0 to 10 min, 30 min, 50 min and 60 min, the potential decreases from 780 V to 764.5 V, 725 V, 681.4 V and 659.3 V, respectively.

According to Fig. 4, with the increase of the pressurization time, the net charge density of the insulating paper near the electrode side is approximately exponential distribution. The distribution range of the mobile electron density near the cathode side is larger than that of the mobile hole density near the anode side. The reason is that the mobility of mobile electrons is twice as high as the mobility of mobile holes, and the mobility of charge is directly proportional to the distribution range on both sides of the insulating paper. It is proved that the mobility is the main factor causing the asymmetric distribution of space charge and electric field.

3.2 Effect of Thickness on Space Charge

The thickness of the insulating paper was set at 1.2 mm and 0.8 mm, and other parameters were kept constant. The corresponding net space charge density curves are shown in Figs. 5 and 6, respectively.

In order to facilitate the description, the space charge distribution is divided into three parts, negative charge region, zero charge region and positive charge region. According to Figs. 4 and 5, when the thickness of insulating paper is increased from 1 mm to 1.2 mm, the zero charge region increases from 0.369 mm to 0.678 mm. According to Figs. 4 and 6, when the thickness of insulating paper is decreased from 1 mm to 0.8 mm, the zero charge region decreases from 0.369 mm to 0.036 mm. When

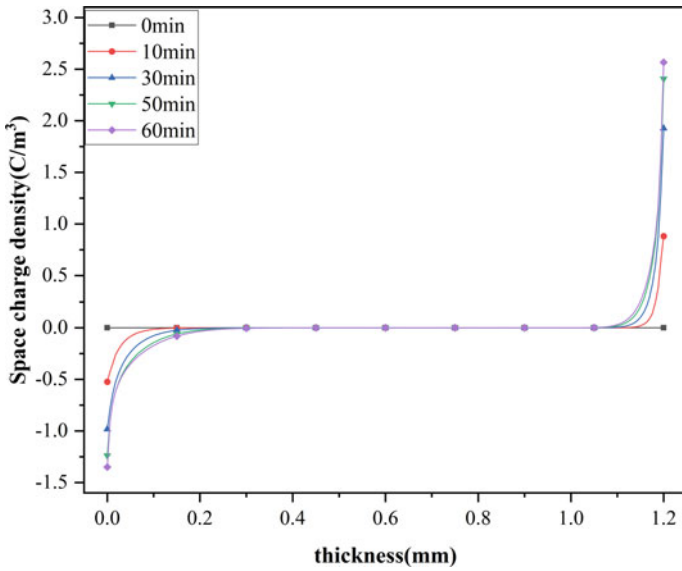


Fig. 5 Net charge density distribution of insulating paper of 1.2 mm thickness

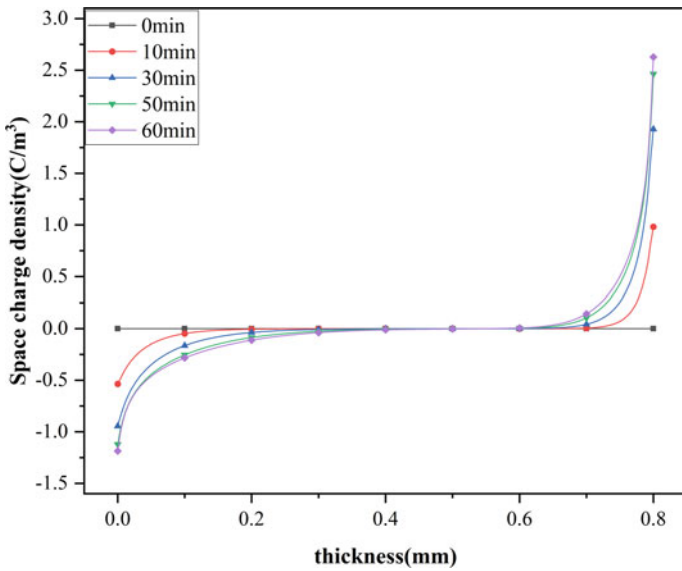


Fig. 6 Net charge density distribution of insulating paper of 0.8 mm thickness

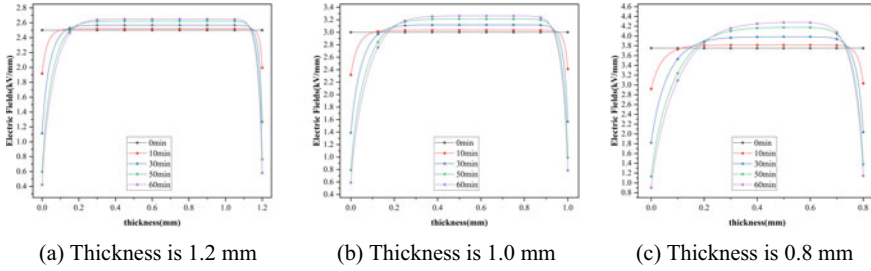


Fig. 7 Electric field intensity distribution inside the insulating paper of thickness 1.2 mm, 1.0 mm and 0.8 mm

the applied voltage time is the same, the slope of the net space charge density curve decreases gradually and the ratio of negative charge region to positive charge region keeps basically constant. The reason is that the trap density on the near electrode side is higher than the intermediate trap density due to the higher electric field strength and temperature on the near electrode side. When the thickness of the insulating paper decreases, it compresses the low trap area in its middle, resulting in an increased degree of electric field distortion inside the dielectric. The electric field strength of different thicknesses of insulating paper is shown in Fig. 7.

In summary, if the insulating paper becomes thinner, the failure rate of the insulating structure will increase due to the space charge characteristics. Further, it affects the service life of the converter transformer.

4 Conclusion

Based on the bipolar charge transport model and the physical processes of mobility, trapping, de-trapping and recombination of carriers such as electrons and holes, it has investigated that the effect of insulation paper thickness inside the converter transformer on the space charge characteristics. There are the following conclusions.

Under DC voltage, it accumulates space charges which has the same polarity as the electrode injection near the electrode side of the insulating paper. It results in a polarity offset of the dielectric instantaneous potential. The different mobility of electron and hole makes the instantaneous potential has a distribution range offset.

The change of insulating paper thickness has little change the polarity offset and distribution range offset of space charge characteristics. However, the low trap region within the dielectric decreases with the decrease of dielectric thickness, and the electric field distortion increases with the decrease of dielectric thickness.

Acknowledgements This work was supported by the Liaoning Provincial Education Department Basic Research Project for Universities (LJKMZ20220513).

References

1. Liu Z, Zhang Q (2013) Study on national grid development model. *Proc CSEE* 33(7):1–10+25 (in Chinese)
2. Matsui K, Tanaka Y, Takada T et al (2005) Space charge behavior in low density polyethylene at pre-breakdown. *IEEE Trans Dielectr Electr Insul* 12(3):406–415
3. Qiu B, He J, Tu D (2010) Mechanism of space charge formation in DC cross-linked polyethylene insulation. *J Insulat Mater* 43(06):39–43 (in Chinese)
4. Zhang Z, Pan J, Lei Q et al (2021) Space charge effects in solid insulating media and applications. *Sci Bull* 66(Z2):3695–3711 (in Chinese)
5. He Y, Wu K, Wu Y et al (2022) Investigation on charge transport model considering the influence of ionized charges. In: 2022 IEEE 4th international conference on dielectrics (ICD), pp 514–517
6. Yeong-II J (2015) Bipolar charge transport model of insulator for HVDC applications. In: COMSOL conference, pp 2–10
7. Le Roy S, Baudoin F, Laurent C et al (2022) Analysis of current-voltage characteristics in insulating polymers using a bipolar charge transport model. *IEEE Trans Dielectr Electr Insul* 29(6):2101–2109
8. Xu X, Gao Y, Li J et al (2021) Numerical simulation on charge transport and DC breakdown in polyethylene-based micro-h-BN/Nano-SiO₂ with filler orientation dependent trap energy. *Energies* 14(15):4645
9. Cai X, Wang X, Pang D et al (2019) Investigation of current density, recombination rate and space charge density in polyethylene thin films based on bipolar charge transport mode. *Mater Res Express* 6(9):096451
10. Le Roy S, Baudoin F, Laurent C, et al (2020) Introduction of ionic contributions to a charge transport model for dielectrics. In: 2020 IEEE 3rd international conference on dielectrics (ICD), pp 509–512
11. Zhong X, Zheng Y, Dang B et al (2016) Polarity effect of polymer space charge distribution under DC electric field. *Proc CSEE* 36(24):6693–6701+6922. (in Chinese)

Preparation and Energy Storage Characteristics of Novel Poly(M-phenylene Isophthalamide) Dielectric Composites



Guangyu Duan, Fengying Hu, Guiyuan Liu, Wenxuan Shao, and Zuming Hu

Abstract Novel polymer-based dielectric composites were prepared by adding core-double-shell structured PDA@TiO₂@BaTiO₃ nanoparticles (PTBP) into Poly(m-phenyleneisophthalamide) (PMIA). In order to suppress the local electric field distortion caused by different dielectric constants and improve the interfacial compatibility between BaTiO₃ (BT) and PMIA, TiO₂ and polydopamine (PDA) were wrapped on BT to fabricate core-double-shell structured PTBP nanoparticles. The obtained results indicate the dielectric constant of PTBP/PMIA dielectric composite obviously increases with increment of PTBP content. When PTBP content reaches up to 10 wt%, the dielectric constant of PTBP/PMIA composite dielectric increases by 57.1% compared with that of as-prepared PMIA at 10³ Hz. The dielectric properties of PTBP/PMIA dielectric composites also maintain stable at high temperature (>150 °C), which is suitable for applications in high-temperature conditions. In addition, PTBP particles significantly improve the energy storage properties of PTBP/PMIA dielectric composites. When the PTBP content is 10 wt%, the maximum values of energy storage density (U_e) and discharge energy density (U_d) are 1.91 J/cm³ and 1.23 J/cm³ at room temperature, respectively, which are 103.2% and 61.8% higher than that of as-prepared PMIA. Consequently, this research provides a new approach to fabricate novel high-temperature polymer-based dielectric composites.

G. Duan (✉) · F. Hu · G. Liu · W. Shao

College of Materials Engineering, Henan University of Engineering, Zhengzhou 450007, China
e-mail: duanguangyu@haue.edu.cn

F. Hu

e-mail: hufengying@haue.edu.cn

G. Liu

e-mail: LGY020712@haue.edu.cn

W. Shao

e-mail: W1963895923@haue.edu.cn

G. Duan · Z. Hu

State Key Laboratory for Modification of Chemical Fibers and Polymer Materials, College of Materials Science and Engineering, Donghua University, Shanghai 201620, China
e-mail: hzm@dhu.edu.cn

© Beijing Paiké Culture Commu. Co., Ltd. 2024

X. Dong and L. Cai (eds.), *The Proceedings of 2023 4th International Symposium on Insulation and Discharge Computation for Power Equipment (IDCOMPU2023)*, Lecture Notes in Electrical Engineering 1100, https://doi.org/10.1007/978-981-99-7393-4_28

293

Keywords PMIA · Barium titanate · TiO_2 · Dielectric · Energy storage property

1 Introduction

To meet the high-temperature requirements of hybrid electric vehicles, oil and gas exploration technologies, and space power systems, aromatic polymers, e.g., polyimide (PI), poly(ether-ether-ketone) (PEEK) and fluorinated polyester (FPE) have been widely utilized to prepare high-temperature polymer-based dielectrics [1, 2]. However, the low dielectric constant and exponentially increasing conductivity loss under high temperature limit the enhancement of energy storage properties of aromatic polymer dielectrics [3].

To enhance the dielectric constant of aromatic polymers, fillers with high dielectric constant, such as barium titanate (BaTiO_3), strontium barium titanate ($\text{Ba}_x\text{Sr}_y\text{TiO}_3$), and strontium titanate (SrTiO_3), have been utilized to achieve the goal [4]. However, the obvious difference of dielectric constants between fillers and polymer always lead to severe electric field distortion at the interface and incur partial breakdown at low electric field [5]. To address this issue, surface modification has been adopted to suppress the local electric field distortion. For example, fillers with high dielectric constant as “core” and low dielectric constant as “shell” have been developed to maintain the high breakdown strength of polymer dielectrics [6].

Besides the dielectric constant and breakdown strength, the leakage current density of polymer dielectrics at high temperature also significantly affects the energy storage properties. As temperature increases, the injection of electrons at electrode/dielectric interface (Schottky conduction) and the thermal excited charge carrier in polymer dielectrics (Poole–Frenkel conduction) both rapidly increase, leading to the remarkable decline of charge–discharge efficiency of polymer dielectric [7]. Consequently, how to effectively suppress the formation of leakage current under high temperature condition is of importance to improve the energy storage performances of polymer dielectrics.

Poly(meta-phenylene isophthalamide) (PMIA) is an aromatic polyamide with exceptional high-temperature resistance, making it capable of stable operation at temperatures up to 200 °C. Hence, for the purpose of preparing high-temperature polymer-based dielectrics, this work employed high dielectric constant BaTiO_3 (BT) nanoparticles as fillers and PMIA as high-temperature polymer. To enhance the interfacial compatibility between fillers and PMIA, and suppress the local electric field distortion, titanium dioxide (TiO_2) and polydopamine (PDA) were wrapped on surface of BT. The effects of PDA@ TiO_2 @BT (PTBP) nanoparticles on dielectric properties, breakdown strength, and energy storage properties of PTBP/PMIA dielectrics were thoroughly investigated.

2 Methods

2.1 Preparation of $\text{TiO}_2@BT$ Nanoparticles

0.5 g of BT nanoparticles were dispersed in 200 mL of anhydrous ethanol under continuous magnetic stirring. Subsequently, 1 mL of triethylamine was added gradually, and followed by sonication for 1 h. The obtained product was denoted as sample A. Simultaneously, 4 mL of tetrabutyl titanate was added to 40 mL of anhydrous ethanol under continuous stirring, and designated as sample B. Finally, sample B was slowly added into sample A under mildly stirring. The TiO_2 layer was formed on surface of BT via the hydrolysis of tetrabutyl titanate, which was catalyzed by triethylamine in an ethanol medium. The resultant precursor solution was filtered and calcined at 550 °C to yield $\text{TiO}_2@BT$ nanoparticles.

2.2 Preparation of $PDA@TiO_2@BT$ Nanoparticles

The poor compatibility between inorganic fillers and polymer can result in migration of space charges under high temperature environments, and leading to high level of conductive loss. Therefore, organic polydopamine (PDA) was employed to adhere to the surface of $\text{TiO}_2@BT$ to improve the interfacial compatibility between $\text{TiO}_2@BT$ nanoparticles and PMIA. Briefly, 1 g of $\text{TiO}_2@BT$ nanoparticles was dispersed in 150 mL of deionized water with ultrasonic treatment. Next, 1.8 g of Tris was added to the dispersion solution, and the pH was adjusted to 8.5 by HCl. Finally, 0.3 g of dopamine hydrochloride was added, and the mixture was stirred for 6 h at room temperature. After the reaction, the modified $\text{TiO}_2@BT$ nanoparticles were centrifuged and washed with deionized water and ethanol several times to obtain $PDA@TiO_2@BT$ (PTBP) nanoparticles.

2.3 Preparation of PTBP/PMIA Films

The PTBP/PMIA films were prepared via solution-casting approach. Initially, a certain amount of PTBP nanoparticles was dispersed in DMAc through ultrasonication for 1 h. The obtained PTBP dispersion was added to PMIA solution, and the solid content of PMIA solution was diluted from 18.5% to 14%. Subsequently, the PTBP/PMIA solution was slowly cast onto clean glass sheets to manufacture PTBP/PMIA films. To completely remove the solvent, the PTBP/PMIA films were dried at 100 °C for 12 h, and then transferred to a vacuum oven at 80 °C for 24 h. The thickness of prepared PTBP/PMIA film was approximately 50 μm , and the PTBP content varied from 0 wt%, 3 wt%, 5 wt%, 7 wt% to 10 wt%. Additionally, the prepared films were denoted as PTBP-0, PTBP-3, PTBP-5, PTBP-7, and PTBP-10

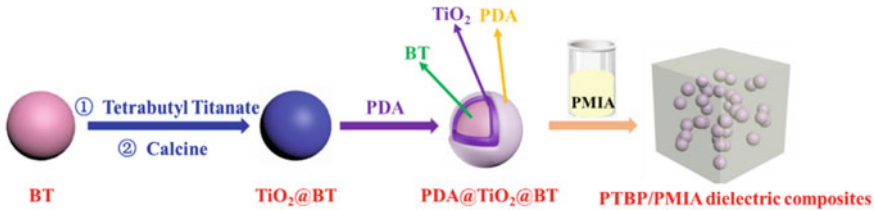


Fig. 1 The schematic illustration for preparation of PTBP/PMIA dielectric composites

based on the content of PTBP. The schematic illustration for preparation of PTBP/PMIA films is illustrated in Fig. 1.

3 Results and Discussion

3.1 Morphologies of Samples

The morphologies of BT, TiO_2 @BT, PTBP and PTBP/PMIA dielectric composites are illustrated in Fig. 2. It is displayed that the TiO_2 @BT (Fig. 2b) and PTBP (Fig. 2c) nanoparticles exhibit comparable morphologies to BT (Fig. 2a). In Fig. 2d, the PTBP nanoparticles show distinct double core-shell structure with PDA layer of approximate 3 nm and TiO_2 layer of around 8 nm. PDA is beneficial to reducing the surface energy of TiO_2 @BT nanoparticles and inhibiting the formation of agglomerations in PMIA, which contributes to enhancing the interfacial compatibility between PTBP nanoparticles and PMIA. The smooth and flat cross-section of PTBP-0 can be seen in Fig. 2f, while the cross-section of PTBP-10 (Fig. 2e) is rougher than that of PTBP-0. Moreover, the PTBP nanoparticles are tightly embedded in PMIA and uniformly distributed, which is favorable for suppressing the dielectric loss of PTBP/PMIA dielectric composites and improving the energy storage properties.

3.2 Dielectric Properties of Samples

The dielectric properties of PTBP/PMIA dielectric composites were evaluated in the frequency range of 10^2 Hz to 10^6 Hz. It is seen from Fig. 3a that the dielectric constant distinctly increases with increasing PTBP content. Specifically, the dielectric constant of PTBP-10 was 57.1% higher than that of PTBP-0 at 10^3 Hz. This improvement can be attributed to following factors: firstly, the high dielectric constant of PTBP nanoparticles is conducive to promoting the dielectric constant of PTBP/PMIA dielectric composites. Secondly, the double core-shell structure of

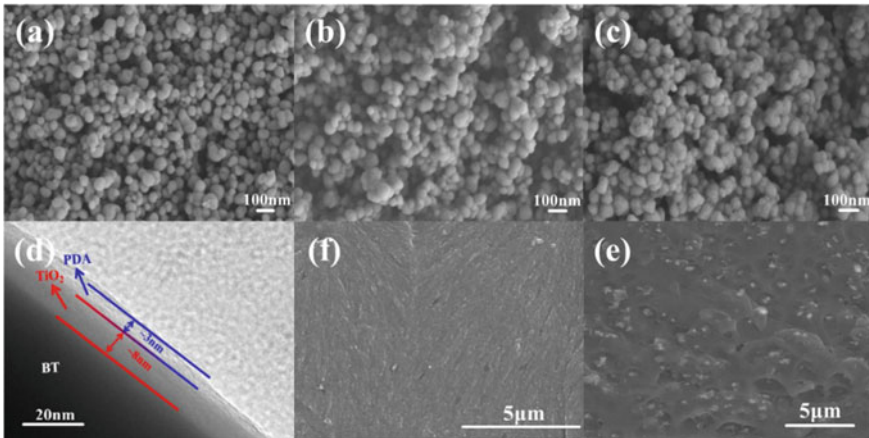


Fig. 2 Morphologies of a BT, b TiO₂@BT, c and d PTBP, e PTBP-0, f PTBP-10

PTBP nanoparticles facilitate the Maxwell–Wagner–Sillars(MWS) interfacial polarization, thus enhancing the dielectric constant of PTBP/PMIA dielectric composites. Additionally, the presence of PTBP nanoparticles are beneficial to enhancing the stability of dielectric constant in the tested frequency range. For instance, the variation rate of PTBP-0 between 10² and 10⁶ Hz is 14.6%, while PTBP-10 exhibits a variation rate of only 8.1% under the same condition.

Dielectric loss of PTBP/PMIA dielectric composite converts the stored electrical energy into joule heat, which not only reduces the charge–discharge efficiency of dielectric capacitors, but also creates thermal effect that cause local breakdown [8]. Hence, suppressing the dielectric loss of polymer dielectric is crucial to improve the energy storage properties. In Fig. 3b, the dielectric losses of PTBP/PMIA dielectric composites were analyzed in the frequency range of 10²–10⁶ Hz. It can be observed that the dielectric loss of PTBP/PMIA dielectric composite slightly increases with increasing content of PTBP in the range of 10²–10³ Hz. This phenomenon is attributed to the difference of conductivity between TiO₂ and BT, resulting in a large number of electrons accumulating at the interface. However, with increasing frequency, the dielectric loss of PTBP/PMIA dielectric composite decreases rapidly,

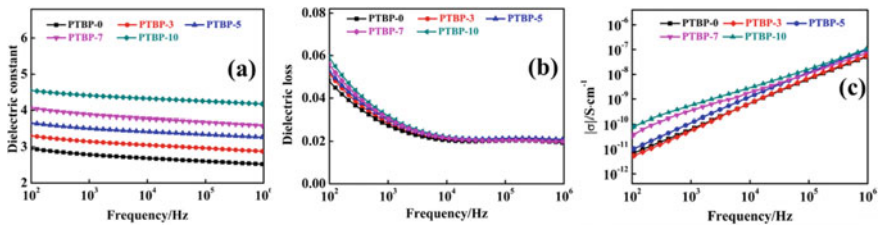


Fig. 3 Dielectric properties of samples

this can be explained by the smaller effect of interfacial polarization and conductivity on dielectric loss at higher frequency region. Furthermore, the dielectric losses of prepared PTBP/PMIA dielectric composites are lower than 0.06 in the tested frequency range, which is capable of meeting the requirement of polymer-based dielectric capacitor.

The conductivities of PTBP/PMIA dielectric composites are depicted as a function of frequency in Fig. 3c. The results reveal a nearly linear relationship between the conductivity and frequency, indicative of good insulation performance of PTBP/PMIA dielectric composites. However, with increasing content of PTBP, the insulation performance of PTBP/PMIA dielectric composite gradually deteriorates. For instance, at 10^2 Hz, the conductivity of PTBP-0 is 6.7×10^{12} ($\text{S} \cdot \text{cm}^{-1}$), while that of PTBP-10 increases to 5.3×10^{12} ($\text{S} \cdot \text{cm}^{-1}$). This behavior can be ascribed to the reason that, at low PTBP content, the PTBP nanoparticles can uniformly dispersed in PMIA, which hinders the mobility of interface carriers and space charges. Nevertheless, when PTBP content exceeds 7 wt%, PTBP nanoparticles tend to contact with each other and leading to the formation of conductive pathways [9].

3.3 Breakdown Strength of Samples

It is known that the breakdown strength is a crucial parameter for evaluating the energy storage properties of polymer dielectrics [10]. Therefore, the Weibull distribution was employed to model the breakdown strength of PTBP/PMIA dielectric composites. Equation (1) is utilized to calculate the Weibull distribution, where $P(E)$ represents the probability of breakdown, E is the breakdown strength of the sample, E_b is the Weibull breakdown strength when the probability of breakdown is 63.2%, and β is the Weibull parameter. A higher β value indicates greater reliability of the numerical breakdown strength.

$$P(E) = 1 - \exp\left[-\left(\frac{E}{E_b}\right)^\beta\right] \quad (1)$$

Equation (2) is employed to compute the corresponding $P(E)$ for each measured breakdown strength E , where i is the rank of measured breakdown strength values in ascending order, and n is the total number of tests for each sample. To achieve more precise Weibull breakdown strength, each sample underwent 7 tests. The fitting results and Weibull breakdown strengths of samples are displayed in Fig. 4.

$$P_i = \frac{i - 0.44}{n + 0.25} \quad (2)$$

Figure 4a shows that the Weibull breakdown strength of PTBP/PMIA dielectric composite gradually decreases with increment of PTBP fillers. It is seen from Fig. 4b

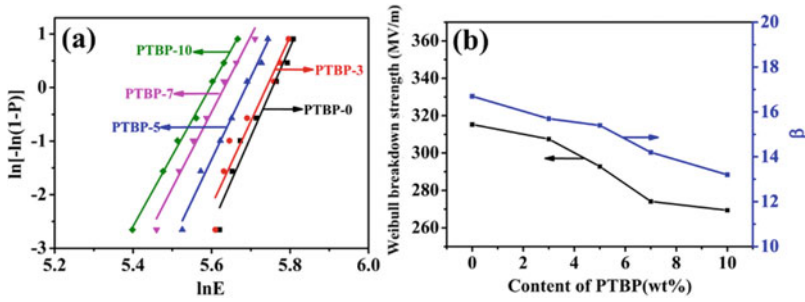


Fig. 4 Breakdown strength of samples

that the Weibull breakdown strength decreases from 315.3 MV/m (PTBP-0) to 269.4 MV/m (PTBP-10), the Weibull distribution parameter also decreases from 16.7 to 13.2 simultaneously. These outcomes imply that, although TiO_2 and PDA contribute to inhibiting the electric field distortion at the interface between PTBP and PMIA, the increase of inner defect and leakage current result in decline of breakdown strength of PTBP/PMIA dielectric composites.

3.4 Energy Storage Properties of Samples

Figure 5a–c present the hysteresis loops and polarization characteristics of PTBP-0, PTBP-5 and PTBP-10, respectively. The results exhibit that the maximum polarization of dielectric composite increases with increasing PTBP content. Specifically, the maximum polarization values of PTBP-5 and PTBP-10 increase by 68.8% and 90.1% at room temperature, respectively, compared with PTBP-0. The obvious enhancement can be attributed to the dual-core-shell structure of PTBP nanoparticles that significantly strengthens the interfacial polarization [11]. Furthermore, the high dielectric constant of BT nanoparticles further improves the maximum polarization of PTBP/PMIA dielectric composites. The improvement of polarization is expected to increase the energy storage density of PTBP/PMIA dielectric composites. Figure 5d, e display the effective polarization of PTBP/PMIA dielectric composites. Obviously, the difference value between P_{\max} and P_r increases with increment of PTBP content, indicating that the discharge energy density of PTBP/PMIA dielectric composite also increases [12]. The energy storage properties of samples are presented in Fig. 5f–h. It is seen that the energy storage density (U_e) and discharge energy density (U_d) of PTBP/PMIA dielectric composites gradually increase with increasing electric field. The U_e and U_d of PTBP-10 are 1.91 J/cm^3 and 1.23 J/cm^3 at electric field of 250 MV/m, respectively, which are 103.2% and 61.8% higher than those of PTBP-0. The outcomes indicate that PTBP nanoparticles can effectively enhance the energy storage properties of PTBP/PMIA dielectric composites. Additionally, the charge–discharge efficiency (η) of PTBP/PMIA dielectric composites gradually decrease

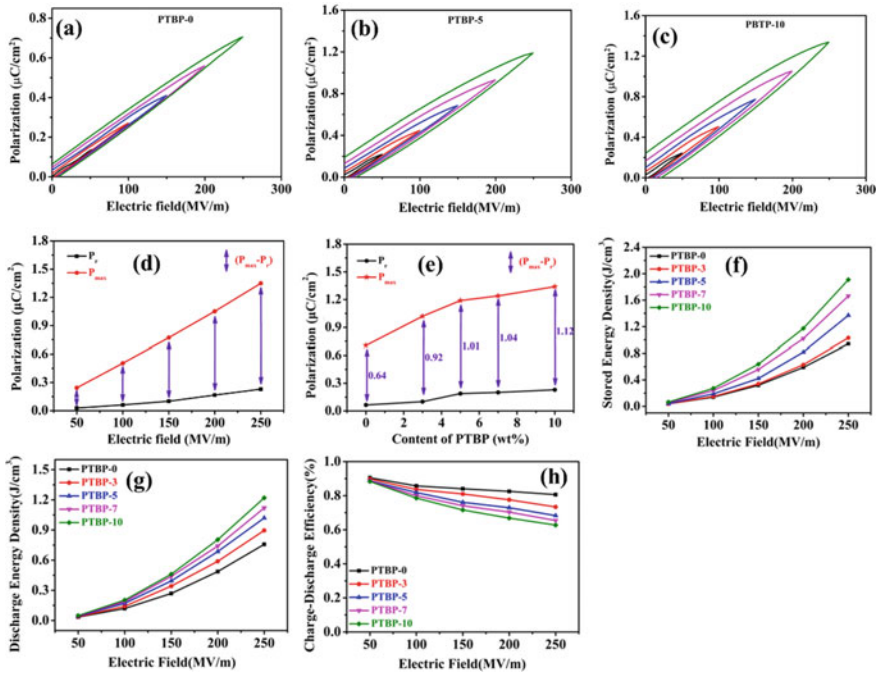


Fig. 5 Energy storage properties of samples

with increasing electric field. This can be ascribed to the increased leakage current in PTBP/PMIA dielectric composites under high electric fields, which incurs the stored energy converts into heat [13]. Nevertheless, it is worth noting that the η of prepared PTBP/PMIA dielectric composites are all above 60% under high electric fields.

4 Conclusion

In this paper, novel high-temperature PTBP/PMIA dielectric composites were successfully fabricated. The results displayed that the dielectric constant of PTBP/PMIA dielectric composites obviously increase with increasing content of PTBP nanoparticles, and the dielectric loss maintained low values. Owing to the increment of inner defects and leakage current, the breakdown strength of PTBP/PMIA dielectric composite decreased slightly. Moreover, the energy storage density (U_e) and discharge energy density (U_d) of PTBP/PMIA dielectric composites gradually increase with increasing content of PTBP. The U_e and U_d of PTBP-10 are 1.91 J/cm³ and 1.23 J/cm³ at 250 MV/m, respectively, which are 103.2% and 61.8%

higher than those of PTBP-0. These consequences indicate that PTBP nanoparticles can effectively enhance the energy storage properties of PTBP/PMIA dielectric composites.

Acknowledgements This research was financially supported by Science and Technology Project of Henan Province (222102240033) and Foundation for Doctorate Research of Henan University of Engineering (D2021009).

References

1. Li H, Zhou Y, Liu Y et al (2021) Dielectric polymers for high-temperature capacitive energy storage. *Chem Soc Rev* 50(11):6369–6400
2. Yuan C, Zhou Y, Zhu Y et al (2020) Polymer/molecular semiconductor all-organic composites for high-temperature dielectric energy storage. *Nat Commun* 11(1):3919
3. Feng Q, Zhong S, Pei J et al (2021) Recent progress and future prospects on all-organic polymer dielectrics for energy storage capacitors. *Chem Rev* 122(3):3820–3878
4. Wu X, Chen X, Zhang Q et al (2022) Advanced dielectric polymers for energy storage. *Energy Storage Mater* 44:29–47
5. Huang X, Sun B, Zhu Y et al (2019) High-k polymer nanocomposites with 1D filler for dielectric and energy storage applications. *Prog Mater Sci* 100:187–225
6. Wang P, Zhou D, Guo H et al (2020) Ultrahigh enhancement rate of the energy density of flexible polymer nanocomposites using core-shell BaTiO₃@MgO structures as the filler. *J Mater Chem A* 8(22):11124–11132
7. Zhou Y, Wang Q (2020) Advanced polymer dielectrics for high temperature capacitive energy storage. *J Appl Phys* 127(24):240902
8. Duan G, Hu F, Xin Z et al (2022) High-temperature PMIA dielectric composites with enhanced thermal conductivity utilizing functionalized BaTiO₃ nanowires-carbon nanotubes fillers. *High Perform Polym* 34(1):54–65
9. Hu J, Zhang S, Tang B (2021) 2D filler-reinforced polymer nanocomposite dielectrics for high-k dielectric and energy storage applications. *Energy Storage Mater* 34:260–281
10. Duan G, Cao Y, Quan J et al (2020) Bioinspired construction of BN@polydopamine@Al₂O₃ fillers for preparation of a polyimide dielectric composite with enhanced thermal conductivity and breakdown strength. *J Mater Sci* 55:8170–8184
11. Zhou W, Cao G, Yuan M et al (2023) Core-shell engineering of conductive fillers toward enhanced dielectric properties: a universal polarization mechanism in polymer conductor composites. *Adv Mater* 35(2):2207829
12. Dong J, Hu R, Xu X et al (2021) A facile in situ surface-functionalization approach to scalable laminated high-temperature polymer dielectrics with ultrahigh capacitive performance. *Adv Func Mater* 31(32):2102644
13. Lin Y, Zhang Y, Sun C et al (2020) Energy storage performance in polymer dielectrics by introducing 2D SrBi₄Ti₄O₁₅ nanosheets. *Ceram Int* 46(10):15270–15275

The Roof Cable Terminal Simulation Calculation Study Based on Electric-Thermal Coupling Physical Field



Xuefei Li, Liankang Zhang, Jingbing Wang, Jiaying Wang, and Guochang Li

Abstract The roof cable accessories of the motor train unit are affected by various factors such as electricity, heat and airflow. Conducting simulation and calculation research based on electric-thermal coupled can effectively guide product development. Also, it can provide technical support for product fault operation and maintenance. The electrothermal coupled simulation model of roof cable terminal is established. The electric field distribution and temperature field distribution of the cable terminal at room temperature and the influence of ambient temperature on the electric-temperature field are studied respectively. The simulation shows that the change of terminal electric field caused by temperature is not significant, and the maximum distortion point occurs at the triple junction point, which is 4.54 kV/mm. The electric field is mainly distributed at the main insulation of the cable, and the electric field strength is 4.10 kV/mm. At steady state, the maximum temperature near the wire core is 47.0 °C. The temperature of the insulating layer decreases in a gradient from the inside to the outside. The temperature of the umbrella skirt part was 26.2 °C. In addition, the ambient temperature has a large impact on the temperature distribution at the terminals. Temperature differences and differences in the thermal conductivity of different materials can create temperature gradients inside the terminals. The change in the internal electric field of the terminal due to temperature change is small in comparison. The work is a guideline for the design and fault analysis of roof cable terminals for motor train units.

Keywords Motor train unit · Cable terminal · Electric-thermal coupled · Electric field simulation

X. Li
CRRC Changchun Railway Vehicles.Co., Ltd, Changchun, China

L. Zhang · G. Li (✉)
Institute of Advanced Electrical Materials, Qingdao University of Science and Technology,
Qingdao, China
e-mail: Lgc@qust.edu.cn

J. Wang · J. Wang
CRRC Qingdao Sifang Rolling Stock Research Institute Co., Ltd, Qingdao, China

1 Introduction

In recent years, the fast development of railway has not only put forward more stringent requirements for the power supply system of motor train unit, but also tested the safety and reliability of the electrical equipment of bullet trains [1]. As a weak link in the transmission and distribution system of the motor train unit, the roof high voltage cable terminal is demanded with good electrical insulation performance and environmental resistance [2–4]. The operating conditions of the roof cable terminal are very complex. The high-speed airflow from train operation, the temperature difference formed by the geographical difference between the north and the south, the moisture and water from rain, snow and ice, as well as the harmonic interference and switching overvoltage caused by train vibration will all affect the overall insulation performance of the high-voltage terminal [5–8]. In the process of locomotive operation, if the heat-shrinkable insulation sleeve of the cable terminal fails, the safe operation at the locomotive will be seriously affected.

At present, scholars have carried many studies on the fault problem at cables through experiments and simulations. Zhu Lin [9] conducted the electric field simulation analysis in the presence of air gap at the cable terminal, and the results showed that air gap is an important reason for the discharge of cable terminal. Illias [10] in Canada found that when the interior contains defects, the electric field distortion at the defects is much greater than the electric field strength in the surrounding area. Clabburn [11] found that too high or too low impedance of stress control tube can cause discharge breakdown of the insulation structure, indirectly revealing the importance of the dielectric parameters of the stress control tube.

The research work of high-voltage system of motor train unit mainly focuses on the numerical analysis about the electric field of insulation structure of cable terminal under various flaws, analysis of material insulation characteristics, etc. All these studies provide the basis for optimal design of terminal structure and upgrading of terminal insulation level. The simulation of roof cable accessories is an important guide for the design and operation maintenance of new products.

In this paper, the physical model of high-voltage cable terminal is established according to the size and material properties about the roof terminal. Calculate the electric field distribution and temperature field distribution inside the high-voltage terminal at room temperature. The temperature field distribution and electric field distribution of the terminal at different ambient temperatures are further discussed.

2 Simulation Calculation Model Construction

As shown in Fig. 1, set the air pressure to standard atmospheric pressure, and establish the two-dimensional geometric model of the cable terminal. The cable terminal electric field simulation uses the finite element method, and the electric field distribution

follows the Poisson equation of the electric field. When the size of the power equipment is much less than one tenth of the wave length, the electric field can be approximated as an electrostatic field [12]. In this paper, the internal electric fields of high-voltage terminals are treated as electrostatic fields. Physical field boundary conditions and material performance parameters are set according to the actual environment and material properties about the terminal.

The losses during cable operation are mainly conducted in the form of heat, when current flows through the cable and the cable core conductors heat up. According to Ohm law, and to neglect the heat loss in the cable conductor, we can get the heat generation per unit length of cable core as $S = I^2R$ [13].

The effective resistance R per unit length of wire core can be calculated by the following formula:

$$R = R_0[1 + \alpha_{25}(T - 25)] \tag{1}$$

In the formula: R is the resistance at temperature T ; R_0 is the resistance of the wire core at 25 °C; α_{25} is the resistance temperature coefficient at 25 °C.

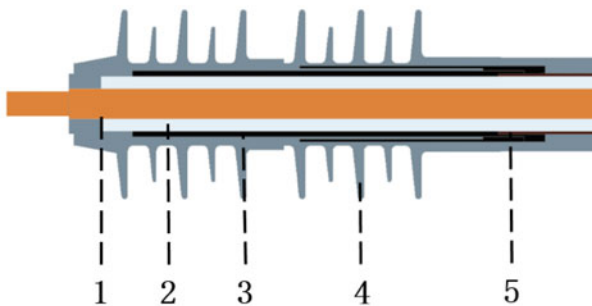
The heat production of a conductor over a period of time can be calculated using Eq. (2):

$$Q = I^2 R t \tag{2}$$

In the formula, Q is the heat production of the line core; I is the current through the cable core; R is the core resistance value; t is the time when the cable is put into operation.

The temperature distribution of the terminal is obtained using Poisson equation for heat conduction [14, 15], and the specific calculation process is as follows:

$$\frac{\partial^2 T}{\partial x^2} + \frac{\partial^2 T}{\partial y^2} + \frac{\phi}{\lambda} = 0 \tag{3}$$



1.copper core; 2. cable insulation; 3.stress control tube; 4.umbrella skirt; 5.semiconducting

Fig.1 Cable terminal geometry model

In the formula, T is the terminal temperature; Φ is the heat producing power; λ is the thermal conductivity of the material.

The cable terminal electric field distribution is obtained using Poisson equation for the electrostatic field, and the second-order Poisson equation for the potential is shown in Eq. 5. The gradient of the electric potential is the magnitude of the electric field. The electric field in cable insulation and casing insulation is inversely proportional to the relative dielectric constant magnitude. The relative dielectric constant of the material used in the calculation is determined by the results of the temperature field distribution combined with experimental data.

$$\nabla^2\phi = -\frac{\rho}{\varepsilon} \quad (4)$$

$$\varepsilon_1 E_1 = \varepsilon_2 E_2 \quad (5)$$

In the formula, ε_1 and ε_2 are the relative dielectric constants of the cable insulation and casing insulation, respectively; E_1 and E_2 are the electric fields inside the cable insulation and casing insulation, respectively.

3 Calculation Results and Analysis

3.1 *Electric Field Distribution of High Voltage Cable Terminals*

In order to evaluate the insulation capability of the high-voltage terminal, a physical field simulation model is established based on the terminal operating conditions and material insulation characteristics. According to the actual operating conditions of the cable terminal on the roof of motor train unit, the voltage is set to 27.5 kV frequency AC, and the simulation current is set to 300 A. The metal shield and outer sheath of the cable are grounded, and the ambient temperature is 25 °C. The potential distribution and electric field distribution of the roof high voltage cable terminal are calculated. The calculation results are shown in Figs. 2 and 3.

The terminal electric potential distribution is shown in Fig. 2. The electric potential of the conductor at the cable termination is 27.5 kV, and the electric potential shows a gradient distribution along the radial direction of the termination. The electric potential contour line are more dense near the cable insulation and stress control tubes. The stress control tube causes the electric potential lines near the break in the semi-conducting shield of the cable to tend to diverge, reducing the electric field distribution inside the nearby insulation. The terminal umbrella skirt electric potential gradually decreases from the top to the bottom, but the contour line density gradually increases.

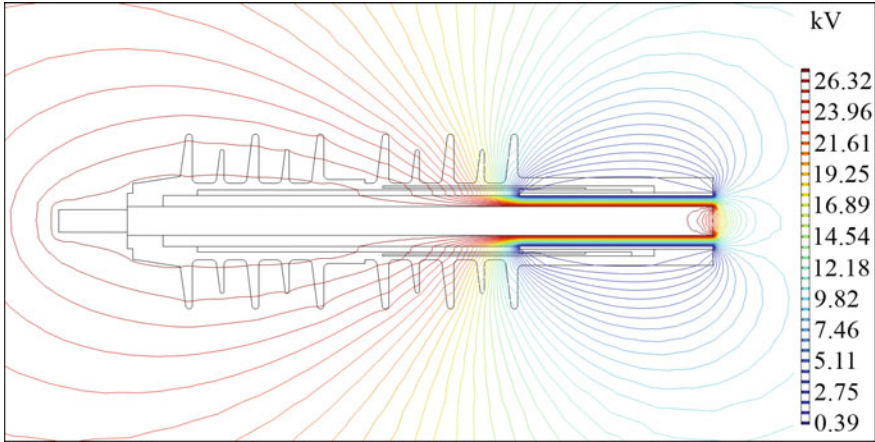


Fig. 2 Cable terminals potential change

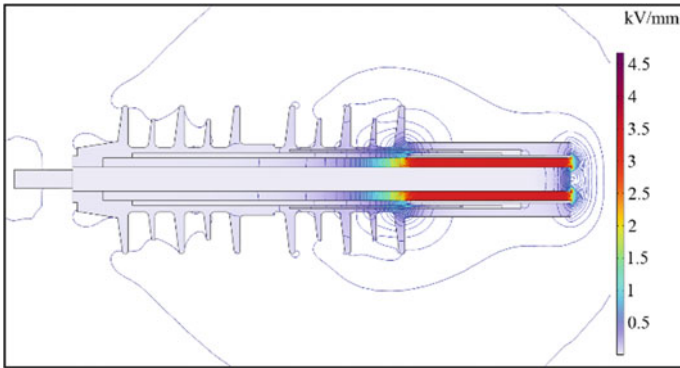


Fig. 3 Cable terminals electric field changes

The electric field distribution of the cable terminal is shown in Fig. 3. Combined with the analysis of the cable terminal electric potential distribution diagram, the electric field is mainly concentrated in the insulating layer, which is about 3.4 kV. The location of the maximum electric field distortion at the terminal is located at the combination of semiconducting, insulating layer and stress control tube. The electric field strength at this location is 4.54 kV/mm, which is the most vulnerable position of the transmission and distribution system of the motor train unit.

Based on the results of the electric field distribution at the terminal, a coordinate system is established along the radial direction of the cable terminal. Taking the copper core center of the cable as the coordinate origin, the electric field distribution along the diameter direction of the terminal is obtained. As shown in Fig. 4, the copper core, the cable insulation, the cable shield, the stress control tube and the umbrella skirt are shown from the origin of the coordinates to both sides. From the figure, it

Fig. 4 Radial electric field distribution at cable terminals

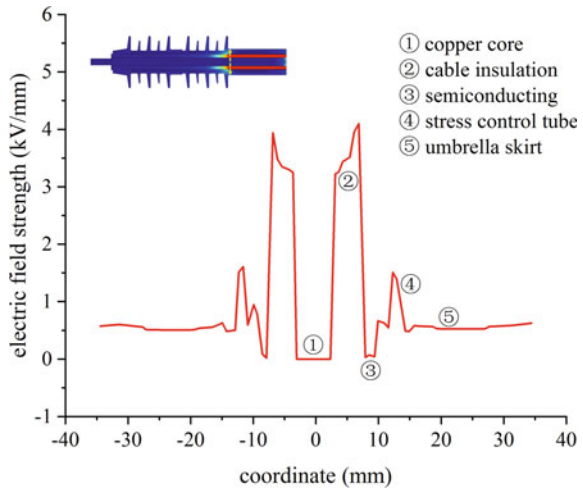


Table 1 Maximum electric field in different areas

Location	Major insulation	Stress control tube	Umbrella skirt
Electric field strength (kV/mm)	4.10	1.94	0.76

can be seen that the electric field strength in the copper core is close to zero. This is because the copper core is a conductor, the dielectric constant is very large, so the electric field strength is close to zero. The location of the most serious electric field distortion is mainly distributed in the junction of insulating layer, semiconducting, and stress tube, semiconducting and stress tube junction. The electric field strength of the distortion is 4.10 kV/mm and 1.51 kV/mm, respectively.

The maximum electric fields in different areas of the cable terminals are shown in Table 1. From Table 1, it can be seen that the maximum electric field of the cable main insulation and stress tube is located at the three bonding points, and the electric field strength is 4.10 kV/mm and 1.94 kV/mm respectively. The maximum electric field of the umbrella skirt is located at the bottom umbrella skirt, and the maximum electric field strength of the umbrella skirt is 0.76 kV/mm.

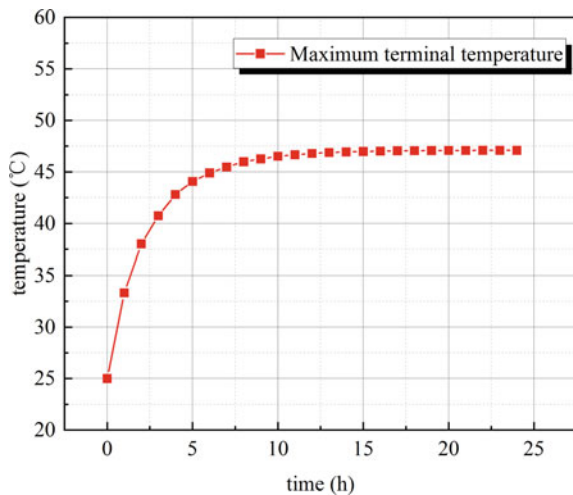
3.2 Temperature Field Distribution of High-Voltage Cable Accessories

Under the action of the cable core for a long time, the continuous high temperature overheating phenomenon easily leads to the aging modification of the internal components of the terminal, and suffers irreversible aging damage. The electrical and mechanical characteristics of the cable deteriorate continuously, leading to a

sharp decline in the overall insulation performance of the terminal, which seriously threatens the safe operation of the motor train unit. According to the actual situation of operation, the simulation results of the cable terminal temperature field are shown in Fig. 5. The maximum temperature of the cable terminal gradually increases with the increase of the operating time and reaches stability around 15 h. The maximum terminal temperature at stabilization is about 47.0 °C.

The internal electric-thermal field distribution of the cable terminal under room temperature operation is calculated by simulation, as can be seen from Fig. 7. As can be seen from the graph, the temperature maximum is located in the core part of the cable, with a maximum value of 47.0 °C. The temperature distribution at the cable core is uniform. The temperature of the insulating layer decreases in a gradient from inside to outside, with a temperature of 46.3 °C at the position close to the copper core and 43.4 °C at the other side. The minimum temperature is 26.2 °C in the umbrella skirt. It can be seen that the temperature of each layer inside the terminal decreases gradually with the increase of radial distance. This is the result of the diffusion of the heat flow generated by the heat source to the outer layers. The closer the material is to the heat source, the less heat is lost and the higher the temperature generated. The farther the material is from the heat source, the greater the heat loss and the lower the temperature generated.

Fig. 5 Maximum temperature change at cable terminals



3.3 Effects of Ambient Temperature on the Electrical-Temperature Field of the Cable Terminal

The high voltage cable terminals are installed in the high voltage box. The temperature inside the box is influenced by the combination of the internal electrical equipment and the external natural environment. During actual operation, the temperature inside the high pressure box can reach 50°C. The high voltage terminals operate not only with the geographical temperature difference between the north and the south in a day, but also with the huge natural temperature difference generated by different seasons. Under the action of high electric fields and extreme temperatures, insulation materials can deteriorate or degrade, leading to potential discharge and breakdown risks in roof-top high-voltage terminals [16].

Set the environmental conditions by extreme weather and calculate the temperature distribution of cable terminals after a period of operation at ambient temperatures of $-30\text{ }^{\circ}\text{C}$, $25\text{ }^{\circ}\text{C}$ and $50\text{ }^{\circ}\text{C}$. The calculation results are shown in Figs. 7 and 8.

As can be seen from Fig. 7, when the ambient temperature is $-30\text{ }^{\circ}\text{C}$, the lowest point of cable terminal temperature is near the umbrella skirt, and its value is $-27.1\text{ }^{\circ}\text{C}$. Influenced by the ambient temperature, the temperature is lower near the air part. The innermost mandrel can reach a maximum temperature of $1.68\text{ }^{\circ}\text{C}$ in low-temperature environments. As shown in Fig. 6, the minimum temperature of the cable termination at room temperature is $26.2\text{ }^{\circ}\text{C}$ near the umbrella skirt and the maximum temperature is $47.0\text{ }^{\circ}\text{C}$ near the core bar. As shown in Fig. 8, when the ambient temperature is $50\text{ }^{\circ}\text{C}$, the temperature near the umbrella skirt reaches $51.1\text{ }^{\circ}\text{C}$ and the cable mandrel temperature reaches $71.9\text{ }^{\circ}\text{C}$. When the cable terminal is running with load, the core temperature forms convection heat dissipation with the air after heat transfer through each layer of the medium. The heat transfer process is accompanied by a large influence of external ambient temperature changes.

Temperature differences and differences in the thermal conductivity property of different materials can create temperature gradients inside the cable terminals.

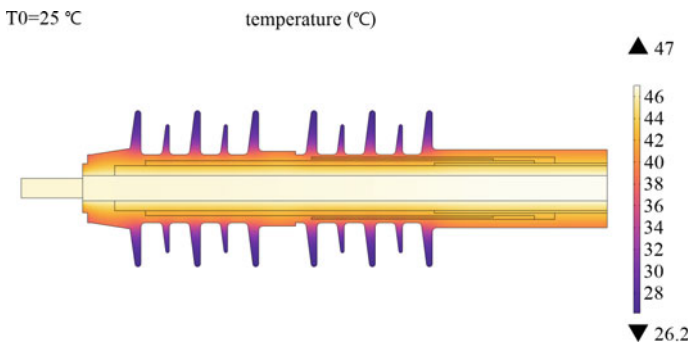


Fig. 6 Cable terminal temperature distribution

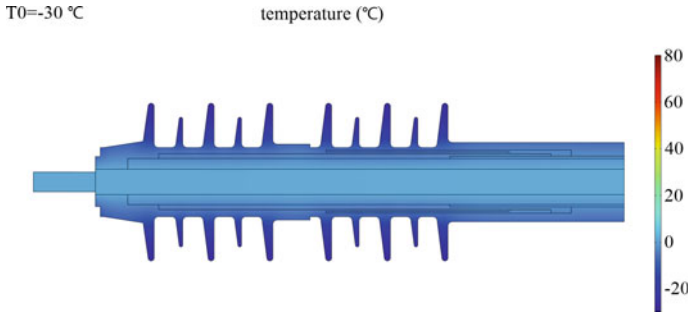


Fig. 7 Ambient temperature -30 °C , terminal temperature distribution

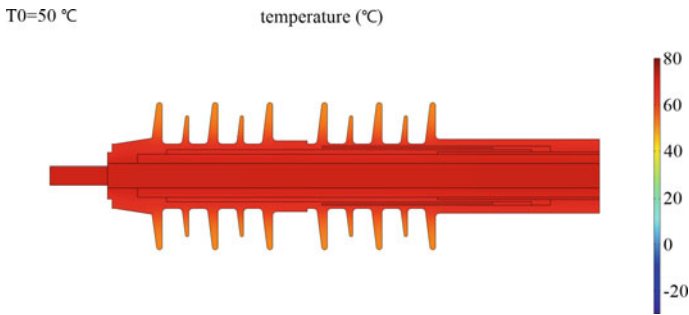
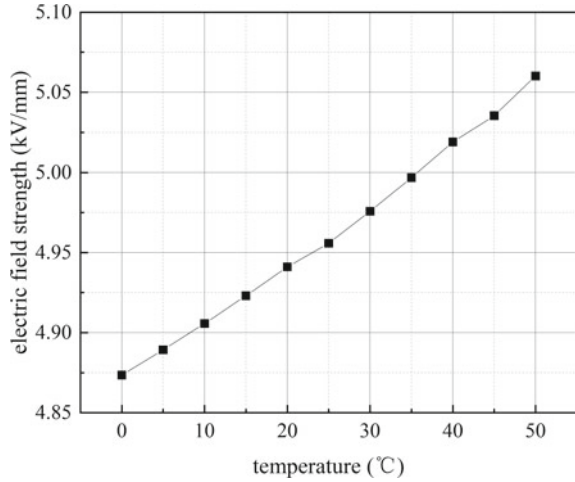


Fig. 8 Ambient temperature 50 °C , terminal temperature distribution

Temperature affects the relative dielectric constant, electrical conductivity, and thermal conductivity of the material. This causes a change in the electric field inside the terminal. Figure 9 shows the variation curves of the maximum electric field of the cable terminals over a period of operation at different external ambient temperatures. The increase in external ambient temperature leads to an increase in temperature at each location of the cable terminal. The increase in temperature leads to a decrease in the relative dielectric constant of cable insulation, stress control tube, etc. This brings about a change in the electric field strength. The maximum field strength increases from 4.83 kV/mm to 5.06 kV/mm when the external ambient temperature increases from 0 °C to 50 °C , and the increase of field strength is about 4%. It can be seen that there is little change in the electric field of the terminal caused by the temperature change.

Fig. 9 Maximum electric field variation under different external environments



4 Conclusion

- (1) The electric field distribution in different areas of the cable terminal was calculated. The maximum distortion of the electric field at the cable terminal occurs at the triple junction point with an electric field strength of 4.54 kV/mm. Secondly, the electric field is concentrated in the main insulation of the cable with an electric field strength of 4.10 kV/mm.
- (2) The natural environment has a large impact on the temperature distribution of cable terminals. Temperature differences and differences in the thermal conductivity of different materials can create temperature gradients inside the cable terminals. The temperature maximum value is distributed near the copper core and the minimum value occurs at the umbrella skirt. The change in the electric field inside the terminal caused by the temperature change is not significant.
- (3) In this study, it is proposed to calculate the internal electric field as well as the temperature field of the high-voltage terminal by simulating the electric-thermal coupled field of the cable terminal. The electric field, potential and temperature field distributions at each critical location of the cable terminals was obtained. This offers a reference for improving the overall insulation level of the terminal.

References

1. Chen WQ (2020) Failure tendency and prevention of railroad locomotive electrical equipment. *Internal Combust Engine Parts* 303(03):164–165
2. Raicevic NB, Aleksic SR, Ilic SS (2011) One numerical method to determine improved cable terminations. *Electric Power Syst Res* 81(4):942–948

3. Alboyaci B, Cinar MA, Demiroglu YB et al (2022) Evaluation of the effect of structural defects in the heat-shrink cable terminal on electric field distribution. *Eng Fail Anal* 132:105920
4. Li S, Cao B, Li J (2023) Review of condition monitoring and defect inspection methods for composited cable terminals. *High Voltage*
5. Zhou LJ, Zhu SB, Bai LL (2019) Influence of stress tubes interface on partial discharge of vehicle cable terminal at low temperatures. *High Voltage Eng* 45(04):1266–1273
6. Bai LL, Zhou LJ, Xing LM (2020) Effect of low temperature on interface discharge characteristics of ethylene rubber cable termination in high-cold environment. *Trans China Electrotech Soc* 35(03):646–658
7. Guo L, Zhu L, Bai LL (2020) Study on Extension and breakdown of discharge channel in flexible cable terminal in electric locomotive operating in alpine region. *J China Railway Soc* 42(04):59–65
8. Li C, Lin L, Qu W (2022) Study on insulation performance optimization of EMU high-voltage equipment box. *J Phys: Conf Series IOP Publishing* 2195(1):012040
9. Zhu L (2018) Electric field simulation and structural optimization of cable termination and line side cubicle for locomotive in alpine region. Southwest Jiaotong University, pp 25–31
10. Illias HA, Lee ZH, Bakar A et al (2012) Electric field distribution in 132 kV one piece premolded cable joint structures. In: International conference on condition monitoring and diagnosis, IEEE
11. Claburn CRJ, Chiang D (2011) The function of stress control tube in cable terminal. *J Electroceramics* 3(4):1509–1517
12. Zhang SD, Su GQ, Liu HJ et al (2022) Study on interface characteristics of xlpe/sir and its influence on electric field distribution for cable accessories. *Shandong Electric Power* 49(08):56–61
13. Zheng J (2021) Temperature simulation calculation of cable intermediate joint based on continuous multi step. *Electric Eng* 09:53–56
14. Liu G, Wang PY, Mao JK et al (2018) Simulation calculation of temperature field distribution in high voltage cable joints. *High Voltage Eng* 44(11):3688–3698
15. Gan DG, Zhang L, Zhang R et al (2019) Surface temperature distribution and statistical characteristics of cable joints under eccentric conditions. *High Voltage Apparatus* 55(6):117–123
16. Wang JB, Wang JX, Li GC (2022) Analysis on properties of high-voltage cable terminal material on motor train unit roof and electro-thermal coupling field simulation. *Insulat Mater* 55(07):64–70

Identification of Series Fault Arc Occurred in Motor with Inverter Circuits Under Vibration Conditions



Yanli Liu , Zhengyang Lv, Lingwei Zhang, Yiyang Liu, Hao Wang, and Huiyang Wang

Abstract One of the safety risks in electricity supply systems is the series fault arc (SAF). The method for identifying SAFs in electrical connectors for industrial motor with inverter circuits under vibrational situations was suggested in this study. Firstly, we adopted a motor with an inverter as a load, and a SAF experiment was conducted under vibrational conditions. To eliminate high-frequency harmonic interference from the inverter, the fault-phase current signal at the back-end of the inverter collected by the experiment was filtered with a finite impulse response low-pass filtering. After that, the filtered current signal was processed by phase space reconstruction (PSR), and the obtained signal was normalized, visualized and gray scaled. Next, the gray level co-occurrence matrix (GLCM) of the processed signal in the 0° , 45° , 90° and 135° directions were calculated, and 24 matrix parameters were selected as the preliminary characteristics of the SAF. Finally, the random forest (RF) algorithm was used to screen out 13 effective features and completed the training of the recognition model. The test results show that the identification method can not only distinguish between the normal data and the SAF data with 100% accuracy, but also classify the normal data and the SAF data with 99.25% accuracy under three different vibration frequencies.

Keywords Vibration · Motor with inverter circuits · SAF · PSR · GLCM · RF

1 Introduction

Three phase asynchronous motors are commonly used loads in industrial systems, and inverters are often used to control the speed and start of motors. When a three-phase asynchronous motor has a vibration fault, it will produce mechanical vibration with a specific vibration frequency. If the electrical connection of the motor is loose, the contact point is prone to generating a SAF under vibration conditions. The prolonged

Y. Liu · Z. Lv (✉) · L. Zhang · Y. Liu · H. Wang · H. Wang
Liaoning Technical University, Huludao 125105, China
e-mail: 1264310854@qq.com

© Beijing Paiké Culture Commu. Co., Ltd. 2024
X. Dong and L. Cai (eds.), *The Proceedings of 2023 4th International Symposium on Insulation and Discharge Computation for Power Equipment (IDCOMPU2023)*, Lecture Notes in Electrical Engineering 1100, https://doi.org/10.1007/978-981-99-7393-4_30

SAF is very prone to serious electrical fires. At present, there is little research on SAF identification under the vibration conditions of AC systems. Therefore, it is necessary to study the identification of SAFs under vibration conditions.

Reference [1] extracted the time domain and frequency domain characteristics of current signals, used random forest method dimensionality reduction, and combined deep neural network to realize load type judgment and fault location. Reference [2] used the optimized generalized S-transform to extract features from aviation current signals, and used the support vector machine (SVM) optimized by particle swarm algorithm to complete the identification of aviation SAFs. Reference [3] performed double-tree complex wavelet transform on current signals and detected SAF by kernel extreme learning machine. Reference [4] converted the high-frequency signal characteristics of current into grayscale images, and realized the SAF identification of home low-voltage distribution system based on convolutional neural network (CNN). Reference [5] converted the current signal into a threshold-free recursive plot, and 21 GLCM parameters are used as the final feature. The SAF identification of household load was realized based on linear discriminant analysis. The result of references [1–5] did not address the problem of SAF diagnosis of motor with inverter circuits in industrial system under vibration conditions.

Reference [6] converted the reconstructed current of wavelet packets into grayscale images, and used grayscale-gradient co-generation matrix and SVM to realize the SAF identification. Reference [7] took the fault phase current and single-phase voltage as the research objects, extracted SAF features by kernel principal component analysis, and realized SAF detection under complex harmonics based on SVM optimized by firefly algorithm. Reference [8] constructed the fault phase current signal after the decomposition of 5 layers of empirical wavelets into an attractor trajectory matrix, which was characterized by the singular value of the matrix, and used SVM to realize the identification of SAFs. References [6–8] mainly focused on the SAF generated at the front end of the inverter, and did not consider the influence of vibration generated during motor vibration fault on SAF identification.

In this paper, the fault phase current signal at the back end of the inverter under vibration conditions was taken as the research object. The SAF features were extracted by PSR and GLCM, and the feature vectors were input into the classification model based on RF algorithm to complete the feature screening and SAF recognition. The following sections explain the work done in this paper from three aspects: experiment, algorithm principle and test analysis.

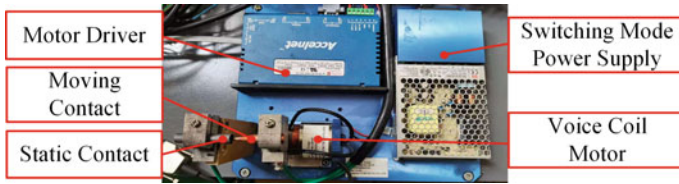


Fig. 1 The vibration SAF generator

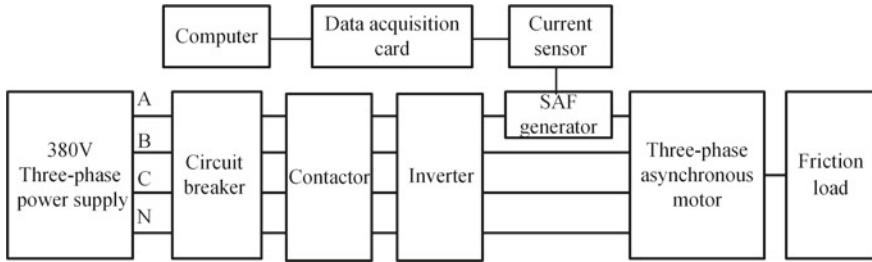


Fig. 2 The overall structure of the vibration fault arc experiment system

2 Experiment

2.1 Experimental Platform

In order to restore the true vibration situation of the electrical contact point under vibration conditions to a greater extent, we designed a vibration SAF experimental system based on a voice coil motor. The vibration SAF generator is shown in Fig. 1. The SAF generator was located at the rear end of the inverter. In order to simulate the vibration of the contact point with poor contact under the vibration fault of the motor, the moving contact and static contact were driven by the voice coil motor to reciprocate.

The overall structure of the experimental system is shown in Fig. 2. The experimental power supply is provided by a 380 V power supply, and the load is selected three-phase asynchronous motor with inverter. The experimental system control and data acquisition circuit consists of LHB100A5VY2 current sensor, USB3200 data acquisition card, switch power supply, Copley motor controller, and computer.

2.2 Experimental Scheme

The experimental plan is shown in Table 1. During the experiment, the working current of the motor was 12 A. The vibration frequencies of 8 Hz, 16 Hz, and

Table 1 Experimental scheme

Experimental group number	1	2	3	4
SAF	No	Yes	Yes	Yes
Vibration frequency (Hz)	/	8	16	25

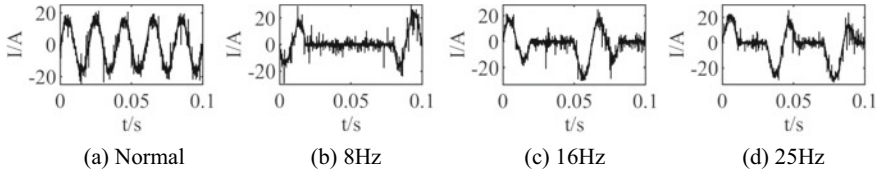


Fig. 3 Initial current waveform

25 Hz generated when the motor experiences vibration faults were selected as the experimental vibration frequencies. During the experiment, the vibration frequency of the voice coil motor was set using CME software. The sampling frequency was set to 50 kHz.

2.3 Experimental Results

The waveform of experimental results is shown in Fig. 3. From Fig. 3, it is found that the current under vibration conditions has a long arc current zero rest zone. And the higher the vibration frequency, the shorter the zero rest zone. This is because after the current crosses zero, under the action of the voice coil motor, the distance between the contacts is long, and the gap cannot be broken down, so the current is 0. As the frequency of vibration increases, the duration of this process becomes shorter, resulting in a shorter zero-break zone.

3 SAF Identification Method Based on PSR–GLCM–RF Algorithm

3.1 Data Low-Pass Filtering

In order to filter out the interference of high-frequency harmonics of the inverter, a finite impulse response low-pass filter with a sampling frequency of 50 kHz and a cutoff frequency of 150 Hz is designed. The current waveform and the spectrogram of current signals before and after filtering are shown in Fig. 4. From Fig. 4, it is found that the filtered current waveform becomes smoother, and there is almost no

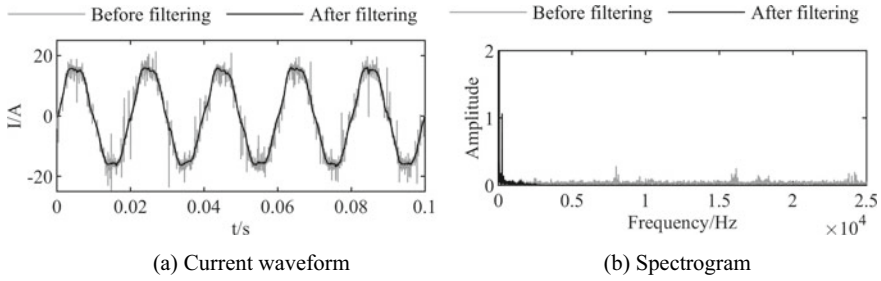


Fig. 4 Analysis of low-pass filtering before and after current signal filtering

loss in the 50 Hz fundamental frequency signal. The amplitude of the fundamental frequency signal in Fig. 4b is not fully displayed.

3.2 PSR and Data Visualization

After filtering the current signal in a low pass, we normalize it. The PSR [9] converts one-dimensional data into matrix through time delay reconstruction method to realize signal dimensionality upgrading. The single sample collected by the data acquisition card is X discrete points of $[u(1), u(2), \dots, u(X)]$ and the matrix after phase space reconstruction is as follows:

$$\begin{aligned}
 U(n) &= [u(n), u(n + \tau), \dots, u(n + (m - 1)\tau)] \\
 n &\in (1, 2, \dots, X - (m - 1)\tau)
 \end{aligned}
 \tag{1}$$

where, m is the dimension of phase space, and τ is the delay constant.

After visualizing and gray scaling the reconstructed matrix, a PSR visualization grayscale image is obtained, as shown in Fig. 5. From Fig. 5, it is found that there is a significant difference between the PSR visualization grayscale images under normal conditions and different fault frequencies.

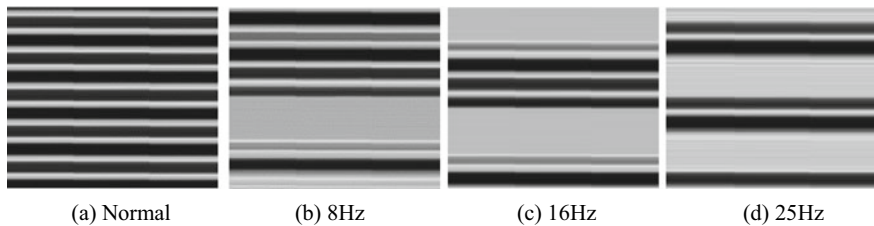


Fig. 5 Grayscale plot of current signal PSR visualization

3.3 Image Digital Texture Features GLCM

Texture analysis can analyze and extract the spatial distribution patterns of image grayscale, and the GLCM [10] is a commonly used digital texture feature in texture analysis. The initial grayscale image in this paper is 256 levels. In order to reduce computational complexity, the grayscale image is compressed to obtain a two-dimensional digital image $f(x, y)$ with a grayscale level of 16. We calculated the GLCM of the $f(x, y)$ at a certain distance from 4 directions, including 0° , 45° , 90° , and 135° . The GLCM of the $f(x, y)$ is as follows:

$$\begin{aligned}
 P(i, j) &= \#\{(x_1, y_1), (x_2, y_2) \in M \times N \mid f(x_1, y_1) \\
 &= i, f(x_2, y_2) = j\} \\
 i, j &\in (1, 16)
 \end{aligned} \tag{2}$$

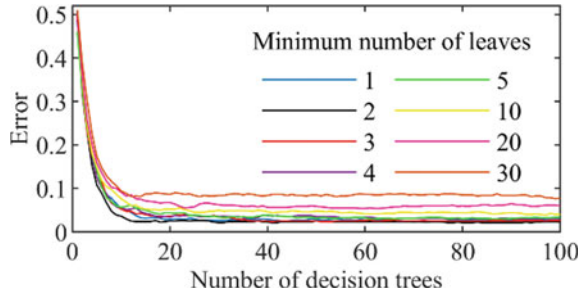
In the equation, $\#()$ represents the number of elements in the set that meet the condition.

This paper selected energy, entropy, contrast, and correlation as 4 features to characterize the GLCM. The energy is the amount that reflects the uniform distribution of image grayscale and texture thickness. The entropy reflects the complexity of the image gray distribution. The contrast reflects the clarity of the image and the depth of the texture grooves. The correlation represents the similarity of elements in the row or column direction of the GLCM. We calculated the 4 features of the GLCM in the 0° , 45° , 90° and 135° directions, and calculated the mean and standard deviation of 4 features in 4 directions. We used these 24 features as preliminary features of the SAF current signal.

3.4 A Data Classification Method Based on RF Algorithm

This paper selected RF algorithm [11] to achieve data classification. The RF algorithm belongs to the guided aggregation algorithm in integrated learning. The RF algorithm is difficult to overfitting and has good anti-interference ability. The number of decision trees and the minimum number of leaves will affect the accuracy and running speed of the model. Their effect on model error is shown in Fig. 6. From Fig. 6, it is found that in order for the model to have low error and run faster, it is necessary to select the appropriate parameter values. In Sect. 4.1, this paper analyzed the importance of 24 initial features.

Fig. 6 RF algorithm classification model error curve



4 Testing of SAF Identification Model

4.1 Feature Screening and Analysis of Test Results

Divide the experimental data into a sample library containing 1200 samples. In Table 1, there are 300 samples for each experimental group, with sample labels 1–4. Randomly select 800 samples from the sample library as the training set, and the remaining 400 samples as the testing set. In this paper, the minimum number of leaves was set to 2 and the number of decision trees was set to 40. The test result confusion matrix and the importance of 24 preliminary features are shown in Fig. 7. The preliminary classification accuracy of the 4 samples of the identification model is 97.5%.

Labels on the horizontal axis of Fig. 7b correspond to different initial characteristics. Labels 1–4 represent the energy of 0°, 45°, 90° and 135° GLCM. Labels 5–8 represent the entropy of 0°, 45°, 90° and 135° GLCM. Labels 9–12 represent the contrast of 0°, 45°, 90° and 135° GLCM. Labels 13–16 represent the correlation of 0°, 45°, 90° and 135° GLCM. Labels 17–24 represent the average and the standard deviation of energy, entropy, contrast and correlation in 4 directions.

This paper arranged the importance of features in order, deleting one feature with the lowest importance each time. Table 2 shows the model recognition accuracy

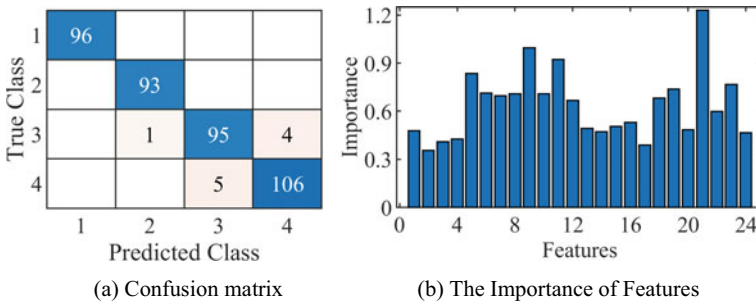


Fig. 7 Preliminary test results

Table 2 The influence of different features on recognition accuracy

Number of features	A1 (%)	A2 (%)
24	100	97.5
20	100	98.25
16	100	98.75
14	100	99
13	100	99.25
12	100	96.25

after partial feature deletion. In Table 2, the A1 shows the accuracy of the distinction between the normal current and the SAF current, and the A2 indicates the classification accuracy of 4 different types of samples. From Table 2, it is found that when the number of features decreases to 12, the accuracy of the identification model begins to significantly decrease. Therefore, this paper selected the most important 13 features as the final SAF features, their corresponding labels are 5, 6, 7, 8, 9, 10, 11, 12, 18, 19, 21, 22 and 23. At this point, the model identification accuracy A2 is 99.25%.

4.2 Comparative Analysis of Different Identification Methods

The GLCM is a digital texture feature of an image, which can be directly classified as a fault arc feature. In order to explore the advantages and disadvantages of using GLCM as a SAF feature and the feature extraction method proposed in this paper, GLCM is directly input into CNN for classification, and its recognition accuracy is compared with the method proposed in this paper. In addition, this paper also tested some methods in the reference literature, and the comparison results of their recognition accuracy are shown in Table 3.

The comparison results in Table 3 show that the A1 value and A2 value of the identification method in this paper are the highest, which shows that the identification method in this paper is more suitable for the SAF identification of the back-end current signal of the inverter under vibration conditions. The identification method

Table 3 Recognition accuracy of different recognition methods

No.	Methods	A1 (%)	A2 (%)
1	Enter GLCM directly into the CNN	98.75	89.25
2	Reference [6]	100	92.25
3	Reference [7]	98.67	67.23
4	Reference [8]	100	82.25
5	Reference [5]	99.76	78.52
6	Proposed method	100	99.25

in this paper not only distinguishes between normal and SAFs with 100% accuracy, but also has a classification accuracy of 99.25% for 4 different types of samples.

5 Conclusion

The high-frequency harmonics generated by the inverter interfered with the SAF identification of the current signal at its back end. After filtering the current signal, we extracted the preliminary SAF features using the PSR-GLCM algorithm. We also use RF algorithms to screen the final SAF features and implement SAF identification. By comparing with other SAF identification methods, we found that the PSR-GLCM-RF algorithm has certain advantages in distinguishing normal current and SAF current, and in classifying SAF under different vibration conditions.

References

1. Jiang J, Li W, Wen Z et al (2021) Series arc fault detection based on random forest and deep neural network. *IEEE Sens J* 21(15):17171–17179
2. Cui RH, Tong DS, Li Z (2021) Aviation arc fault detection based on generalized S transform. *Proc CSEE* 41(23):8241–8250 (in Chinese)
3. Yin ZD, Wang L, Zhang B et al (2021) An integrated DC series arc fault detection method for different operating conditions. *IEEE Trans Industr Electron* 68(12):12720–12729
4. Chu RB, Schweitzer P, Zhang RC (2020) Series AC arc fault detection method based on high-frequency coupling sensor and convolution neural network. *Sensors* 20(17):4910
5. Ferracuti, F., Patrick, S., Andrea, M.: Arc fault detection and appliances classification in AC home electrical networks using recurrence quantification plots and image analysis. *Electric Power Systems Research* 201, 1–12, Art no. 107503 (2021).
6. Guo FY, Deng Y, Wang ZY et al (2018) Series arc fault characteristics based on gray level-gradient co-occurrence matrix. *Trans China Electrotech Soc* 33(01):71–81 (in Chinese)
7. Han CX, Wang ZY, Tang AX et al (2021) Recognition method of AC series arc fault characteristics under complicated harmonic conditions. *IEEE Trans Instrument Measure* 70:1–9, Art no. 3509709
8. Gao HX, Wang ZY, Han CX et al (2022) Feature extraction method of series arc fault occurred in three-phase motor with inverter circuit. *IEEE Trans Power Electron* 37(9):11164–11173
9. Cui RH, Li Z, Dong DS (2021) Arc fault detection based on phase space reconstruction and principal component analysis in aviation power system. *Proc CSEE* 41(14):5054–5065 (in Chinese)
10. Yang XZ, Ding Y, Zhang XY et al (2022) Spatial-temporal-circulated GLCM and physiological features for In-Vehicle people sensing based on IR-UWB radar. *IEEE Trans Instrument Measure* 71:1–13, Art no. 8502113
11. Dong XH, Taylor CJ, Cootes TF (2021) A random forest-based automatic inspection system for aerospace welds in X-ray images. *IEEE Trans Autom Sci Eng* 18(4):2128–2141

Electric Field Simulation and Defect Analysis of Transformer Oil-Paper Capacitive Bushing



Yu Rui, Lei Xu, Tao Jiang, Bowen Yao, Fanhua Zhang, Beibei Wang, and Binbin Wei

Abstract In order to study the insulation performance of oil-paper capacitive bushing, the finite element model of 40.5 kV transformer oil-paper capacitive scaled bushing with field strength similar to that of actual 1000 kV bushing is established based on COMSOL software. Based on this model, the 2D electric field analysis is carried out. The field strength distribution and potential distribution of the bushing under different defects are calculated, and the degree of electric field distortion at the defects is obtained. The calculation results show that the design of the capacitor core of the casing can effectively uniform the electric field distribution in the casing under normal working conditions. When the fault occurs, the internal electric field distorts in different degrees at the defect. Therefore, it is very important to avoid bushing the dirty and wrinkled capacitive screen, keep the bushing environment dry and avoid the humidity of the capacitor core.

Keywords Oil-paper capacitive bushing · The finite element model · COMSOL · Electric field distribution

1 Introduction

Oil-paper insulated bushing is an important part of transformer, which is widely used in power system [1]. Oil-paper capacitive transformer bushing is an important outlet device of transformer, which acts as a carrier for introducing or leading out the high, medium and low voltage side currents of transformer and insulates the oil tank shell of transformer [2]. Once the transformer bushing fails, it will pose a serious threat to

Y. Rui · L. Xu · T. Jiang · B. Yao · F. Zhang · B. Wang
State Grid Ji'ning Power Supply Company, State Grid Shandong Electric Power Company,
Ji'ning 272000, China

B. Wei (✉)
School of Electrical Engineering, Shandong University, Ji'nan 250061, China
e-mail: 202234750@mail.sdu.edu.cn

the transformer and nearby equipment, and even cause a large-scale power outage and personal injury, resulting in social disorder and significant economic losses [3, 4].

In the process of operation, the insulation performance of the casing will gradually deteriorate due to the long-term action of strong mechanical force, large current and high voltage, as well as the influence of wet weather and pollutants [5, 6]. Under the action of high field strength for a long time, these defects may cause a series of problems such as local overheating or partial discharge, which will lead to accidents such as casing breakdown and damage [7]. Therefore, for the operation and maintenance of casing equipment, the electric field simulation calculation of high-voltage casing can effectively provide guidance for the optimal design of casing [8, 9].

Therefore, this paper comprehensively analyzes the typical faults of oil-immersed capacitive bushing, and based on the principle of electric field strength equivalence [10], establishes a finite element simulation model of 40.5 kV bushing scale model with field strength similar to that of actual 1000 kV bushing [11]. Based on the electric field simulation analysis of COMSOL electrostatic module, the electric field simulation calculation of normal and typical fault conditions of bushing is carried out, and the insulation performance of bushing is analyzed. Finally, based on the results of electric field distribution under different fault types, effective preventive measures are put forward.

2 Simulation Calculation of Electric Field of Oil-Paper Capacitive Bushing

2.1 Mathematical Model and Boundary Conditions of Electric Field Calculation

The bushing works under electrostatic field at any time, which is $-\frac{\partial B}{\partial t} = 0$ [3]. Therefore, the physical field to be solved in this paper is a two-dimensional electrostatic field.

The finite element method is suitable for solving electromagnetic problems, and the electromagnetic field is established according to Maxwell's equation, which describes the differential form of the quasi-static electric field as follows (differential form):

$$\nabla \times \vec{E} \approx 0 \quad (1)$$

$$\nabla \times \vec{H} = \vec{J} = \frac{\partial \vec{D}}{\partial t} \quad (2)$$

$$\nabla \bullet D = \rho \quad (3)$$

where, \vec{E} represents the electric field intensity, and the unit is V/m ; \vec{H} is the magnetic field strength, and the unit is A/m ; \vec{D} is the electric displacement, and the unit is C/m^2 ; ρ represents the density of free charge body, and the unit is C/m^3 ; \vec{J} represents the conduction current density, and the unit is A/m^2 ; $\frac{\partial D}{\partial t}$ represents the displacement current density.

The relationship between the above parameters in the dielectric is as follows:

$$\vec{D} = \varepsilon E \quad (4)$$

$$\vec{J} = \gamma \vec{E} \quad (5)$$

where, ε represents the dielectric constant, and the unit is F/m ; γ represents the electrical conductivity, and the unit is S/m^2 .

In the quasi-static electric field, the electric field is regarded as irrotational, so the relationship between electric field and potential in the field is as follows:

$$\vec{E} = -\nabla\varphi \quad (6)$$

The partial differential equation-Poisson equation which describes the potential distribution of electrostatic field is obtained from Eqs. (3), (4) and (6):

$$\nabla^2\varphi = -\frac{\rho}{\varepsilon} \quad (7)$$

Equation (7) considers the influence of free charge on the potential distribution in the electrostatic field. When there is no free charge in the field, the formula can be simplified as:

$$\nabla^2\varphi = 0 \quad (8)$$

Equation (8) can be used to solve and calculate the potential distribution of steady-state current field.

In electric field calculation, the initial conditions are expressed as:

$$\varphi|_{t=0} = \varphi_{x,y,z}(0) \quad (9)$$

There are two kinds of boundary conditions in the electric field calculation of oil-paper capacitive bushing.

A kind of boundary of electric field is called reinforced boundary, which needs to be given in finite element simulation in advance in calculation. A kind of boundary constrains the boundary potential. This boundary is also called Dirichlet boundary

condition, and its expression is:

$$\varphi|_{r_1} = \varphi \quad (10)$$

The second boundary of electric field is called automatic boundary, which accords with variational conditions in calculation. The second boundary condition constrains the normal reciprocal of the boundary potential. This boundary is also called Newman boundary condition, and its expression is:

$$\frac{\partial \varphi}{\partial n}|_{r_2} = \varphi(x, y, z) \quad (11)$$

Therefore, only one kind of boundary needs to be set before calculation.

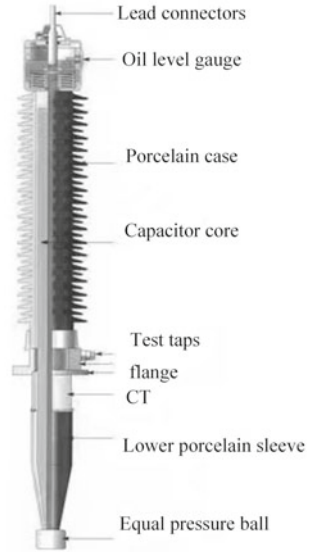
2.2 Casing Structure and Scale Model Parameters

This paper mainly analyzes the electric field of transformer bushing through simulation. For transformer bushing with high voltage level, on the one hand, the number of plates at the inner insulation is often more, and the number of plates of transformer capacitor bushing with general voltage level greater than 10, 1000 kV will reach about 190 layers [12]. Building a 1:1 simulation model of high voltage bushing will undoubtedly increase the complexity of the simulation model and greatly increase the amount of calculation. On the other hand, the capacitance core of oil-paper capacitive insulation sleeve is only about 0.08–0.12 mm for each layer of insulation paper and 0.01 mm for each layer of polar plate. In the simulation software, due to the extremely thin thickness of insulation oil paper, it is often impossible to realize fine grid division in grid division calculation, which leads to a large error in the final field strength calculation result and a low calculation rate. Based on the above analysis, the finite element simulation model of 40.5 kV casing scale model with field strength similar to that of actual 1000 kV casing is selected and established in this paper.

Oil-paper capacitance is widely used in bushings with voltage levels of 110 kV and above to evenly distribute the internal electric field. The oil-paper capacitive bushing structure of transformer is shown in Fig. 1. Oil-paper capacitive bushing is mainly composed of central conducting rod, outer insulating upper and lower porcelain sleeves, and inner insulating capacitor core, insulating oil, oil conservator, mounting flange, bottom equalizing ball and oil tank [13].

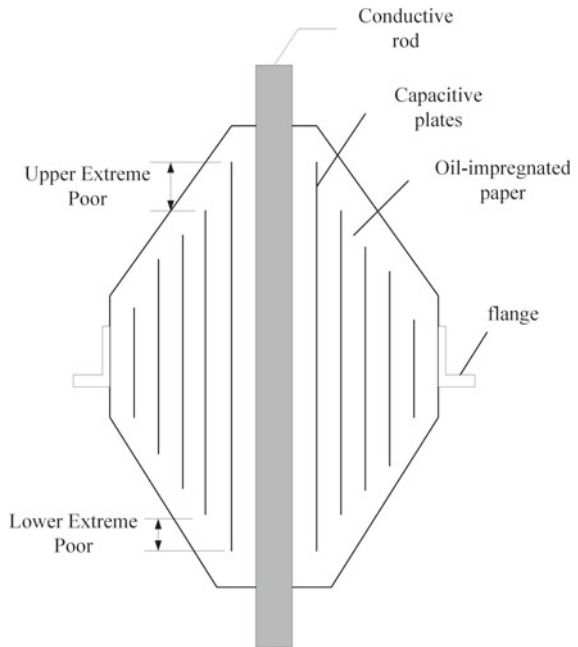
The inner insulation of oil-paper capacitive bushing is the capacitor core, which is the focus of bushing design. The capacitor core is a coaxial series capacitor consisting of a layer of aluminum foil tightly wound with oil-immersed cable paper every certain layer outside the central copper guide rod as the polar plate. One side is connected with the copper conductive rod, and the other side has a lead wire led out through

Fig. 1 Structural schematic diagram of oil-paper capacitive bushing



the measuring terminal. The inside of the sleeve is vacuumized and dried and filled with insulating oil [4]. The structure of the capacitor core is shown in Fig. 2.

Fig. 2 Schematic diagram of capacitor core structure



In this simulation, the scale model of oil-paper capacitive bushing is adopted. The maximum voltage is 40.5 kV, the total length of bushing is 1137 mm, the diameter of conductive rod is 35 mm, the aluminum foil electrode plate is 10 layers, and the oil tank is insulating oil. Specific parameters of scaled casing are as follows (Table 1).

The scale model of bushing is mainly to make the internal field strength of the capacitor core of the model equivalent to that of the actual 1000 kV bushing by changing the length of the plates and the distance between the plates. The specific plate size of 40.5 kV bushing is shown in Table 2.

Table 1 Parameters of 40.5 kV Casing

Technical parameter	Numerical value
Maximum voltage (um) (kV)	40.5
Rated current (A)	630
Imin power frequency withstand voltage (kV)	95
Lightning full-wave impulse withstand voltage (kV0)	200
Dielectric loss factor at 20 °C (under Um)	≤ 0.005
Maximum partial discharge (under um) (pC)	≤ 10
Minimum creepage distance of external insulation (mm)	1260
External insulation flashover distance (mm)	485
Bending tolerance load (N)	1600
Maximum installation angle with vertical direction (°C)	30

Table 2 Design dimensions of 40.5 kV bushing capacitor core

Plate layer number	Length of polar plate (mm)	Superior difference (mm)	Lower grade difference (mm)	Diameter (mm)
Zero screen	681			45
1	638	31	12	47.057
2	595	31	12	49.137
3	552	31	12	51.217
4	506	31	15	53.297
5	460	31	15	55.897
6	414	31	15	58.497
7	368	31	15	61.097
8	320	32	16	63.177
9	272	32	16	65.257
10	224	32	16	67.337

Table 3 Relative dielectric constant of casing materials

Material	Insulator	Insulating oil paper	Dielectric oil	Copper	Aluminium
Relative dielectric constant ϵ_r	6	3.8	2.2	2000	2000

2.3 Establishment of Scaled Casing Simulation Model

As can be seen from the bushing structure diagrams in Figs. 1 and 2, the oil-paper capacitor bushing is an axisymmetric structure, and the electrode screen inside the capacitor core is very thin and has many layers. Therefore, when establishing the simulation calculation model, this paper chooses to establish a two-dimensional axisymmetric model, and the electrode screen of the capacitor core is replaced by a line [14]. The boundary condition is that the operating voltage of the conductive rod, oil conservator, equalizing ring and zero screen is 23.4 kV, the last screen, flange and oil tank shell are at zero potential, and the other capacitive screens are set as dielectric shields. Only the relative dielectric constant needs to be considered in the material setting. The parameters are shown in Table 3.

After the simulation model of casing structure is built based on the above data, it is necessary to mesh according to the structure of casing model, in order to ensure the accuracy of calculation, save computer memory and ensure the calculation speed [15]. The insulation thickness between the electrode screens of the capacitor core is all about 1 mm. In order to ensure the calculation accuracy, high-density grid elements are selected in this part during grid division. The internal structure of oil tank, air, insulating oil layer and other parts are single, and rough grid can be selected for division. At the corner structure of the structure, the mesh generation at the corner is refined by the method of corner thinning. The finite element model diagram and mesh generation diagram of casing are shown in Fig. 3.

3 Analysis of Simulation Results

3.1 Electric Field Distribution of Casing Under Normal State

Based on the finite element model of transformer bushing established in Sect. 1.2, the bushing is numerically simulated by using finite element software, and the potential distribution diagram of bushing model shown in Fig. 4 and the radial potential distribution diagram of capacitor core of bushing model shown in Fig. 5 are obtained respectively.

As can be seen from the potential distribution in Fig. 4, the red area indicates high potential, the blue area indicates low potential, and other color areas indicate the transition of different potentials. The overall potential of the bushing is in a state of gradual transition from the high voltage area of the central conductor and the

Fig. 3 Finite element model and mesh generation diagram of casing

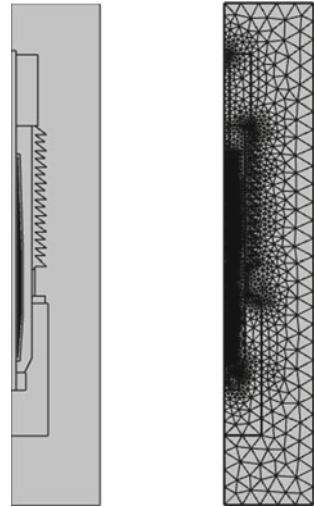


Fig. 4 Overall and local potential distribution diagram of casing

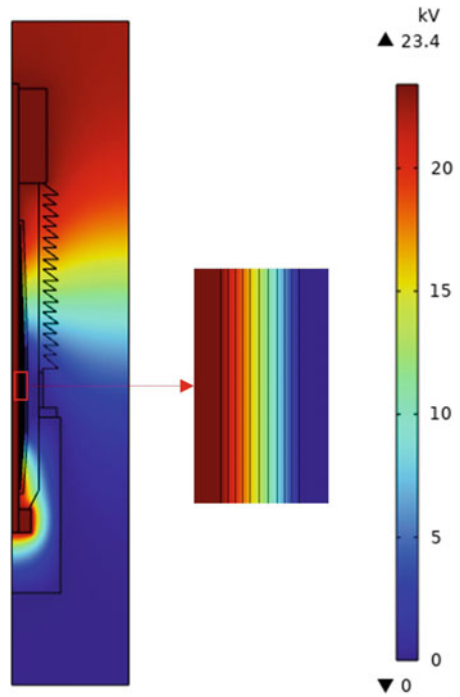
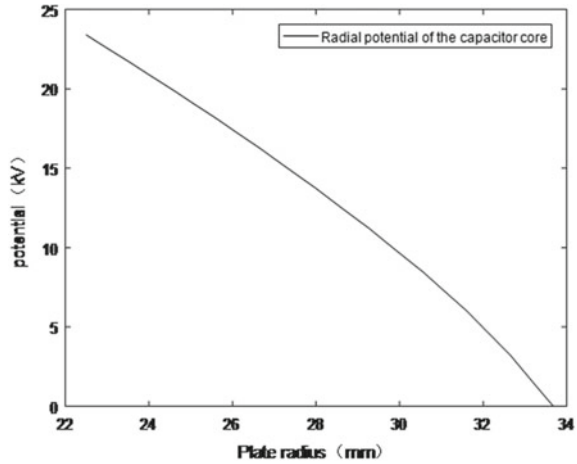


Fig. 5 Radial potential distribution of capacitor core

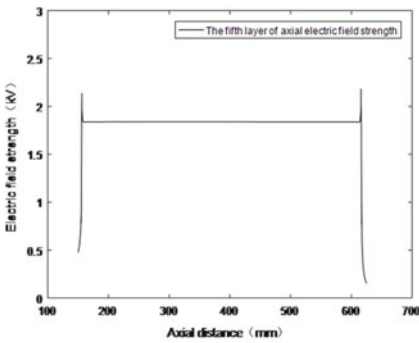
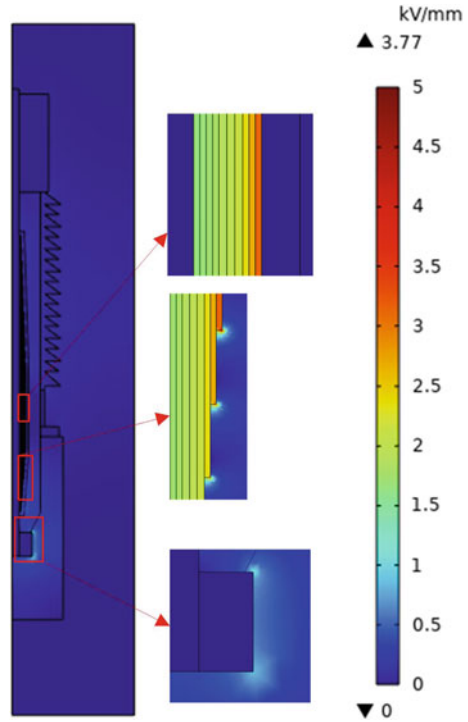


equalizing ball to the low voltage area of the oil tank and sleeve. It can be seen from the radial potential distribution diagram in Fig. 5 that the aluminum foil polar plate makes the potential inside the capacitor core decrease uniformly from the zero screen to the last screen, which conforms to the boundary conditions of loading.

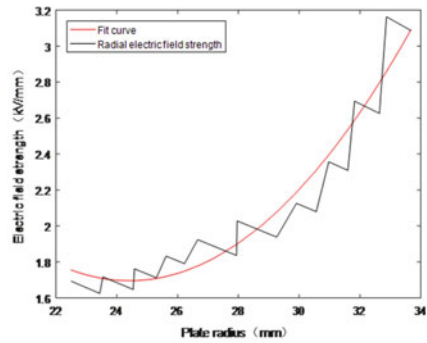
According to the electric field diagram of the bushing in Fig. 6, the electric field distribution of the bushing as a whole is uneven, and the electric fields at the bushing tail, the surface of the equalizing ball and the capacitor core are concentrated, and the electric fields in the insulating oil and the area far from the core are low. Among them, the field strength in the capacitor core is much higher than that in other areas. From the local enlarged diagram, it can be seen that the electric field distortion at the bottom of each layer of electrode plate and the surface of the equalizing ball is serious, forming a local strong electric field area, which will improve the requirements for insulation performance at these positions, and the bushing is more prone to discharge, breakdown and other failures.

As shown in Fig. 7, due to the voltage equalization of aluminum foil plates, the forced electric field is perpendicular to the aluminum foil. The axial electric field between the plates is approximately uniform to avoid partial discharge due to too high field strength. However, the electric fields at the upper and lower ends of the plates are seriously distorted. The radial electric field of the capacitor core decreases first and then increases outward from the zero-layer plate, and the overall distribution is “U”. The electric field near the inner and outer plates is higher, but the electric field in the middle plate is lower. The maximum electric field intensity in the radial direction of the capacitor core appears on the insulating paper near the zero screen of the main insulation of the bushing, which is 3.1835 kV/mm and the minimum electric field intensity is 1.6256 kV/mm.

Fig. 6 Overall and local electric field distribution of casing



(a) Axial field strength diagram.



(b) Radial field strength diagram.

Fig. 7 Axial and radial electric field distribution of capacitor core

3.2 Electric Field Distribution Under Casing Fault Condition

Based on the finite element model of bushing in Sect. 1.2, five fault conditions, such as uniform damping of bushing, floating of end screen, plate deviation, folding and

breakage of capacitor core, are simulated respectively, and the influence of defects on the electric field distribution of bushing model is compared and analyzed.

The following respectively introduce the simulation methods of five kinds of casing faults on the finite element model:

- (a) In the simulation model, the relative dielectric constant of the material is changed to simulate the damp defect. After the material is damp, the relative dielectric constant will become larger [16]. In this simulation experiment, the relative dielectric constants of transformer oil and insulating paper are changed to 5, which simulates the uniform moisture defect.
- (b) The transformer bushing is grounded in normal operation. If the terminal screen is imperfect or poorly grounded in operation, a high floating voltage will be formed between the terminal screen and the ground, which will cause the terminal screen to discharge to the ground, burn the nearby insulation, and even lead to a serious bushing explosion accident. In the simulation experiment, the grounding failure of the last screen can be simulated by setting the last screen to the floating potential.
- (c) The number of layers of plates in the capacitor core of transformer bushing may cause the internal plates to shift under the circumstances of bushing collision and vibration, that is, the plate deviation defect. In the finite element model, the plate offset defect is arranged on the seventh layer plate, and the sinking distance is set to 20 mm.
- (d) Arranging the fold defect in the middle of the fifth layer plate in the simulation model capacitor core, and arranging a triangular defect with a height of about 0.3 mm to simulate the fold defect.
- (e) The arrangement position and method of the bushing model damage defect are the same as those of the fold defect, and a rectangle of $0.1 * 1$ mm is set in the middle of the fifth layer plate to simulate the capacitor core damage defect. Because the capacitor core is always immersed in insulating oil, the damaged part will eventually be filled with insulating oil, so the relative dielectric constant of the damaged part is set to 2.2.

As shown in Fig. 9, it can be seen that the damp of the capacitor core basically does not affect the electric field distribution in the bushing, and the maximum radial field strength of the capacitor core is 3.1565 kV/mm and the minimum is 1.6527 kV/mm. Figure 8a shows the distribution map of the field strength at the end screen-flange when the end screen is suspended. It can be found that the field strength in this area is obviously increased, and the electric field distortion at the chamfer of the flange is obvious. Figure 9 shows that the electric field in the plate area presents a “U” shape from the inside to the outside, and the electric field intensity is much smaller than that in the defect-free model, when the maximum electric field intensity in the plate area is only 0.38914 kV/mm. Figure 8b is a local enlarged view of the field strength after the offset of the polar plate. Compared with the defect-free model, it can be found that the sinking of the polar plate has no influence on the overall electric field distribution, but there is a certain degree of electric field concentration at the tip of the sinking polar plate. The electric field intensity at the tip is 3.3053 kV/mm,

which is about 1.5 times compared with the 2.1248 kV/mm of the defect-free model. Figure 8c shows the electric field distribution at the fold. Combining with the radial field intensity curve in Fig. 9, it can be found that the fold defect has little influence on the overall electric field distribution, and the electric field intensity of insulating oil and other far-field areas is close to zero. However, serious electric field distortion will be found by observing the position of the fold of the capacitor core plate, and the maximum electric field at the tip of the model is about 4.6473 kV/mm. The electric field concentration area will be formed outside the sharp corner of the defect, and the electric field distortion here is about 2–3 times that of the defect-free model. On the contrary, the inner side of the sharp corner of the defect will form a low field strength region; Fig. 8d shows the electric field distribution at the damaged electrode plate. Compared with the model with damaged defects and the model without defects, the electric field distribution of the whole casing has not changed obviously, but there is obvious electric field concentration at the damaged hole.

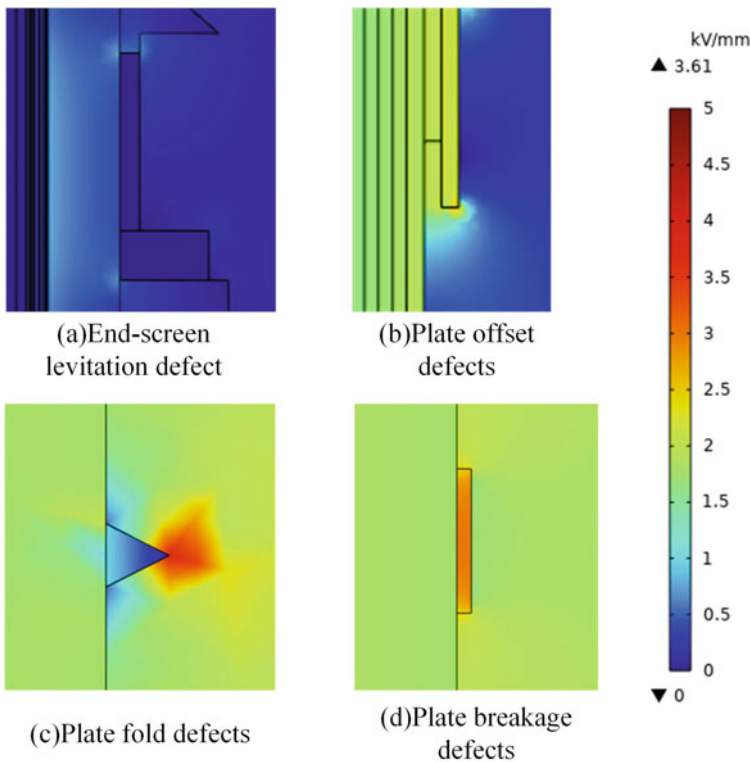


Fig. 8 Electric field distribution of casing fault condition

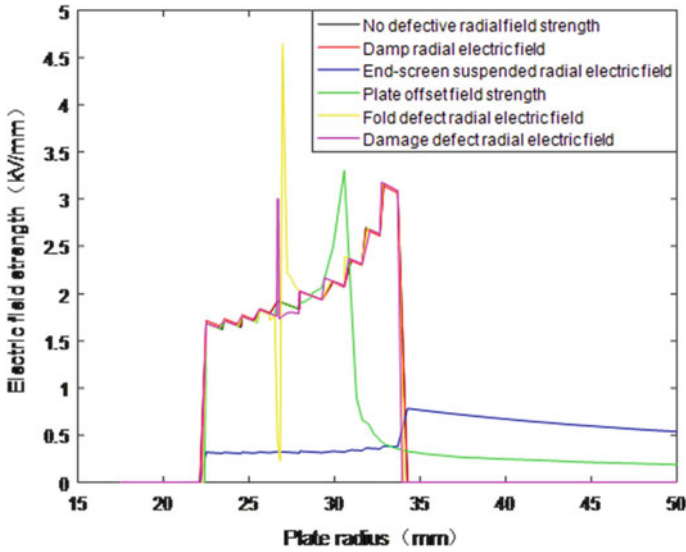


Fig. 9 Variation curves of radial field strength under normal and fault conditions

3.3 Impact Analysis of Casing Insulation and Suggestions for Operation and Maintenance

From the above analysis of the calculation results and distribution of the electric field of the bushing, it can be seen that, on the one hand, the positions such as the tail of the bushing, the surface of the equalizing ball and the capacitor core belong to the areas where the field strength is concentrated, so it is necessary to reasonably adjust the length of the plate, the range between the top and bottom and the gap distance between the plates, which can effectively improve the electric field distribution in the high field strength area and reduce the occurrence of insulation accidents. On the other hand, based on the analysis of the field strength distribution of typical faults of casing, it is known that the defects in the casing manufacturing process are also harmful to the insulation of casing. So the process should be improved in the manufacturing process, meanwhile materials with better performance should be used to avoid air gaps, burrs and bulges.

The following preventive measures are proposed for production, transportation, operation and maintenance:

- (a) Improve product quality control, and avoid burr defects on the surface of the conductive rod, dirty and wrinkled capacitive screen, etc.
- (b) During transportation, the fixation should be firm to avoid the displacement of internal structures such as polar plates caused by collision.

- (c) Pay attention to keep the casing environment dry, and replace the sealing washer immediately after taking and replenishing oil to prevent the water from getting damp due to the failure of the sealing washer.
- (d) During maintenance, always pay attention to the integrity of casing grounding performance, and try not to install an online monitoring device for the grounding lead of the last screen as much as possible. If necessary, the spring-pressed grounding mode can be changed to a direct lead-out grounding mode to ensure the integrity of the grounding of the last screen.

4 Conclusion

In this paper, the finite element simulation model of 40.5 kV bushing scale model with field strength similar to that of actual 1000 kV bushing is established. The electric field simulation calculation of bushing under normal operation and typical fault conditions is carried out.

- (a) Under the normal working condition of the bushing, the overall potential gradually transits from the high voltage area of the central conductor and the equalizing ball to the low voltage area of the oil tank and the bushing. The electric field is concentrated at the tail of the bushing, the surface of the equalizing ball and the capacitor core. The radial electric field of the capacitor core first decreases and then increases from the zero-layer plate, and the overall distribution shows a “U” shape.
- (b) Due to the floating defect of the last screen, the high electric field is concentrated at the fuel tank, with serious electric field concentration at both ends of the flange. When the electrode plate is folded, deviated and damaged, the electric field of the casing is seriously distorted at the defect.
- (c) Optimize the structural parameters such as the spacing and thickness of the capacitor cores to make the internal electric field distribution more reasonable.

Acknowledgements This work was supported by the State Grid Shandong Electric Power Company Science and Technology Project Funding “Research on non-contact insulation status monitoring and fault warning technology of large transformer bushing based on advanced sensing” (Project No.520606220006).

References

1. Neng W et al (2022) Insulation state evaluation method of oil immersed paper bushings based on multi-dimensional electrical characteristic parameters. In: 2022 IEEE international conference on high voltage engineering and applications (ICHVE), Chongqing, China. IEEE, pp 1–4
2. Yongqi W, Guangning W, Kai L, Mu L, Zhen D, Hao T (2022) Development course and challenges of transformer bushing. *Sichuan Electr Power Technol* (in Chinese) 45(6):59–67

3. Xiaoying X (2021) Analysis and treatment of typical defects of oil-paper insulation bushing of transformer (in Chinese). Xiamen Institute of Technology
4. Wenxiu G (2021) Study on partial discharge characteristics and identification of typical defects in oil-paper capacitive bushing (in Chinese). Shandong University
5. Smith DJ, McMeekin SG, Stewart BG, Wallace PA (2011) The electric field modelling of a high voltage bushing with contaminants on the lower porcelain surfaces. In: 2011 annual report conference on electrical insulation and dielectric phenomena, Cancun, Mexico, pp 555–558
6. Yang D, Zhang W, Hao J, Du Z (2022) Diagnosis of moisture defects in insulation of 252 kV main transformer bushing. In: 2022 5th international conference on energy, electrical and power engineering (CEEPE), Chongqing, China, pp 6–10
7. Xinyi Q, Wei T (2022) Analysis and treatment of partial discharge in transformer bushing. *Electr Power Saf Technol* (in Chinese) 24(9):60–62
8. Yu N et al (2022) Study on partial discharge characteristics of typical defects of oil-paper capacitor bushing. In: 2022 IEEE 6th information technology and mechatronics engineering conference (ITOEC), Chongqing, China, pp 625–629
9. Yuxi C (2011) Study on electric field distribution of UHVDC bushing (in Chinese). Shandong University
10. Yi Z, Cheng C, Yue ZG, Guojun X (2015) Optimal design of transformer bushing capacitor core structure. *Electr Switch* (in Chinese) 53(4):66–68+73
11. Yubin W (2022) Common faults of transformer bushing and their countermeasures. *Min Equipment* (in Chinese) 2022(3):261–263
12. Shujian D, Ping H, Yue W (2008) Development of 1100 kV AC UHV transformer bushing. *Electr Porcelain Arrester* (in Chinese) 2008(2):1–6
13. Suman S, Ola SR, Mahela OP (2016) A study of industrial manufacturing and testing procedures for press board transformer insulation. In: 2016 IEEE 1st international conference on power electronics, intelligent control and energy systems (ICPEICES), Delhi, India, pp 1–6
14. Tianwei L, Bing L, Lei L, Bai L, Tang L (2018) Electric field calibration and software development of 500 kV transformer bushing. *Autom Instrum* (in Chinese) 2018(11):186–190
15. Hao C, Zurong H, Mengtao C, Dongdong Z, Xiaoning H, Jin L (2020) Study on spatial electric field characteristics of transformer bushing surface. *Guangdong Electr Power* (in Chinese) 33(7):107–112
16. Zhenghua H (2000) Study on relative dielectric constant of oil-water mixed media. *Oil Gas Field Surf Eng* (in Chinese) 2000(2):8–9+16

Coupling Simulation Study on Dislocation Slip of Self-Elastic Arcing Contact Sets of SF6 Circuit Breaker



Yakui Liu, Fengchao Wang, and Hongyun Li

Abstract High voltage circuit breaker plays a very important role in the safe operation of the power grid. One of the core components, self-elastic contacts made of tungsten-copper alloy, undertakes the task of switching circuits in its operation. The mechanical properties of the contacts are degraded during operation due to defects such as stress relaxation and metal fatigue. So that the contact force between the movable contact and stable contact decreases, which will lead to a serious failure of the circuit breaker. Since the contacts are inside the arc-extinguishing chamber and surrounded by SF₆ gas, it is difficult to achieve an accurate measurement of their mechanical properties. Therefore, the relationship between the plastic stress–strain of the contact and the change of the circuit breaker opening and closing must be calculated with the help of simulation technology. MATLAB and ABAQUS are combined to establish a discrete dislocation dynamics finite element coupling simulation program for tungsten-copper alloy self-elastic contacts, to simulate the dislocation evolution, and then to establish the contact plastic stress–strain relationship. The establishment of the model helps to understand the mechanical properties of the contacts during the operation of the circuit breaker, and this method is important for maintaining the safe and stable operation of the circuit breaker.

Keywords Self-elastic contacts · Finite element analysis · Dislocation evolution law

Y. Liu (✉) · F. Wang · H. Li
Qingdao University of Technology, Qingdao 266520, China
e-mail: lykppqq@163.com

Y. Liu
State Key Laboratory of Electrical Insulation and Power Equipment, Xi'an Jiaotong University,
Xi'an 710049, China

© Beijing Paiké Culture Commu. Co., Ltd. 2024
X. Dong and L. Cai (eds.), *The Proceedings of 2023 4th International Symposium on
Insulation and Discharge Computation for Power Equipment (IDCOMPU2023)*, Lecture
Notes in Electrical Engineering 1100, https://doi.org/10.1007/978-981-99-7393-4_32

341

1 Introduction

The dynamic mechanical behavior of materials has been a common concern of solid mechanics and materials science. It has been found through numerous microscopic experiments that when the microstructural scale of a material decreases to the micron scale, the strength of the material tends to increase significantly, exhibiting a significant microscale effect [1], and the scale effect has long been attributed to the presence of dislocations within the material. The dynamic mechanical behavior of crystalline materials is mainly controlled by dislocation dynamics, and the lamellar dislocation energy [2], Peierls stress [3], solid solution atoms [4], and precipitation-reinforced particles [5] are all influenced by the motion of dislocations and thus have an impact on the macroscopic mechanical behavior of materials, so dislocation dynamics is an important basis for studying the macroscopic mechanical behavior of materials [6].

Tungsten copper alloy contacts are subjected to strong mechanical shock and arc ablation during operation. At present, there are relatively few studies on the dislocation dynamics model of contacts. Self-actuated contacts work inside the interrupter chamber and are surrounded by SF₆ gas, and the mechanical properties of the contacts cannot be measured by conventional means. This paper combines MATLAB and ABAQUS to establish a discrete dislocation dynamics finite element coupled simulation model of tungsten-copper alloy self-actuated contacts, and obtains the dislocation evolution law of copper-tungsten alloy, and then obtains the plastic stress–strain relationship diagram of the contacts, which helps to analyze the mechanical property changes of the contacts during the operation of the circuit breaker.

2 Dislocation Motion

2.1 Dislocation Slip Speed

Dislocations are a kind of linear defects in crystals that can slip within their slip surfaces, and therefore are regarded as carriers of plastic flow of materials. The slip motion of a large number of dislocations inside the crystal constitutes the plastic deformation of materials on a macroscopic scale. Based on the previous analysis, both stress relaxation and metal fatigue can be regarded as the result of dislocation motion inside the crystal in essence.

Since it is difficult to measure the dislocation motion directly, simulation studies are needed to investigate the dislocation slip of self-actuated contacts of tungsten-copper alloy. This project is based on the 2D discrete dislocation dynamics simulation framework proposed by Needleman, which only considers the existence of edge dislocations in the crystal and ignores the role of spiral dislocations and mixed dislocations. There are several types of dislocation motions in the crystal: dislocations slip on the slip plane under stress, dislocations of opposite sign in the same slip

plane annihilate each other, dislocations in different slip systems are close to each other and block into forest dislocations, dislocations move to the crystal boundary and are adsorbed and plugged, and dislocation sources proliferate. According to the dislocation theory, the stress field between dislocations can be expressed as:

$$\sigma_x = \frac{-Gb(1-v)y(3x^2+y^2)}{2\pi(x^2+y^2)^2} \quad (1)$$

$$\sigma_y = \frac{Gb}{2\pi(1-v)} \frac{y(x^2-y^2)}{(x^2+y^2)^2} \quad (2)$$

$$\tau_{xy} = \frac{Gb}{2\pi(1-v)} \frac{x(x^2-y^2)}{(x^2+y^2)^2} \quad (3)$$

where G is the shear modulus, b is the dislocation Burgers vector, and v is the Poisson's ratio.

After finding the stress field, the interaction force between dislocations $f^{(J)}$ can be calculated as:

$$f^{(J)} = \left(\sigma + \sum_{K \neq J}^n \sigma^K \right) b^{(J)} m^{(J)} \quad (4)$$

where: σ is the external load on the dislocation (Pa); $\sigma^{(K)}$ is the force of dislocation K on dislocation J ; $b^{(J)}$ is the Burgers vector of dislocation J ; $m^{(J)}$ is the normal direction of the slip surface where dislocation J is located.

The dislocations are not only subject to external forces and inter-dislocation forces, but also subject to the lattice resistance piezoelectric force f_{P-N} during the slip motion, which can be expressed as the combined force on the dislocations as:

$$f_{P-N} = \frac{2G}{1-v} e^{-\frac{2\pi\xi}{b}} \quad (5)$$

The combined force on the dislocation is:

$$f_0 = f^{(J)} - f_{P-N} \quad (6)$$

After finding the stress on the dislocation, we can find the dislocation slip velocity:

$$v^{(J)} = \frac{f_0}{B_g} \quad (7)$$

where: $v^{(J)}$ is the slip velocity of dislocation J ; $B_{(g)}$ the linear resistance coefficient.

2.2 Unit Plasticity Strain Variables

Discrete dislocation dynamics simulation requires a large number of numerical calculations for solving the model dislocation motion, dislocation source multiplication and dislocation barriers. In this paper, we use MATLAB software to write a discrete dislocation dynamics simulation program. Firstly, the initialization pre-processing is carried out, including the establishment of a two-dimensional model, the initialization of pre-stored dislocations, dislocation sources and dislocation barriers in the model, etc.

The numerical field generated by the external load is calculated by means of finite elements and substituted into the dislocation dynamics to solve for the strain rate and other parameters, and then the plastic strain is brought into the finite elements to solve for the corresponding correction field, and the final numerical solution can be solved by superimposing the dislocation field and the correction field to obtain the total stress σ_0 and the total strain ε_0 respectively:

$$\sigma_0 = \sigma_{\text{fem}} + \sigma_{\text{DD}} \quad (8)$$

$$\varepsilon_0 = \varepsilon_{\text{fem}} + \varepsilon_{\text{DD}} \quad (9)$$

where: σ_{fem} is the elastic stress provided by the finite element; ε_{fem} is the elastic strain provided by the finite element; σ_{DD} is the plastic stress provided by the discrete dislocation dynamics; ε_{DD} is the plastic strain provided by the discrete dislocation dynamics.

In this paper, we use the MATLAB discrete dislocation dynamics program to call the ABAQUS software to calculate the finite element boundary load conditions in the simulation in order to improve the simplicity and versatility of the simulation. The calculated finite element stresses need to be input into the MATLAB dislocation dynamics program, and the stresses and strains from the dislocation dynamics solution are superimposed on the finite element field. ABAQUS is used in the program to provide the stresses needed for the dynamics calculations. When the finite element stresses are transferred to the dislocations, procedures such as dislocation multiplication are started. The material instanton equation in the finite element part of the coupled simulation contains only the elastic modulus, and the dislocations start to multiply and move after the material stresses reach the yield stress. The strain increment per unit time ε^p is:

$$\varepsilon^p = \frac{1}{2} \sum v_i (n_i b_i + b_i n_i) \quad (10)$$

where: v_i is the slip velocity of the dislocation; n_i is the slip direction normal unit vector of the dislocation; b_i is the Burgers vector of the dislocation.

By using the above equation, the incremental plastic strain within the cell can be calculated and combined with the iterative unit time, the plastic strain value of the cell at the current moment can be solved.

3 Analysis of the Theoretical Framework of Discrete Dislocation Dynamics

Discrete dislocation dynamics uses the defect-dislocation in a crystal as the basic unit to calculate the mechanical properties of a material at the macroscopic level by means of a dislocation field composed of dislocated dislocation behavior. As a new simulation framework proposed in the 1990s and gradually developed in the new century, it is able to balance computational efficiency and computational accuracy. It provides a new perspective and bottom-up interpretation of the scale effects of small-scale crystals. Understanding, developing, and refining this approach will have a positive effect on a deeper understanding of the mechanistic aspects of the plastic behavior of crystals. The theoretical framework of discrete dislocation dynamics based on this project is analyzed as follows:

Stress relaxation is a thermally activated process of movable dislocation motion driven by elastic strain energy. In this process, the elastic deformation of the material is gradually converted to plastic deformation, which gradually forms permanent plastic deformation after the continual accumulation of time. In addition, as time proceeds, the density of movable dislocations continues to decrease, while the rate of stress relaxation also decreases.

This project is based on the 2D discrete dislocation dynamics simulation framework proposed by Needleman, which only considers the existence of edge dislocations in the crystal and ignores the role of spiral dislocations and mixed dislocations. The dislocation motions in the crystal are mainly as follows: dislocations slip on the slip plane under stress, dislocations of opposite sign in the same slip plane annihilate each other, dislocations in different slip systems are blocked close to each other to form forest dislocations, dislocations move to the crystal boundary and are adsorbed and plugged, and dislocation sources proliferate.

The discrete dislocation dynamics simulation requires a lot of numerical calculations to solve the model dislocation motion, dislocation source proliferation and dislocation obstruction. The MATLAB software is used to write the discrete dislocation dynamics simulation program. Firstly, the initialization pre-processing is carried out, including the establishment of a two-dimensional model, the initialization of pre-stored dislocations, dislocation sources and dislocation barriers in the model, etc.

4 Finite Element Coupled Simulation Model

First, the model to be simulated is established in the finite element program and the boundary conditions are applied. At this time, no solution is required and the Inp file of ABAQUS is saved. When building the contact finite element simulation model, it is necessary to set up various material parameters, such as material properties in Table 1, stress–strain relationships in Table 2 and model properties in Table 3. Make the data parameters simulate the material properties of tungsten-copper alloy as much as possible, so that the subsequent calculation and analysis can better simulate the real situation and produce more accurate results.

Since this project mainly analyses the dislocation behaviour of the moving contact and the stress–strain change law, the motion of the static contact can be set relative to the reference system fixed on the moving contact by the relative motion, so the moving contact is stationary and the static contact is in motion. When the boundary conditions are applied to the dynamic contact because only one of the six degrees of freedom is open, the static contact of this analysis can be completely assumed as a rigid body, and thus ignore the static contact analysis calculation. Combining the settings of the contact analysis motion module with the boundary condition application method, the

Table 1 Material properties

Density/g/cm ⁻³	15.688
Yield strength/MPa	1000
Modulus of elasticity	334,000
Poissonbee	0.34

Table 2 Stress–strain relationship

	Yield stress	Plastic strain
1	1000	0
2	1100	0.000353
3	1300	0.000354
4	1500	0.000355
5	1800	0.000357

Table 3 Model attributes

Type	Setting method
Surface-to-surface contact	Finite slip
Normal phase behaviour	Tangential behaviour
Pressure overfills hard contact	Frictionless
Field output request	Course output request
Frequency: every <i>n</i> increments	Frequency: every <i>n</i> increments
Output variables: <i>S</i> , <i>U</i>	Output variables: ALLEN

ABAQUS finite element analysis part of this project effectively reduces the difficulty of the coupling calculation, greatly improves the analysis accuracy, and reduces the calculation time, making the research efficiency effectively improved.

After initializing the boundary conditions in ABAQUS and applying external conditions such as external forces or velocities, the total stress and strain occurring in the 3D contact model under the action of external forces can be simulated. The contact force generated by the dynamic contact movement colliding with the static contact during circuit breaker closing is the root cause of the contact strain. To analyse the mechanical properties of the contacts, the collision contact stresses of the moving and static contacts are first simulated and calculated. The values of stress and strain at each point will change with time so that all data can be exported in csv format, including total stress and total strain, which can be received by MATLAB and used as the initial condition to start the dislocation movement, and finally MATLAB will get the changes of plastic stress and plastic strain with time and save them in csv format for ABAQUS. When the data is received by ABAQUS, the second collision simulation can be performed.

See Figs. 1, 2 and 3.

The algorithm flow is shown in Fig. 1. After initializing the boundary conditions in ABAQUS, external conditions such as external forces or velocities are applied to simulate the total stress and strain occurring in the three-dimensional contact model under the action of external forces. To analyse the mechanical properties of the contacts, the collision contact stresses of the moving and static contacts are first simulated and calculated. The stress and strain values at each point change over time, and the data can be exported in csv format, including total stress and total strain. The exported data from ABAQUS can be received by MATLAB and used as the initial condition to make the dislocation start to move, and finally MATLAB will get the change of plastic stress and plastic strain over time and save them in csv format for ABAQUS to receive. This process is the coupling process of MATLAB and ABAQUS.

Since the plastic strain cannot be recovered, the plastic strain and plastic deformation can only increase as shown in Fig. 3. The total stress, including elastic stress and plastic stress, starts to increase at the moment of contact, and the total stress is positively correlated with the total strain. If plastic deformation occurs, when the contact is disconnected, the total stress is plastic stress.

The subsequent bit error calculation is performed and the updated data is obtained as shown in Fig. 2.

5 Conclusions

In this paper, a discrete dislocation kinetic-finite element coupling simulation program for the self-actuated contacts of tungsten-copper alloy is established by combining relevant mechanical calculations and finite element analysis, and the

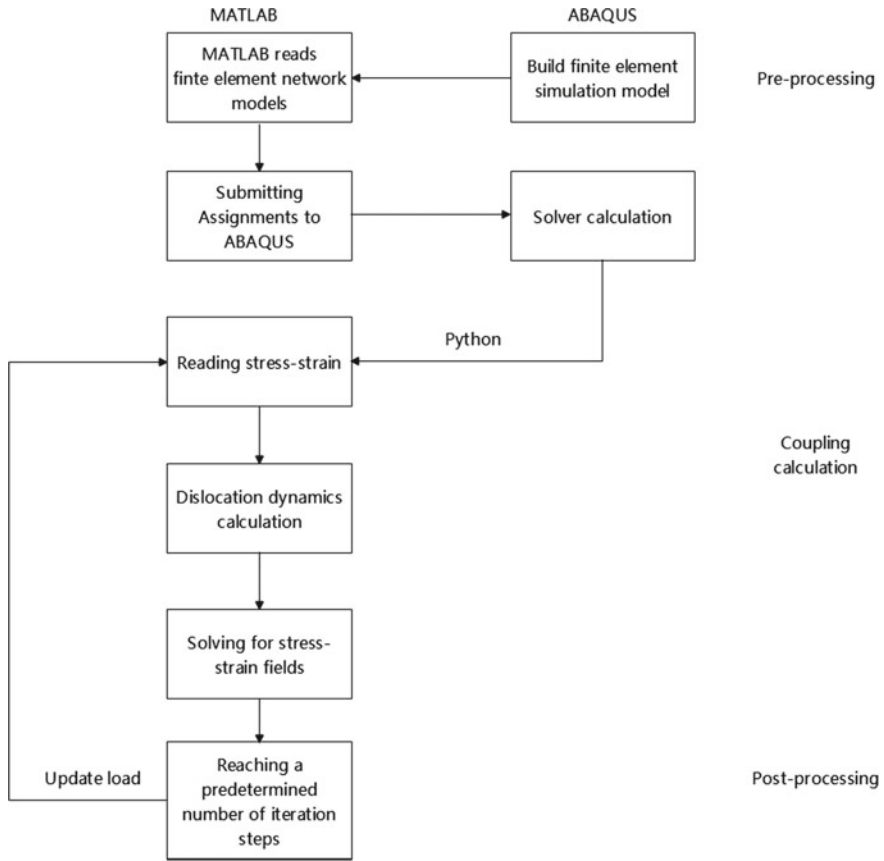


Fig. 1 Finite element coupling operation flow

dislocation evolution law of copper-tungsten alloy is obtained by simulation. The following conclusions are drawn:

- (1) According to the finite element analysis, the maximum stress is at the root of the dynamic contact at the moment of contact and the stress reaches the yield limit when the tungsten-copper alloy contact reaches 1000 MPa, followed by plastic strain.
- (2) A plot of plastic stress as a function of strain as a function of time for the contacts is obtained by MATLAB correlation calculations.

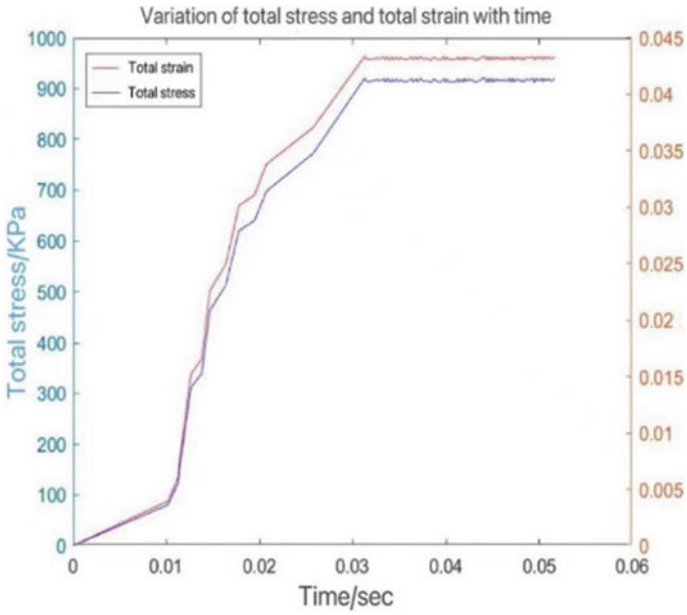


Fig. 2 Total stress–strain relationship diagram

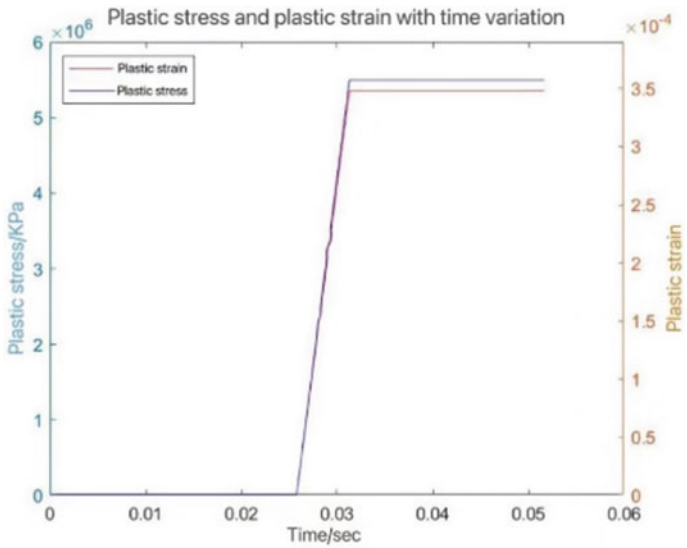


Fig. 3 Plastic stress and plastic strain with time variation

Acknowledgements This work was supported in part by the Natural Science Foundation of Shandong Province (ZR2021QE289), and in part by State Key Laboratory of Electrical Insulation and Power Equipment (EIPE22201).

References

1. Greer JR, De Hosson JTM (2011) Plasticity in small-sized metallic systems: Intrinsic versus extrinsic size effect [J]. *Prog Mater Sci* 56(6):654–724
2. Guo X, Sun C, Wang C et al (2021) Study of dislocation-twin boundary interaction mechanisms in plastic deformation of TWIP steel by discrete dislocation dynamics and dislocation density-based modeling [J]. *Int J Plast* 145:103076
3. Joos B, Duesbery MS (1997) The Peierls stress of dislocations: an analytic formula [J]. *Phys Rev Lett* 78(2):266
4. Sun L, Dong N, Wang J et al (2022) Effect of solid solution Zn atoms on corrosion behaviors of Mg-2Nd-2Zn alloys [J]. *Corros Sci* 196:110023
5. Zhou K, Wang Z, He F et al (2020) A precipitation-strengthened high-entropy alloy for additive manufacturing [J]. *Addit Manuf* 35:101410
6. Zbib HM, De La Rubia TD, Rhee M et al (2000) 3D dislocation dynamics: stress–strain behavior and hardening mechanisms in fcc and bcc metals [J]. *J Nucl Mater* 276(1–3):154–165

Analysis of Aging Degree of Composite Insulators Based on Joint Relaxation Spectrum



Ding Zhang, Xinwen Hou, Yufei Zhang, Chuangang Zhu, Xiaonan Li, Xiong Ge, Ran Zhong, and Yu Lei

Abstract In power systems, composite insulators are subjected to strong electric fields and environmental corrosion, and will age and affect the electrical insulation effect; however, existing insulator aging detection methods are limited by the test environment, and it is difficult to intuitively reflect the microchemical structure changes of silicone rubber materials. In this paper, the NMR relaxation spectrum analyzer and CPMG signal were used to verify the feasibility of T_2 relaxation spectrum for aging degree detection, and the combined sequence of IR-CPMG was proposed to experiment on composite insulators with different aging years. The results show that detecting the signal amplitude of the joint sequence and inverting the two-dimensional relaxation spectrum can visually characterize the change of the main hydrogen-containing group from the height and volume of the joint spectral peak, and effectively distinguish the composite insulators with different aging degrees.

Keywords Composite insulators · Nuclear magnetic resonance · IR-CPMG · Joint relaxation spectrum

1 Introduction

In transmission systems, insulators can be divided into ceramic insulators, glass insulators, and silicone rubber composite insulators according to their insulation materials, among which composite insulators have the advantages of high mechanical strength, unbreakably, and good stain resistance, and have been widely used in recent years [1–3]. However, under the strong electric field distribution of the working environment and the corrosion of the natural environment, molecular group fractures

D. Zhang · X. Hou · C. Zhu · X. Ge · R. Zhong · Y. Lei
UHV Company of State Grid Hubei Electric Power Co., Ltd, Wuhan 430050, China

Y. Zhang · X. Li (✉)
Institute of Electrical Engineering, Chinese Academy of Sciences, Beijing 100190, China
e-mail: lxn@mail.iee.ac.cn

© Beijing Paiké Culture Commu. Co., Ltd. 2024
X. Dong and L. Cai (eds.), *The Proceedings of 2023 4th International Symposium on Insulation and Discharge Computation for Power Equipment (IDCOMPU2023)*, Lecture Notes in Electrical Engineering 1100, https://doi.org/10.1007/978-981-99-7393-4_33

will occur inside the silicone rubber composite insulator [4], which affects the electrical insulation effect between the wire and tower; therefore, it is of great significance to detect the aging state of the composite insulator. Currently, the commonly used composite insulator aging detection methods include the direct observation method, hydrophobic detection method, leakage current method, ultraviolet detection method, etc. [5–7]; the subjective judgment of testers limits some of these methods, some are demanding on the test environment, and it is difficult to reflect the microstructural changes in silicone rubber materials intuitively. In contrast, nuclear magnetic resonance (NMR) technology is a phenomenon of precession evolution of material spin ensembles under the action of an applied magnetic field, which is widely used to study the structure and dynamic properties of rubber and polymer materials and is currently used in chemical analysis, medical imaging, geological exploration, and other fields for microstructure reproduction and molecular dynamics information extraction [8–11]. As a powerful nondestructive testing technology, finding the intrinsic relationship between relaxation parameters and the aging of composite insulator umbrella skirts has excellent theoretical and practical significance for the research on the aging characteristics and mechanism of silicone rubber composite insulator umbrella skirt sheaths and scientifically evaluating the service life of composite insulators.

Detection methods based on NMR relaxation spectra can be used stably and reliably to analyze insulator aging. The NMR relaxation spectrum mainly adopts the transverse relaxation time T_2 spectrum analysis detection method [12–14]. The collected time-domain echo signal is a Laplace transform, and the analysis results of the transformation are compared with the detection results of other methods. In 2002, Song et al. proposed a fast two-dimensional T_1 – T_2 correlation spectral Laplace inversion algorithm [15], marking the beginning of Laplace's multidimensional NMR technology. The two-dimensional relaxation spectrum adds the relaxation information of T_1 based on the T_2 spectrum [16], which effectively distinguishes substances with significant differences in the diffusion coefficient and is widely used in petrophysical research. At present, the chemical structure and aging mechanism of composite insulators are analyzed, and the laboratory Newman relaxation spectrum analyzer is used to carry out T_2 relaxation spectrum and T_1 – T_2 combined relaxation spectrum detection, which verifies the feasibility of using the T_1 – T_2 combined relaxation spectrum to measure the aging degree of composite insulators.

2 Analysis of Aging Mechanism of Insulators

The main component of the silicone rubber composite insulator umbrella skirt is polydimethylsiloxane, which mainly contains C–Si bonds, Si–O bonds, etc., owing to the influence of the external strong electric field and harsh working environment; C–Si bonds, Si–O bonds, and other bonds can be weakened or even broken; some molecular groups break away from the main group and the oxygen and water molecules in the air chemical reaction, producing $\cdot\text{H}$, $\cdot\text{CH}_3$ and Free radicals, as shown in Fig. 1.

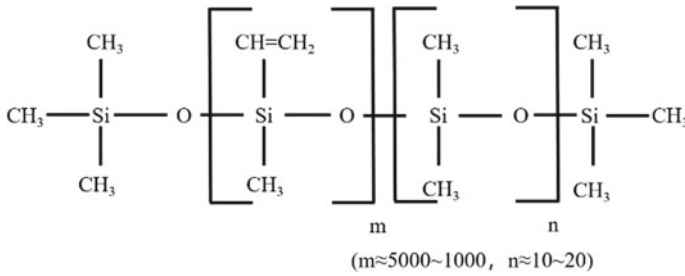


Fig. 1 Molecular formula of polydimethylsiloxane

In the chemical mentioned above reactions that cause the degradation of insulation performance, the number and state of H-containing groups in the composite insulator will change, and this structural change will lead to a decrease in the non-polarity of the composite insulator, a decrease in hydrophobicity, and different degrees of pulverization and embrittlement. Therefore, detecting and analyzing the NMR relaxation spectrum of the umbrella skirt can indirectly determine the degree of aging of the insulator.

3 Nuclear Magnetic Resonance and Detection Signal

Nuclear magnetic resonance is a physical phenomenon in which the nuclear magnetic moment of a material atom splits at an energy level under the action of an external magnetic field and produces an energy level transition under the action of an applied radio frequency magnetic field. When the magnetic nucleus is in a uniform external magnetic field B_0 , the nucleus is subjected to the action of the magnetic moment, which is manifested as follows: while the nucleus rotates around its axis, it must show precession in the direction of the applied magnetic field, which is called the La-more precession. The Lamore precession angle frequency, ω_0 , was determined using the Lamore precession equation.

In the detection of the composite insulator aging NMR relaxation spectrum, the main factors affecting the signal amplitude are the ambient temperature, sample quality, gain of the amplifier of the detection device, and the continuous spin-echo sequence used. Under the given conditions, the signal size depends on the proton density of the sample, transverse relaxation time T_2 , and longitudinal relaxation time T_1 . The acquired signal strength of an RF echo scan sequence can be expressed as Eq. (1)

$$S = K \cdot [H] \cdot (1 - e^{-TR/T_1}) \cdot e^{TE/T_2} \tag{1}$$

where K is the proportion factor of the detection device, which is related to the factors of the detection instrument itself; $[H]$ is the proton density, which is related to the

mass of the sample being measured; TR is the sequence repeat time; and TE is the echo time. It can be seen from Eq. (1) that for the detection of the relaxation spectrum curve of the insulator aging degree inversion, the e-index factor terms can reflect the aging degree of insulators under different ages and grid conditions.

For the measurement of longitudinal relaxation time T_1 , the Inverse Recovery signal is often used for testing. One period of the pulse train is that a 180° pulse is first applied, a 90° pulse is applied after the reversal time, and after a while, the 180° pulse is applied again to refocus and acquire the signal echo, as shown in Fig. 2. Different reversal times TI is set for n periods of pulse trains to obtain a longitudinal magnetization strength recovery curve.

Since the CPMG sequence (Carr-Purcell-Meiboom-Gill) can greatly eliminate the signal attenuation caused by the inhomogeneity of the external magnetic field, the self-selected pulse train signal is usually selected for the transverse relaxation time T_2 for testing. The pulse consists of a 90° pulse and several 180° pulses, as shown in Fig. 3. For molecular systems with simple structures, the attenuation signal of the measured echo peak.

In this study, the T_1 - T_2 combination method is adopted; that is, the combination of IR-CPMG is used to detect the aging degree of the composite insulator, and the pulse train signal is shown in Fig. 4.

Fig. 2 The signal of inverse recovery

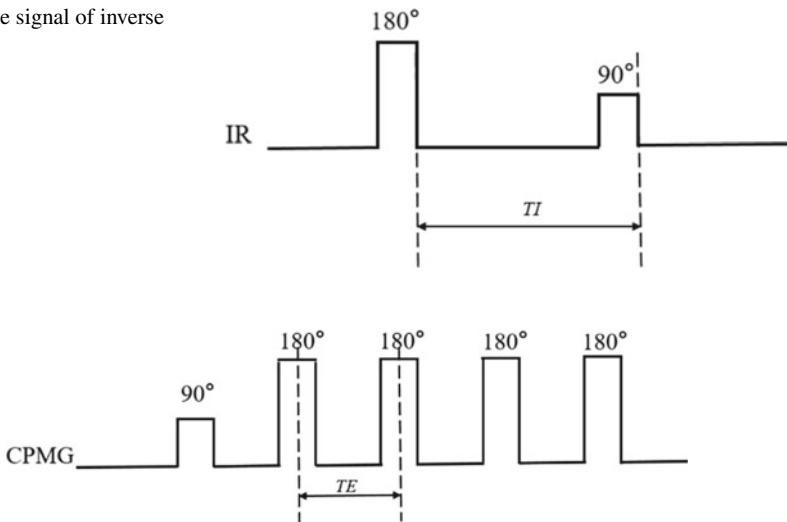


Fig. 3 The sequence of CPMG

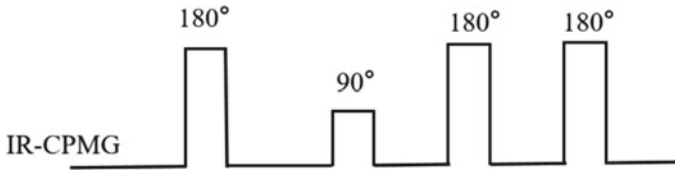


Fig. 4 The sequence of IR-CPMG

4 Insulator Aging Degree Detection

The record information of aging composite insulator samples is shown in Table 1, the service life of the three composite insulators is 7 years, 5 years and 12 years, respectively, and the samples sent for inspection are collected from the same part at the middle end of the composite insulator.

In this experiment, the Suzhou Newman Insulator Aging Relaxation Spectrum Analyzer was used for data acquisition and inversion, the magnet field strength in the analyzer was 0.5T, and the temperature control of the permanent magnet by the instrumentation was constant at 32 °C; to improve the smoothness of the distribution of T_2 one-dimensional spectral data, the SIRT algorithm was used for signal inversion.

The experiment first uses a standard NMR continuous echo sequence, that is, the CPMG signal, to measure the T_2 relaxation spectrum time-domain signal of the sample; the parameters of the CPMG sequence in the experiment are shown in Table 2.

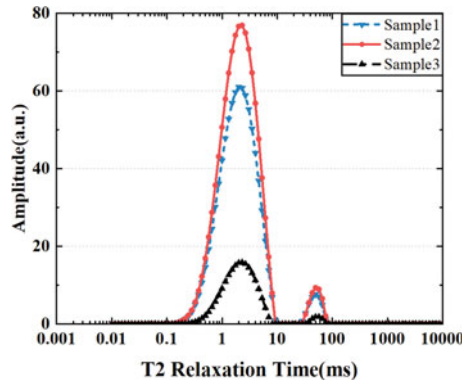
Table 1 The information of aging insulators

Sample number	The age of the sample	Degree of aging	Voltage level (kV)	Production location
1#	7 years	Slight chalking and cracking	±500	Zibo, Shandong
2#	5 years	No chalking, and slight cracking	500	Cangzhou, Hebei
3#	12 years	Severe chalking and cracking	1000	Xiang Yang, Hubei

Table 2 CPMG sequence parameters

Sequence Parameters	Center frequency (MHz)	90° pulse width (μs)	180° pulse width (μs)	Echo time (ms)	Number of echoes	Number of accumulations
Value	20.5539	7	11.04	1	200	4

Fig. 5 The T_2 lateral relaxation time spectrum of three samples



In the T_2 relaxation spectrum, the lateral relaxation time T_2 of the H atoms in the atomic cluster is the abscissa corresponding to the respective peaks, and the area enclosed by the peaks and the transverse axis can be the tent of the H atoms in the crest atomic cluster, as shown in Fig. 5.

From the area of the curve, sample 2 measured the largest inversion crest area. The area of the principal peak was 1062.874. The area of the secondary peak was 38.275, followed by the crest area of sample 1, the area of the principal peak was 874.422, and the area of the secondary peak was 31.544; In contrast, the crest area of sample 3 was much smaller than that of sample 1 and sample 2; the area of the two peaks was 192.627 and 7.92, respectively. The measurement results are consistent with the corresponding aging degree of the experimental sample in Table 1; that is, sample 3 has the most aging severe degree, the umbrella skirt pulverized and cracked seriously, followed by sample 1, with the umbrella skirt pulverized and slightly cracked, and the lightest aging degree is only slightly cracked sample 2.

In general, the lateral relaxation time of NMR can reflect the proximity between hydrogen atoms, and the lateral relaxation time is an essential characteristic quantity that reflects the state of hydrogen atoms in a substance. From the relaxation time of the prominent peaks of the three samples, the relaxation time of samples 1 and 2 was the shortest, the T_2 relaxation time corresponding to the two prominent peaks was the same as 2.31 ms, and the T_2 relaxation time corresponding to the main peak of sample 3# was 2.01 ms. With increasing sample aging, the T_2 relaxation time of the main peak showed an overall decreasing trend.

In order to more intuitively reflect the aging degree of composite insulator samples of different ages and distinguish atomic groups more intuitively, we used the method of T_1 - T_2 joint inversion and used IR-CPMG sequence for testing. The inverted time series of the IR signal is shown in Table 3.

For the CPMG signal in this joint sequence, we take the same parameters as in Table 2, and the measured two-dimensional relaxation spectrum is shown in Fig. 6.

From the combination of the T_1 - T_2 spectra, we obtained the distribution curve of $\log(T_1/T_2)$, as shown in Fig. 6. There were four peaks in the distribution curve, and the T_1/T_2 ratio for each peak in the three samples did not change significantly.

Table 3 The inverted time series of the IR signal

Serial number	1	2	3	4	5
Reversal time (ms)	0.09	0.17	0.51	1.50	4.43
Serial number	6	7	8	9	10
Reversal time (ms)	13.09	38.70	114.42	338.27	1000

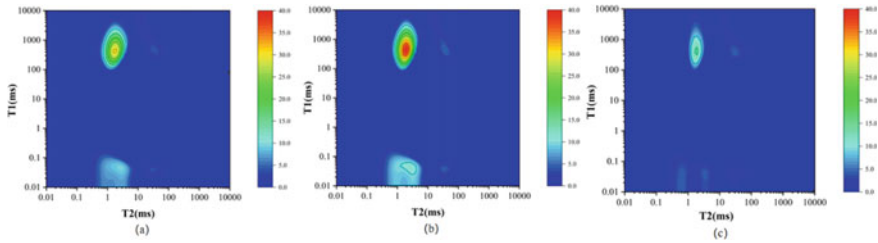


Fig. 6 IR-CPMG combined relaxation spectrum

The lower peak of $T1/T2$ corresponds to the brightest peak in the $T1-T2$ spectrum in Fig. 6, representing the most crucial hydrogen-containing group in silicone rubber insulators. The height of the joint relaxation spectrum varies for insulator samples with different aging ages. The height of the relaxation spectrum of sample 2 was 39.85, followed by the height of the relaxation spectrum of sample 1 was 30.41, and the height of the relaxation spectrum of sample 3 was 13.77.

In addition, we analyzed the integral values of the height under the combined relaxation spectrum of $T1-T2$, as shown in Table 4. The integral values corresponding to peaks 1 and 2 decreased significantly with the change in aging degree, representing the two hydrogen-containing groups with the most significant influence on the aging degree. In contrast, the integral value changes of peaks 3 and 4 did not seem obvious. Proportionally, with an increase in aging years, the integral proportions of peaks 3 and 4 were 7.1%, 7.7%, and 17.4%, respectively, and the proportion increased with an increase in the aging age of the sample.

Compared with the $T2$ relaxation spectrum excited by a single CPMG signal, the $T1-T2$ combined relaxation spectrum measured by the IR-CPMG sequence can more intuitively reflect the hydrogen-containing groups in the sample. From the leading hydrogen-containing group of the joint spectrum, the peak height and integration of the sample decreased significantly with increasing aging age. In future research, other

Table 4 The integral value of the spectral peak

Spectral peak serial number	1	2	3	4
Sample1	1877.397	982.651	166.097	69.748
Sample2	2268.932	1238.664	188.125	79.587
Sample3	635.737	445.308	157.781	69.745

sequences such as PIR-CPMG and BE-CPMG can be considered for the inversion of two-dimensional relaxation spectra. The specific changes and cleavage processes of internal hydrogen-containing groups can be analyzed from a microscopic perspective according to multiple sets of two-dimensional relaxation spectra.

5 Conclusion

In this study, relaxation spectrum analysis of insulator samples with different running hours of the hanging network was carried out using a nuclear magnetic resonance relaxation spectrum detection instrument. First, the CPMG sequence was used to analyze the aging degree of the existing insulator samples, which verified the feasibility of the T_2 relaxation spectrum for aging detection. The IR-CPMG signal was used to measure the T_1 – T_2 two-dimensional relaxation spectrum, and it was found that the height and integral value of the combined relaxation spectrum changed significantly with an increase in the aging age of the composite insulator, which would be more conducive to the analysis of the aging degree of the composite insulator. The analysis of the T_1 – T_2 combined relaxation spectrum in this study provides a new method for evaluating the aging degree of composite insulators for inspection work in power systems.

Acknowledgements Project Supported by the Science and Technology Project of State Grid Corporation of China(SGHBCG00JMJS2200873; SGHBCG00JMJS2200874).

References

1. Zhang Z, Liang T, Xiang Y et al (2022) Effect of depowdering on the performance of silicone rubber composite insulator. *Trans China Electrotech Soc* 37(08):2126–2135
2. Li T, Tao R, Zhang R et al (2022) Infrared characteristic of typical composite insulator heating defects and selection of field unmanned aerial vehicle infrared test parameters. *High Voltage Eng* 48(03):865–875
3. Cao W, Feng H, Xue H et al (2021) Mechanisms and influence factors of dynamic behavior of water droplets on the composite insulator surface under AC Electric field. *Progr Electromagn Res Lett* 98:9–18
4. Kaneko T, Ito S, Minakawa T et al (2019) Degradation mechanisms of silicone rubber under different aging conditions. *Polym Degrad Stab* 168:108936
5. Fan H, Liu Y, Wang L et al (2021) Influence of closing joints of epoxy resin insulator on water diffusion test. *Power Syst Technol* 45(06):2420–2426
6. Tian S (2020) Study on the influence of surface texture of silicone rubber insulator on its anti icing performance. China Three Gorges University
7. Fang C, Wang J, Hu C et al (2012) Research on discharge phenomena of composite insulators during tracking wheel test and analysis on leakage current characteristic. *Power Syst* 36(04):242–246

8. Camilloni C, De Simone A, Vranken WF et al (2012) Determination of secondary structure populations in disordered states of proteins using nuclear magnetic resonance chemical shifts. *Biochemistry* 51(11):2224–2231
9. Ji Y, He W, Wu G et al (2015) Optimization of RF coil in single-sided NMR system. *Adv Technol Electr Eng Energy* 34(09):75–80
10. Zhou K, Liu T, Hu Z (2018) Exploration of damage evolution in marble due to lateral unloading using nuclear magnetic resonance. *Eng Geol* 244:75–85
11. Li J (2022) Structure design of portable NMR main magnet system and RF coil. Northeast Electric Power University
12. Zhang Z, Pang G, Lu M et al (2022) Research on silicone rubber sheds of decay-like fractured composite insulators based on hardness, hydrophobicity, NMR, and FTIR. *Polymers* 14(16):3424
13. Xia Y, Song X, He W (2020) Nuclear magnetic resonance method for analyzing aging status of composite insulators. *High Voltage Apparatus* 56(02):197–201+209
14. Yu C, Gong W, Xu X et al (2021) Design of a portable unilateral magnetic resonance sensor for aging detection of silicone rubber insulators. *Electr Eng* 05:118–121
15. Song YQ, Venkataramanan L, Hürlimann MD et al (2002) T1–T2 correlation spectra obtained using a fast two-dimensional Laplace inversion. *J Magn Reson* 154(2):261–268
16. Zhang B, Chen J (2014) Characterization of shale oil rocks using retort and NMR. In: SPE unconventional resources technology conference, USA, pp 78–100

Simulation for the Chain Formation of Cellulose Particles in Flowing Transformer Oil Under DC Voltage



Yuhang Yao, Mengyue Yu, Cheng Pan, Suyi Xia, and Ju Tang

Abstract The formation of impurity bridges in transformer oil can be altered by the oil flow, which in turn influences the breakdown progress of contaminated oil. In this paper, a solid–liquid two-phase flow model that incorporated both uniform and non-uniform electric fields was developed. The chain-forming behaviors in oil were simulated under various flow velocities and the experimental verification was carried out. It was shown that in stationary oil, the cellulose particles would gradually converge along the direction of electric field. Then particle chains were established across the gap, starting and ending with the adsorbed particles on the electrode surface. In non-uniform electric fields, the chains were broader and particles accumulated more tightly. However, the formation of particle chains was inhibited when the transformer oil flowed. Furthermore, complete chains could not be formed after the flow velocity increased to 20 mm/s. Finally, the mechanism of particle chain formation and the effect of flow velocity on the bridge-forming were discussed in relation to the changes in the force conditions.

Keywords Transformer oil · Cellulose particles · Flow velocity · DEP force · Impurity bridges

1 Introduction

The converter transformer is one of the key equipment in the High-voltage direct current (HVDC) system, which plays a crucial role in ensuring safe and stable operation of system [1]. The oil-paper composite insulation is mainly employed in converter transformers, where the quality of the oil has a significant impact on overall insulation performance [2]. Nevertheless, during the manufacturing, installation, operation, and maintenance, transformer oil is inevitably contaminated by solid particles, such as metallic particles and cellulose particles. Among them, cellulose

Y. Yao · M. Yu · C. Pan (✉) · S. Xia · J. Tang

School of Electrical Engineering and Automation, Wuhan University, Wuhan 430072, China
e-mail: pancheng1986@whu.edu.cn

© Beijing Paiké Culture Commu. Co., Ltd. 2024

X. Dong and L. Cai (eds.), *The Proceedings of 2023 4th International Symposium on Insulation and Discharge Computation for Power Equipment (IDCOMPU2023)*, Lecture Notes in Electrical Engineering 1100, https://doi.org/10.1007/978-981-99-7393-4_34

361

particles account for more than 90% of the total impurities [3]. It has been shown that the accumulation of solid impurities in the oil gap can cause a significant degradation of the insulation performance, causing serious damage to the liquid-phase insulation of transformers [4].

At present, the classic “particle bridge theory” is commonly used to explain transformer oil breakdown due to the impurities. That is, solid particles will accumulate in areas of high field strength under the action of electric field forces, forming an “impurity bridge” across the gap and causing insulation breakdown [5]. The bridge-forming behaviors of cellulose particles in transformer oil have been investigated. Shekhar Mahmud et al. studied the bridge formation behaviors of cellulose particles in transformer oil under DC, AC, and AC/DC combined voltages. They founded that only when a stable DC electric field was applied, particle bridges would appear across both electrodes. And the small particles would form bridges faster [6]. Dan et al. studied the aggregation characteristics of cellulose particles in oil under AC and DC voltages and analyzed the morphological characteristics of particle bridge under different voltages. It was found that particles were adsorbed on the electrode surface in the form of short whiskers under AC voltage, while they were interconnected to form fiber bridges across both poles under DC voltage [7]. Li et al. studied the generation and growth of impurity bridges in oil-paper insulation systems under constant negative DC voltage. They divided the development of bridges into three stages: pre-generation, growth, and initiation of breakdown. It was concluded that the high-risk bridges generated in the third stage were the key factors that trigger insulation damage, and the breakdown always occurred along the bridges [8].

Existing studies on the bridge formation characteristics have always been conducted in static transformer oil. However, the transformer oil in actual equipment keeps flowing due to oil circulation cooling system and temperature gradient [9]. The oil flow changes the force on particles and in turn affects the bridging approach. Our group conducted an experimental study on the bridging characteristics of cellulose particles in flowing oil [10]. A high-speed camera was used to capture images of bridge formation at different flow rates. The results showed that the oil flow changes the morphology of bridges and the formation of bridges is delayed or even destroyed at higher flow rates. However, the above study only provided a superficial analysis of the experimental phenomena. The bridge formation mechanism of particles in flowing oil still needs to be further explored.

Based on the insufficiency of the previous study, this paper presents an exhaustive force analysis of cellulose particles in oil. And a simulation model of solid-liquid two-phase flow coupled with uniform and non-uniform electric fields was established, respectively. The bridge-forming behaviors of particles in oil at different flow velocities were simulated. Finally, the mechanism of influence of oil flow on particle chain formation was discussed, which supports the next explanation of the breakdown for flowing oil.

2 Numerical Modelling of Chain Formation

2.1 Equations of Continuous Phase

The schematic diagram of the solid–liquid two-phase flow model is shown in Fig. 1, where the continuous phase is set as transformer oil in the electrode gap, and the discrete phase is the cellulose particles. Since the volume fraction of particles is much less than 10%, the discrete phase is considered to be dispersed and the Eulerian–Lagrangian method can be used to solve for the particle motion. Assuming that the transformer oil is an incompressible Newtonian fluid, the Navier–Stokes equation is used to solve for the continuous phase [11]. The continuity equation is expressed in Eq. (1), where \mathbf{u} is the oil flow velocity, p is the fluid pressure, ρ is the transformer oil density. η is the dynamic viscosity and ∇^2 is the Laplace operator. \mathbf{F}_v characterizes the coupling relationship between the discrete phase and the continuous phase, as shown in Eq. (2). $\mathbf{F}_{D,i}$ is the traction force of the fluid on the i th particle. \mathbf{r} is the arbitrary position vector in the fluid and \mathbf{r}_i refers to the position vector of the i th particle. δ is the Dirac function and N is the total number of particles.

$$\rho \frac{\partial \mathbf{u}}{\partial t} + \rho(\mathbf{u} \cdot \nabla)\mathbf{u} = \rho \mathbf{g} - \nabla p + \eta \nabla^2 \mathbf{u} + \mathbf{F}_v \tag{1}$$

$$\mathbf{F}_v = - \sum_{i=1}^N \mathbf{F}_{D,i} \delta(\mathbf{r} - \mathbf{r}_i) \tag{2}$$

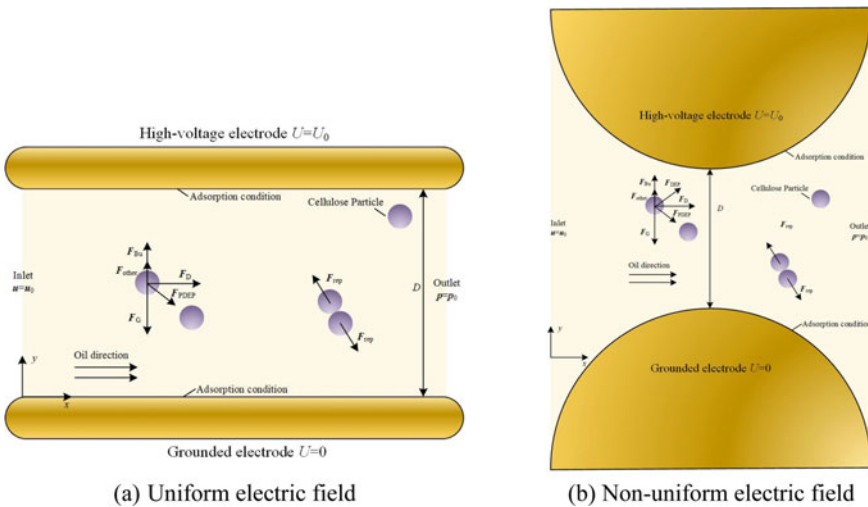


Fig. 1 Schematic diagram of solid–liquid two-phase flow model

2.2 Equations of Discrete Phase

The kinetic equations in the Lagrangian coordinate system are used to calculate the state of motion of the particles:

$$\frac{4}{3}\pi R^3 \rho_p \frac{d\mathbf{v}_p}{dt} = \mathbf{F}_G + \mathbf{F}_{Bu} + \mathbf{F}_{rep} + \mathbf{F}_D + \mathbf{F}_{DEP} + \mathbf{F}_{PDEP} + \mathbf{F}_{others} \quad (3)$$

where R and ρ_p are the radius and density of cellulose particles, \mathbf{v}_p is the particle velocity. Particles in oil will be subjected to gravitational force (\mathbf{F}_G), buoyancy force (\mathbf{F}_{Bu}), collision force (\mathbf{F}_{rep}), dielectrophoretic force (\mathbf{F}_{DEP}), secondary dielectrophoretic force (\mathbf{F}_{PDEP}), \mathbf{F}_{others} mainly includes additional mass force, pressure gradient force, Magnus force, etc., which can be found in Ref. [11]. Among them, the gravitational and buoyancy forces on the particles can be calculated by the following equations:

$$\mathbf{F}_G = \frac{4}{3}\pi R^3 \rho_p \mathbf{g} \quad (4)$$

$$\mathbf{F}_{Bu} = -\frac{4}{3}\pi R^3 \rho \mathbf{g} \quad (5)$$

The generation mechanism of the dielectrophoretic force on cellulose particles is attributed to the non-uniform distribution of the electric field, and its action can be divided into global and local effects. Global dielectrophoretic is the motion generated by the interaction of the polarized particles with a non-uniform electric field. When the particles are suspended in solution, the charges inside the particles and inside the solution under the action of the external electric field produce directional movement along the direction of the electric field, forming an electric dipole parallel. The different forces on the two ends of the dipole in the non-uniform electric field cause the particles to move [12]. The equation for the dielectrophoretic force can be shown by Eq. (6), where, \mathbf{p} is the equivalent dipole moment formed, which can be calculated by Eq. (7). In the equation, ε_0 ε_m ε_p are the vacuum dielectric constant, the relative dielectric constants of the solution and the particles, respectively.

$$\mathbf{F}_{DEP} = (\mathbf{p} \bullet \nabla) \mathbf{E} \quad (6)$$

$$\mathbf{p} = 4\pi \varepsilon_0 \varepsilon_m R^3 \frac{\varepsilon_p - \varepsilon_m}{\varepsilon_p + 2\varepsilon_m} \mathbf{E} \quad (7)$$

From a microscopic view, when particles are close to each other, the positive charge on each electric dipole will attract the negative charge on another dipole, pushing the particles close to each other and connect together to form a chain. This effect calls the secondary dielectrophoretic effect [13]. The specific calculation formula of \mathbf{F}_{PDEP} between the i th and j th particle is:

$$\begin{aligned} \mathbf{F}_{\text{PDEP},ij} = & \frac{1}{4\pi\epsilon_0\epsilon_m} \frac{3}{R_{ij}^5} [\mathbf{R}_{ij}(\mathbf{p}_i \bullet \mathbf{p}_j) + (\mathbf{R}_{ij} \bullet \mathbf{p}_i)\mathbf{p}_j \\ & + (\mathbf{R}_{ij} \bullet \mathbf{p}_j)\mathbf{p}_i - \frac{5}{R_{ij}^2} \mathbf{R}_{ij}(\mathbf{p}_i \bullet \mathbf{R}_{ij})(\mathbf{p}_j \bullet \mathbf{R}_{ij})] \end{aligned} \quad (8)$$

where \mathbf{R}_{ij} is the Eulerian distance vector between particle i and j . For the particles in oil, they can be equated as isotropic cellulose spheres of radius a . In this way, the dipole moments of each particle in the uniform electric field are of the same magnitude and direction. Based on this, \mathbf{F}_{PDEP} in the uniform electric field can be reduced to Eq. (9), where θ is the angle between \mathbf{R}_{ij} and \mathbf{p} .

$$\begin{cases} F_x = \frac{3p^2 \sin\theta(1-5\cos^2\theta)}{4\pi\epsilon_0\epsilon_m R_{ij}^4} \mathbf{i}_x \\ F_y = \frac{3p^2 \cos\theta(3-5\cos^2\theta)}{4\pi\epsilon_0\epsilon_m R_{ij}^4} \mathbf{i}_y \end{cases} \quad (9)$$

To ensure that no overlap occurs between particles, collision forces need to be considered. A hard sphere collision model is used to calculate the elastic collision forces between particles when they collide with each other [14]:

$$\mathbf{F}_{\text{rep}} = -K_0 \sum_{i=1}^N \exp\left[-\kappa\left(\frac{R_{ij}}{\delta_{\min}} - 1\right)\right] \frac{\mathbf{R}_{ij}}{R_{ij}} \quad (10)$$

where K_0 is the collision force constant, whose magnitude is comparable to the value of dielectrophoretic force; $1/\kappa$ is the range of collision force action and the truncation distance $R_c = 2a$ is set to reduce the operation cost. δ_{\min} is the minimum particle spacing.

When the particles move in the transformer oil, they will receive the drag force exerted by the oil flow, which is calculated by Eq. (11), where λ_d is the traction correction factor [11].

$$\mathbf{F}_D = -6\lambda_d\pi\eta R(\mathbf{u} - \mathbf{v}_p) \quad (11)$$

In addition, a large number of experiments have shown that cellulose particles will adsorb on the surface after contacting the metal electrode [3, 10]. So, adsorption boundary conditions are set on the upper and lower electrode surfaces. Table 1 shows main simulation parameters for reference and verification. The simulation duration is 120 s and the time step is set to 10 s^{-6} .

Table 1 Table captions should be placed above the tables

Parameters	Values	Units
ρ	0.85	g cm^{-3}
U_0	1500	V
η	0.0059	Pa s
p_0	101,325	Pa
ε_r	2.2	1
ε_m	4.4	1
u_0	0–20	mm s^{-1}
ρ_p	0.93	g cm^{-3}
R	50	μm
g	9.85	m s^{-2}
D	1.5	mm

3 Simulation Results

3.1 Chain-Formation Between Uniform Electric Fields

Cellulose particles with a mass fraction of approximately 0.005% were released into the oil gap between uniform electric fields randomly. The chain formation process at various flow rates between uniform electric fields is illustrated in Fig. 2.

Initially, when the transformer oil was stationary, the cellulose particles in the oil were randomly distributed within the uniform electric field at $t = 0$ s. Some particles contacted the electrode surface and became adhered. Over time, particles in the oil gradually aggregated along the electric field lines. Particle chains were formed spanning the gap, which began and ended with particles adsorbed on the electrode surface. At approximately $t = 10$ s, complete particle chains were observed in the gap. Furthermore, after the simulation duration reached 20 s, three complete chains could be observed within the gap.

When the transformer oil flowed at 5 mm/s, after being randomly introduced to the gap, the cellulose particles were propelled along with the oil flow by the drag force. During migration, particles aggregated along the electric field lines, connected with others head to tail and finally formed chains. However, the particle chains formed under the influence of oil flow took on an arc shape. At $t = 10$ s, the initial particle chain was disrupted. And the particles adsorbed on the electrode surface formed short chains, which tilted along the flow direction. Over time, the lengths of the short chains decreased, and their numbers reduced. This trend became more pronounced when the flow velocity was increased to 20 mm/s. As the rate of particle migration with oil flow accelerated, complete long chains of particles would no longer be formed, and only several short chains of particles remained on the electrode surface. Their lengths were significantly shorter than those observed at 5 mm/s. Collectively, the

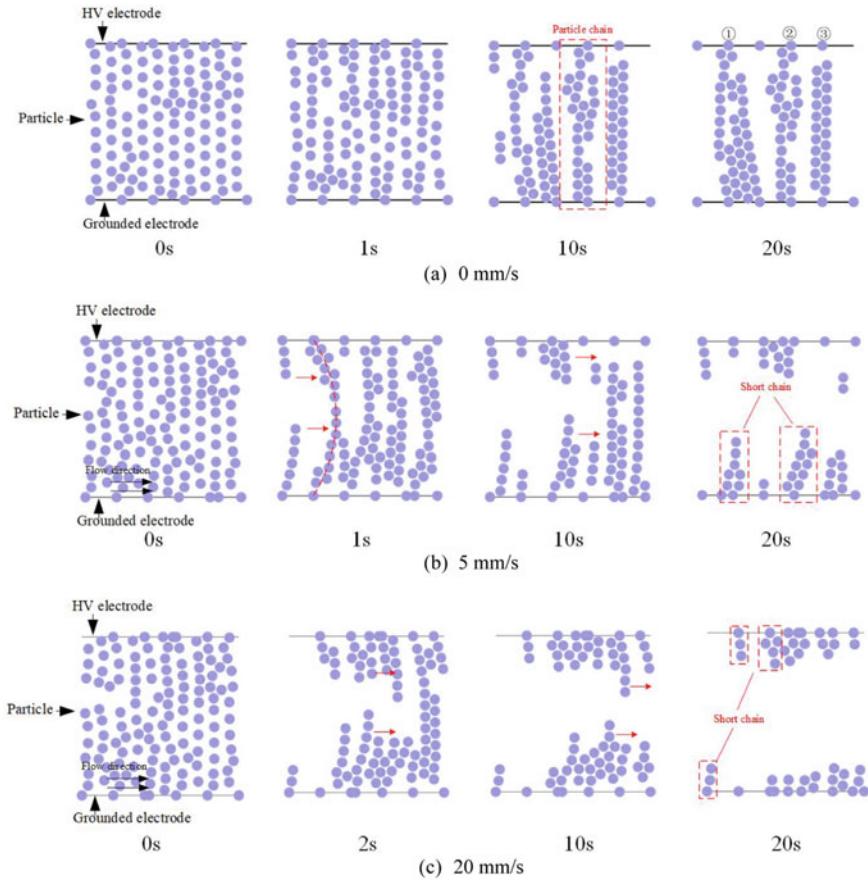


Fig. 2 Chain formation of cellulose particles in uniform electric field at different flow velocities

results indicated that oil flow disrupted the bridging behaviors of cellulose particles spanning the gap.

3.2 Chain-Formation Between Non-uniform Electric Fields

Figure 4 shows the simulation results of the chain formation behaviors of fiber particles in a non-uniform electric field. In the stationary transformer oil, cellulose particles were randomly released into the oil gap at 0 s. After that several particles migrated toward the arc-top of the ball electrodes and remained on the electrode surface upon contacted. As time elapsed, discrete particles in the oil gap gradually converged towards the high field strength region and began to connect with each other. Particle chains between two electrodes were built, i.e., the impurity particles

bridge. In contrast to the particle chain formed in a uniform electric field, the particle bridge in the non-uniform electric field was thicker and the particles accumulated more closely.

When the transformer oil flowed at 5 mm/s, the chain-forming behaviors were simulated, as depicted in Fig. 3b. Similar to the scenario in the uniform electric field, the particles also migrated with the oil flow upon released. The particles located in the vicinity of the electrode surface were the first to adhere to it. Subsequently, the particles at the entrance migrated towards the high field strength region with the oil flow and gradually converged to the particle pile at the top of the electrode arc. However, only a fraction of particles at the exit could be adsorbed by the particle chains. A few particles migrated out of the simulation region with the oil flow, thereby not participating in the chain formation. At 10 s, a complete particle chain could be observed between the gaps. However, the presence of oil flow resulted that the center of this chain became slightly shifted in the direction of oil flow, leading to a reduction in the thickness at this location. Nevertheless, with a further increase in the flow rate, the migration rate of particles increased and the number of particles that could be adhered decreased. After 20 s, the particles could only form particle mounds at the arc-top of the electrodes, and a complete particle chain could not be observed.

4 Experimental Verification

To verify the simulation results obtained in this study, the platform for observing cellulose particles in oil was established, as described in detail in the [10]. Experimental observations of particle chains in uniform and non-uniform electric fields were conducted. The electrode spacing was set to 2.5 mm, and the applied voltage was +2.5 kV, to ensure that the electric field strength corresponded to the simulation model. The total observation time was 60 s, and images were captured at 0, 5, 20, and 60 s, respectively.

The observed images of the chain formation in a uniform electric field are presented in Fig. 4. When the oil flow was stationary, the cellulose particles in the oil gradually converged in the direction of the electric field, forming several complete chains. As time progressed, the number of particle chains increased. When the flow velocity was 5 mm/s, particle chains were already observed at 5 s. As time passed, the particle chains would migrate with the oil flow, and eventually, only a few short chains could be formed in the gap. When the flow velocity increased to 20 mm/s, complete particle chains could not be formed and the length of the particle short chains on the electrode surface decreased.

The observed results of the forming process in a non-uniform electric field are presented in Fig. 5. In stationary oil, the cellulose particles rapidly converged towards the center of the gap after the electrodes were energized and oriented themselves into a long chain connecting the two electrodes, namely “particle bridge”. As time progressed, the particle chain became thicker. When the flow velocity increased to 5 mm/s, coherent chains of particles could still be formed in the oil gap, but their

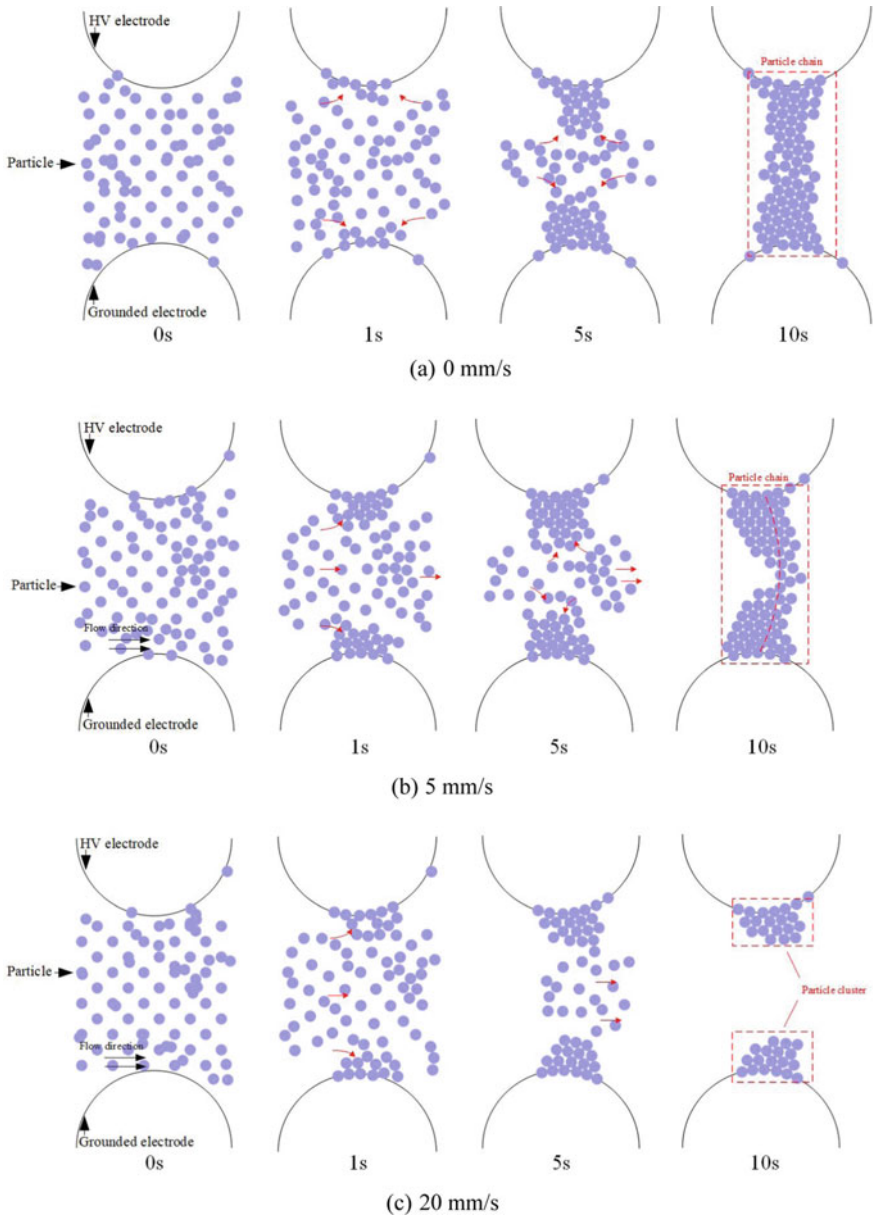


Fig. 3 Chain formation of cellulose particles in non-uniform electric field at different flow velocities

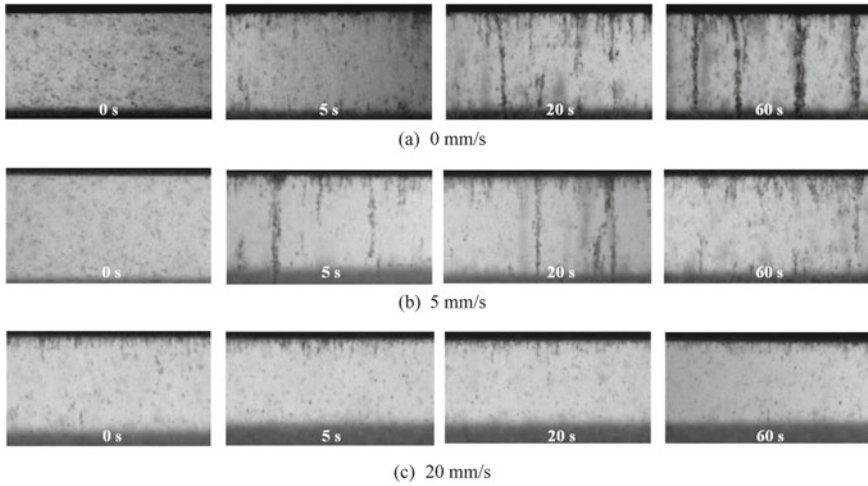


Fig. 4 Chain formation images of particle chains in uniform electric field

morphology changed. The center of the long chains tilted in the direction of the flow velocity, resulting in a curved shape. And the chains would become progressively wider with time. However, when the oil velocity increased to 20 mm/s, the formation of chains was inhibited and the cellulose particles only formed short whisker-like chains on the electrode surfaces. In summary, the experimental observations were consistent with the simulation results, indicating that the formation of particle chains was influenced by the oil flow.

5 Discussion

5.1 Mechanism of Chain-Forming of Cellulose Particles in Transformer Oil

To investigate the mechanism behind the formation of cellulose particle chains in oil, it is necessary to conduct a thorough analysis of the force conditions on particles. Specifically, the force changes on a certain particle (No. 105) in the uniform electric field were evaluated as it interacted with the particle chain, as shown in Fig. 6a. Prior to 0 ms, the particle was free in transformer oil and gradually approached the particle chain due to F_{PDEP} . At 0 ms, the particle contacted with the particle chain, resulting in a significant increase in F_{PDEP} . The interparticle collision led to a rapid surge in F_{rep} . This sudden collision also caused the particle's velocity to rapidly decrease to zero, in turn reduced F_{D} to zero. Subsequently, the particle was adsorbed by the particle chain, and F_{rep} and F_{PDEP} balanced each other.

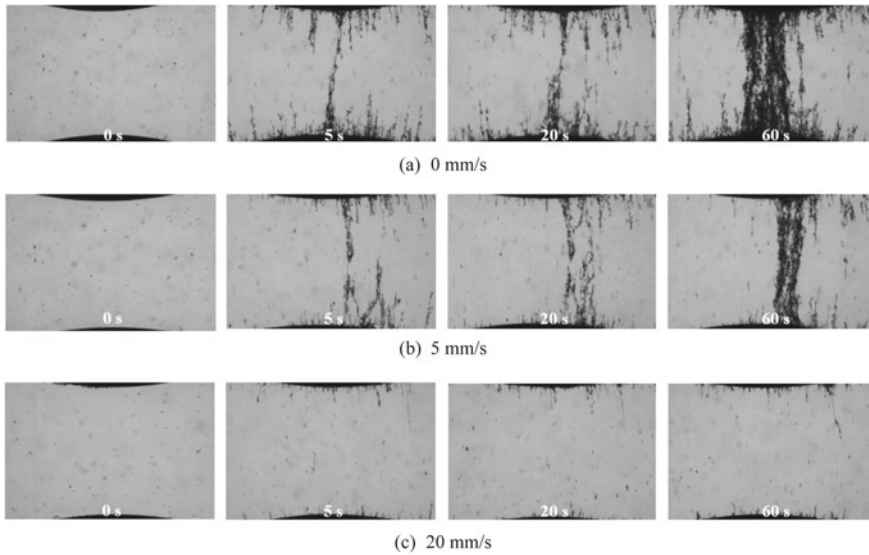


Fig. 5 Chain formation images of particle chains in non-uniform electric field

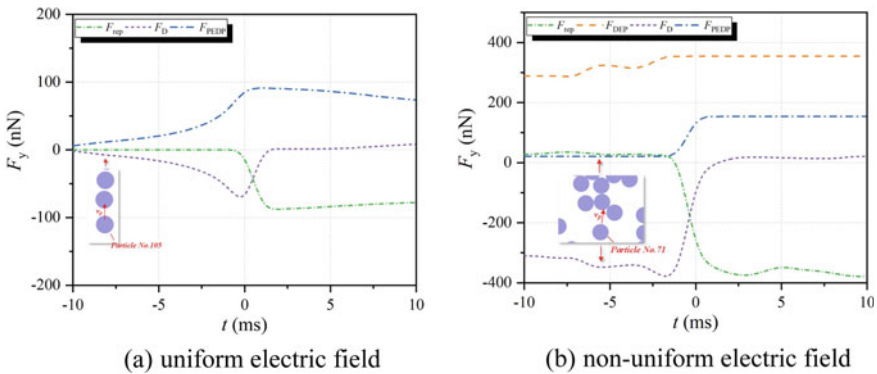


Fig. 6 Changes on force conditions on the cellulose particle during chain formation

For the non-uniform electric field, we analyzed the variation of force conditions on a typical particle (No. 71) in the static oil. Figure 6b illustrates force changes in the vertical direction before and after convergence into the particle chain. In the non-uniform electric field, the particle experienced a dielectrophoretic force (~ 300 nN) that drove it towards the electrode surfaces. The particle then contacted the particle stack at 0 ms. As the distance between the particles shortened, F_{PDEP} and F_{REP} between particles instantaneously increased, causing the particle velocity to rapidly decrease to zero. Then, this particle was adsorbed by the particle chains. F_{DEP} , F_{PDEP} , and

F_{rep} which was in the opposite direction balanced each other, thereby maintaining the formation of the particle chain.

In summary, F_{PDEP} plays a pivotal role in the process of particle chain formation. It makes the particles adsorb each other and maintains the stable state of particle chains. Additionally, F_{DEP} in the non-uniform electric field can drive particles towards regions of high field strength, promoting the chain formation.

5.2 Effect of Flow Velocity on the Chain-Forming of Cellulose Particles

Based on the result in Sect. 3, it is evident that the oil flow will hamper the formation of particle chains. Complete chains are hard to be constructed at higher flow velocities. To investigate the effect of flow velocity on particle chain formation, we examined the forces acting on a certain particle within the particle chain in flowing oil, as illustrated in Fig. 7.

In the uniform electric field, particle No. 20, which was situated at the end of an inclined particle chain, mainly experienced the F_D and the F_{PDEP} in the horizontal direction. These two forces acted in opposite directions but were of similar magnitude. They allow the particle to maintain its position without being carried away by the oil flow. Additionally, the F_D exerted on the particle was calculated when the flow velocity increased to 20 mm/s. The result shows that the increase in flow velocity led to a significant rise in the horizontal component of the F_D , rendering the particle unable to maintain force equilibrium. This, in turn, led to the fragmentation of the particle chain.

As for the non-uniform electric field, particle No. 80 was located at the center of the oil gap, where the particle chain was the most slender and fragile. At this point, the particles were primarily subject to F_{DEP} , F_{PDEP} , F_D , and F_{rep} . The F_{DEP} balanced F_D

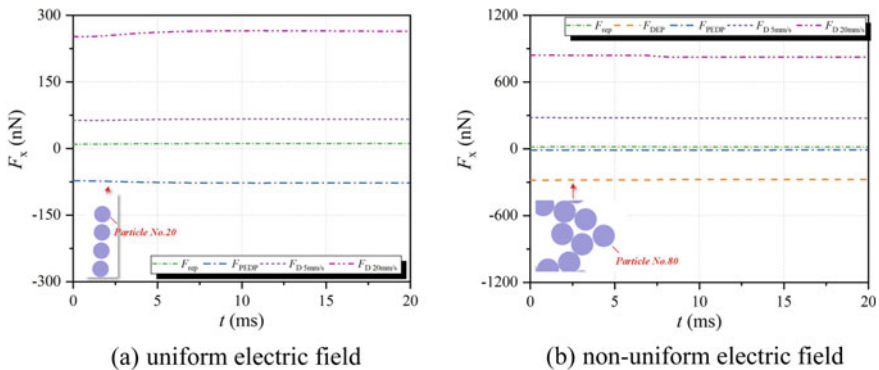


Fig. 7 Force conditions on the cellulose particle in flowing transformer oil

in the horizontal direction, ensuring the formation of complete chains in flowing oil. However, as the flow velocity increased further, the drag force significantly increased and overwhelmed F_{DEP} , destructing of the particle chains.

In conclusion, the oil flow will disrupt the formation of particle chains. In the uniform electric field, the F_{PDEP} is crucial for maintaining the morphology of the particle chains. The chain-forming will be inhibited due to the increasing of the F_{D} . In the non-uniform electric field, the F_{DEP} can counteract the F_{D} in the horizontal direction to a certain extent, allowing the formation of particle chains at low flow velocity. However, the oil flow will destroy and fragment the particle chains as the velocity further increases.

6 Conclusion

When the transformer oil is stationary, cellulose particles will gradually converge along the direction of the electric field, forming a long chain across the gap. Particles accumulate more closely in the non-uniform electric field and the particle chains formed will be wider. However, when the transformer oil flows, the formation of the particle chains will be hindered. Complete particle chains even cannot be formed when the flow velocity increases to 20 mm/s.

The secondary dielectrophoretic force is the main reason for the arrangement of cellulose particle chains. And the dielectrophoretic force in the non-uniform electric field can push the particles to the high field strength region, promoting the formation of particle chains. However, as the transformer oil flows at a higher velocity, the drag force in the horizontal direction becomes significantly higher, and the secondary dielectrophoretic force and the dielectrophoretic force cannot balance its effects. The equilibrium state of particles is broken and the particle chains are difficult to form.

Acknowledgements The authors appreciate the financial supports from the National Natural Science Foundation of China (51977158).

References

1. He C, Xie Q, Ma G et al (2018) Behavior of ± 800 kV UHV converter transformer and bushing system. *High Voltage Eng* 44(6):1878–1883 (in Chinese)
2. Zhao T, Liu Y, Lv F et al (2018) Study of cellulose particle motion effect on impulse breakdown in transformer oil. *IEEE Trans Dielectr Electr Insul* 25(1):235–244
3. Dan M, Hao J, Qin W et al (2018) Effect of different particles on breakdown and conductivity properties of mineral oil under non-uniform DC electric field. In: *IEEE international conference on dielectrics*, no 8468412
4. Guo R, Wang Z, He C et al (2021) Impulse breakdown characteristics of transformer oil with cellulose particles in quasi-uniform field. *IEEE Trans Dielectr Electr Insul* 28(1):107–115

5. Wadhwa C (2012) High voltage engineering. New Age International Publishers, England
6. Mahmud S, Golosnoy IO, Chen G (2014) Effect of different shapes of electrodes on bridging in contaminated transformer oil. In: IEEE conference on electrical insulation and dielectric phenomena, pp 114–117
7. Dan M, Hao J, Liao R et al (2019) Accumulation behaviors of different particles and effects on the breakdown properties of mineral oil under DC voltage. *Energies* 12(12):2301–2315
8. Li Y, Zhang Q, Li J et al (2016) Study on micro bridge impurities in oil-paper insulation at DC voltage: their generation, growth and interaction with partial discharge. *IEEE Trans Dielectr Electr Insul* 23(4):2213–2222
9. Pan C, Tang J, Tao X et al (2018) Partial discharge and breakdown characteristics of moving transformer oil contaminated by metallic particles. *IEEE Trans Dielectr Electr Insul* 25(5):1774–1784
10. Xia S, Pan C, Yao Y et al (2023) Bridging characteristics of cellulosic particles in flowing transformer oil. *IEEE Trans Dielectr Electr Insul* (Early Access)
11. Luo X, Pan C, Yao Y et al (2021) Observation and simulation for the movement of metallic particles in flowing transformer oil under AC/DC and combined voltages. *IEEE Trans Dielectr Electr Insul* 28(3):1034–1043
12. Xie C, Chen B, Ng C et al (2015) Numerical study of interactive motion of dielectrophoretic particles. *Eur J Mech-B/Fluids* 49(1):208–216
13. Lebey T, Belijar G, Diahm S et al (2017) Dynamics of particle chain formation in a liquid polymer under AC electric field: modeling and experiments. *J Phys D Appl Phys* 50(1):025303
14. Li J, Shui J (1996) Simulation of a three-dimensional electrorheological suspension. *J Appl Phys* 79(9):7312–7317

Calculation and Analysis of Induced Voltage in Overhead Ground Lines of UHVDC Transmission Lines After Ground Insulation Modification



Wei Li, Xinmin Li, Yanhua Han, Panfeng Hu, Lu Zhang, and Mingxi Zhu

Abstract The insulated ground wire of ultra-high voltage direct current (UHVDC) transmission lines may produce induced voltage due to proximity to operating lines after insulation modification, which can affect the safety of the equipment and operators in the deicing circuit. In this paper, a calculation model for induced voltage after the insulation modification of UHVDC transmission line ground wire was established. The influence of model symmetry, grounding switch status, and soil resistivity on induced voltage was quantitatively studied, and field tests were conducted on ± 800 kV transmission lines for verification. The results show that the asymmetry of the ground wire and optical cable in UHVDC transmission lines is an important factor affecting calculation accuracy. When there is a grounding point in the deicing circuit, the main influencing factor of induced voltage changes from the electrostatic induction component generated by the DC voltage to the electromagnetic induction component generated by the ripple current, with an effective value of 783 V in this project. The calculation and measurement results in this paper can provide reference and basis for the design and construction of ground deicing devices and deicing circuits in UHVDC transmission projects.

Keywords UHVDC transmission line · Live-line deicing of ground wire · Induced voltage · Electromagnetic induction · Electrostatic induction

W. Li (✉) · X. Li · Y. Han

Power Research Institute of State Grid Shaanxi Electric Power Company Limited, Xi'an 710100, China

e-mail: 175526631@qq.com

P. Hu · L. Zhang · M. Zhu

State Grid Shaanxi Electric Power Co., Ltd., Xi'an 710048, China

© Beijing Paiké Culture Commu. Co., Ltd. 2024

X. Dong and L. Cai (eds.), *The Proceedings of 2023 4th International Symposium on Insulation and Discharge Computation for Power Equipment (IDCOMPU2023)*, Lecture Notes in Electrical Engineering 1100, https://doi.org/10.1007/978-981-99-7393-4_35

375

1 Introduction

Ultra-high voltage (UHV) transmission is one of the important indicators of the development level of the power industry, and is an inevitable requirement for long-distance power transmission. UHV transmission can increase transmission capacity and transmission distance, reduce the engineering cost of unit power transmission, reduce line losses, and save land occupation for transmission corridors. It conforms to China's national conditions, conforms to the development trend of the power grid, and has significant comprehensive economic and social benefits [1, 2].

As global climate change continues, the 0 °C line in China is moving northward and westward, and the harm of icing to transmission lines is becoming increasingly serious. In early 2022 alone, a series of UHVDC transmission lines including Qishao, Binjin, Shanwu, and Yahuhad incidents of ground wire (including optical cable, etc.) breakage, tension clamp detachment, suspension clamp fracture, and crossarm bending caused by icing. Icing on ground wires has become the main threat to the safe and reliable operation of UHVDC transmission lines.

In response to the induced voltage on the transmission lines of ultra-high voltage direct current (UHVDC) caused by ice melting, many scholars at home and abroad have conducted sufficient research. Guo et al. [3] studied the induced voltage generated at the ice melting device on the operating line of a UHV double-circuit AC transmission line and a stopped line. Yu et al. [4] proposed measures to suppress induced voltage and current using a segmented ice melting device on the same UHV double-circuit AC transmission line during one circuit operation and one circuit stoppage. Chen et al. [5] studied the electrical requirements of the insulation of the ground wire insulator and the parallel discharge gap after the insulation modification of the fiber composite overhead ground wire, but did not analyze the induced voltage in the ground wire after modification. Zhu et al. [6] established a mathematical model of ice melting vibration characteristics based on the temperature distribution characteristics during the ground wire icing process and analyzed the DC ice melting temperature and ground wire vibration characteristics. Chen [7] developed a voltage-adjustable DC ice melting power source to meet the demand for OPGW ice melting. Zasytkin et al. [8] analyzed the calculation method of overcurrent and undercurrent relay protection current values in the relay protection composite unit of steel lightning protection wires for AC ice melting schemes in overhead transmission lines and adjusted the corresponding protection accordingly. Zha et al. [9] studied the induced voltage of overhead ground wires for different tower types, ground wire models, line lengths, and replacement methods under different operation modes of 500 kV AC and ± 500 kV DC transmission lines. They concluded that when the ground wire is insulated and has no grounding point, the induced voltage increases with the line length, and the static induction voltage of the ± 500 kV DC ground wire decreases significantly as long as there is one grounding point.

However, there is a lack of research on the issue of induced voltages in the circuit during the process of grounding wire (including optical cable, etc.) ice melting for

ultra-high voltage direct current transmission lines, especially when the lines are energized.

Compared with the transmission lines, the ground wire (including optical cables) of UHVDC transmission lines is more susceptible to icing because of its higher height, higher wind speed at the corresponding position, and no current passing through it during normal operation. In order to achieve ground wire live ice-melting without affecting the normal operation of UHVDC transmission lines, insulation modification is required for the ground wire originally connected to the tower grounding grid. Furthermore, because the optical cable has both lightning protection and communication functions, excessive temperature rise during ice-melting will cause irreversible damage to the optical cable core. Therefore, strict control of the temperature rise of the optical cable during ice-melting is necessary. Compared to other power transmission lines, ultra-high voltage direct current (UHVDC) transmission lines require longer distances, taller towers, and higher levels of operational reliability. Therefore, the difficulty of UHVDC ground wire icing melting technology is greater, and there has been no successful experience of UHVDC ground wire icing melting both domestically and internationally. Compared with conductors, the overhead ground wire of UHVDC transmission lines is more susceptible to icing due to its higher height and greater wind speed at corresponding positions, and it does not pass operating current during normal operation. To achieve ground wire de-icing without affecting the normal operation of UHVDC transmission lines, it is necessary to carry out live-line de-icing of the ground wire. At this time, insulation transformation needs to be carried out on the ground wire originally connected to the tower grounding grid. Since optical cables have both lightning protection and communication functions, and UHVDC transmission lines have longer distances, higher towers, and higher requirements for operational reliability than other lines, the difficulty of live-line de-icing technology for UHVDC ground wires is also greater, and the requirements for equipment safety and personal safety are higher. Therefore, the calculation and verification of induction voltage are even more important.

This paper conducts numerical calculations on the induced voltage on the ground wire in the ice melting section of the Shaanxi section of the ± 800 kV Qishao line after the insulation transformation, providing a basis for overvoltage protection and insulation coordination of the output port of the deicing device. After the insulation transformation of the ground wire and the construction of the deicing device, field tests of the induced voltage were carried out at the output port to verify the accuracy of the simulation results.

2 Theoretical Analysis

2.1 Classification of Induced Voltage and Induced Current

The electromagnetic induction parameters between operating lines and maintenance lines can mainly be classified into four categories. Due to the mutual capacitance between conductors and their capacitive coupling to ground, the operating lines will produce electrostatic induction voltage and electrostatic induction current on the out-of-service lines. Due to the electromagnetic induction of conductors in alternating magnetic fields, there is mutual inductance between AC lines that are installed on the same tower, run in parallel or cross over each other and the out-of-service lines. The AC lines will produce electromagnetic induction voltage and electromagnetic induction current on the out-of-service lines.

- (1) When neither end of the line is grounded, the current is zero. At this time, the electrostatic coupling component plays a decisive role in the induced voltage, and the value is mainly related to the capacitance between circuits, the capacitance between conductors and ground, and the operating voltage of the line.
- (2) When only one end of the line is grounded, the grounding point will pass through the induced current, which is determined by the electrostatic coupling component and is approximately equal to the electrostatic coupling current. At the same time, the other end of the line will produce a high induced voltage, which is determined by the electromagnetic induction voltage.
- (3) When both ends of the line are grounded, i.e., under maintenance conditions, the grounding point will produce an induced current, which is determined by the electromagnetic induction component and is mainly related to the line.

2.2 Theoretical Calculation Model

Based on the distributed parameter method, the equations for current I and voltage U at any point on the line g are [10]:

$$-\frac{\partial \dot{U}}{\partial l} = j\omega L \dot{I} + j\omega M_{A_g} \dot{I}_A + j\omega M_{B_g} \dot{I}_B \quad (1)$$

$$-\frac{\partial \dot{I}}{\partial l} = j\omega C_0 \dot{U} + j\omega C_{A_g} (\dot{U} - \dot{U}_A) + j\omega C_{B_g} (\dot{U} - \dot{U}_B) \quad (2)$$

where:

\dot{U}_A , \dot{U}_B , \dot{I}_A and \dot{I}_B are the voltages and currents of the operating line, respectively; C_0 is the unit-length ground capacitance of the adjacent line g ;

C_{Ag} and C_{Bg} are the unit-length mutual capacitances between the polar conductors of the operating line and line g, respectively;

M_{Ag} and M_{Bg} are the unit-length mutual inductances between the polar conductors of the operating line and the adjacent line g, respectively.

The simplified general calculation formula is:

$$\dot{U}_2 = \dot{U}_1 \cos \gamma l - j \dot{I}_1 Z_C \sin \gamma l + \frac{\alpha}{\gamma^2} \dot{U}_A (1 - \cos \gamma l) - j \frac{M}{L} Z_C \dot{I}_A \sin \gamma l \quad (3)$$

$$\dot{I}_2 = -j \frac{\dot{U}_1}{Z_C} \sin \gamma l + \dot{I}_1 \cos \gamma l + j \frac{\alpha}{\gamma^2 Z_C} \dot{U}_A \sin \gamma l + \frac{M}{L} \dot{I}_A (\cos \gamma l - 1) \quad (4)$$

where:

γ is the propagation constant, $\gamma = j\omega\sqrt{L(C_0 + C_{Ag} + C_{Bg})}$.

M is the equivalent mutual inductance, $M = M_{Ag} + M_{Bg}$.

α is the equivalent capacitance, $\alpha = -\omega^2 L(C_{Ag} + C_{Bg})$.

Z_C is the characteristic impedance, $Z_C = \sqrt{L/(C_0 + C_{Ag} + C_{Bg})}$.

(1) Line with both ends open

When both ends of the line are open, $I_1 = I_2 = 0$, for a typical line $\gamma l \ll 1$, we have:

$$\dot{U}_1 \approx \dot{U}_2 \approx \frac{\alpha}{\gamma^2} \dot{U}_A = \frac{C_{Ag} \dot{U}_A + C_{Bg} \dot{U}_B}{C_{Ag} + C_{Bg} + C_0} \quad (5)$$

(2) Line with one end grounded

Assuming that the line is grounded at one end, we have $I_1 = 0$, $U_2 = 0$, and:

$$|\dot{U}_1| \approx |j(M/L)Z_C \dot{I}_A \tan \gamma l| = |j\omega l(M_{Ag} \dot{I}_A + M_{Bg} \dot{I}_B)| \quad (6)$$

$$|\dot{I}_2| \approx |j(\alpha/\gamma^2 Z_C) \dot{U}_A \tan \gamma l| = |j\omega l(C_{Ag} \dot{A}_A + C_{Bg} \dot{B})| \quad (7)$$

(3) Line with both ends grounded

When both ends of the line are grounded, $U_1 = U_2 = 0$, and:

$$\dot{I}_1 \approx \dot{I}_2 = -(M_{Ag} \dot{I}_A + M_{Bg} \dot{I}_B)/L \quad (8)$$

3 The Main Factors Influencing Induced Voltage

The Qishao ± 800 kV transmission line (Shaanxi section) #2484–#2509 is 14.446 km long, with a length of 6481 m from section #2484 to #2495 and a length of 7965 m from section #2495 to #2509. The overhead ground wire type for the section is JLB20A-150-19, and the optical cable model is OPGW-24B1(ULL)-155. The schematic diagram of the ice-melting circuit is shown in Fig. 1.

As shown in Fig. 1, the overhead ground wire and optical cable of the ± 800 kV Qishao transmission line (Shaanxi section) in the #2484–#2509 section have been insulated and upgraded. The overhead ground wire and optical cable are short-circuited at the #2484 and #2509 tower positions. At the #2495 tower, the overhead ground wire and optical cable are respectively led down and connected to the DC ice-melting device through a 10 kV output cable. The operating conditions that were calculated and tested in this study were as follows: The ice-melting device was disconnected from the ice-melting output cable, and the grounding of the ice-melting output cable was controlled by a knife switch. Induced voltage was measured at the point where the ice-melting output cable was disconnected.

According to the on-site investigation, there are no parallel or intersecting ultra-high or extra-high voltage AC transmission lines within 3 km of the ± 800 kV Qishao Line (Shaanxi section) #2484–#2509 section. Therefore, in normal operation of the line, this section mainly considers the static induction caused by ultra-high voltage DC transmission when calculating the induced voltage on the ground wire.

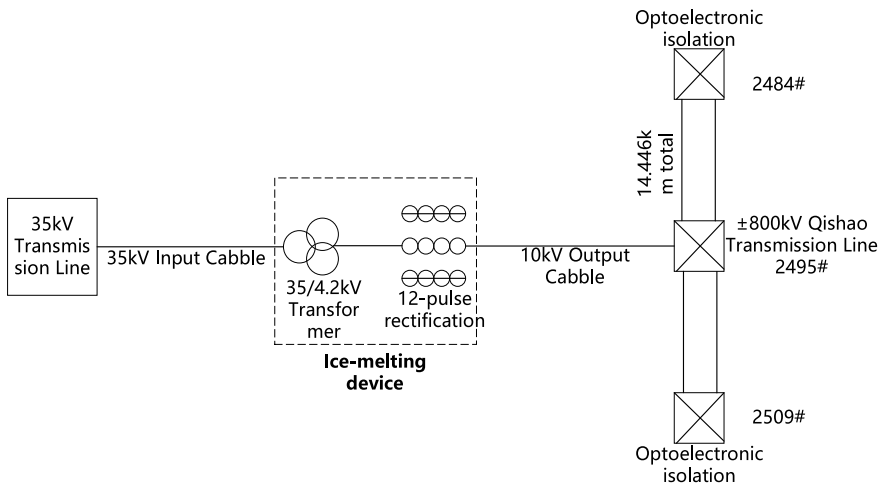


Fig. 1 Schematic diagram of ice-melting circuit

3.1 The Effect of Model Symmetry on Induced Voltage

In practical engineering, on the one hand, the differences in parameters of overhead ground wires and optical cables lead to different temperature characteristics and sag, resulting in differences in the distance between the wires. On the other hand, the power lines are not arranged completely straight and horizontally, and there are differences in inner angle side, outer angle side, and height, which make the two sides of the ground wire slightly lose model symmetry with the change of the line direction. Therefore, in practical engineering, the distance D_1 between the optical cable and the wire and the distance D_2 between the overhead ground wire and the wire are not exactly equal. In other words, in actual working conditions, there exists a distance difference $D = |D_1 - D_2|$ between the two, which is difficult to accurately obtain. Based on operation and maintenance experience and field observations, the estimated D value within the actual ice melting section is no more than 3 m. Therefore, when the distance is 1, 2, and 3 m respectively, the induced voltage in the ice melting circuit is calculated, and the results are shown in Table 1 and Fig. 2.

From Table 1 and Fig. 2, it can be seen that the calculated induced voltage of the ice melting circuit is close to 0 when $D = 0$. This is because in the ice melting circuit after the short-circuit between the overhead ground wire and the optical cable, the induced voltage generated by one pole wire on the overhead ground wire cancels

Table 1 The effect of distance difference D on induced voltage

D (m)	Induced voltage (V)
0	0.520
1	5603
2	11,130
3	16,130

Fig. 2 The effect of distance difference D on induced voltage

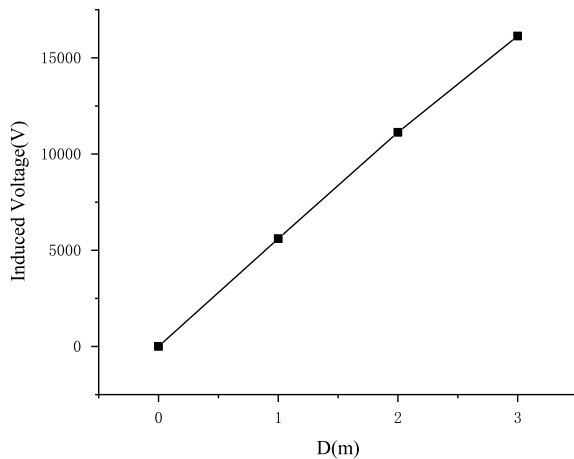


Table 2 The effect of grounding switch state on induced voltage

Condition	One open	Both grounded	Both open
Induced voltage (V)	0.0026	0.0014	16,128

out with the induced voltage generated by the other pole wire on the optical cable. With the change of distance D , the symmetry of the model is lost, and the induced voltage in the ice melting circuit increases linearly. It reaches 16.13 kV when $D = 3$ m. Therefore, in the calculation and analysis of actual engineering, it is necessary to pay attention to the influence of model symmetry, otherwise it will lead to a large deviation between the calculation results and the actual situation.

3.2 The Effect of Grounding Switch State on Induced Voltage

According to the theoretical analysis in the previous section, the induced voltage in the icing circuit has significant differences when the circuit is open at both ends, grounded at one end, or grounded at both ends. Here, we continue to validate the asymmetric model and present the calculation results in Table 2.

From Table 2, it can be seen that when the circuit is open at both ends, there is a significant induced voltage in the ice melting circuit due to the influence of the nearby operating ultra-high voltage direct current transmission lines. However, once there is a grounding point in the entire circuit, the induced voltage will rapidly drop to near zero, consistent with the theoretical analysis results.

3.3 The Effect of Earth Resistivity on Induced Voltage

The induced voltage at the end of the ice melting ground wire was calculated when the ice melting ground wire was open at the ice melting device in earth with equivalent uniform resistivity of 100 Ω m, 500 Ω m, 1000 Ω m and 2000 Ω m, and the results are shown in Table 3 and Fig. 3.

Table 3 The effect of earth resistivity on induced voltage

Earth resistivity (Ω m)	Induced voltage (V)		
	One open	Both grounded	Both open
100	0.0015	0.0003	16,128
500	0.0026	0.0014	16,128
1000	0.004	0.0028	16,128
2000	0.0067	0.0056	16,128

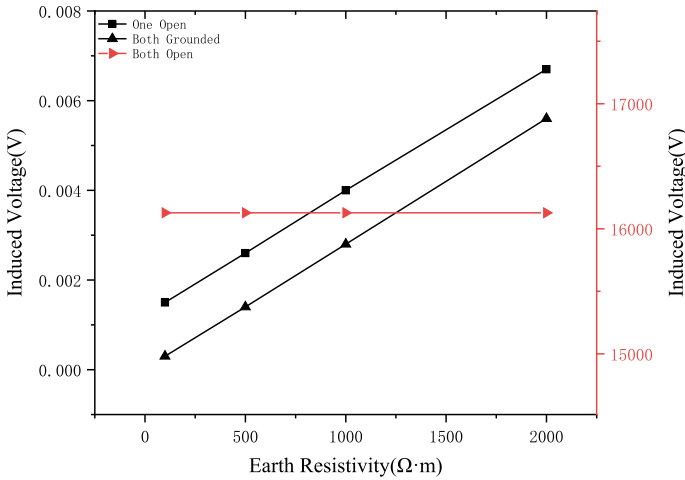


Fig. 3 The effect of earth resistivity on induced voltage

As shown in Table 3 and Fig. 3, the earth resistivity has little effect on the induced voltage on the ice melting ground wire when the circuit is open at both ends. As shown in Fig. 2, under the condition of grounding at one end or both ends, the earth resistivity indirectly affects the induced voltage at the grounding point by influencing the grounding resistance at the grounding point. This results in the induced voltage increasing linearly with earth resistivity. However, since the static induced voltage in both of these conditions is overall close to zero, it can be ignored.

4 Results of Field Testing

Measurements were taken on the induced voltage/induced current on the overhead ground wire/fiber optic cable of the #2484–#2509 section of the ±800 kV Qishao transmission line after its insulation was upgraded. The test results were compared with the calculated results as shown in Table 4.

As shown in Table 4, the measured DC component of the induced voltage on the overhead ground wire/fiber optic cable of the ±800 kV Qishao transmission line #2484–#2509 section after the insulation upgrade corresponds to the $D = 2.51$ m

Table 4 Measured value of induced voltage

Condition	Induced voltage (DC) (V)	Induced voltage (AC) (V)
Both open	13,716	412
One open	0	783

condition under the open circuit condition in the calculated results obtained by interpolation. Once there is a grounding point in the ice melting circuit, the DC component rapidly returns to zero, consistent with the theoretical analysis and calculated results.

However, in the actual measurement, there is still an AC component with an effective value in the ice melting circuit, as shown in Fig. 4. According to the on-site investigation, there are no ultra-high voltage AC transmission lines around the entire ice melting circuit section, so the AC component was not considered in the calculation, resulting in a difference between the calculated and measured results.

The AC induced voltage waveform in Fig. 4 was subjected to Fourier analysis, and the results are shown in Fig. 5.

According to the Fourier analysis results, the main frequency of the induced voltage is distributed at 1500 Hz, followed by frequencies of 1200 Hz, 900 Hz, 300 Hz, and 1800 Hz, which are speculated to be caused by the ripple voltage electromagnetic induction generated by the ± 800 kV ultra-high voltage DC transmission line.

Further, the induced voltage value caused by the ripple voltage was calculated based on the $D = 2.51$ m model, and the calculation results are shown in Table 5 and Fig. 6.

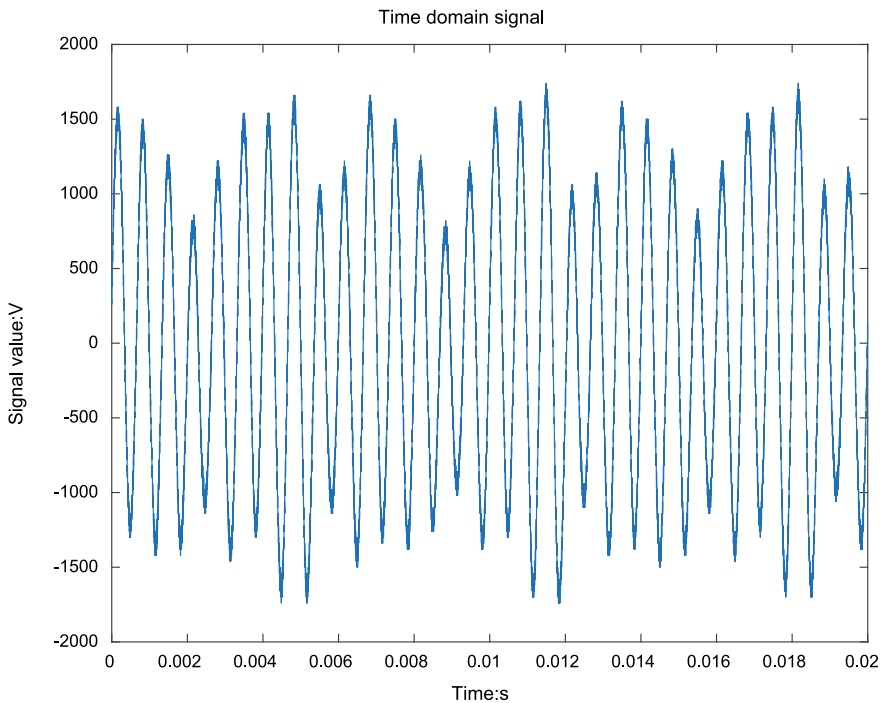


Fig. 4 Measured AC component of induced voltage on overhead ground wire/fiber

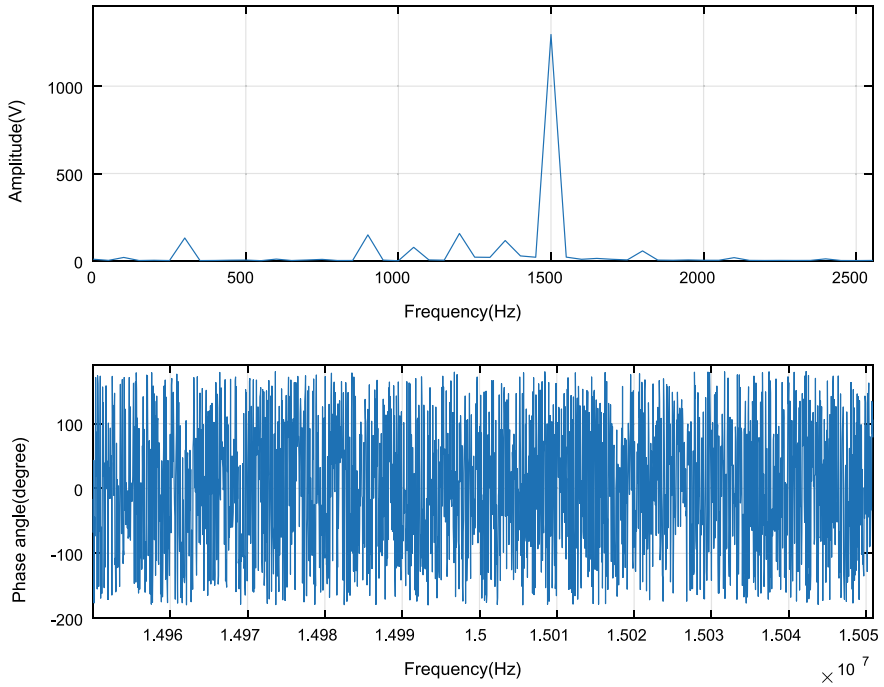


Fig. 5 The FFT result of measured AC component of induced voltage

Table 5 The effect of rippled voltage and rippled current on induced voltage

Rippled voltage (V)	Rippled current (A)	Induced voltage (V)
500	3	797
1000	3	797
5000	3	797
5000	30	7966
5000	300	77,872

From the calculation results, it can be seen that under the condition of grounding at one end of the ice melting loop, the induced voltage is mainly affected by electrostatic induction, and it increases linearly with the increase of ripple current, regardless of the value of ripple voltage (Fig. 7), which is consistent with theoretical analysis. Based on numerical fitting, taking the measured electromagnetic induced voltage at a frequency of 1500 Hz as an example, the corresponding value of ripple current is 4.88 A.

Fig. 6 The effect of rippled current on induced voltage

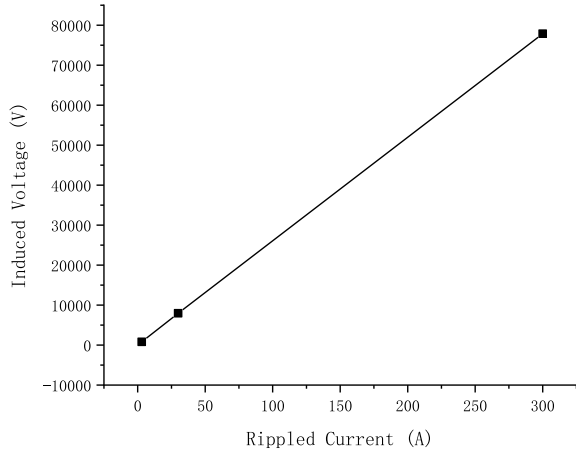
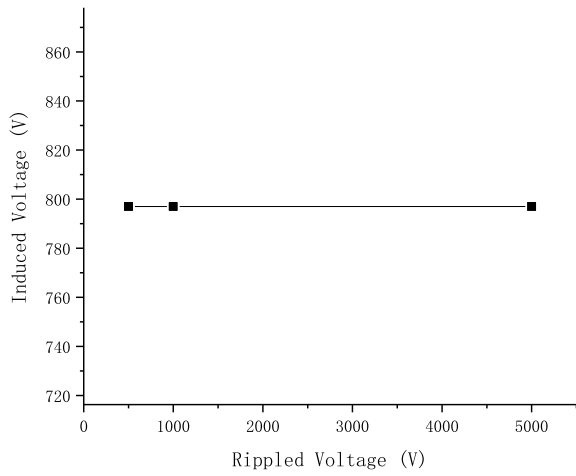


Fig. 7 The effect of rippled voltage on induced voltage



5 Conclusion

- (1) Ultra-high voltage transmission lines usually use double ground wires (one of which is OPGW). Although the hanging points of the designed ground wires are symmetrical, the actual engineering often causes the model to lose symmetry due to different sagging and other reasons, which should be taken seriously in simulation calculations, otherwise significant computational errors may occur.
- (2) After the insulation transformation of the ground wire, the induced voltage in the ground wire is mainly affected by the electrostatic induction voltage of the operating line, and once there is a grounding point in the loop, the DC electrostatic induction voltage will quickly decrease to near zero as the voltage of the operating line linearly changes.

- (3) In the ground wire icing circuit with a single point of grounding, the induced voltage is mainly caused by the electromagnetic induction of the ripple voltage of the ultra-high voltage DC transmission line, which increases linearly with the increase of the ripple voltage. In this project, the induced voltage value reaches 783 V. The calculation and measurement results of this article provide a typical value of induced voltage for the ground wire icing circuit of ultra-high voltage projects, which can provide reference for the design of ground wire icing devices and induced voltage suppression in subsequent ultra-high voltage projects.

Acknowledgements Sincerely gratitude for the project supported by State Grid Corporation of China Scientific and Technological Project “Research on Key Technologies of On-Site Rapid Detection and Performance Improvement of New Grounding Materials” (5500-202232127A-1-1-ZN).

References

1. Liu Z (2013) Technical innovation of ultra-high voltage AC transmission in China. *Power Syst Technol* 37(03):567–574. <https://doi.org/10.13335/j.1000-3673.pst.2013.03.020> (in Chinese)
2. Peng K (2015) Study on induction voltage and current of 1000kV AC ultra-high voltage transmission line on 500 kV AC transmission line conductor. Shanghai Jiao Tong University (in Chinese)
3. Guo Z, Lu J, Yu Z, Tan Y, He J, Hu J, Li B, Zhang H (2013) Analysis of induced voltage in de-icing devices for special high-voltage double-circuit transmission lines on the same tower. *Power Syst Technol* 37(11):3015–3021. <https://doi.org/10.13335/j.1000-3673.pst.2013.11.010> (in Chinese)
4. Yu Z, Guo Z, Lu J, Tan Y, He J, Hu J (2014) Suppression measures for induced voltage and current in segmented de-icing devices of special high-voltage double-circuit transmission lines on the same tower. *High Voltage Eng* 40(05):1332–1338. <https://doi.org/10.13336/j.1003-6520.hve.2014.05.007> (in Chinese)
5. Chen X, Xia C, Zhu H, Ma Z, Yin Y, Zhang Y (2017) Electrical requirements for insulators and parallel discharge gaps of composite fiber overhead ground wires in DC de-icing insulation transformation. *High Voltage Eng* 43(08):2733–2738. <https://doi.org/10.13336/j.1003-6520.hve.20170731039> (in Chinese)
6. Zasytkin AS, Nagay VI (2021) The calculation method of ice melting schemes’ relay protection settings and clarification of the ice depositions control method on steel lightning protection wires. *J Phys Conf Ser* 2096(1). <https://doi.org/10.1088/1742-6596/2096/1/012045>
7. Chen H, Zi ZN, Hua Z (2022) Research and application of ice melting power supply for OPGW. *IET Conf Proc* 2022(5):685–689. <https://doi.org/10.1049/cp.2022.0516>
8. Zhu H, Han Z, Xing H, Xu D, Zhang R, Liu C, Chen W (2023) DC ice-melting operation of the ground wire based on the characteristic investigation of the thermal structure coupling effect. *Electr Power Syst Res* 218, Article 107586. <https://doi.org/10.1016/j.epsr.2022.107586>
9. Zha ZP, Li ZQ, Ying L, Mian F (2022) Study on overhead ground wire induced voltage of 500 kV AC/DC transmission lines for ice melting. In: *Proceedings—2022 7th Asia conference on power and electrical engineering, ACPEE 2022*, pp 1704–1711. <https://doi.org/10.1109/ACPEE53736.2022.00181>
10. Wang Y (2008) Simulation experiment research on induced voltage and current of 500 kV double-circuit transmission line on the same tower. Shenyang University of Technology, Shenyang (in Chinese)

Numerical Modeling of the Arc in Switching-Type SPD



Yipeng Zhang, Qibin Zhou, Yijie Xiao, Xiaoyan Bian, and Zhenyu Pang

Abstract Surge protection is very important for the safe operation of power system. The application of Surge Protective Device (SPD) is the one of key measures of surge protection. Due to its high surge absorption capability, switching-type SPD is widely used in various scenarios of power systems. The follow current in the switching-type SPD which will generate continuous arc is one of the main problems to this type of SPD. How to extinguish the follow current arc is the key problem of developing switching-type SPD. In this paper, a two-dimensional numerical model of follow current arc inside a switching-type SPD is established based on the magneto hydro dynamic (MHD) model. The simulation results show that the air flow and the configuration of splitter plates in the arc extinguish chamber greatly affect the extinguishment of the arc. The stronger air flow and the convex configuration of splitter plates make the arc extinguished more easily. The conclusion of this paper will be beneficial for the optimization of switching-type SPD design.

Keywords Switching-type SPD · Arc · Air flow · Splitter plates configuration

Y. Zhang (✉) · Q. Zhou · Y. Xiao
School of Mechatronic Engineering and Automation, Shanghai University, Shanghai 200444,
China
e-mail: zhangyipeng@shu.edu.cn

Q. Zhou
e-mail: zhouqibin@shu.edu.cn

Y. Xiao
e-mail: 21721826@shu.edu.cn

X. Bian · Z. Pang
College of Electrical Engineering, Shanghai University of Electric Power, Shanghai 200090,
China

1 Introduction

For all kinds of AC and DC systems, surge can pose a great threat to the equipment. For instance, some PV systems are not sufficiently protected against lightning, accounting for approximately 26% [1]. Therefore, measures of lightning protection should be adopted to reduce the risk to a tolerable level in indirect and direct lightning strikes.

Due to the special non-linear voltage-current characteristic, Surge Protective Device (SPD) is generally used to absorb the surge current and discharge to the earth. In IEC 62305-4:2020, the Surge Protection Measures (SPM) is formed with different types of SPDs [2]. There have been many researches on SPD nowadays. For instance, Luis Ignacio Colina Jimenez discussed a problem how the creeping discharge spark gap (CDSG) principle can be applied to SPDs [3]. Falun Song analyzed the relationship between the breakdown voltage and the optimal operation frequency [4].

In IEC 61643-11, SPD is divided into two kinds [5]. Among them, the switching-type SPD is widely used in various power supply systems due to its surge absorption ability. Some problems will be caused in practice by the defective design of the spark gap which is the main component of SPD. When the surge is passed by the switching-type SPD, an arc will be generated in the spark gap. The arc burns continuously because of the line voltage applied at the ends of the SPD, which will make the device on fire resulting in significant economic loss and outage. Therefore, it is of great significance to study the development and extinguishment of the arc in the spark gap.

Magneto hydro dynamics (MHD) methods are often used to establish the mathematical model of arc [6–8]. This paper discusses a special-designed spark gap with an arc extinguisher. Section 2 introduces the arc modeling theory and the magneto hydro dynamics (MHD) model. The model is established and simulated in Sect. 3. The simulation results is analyzed in Sect. 4. Through simulation and analysis, the ability to extinguish the arc will be improved in the switching-type SPD, which enhances the safety of power systems.

2 Modeling Methodology

In microcosmic view, arc is a kind of plasma containing many charged particles. In macroscopic view, arc can be viewed as a magnetic fluid consisting of four physical fields—electric, magnetic, temperature, and fluid fields. The magneto hydro dynamic (MHD) model, which consists of several equations for these four physical fields, can calculate the state of the arc.

Figure 1 shows how the MHD model is coupled. The temperature field affects the electric field by changing the conductivity of air at different temperatures, so as to solve the current density J . The current density solved in the electric field affects the spatial magnetic field distribution B through the Ampere theory. Lorentz force F is

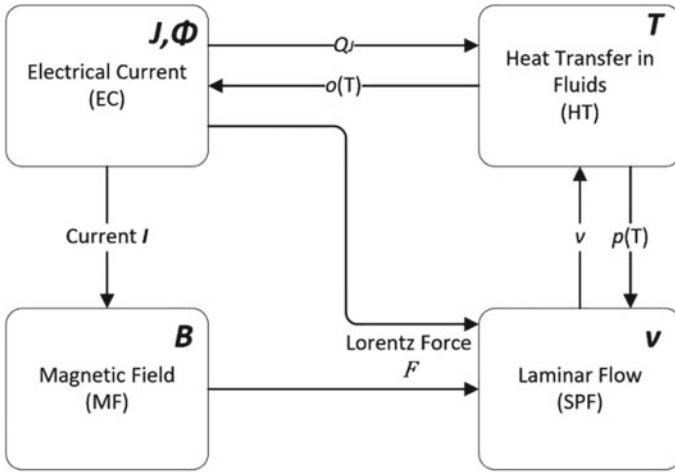


Fig. 1 Coupling mechanism of MHD model

formed under the combined action of magnetic field distribution and space current. Lorentz force causes the flow field to shrink and further affects the space temperature change.

Based on the coupling of the above four physical fields, the MHD model can be established and the arc properties can be calculated.

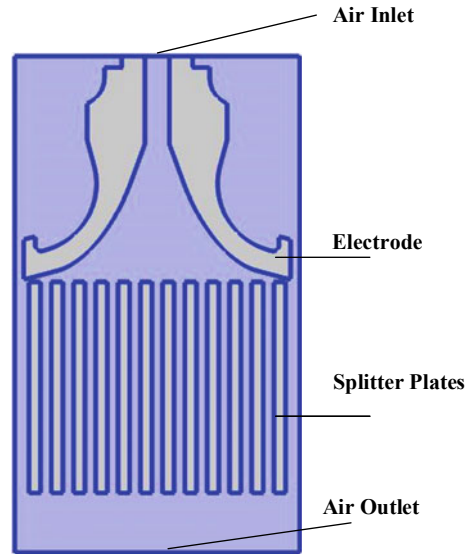
3 Simulation Model and Its Boundary Condition

According to the modeling approach in Sect. 2, this section simplifies the arc model. A two-dimensional arc simulation model is established in COMSOL-Multiphysics. As shown in the Fig. 2, the simulation area is concentrated between two electrodes and grid area. The model mainly includes copper electrodes, iron splitter plate group, inlet and outlet.

In order to facilitate the convergence of simulation calculation and reduce the complexity of simulation, some assumptions are introduced in the simulation:

- (1) Without considering the initial process of arc formation, assuming that the arc is already stably burning between the electrodes at the beginning of the calculation ($t = 0.05$ ms).
- (2) Assuming that the arc plasma always satisfies the local thermodynamic equilibrium (LTE) state.
- (3) The flow of the arc plasma generated by electromagnetic force is laminar.
- (4) The air flow generated by the material is simulated by a constant pressure.

Fig. 2 Simulation model of switch-type SPD



4 Simulation Results and Discussion

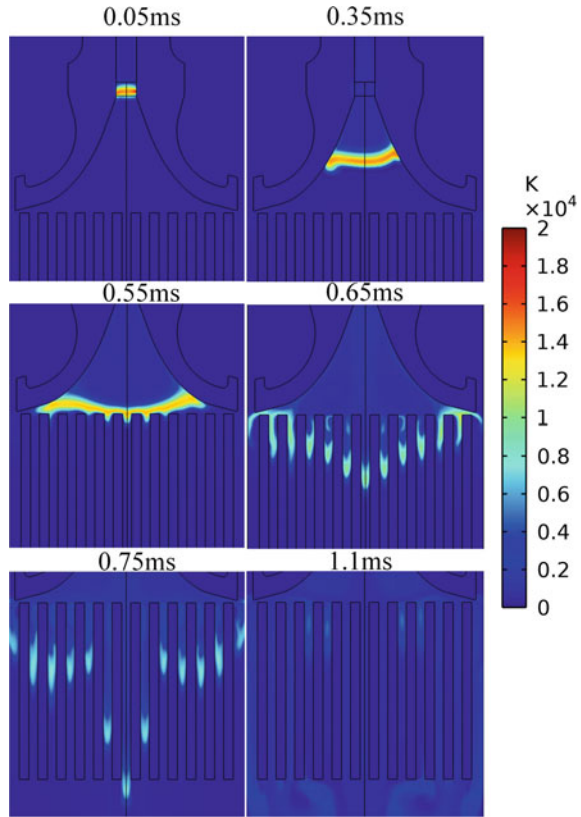
4.1 Simulation of Arc Development Process

In this section, the elongation, bending and extinguishing process of the arc under the effect of air flow and Lorentz force were simulated. During this process, the distribution of arc voltage and temperature was obtained.

The arc temperature distribution at different times is shown in Fig. 3. At 0.05 ms, there is a fluid with a high central temperature in the middle of the electrode. This hot fluid is the arc at the initial moment. The temperature of the arc is very high. Its maximum temperature at the arc root can even reach more than 20000 K. The arc is forced downward by the Lorentz force and the air blow. At 0.35 ms, under the effect of force, the arc develops steadily down the chamber wall. As the arc is gradually stretched, its temperature also drops. At 0.55 ms, when the arc enters the metal splitter plates, the arc is squeezed and curved. At 0.65 ms, the arc completely enters the splitter plates and is divided into several independent short arcs. The maximum temperature of the arc decreased significantly. At 0.75 ms, under the Lorentz force and air flow field, the short arc located in the middle part of the splitter plates group first spray out of the splitter plates area, and the maximum temperature of the arc continued to decrease. It is generally believed that the arc is successfully extinguished at this time. The temperature profile at 1.1 ms also verified this conclusion. The arc has mostly dissipated and the temperature is gradually dropping to space temperature.

The voltage, current and maximum temperature curves of the arc is shown in Fig. 4. As time goes by, the arc is gradually elongated. Therefore, the arc voltage

Fig. 3 Arc temperature distribution at different times



gradually increases while the arc current decreases with time. The arc is extinguished when the current value is reduced to 0 A or the potential difference reaches 220 V. The maximum temperature of the arc gradually decreases. In particular, the maximum temperature decreases rapidly from 0.65 to 0.75 ms. It is the time for the arc to enter the splitter plates. The arc energy dissipates rapidly under the effect of the splitter plates.

4.2 Simulation of Arcs Under Different Air Blowing Strength

During the process of arc development, the air-producing materials in the arc extinguish chamber are decomposed and vaporized by high temperature of the arc. This makes the pressure in the arc extinguish chamber increase. As the air is discharged through the outlet, it forms a high-speed air stream that helps to blow out the arc. In this section, the influence of different strength of air inflow on the dynamic process of

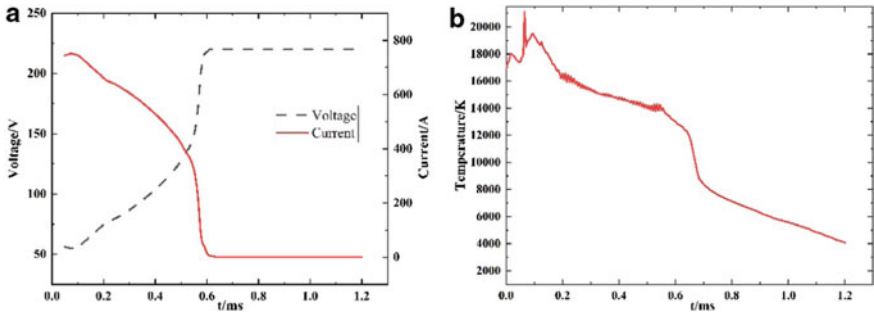


Fig. 4 Voltage, current and maximum temperature curves of arc. **a** Voltage and current, **b** temperature

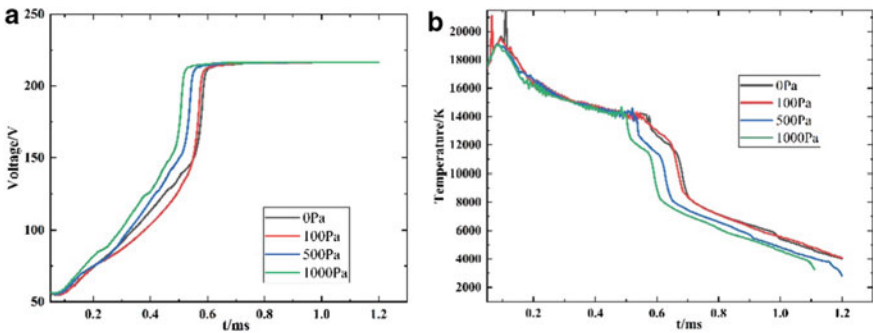


Fig. 5 Voltage and maximum temperature curves of arc under different blowing strength. **a** Voltage, **b** temperature

arc is explored. In the simulation, the air flow generated by the material is simulated by a constant pressure air flow entering. The results are shown in Fig. 5.

For the model of arc extinguish chamber with outlet, the inflow of air can drive the arc to bend and elongate quickly. Then the arc is directly driven to the splitter plates area, so that the extinguishment of the arc is accelerated. As shown in Fig. 5, the development trend of voltage is similar, which means that the arc can be successfully extinguished under several different blowing intensities. Besides, the arc voltage rises faster with the increase of blowing strength. Similarly, with the increase of the strength of air blowing, the decrease rate of the maximum temperature of the arc is faster. With the increase of air blowing strength, air flow makes the power of convective heat dissipation increase, which means that the cooling effect of air on the arc is enhanced. On the other hand, the increase of air blowing strength directly makes the arc enter the splitter plates more quickly. The splitter plate has a strong limiting effect on arc, which speeds up the extinguishment of arc. It can be concluded that the arc is extinguished more quickly, while the pressure of the inflow airflow is bigger.

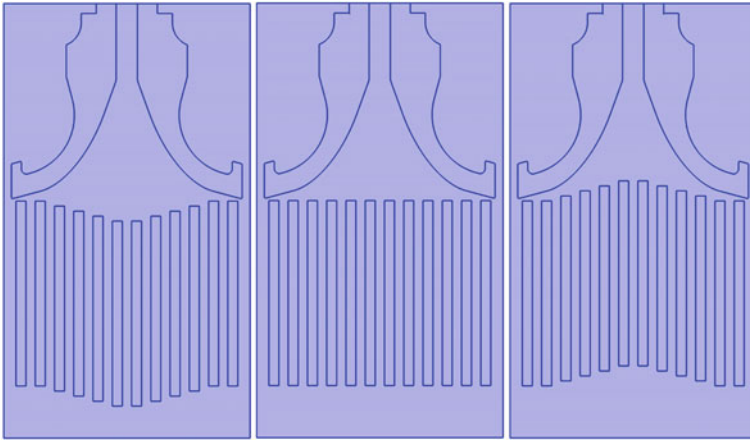


Fig. 6 Different configurations of splitter plates

4.3 Simulation of Arcs in Different Configurations of Splitter Plates

The configuration of the splitter plates in the arc extinguish chamber will have some influence on the internal air flow. In this section, the arc development in an arc extinguishing chamber with different configurations of splitter plates is simulated and analyzed. As shown in Fig. 6, convex, flush and concave configurations modes are designed respectively. The same boundary conditions are set.

Figure 7 shows the temperature distribution of arc at 0.5 ms. The arc development speed is similar in different configurations. The difference is that the arc in the arc extinguish chamber with the convex configuration reaches the splitter plates the earliest while the arc in the arc extinguish chamber with the concave configuration reaches the latest. What’s more, in the simulation of the concave configuration, the arc root at the cathode appears disturbance. This phenomenon does not appear in the other two simulations. The change of splitter plates configuration has the greatest influence on the distribution of internal airflow field in the arc extinguish chamber. Therefore, the simulation of its airflow velocity distribution is continued.

In the airflow distribution shown in Fig. 8, it is found that in the simulation of concave splitter plates, air eddies will appear between the electrode and the splitters. This will affect the arc root near the electrode and cause disturbance to the arc root. Air eddies are considered the main cause of arc root disturbance. When the arc root is disturbed, it can cause unstable movement and irregular shape of the arc, as well as uneven distribution and incomplete dissipation of the arc energy. This not only results in uneven temperature distribution of the arc and concentration of thermal stress, but may also cause a secondary breakdown, which is should be avoided in practical applications.

The curves of arc parameters in different configurations can be seen Fig. 9.

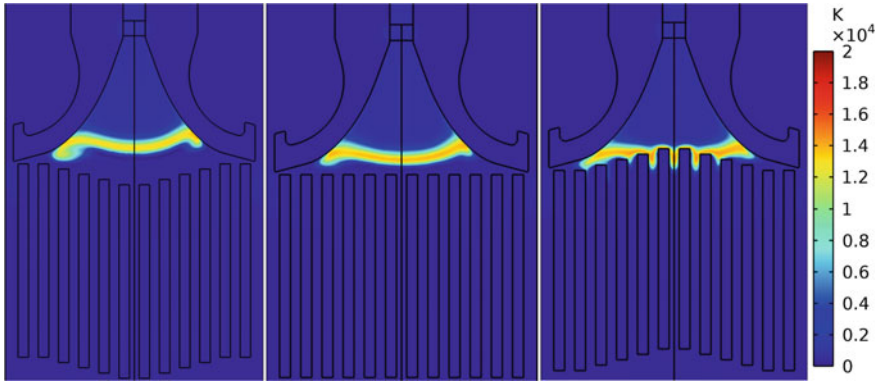


Fig. 7 Temperature distribution of arc at 0.5 ms

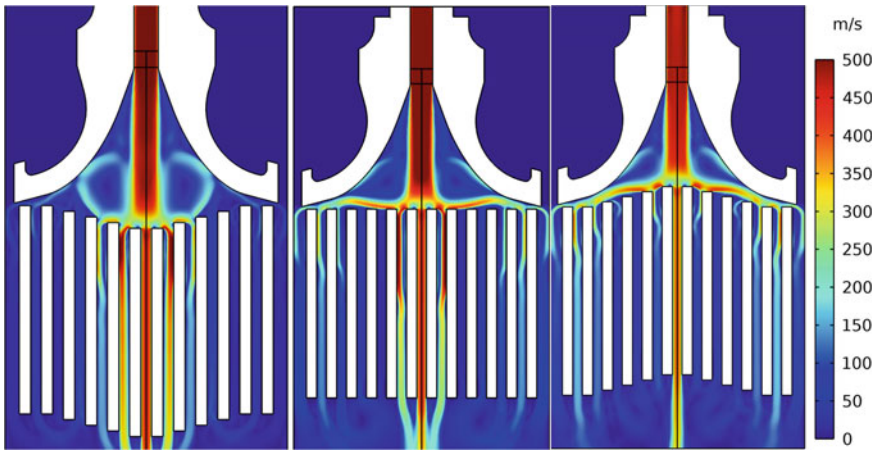


Fig. 8 Airflow velocity field distribution of arc

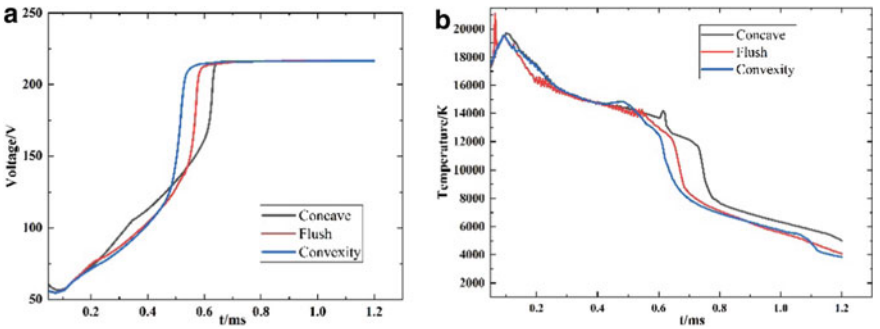


Fig. 9 Voltage and maximum temperature curves of arc in different configurations of splitter plates. a Voltage, b temperature

Among the three configurations, the convex configuration can more quickly extinguish the arc, with the voltage reaching 220 V and the current becoming 0 A earliest. The flat configuration ranks second, while the concave configuration of the splitter plates has the slowest arc extinguishing speed. Moreover, it can be found from the previous conclusion that the concave configuration of the splitter plates will create a swirling airflow between the splitter plates and the electrode, which will disturb the arc root position. This is not conducive to the movement and energy dissipation of the arc. It may also cause secondary breakdown and reduce the reliability and lifespan of the equipment. Therefore, the concave configuration of the splitter plates should be avoided. However, the convex configuration of the splitter plates should be chosen to improve the performance and reliability of arc extinguishment in the equipment.

5 Conclusion

This paper discusses the problem on the development and extinguishment of the arc in switching-type SPD. Based on the MHD model, a two-dimensional numerical model of arc is established by the multi-field coupling method. The main conclusions of the study can be listed as follows:

- (1) The extinguishing time of the arc is greatly affected by the air flow. As the air flow strength increases, the arc will move faster and enter the splitter plates earlier.
- (2) The arc extinguishment is affected by the different configurations of splitter plates. Among the three configurations, the convex one has the best performance on the arc extinguishment.

References

1. Kisielewicz T, Piparo GBL, Mazzetti C, Rousseau A (2014) Dimensioning of SPD for the protection against surges due to lightning to LV overhead lines. In: 2014 international conference on lightning protection (ICLP), Shanghai, China, pp 141–145
2. Protection against lightning part 4: Electrical and electronic systems within structures. IEC Standard 62305-4, Geneva, Switzerland (2010)
3. Colina Jimenez LI, Rock M (2021) Measurements of surface breakdown voltage of a creeping discharge spark air gap using POM as insulation material. In: 2021 35th international conference on lightning protection (ICLP) and XVI international symposium on lightning protection (SIPDA), Colombo, Sri Lanka, pp 01–05
4. Song F et al (2019) Analysis of the optimal operation frequency with lowest time-delay jitter for an electrically triggered field-distortion spark gap. *IEEE Trans Plasma Sci* 47(10):4708–4712
5. Low-voltage surge protection device part 1: surge protection device connected to low-voltage power distribution systems—requirements and tests. IEC Standard 61643-1 (1998)

6. Lin Q, Huang X, Liu X (2021) Simulation analysis of arc motion of high voltage DC Relay under non-uniform magnetic field. In: 2021 IEEE 2nd China international youth conference on electrical engineering (CIYCEE), Chengdu, China, pp 1–6
7. Liu X, Huang X, Cao Q (2021) Simulation and experimental analysis of DC arc characteristics in different gas conditions. *IEEE Trans Plasma Sci* 49(3):1062–1071
8. Park Y, Song T (2022) Plasma arc simulation of high voltage circuit breaker with a hybrid 2D/3D model. In: 2022 6th international conference on electric power equipment-switching technology (ICEPE-ST), Seoul, Republic of Korea, pp 190–193

Research on Relationship Between Aerodynamic Configuration and Ability to Extinguish Arc in Switching-Type SPD



Yijie Xiao, Qibin Zhou, Yipeng Zhang, and Xiaoyan Bian

Abstract The application of surge protective devices plays an important role in ensuring the safe operation of power systems. Among all kinds of SPD, switching-type SPD is widely used in power systems due to its great surge absorption capacity. Spark gap is the main structure in switching-type SPD. It has the problem that the follow current arc in the spark gap will continue to burn due to the voltage at the SPD after discharging the surge current. This paper analyzes the development of the arc in the SPD arc extinguish chamber based on the magneto hydro dynamic (MHD) model. The relationship between aerodynamic configuration and ability to extinguish arc can be concluded. The result will be benefit for the structural optimization design of the SPD arc extinguish chamber. It also improves the safety and reliability of the equipment.

Keywords Switching-type SPD · Arc extinguishment · MHD model · Aerodynamic configuration

Y. Xiao (✉) · Q. Zhou · Y. Zhang
School of Mechatronic Engineering and Automation, Shanghai University, Shanghai 200444,
China
e-mail: 846707560@qq.com

Q. Zhou
e-mail: zhouqibin@shu.edu.cn

Y. Zhang
e-mail: zhangyipeng@shu.edu.cn

X. Bian
College of Electrical Engineering, Shanghai University of Electric Power, Shanghai 200090,
China

1 Introduction

Surge protection is essential for power systems. IEC 62305-4:2010 describes the Surge Protection Measures (SPM) formed by different types of surge protective devices (SPDs) [1], which can suppress the overvoltage in the circuit and divert the lightning energy to the ground. The application of surge protective devices plays an important role in ensuring the safe operation of power systems.

Many researches about SPD have been conducted in the past decade. For instance, American Skuletic [2] and He [3] got the results of the energy coordination and effective protective distance of SPDs in low voltage power systems by calculating the coordination of SPDs with different loads. Kisielewicz et al. [4] proposed rules for SPD selection on the basis of the voltage protection level of the SPD. In these studies, researchers have found important differences between different types of SPD in lightning protection systems, including parameters such as residual voltage and response time.

In IEC 61643-11, SPD can generally be divided into several types according to the different non-linear components [5]. One is switching-type SPD, which usually uses a spark gap inside. The typical structure of the switching-type SPD is an air gap with two electrodes. Another one is clamping-type SPD, which generally uses a metal oxide varistor (MOV) inside. Compared with the clamping-type SPD, switching-type SPD has great surge absorption capacity. Currently, research on switching-type SPDs has focused on the effects of gap structure on protection characteristics [6], arc characteristics [7] and the improvement of gap performance by coupled triggering circuits and trigger methods [8, 9]. However, there are still some problems in the spark gap in practice [10, 11]. After discharging the surge current, the arc in the spark gap will continue to burn due to the voltage at the SPD, which generates a lot of heat. It will bring great threat to the protected equipment. Therefore, it is necessary to study the extinguishment of the arc in the spark gap.

In this paper, to calculate the reliability of the arc extinguishment in the switching-type SPD, a cambered spark gap with an arc extinguish chamber is modeled. The arc modeling theory is mainly introduced in Sect. 2. The model is established and simulated in Sect. 3. The analysis of the calculation results is introduced in Sect. 4. Through simulation and analysis, the ability to extinguish the arc will be improved in the switching-type SPD.

2 Modeling Methodology

The magneto hydro dynamic (MHD) model is generally used to express the arc. It consists of several equations for four physical fields including electric, magnetic, temperature, and fluid fields.

2.1 Electric Fields

The electric field is necessary for the formation of the arc. Solving for the current density and electric field distribution through the electric field provides the basis for calculations of the magnetic and flow fields.

$$\nabla \cdot \mathbf{J} = 0 \quad (1)$$

Equation (1) is current conservation equation. \mathbf{J} indicates current density.

$$\mathbf{J} = \sigma \mathbf{E} + \frac{\partial \mathbf{D}}{\partial t} + \mathbf{J}_e \quad (2)$$

Equation (2) explains the generation of current density. In Eq. (2), σ for specific conductivity, \mathbf{E} for electric field intensity, \mathbf{D} for electric displacement vector, t for time, \mathbf{J} for external current density.

2.2 Magnetic Field

Lorentz force is the reason why the arc is able to keep burning. The equations of magnetic field can be solved for the magnetic induction strength. The Lorentz force can be obtained by calculating the magnetic induction strength and the current density.

$$\nabla \times \mathbf{H} = \mathbf{J} \quad (3)$$

Equation (3) is Ampere's law. \mathbf{H} for magnetic field strength.

$$\mathbf{J} = \sigma \mathbf{E} + \sigma \mathbf{v} \times \mathbf{B} + \mathbf{J}_e \quad (4)$$

Equation (4) represents the source of the current that forms the magnetic field.

$$\mathbf{E}_m = -\frac{\partial \mathbf{A}}{\partial t} \quad (5)$$

Equation (5) represents Faraday's law of electromagnetic induction. It illustrates that a changing magnetic field produces an electric field.

2.3 Temperature Field

The change of the temperature is related to the energy. The energy of the MHD model is from a power source, which is represented by changes in arc and electrode temperature.

$$\rho C_p \left(\frac{\partial T}{\partial t} + v \cdot \nabla T \right) - \nabla \cdot (k \nabla T) = Q + Q_p + Q_{vd} \quad (6)$$

$$Q = \frac{\partial}{\partial T} \left(\frac{5k_B T}{2e} \right) (\nabla T \cdot \mathbf{J}) + \mathbf{E} \cdot \mathbf{J} + Q_{\text{rad}} \quad (7)$$

Equation (6) is a thermodynamic equation. For the MHD model, internal heating Q is the main factor. Equation (7) shows that arc heating consists of three parts including enthalpy change heat, Joule heat and radiant heat of plasma.

2.4 Fluid Field

The plasma is treated as a fluid. The laminar flow theory based on Navier–Stokes equation (Eq. 8) is used to describe the arc flow.

$$\rho \left(\frac{\partial v}{\partial t} + v \cdot \nabla v \right) = \nabla \cdot [-p \mathbf{I} + \mu (\nabla v + (\nabla v)^T)] + \mathbf{F} + \rho \mathbf{g} \quad (8)$$

$$\mathbf{F} = \mathbf{J} \times \mathbf{B} \quad (9)$$

$$\rho \nabla \cdot (v) = 0 \quad (10)$$

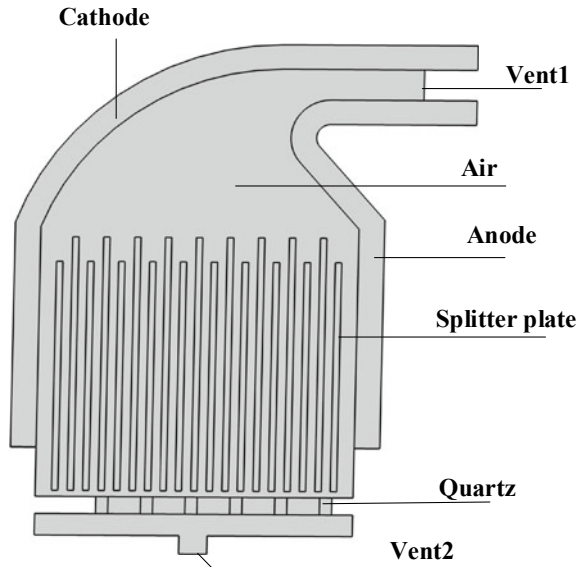
Equation (9) represents the Lorentz force, which is the main source of forces in the fluid field. Equation (10) represents the conservation of mass in the fluid.

To sum up, the macro state of the arc can be obtained by coupling calculation of the above physical fields.

3 Simulation Model

This paper simplifies the internal structure of SPD. The arc extinguish chamber model used in this paper is shown in Fig. 1. A two-dimensional model was established with a size of 35 mm × 40 mm in the x–y direction. The initial gap between the cathode and anode is 2 mm. Both the cathode and anode are made of copper material. In

Fig. 1 Arc extinguish chamber model



addition, 19 silicon steel grating plates are arranged in the arc extinguish chamber. The parts from the two electrodes to Vent2 are insulated sidewalls and 5 air channels.

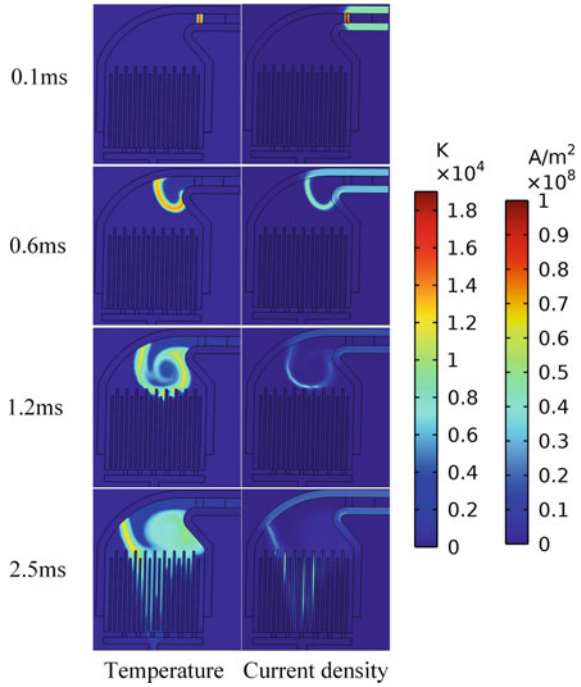
4 Simulation Results

4.1 The Development of the Arc

This part reproduces the development of the arc in the arc extinguish chamber. The input source is set as DC1000 A/220 V and the initial temperature is 293 K. The distribution of temperature and current density at different times are shown in Fig. 2. The development of the arc can be judged by its temperature and current density.

At $t = 0.1$ ms, a stable cylindrical arc has been formed between the cathode and anode. The two electrodes have already been connected by the arc. At $t = 0.6$ ms, the arc is influenced by the Lorentz force and the driving force of the airflow. Thus, it moves smoothly along the two stages towards the splitter plates. At $t = 1.2$ ms, the arc begins to contact the splitter plates and his maximum temperature drops significantly. In addition, the arc root tailing phenomenon appears at the position of the anode arc root. The incorrect structural design of the arc extinguish chamber caused an abnormal aerodynamic configuration inside it. Figure 3 shows the velocity vector distribution diagram of the airflow field at this time. There is a small vortex of air at that position. The vortex causes the arc root to experience a force opposite to the direction of the arc column. This causes the arc column to expand forward

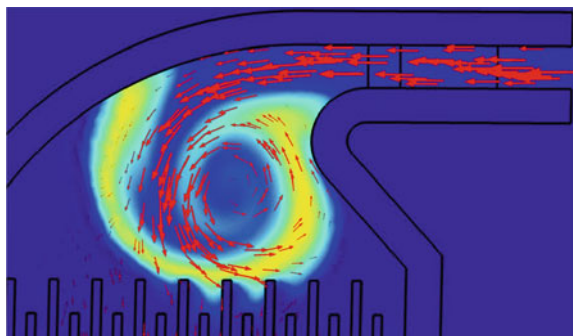
Fig. 2 The distribution of temperature and current density of the arc



under the electromagnetic force, while the arc root stagnates. As this phenomenon continues to develop, it will gradually become an arc trailing. The distribution of temperature and current density at $t = 2.5$ ms showed that the arc was divided into several independent short arcs after entering the splitter plates. The maximum arc temperature drops.

However, due to defects in the design of the arc extinguish chamber, the arc has been vibrating at the upper of the splitter plates and cannot be extinguished successfully. Figure 4 shows the arc voltage and temperature curve versus time. The arc voltage is maintained below 150 V. It can be proved that the arc is not completely

Fig. 3 The velocity vector distribution diagram of the airflow field



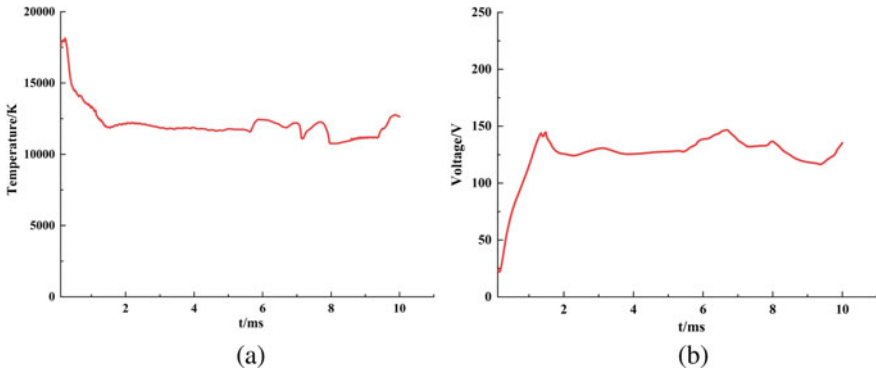


Fig. 4 Arc voltage and temperature versus time. **a** Temperature, **b** voltage

extinguished after 2 ms. At the same time, its maximum temperature is maintained above 10,000 K. Due to the long-time burning, the energy of arc is very large, which is easy to destroy the arc extinguish chamber in practice. Further simulation is needed to explore the method to successfully extinguish the arc.

4.2 The Simulation of Different Vent Sizes

The outlet (Vent2) size of arc extinguish chamber will have great influence on the airflow field. In addition, the arrangement of the splitter plates in the arc extinguish chamber will also affect the airflow field. The arc will eventually move into the splitter plates, so the different arrangement of the splitter plates may also affect the shape of arc. Currently, it is speculated that the reason why the arc cannot be successfully extinguished may be related to the aerodynamic configuration inside the arc extinguish chamber. Therefore, the air outlet (Vent2) under the arc extinguish chamber is enlarged. The situations under different numbers of splitter plates are simulated. Simulation results are shown in Fig. 5.

After increasing the width of the Vent2, the ability to extinguish arc is obviously improved. With the development of the arc, especially after entering the splitter plates, the temperature drops rapidly and the arc voltage rises to about 220 V rapidly. The effect of arc extinguishment effect is better when only 9 or 10 splitter plates is retained. Too many splitter plates may affect the airflow speed and direction in the arc extinguish chamber, which will hinder the normal flow of air. In the simulation with 19 splitter plates, a peak appears at about 4 ms in the arc parameter curve. After this time, the maximum temperature rises and the voltage drops again. There is an arc secondary breakdown.

As shown in Fig. 6, at the upper corner of the arc extinguish chamber, the phenomenon of secondary breakdown occurs. The electrode is re-broken, causing

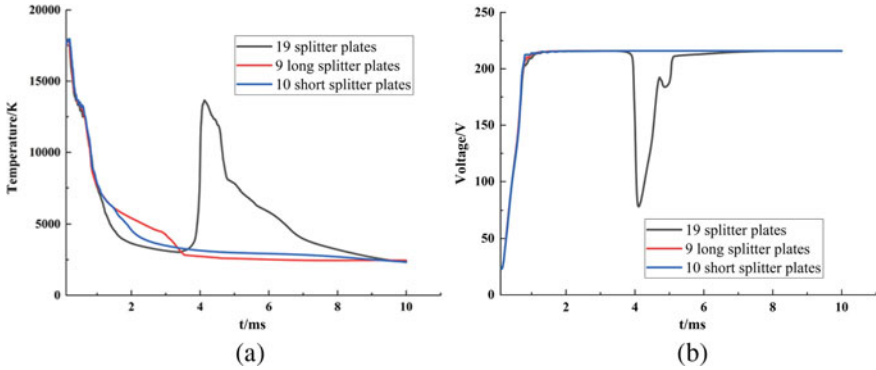


Fig. 5 Arc voltage and temperature versus time. **a** Temperature, **b** voltage

the temperature rises and the voltage drops again. Then, the reignited arc enters the quench chamber again and finally is extinguished.

Increasing the width of the outlet (Vent2) is beneficial to improving the airflow distribution and enhancing the arc extinction ability of the extinguish chamber. However, there is still a secondary breakdown phenomenon. Although the arc produced by the secondary breakdown enters the arc extinguish chamber again and is interrupted, the high temperature generated by multiple arcs will accelerate the damage of the product, so it is still necessary to avoid this phenomenon as much as possible. Therefore, it is necessary to continue to improve the design and further optimize the airflow distribution.

Fig. 6 Arc reignition

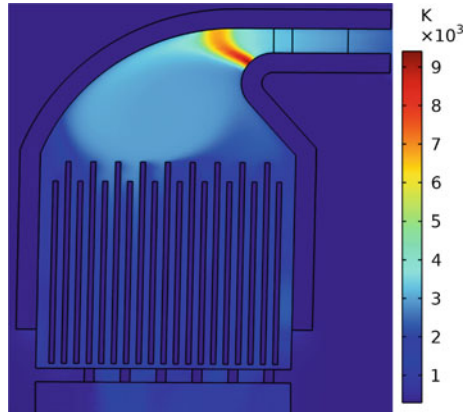


Fig. 7 New arc extinguish chamber with six air channels

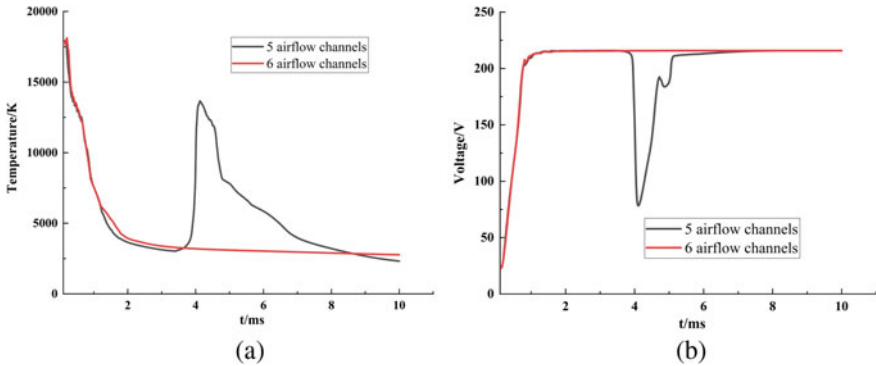
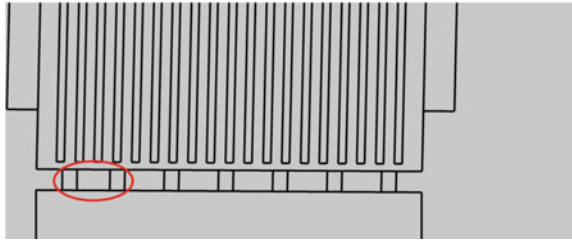


Fig. 8 Arc voltage and temperature versus time: **a** temperature, **b** voltage

4.3 The Simulation of 6 Air Flow Channels

As shown in Fig. 7, an airflow channel (shown in the red circle) is added to the left side of the model. The parameter change of arc is analyzed by simulation again. The results are shown in Fig. 7

As can be seen in Fig. 8, the secondary breakdown phenomenon disappeared after adding an airflow channel. The arc voltage rises to 220 V and don't fall again, which is proved that the arc is extinguished successfully. It can be considered that adding one more airflow channel is beneficial to improve the airflow distribution of the arc extinguish chamber and increase the ability to extinguish the arc.

5 Conclusion

The aerodynamic configuration inside the arc extinguish chamber has a significant impact on arc extinguishment. A too small outlet will cause air flow obstruction, leading to the failure of the arc extinguish. This paper analyzes the development of the arc in the SPD arc extinguish chamber through simulation. Based on the simulation results, The main conclusions of the study can be listed as follows:

- (1) Excessive and too dense splitter plates will hinder the flow of air. It can improve the ability of arc extinguishment by reducing the number of splitter plates appropriately.
- (2) A too small vent will hinder the air flow. The air flow can be improved by increasing the number of air channels and the width of vent2, thereby enhancing the ability of arc extinguishment.

References

1. Protection against lightning Part 4: electrical and electronic systems within structures. IEC Standard 62305-4, Geneva, Switzerland (2010)
2. Skuletic S, Radulovic V (2008) Effective protection distance from cascade coordinated surge protective devices to equipment in low-voltage AC power circuits. In: 2008 43rd international universities power engineering conference, pp 1–5
3. He J (2015) Discussions on factors influencing the effective protection distance of SPD to loads. In: 2015 Asia-Pacific symposium on electromagnetic compatibility (APEMC), pp 420–423
4. Kisielewicz T, Piparo GBL, Mazzetti C, Rousseau A (2014) Dimensioning of SPD for the protection against surges due to lightning to LV overhead lines. In: 2014 international conference on lightning protection (ICLP), Shanghai, China, pp 141–145
5. Low-voltage surge protection device—Part 11: surge protection device connected to low-voltage power systems—requirements and tests. IEC Standard 61643-11 (2011)
6. Liu S, Liu X, Shen X, Feng L, Tie W, Zhang Q (2017) Discharge characteristics of a dual-electrode gas switch triggered by ejected plasma in N₂ and SF₆. *IEEE Trans Plasma Sci* 45(6):969–974
7. Kopp TH, Runge T, Kurrat M (2018) Analysis of arc behavior in a model spark gap after surge currents. *IEEE Trans Compon Packag Manuf Technol* 8(6):958–965
8. Kopp TH, Kurrat M, Schottel B (2014) Circuit behavior during operation duty test applying spark gap technology based arresters. In: 2014 international conference on lightning protection (ICLP), pp 1365–1369
9. Park Y, Song T (2022) Plasma arc simulation of high voltage circuit breaker with a hybrid 2D/3D model. In: 2022 6th international conference on electric power equipment-switching technology (ICEPE-ST), Seoul, Republic of Korea, pp 190–193
10. Lin Q, Huang X, Liu X (2021) Simulation analysis of arc motion of high voltage DC relay under non-uniform magnetic field. In: 2021 IEEE 2nd China international youth conference on electrical engineering (CIYCEE), Chengdu, China, pp 1–6
11. Liu X, Huang X, Cao Q (2021) Simulation and experimental analysis of DC arc characteristics in different gas conditions. *IEEE Trans Plasma Sci* 49(3):1062–1071

Study on Voltage Control Method of Energy Router Based on Common DC Voltage Bus



Shuxi Liu, Qin Luo, Jianhong Chen, and Yufei Qu

Abstract In order to relieve the pressure caused by the direct input of all kinds of distributed energy to the stable operation of distribution network, a kind of multi-port energy router with common DC bus is studied. The energy router provides five standardized interfaces that enable “plug and play” for photovoltaic, energy storage, diesel generators, DC loads and distribution network ports. The virtual motor control algorithm is introduced into the interface control link of energy router, which can increase the damping and inertia of the system, effectively reduce the voltage fluctuation of DC bus, and realize the friendly interconnection between distributed energy and distribution network. At the same time, an improved virtual synchronous motor control algorithm is introduced to make the energy router run stably under the voltage drop of power grid. Finally, an experimental model is built by simulation software to verify the feasibility and effectiveness of the proposed control algorithm.

Keywords Energy routers · Virtual AC motor control · Virtual DC motor control · Network fault

1 Introduction

With the rapid development of economic construction and the iterative renewal of industrial production, renewable distributed energy sources such as photovoltaic and wind power are being vigorously built as well as grid-connected, but the fluctuating and intermittent nature of their power generation poses a great burden on the stable power supply of traditional distribution grids [1, 2]. With the help of mature power electronics technology, the multi-port energy router, a highly integrated device, can not only provide standardized power interfaces, but also realize

S. Liu · Q. Luo (✉) · J. Chen · Y. Qu
Chongqing University of Technology, Chongqing 400054, China
e-mail: 798569195@qq.com

S. Liu
Chongqing Energy Internet Engineering Technology Research Center, Chongqing 400054, China

© Beijing Paiké Culture Commu. Co., Ltd. 2024
X. Dong and L. Cai (eds.), *The Proceedings of 2023 4th International Symposium on Insulation and Discharge Computation for Power Equipment (IDCOMPU2023)*, Lecture Notes in Electrical Engineering 1100, https://doi.org/10.1007/978-981-99-7393-4_38

the balanced flow of energy between interfaces through the controller to enhance the reliability of distributed energy supply, which is the core device to realize the future energy Internet.

Literature [3] proposes a new energy router structure that can access multiple voltage levels simultaneously. In [4], a hybrid AC-DC energy router is studied, and four operating modes and their switching methods are analyzed. In [5], an energy router for DC micro-grid is studied and a droop phase shift control method with normalization is proposed to achieve a reasonable distribution of micro-grid energy between different operating conditions. In [6], a virtual synchronous motor control strategy is used to improve the damping and inertia of the system. The literature [7] introduced a PI controller in the power loop of the Virtual Synchronous Generator (VSG) to enable the VSG to improve the output current under grid faults to some extent. The literature [8, 9] proposes the application of Virtual DC Motor (VDCM) in PV, energy storage environment. The literature [10, 11] introduces virtual motor control in energy routers, adding some inertia and damping to the AC output side.

Based on the above analysis, this paper proposes an improved voltage stabilization control strategy for a multi-port energy router with common DC bus, which increases the bus voltage inertia and damping by adopting a virtual motor control algorithm, and also improves the virtual AC motor control for the AC interface, so that the energy router can operate stably in grid faults within a certain range, while reducing the DC bus voltage disturbance. Finally, the correctness and effectiveness of this voltage stabilization control algorithm is derived by building a model and conducting an experimental analysis of the control strategy.

2 Topology of the Energy Router

The energy router studied in this paper is shown in Fig. 1a. The core of the operation of the multi-port energy router is to maintain the stability of the DC bus voltage and to distribute the energy between the ports via the DC bus. Various power electronics and corresponding control strategies are used to realize the flow of energy between the various electrical sources and the change of voltage levels.

As shown in Fig. 1b, the AC interface uses a virtual synchronous motor control strategy to reduce the impact on the grid and output a smoother three-phase sinusoidal AC voltage during the energy transfer conversion process. The energy storage interface, as the core device of the energy router, uses virtual DC motor control, which can better smooth out DC bus voltage fluctuations compared to the traditional constant voltage control mode. The photovoltaic power port uses a unidirectional Boost converter and is operated in Maximum Power Point Tracking (MPPT) mode, considering the use of green and clean energy wherever possible. The diesel generator port can be used as an emergency power supply in the energy router due to the controllable power output.

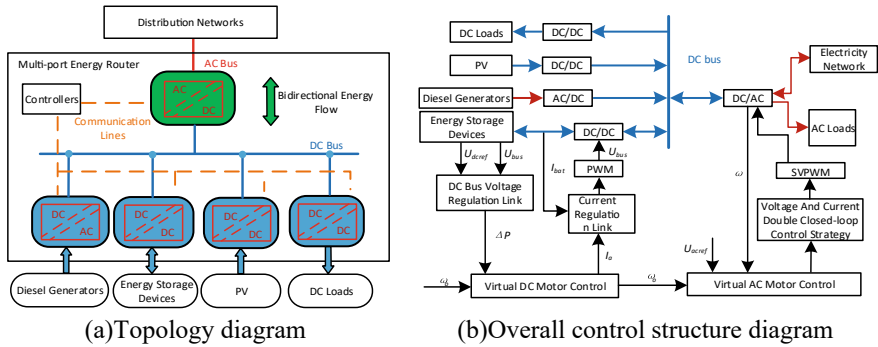


Fig. 1 Energy router

3 Virtual Motor Control

3.1 VDCM Control of the Energy Storage Interface

The introduction of VDCM control at the energy storage interface allows a certain damping factor to be added to the DC bus to prevent fluctuations in the DC bus voltage during the power flow between the interfaces in the energy router, acting as a balancing voltage regulator. Figure 2 shows the Buck-Boost topology and the equivalent structure of the DC motor. It is easy to see from the figure that the DC motor and the Buck-Boost circuit have a similar structure and a pairwise relationship. The energy stored in the DC motor comes from the kinetic energy generated by the rotor rotation $E_k = J\omega^2/2$, while the energy contained in the energy storage capacitor is $W_c = CU_{dc}^2/2$, thus further proof the feasibility of the VDCM.

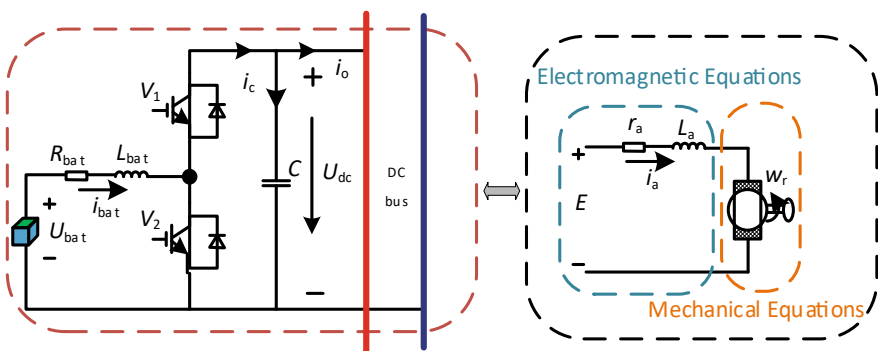


Fig. 2 Virtual DC motor coupling schematic

3.2 Virtual AC Motor Control Under Grid Fault

Conventional controller in the event of a grid fault can cause large fluctuations in the DC bus voltage amplitude, resulting in the energy router being unable to maintain a stable output current and power. This paper proposes an improved VSG controller to cope with grid faults. It is able to stabilize the output power of the grid-connected interface when the grid voltage drops to 20% and also reduces the double-frequency disturbing component in the DC bus voltage.

When the three-phase grid voltage drops, the output power of the VSG is calculated according to the instantaneous power theory, and the coordinate transformation is carried out to obtain Eq. (1):

$$\begin{bmatrix} \bar{p} \\ \bar{q} \\ P_{s2} \\ P_{c2} \\ Q_{s2} \\ Q_{c2} \end{bmatrix} = \frac{3}{2} \begin{bmatrix} u_{gd}^+ & u_{gq}^+ & u_{gd}^- & u_{gq}^- \\ u_{gq}^+ & -u_{gd}^+ & u_{gq}^- & -u_{gd}^- \\ u_{gq}^- & -u_{gd}^- & -u_{gq}^+ & u_{gd}^+ \\ u_{gd}^- & u_{gq}^- & u_{gd}^+ & u_{gq}^+ \\ u_{gq}^- & -u_{gd}^- & u_{gq}^+ & -u_{gd}^+ \\ -u_{gd}^- & -u_{gq}^- & u_{gd}^+ & u_{gq}^+ \end{bmatrix} \begin{bmatrix} i_d^+ \\ i_q^+ \\ i_d^- \\ i_q^- \end{bmatrix} \quad (1)$$

Among them, i_d^+ , i_q^+ , i_d^- , i_q^- not only changes the positive and negative sequence output power values in the system, but also controls the output current. The design of the current loop control is therefore central to ensuring the stability of the VSG system. In order to keep the output current stable, the magnitude of the negative sequence current needs to be controlled, where the positive and negative component can be separated by a second order generalized integrator.

In the case of a sudden drop in grid voltage, the analysis is simplified by neglecting the effect of the filter capacitor to derive the output voltage of the VSG, which is converted to a pull-form, with s tending to zero in the steady state due to the final value theorem, and then converted to the time domain, as follows:

$$\begin{cases} i_d^{+*} = \frac{R(u_{1d}^+ - u_{gd}^+) + \omega_g L(u_{1q}^+ - u_{gq}^+)}{R + (\omega_g L)^2} \\ i_q^{+*} = \frac{R(u_{1q}^+ - u_{gq}^+) - \omega_g L(u_{1d}^+ - u_{gd}^+)}{R + (\omega_g L)^2} \end{cases} \quad (2)$$

Equation (2) shows that if only the negative sequence current is zero-tracked, there are still active and reactive double-frequency component. Therefore, the active and reactive power doublings need to be suppressed and the negative sequence currents need to be selected for control again.

If the active double-frequency component needs to be suppressed, it is necessary to keep P_{s2} , P_{c2} equal to zero and bring in Eq. (1). The calculation formula of negative sequence current is as follows:

$$\begin{bmatrix} i_d^{-*} \\ i_q^{-*} \end{bmatrix} = -\frac{1}{(u_{gd}^+)^2 + (u_{gq}^+)^2} A \begin{bmatrix} i_d^{+*} \\ i_q^{+*} \end{bmatrix}$$

$$A = \begin{bmatrix} -u_{gq}^+ u_{gq}^- + u_{gd}^+ u_{gd}^- & u_{gq}^+ u_{gd}^- + u_{gd}^+ u_{gq}^- \\ u_{gd}^+ u_{gq}^- + u_{gq}^+ u_{gd}^- & -u_{gd}^+ u_{gd}^- + u_{gq}^+ u_{gq}^- \end{bmatrix} \quad (3)$$

Similarly, if the reactive double-frequency component needs to be suppressed, it is necessary to keep Q_{s2} , Q_{c2} equal to zero and bring in Eq. (1). The calculation formula of negative sequence current is as follows:

$$\begin{bmatrix} i_d^{-*} \\ i_q^{-*} \end{bmatrix} = \frac{1}{(u_{gd}^+)^2 + (u_{gq}^+)^2} A \begin{bmatrix} i_d^{+*} \\ i_q^{+*} \end{bmatrix} \quad (4)$$

Based on the mathematical model analyzed above, the control block diagram for the VSG under grid voltage drop can then be derived as shown in Fig. 3.

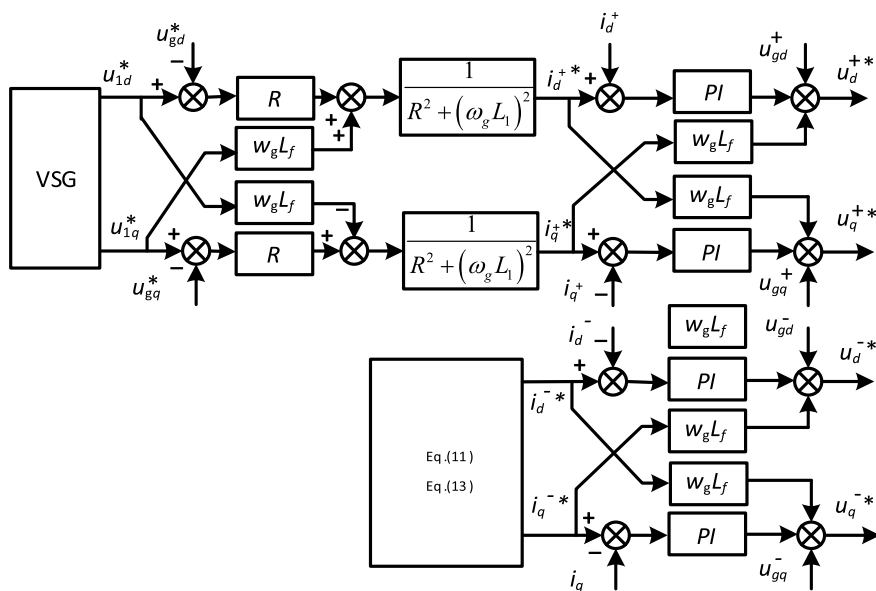


Fig. 3 VSG control block diagram under grid voltage drop

Table 1 VSG controller main circuit parameters

Parameter	Value	Parameter	Value
DC voltage U_{dc}	400 V	Net-side voltage U	220 V
Filter inductor L_1	4.8 mH	Filter resistor R_1	0.1 Ω
Filter capacitor C	50 μ F	Switching frequency f	10 kHz
Active inertia link J	1000	Active damping factor D_p	50
Reactive droop coefficient D_q	480	Reactive inertia coefficient K	1600
Line equivalent inductance L_2	3 mH	Line equivalent resistance R_2	0.1 Ω

4 Experimental Results and Analysis

4.1 Comparative Experiments of VSG Under Grid Faults

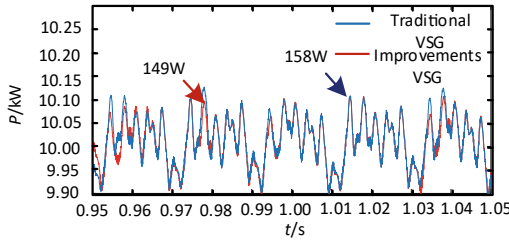
In order to verify the superiority of VSG control, an experimental module was built in Matlab/Simulink to simulate a three-phase voltage fault in the grid. Among other things, the main parameters within the system can be seen in Table 1. The simulation duration was set to 1.5 s, with a grid fault occurring at 0.8 s and the system returning to stability after 1.2 s.

Three-phase Voltage Drop to 0.2 pu. When the three-phase voltage drop to 20% of the rated voltage value, Fig. 4 shows the three-phase voltage fault waveform, from which it can be seen that the power fluctuation of the conventional VSG is about 158 W, while the power fluctuation of the improved VSG is reduced to 149 kW. And it can be concluded that the THD of the improved VSG control strategy is reduced to 0.47%. The analysis leads to the conclusion that the improved VSG improves the output power and output current under grid faults.

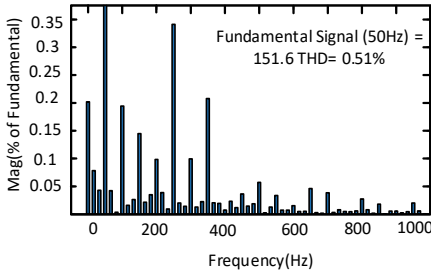
4.2 Energy Router Voltage Regulation Control Comparison Experiments

To verify that VDCM control can stabilize the DC bus voltage and improve bus voltage fluctuations, experiments were set up in Simulink. Various scenarios such as sudden changes in PV output, sudden changes in DC load and single-phase grid faults were classified and verified against conventional droop control. The simulation parameters for the energy storage interface are shown in Table 2.

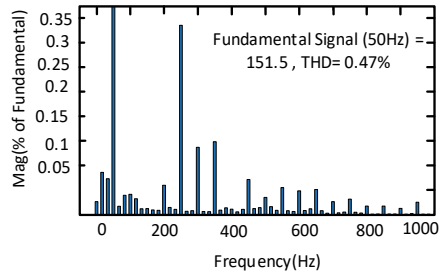
Mutation experiments. The simulation duration was set to 1 s for experiments with sudden changes in PV and sudden changes in load. In Fig. 5a with a DC load of 5 kW and the PV running in MPPT mode, the light intensity rises from 750 to 1000 W/m² at 0.4 s and then drops to 800 W/m² at 0.8 s. In Fig. 5b, the light intensity is set to 1000 W/m² and the DC load power rises from 3 to 8 kW at 0.5 s. The comparison



(a) Comparison of active power output under a three-phase voltage fault



(b) Traditional VSG control



(c) Improved VSG control

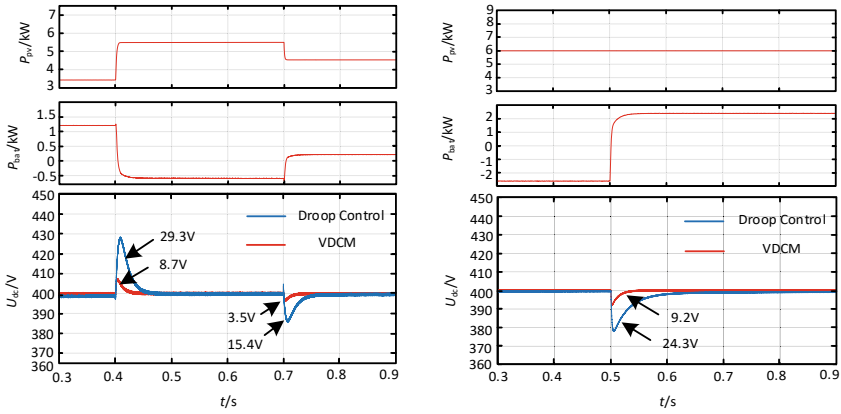
Fig. 4 Three-phase voltage fault waveform diagram

Table 2 System simulation parameters

Parameters	Numerical values
DC bus voltage U_{dc}/V	400
Battery terminal voltage U_{dc}/V	150
C_T/Φ	5.1
Armature Equivalent Resistance R_a/Ω	0.2
Damping factor D	15
Inertia coefficient out J	2

shows that the use of VDCM is effective in mitigating voltage fluctuations and that the VDCM control has a faster recovery than conventional droop control.

Simulation and Comparison Analysis of Single-phase Faults at the AC Interface. The light intensity was set to 1000 W/m^2 and the DC load interface power was kept at 5 kW. A single-phase fault at the AC interface was considered, with the resulting double-frequency component causing disturbances to the DC bus voltage. To verify the above improvements in the VSG and VDCM at the energy router interface, the AC interface a-phase voltage was set to plunge to 20% at 0.6 s. As can be seen in Fig. 6, when a voltage fault occurs at the grid-side interface, it causes the power output of the energy storage system to have a double-frequency disturbance, but the overall fluctuation has little impact on the system due to the VSG

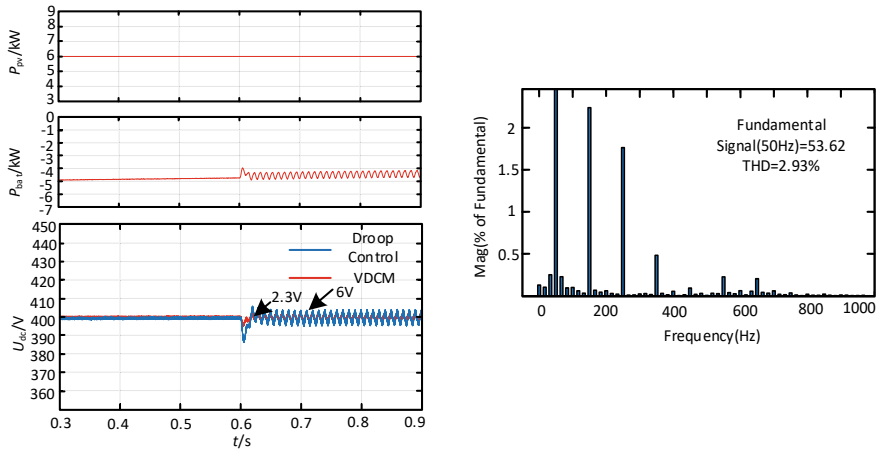


(a) Photovoltaic output sudden change (b) DC load sudden change

Fig. 5 Contrast waveform graph

control improvements. Compared to droop control, VSG and VDCM provide better suppression of voltage fluctuations.

The simulation verification analysis shows that the proposed energy router voltage regulation control can operate correctly in a multi-port system. A combined simulation of PV sudden change, load sudden change and access to a diesel generator in emergency mode and a single phase fault on the network side is set up and the conventional droop control and VDCM control are compared. The traditional droop control has a larger fluctuation range and the overshoot is much higher than the



(a) Comparison waveform of single-phase faults

(b) The input current THD

Fig. 6 AC interface

VDCM control, so the VDCM control is more suitable for the energy storage interface. Make the energy storage interface add a certain inertia link and damping factor to make the system DC bus voltage operation more smooth and stable.

5 Conclusion

In this paper, an energy router voltage stability control method for common DC bus is presented. Firstly, by introducing the output external characteristics of a conventional generator into the interface control link of the energy router, the energy router system adds a certain inertia and damping factor, which can effectively reduce bus voltage fluctuations compared to conventional droop control, and make the DC bus voltage more stable when the voltage changes caused by power delivery between internal interfaces smoother and more stable. An improved VSG for grid faults is then investigated to enable the energy router to provide some support in the event of a voltage drop, providing a guarantee for the safe operation of the power system. Finally, an experimental model is built through a simulation platform, and the feasibility and effectiveness of this voltage stability control algorithm is verified through experiments.

Acknowledgements This research is the Chongqing Education Science and Technology Research Project (KJZD-K201901102).

References

1. Chi J (2020) World energy revolution and enlightenment to China Land and. *Resour Inf* 01:25–30 (in Chinese)
2. Bhattacharya S, Ramachandran T, Somani A, Hammerstrom DJ (2022) Impacts of energy flexibility in transactive energy systems with large-scale renewable generation. *IEEE Trans Ind Electron* 10:14870–14879
3. Ai X, Rong J, Lü Z (2019) Research on a new type of energy router structure and its control strategy. *Power Syst Technol* 43(4):1202–1210 (in Chinese)
4. Hussain SMS, Aftab MA, Nadeem F, Ali I, Ustun TS (2020) Optimal energy routing in microgrid with IEC 61850 based energy routers. *IEEE Trans Ind Electron* 67(6):5161–5169
5. Tu C, Xiao F, Lan Z, Guo Q, Shuai Z (2019) Analysis and control of a novel modular-based energy router for DC microgrid cluster. *IEEE J Emerg Select Topics Power Electron* 7(1):331–342 (in Chinese)
6. Jia J, Pang S, Dong R (2019) AC/DC coordinated control of energy router based on virtual synchronous generator control technology. *Mod Electr Power* 36(2):33–39 (in Chinese)
7. Bandla KC, Prasad Padhy N (2022) An improved virtual synchronous generator control for decentralized and coordinated sharing of transient response in hybrid AC-DC microgrids. In: 2022 IEEE IAS global conference on emerging technologies (GlobConET), Arad, Romania, pp 769–774
8. Zhi N, Ding K, Huang Q, Li W, Zhang H (2021) Virtual DC motor control strategy based on P-U droop characteristics. *Trans China Electrotech Soc* 36(6):1238–1248 (in Chinese)

9. Navarro-Rodríguez Á, García P, Gómez-Aleixandre C, Blanco C (2022) Cooperative primary control of a hybrid AC/DC microgrid based on AC/DC virtual generators. *IEEE Trans Energy Convers* 37(4):2837–2850
10. Gonzalez O et al (2022) Model predictive current control of six-phase induction motor drives using virtual vectors and space vector modulation. *IEEE Trans Power Electron* 37(7):7617–7628
11. Lan Z, Tu C, Jiang F (2019) Flexible interconnection strategy of DC microgrid and main power grid based on virtual motor technology. *Trans China Electrotech Soc* 34(8):1739–2174 (in Chinese)

Structural Parameters on the Performance of Magnetic Field Sensor Based on Faraday Effect



Meng Huang, Haomin Lv, Lei Zhang, and Bo Qi

Abstract The existing research direction focuses on non-metallic magnetic field sensors based on Faraday effect. The relationship between the structure and performance of such sensors is not clear. Therefore, this paper simulates the structural parameters of non-metallic magnetic field sensors based on Faraday effect. The main structures include magneto-optical crystals, polarizers and polarizers. The effects of the length of magneto-optical crystals, the initial angle between polarizers and polarizers, and the material of magneto-optical crystals on the range and sensitivity of magnetic flux leakage sensors are compared and analyzed. It is concluded that as the length of magneto-optical crystals decreases, the range increases, and the maximum range is 4 T when the initial angle between polarizers and polarizers is 45°. The range of magneto-optical crystal material TGG is 42.5% larger than that of TSAG, and the corresponding sensitivity is 60.3% smaller. In practical engineering, the selection of non-metallic magnetic field sensors with appropriate structural parameters is conducive to the use in scenarios requiring large range and high sensitivity.

Keywords Faraday effect · Magnetic field sensor performance · Structural parameters

1 Introduction

The main principle of the magnetic field sensor used in engineering is Faraday electromagnetic induction [1]. The main structure is passive detection coil, but it contains metal components. In the presence of electric field, it will bring serious insulation problems. It is easy to cause internal breakdown during built-in measurement, damage sensors and windings, and bring danger to testers. Due to the limitation of its own

M. Huang (✉) · H. Lv · L. Zhang · B. Qi
State Key Laboratory of Alternate Electrical Power System with Renewable Energy Sources,
North China Electric Power University, Beijing 102206, China
e-mail: huang_m2011@163.com

© Beijing Paiké Culture Commu. Co., Ltd. 2024
X. Dong and L. Cai (eds.), *The Proceedings of 2023 4th International Symposium on Insulation and Discharge Computation for Power Equipment (IDCOMPU2023)*, Lecture Notes in Electrical Engineering 1100, https://doi.org/10.1007/978-981-99-7393-4_39

metal materials, the measurement error will be relatively large in a complex electromagnetic environment, which cannot meet the measurement requirements. The Hall effect is widely used in magnetic field measurement. However, its probe contains metal materials, which has the same fatal disadvantage as Faraday electromagnetic induction method [2].

In engineering, magnetostrictive material is also used in combination with fiber grating for magnetic field measurement [3, 4]. The principle is that magnetostrictive material deforms in the magnetic field, causing the attached fiber grating to deform, so that the central wavelength changes, and magnetic field measurement is realized by detecting wavelength changes. Through optical fiber communication, the transmission of optical signal is not affected by strong electromagnetic interference. However, the measurement range of this principle is below 0.1 T, which cannot meet the requirements of large range in engineering [5, 6].

Therefore, the current research direction focuses on the study of magnetic field sensors based on Faraday effect [7–9]. The main structures include magneto-optical crystals, polarizers and polarizers, etc., excluding metal devices. They are not affected in complex electromagnetic environments, and can be used in the presence of strong electric fields. It will not bring serious insulation problems, and can guarantee the safety of the tester to the greatest extent, and its measurement range is larger than the magnetostrictive effect.

This paper simulates the structural parameters of non-metallic magnetic field sensors based on Faraday effect. The main structures include magneto-optical crystals, polarizers and polarizers. The influence of the results parameters such as the length of the magneto-optical crystal, the initial angle between the polarizer and the polarizer, and the magneto-optical crystal material on the performance of the magnetic flux leakage sensor such as range, resolution and sensitivity is compared and analyzed.

2 Principle of Magnetic Field Sensor Based on Faraday Effect

The principle of non-metallic magnetic field sensors is based on the Faraday effect. In 1845, Faraday first discovered the Faraday effect [10]: under the action of a magnetic field parallel to the direction of light transmission, the polarization direction rotates during the transmission of linearly polarized light in magneto-optical materials. The rotation angle is called the Faraday rotation angle. The schematic diagram is shown in Fig. 1.

The main component of the built-in magnetic field sensor based on Faraday effect is a sensing probe containing a magneto-optical crystal. When the incident linearly polarized light passes through the magneto-optical crystal in the sensing probe, the polarization plane of the linearly polarized light rotates θ , and its relationship with the leakage magnetic field is:

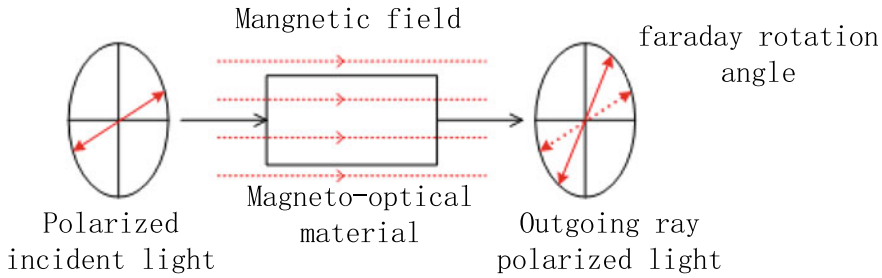


Fig. 1 Faraday effect principle diagram

$$\theta = BVL \tag{1}$$

Among them, B is the leakage flux density at the position of the magneto-optical crystal; V is the Verdet constant of magneto-optical crystal. Verdet constant is the standard to measure the Faraday effect of magneto-optical materials. In many magneto-optical materials, the Faraday effect is very weak and cannot be effectively utilized. After a lot of exploration experiments, it is found that some garnet materials have obvious Faraday effect. In addition, Verdet constant depends not only on the type of magneto-optical materials, but also on the wavelength of optical signals and the ambient temperature of magneto-optical crystals. L is the length of the optical signal transmitted in the magneto-optical crystal.

The light wave output by the light source is generally a partially polarized light composed of natural light, linearly polarized light and other light. It cannot be directly used as an incident linearly polarized light. It is necessary to pass the output light of the light source through the polarizer to produce the incident linearly polarized light that meets the requirements.

It is difficult to directly measure the polarization direction of the incident ray polarized light and the outgoing ray polarized light, which makes it difficult to directly measure the Faraday rotation angle. Therefore, a polarizer is usually set after the outgoing ray polarized light carrying the magnetic field information. The Faraday rotation angle that reflects the size of the magnetic field is transformed into the change of light intensity. By measuring the change of light intensity, the Faraday rotation angle is obtained indirectly, and then the magnetic field measurement is realized. Among them, the light intensity P of the output light after the polarizer mainly depends on the light intensity of the incident light, the angle of the polarizer and the Faraday rotation angle. Let the angle between the polarizer and the x -axis be 0° , and the angle between the analyzer and the polarizer be α , then:

$$P = \frac{1}{2}I[1 + \cos(2\theta - 2\alpha)] \tag{2}$$

where I is the light intensity before the input magneto-optical crystal after passing through the polarizer.

The frequency of alternating current is mostly 50 Hz or 60 Hz, and 50 Hz is mainly used in China. Therefore, this paper takes the magnetic field frequency of 50 Hz as an example. When α is 45° . Combining Eqs. (1) and (2), the change of probe output light intensity caused by magnetic field can be expressed as Eq. (3).

$$P = \frac{I}{2} \cdot \{1 + \sin[2VLB \cos(\omega_0 t)]\} \tag{3}$$

where t is time, ω_0 is the angular frequency of the magnetic field, and its value is 314.16 rad/s.

The second term on the right side of Eq. (3) can be simplified by using the characteristics of the first kind of Bessel function.

$$\sin(2VLB \cos \omega_0 t) = -2 \sum_{n=1}^{\infty} (-1)^n J_{2n-1}(2VLB) \cos[(2n - 1)\omega_0 t] \tag{4}$$

If the higher order term is omitted, then (3) is simplified by Bessel function and becomes

$$P = \frac{I}{2} \cdot [1 + A_3 \cos(\omega_0 t)] \tag{5}$$

It can be seen from the above derivation process that A_3 is obtained by the change of $\sin(2VLB)$ through the first Bessel function, and B can be obtained by A_3 .

The 50 Hz component of the output light intensity of the sensor is only related to the measured magnetic field. The amplitude P_0 of the 0 Hz component and the amplitude P_{50} of the 50 Hz component are obtained by fast Fourier transform of the output light intensity:

$$\begin{cases} P_0 = \frac{I}{2} \\ P_{50} = \frac{I}{2} A_3 \end{cases} \tag{6}$$

The amplitude of the two components is directly divided to obtain a value independent of the light intensity and only related to the magnetic field. The leakage magnetic field measurement results obtained by the signal cross-contrast method are as follows:

$$A_3 = \frac{P_{50}}{P_0} \tag{7}$$

In summary, the measured magnetic field can be obtained from A_3 , and the factors affecting A_3 include the angle between the polarizer and the polarizer is α , the Feld constant V of the magneto-optical crystal, and the length L of the optical signal transmitted in the magneto-optical crystal. Next, the influence of three structural factors on A_3 will be simulated and analyzed, and the influence of three structural factors on the performance of the sensor will be obtained.

3 The Influence of Three Structural Factors on Performance

3.1 Angle Between Polarizer and Polarizer A

The above selection α is equal to 45° for theoretical derivation, and now the simulation analysis proves that the magnetic field sensor range is the largest when α is equal to 45° . The simulation analysis α is equal to 30° and 45° are compared. By the control variable method, L is 8, and the magneto-optical crystal material is TSAG. The simulation results are shown in Fig. 2.

The simulation results show that the black line is A_3 . When A_3 begins to decline, it is considered to be saturated, and the magnetic field sensor reaches the upper limit of the range, because the A_3 does not meet the Bessel function expansion condition at this time. At this time, the B_m corresponding to A_3 has two values, which can not distinguish the specific magnetic field value. The red line is dA_3/dB_m , and the maximum value is the sensitivity of the magnetic field sensor.

From the simulation results, it can be concluded that when α is equal to 45° , as shown in the black line on of Fig. 2a, the range of the magnetic field sensor is greater than 2000 mT, and it has not yet reached saturation at 2000 mT, up to 4000 mT. When α is equal to 30° , as shown in the black line of Fig. 2b, the maximum range of the magnetic field sensor reaches saturation at 1000 mT, which can not meet the measurement requirements of large range in engineering. Therefore, when analyzing the influence of other structural parameters on the performance of the sensor, the angle between the polarizer and the polarizer is 45° .

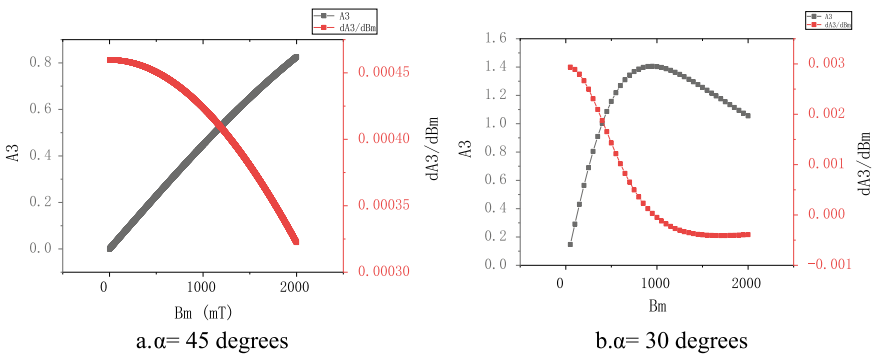


Fig. 2 Performance comparison of different α

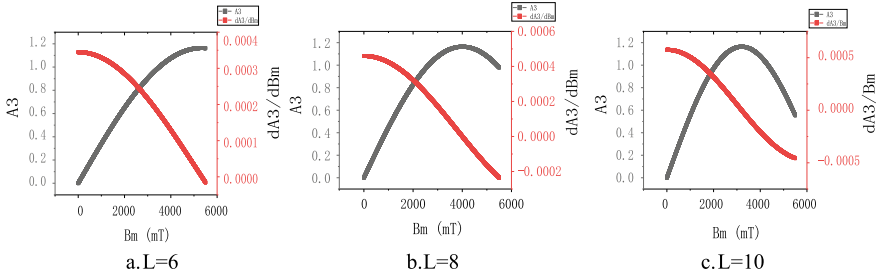


Fig. 3 Performance comparison of different L

3.2 Magneto-optical Crystal Length L

In this paper, the performance changes of magnetic field sensors with three lengths of 6, 8 and 10 mm are simulated and analyzed. By the control variable method, the α is 45° , and the magneto-optical crystal material is TSAG. The simulation results are as shown in Fig. 3.

From the simulation results, it can be concluded that when the maximum L is 10, the range is the smallest and reaches saturation near 3300 mT. When the minimum L is 6, the range is the largest and is close to saturation at 5000 mT. In terms of sensitivity, from the maximum value of the red line dA_3/dBm , it can be seen that the sensitivity is 0.00037 when the minimum L is 6, and the sensitivity is 0.0006 when the maximum L is 10. Therefore, in practical engineering, it is necessary to consider both the range and sensitivity requirements, and consider the appropriate magneto-optical crystal length L by combining the two.

3.3 The Feld Constant V of Magneto-optical Crystal Material

In this paper, the influence of two kinds of magneto-optical crystal materials, TSAG crystal and TGG crystal, on the performance of the sensor is simulated and analyzed. By the control variable method, L is 8 and α is 45° . The simulation results are as shown in Fig. 4.

The analysis results show that the TSAG crystal is close to saturation at 4000 mT, and the TGG crystal is close to saturation at 5500 mT. In terms of sensitivity, the maximum value of TSAG crystal is 0.0004, which is greater than the sensitivity of TGG crystal. In practical engineering, it is necessary to consider the range and sensitivity of the sensor to flexibly select the magneto-optical crystal material.

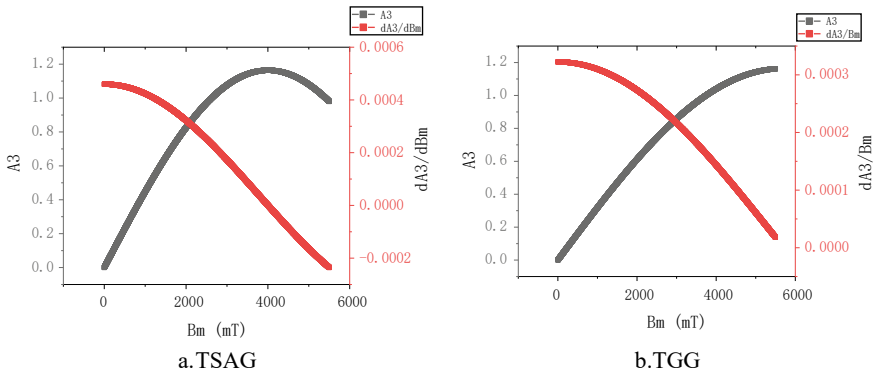


Fig. 4 Performance comparison of different V

4 Conclusion

1. In this paper, the minimum L is 6 mm, for example, it is close to saturation at 5000 mT, the range is the smallest when the maximum L is 10, and it reaches saturation near 3300 mT. When the initial angle between the polarizer and the polarizer is 45°, the maximum range is 4000 mT, which is much larger than the range when the initial angle is 30°.
2. With the decrease of the length of the magneto-optical crystal, the sensitivity decreases. In this paper, the minimum L is 6, for example, when the sensitivity is 0.00037 and the maximum L is 10 mm, the sensitivity is 0.0006.
3. This paper provides the relationship between the structural parameters and the performance of the magnetic field sensor based on Faraday effect, which can be used in practical engineering to select the appropriate structural parameters through the range and sensitivity requirements.

Acknowledgements This research was funded by the Science and Technology Project of SGCC (No. 5206002000D6, Research on key technologies of leakage magnetic field and stress field sensing for power transformer transparency).

References

1. Jiang Z, Zhao W, Qu K (2008) Development and application of magnetic field measurement technology. *Electr Meas Instrum* 04:1–5 (in Chinese)
2. Chen Y, Feng M, Meng Q et al (2013) Detection and analysis of magnetic field distribution in transformers. *Transformers* 50(03):49–55 (in Chinese)
3. Schukar V, Koppe E, Hofmann D et al (2016) Magnetic field detection with an advanced FBG-based sensor device. *Procedia Eng* 168:1270–1274

4. Dai Y, Yang M, Xu G et al (2013) Magnetic field sensor based on fiber Bragg grating with a spiral microgroove ablated by femtosecond laser. *Opt Express* 21(14):17386–17391
5. Ribeiro ABL, Frazão O, Jorge PAS (2012) Magnetic field sensor with Terfenol-D thin-film coated FBG. *International Society for Optics and photonics*, pp 1–34
6. Kersey AD, Marrone MJ (1991) Polarisation-insensitive fibre optic Michelson interferometer. *Electron Lett* 27(6):518–520
7. Li J et al (2021) An optical fiber magnetic field sensor based on Faraday effect for transformer leakage magnetic field measurement. In: 2021 IEEE electrical insulation conference (EIC), Denver, CO, USA, pp 137–140. <https://doi.org/10.1109/EIC49891.2021.9612256>
8. Jiang J et al (2021) A new approach to measure magnetic field of high-temperature superconducting coil based on magneto-optical Faraday effect. *IEEE Trans Appl Supercond* 31(1):1–5, Art no. 9000105. <https://doi.org/10.1109/TASC.2020.3032134>
9. Dias da Silva AA, Alves HP, Marcolino FC, do Nascimento JC, Martins-Filho JF (2020) Computational modeling of optical fiber-based magnetic field sensors using the Faraday and Kerr magneto-optic effects. *IEEE Trans Magn* 56(9):1–9, Art no. 4001109. <https://doi.org/10.1109/TMAG.2020.3010108>
10. Lin S (2010) Study on the characteristics of optical current sensor based on Faraday magneto-optical effect. Chongqing University (in Chinese)

Study on the Effect of O₂ Content on the Decomposition Characteristics of C₅F₁₀O Under Different Buffer Gases



Long Li, Liangjun Dai, Baojia Deng, Qiang Yao, Ying Zhang, Huaxia Yang, Yifan Wang, and Yi Li

Abstract In recent years, C₅F₁₀O has aroused a lot of notice as a potential SF₆ alternative gas. As a new kind of environmentally friendly insulated gas, the research on the effect of O₂ content on the decomposition characteristics of C₅F₁₀O mixed insulating gas is still insufficient. In this paper, partial discharge tests of C₅F₁₀O/N₂/O₂ mixed gas and C₅F₁₀O/CO₂/O₂ mixed gas are carried out to imitate the work condition of gas insulation equipment under the severe non-homogeneous field. The impact of O₂ content in the mixed gas on its decomposition characteristics is analyzed, and the difference of decomposition characteristics under two buffer gases is compared. We found that under the condition that N₂ is the background gas, when the oxygen ratio is around 4%, the overall concentration of decomposition by-products generated by mixed gas partial discharge is the lowest. In addition, the influence of two background gases on the partial discharge decomposition of C₅F₁₀O are totally different. When N₂ is the background gas, there exists an obviously trend to reduce the decomposition. But when CO₂ is the background gas, it even exacerbates the decomposition to a certain extent.

Keywords C₅F₁₀O gas mixture · O₂ · Partial discharge · Decomposition characteristic

1 Introduction

Sulfur hexafluoride (SF₆) is a colourless, odorless and non-toxic gas. As a prominent insulation medium, it is usually applied in gas insulated equipment (GIE). However, the greenhouse effect of SF₆ is high, and its GWP value is about 25,200 times that

L. Li · L. Dai · B. Deng · Q. Yao · Y. Zhang · H. Yang
State Grid Chongqing Electric Power Research Institute, Chongqing, China
e-mail: Yaoqiang212@aliyun.com

Y. Wang (✉) · Y. Li
School of Electrical Engineering and Automation, Wuhan University, Wuhan 430072, China
e-mail: 903067746@qq.com

© Beijing Paiké Culture Commu. Co., Ltd. 2024
X. Dong and L. Cai (eds.), *The Proceedings of 2023 4th International Symposium on Insulation and Discharge Computation for Power Equipment (IDCOMPU2023)*, Lecture Notes in Electrical Engineering 1100, https://doi.org/10.1007/978-981-99-7393-4_40

of CO_2 , which is one of the six prohibited greenhouse gases listed in the ‘Kyoto Protocol’ [1]. At present, SF_6 emissions from the power industry account for a very high proportion of total SF_6 emissions [2]. Therefore, it is necessary to find a gas with good environmental protection characteristics and physical and chemical properties as an insulating medium to replace SF_6 , that is, to develop SF_6 alternative technology, which can fundamentally reduce the use of SF_6 [3].

At present, the perfluoroketone insulating gas proposed by ABB Company has great application potential in electrical equipment. The insulating medium $\text{C}_5\text{F}_{10}\text{O}$ is stable, and its GWP value is close to 1, and the insulation strength is about 2 times that of SF_6 gas [4]. It is suitable for medium voltage gas insulated metal-enclosed switchgear and control equipment [5]. For the insulation and discharge decomposition performance of $\text{C}_5\text{F}_{10}\text{O}$, domestic and foreign researchers have also made some progress [6–8]. The liquefaction temperature of $\text{C}_5\text{F}_{10}\text{O}$ is high, which is 26.9°C . Therefore, it needs to be mixed with commonly used buffer gases (N_2 , CO_2) to satisfy the minimum temperature of operating [9]. In addition, Wei et al. found that the breakdown voltage of $\text{C}_5\text{F}_{10}\text{O}/\text{N}_2$ mixed gas boosts with the enhancing of oxygen concentration [10]. Therefore, we use the needle-plate electrode to imitate the work condition of GIE under the severe non-homogeneous field and carried out partial discharge tests of $\text{C}_5\text{F}_{10}\text{O}/\text{N}_2/\text{O}_2$ mixed gas and $\text{C}_5\text{F}_{10}\text{O}/\text{CO}_2/\text{O}_2$ mixed gas. After partial discharge tests, we measured the gas decomposition components. The influence of O_2 content in the mixed gas on its decomposition characteristics is analyzed, and the difference of decomposition characteristics under two buffer gases is compared. It provides a reference for the selection of O_2 concentration and buffer gas in low and medium voltage GIE based on $\text{C}_5\text{F}_{10}\text{O}$.

2 Platform and Method

2.1 Test Platform

Figure 1 shows the illustrative diagram of the test platform. The main equipment includes an induction voltage regulator (providing an AC voltage of 0–380 V for the test transformer), a protection resistor ($10\text{ k}\Omega$) to limit the short-circuit current when the breaks down occurs and prevent test transformer from over-loading. The voltage divider capacitor (1/1000) and the non-inductive detection impedance ($50\ \Omega$) transfer the PD current signal to a voltage signal. The PD signals are stored in a digital oscilloscope (Tektronix MDO3054, maximum sampling rate is 10 GS/s). In our tests, the discharge decomposition components of $\text{C}_5\text{F}_{10}\text{O}$ mixed gas were detected by Shimadzu QP 2010 Ultra gas chromatography-mass spectrometry (GC–MS).

In order to imitate the severe non-homogeneous field inside GIE, the needle-plate electrode is selected for the experiment. The structural parameters are shown in Fig. 2. The needle is tungsten copper needle. Because tungsten has the characteristics of good thermal and electrical conductivity, it is not easy to be ablated under partial

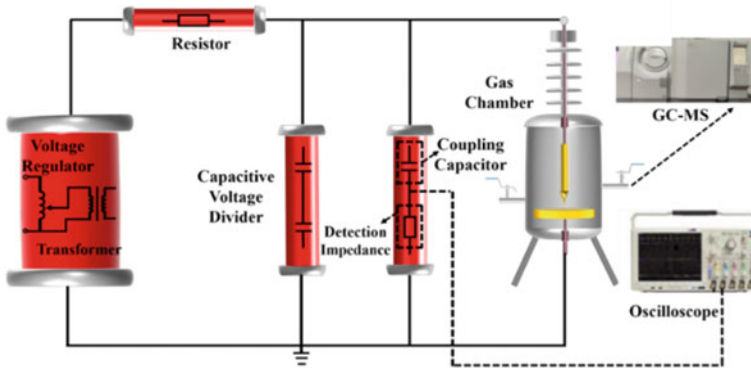
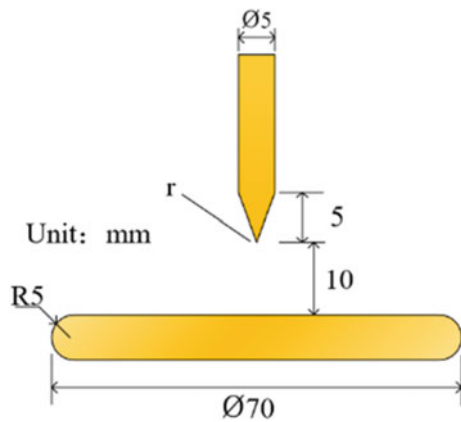


Fig. 1 Schematic diagram of test platform

discharge for a long time, resulting in the needle tip becoming bald, which affects the measurement of partial discharge charge and partial discharge. The total length of the needle is 17 mm, the bottom diameter is 5 mm, and the length of the needle tip is 5 mm. The sharper the tip, the more prone to partial discharge. In order to avoid the error of the test results of different needle electrodes, the curvature radius of the needle electrode tip is set to 0.3 mm. The plate electrode material is brass, 8 mm thick and 70 mm in diameter. In the experiment, the needle tip was set to 10 mm from the center of the plate electrode.

Fig. 2 Structure parameter diagram of needle-plate electrode



2.2 Test Method

Before each test, the gas chamber and the electrode were wiped roundly to avoid the influence of impurities and dust in the air chamber or the possible residual solid decomposition products in the previous experiment on the experimental results. After drying with anhydrous ethanol, the electrode model is installed on the conductive rod, the electrode spacing is adjusted, and the powder-free rubber gloves are worn for overall operation. Then we washed the gas chamber with buffer gas. After washing the gas three times and vacuuming the gas chamber, the gas is filled with the vacuum chamber in the proportion required for our test and then the subsequent tests can be started.

3 Result and Discussion

3.1 Influence of O_2 Content on the Decomposition Characteristics of $C_5F_{10}O/N_2/O_2$ Mixed Gas

Figure 3 shows the concentrations of gaseous by-products under the pressure of 0.3 MPa and the $C_5F_{10}O$ partial pressure is 10.5 kPa, and the $C_5F_{10}O/N_2/O_2$ mixed gas is with 0, 4% and 8% oxygen respectively. We found that with the addition of oxygen, the kind of gaseous PD decomposition by-products were not changed, but the formation characteristics of products was influenced. The addition of oxygen may lead to changes in the decomposition characteristics of the mixed gas. In order to maintain the insulation reliability of the $C_5F_{10}O$ mixed gas, we researched the relationship between the main products concentration and the oxygen content, which provided a reference for selecting the oxygen ratio in practical applications.

It can be seen from the above figure that with the enhancement of oxygen content, the concentration of CF_4 , C_2F_6 , C_3F_8 and C_3F_6 decomposition products is greatly reduced due to the addition of oxygen, except that C_2F_4 is not produced by decomposition. CHF_3 decreases slightly after the addition of oxygen, while the characteristic curve of C_3HF_7 shows a “V” shape. It decreases greatly first when the oxygen concentration is less, and then enhances slightly with the multiplication of oxygen. Different from other products, the content of CO increases significantly with the enhancing of oxygen content. At the same partial discharge time when the oxygen concentration is 8%, the concentration at the peak is 9 times and 7.5 times higher than that when the oxygen concentration is no oxygen and 4% oxygen respectively. The peak area diagram of COF_2 shows another different characteristic, which is most obvious at 4% oxygen, while the concentration at 8% oxygen is basically the same as that without oxygen. In comprehensive consideration, when the oxygen ratio is around 4%, the overall concentration of decomposition by-products generated by PD decomposition of $C_5F_{10}O$ mixed gas is the lowest.

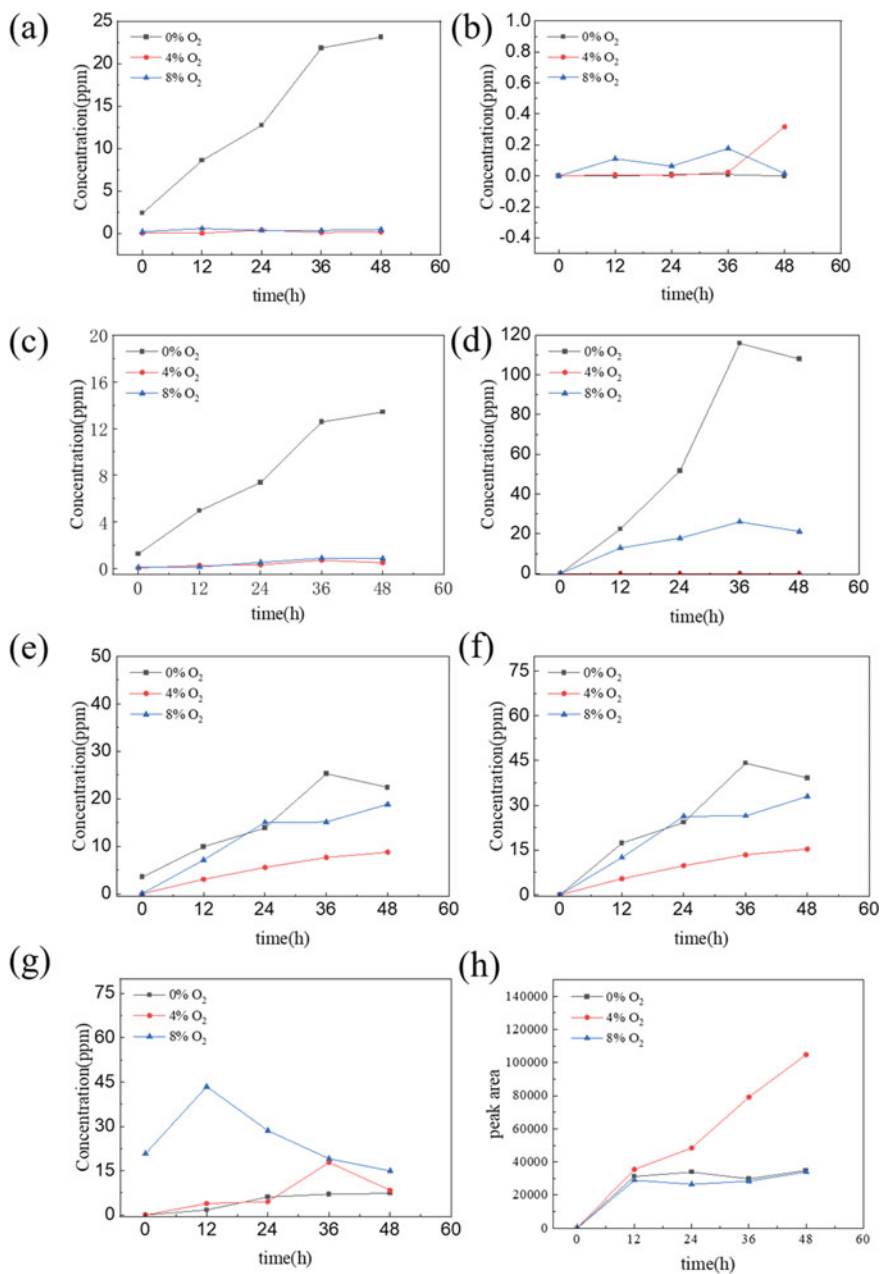


Fig. 3 Decomposition characteristics of C₅F₁₀O/N₂/O₂ mixed gas. **a** CF₄, **b** C₂F₄, **c** C₂F₆, **d** C₃F₆, **e** C₃F₈, **f** CHF₃, **g** CO, **h** COF₂

3.2 Effect of O₂ Content on the Decomposition Characteristics of C₅F₁₀O/CO₂/O₂ Mixed Gas

Figure 4 shows the concentrations of gaseous by-products under the pressure of 0.3 MPa and the C₅F₁₀O partial pressure is 10.5 kPa, and the C₅F₁₀O/CO₂/O₂ mixed gas is with 0, 4% and 8% oxygen respectively.

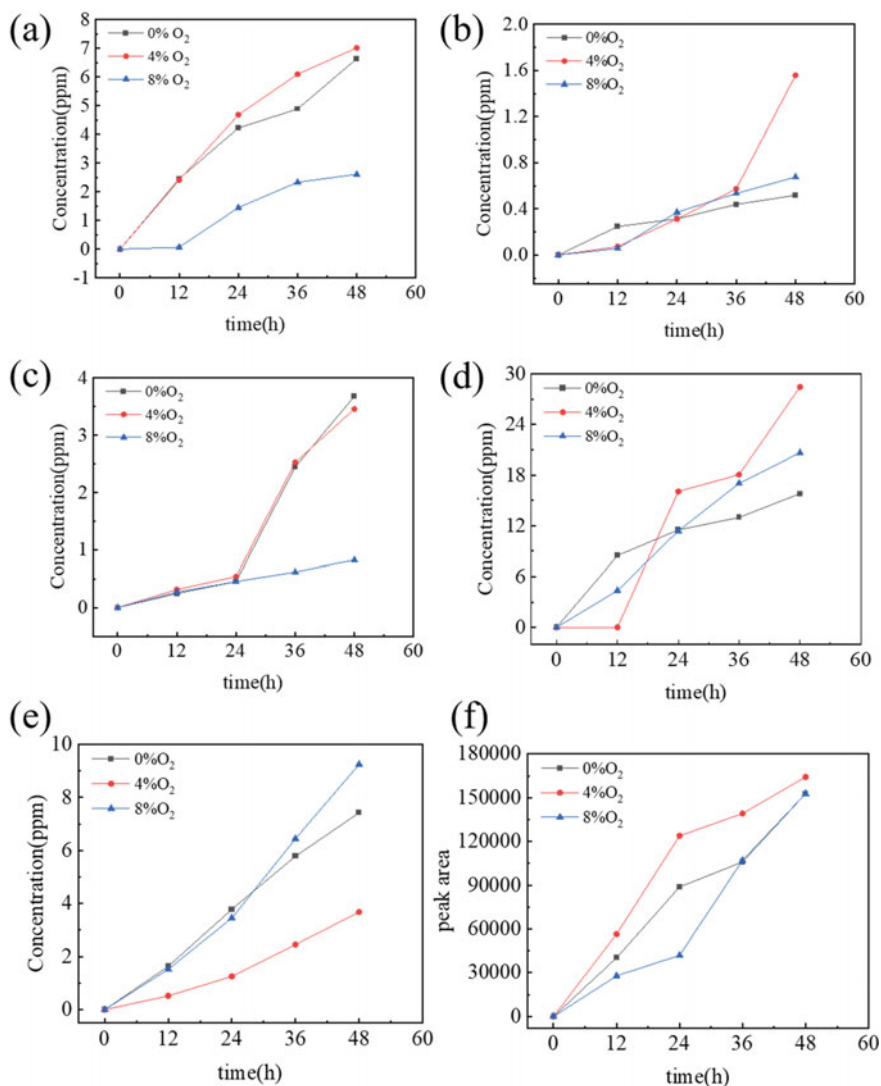


Fig. 4 Decomposition characteristics of C₅F₁₀O/CO₂/O₂ mixed gas. **a** CF₄, **b** C₂F₆, **c** C₃F₈, **d** C₃F₆, **e** CO, **f** COF₂

Different from that when the background gas is N₂, when the background gas is CO₂, after adding oxygen, the concentration of CF₄, C₂F₆, C₃F₈, C₂F₄, C₃F₆ and other gaseous by-products is basically unchanged or slightly increased compared with that when there is no oxygen, in which the concentration of CF₄, COF₂, C₃F₆, C₂F₆, C₃F₈ changes most obviously. To sum up, under the same test conditions, the influence of two background gases on the PD decomposition characteristics of C₅F₁₀O mixed gas are different. When N₂ is used as the background gas, there exists a clear tendency to reduce the decomposition. While when CO₂ is used as the background gas, the decomposition of mixed gas is promoted.

4 Conclusion

Under the buffer gas of N₂, with the enhancing of oxygen content, the concentration of CF₄, C₂F₆, C₃F₈ and C₃F₆ in the decomposition products is greatly reduced due to the addition of oxygen. The concentration of CHF₃ decreases slightly after the addition of oxygen, while the content of CO increases significantly with the gain of oxygen. The peak area of COF₂ increases most obviously at 4% oxygen, while the concentration at 8% oxygen is basically the same as that without oxygen. Considering comprehensively, when the oxygen ratio is near 4%, the overall concentration of PD induced decomposition by-products generated by C₅F₁₀O mixed gas is the lowest.

When the buffer gas is CO₂, after adding oxygen, the concentration of gaseous products such as CF₄, C₂F₄, C₂F₆, C₃F₈ and C₃F₆ is basically unchanged or slightly increased compared with that without oxygen, among which the concentration of COF₂, CF₄, C₂F₆, C₃F₈ and C₃F₆ changes most obviously. Based on the above, the impact of two background gases on the PD decomposition characteristics of C₅F₁₀O mixed gas are different under the same conditions. When N₂ is the background gas, there is a clear trend to reduce the decomposition. While when CO₂ is the background gas, the decomposition of mixed gas multiplies.

References

1. Zhou Z, Han D, Zhao M, Zhang G (2020) Review on decomposition Characteristics of SF₆ alternative gases. *Trans China Electrotech Soc* 35(23):4998–5014
2. Zhang B, Chen L, Li X et al (2020) Evaluating the dielectric strength of promising SF₆ alternatives by DFT calculations and DC breakdown tests. *IEEE Trans Dielectr Electr Insul* 27(4):1187–1194
3. Yan X, Gao K, Zheng Y et al (2018) Research progress of SF₆ mixed gas and substitute gas. *Grid Technol* 42(06):1837–1844
4. Li X, Zhao H, Murphy AB (2018) SF₆-alternative gases for application in gas-insulated switchgear. *J Phys D-Appl Phys* 51(15):19
5. Hyrenbach M, Hintzen T, Müller P et al (2015) Alternative gas insulation in medium-voltage switchgear. In: *Proceedings of the 23rd international conference on electricity distribution, Lyon, CIRED*

6. Su D, Zeng F, Chen X et al (2023) Experimental research on V-t characteristics of $C_5F_{10}O/CO_2$ gas mixture under lightning impulse voltage. *IEEE Trans Dielectr Electr Insul* (Early Access). <https://doi.org/10.1109/TDEI.2023.3276336>
7. She C, Zeng F, Dai L et al (2022) Theoretical analysis on the self-recovery ability of $C_5F_{10}O$: An environmental-friendly substitute for SF_6 . *IEEE Trans Plasma Sci* 50(11):4620–4627
8. Wang X, Yuan H, Yang A et al (2022) Decomposition products and mechanism of $C_5F_{10}O/N_2$ gas mixture by electron attachment mass spectrometry. *IEEE Trans Dielectr Electr Insul* 29(3):1127–1134
9. Li Y, Zhang X, Xiao S et al (2018) Study on the discharge decomposition characteristics of an environmental-friendly insulating medium $C_5F_{10}O$. *Proc CSEE* 38(14):4298–4306
10. Wei Z, Study on the influence of O_2 on the discharge and decomposition characteristics of $C_5F_{10}O/CO_2$. Wuhan University, Wuhan, TM21310486

Investigation of Gas Adsorption Properties Between CrB and SF₆ Decompositions: A Theoretical Study



Xiangyu Tan, Fangrong Zhou, Zhimin Na, Dibo Wang, Ran Zhuo, Peng Wu, and Yi Li

Abstract CrB, as a new type of two-dimensional material, possesses both high conductivity, large specific surface area, and high activity similar to MXenes, as well as good antioxidant properties, showing potential as a gas sensing material. In this paper, the performance of CrB as a gas sensing material for SF₆ decomposition components (H₂S, SO₂, SOF₂, and SO₂F₂) was explored by applying first-principles calculations. The results show that the adsorption of the four gases is all attributed to strong chemical adsorption, and significant structural changes occur in H₂S, SOF₂, and SO₂F₂ during the interaction. Through the analysis of the differential charge density map and the density of states map, it is found that, except for the SO₂ molecule, both the H-S and S-F bonds in the other gas molecules are broken and new chemical bonds are formed with the Cr atoms on the substrate surface. This work reveals the relevant mechanism of interaction between CrB and SF₆ decomposition components, indicating that the material has high sensitivity to H₂S, SO₂, SOF₂, and SO₂F₂ and has potential for application as a sensing material.

Keywords CrB · Gas sensing · SF₆ decomposition

X. Tan · F. Zhou

Power Science Research Institute of Yunnan Power Grid Co., Ltd., Kunming 650214, China

Z. Na

Qujing Power Supply Bureau of Yunnan Power Grid Co., Ltd., Qujing 655099, China

D. Wang · R. Zhuo

Electric Power Research Institute, China Southern Power Grid, Guangzhou 510623, China

P. Wu · Y. Li (✉)

School of Electrical Engineering and Automation, Wuhan University, Wuhan 430072, China

e-mail: li_yi@whu.edu.cn

© Beijing Paiké Culture Commu. Co., Ltd. 2024

X. Dong and L. Cai (eds.), *The Proceedings of 2023 4th International Symposium on Insulation and Discharge Computation for Power Equipment (IDCOMPU2023)*, Lecture Notes in Electrical Engineering 1100, https://doi.org/10.1007/978-981-99-7393-4_41

435

1 Introduction

SF₆ gas has been widely used in gas insulated equipment due to its excellent insulation performance and arc-extinguishing ability [1, 2]. However, during long-term operation, local discharge or local overheating faults caused by insulation defects inevitably occur inside the equipment. Under the continuous action of these faults, the insulation state inside the equipment will continue to deteriorate and ultimately lead to more serious consequences [3]. During the occurrence of local discharge, SF₆ will undergo a certain degree of decomposition and generate stable decomposition products such as H₂S, SO₂, SOF₂, and SO₂F₂ under the action of trace water and oxygen [4]. By detecting the concentration and type of these gas products, on-site operators can take timely measures to prevent the further development of faults and reduce the losses and negative impacts of insulation accidents.

Currently used gas detection methods include gas chromatography-mass spectrometry (GC-MS), spectroscopy, electrochemistry, and resistance-based sensors based on nanomaterials. Among them, resistance-based sensors have received widespread attention in the field of SF₆ decomposition component detection due to their low cost, simple structure, low energy consumption, small size, and high integrability [5]. It has been reported that materials such as graphene, metal oxides, transition metal disulfides, graphene, and MXenes can all respond to SF₆ decomposition components. However, sensors based on these materials have problems such as high operating temperatures or poor stability. MBenes, (obtained by etching MAB, composed of an early transition metal (M), metals from groups 13 and 14 of the periodic table (A), and boron (B)), as a new type of two-dimensional material, has large specific surface area, high conductivity, rich surface functional groups, and good stability, making it suitable for sensing and has high application potential. So far, there have been few studies on the interaction between MBenes and gases. Chen et al. explored the adsorption effect of MoB on CO, NO, SO, and SO₂. The results revealed that MoB had strong interaction with NO, SO, and SO₂, and the interaction energy reached above -2 eV and could not be desorbed at room temperature, showing potential as an irreversible high-sensitivity sensor [6]. Shukla et al. explored the performance of Mo₂BX₂ (X = H, OH, O) as adsorbents for capturing and storing NO₂, SO₂, CO₂, and NH₃, and found that MBenes were appropriate for CO₂ capture and selective removal of NO₂ and SO₂ gases. The moderate adsorption energy for NH₃ reveals that MBenes and their functionalized derivatives are promising sensing/capturer materials for NH₃ detection [7]. Mir et al. studied the adsorption of CO₂ on various MBenes and obtained the adsorption strength ranking of the studied MBenes based on adsorption energy as Sc₂B₂ > Ti₂B₂ > V₂B₂ > Cr₂B₂ > Mn₂B₂ > Fe₂B₂ [8]. Considering the potential application of MBenes in the sensing field, it is necessary to conduct related theoretical calculations to explore the application possibilities of these materials in relevant industries, providing a reference for the application of this material while serving modern production.

In this paper, first-principles calculations were used to analyze the sensing and capturing effect of CrB on SF₆ decomposition components. By analyzing the adsorption energy, charge transfer, density of states, and other parameters of the adsorption system after structure optimization, it was found that CrB can strongly adsorb the four SF₆ decomposition components, and the adsorption strength order is SOF₂ > SO₂F₂ > H₂S > SO₂. During the interaction process, the structures of H₂S, SOF₂, and SO₂F₂ underwent significant changes. The analysis of the differential charge density map and the energy density of states map suggest that bonding and breaking behaviors occur during the adsorption process. The structure of SO₂ did not change significantly, so the corresponding system had the lowest adsorption energy among the four systems. These results indicate that CrB has high sensitivity to the four SF₆ decomposition components and has the potential to be used as a gas-sensitive material for SF₆ decomposition component detection.

2 Method

Calculations of multiple properties of CrB, including geometric optimization, band structure, and density of states, were carried out using the VASP software based on the plane wave pseudopotential method. The exchange–correlation functional approximation method used the Perdew–Burke–Ernzerhof (PBE) function, which is based on the generalized gradient approximation (GGA) in density functional theory. Although this method has lower accuracy than hybrid functionals, its efficiency is nearly 1000 times higher, making it the most widely used exchange–correlation functional approximation method. The outer and inner electrons were treated using the projected augmented wave (PAW) method, and the plane wave cutoff energy (E_{cut}) was set to 520 eV. The convergence criterion for the system energy calculation was set to a difference of less than 1×10^{-5} eV between two consecutive calculations. The block Davidson iteration method was used for geometric structure optimization, and the convergence criterion was defined as the maximum force on each atom not exceeding 0.02 eV/Å. To consider weak van der Waals forces, the DFT-D3 dispersion correction program developed by Grimme was introduced. The initial structure was set as a $4 \times 4 \times 1$ supercell composed of the minimum unit cell, and the k-point mesh for geometric optimization and electronic structure calculation was set to $4 \times 4 \times 1$ in the Monkhorst–Park grid. The atomic charge calculation results in the system were processed using Bader charge analysis, and all calculations did not include spin polarization.

For the optimized system structure, the adsorption energy (E_{ads}) was used to describe the strength of the interaction between gas molecules and CrB, which was defined as follows:

$$E_{\text{ads}} = E_{\text{gas/CrB}} - E_{\text{gas}} - E_{\text{CrB}} \quad (1)$$

3 Results and Discussion

3.1 Geometrical Structures

From Fig. 1a, it can be seen that the structure of the single-layer CrB appears as a cross-distribution of B atomic chains and Cr atomic chains when viewed from the top, while the arrangement of four layers of Cr-B-B-Cr from top to bottom is close to a sandwich structure. The optimized lattice constants of the crystal cell are $a = b = 2.913 \text{ \AA}$, and the bond length between B atoms is 1.800 \AA , while the distance between adjacent layers of B atoms and Cr atoms is 2.126 \AA , which is attributed to the large atomic diameter of Cr. The band structure of CrB is shown in Fig. 1b, where the calculated results show that the conduction band minimum (CBM) and valence band maximum (VBM) are located at -1.784 eV and -1.930 eV , respectively, indicating that the structure has no band gap and has good metallic conductivity. The structures of the four SF₆ decomposition components are shown in Fig. 1c–f, respectively. Considering the symmetry of the CrB surface, all gas molecules are placed at the highlighted positions in Fig. 1a with different initial molecular orientations for adsorption calculations. For the SO₂ and H₂S gas molecules, they are arranged parallel and perpendicular to the CrB plane, respectively, while SOF₂ and SO₂F₂ are placed in the corresponding initial positions considering the molecular symmetry. The optimal adsorption results of the four gas molecules on the single-layer CrB surface are shown in Fig. 2.

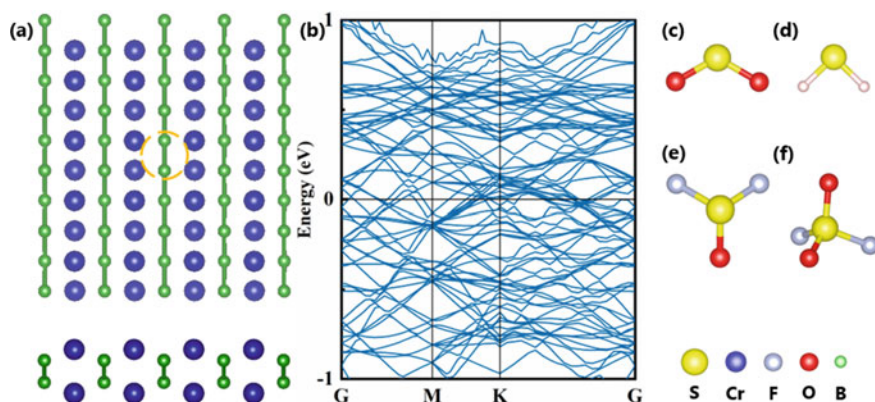


Fig. 1 Geometrical and electronic structures of **a** and **b** CrB **b** SO₂ **c** H₂S **d** SOF₂ **e** SO₂F₂

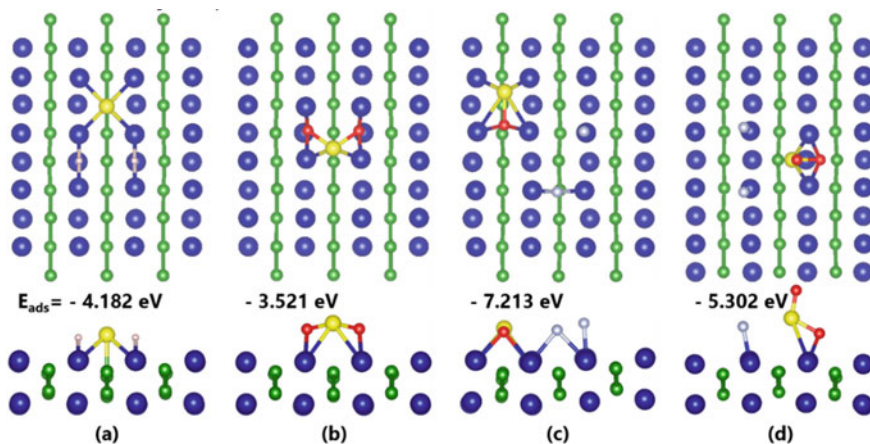


Fig. 2 Optimized structures of **a** H₂S adsorption system, **b** SO₂ adsorption system, **c** SOF₂ adsorption system, **d** SO₂F₂ adsorption system

3.2 Optimized Adsorption Structures

In the adsorption systems of H₂S, SOF₂ and SO₂F₂ in Fig. 2a, the gas molecules underwent significant twisting and deformation under the influence of interaction forces. For H₂S, the distance between the two H atoms and the S atom increased from the original 1.348 Å to 3.136 Å and 3.139 Å, respectively, which is much larger than the range of the hybridization of S and H atomic orbitals, indicating complete decomposition of the H₂S molecule. In addition, the minimum distances between the S or H atoms and the Cr atoms on the CrB surface decreased from 3.800 Å and 2.713 Å to 2.386 Å and 1.783 Å, respectively, revealing strong binding of the gas molecule to the substrate surface. In the SOF₂-CrB and SO₂F₂-CrB adsorption systems, the strong binding force of the substrate surface on the gas molecules weakened the chemical bond between the S and F atoms, and increased the distance between them, and they were respectively attracted and captured by different Cr atoms. However, the O atoms, which remain close to the S atom in the two optimized structures, indicate that the strength of the S–O bond is significantly stronger than that of the S–F bond, with the S–O bond lengths in the SO₂F₂ and SOF₂ systems being 1.470 Å, 1.654 Å, and 1.708 Å, respectively. Due to the structural changes during the adsorption process, all three systems experienced drastic energy changes. According to Eq. (1), the adsorption energies of H₂S, SOF₂, and SO₂F₂ on the CrB surface were -4.182 eV, -7.213 eV, and -5.302 eV, respectively, which belong to strong chemical adsorption. In the optimized SO₂-CrB adsorption system, the distance between the O atom and the closest Cr atom on the substrate surface decreased from 2.600 Å to 2.061 Å, while the distance between the S atom and the closest Cr atom decreased from 3.217 Å to 2.419 Å. During the adsorption process, compared with the gas molecules in other adsorption systems, the SO₂ molecule did not undergo significant structural changes.

The S–O bond was slightly elongated (from 1.448 Å to 1.619 Å) under the influence of CrB, and it had the smallest adsorption energy (−3.521 eV) among the four systems. In addition to the changes in the gas molecules, the CrB substrate in the vicinity of the gas molecules was also subjected to some traction, resulting in upward protrusion of some local Cr atoms. Based on the structural optimization analysis, it can be inferred that the four SF₆ gas molecules underwent drastic structural deformation and accompanied by significant adsorption energies during the interaction with CrB. Therefore, it is speculated that the formation and breaking of chemical bonds occurred during the adsorption process, which will be verified by the analysis of the density of states and the differential charge density in the following analysis.

3.3 Electronic Structure Analysis

In order to further investigate the interaction between gas molecules and single-layer CrB substrate, Bader charge analysis was used to calculate the charge transfer behavior during the adsorption process, as shown in Fig. 3, where the direction of the arrow indicates the direction of electron transfer from the CrB substrate to the gas molecule, with Q_t being positive if the gas molecule gains electrons, and negative otherwise. In addition, the differential charge density maps obtained after the four SF₆ decomposition components were adsorbed on the CrB surface are also shown in Fig. 3, where the yellow regions indicate an increase in charge density and the blue regions indicate a decrease. The results show that all gas molecules act as electron acceptors, with the number of electrons acquired in order of magnitude corresponding to the order of adsorption energy, namely SOF₂ (2.181 e) > SO₂F₂ (1.862 e) > H₂S (1.595 e) > SO₂ (1.058 e). Furthermore, the results from the differential charge density maps show that the electrons gained by the gas molecules mainly come from the Cr atoms with a significant decrease in charge density on the surface, indicating that Cr atoms play a major role in the adsorption of the decomposition components.

In order to analyze the bonding situation and changes in conductivity of the SF₆ decomposition components after adsorption, the partial density of states (LDOS) and total density of states (TDOS) of each adsorption system are given in Fig. 4. From the TDOS of the pristine CrB in Fig. 4, it can be seen that there is a clear peak of the partial density of states (PDOS) at the Fermi level, which verifies its metallic character. After the adsorption of gas molecules, a reduction in the TDOS peak at the Fermi level can be observed to varying degrees in Fig. 4a–d, indicating a weakening of the conductivity of CrB and a macroscopic increase in resistance. In the LDOS, obvious hybridization is observed at positions of 0.64 eV, −0.66 eV, −2.68 eV, −3.85 eV, −5.80 eV, and −6.78 eV between S 3p, H 1 s, and Cr 3d orbitals in the H₂S adsorption system, indicating that H₂S molecules may have formed new chemical bonds with Cr atoms after bond cleavage. Similarly, obvious hybridization peaks can be observed in the SOF₂ and SO₂F₂ systems, such as −4.77 eV, −5.53 eV, −7.25 eV in Fig. 4c, and −4.88 eV, −5.54 eV, −6.77 eV, −7.52 eV in Fig. 4d, where the atomic orbitals of the gas molecules overlap with the 3d orbitals of Cr atoms on

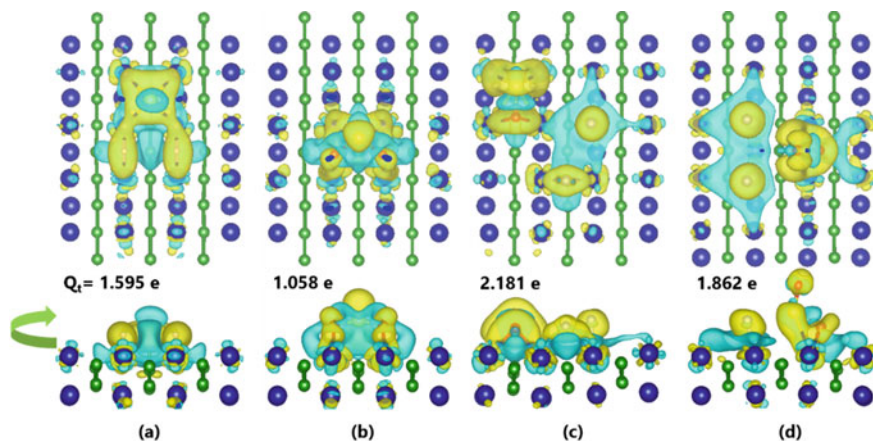


Fig. 3 Charge density deformation results of adsorption system, **a** H₂S adsorption system, **b** SO₂ adsorption system, **c** SOF₂ adsorption system, **d** SO₂F₂ adsorption system

the surface of CrB, indicating the formation of new chemical bonds. In the LDOS of SO₂, hybridization between the S 3p, O 2p, and Cr 3d orbitals at $-2.91 eV$, $-7.28 eV$, and $-7.93 eV$ can be observed, indicating that the bond between S and O atoms is still present, which is consistent with the previous speculation.

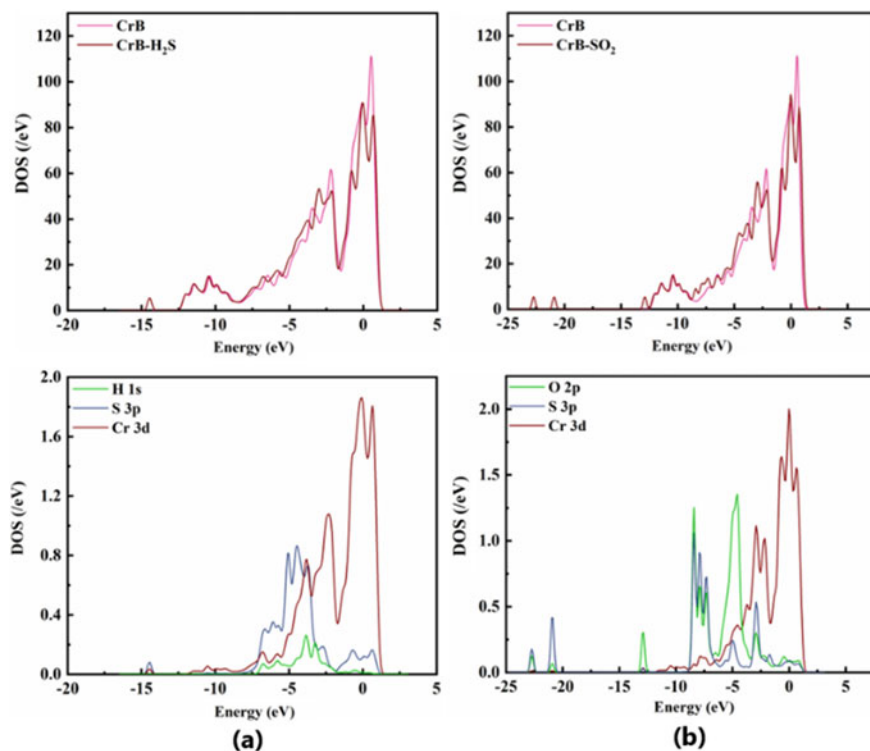


Fig. 4 TDOS and PDOS of **a** H₂S adsorption system, **b** SO₂ adsorption system, **c** SOF₂ adsorption system, **d** SO₂F₂ adsorption system

4 Conclusion

In summary, this study calculated the geometric and electronic structure parameters of single-layer CrB after adsorbing H₂S, SO₂, SOF₂, and SO₂F₂. By analyzing parameters such as adsorption energy, charge transfer, and density of states, it was found that CrB had the highest adsorption energy for SOF₂ at -7.213 eV, followed by SO₂F₂ at -5.302 eV and H₂S at -4.182 eV, with the lowest adsorption energy of SO₂ at -3.521 eV. All gas molecules were strongly chemisorbed and acted as electron acceptors during the adsorption process. Analysis of the differential charge density map and density of states showed that the adsorption of H₂S, SOF₂, and SO₂F₂ resulted in the breaking of H–S and S–F bonds and the formation of H–Cr and F–Cr bonds, indicating a strong interaction between gas molecules and the substrate. The relevant calculation results provide a first understanding of the mechanism of CrB adsorbing SF₆ decomposition components and broaden the application field of CrB as a two-dimensional material.

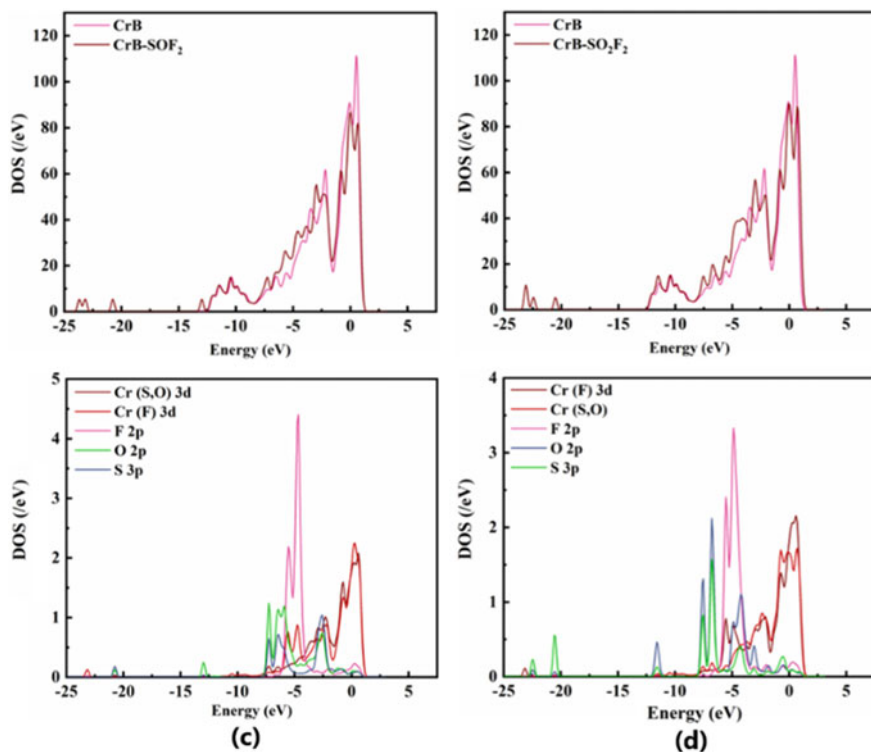


Fig. 4 (continued)

Acknowledgements This work was supported by the science and technology project of China Southern Power Grid (Grant number YNKJXM20222118, YNKJXM20222131, YNKJXM20222043).

References

1. Nisar J, Topalian Z, De Sarkar A, Osterlund L, Ahuja R (2013) TiO₂-based gas sensor: a possible application to SO₂. *ACS Appl Mater Interfaces* 5(17):8516–8522
2. Cui H, Zhang X, Zhang J, Zhang Y (2019) Nanomaterials-based gas sensors of SF₆ decomposed species for evaluating the operation status of high-voltage insulation devices. *High Volt* 4(4):242–258
3. Gui Y, Zhang X, Lv P, Wang S, Tang C, Zhou Q (2018) Ni-CNT chemical sensor for SF₆ decomposition components detection: a combined experimental and theoretical study. *Sensors (Basel)* 18(10):1–11
4. Guo H, Zheng K, Cui H, Zhang F, Yu J, Tao L-Q, Li X, Chen X (2020) High sensitivity gas sensor to detect SF₆ decomposition components based on monolayer antimonide phosphorus. *Chem Phys Lett* 756:137868

5. Yang A, Wang D, Lan T, Chu J, Li W, Pan J, Liu Z, Wang X, Rong M (2020) Single ultrathin WO_3 nanowire as a superior gas sensor for SO_2 and H_2S : selective adsorption and distinct I-V response. *Mat Chem Phys* 240:122165
6. Chen C, Xu B, Zhang J, Ma S, Wang Y, Li J, Yi L (2023) Gas sensing potential of monolayer MoB: a first principles study. *Vacuum* 210:111883
7. Shukla A, Sharma G, Krishnamurthy S (2023) Functionalized Mo_2BX_2 ($X = \text{H}, \text{OH}, \text{O}$) MBenes as a promising sensor, capturer and storage material for environmentally toxic gases: a case study of 1T and 2H phase. *Appl Surf Sci* 615:156299
8. Mir SH, Yadav VK, Singh JK (2022) Efficient CO_2 capture and activation on novel two-dimensional transition metal borides. *ACS Appl Mater Interfaces* 14(26):29703–29710

Study About the Surface Charge Accumulation and Dissipation of Insulators Under Corona Condition



Fan Yi, Wenli Xu, Xiaoshan Yao, Naifa Gong, Dazhao Zhang, Zhiye Du, Hao Meng, and Guohua Yue

Abstract The insulator surface charge buildup issue is a significant element impacting the electric field on the insulator surface in HVDC transmission. The electrostatic probe method is used to measure the surface potential of various insulators under the corona situation in order to acquire insulator surface charge buildup and dissipation regularity under DC high voltage. A charge density inversion approach for curved surfaces is suggested in this study. The chosen measurement points are used to create triangular meshes from the curved surface. Based on the measured potential, surface charge density is inverted. According to the findings, an insulator with a PRTV coating on its surface is easily charged. The surface potential attenuation trend of the insulator shed sprayed with PRTV coating is exponential attenuation. The peak value of insulator shed sprayed with PRTV coating surface charge density is about $-0.5\mu\text{C}/\text{m}^2$.

Keywords Insulator · Surface potential · Charge accumulation · Charge inversion

1 Introduction

In HVDC power system, corona generates space charge, which accumulates on the surface of insulator shed under the action of constant electric field. The space charge on insulator shed surface will change the potential distribution and electric field distribution, cause the electric field intense distortion along the surface, and electric field distortion along the surface will reduce the flashover voltage of insulators. At the same time, the space charge on the insulators surface will accelerate the aging of insulating materials.

F. Yi (✉) · W. Xu · X. Yao · N. Gong · D. Zhang · H. Meng
Air Force Early Warning Academy, Wuhan, China
e-mail: yifan10101546@qq.com

Z. Du · G. Yue
School of Electrical Engineering and Automation, Wuhan University, Wuhan, China

With the rapid development of UHVDC, it is urgent to clarify the law of insulators surface charge accumulation and dissipation, and the method is found to control surface charge of insulator shed to improve the insulation performance of insulator.

The surface potential distribution of different insulators under corona condition are measured by electrostatic probe method. In order to obtain the surface charge density distribution of insulator shed, a surface charge density inversion method is proposed in this paper. The surface electrostatic potential of insulator shed is inverted to the charge density, and the law of charge accumulation and dissipation on insulator surface is obtained.

2 Insulator Shed Surface Charge Accumulation and Dissipation Test

2.1 Surface Potential Measurement System

Figure 1 depicts an insulator surface potential measurement apparatus.

During the experiment, a high voltage is supplied to the spherical electrode, causing it to discharge and create corona. After a set period of time, the high voltage is withdrawn and the spherical electrode has finished discharging. The multi axis motion controller can precisely regulate the location of the electrostatic probe to complete radial and full surface scanning of various insulator surfaces [1]. Electrostatic probes may detect the electrostatic potential of an insulator's surface, generating a picture of the potential's change over time and obtaining electrostatic potential changes exponentially with time [2].

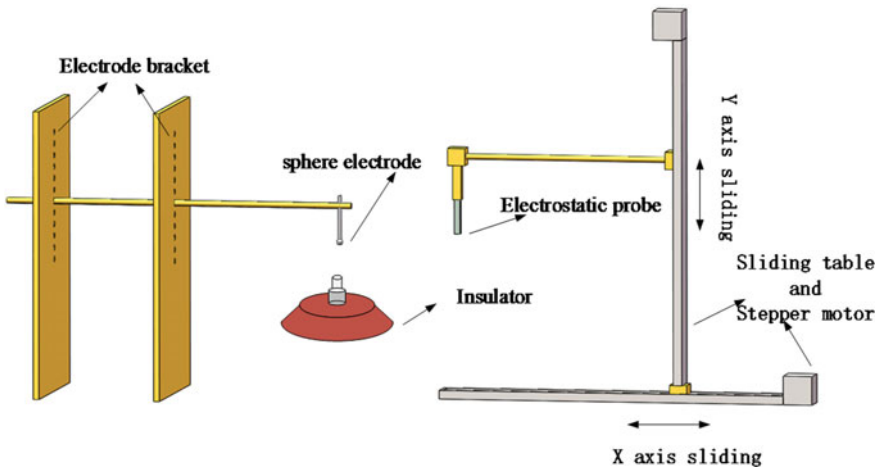


Fig. 1 The surface potential measurement system is depicted in a diagram

2.2 Test Insulators and Selection of Potential Measurement Points

Several kinds of insulators commonly used in engineering are selected to measure the surface potential changes after corona. The tested insulators are divided into three types: ceramic material, glass material and surface spraying PRTV coating. Different insulators are shown in the figure (Fig. 2).

Corona spherical electrodes are placed in the center of insulators in the test platform, and both insulators and spherical electrodes are spherically symmetrical, so the electric field in the whole test space also presents spherically symmetrical distribution, and the charge accumulation on the insulator shed surface also presents spherically symmetrical distribution. Therefore, a point potential on the insulator surface can present each point potential on the circumference. So the paper measure one axis potential change of insulator shed to analyze the law of charge accumulation and dissipation.

When measuring the potential changes at different points on an axis of insulator shed surface, each potential measuring point is selected from the outside to the inside equidistantly [3]. The distance between each measuring point is about 1 cm. The first potential measuring point near the edge of insulator shed is marked as 1. The number gradually increases from the outside to the inside. According to the size of insulator shed, 9–13 potential measuring points are selected respectively. The schematic diagram of the measuring points selection for insulator shed surface potential is shown in Fig. 3.

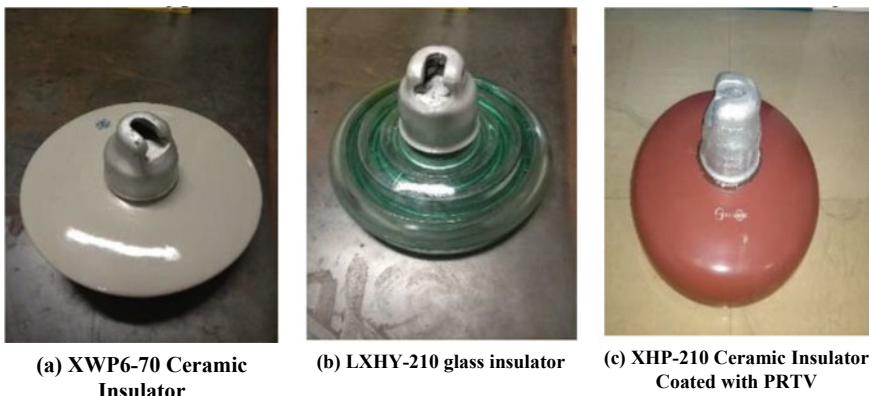


Fig. 2 Physical drawings of different insulators

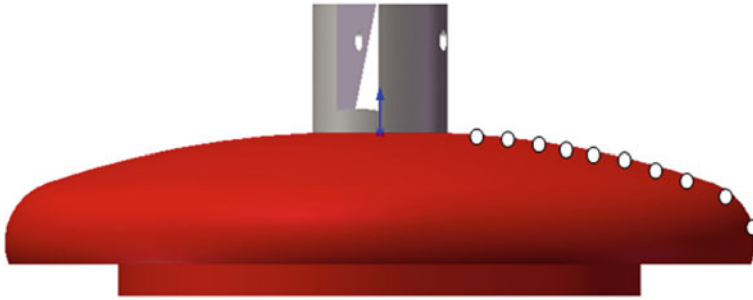


Fig. 3 Measuring points selection of insulator

2.3 Insulator Shed Surface Potential Change

The surface potential distribution of XWP6-70 ceramic insulator was shown in Fig. 4, and LXHY-210 glass insulator surface potential distribution was shown in Fig. 5, and the surface potential of XHP-210 ceramic insulator sprayed with PRTV coating changed with time as shown in Fig. 6.

From the above figure, it can be seen that the surface potential of ceramic and glass insulator shed is very low, and there is no trend of potential decay in a short time. Because the surface potential is approximately linear with the surface charge density, the surface charge density of insulator shed is also very low. It can be judged that under high voltage DC corona, the surface of ceramic and glass insulator shed hardly accumulates charge, So it is not necessary to invert the potential into charge density.

For insulators sprayed with PRTV coating, the surface accumulated charge increases sharply. At the same time, the insulator shed surface near the insulator cap is difficult to accumulate charge, and the charge density at the edge of the insulator shed

Fig. 4 Surface potential distribution of XWP6-70 ceramic insulator shed after corona

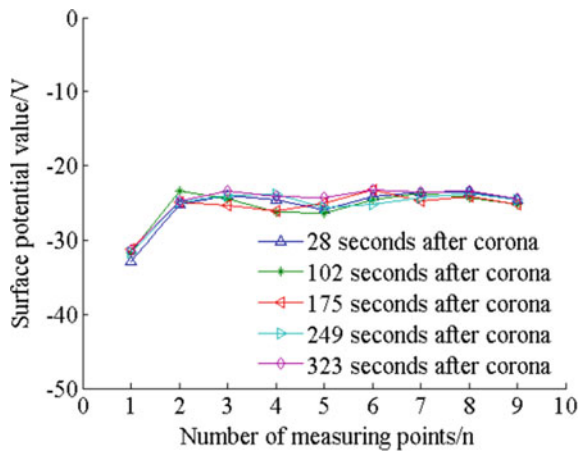


Fig. 5 Surface potential distribution of LXHY-210 glass insulator shed after corona

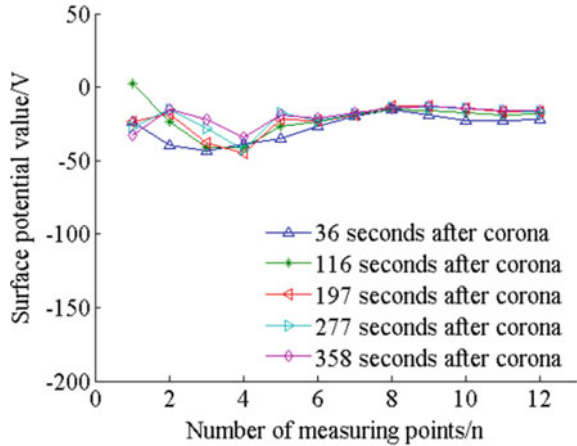
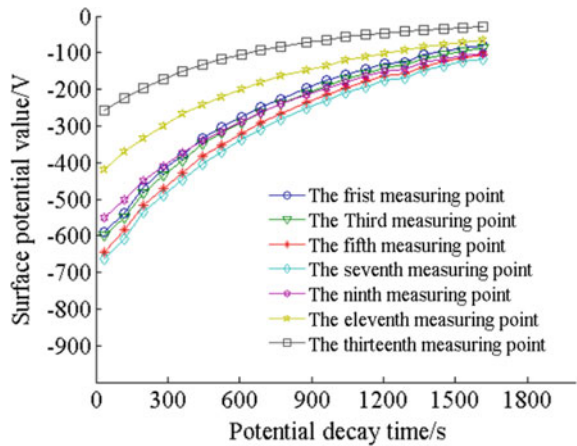


Fig. 6 Surface potential of XHP-210 ceramic insulator shed coated with PRTV change with time



is not as high as that in insulator shed middle part, and the surface potential distribution presents a “spoon” shape. The attenuation of surface potential at the measuring point far away from the insulator cap is consistent, and the trend of surface potential attenuation curve is almost the same, approximating an exponential attenuation. The surface charge of XHP-210 ceramic insulator coated with PRTV coating basically dissipated in 1500 s after corona.

3 Curved Surface Charge Inversion Method

3.1 Introduction of Charge Inversion Method

Polarized charges and free charges are present on the insulator surface following corona discharge. The superposition theorem states that the potential and electric field intensity produced by these two charges at any given point superimpose to yield the $\varphi(P)$ and $E(P)$ of every given point [4].

$$\sigma_a = \sigma + \sigma' \tag{1}$$

σ represent free charge density; σ' represent polarized charge density.

The insulating surface is divided into n meshes in accordance with the principles of the finite element approach. When n is large enough, it may be said that the distribution of electric charges within each mesh is uniform [5, 6]. Currently, the representations of potential and electric field intensity for each mesh may be expressed as follows:

$$\varphi_j = \frac{1}{4\pi\epsilon_0} \sum_{i=1}^n (\sigma_a)_i \int_{S_i} \frac{1}{r_{ij}} dS \tag{2}$$

$$E_j = \frac{1}{4\pi\epsilon_0} \sum_{i=1}^n (\sigma_a)_i \int_{S_i} \frac{\mathbf{r}}{r_{ij}^3} dS \tag{3}$$

The following matrix equation describes the relationship between surface potential and charge density of an insulating surface:

$$\begin{bmatrix} \varphi_1 \\ \varphi_2 \\ \vdots \\ \varphi_n \end{bmatrix} = \begin{bmatrix} P_{11} & P_{12} & \cdots & P_{1n} \\ P_{21} & P_{22} & \cdots & P_{2n} \\ \vdots & \vdots & & \vdots \\ P_{n1} & P_{n2} & \cdots & P_{nn} \end{bmatrix} \begin{bmatrix} (\sigma_a)_1 \\ (\sigma_a)_2 \\ \vdots \\ (\sigma_a)_n \end{bmatrix} \tag{4}$$

The potential coefficient matrix P is defined as follows:

$$P = \begin{bmatrix} P_{11} & P_{12} & \cdots & P_{1n} \\ P_{21} & P_{22} & \cdots & P_{2n} \\ \vdots & \vdots & & \vdots \\ P_{n1} & P_{n2} & \cdots & P_{nn} \end{bmatrix} \tag{5}$$

Each unit's charge density equation is as follows:

$$\begin{bmatrix} (\sigma_a)_1 \\ (\sigma_a)_2 \\ \vdots \\ (\sigma_a)_n \end{bmatrix} = P^{-1} \begin{bmatrix} \varphi_1 \\ \varphi_2 \\ \vdots \\ \varphi_n \end{bmatrix} \quad (6)$$

Free charge density is expressed as follows for any cell:

$$\sigma_i = (\varepsilon_2 \vec{E}_{i2} - \varepsilon_1 \vec{E}_{i1}) \cdot \vec{n}_i \quad (7)$$

ε_1 and ε_2 refer to the dielectric constant of insulating material and air respectively; \vec{E}_{i1} and \vec{E}_{i2} refer to the electric intensity of insulating surface and air surface at the interface respectively; \vec{n}_i refer to the unit normal vector from the interface to the air side [7].

Free charge density and visible charge expressed as matrices:

$$\begin{bmatrix} \sigma_1 \\ \sigma_2 \\ \vdots \\ \sigma_n \end{bmatrix} = \begin{bmatrix} F_{11} & F_{12} & \cdots & F_{1n} \\ F_{21} & F_{22} & \cdots & F_{2n} \\ \vdots & \vdots & & \vdots \\ F_{n1} & F_{n2} & \cdots & F_{nn} \end{bmatrix} \begin{bmatrix} (\sigma_a)_1 \\ (\sigma_a)_2 \\ \vdots \\ (\sigma_a)_n \end{bmatrix} \quad (8)$$

Definited matrix F is as follows:

$$\mathbf{F} = \begin{bmatrix} F_{11} & F_{12} & \cdots & F_{1n} \\ F_{21} & F_{22} & \cdots & F_{2n} \\ \vdots & \vdots & & \vdots \\ F_{n1} & F_{n2} & \cdots & F_{nn} \end{bmatrix} \quad (9)$$

The following are the computational expressions for each component of matrix F:

$$F_{ij} = \begin{cases} (\varepsilon_2 - \varepsilon_1) \frac{1}{4\pi \varepsilon_0} \int_{S_i} \frac{\vec{r}_{ij} \cdot \vec{n}_i}{r_{ij}^3} \\ \frac{\varepsilon_1 + \varepsilon_2}{2\varepsilon_0}, & i = j \end{cases} \quad (10)$$

The following formula may be used to calculate any component of the potential matrix P:

$$P_{ij} = \begin{cases} \frac{S_i}{4\pi \varepsilon_0 R_{ij}}, & i \neq j \\ \frac{R_i}{2\varepsilon_0}, & i = j \end{cases} \quad (11)$$

3.2 Charge Inversion of Curved Surface Structures

According to the charge inversion calculation principle, there are two main differences in the charge inversion calculation of plane surface and curved surface materials.

- (1) In surface meshing of planar materials, planar materials can be simplified to a two-dimensional model. The location of each element can be represented by only two coordinates, x and y . While the curved surface material is divided into elements, it needs three coordinates, x , y and z , to represent the position of each element [8, 9].
- (2) Formula (7) is expressed differently in computation. Specifically, When $i \neq j$, $F_{ij} = 0$ for planar materials. For curved surface material, we need to calculate the unit normal vector \mathbf{n}_k at the center of each element. Then the angle between two vectors \mathbf{r}_{ik} and \mathbf{n}_k is calculated. The angle between \mathbf{r}_{ik} and \mathbf{n}_k is recorded as θ . In the actual calculation of charge density, F_{ij} expression can be simplified as follows:

$$F_{ij} = (\epsilon_2 - \epsilon_1) \frac{S_i \cos \theta}{4\pi\epsilon_0 r_{ik}^2} \tag{12}$$

For the curved surface of known surface equation, the normal vector of each point can be obtained directly by surface equation derivation. But in practical engineering, the method of surface equation derivation can not be applied to measure the curved surface of unknown surface equation such as insulators. Therefore, a general solution method suitable for all curved surface should be created [10].

According to the geometry, a plane is determined at three points. As shown in Fig. 1, $\triangle ABC$ is a mesh after the curved surface is meshed. The region in which each mesh is located is thought to be a plane since the mesh is so narrow. The grid's three vertices are points A , B , and C , its center is O , and the plane it is situated in has a normal vector called \mathbf{n} . When the mesh is divided into quadrilateral elements, the mesh will be further divided into two triangular elements according to the diagonal line. The coordinates of A , B and C can be obtained by meshing. When the coordinates of A , B and C are $A(x_1, y_1, z_1)$, $B(x_2, y_2, z_2)$ and $C(x_3, y_3, z_3)$, the normal vector $\mathbf{n} = (a, b, c)$ of the mesh is set [11] (Fig. 7).

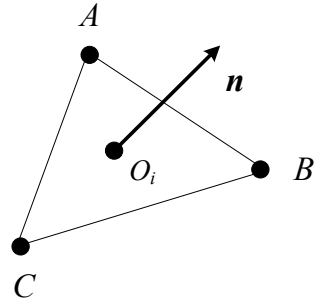
According to the geometry, it can be seen that:

$$\vec{n} = \vec{CB} \times \vec{CA} \tag{13}$$

The coordinates of the normal vector \mathbf{n} are as follows:

$$\begin{aligned} a &= (y_2 - y_3)(z_1 - z_3) - (z_2 - z_3)(y_1 - y_3) \\ b &= (z_2 - z_3)(x_1 - x_3) - (x_2 - x_3)(z_1 - z_3) \\ c &= (x_2 - x_3)(y_1 - y_3) - (y_2 - y_3)(x_1 - x_3) \end{aligned} \tag{14}$$

Fig. 7 Normal vector solution schematic diagram



Therefore, the first item in the inversion calculation formula (10) can be written in the form as follows:

$$\begin{aligned}
 F_{ij} &= (\varepsilon_2 - \varepsilon_1) \frac{1}{4\pi\varepsilon_0} \int_{S_i} \frac{\mathbf{r}_{ij} \cdot \mathbf{n}_i}{r_{ij}^3} dS \quad i \neq j \\
 &= (\varepsilon_2 - \varepsilon_1) \frac{S_i}{4\pi\varepsilon_0} \frac{r_1m + r_2n + r_3p}{r_{ij}^3} \tag{15}
 \end{aligned}$$

Among them: S_i is the area of the grid; r_1 、 r_2 and r_3 are three coordinates of vector \mathbf{r}_{ij} ; r_{ij} is the length of vector \mathbf{r}_{ij} . For mesh generation, the area S_i of each mesh is determined and known, and the coordinates of vector \mathbf{r}_{ij} can also be obtained by the central coordinates of each mesh. Therefore, F_{ij} can be obtained directly [12].

4 Surface Charge Distribution of Insulators Coated with PRTV Coating

According to the measured potential, it is considered that the potential on the circle where the point is located is equal. 30 points of equal distance are selected for each circle, and the selected potential inversion point is shown in Fig. 8. According to the measured potential, the charge density distribution on the insulator shed surface is obtained by charge inversion. The surface charge density distribution of insulator shed is shown in the Fig. 9. After corona, the peak value of insulator shed surface charge density is about $-0.5\mu\text{C}/\text{m}^2$.

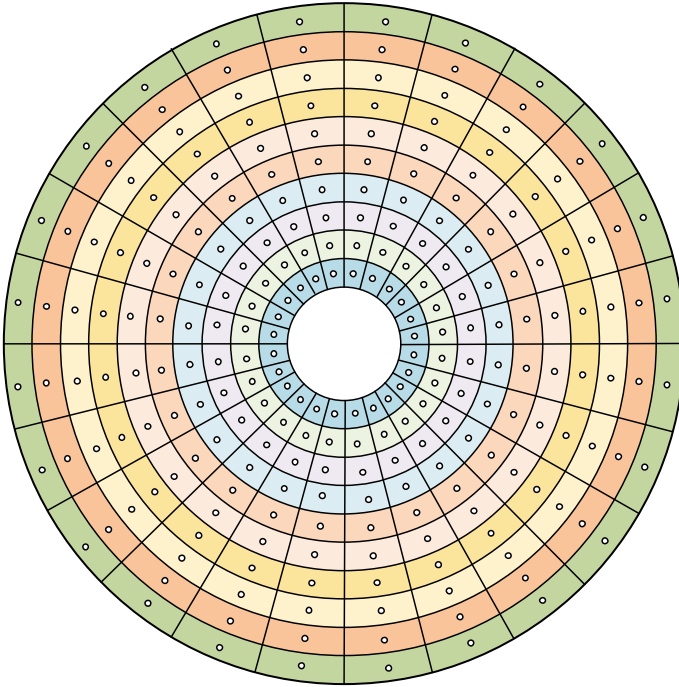
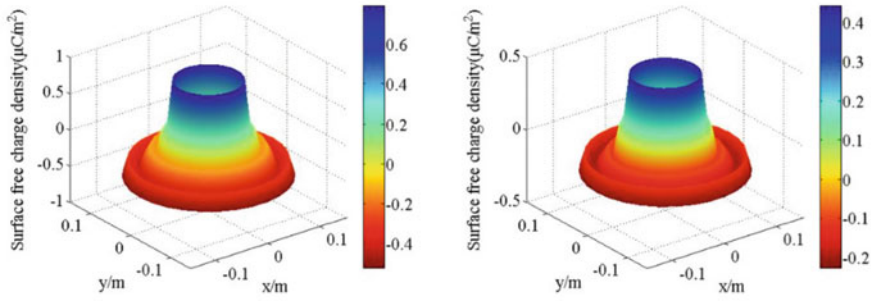
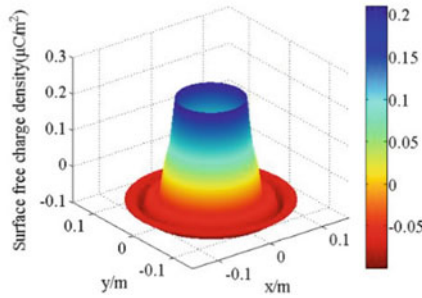


Fig. 8 Schematic diagram of insulator surface potential distribution



(a)Surface Charge Distribution at 35s after Discharge

(b)Surface Charge Distribution at 687s after Discharge



(c)Surface Charge Distribution at 1456s after Discharge

Fig. 9 Surface charge density of XHP-210 ceramic insulator coated with PRTV

5 Conclusion

1. In this paper, an inversion algorithm for calculating surface charge density is proposed. Meshes of triangles are used to partition the surface. The normal vectors at each mesh are obtained by using geometric method, and the F matrix is obtained. Then the surface charge density is obtained by inversion.
2. Ceramic and glass insulator shed hardly accumulates charge, while insulators sprayed with PRTV coating are easy to accumulate charges. The surface potential attenuation trend of the insulator shed sprayed with PRTV coating is exponential attenuation. The peak value of insulator shed sprayed with PRTV coating surface charge density is about $-0.5\mu C/m^2$.

References

1. Wang Q, Zhang G, Wang X (2012) Characteristics and mechanisms of surface charge accumulation on a cone-type insulator under DC voltage. *IEEE Trans Dielectr Electr Insul* 19(19):150–155
2. Hama H, Hikosaka T, Okabe S et al (2007) Cross-equipment study on charging phenomena of solid insulators in high voltage equipment. *IEEE Trans Dielectr Electr Insul* 14(2):508–519
3. Zhang B, Zhang G, Wang Q et al (2015) Suppression of surface charge accumulation on Al₂O₃-filled epoxy resin insulator under DC voltage by direct fluorination. *AIP Adv* 5(12):127207
4. Ootera H, Nakanishi K (1988) Analytical method for evaluating surface charge distribution on a dielectric from capacitive probe measurement-application to a cone-type spacer in ± 500 kV DC-GIS. *IEEE Trans Power Delivery* 3(1):87–89
5. Upadhyay AK, Reddy CC (2020) Analytical model for homocharge accumulation in LDPE—Role of conduction, injection and diffusion[J]. *IEEE Trans Dielectr Electr Insul* 27(2):565–573
6. Tian F, Zhang S, Hou C (2021) Effects of trapping characteristics on space charge and electric field distributions in HVDC cable under electrothermal stress. *Energies* 14(5):1313–1334
7. Zhou Y, Gao B, Wang W et al (2022) Influence of polarity reversal period and temperature gradient on space charge evolution and electric field distribution in HVDC extruded cable. *Energies* 15(3):985–991
8. Hallak K, Baudoin F, Griseri V et al (2021) A New approach for optimizing a bipolar charge transport model for dielectric materials: theoretical framework. *IEEE Trans Dielectr Electr Insul* 28(3):872–879
9. Hallak K, Baudoin F, Griseri V et al (2020) Numerical optimization applying trust region algorithm to optimize parameters related to charge transport model in LDPE. *IEEE Trans Dielectr Electr Insul* 27(6):2048–2055
10. Farooq U, Yang F, Shaikh JA, et al (2021) Temperature field simulation and ampacity optimization of 500 kV HVDC submarine transmission cable. In: 2021 International Conference on Advanced Electrical Equipment and Reliable Operation. Beijing, China, IEEE, 1–6
11. Frobin SJ, Freye C, Niedik CF et al (2018) Generic field simulation framework for HVDC Cables. In: 2018 IEEE 2nd International Conference on Dielectrics. Budapest, Hungary, IEEE, 1–5
12. Tian F, Zhang J, Peng X et al (2017) Interface trapping effects on the charge transport characteristics of LDPE/ZnO nanocomposites. *IEEE Trans Dielectr Electr Insul* 24(3):1888–1895

Influence of Oxygen on Characteristic Law of C₅F₁₀O/N₂ Mixture Partial Discharge Statistical Characteristic



Long Li, Qiang Yao, Baojia Deng, Liangjun Dai, Ying Zhang, Shiling Zhang, Ke Li, and Haoran Xia

Abstract In recent years, C₅F₁₀O (Perfluoro(3-methyl-2-butanone), as a potential substitute gas for SF₆, has attracted extensive attention from researchers. C₅F₁₀O has high molecular freedom and strong energy absorption ability. Due to the high fluorine content in C₅F₁₀O gas, it has excellent insulation characteristics, more than twice that of SF₆ under the same conditions. It is considered to be the most promising alternative gas for SF₆. C₅F₁₀O mixed ratio insulating gas is a new type of environmentally friendly insulating gas, and its partial discharge statistical characteristics are rarely studied at home and abroad. In this paper, the statistical characteristics of partial discharge in C₅F₁₀O/N₂ gas mixtures under extremely inhomogeneous electric field conditions are studied, and the characteristics of their statistical characteristics are analyzed. It is found that the addition of oxygen changes the partial discharge decomposition characteristics of the C₅F₁₀O/N₂ gas mixture, degrades the partial discharge characteristics of the C₅F₁₀O/N₂ gas mixture, making the more severe the electron dissociation, and increases the electric field distortion near the needle tip, thereby promoting the discharge on both sides of the sinusoidal voltage peak (around 270°).

Keywords New environmental protection insulating gas · C₅F₁₀O/N₂ mixed gas · Partial discharge · Discharge statistical characteristics

1 Introduction

In the field of high voltage, the excellent insulation characteristics of SF₆ gas make it always occupy a leading position in the electrical field and power industry. Nearly 80% of the usage of SF₆ gas is used in the electrical field and power industry every

L. Li · Q. Yao · B. Deng · L. Dai · Y. Zhang · S. Zhang · K. Li
State Grid Chongqing Electric Power Research Institute Chongqing, Chongqing, China
e-mail: Yaoqiang212@aliyun.com

H. Xia (✉)
School of Electrical Engineering and Automation, Wuhan University, Wuhan 430072, China
e-mail: 1043101352@qq.com

© Beijing Paiké Culture Commu. Co., Ltd. 2024
X. Dong and L. Cai (eds.), *The Proceedings of 2023 4th International Symposium on Insulation and Discharge Computation for Power Equipment (IDCOMPU2023)*, Lecture Notes in Electrical Engineering 1100, https://doi.org/10.1007/978-981-99-7393-4_43

year [1]. However, SF₆ also has the disadvantages of long atmospheric life and greatly aggravating the greenhouse effect [2]. The Kyoto Protocol and the Paris climate agreement all list SF₆ as a gas that needs to be limited [3]. In addition, the decomposition of SF₆ by discharge will produce toxic low fluoride substances that seriously threaten human health, such as SF₄ and S₂F₁₀. Therefore, it is particularly important to find new environmentally friendly insulating gases that can replace SF₆ in order to reduce the emission of SF₆ for the sustainable development of power industry and environment.

In recent years, C₅F₁₀O, as a potential alternative gas to SF₆, has attracted extensive attention of researchers. It has excellent dielectric properties and environmental protection characteristics [4]. C₅F₁₀O has high degree of freedom and strong energy absorption capacity [5]. The high fluorine content in the molecule also makes its insulation performance extremely excellent, which is more than twice that of SF₆ under the same conditions. C₅F₁₀O has stable chemical properties, the global warming potential (GWP) is about 1, and the atmospheric life is about 15 days. It is not destructive to the ozone layer. Compared with SF₆, the negative impact on the natural environment is greatly reduced. However, due to the high liquefaction temperature of C₅F₁₀O, the liquefaction temperature at one atmospheric pressure is about 26.5 °C [6], so it can not be used alone. It needs to be mixed with buffer gas with low liquefaction temperature to avoid liquefaction, and the selection and proportion of mixed background gas is a major topic. Mantilla J D, gariboldin studied the power frequency breakdown voltage of C₅F₁₀O mixed with N₂ and CO₂, and found that N₂ and CO₂ as background gases have good effects [7, 8]. Therefore, this paper selects N₂, which is more abundant and common in nature, as the background gas of the mixed gas for experimental research.

As a new type of environment-friendly insulating gas, there is less research on the performance of C₅F₁₀O at home and abroad, and less research on the appropriate proportion of C₅F₁₀O in the mixed gas [9]. Therefore, this paper uses the needle plate electrode simulation equipment to operate in a slightly uneven electric field environment, carries out the partial discharge experiment of C₅F₁₀O/N₂ mixed gas by using the power frequency partial discharge experimental platform, and changes the proportion of C₅F₁₀O in the mixed gas, Collect and measure the gas decomposition components after partial discharge to analyze their decomposition characteristics, so as to provide experimental basis for the environmental protection substitution of C₅F₁₀O and N₂ mixed gas, and provide theoretical basis for the substitution of environmental protection insulating gas in high-voltage electrical equipment [10, 11] (Table 1).

Table 1 Comparison of the basic properties of C₅F₁₀O with SF₆, N₂ and CO₂

Chemical formula	Dielectric strength relative to SF ₆	Boiling point (°C)	GWP/100-years
SF ₆	1	-64	23,500
C ₅ F ₁₀ O	2	24	1
N ₂	0.32–0.37	-79	1
CO ₂	0.34–0.43	-196	-

2 Methodology

2.1 Test Platform

The equivalent circuit diagram of the partial discharge testing platform in this article is shown in Fig. 1. The AC Pressure regulator has a range of 0–380 V, which is used to control the output voltage of the test transformer; The protective resistor R has a resistance value of 10kΩ, which plays a role in avoiding overcurrent and protecting the circuit [12]. The circuit model of high voltage power frequency experimental platform is shown in Fig. 1.

The experimental gas chamber is made of stainless steel and can withstand the pressure of 0–0.6 MPa [13]. In the partial discharge experiment, the needle plate electrode is used to simulate a slightly uneven electric field. The needle electrode is made of tungsten copper and the plate electrode is made of brass.

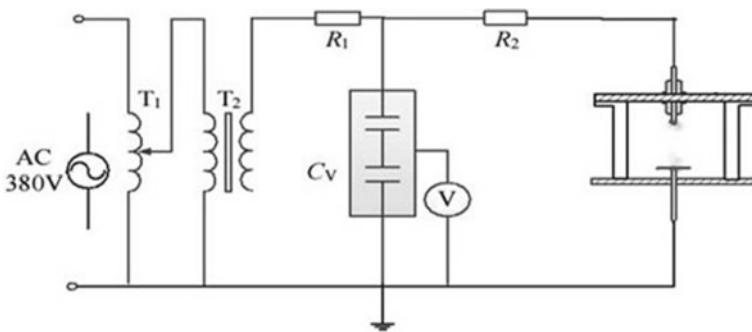


Fig. 1 Circuit of the AC partial discharge testing platform

3 Results

3.1 *C₅F₁₀O/N₂ Gas Mixture PD Statistical Characteristics*

In order to explore the characteristic law of the statistical characteristic quantity of partial discharge of C₅F₁₀O/N₂ gas mixture, this section uses software MATLAB to create a map reflecting the discharge quantity and discharge times. The following figure shows the PRPD map of partial discharge of C₅F₁₀O/N₂ gas mixture for 48 h under oxygen-free conditions. The left and right sides are respectively C₅F₁₀O/N₂ mixed gas, Q-φ (Discharge Phase) Graph and n-φ (Discharge times phase) atlas.

3.2 *Discharge Quantity Phase Diagram and Discharge Frequency Phase Diagram*

According to Fig. 2, the discharge times phase patterns at 12 h, 24 h, 36 h, and 48 h all conform to the Gaussian distribution characteristics. PD mostly occurs in the negative half cycle of power frequency, and the discharge amount and discharge times of the negative half cycle PD pulse at different times are much greater than the positive half cycle, indicating that the C₅F₁₀O/N₂ gas mixture has a polarity effect. The polarity effect is related to the space charge formed around the needle tip during the discharge process, that is, the ionization near the negative potential needle tip generates a large number of positive ions to form a space charge layer, and the direction of the space electric field is the same as that of the applied electric field, resulting in an increase in the intensity of the electric field near the needle tip, which is more prone to self-sustaining discharge and the generation of PD. Similarly, the positive polarity space charge near the electrode of the positive potential probe will weaken the field strength near the tip and inhibit the occurrence of PD. The peak value of the discharge frequency basically occurs at the phase of 270°, which is near the peak value of the sinusoidal voltage. Within 48 h, the discharge capacity basically maintained at around 50pC/pulse, while the discharge frequency showed a trend of increasing first and then decreasing, from 10 times in 12 h to 25 times in 24 h, then to 15 times in 36 h, and finally less than 10 times in 48 h. This is due to the fact that the experimental voltage remained at 24.5 kV, and the discharge amount remained basically unchanged without significant changes in the electrode plate and background gas. However, due to the continuous progress of partial discharge, the discharge frequency first increased with time, after a long time of partial discharge, the needle tip of the needle plate electrode will be ablated, and the needle tip will become increasingly bald after a long time of partial discharge, resulting in a decrease in the number of discharges.

The following figure shows the statistical characteristic map of 48 h PD with an oxygen concentration of 8% (O₂ concentration of 24 kPa) and other conditions unchanged.

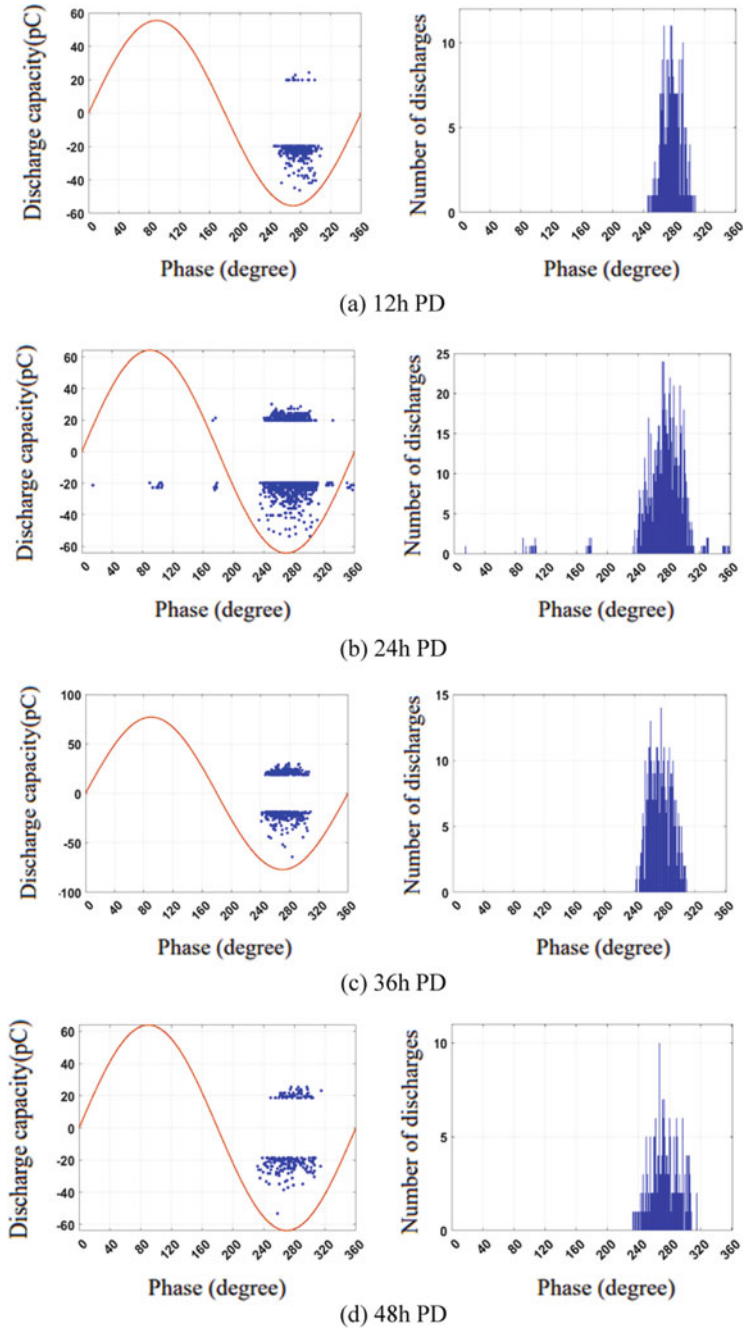


Fig. 2 PRPD spectrum of C₅F₁₀O/N₂ at 0.3 MPa

From Fig. 3, it can be seen that, unlike in the absence of oxygen, after adding 8% O₂, the discharge is more concentrated in the positive half cycle, that is, PD mostly occurs in the positive half cycle of the power frequency. And the PRPD pattern has different characteristics from that in the absence of oxygen. The discharge frequency phase diagram has changed from one peak to two main peaks, and the discharge frequency at the phase of 270° (at the peak of sinusoidal voltage) has greatly decreased. As shown in the figure, the maximum discharge frequency can reach 50 times at 230°, and the discharge quantity at the phase of 270° (at the peak of sinusoidal voltage) in the discharge frequency phase diagram is smaller than the discharge quantity on both sides.

The reason for this may be that the addition of oxygen changes the partial discharge decomposition characteristics of the C₅F₁₀O/N₂ gas mixture and degrades the PD characteristics of the C₅F₁₀O/N₂ gas mixture. From the perspective of gas discharge, due to the negative potential of the needle electrode, gas discharge causes electrons to dissociate, and the gas molecules collide with the free electrons emitted from the cathode to ionize. The ionized free electrons can continue to collide with the gas molecules to cause secondary electron avalanches, forming streamer channels. After the development of the streamer, there is a large and uniformly distributed space charge layer near the tip of the needle. The existence of the space charge layer weakens the front electric field near the tip, with a phase of 270° (at the peak of the sinusoidal voltage) having the strongest shielding effect on the tip, and with very small electric field distortion. However, due to the degradation of PD characteristics of C₅F₁₀O/N₂ gas mixtures by oxygen, the more serious the electron dissociation is, the greater the electric field distortion near the tip of the needle increases, thereby promoting discharge on both sides of the sinusoidal voltage peak (around 270°).

4 Conclusion

To sum up, using a power frequency high-voltage gas insulation test platform, the PD characteristics of C₅F₁₀O under two different background gases, N₂ and CO₂, were systematically investigated, and the PD statistical characteristics of C₅F₁₀O under two different background gases were analyzed theoretically. The following conclusions were obtained:

The addition of oxygen changes the partial discharge decomposition characteristics of the C₅F₁₀O/N₂ gas mixture, and degrades the PD characteristics of the C₅F₁₀O/N₂ gas mixture. The more severe the electron dissociation, the greater the distortion of the electric field near the needle tip, thereby promoting the discharge on both sides of the sinusoidal voltage peak (around 270°).

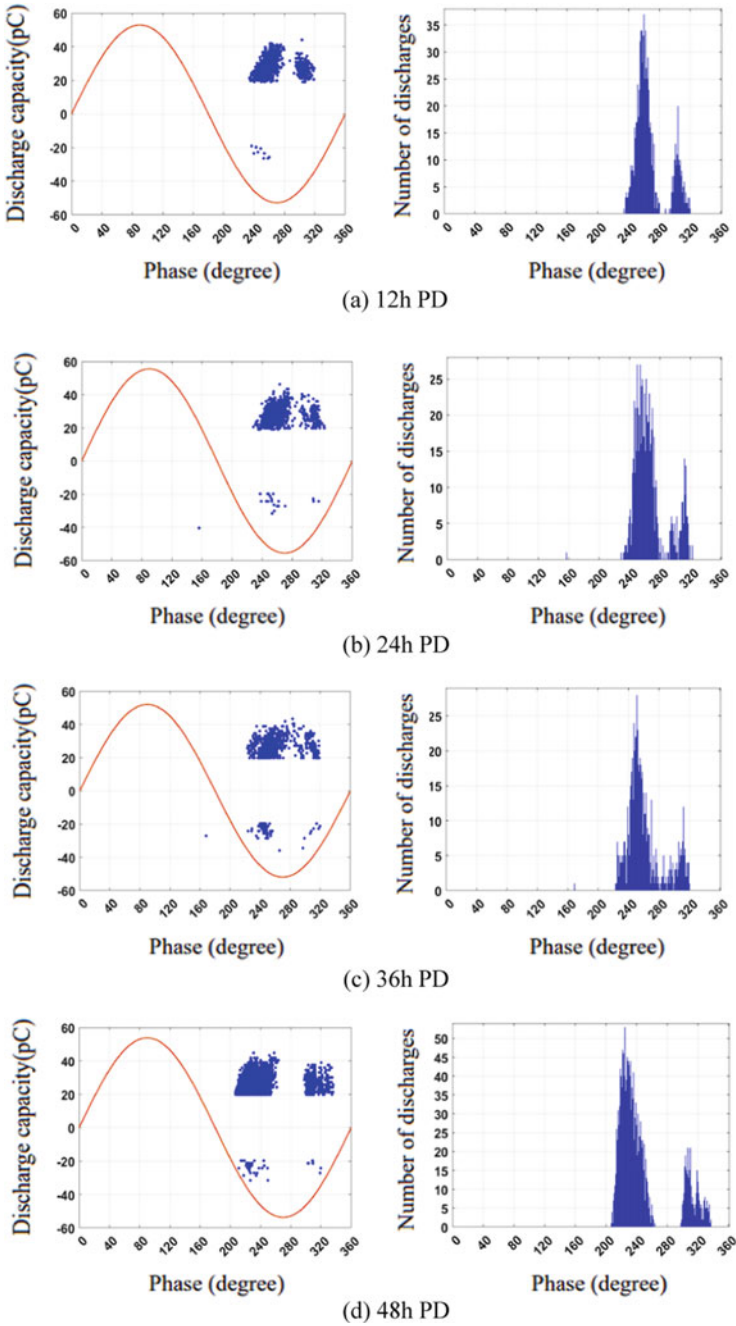


Fig. 3 PRPD spectrum of C₅F₁₀O/N₂/O₂ at 0.3 MPa

References

1. Maiss M, Brenninkmeijer CA (1998) Atmospheric SF₆: trends, sources, and prospects. *Environ Sci Technol* 32(20):3077–3086
2. Beroual A, Haddad AM (2017) Recent advances in the quest for a new insulation gas with a low impact on the environment to replace sulfur hexafluoride (SF₆) gas in high-voltage power network applications. *Energies* 10(8):1216
3. Eves M, Kilpatrick D, Edwards P, Berry J (2018) A Literature review on SF₆ gas alternatives for use on the distribution network. *Western Power Distribution*
4. Pan BF, Wang GM, Shi HM, Shen JH, Ji HK, Kil GS (2020) Green gas for grid as an eco-friendly alternative insulation gas to SF₆: a review. *Appl Sci-Basel* 10(7)
5. Mantilla JD, Claessens M, Kriegel M (2016) Environmentally friendly perfluoroketones-based mixture as switching medium in high voltage circuit breakers. *Cigre*, Paris, France
6. Simka P, Ranjan N (2015) Dielectric strength of C₅ perfluoroketone. In: 19th international symposium on high voltage engineering. Pilsen, Czech Republic
7. Tuma PE (2008) Fluoroketone C₂F₅C(O)CF(CF₃)₂ as a heat transfer fluid for passive and pumped 2-phase applications. In: Annual IEEE semiconductor thermal measurement & management symposium. San Jose, CA, USA, pp 173–179
8. Fu Y, Wang X, Li X et al (2016) Theoretical study of the decomposition pathways and products of C₅-perfluorinated ketone (C₅ pfk). *AIP Adv* 6(8):085305
9. Zhang BY, Xiang JY, Chen L et al (2020) Fundamental physicochemical properties of SF₆-alternative gases: a review of recent progress. *J Phys D-Appl Phys* 53(17):25
10. Zhang X, Li Y, Xiao S, Tang J, Tian S, Deng Z (2017) Decomposition mechanism of C₅F₁₀O: an environmentally friendly insulation medium. *Environ Sci Technol* 51(17):10127–10136
11. Hao M, Zhang B, Li X, Xiong J (2021) Electron swarm parameters and dielectric strength of C₅F₁₀O and its mixtures with CO₂ and dry air. *J Phys D Appl Phys* 55(12):125205
12. Li Y, Zhang X, Wang Y, Li Y, Zhang Y, Wei Z et al (2019) Experimental study on the effect of O₂ on the discharge decomposition products of C₅-PFK/N₂ mixtures. *J Mater Sci: Mater Electron* 30(21):19353–19361
13. Zhang Y, Zhang X, Li Y, Li Y, Chen Q, Zhang G et al (2019) Effect of oxygen on power frequency breakdown voltage and decomposition characteristics of the C₅F₁₀O/N₂/O₂ gas mixture. *RSC Adv* 9(33):18963–18970

Influence of Operating Environment on the Aging Characteristics of Composite Insulators



Dong Yang, Chengjun Xu, Jian Zhang, Jianjun Yang, Shuaiwei Wang, Sile Chen, and Zhaoquan Chen

Abstract Composite insulators are widely used in power transmission lines due to the excellent electrical properties. However, the aging effect of composite insulators can be observed after a long-term operation under the influence of various factors. In this paper, the aging characteristics of composite insulators operating for 10 years in different environments of Maanshan are studied. The surface physical and chemical properties of composite insulators are evaluated by the water contact angle, surface roughness, surface morphology, infrared spectrum and X-ray photoelectron spectroscopy, while the electrical properties are characterized by the flashover voltage, dielectric characteristics, and trap characteristics. The difference of composite insulator properties under different environment are compared. The results showed that the water contact angle and surface roughness of the aged insulators increased, and the chemical compositions are changed, resulting in the electrical performance degradation. However, the aging states of composite insulators in different environment are different. The performances of insulators operating near a steel plant with serious industrial pollution degrade obviously, while the performances of insulators operating near a closed mine pit after ecological restoration are still relatively good.

Keywords Composite insulator · Silicone rubber · Aging characteristics

D. Yang · C. Xu · J. Zhang · J. Yang · S. Wang
State Grid Anhui Electric Power Company Co.Ltd., Maanshan Power Supply Company,
Maanshan 243000, Anhui Province, China

S. Chen (✉) · Z. Chen
School of Electrical and Information Engineering, Anhui University of Technology,
Maanshan 243032, Anhui Province, China
e-mail: silechen@ahut.edu.cn

© Beijing Paiké Culture Commu. Co., Ltd. 2024
X. Dong and L. Cai (eds.), *The Proceedings of 2023 4th International Symposium on Insulation and Discharge Computation for Power Equipment (IDCOMPU2023)*, Lecture Notes in Electrical Engineering 1100, https://doi.org/10.1007/978-981-99-7393-4_44

1 Introduction

Composite insulators are widely used in power transmission lines. The excellent electrical properties and surface hydrophobicity make the composite insulators perform well in the withstanding strength of pollution and wet flashover [1, 2]. However, the anti-aging ability of composite insulators is weak compared with the ceramic or glass insulators. Under the influence of various factors, the electrical performances of composite insulators degrade after a long-term operation, which may further result in the insulation failure.

To prevent accidents caused by aging of composite insulators, researchers have done a lot of work about the aging characteristics [3, 4], insulation monitoring [5, 6] and performance improvement [7, 8] of composite insulators. Research shows that the operating environment has significant influences on the aging of composite insulators. For example, in the high humidity environment along the southeastern of China or the high-altitude mountains, the surface hydrophobicity gradually loses with the aging time increase [9, 10]. The electrical performance degradation of composite insulators during the aging process is relevant to environmental characteristics. It is necessary to model the aging characteristics of composite insulators based on the local environment.

In this paper, the composite insulators operating under several typical environments in Maanshan are sampled. The surface physical–chemical and electrical characteristics are measured. The results can provide reference for the replacement and maintenance of composite insulators in Maanshan.

2 Experimental Materials and Methods

2.1 Materials

The samples are obtained from the real composite insulators of the same type and voltage level, which have been operating for 10 years in three typical environments. The first group marked as M1 is located near the Hudongnan Road, Maanshan, which is a main road leading to the outskirts of the city with a high traffic volume. The second group marked as M2 comes from Aoshan Mine, which is a large open-pit mining site closed in 2017 because of resource depletion. The Aoshan mine has undergone ecological restoration and has been developed into a park. The third group marked as M3 is originated from the industrial factory area of Maanshan Iron and Steel Co., Ltd (Masteel) with serious pollution. In addition, the control group from new composite insulators is marked as M0.

2.2 Methods

The surface physical and chemical characteristics of composite insulator samples are evaluated by the static water contact angles (WCAs, Chengde Dingsheng, JY82A), surface roughness (Mar Surface 300C), scanning electron microscope (SEM, Tescan, MAIA3 LMH), Fourier transform infrared spectroscopy (FTIR, Bruker Vetex 70) and X-ray photoelectron spectrometer (XPS, Thermo Fisher ESCALAB Xi+). The samples are cleaned in the ultrasonic cleaner in the SEM and XPS measurements because of the instrument requirements.

The electrical characteristics of composite insulator samples are evaluated by the flashover voltage, dielectric characteristics and trap characteristics. The flashover voltages are tested using crimp-type plate electrodes with a gap distance of 5 mm under 50 Hz AC high voltage. The dielectric characteristics are measured by a dielectric response analyzer (Omicron, DI-RANA). The trap characteristics are obtained by the method of isothermal surface potential decay [11]. All the measurements are repeated for 3 times and the averages or typical results are displayed.

3 Results

3.1 Physical and Chemical Characteristics

Water contact angle. The WCAs of composite insulator samples from different groups are shown in Fig. 1a. Three samples are selected from each group, and the WCA in five random regions are measured. The WCAs of virgin samples are ranged from 110 to 120°, while the WCAs of all the aged samples are ranged from 140 to 150°. The WCAs of the aged samples increase instead of surface hydrophobicity loss, which is different from the results of those in the high humidity environment [9, 10]. It is indicated that the operating environment has significant influences on the aging characteristics of composite insulators.

Surface roughness. The arithmetic mean roughness (R_a) of the composite insulator samples from different groups are shown in Fig. 1b. Compared with the virgin samples, the R_a of all the aged samples increase obviously, especially the M2 and M3 groups. Besides, the errors of M2 and M3 groups are greater. It may result from the factors which make the roughness increase are unstable.

Surface morphology. The SEM images of the composite insulator samples from different groups are shown in Fig. 2. The surface of the virgin samples is relatively smooth with several flaws. Overall, the samples from M1 group are in good conditions, but some cracks can be observed on the surface. The situation of M2 and M3 groups are worsened. Because of the macromolecule degradation and pollutant deposition, the surface pulverization occurs with cracks and holes.

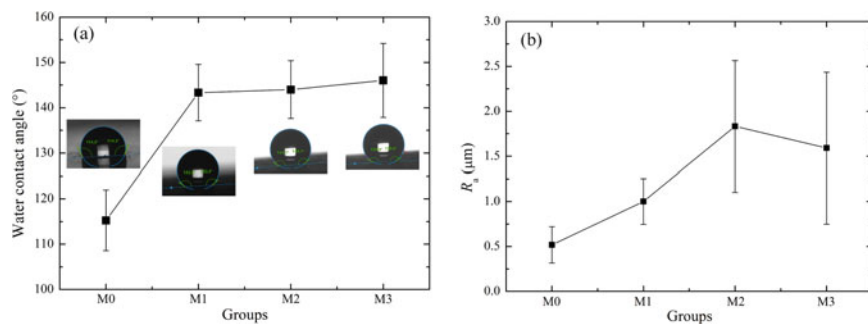


Fig. 1 The **a** WCA and **b** surface roughness of the samples from different groups

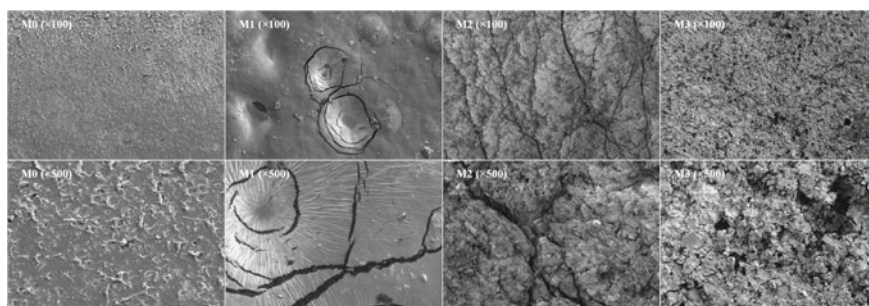


Fig. 2 The SEM images of the samples from different groups

Surface chemical composition. The surface chemical composition of the composite insulator samples from different groups are evaluated by the FTIR and XPS, which are shown in Fig. 3a, b. The functional groups, Si-(CH₃)₂, Si-O-Si, Si-CH₃, C-H and O-H are observed in the FTIR spectrum. The contents of all the functional groups in the aged samples significantly decrease, which means the molecular chains of silicone rubber are severely broken.

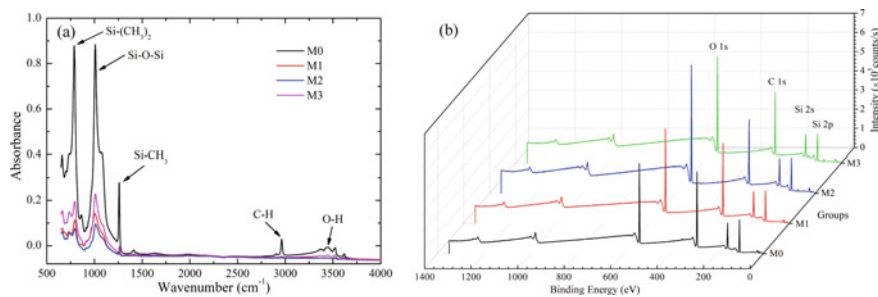


Fig. 3 The **a** FTIR and **b** XPS spectrum of the samples from different groups

Table 1 The surface chemical compositions of the samples from different groups

Groups	Chemical composition (Atom%)			
	C 1 s	O 1 s	Si 2 s	Si 2p
M0	42.44	19.11	19.27	19.38
M1	42.71	20.34	18.41	18.54
M2	32.56	29.59	18.90	18.95
M3	36.80	25.80	18.30	19.00

The O 1 s, C 1 s, Si 2 s and Si 2p peaks are observed in the XPS spectrum. The content (atomic rate) of each element is listed in Table 1. The silicon content of the aged samples is slightly lower than that of the virgin samples, which means the fracture and loss of silicone rubber molecules. Considering the ultrasonic cleaning before XPS measurement, the silicon content of the outermost pollutant layer is even lower. The carbon and oxygen contents of samples from M1 group are similar to those of virgin samples. However, in the M2 and M3 groups, the carbon content decreases while the oxygen content increases.

3.2 Electrical Characteristics

Flashover voltage. The flashover voltages of samples from different groups are tested and shown in Table 2. Three samples are selected from each group, and the test for each sample is repeated for three times. The average values are taken into account. The flashover voltages of aged samples are slightly lower than those of the virgin samples from the results. The flashover voltage errors of M2 and M3 groups are obviously higher. It is considered that the aging of M2 and M3 groups on the surface is nonuniform, which is similar to that of surface roughness. Moreover, the greater error indicates the greater dispersion of flashover voltage, which is probable due to the insulation weakness on the surface.

Dielectric characteristics. The relative dielectric constant (ϵ_r) and dielectric loss tangent ($\tan \delta$) of the samples from different groups are shown in Fig. 4a, b. The ϵ_r and $\tan \delta$ of the aged samples are higher than those of the virgin samples, especially in low frequency. Among the aged samples, the samples from M3 group have the highest ϵ_r and $\tan \delta$, followed by M1 group. Notably, the ϵ_r and $\tan \delta$ of the samples

Table 2 The AC flashover voltage of the samples from different groups

Groups	M0	M1	M2	M3
Flashover voltage (kV)	11.18 ± 0.25	10.88 ± 0.21	10.90 ± 0.35	10.73 ± 0.58

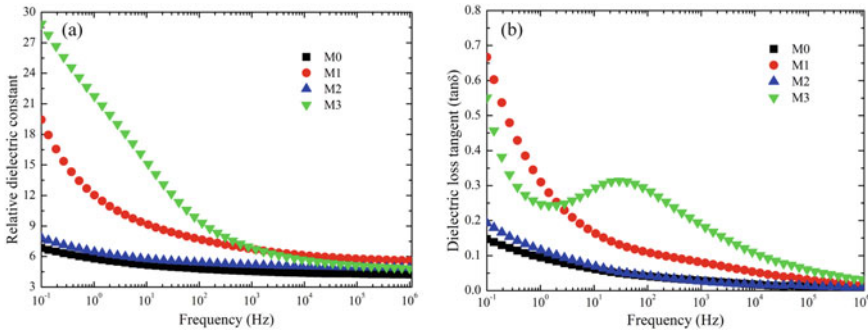
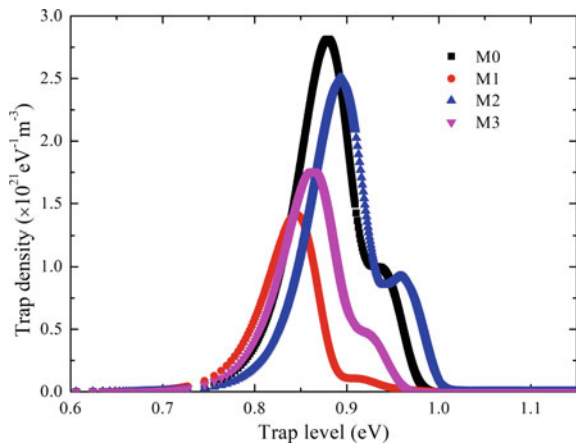


Fig. 4 The **a** relative dielectric constant and **b** dielectric loss tangent of the samples from different groups

from M2 group is only slightly higher than those of the M0 group. It means the electrical performance of the samples from M2 group is still relatively good.

Trap characteristics. The surface trap characteristics of samples from different groups are shown in Fig. 5. The trap densities of the samples from M2 group are slight lower than those of virgin samples, which are on the order of $10^{21} \text{ eV}^{-1} \text{ m}^{-3}$. The maximum trap densities of the samples from M1 and M3 group obviously decrease, about 50–60% of those of the virgin samples. The higher trap density is responsible for the quicker dissipation rate of surface charge, further reducing the flashover caused by the electric field distortion from surface charge. Therefore, the samples from M2 group show good performance. Among all the samples, the difference in energy levels corresponding to the maximum trap density is not significant.

Fig. 5 The surface trap characteristics of the samples from different groups



4 Discussion

In this paper, the samples are taken from the real composite insulators of the same type and voltage level, which is aged for 10 years. Therefore, the difference in insulation performance of the samples mainly results from the different operating environments. The main pollutants of M1 group are nitrogen oxides and particulate matters from the passing vehicles. The pollution is relatively light but long-lasting and stable. The samples from M2 group are heavily contaminated with dusts and particulate matters. Due to the open space and topographical difference around the mine pit, the insulators also need to withstand wind erosion and stress. However, the harsh environment only accounts for about half of the operating time. After the ecological restoration, the mine pit is developed into a park with green plants and oxygen-rich environment, which can be inferred from the oxygen content of the XPS spectrum. The environment of M3 group near the Masteel plant is the worst, which contains large amounts of dusts, particulate matters, nitrogen oxides, sulfide, fluoride, smoke and so on. The amounts of pollutants depend on the output of steel.

From the results of the aging characteristics, the samples from M3 group have the worst overall performances, especially the surface morphology, flashover voltage and dielectric characteristics. It is considered that the polluted environment affects the aging characteristics, reducing the electrical performances. The overall performances of the samples from M1 group also degrades obviously compared with those of virgin samples but better than those of M3 group. It means that long-term mild pollution also has important influences on the performances. Among the aged samples, the samples from M2 group present relatively good performances like dielectric and trap characteristics. Though the samples from M2 group are in the harsh environments for nearly half of the operating time, they are operating in a good environment for the other half time. Therefore, a good environment can extend the lives of composite insulators.

Different operating environments have different influences on the performances of composite insulators. In Maanshan, the WCAs of the samples from aged insulator increase compared with those of virgin samples, which is different from the results in coastal areas. The reason may be that the multiple pollutants deposit on the surface of insulators and form the new hydrophobic structures. Considering the environmental characteristics, once the WCAs of the insulators obviously deviates from the normal value (not just the decrease in WCAs), attention should be paid for the insulation status.

5 Conclusion

In this paper, the composite insulators operating for 10 years in three typical environments of Maanshan are sampled. The surface physical and chemical properties, and the electrical characteristics of the samples are measured and analyzed. The main conclusions are as follows:

- (1) The performances of composite insulators decrease with increasing operating time, and the environment has significant influence on the aging characteristics.
- (2) A good environment can delay the aging process of composite insulators, while a polluted environment can accelerate the performance degradation.
- (3) Different environments have different influences on the performances of composite insulators. In Maanshan, the WCAs of insulators increase over time. It is proposed to pay timely attention to the insulation status once the WCAs deviates from the normal value.

Acknowledgements This work is partly supported by the National Science Foundation of China (Grant Nos. 52207147 and 52177126), and the Anhui Provincial Natural Science Foundation (Grant No. 2208085QE168).

References

1. Zeng Z, Guo P, Zhang R et al (2023) Review of aging evaluation methods for silicone rubber composite insulators. *Polymers* 15:1141
2. Akbar M, Ullah R, Alam S (2019) Aging of silicone rubber-based composite insulators under multi-stressed conditions: an overview. *Materials Res Exp* 6:102003
3. Li X, Zhang S, Chen L et al (2022) A study on the influence of end-sheath aging and moisture absorption on abnormal heating of composite insulators. *Coatings* 12:898
4. Chen L, Guo F, Yang T et al (2021) Aging characteristics and self-healing properties of laser-textured superhydrophobic silicone rubber for composite insulators. *Polymer Degradation Stability* 192:109693
5. Li B, Li H, Zhao B (2022) Non-destructive aging evaluation of 500-kV field-serviced silicone rubber composite insulators with photothermal radiometry. *J Appl Phys* 131:075108
6. Qiao X, Zhang Z, Jiang X et al (2019) A new evaluation method of aging properties for silicon rubber material based on microscopic images. *IEEE Access* 7:15162–15169
7. He W, Zhang F, Zhang F et al (2023) Effect of CeO₂ on UV aging of composite insulators prepared by template-spraying method. *J Appl Polym Sci* 140:e53274
8. Rashid A, Saleem J, Amin M et al (2021) Long-term aging characteristics of co-filled nano-silica and micro-ATH in HTV silicone rubber composite insulators. *Polym Polymer Comp* 29:40–56
9. Zhou J, Fang Y, Deng Y et al (2020) Ageing characteristics of silicone rubber for composite insulator in southeast coastal area. *Insulat Mat* 53(3):14–21 (In Chinese)
10. Zhang Z, Zhang Y, Jiang X et al (2020) Study on aging characterization methods of composite insulators aging in natural environment for different years. *Trans China Electrotech Soc* 35(6):1368–1376 (In Chinese)
11. Shen W, Mu H, Zhang G et al (2013) Identification of electron and hole trap based on isothermal surface potential decay model. *J Appl Phys* 113(8):083706

Self-Powered Insulating Oil Condition Monitoring System Based on Oil-Solid Contact Electrification



Xiangyu Tan, Fangrong Zhou, Zhimin Na, Ran Zhuo, Dibo Wang, Haoying Wu, Song Xiao, and Yi Li

Abstract Insulating oil condition monitoring is one of the important ways of ensuring stable operation of power system, however, the existing detection methods can't achieve real-time online detection. In this paper, a tubular oil solid triboelectric nanogenerator is designed and a self-powered real-time online sensing system for insulating oil condition is constructed. The output performance characterization platform was built, which can realize the accurate perception of pA level tiny current and meet the measurement accuracy of the output signal of oil-solid contact electrification. We tested the influence of oil flow rate on output performance, and found that the output current is approximately proportional to the flow rate in the range of 100–500 ml/min. Finally, the sensitivity of the sensor system is verified by the micro-water response test results, and the detection accuracy can reach 10 ppm. Relevant research results are of great significance for the construction of micro-water sensing system in insulating oil and the improvement of intelligent operation and maintenance level of transformer.

Keywords Contact electrification · Oil condition · Triboelectric nanogenerator

X. Tan · F. Zhou

Power Science Research Institute of Yunnan Power Grid Co., Ltd, Kunming 650214, China

Z. Na

Qujing Power Supply Bureau of Yunnan Power Grid Co., Ltd, Qujing 655099, China

R. Zhuo · D. Wang

Electric Power Research Institute, China Southern Power Grid, Guangzhou 510623, China

H. Wu (✉) · S. Xiao · Y. Li

School of Electrical Engineering and Automation, Wuhan University, Wuhan 430072, China

e-mail: wuhaoying@whu.edu.cn

© Beijing Paiké Culture Commu. Co., Ltd. 2024

X. Dong and L. Cai (eds.), *The Proceedings of 2023 4th International Symposium on Insulation and Discharge Computation for Power Equipment (IDCOMPU2023)*, Lecture Notes in Electrical Engineering 1100, https://doi.org/10.1007/978-981-99-7393-4_45

473

1 Introduction

With the development of intelligent and informatization construction of power grid, the state perception of transmission and distribution equipment represented by oil-immersed transformer has higher requirements. As the “blood” of oil-immersed transformer, the condition of insulating oil has always been an important source of information. Analyzing the content of impurities such as trace water is one of the main methods to monitor the life cycle of oil, and it is also an important means to monitor the internal potential faults of equipment. At present, the main detection methods of trace water include Coulomb method, gas chromatography, etc. [1, 2], but they have shortcomings such as complex detection system, complicated operation, and inability to achieve on-site real-time detection, which limits the use scenario and cannot ensure the timeliness of detection.

Contact electrification is a phenomenon that describes the charge transfer that occurs when two interfaces come into contact, which occurs at the solid–solid interface as well as at the liquid–solid interface [3–5]. Triboelectric nanogenerators based on liquid–solid contact electrogenicity can convert dispersed and multi-source mechanical energy into electrical energy in the environment. At the same time, the response characteristics of the output signal are jointly determined by the liquid and solid interface, so the output signal can also be used as the sensing signal, realizing the self-powered sensing without external power supply of physical and chemical quantity of insulating oil [6–9]. When the insulating oil contains a trace amount of water, the output signal will change compared with the pure insulating oil because the water molecules change the charge distribution at the oil–solid contact interface and the formation process of electric double layer [10, 11]. Based on the oil–solid contact electrification, the kinetic energy of oil flow in the process of forced oil circulation of insulating oil under actual working conditions was collected, and the self-powered insulating oil condition sensing system was constructed, which could realize the real-time online detection of trace water in insulating oil.

In this paper, we designed a tubular oil–solid triboelectric nanogenerator and build an insulating oil condition testing system as self-powered sensor for trace water detection in transformer oil. In this paper, we designed a tubular oil–solid triboelectric nanogenerator, and built a performance characterization platform to realize self-powered oil state sensing. Firstly, we designed a tubular triboelectric nanogenerator and its performance characterization platform, which can simulate the transformer oil channel and measure the oil–solid contact signal. Secondly, the influence of oil flow rate on the output characteristics was studied, and the influence of the inner working conditions of the real transformer on the output characteristics was simulated. Finally, we tested the response characteristics of the sensing system to the moisture content in the insulating oil, which verified the high sensitivity of the developed sensing system.

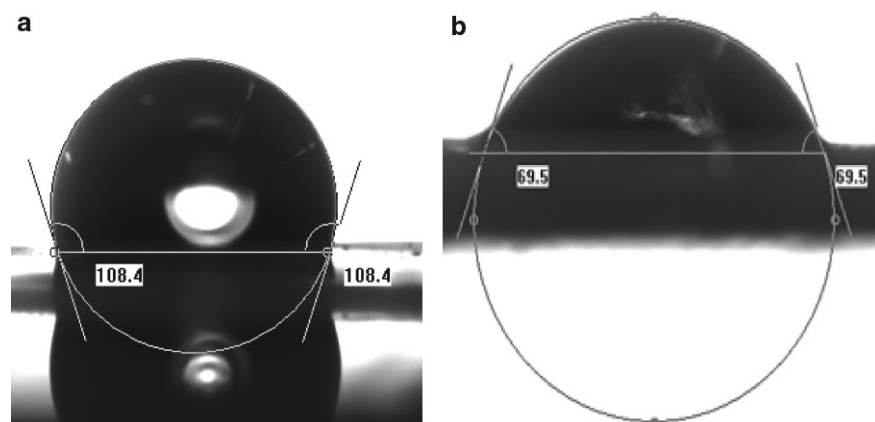


Fig. 1 Oil contact Angle of the FEP film **a** treated, **b** untreated

2 Results and Discussion

2.1 Material

The friction layer materials of triboelectric nanogenerator are mainly polymer films, which have strong electronegativity and are often hydrophobic. However, for insulating oil with low surface tension, these materials are lipophilic. When the oil flow flows through, there will be oil stains remaining, which will affect or even shield the output signal. Therefore, in this paper, by spraying 1H,1H,2H,2H-Perfluorodecyltriethoxysilane on the surface of FEP film to reduce its surface energy, we can avoid the production of oil stains and improve the output performance. The contact Angle between 25# transformer oil and film before and after treatment is shown in Fig. 1. After spraying, the oil contact Angle of the film is increased from 69.5° to 108.4°.

2.2 Tubular Triboelectric Nanogenerator

The tubular triboelectric nanogenerator designed in this paper was shown in Fig. 2a. The tubular triboelectric nanogenerator consist of three layers: the inner layer was FEP film with strong electronegativity, which was used for charge transfer; The middle layer was a layer of gold-plated electrodes that conduct triboelectric charges to the measuring system through electrostatic induction, and the outermost layer was a layer of nylon tubes that act as supports and anchors.

In this paper, a 10 cm long nylon tube with an inner diameter of 6 mm and an outer diameter of 8 mm was used to simulate the transformer oil passage, and gilded FEP

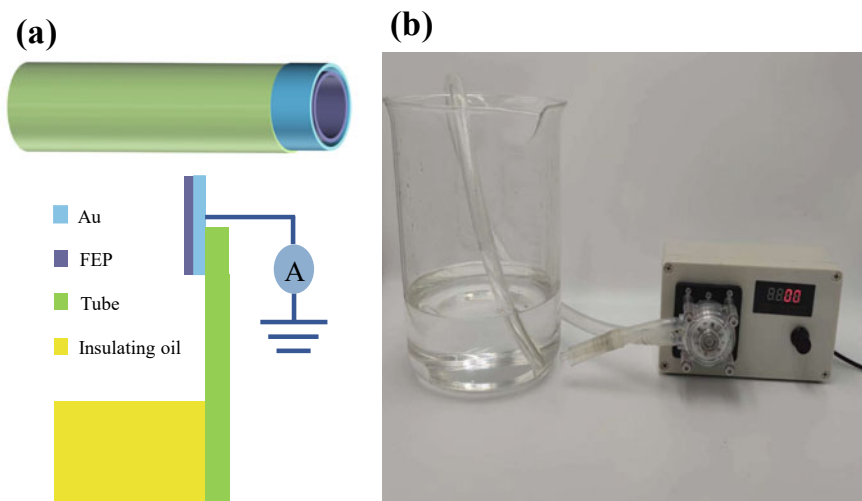


Fig. 2 The tubular triboelectric nanogenerator **a** structure, **b** photograph of the measuring platform

film was pasted inside to make a tubular triboelectric nanogenerator. The thickness of the FEP film is 0.1 mm and the length is 2 cm. The gold electrode is made by using magnetron sputtering on the back of the FEP film for 100 s, and the thickness is about 0.05 mm.

Figure 2b shows the measuring platform of the triboelectric nanogenerator. The platform consists of a peristaltic pump, a tubular triboelectric nanogenerator, and a nylon tube. The peristaltic pump adopts three coaxial stepper motor, adjustable speed range is 0–610 ml·min⁻¹, flow error is less than 1%. The peristaltic pump is connected to the triboelectric nanogenerator through a silicone tube with weak electronegativity. The measuring device is a high resistance meter (Keithley 6517B). Its working principle is as follows: oil flow is driven through the current meter by an adjustable peristaltic pump to control and record the oil flow velocity; The oil flow enters the nylon tube through the tubing. Then the oil flow contacts the tubular triboelectric nanogenerator and generates charge transfer. The electrical signal output is measured by the high resistance meter. The output signal of the high resistance meter is imported into the oscilloscope, and the output result is displayed by the computer; After the oil flow through the pipeline, through the earth electrode to neutralize the charge of the oil flow, back to the peristaltic pump, start a new cycle process.

The charge transfer principle of triboelectric nanogenerator is described in Fig. 3. Figure 3a, b shows the initial triboelectrical charge transfer process from the initial oil-free stage to the triboelectrical interface charge saturation state. In this process, the initial small amount of oil flow will contact and charge the uncharged FEP film, resulting in the FEP film the negative charged, while the oil flow near the film has the same amount of positive charge adsorbed near the film. Subsequently, when the

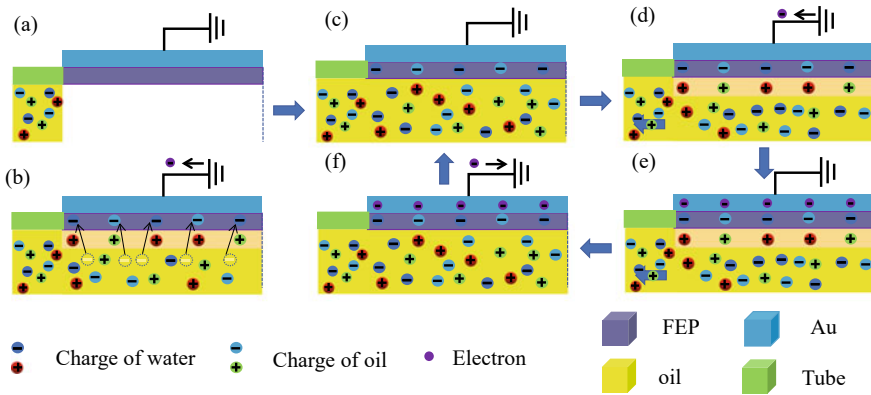


Fig. 3 The working principle of the tubular triboelectric nanogenerator

initial oil flow flows out and the subsequent uncharged oil flow continues to flow in, the negatively charged film will attract the charge in the oil to form electric double layer (Fig. 3d). Due to the electrostatic induction effect, the electrons on the gold electrode flow from the earth to the electrode region until they reach a new equilibrium state (Fig. 3e). Then, as the oil in this part flows out of the pipeline, the electrons generated by electrostatic induction effect on the gold electrode flow back to the earth, the negative charge on the gold electrode gradually decreases Fig. 3f), and finally returns to the initial state (Fig. 3c), and restarts a new oil flow cycle process.

2.3 Output Characteristic

In this paper, the effects of flow rate on output characteristics are tested. Figure 4a shows that the output current of the tubular triboelectric nanogenerator is almost proportional to the flow rate in the flow range from 100 to 500 ml/min. The flow rate of oil flow is reflected in the charge transfer process described in Fig. 3 as the cycle period. The larger the flow rate, the shorter the cycle required by the cycle process, and the higher the output charge within the same time. Therefore, the external output current is approximately proportional to the flow rate.

2.4 Trace Water Detection

The short-circuit current response of the tubular oil-solid triboelectric nanogenerator containing 10–100 $\mu\text{L.L}^{-1}$ trace water at a flow rate of 100 mL.min^{-1} is showed in Fig. 4b, the output response of insulating oil containing only 10 ppm of trace water is about 35% higher than that of pure insulating oil, indicating that the system

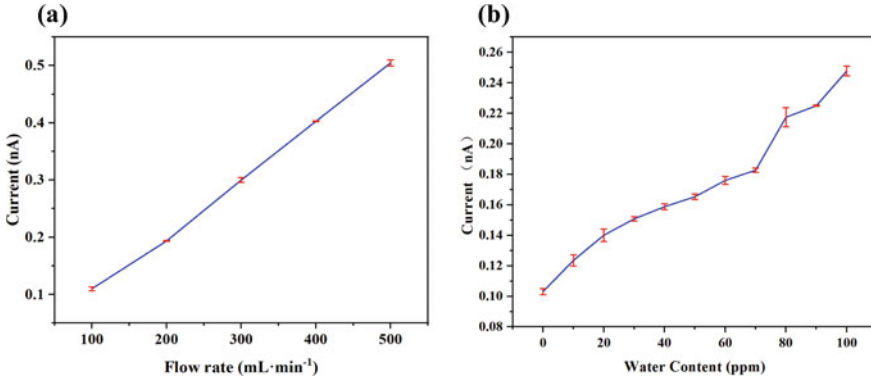


Fig. 4 The short-circuit current response of the tubular triboelectric nanogenerator **a** insulating oil containing 10–100 $\mu\text{L}\cdot\text{L}^{-1}$ trace water

has excellent sensitivity to sensing trace water in insulating oil. When the water content increases gradually, the output current signal also increases gradually, and the two have strong positive correlation. This conclusion lays a theoretical foundation for further research on moisture content in insulating oil and sensing system, and provides guidance for constructing inversion relationship between response parameters and moisture content, so as to realize the monitoring of moisture content in insulating oil (Fig. 4).

3 Conclusion

In this work, an oil-solid triboelectric nanogenerator with tubular structure was developed based on oil-solid contact electrification, and a self-powered sensor was constructed, which could be used to monitor the condition of insulating oil and realize the high sensitivity detection of trace water. We designed a tubular triboelectric nanogenerator and built a performance characterization test platform to reveal the influence of different flow rates on the output characteristics, and measured the output response characteristics corresponding to the change of trace water content in insulating oil. The developed sensor has successfully realized the real-time online monitoring of water content in insulating oil, and can serve the needs of the new power system for the panoramic information perception and intelligent operation and maintenance of transmission and distribution equipment.


Acknowledgements This work was supported by the science and technology project of China Southern Power Grid (Grant number YNKJXM20222118, YNKJXM20222131, YNKJXM20222043).

References

1. Yao Y, Li Y, Pan C, Tang J et al (2022) Motion behaviours and PD characteristic of free metallic particles in flowing transformer oil with paper-covered electrodes. *IET Gener Transm Distrib* 16(13):2559–2572
2. Pan C, Tang J, Tao X et al (2018) Partial discharge and breakdown characteristics of moving transformer oil contaminated by metallic particles. *IEEE Trans Dielectr Electr Insul* 25(5):1774–1784
3. Wang ZL (2021) From contact electrification to triboelectric nanogenerators. *Reports Prog Phys* 84(9): 096502
4. Wang ZL (2020) Triboelectric nanogenerator (TENG)—sparking an energy and sensor revolution. *Adv Energy Mat* 10(17):2000137
5. Kim WG, Kim DW, Tcho IW et al (2021) Triboelectric nanogenerator: Structure, mechanism, and applications. *ACS Nano* 15(1):258–287
6. Loh ZH, Doumy G, Arnold C et al (2020) Observation of the fastest chemical processes in the radiolysis of water. *Science* 367(6474):179–182
7. Zhou Q, Pan J, Deng S, et al (2021) Triboelectric nanogenerator-based sensor systems for chemical or biological detection. *Adv Mat* 33(35):2008276
8. Chang A, Uy C, Xiao X, et al (2022) Self-powered environmental monitoring via a triboelectric nanogenerator. *Nano Energy*, 107282
9. Li C, Liu X, Yang D et al (2022) Triboelectric nanogenerator based on a moving bubble in liquid for mechanical energy harvesting and water level monitoring. *Nano Energy* 95:106998
10. Zhao J, Wang D, Zhang, F et al (2022) Self-powered, long-durable, and highly selective oil–solid triboelectric nanogenerator for energy harvesting and intelligent monitoring. *Nano-Micro Lett* 14(1):160
11. Zhao J, Wang D, Zhang F et al (2021) Real-time and online lubricating oil condition monitoring enabled by triboelectric nanogenerator. *ACS Nano* 15(7):11869–11879

Research on Fast Calculation Method of Lightning Distribution in Mountainous Area Based on Conformal Mapping



Nengxing Guo , Ruifang Li, Qian Lei, Jiayu Zhao, Chengzhi Li, Yujing Liang, and Xiaobin Cao

Abstract The study of lightning distribution is crucial for implementing differentiated lightning protection measures, with lightning channel simulation serving as the foundation for such research. Particularly in mountainous areas, lightning protection presents unique challenges due to complex terrain. However, current numerical calculation methods for simulating lightning channels in mountainous regions suffer from lengthy computation times that fail to meet the requirements of lightning distribution research. Additionally, existing lightning channel models are overly simplified, necessitating the exploration of faster and more accurate simulation methods. To address these limitations, this paper proposes a rapid calculation approach utilizing conformal mapping to project the mountainous electric field onto flat terrain, resulting in accelerated computation speeds. The accuracy of the electric field calculation is verified using COMSOL. Furthermore, a Cooray distribution-based lightning channel model is employed to represent the spatial characteristics of mountainous regions. Combining fractal theory, the study simulates lightning channels within mountainous terrains and efficiently calculates the lightning distribution in typical mountainous topographies. The results demonstrate a significant reduction in lightning strike time to 10 s when employing the Cooray distribution-based lightning channel model, which exhibits paths and distribution closer to actual observations compared to uniformly distributed lightning channels. The findings of this study provide valuable insights for future differentiated lightning protection in mountainous areas.

Keywords Cooray lightning channel · Conformal mapping · Rapid calculation · Typical mountain

N. Guo (✉) · R. Li · Q. Lei · J. Zhao · C. Li · Y. Liang · X. Cao
Southwest Jiaotong University, Chengdu 611756, China
e-mail: 2500641313@my.swjtu.edu.cn

© Beijing Paiké Culture Commu. Co., Ltd. 2024
X. Dong and L. Cai (eds.), *The Proceedings of 2023 4th International Symposium on Insulation and Discharge Computation for Power Equipment (IDCOMPU2023)*, Lecture Notes in Electrical Engineering 1100, https://doi.org/10.1007/978-981-99-7393-4_46

1 Introduction

Research on lightning protection, particularly in mountainous areas, is crucial due to the complex terrain and the need for effective strategies [1]. Lightning distribution studies rely on simulating lightning channels and calculating electric fields [2–5]. Previous studies by Yao et al. and Tao et al. considered terrain impact but had over-simplified lightning channel models and time-consuming field calculations [6]. To address this, faster and more accurate methods are needed. Analytical and numerical methods are used to calculate electric fields, with conformal mapping theory transforming complex boundaries [7]. Cooray et al. developed a dynamic simulation model considering space charge influence on lightning initiation and propagation [8]. This study aims to use a coordinate transformation method based on conformal mapping to accelerate the calculation of lightning distribution in mountainous terrain, specifically focusing on the Cooray charge distribution channel.

2 Conformal Mapping Function

2.1 Mapping Function for Typical Mountainous Terrain

In mountainous regions, when dividing the area into a two-dimensional plane from a vertical cross-section, the boundary curve of the mountains is composed of basic mountain shape functions (such as valleys, ridges, etc.). When calculating the electric field in actual mountainous areas, the boundary curve is first extracted, and then a suitable conformal mapping function is selected to map the undulating mountain curve to a straight line. At the same time, the mountainous region is mapped to the space above the straight line, and the problem of electromagnetic field with a complex boundary is transformed into a problem with a simple boundary. The key to this simplification lies in the mapping function. In this analysis, the conformal mapping function for basic mountain shapes is examined, where the basic mountain shapes include valleys and ridges, both of which exhibit a symmetric pattern [9].

For valleys and ridges, we choose the following conformal mapping formulas [4]:

$$\begin{cases} w = \sqrt{z^2 + d^2} & \text{valleys} \\ w = \sqrt{z^2 - d^2} & \text{ridges} \end{cases} \quad (1)$$

In the equation, $w = u + iv$ and $z = x + iy$. Here, u and v represent the horizontal and vertical coordinates in the w -plane, while x and y represent the horizontal and vertical coordinates in the z -plane. d is a conformal mapping parameter used to control the size of the mountain shape.

The analytical expression for the shape of the ridge in the z -plane can be obtained as follows:

$$y = v \cdot \sqrt{1 + \frac{d^2}{v^2 + x^2}} \tag{2}$$

The variable v in Eq. (2) represents an equipotential surface in the w -plane. When $v = c$ is a constant, it corresponds to a horizontal equipotential surface parallel to the u -axis in the w -plane. This equipotential surface is mapped onto the z -plane through the conformal mapping function, representing the boundary of the mountain. In this case, the undulating mountain shape curve is transformed into a flat straight boundary, and Eq. (2) is accordingly rewritten as:

$$y = c \cdot \sqrt{1 + \frac{d^2}{c^2 + x^2}} \tag{3}$$

According to Eq. (3), the conformal mapping parameters c and d jointly determine the shape of the terrain mountain simulation model. When x approaches infinity and y equals c , Eq. (3) has an asymptote line $y = c$, which can be considered as the horizon. When $x = 0$, we can obtain $y = \sqrt{c^2 + d^2}$, establishing a relationship between the mountain height and the conformal mapping parameters.

$$H = \sqrt{c^2 + d^2} - c \tag{4}$$

The shape of the ridge determined by Eq. (4) is illustrated in Fig. 1.

The height H of the mountain can be obtained through actual measurements. The choice of ground elevation values will affect the calculation results of the slope. To avoid this influence, this paper adopts the ratio of half the mountain height to half the width of the mountain waist for calculation, as shown in Fig. 2.

As shown in Fig. 2, when $y = \frac{H}{2} + c$, Eq. (2) can be solved to obtain the half-width L :

$$L = 2 \cdot \sqrt{\frac{4c^2d^2}{H^2 + 4Hc} - c^2} \tag{5}$$

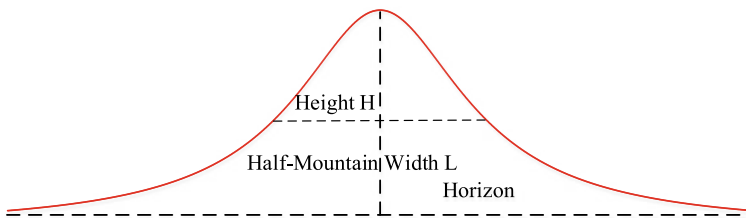


Fig. 1 Ridge shape diagram (mountain height)

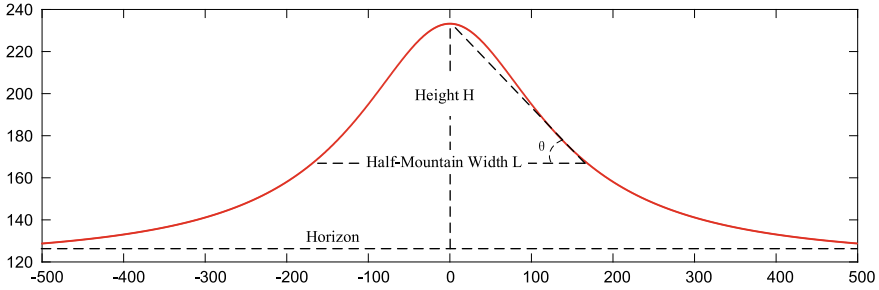


Fig. 2 Ridge shape diagram (mountain slope)

By combining Eqs. (3), (4), and (5), we can solve the following system of equations:

$$\begin{cases} d = \sqrt{H^2 + 2cH} \\ 16c^3 + 12c^2H - 4cL^2 - L^2H = 0 \end{cases} \quad (6)$$

According to the above formulas, if the parameters c and d of the mountain mapping function are known, we can use Eq. (6) to solve for the actual mountain height H and half-width L , thus determining the actual shape of the mountain. In this way, we can use the conformal mapping function to solve the corresponding electrostatic field problems.

Let’s consider a point charge Q located at coordinates (x_0, y_0) above the ridge. In the transformed space after conformal mapping, where the mountain boundary becomes a horizontal line, the charge remains the same, but the coordinates transform to (u_0, v_0) , and any point in space transforms to (u, v) .

2.2 Accuracy Verification

Introduce a static electric charge in the z -plane space and calculate the potential values of points in the mountainous space using the mapping function.

Considering an actual basic mountain ridge with a height of 316 m and a half-width of 153 m, we can solve for the parameters of the mapping function, $d = 300$ and $c = 100$, using Eq. (6). Taking a point charge of 1C located at coordinates $(0, 1000)$, we calculate the spatial electric field using the ridge conformal mapping function in MATLAB. Additionally, using the finite element simulation software COMSOL with the same parameters, we simulate the aforementioned three-dimensional mountain model. The simulated results of the potential in the xz -plane due to the point charge are shown in Fig. 3.

To validate the accuracy of the algorithm results, we selected several points along the z -axis in Fig. 3, using the same parameters as those used in the conformal mapping

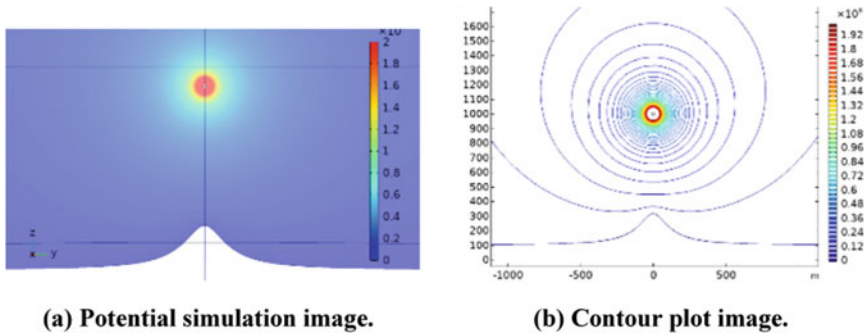


Fig. 3 Electric field results

Table 1 Comparison of potential simulation results of three-dimensional mountain model

Z-axis	Simulation result (V)	Conformal mapping result (V)	Relative error (%)
600	1.579×10^7	1.36×10^7	0.138
700	2.4042×10^7	2.15×10^7	0.105
800	3.9516×10^7	3.63×10^7	0.081
900	8.4962×10^7	7.97×10^7	0.062

and finite element simulation. We compared their potential values with the results obtained from the conformal mapping algorithm. The specific data are presented in Table 1.

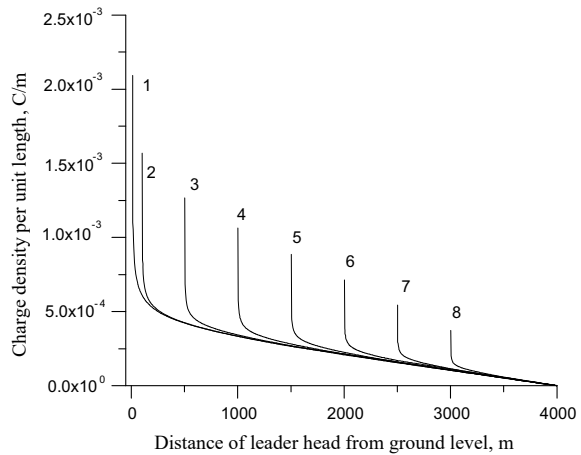
By observing Table 1, we can see that the numerical results obtained from conformal mapping are very close to the results of the finite element simulation for the three-dimensional rotating model. The contour plots of the two methods exhibit a striking similarity, and the relative errors in potential values at each point are relatively small. This result confirms the accuracy of the algorithm.

3 Cooray Distribution

3.1 Simulation of the Lightning Channel

When the leader tip is located at different heights, the charge distribution along the leader channel varies. As the leader propagates downward, the channel charge density is highest at the leader head. As the leader head moves downward, the charge density in the channel gradually decreases and eventually approaches the value corresponding to a fully developed leader channel. Figure 4 illustrates the charge distribution along the leader channel when the tip is located at different heights above the ground.

Fig. 4 Charge distribution along the lightning channel at different heights of the leader head above the ground: (1) 10 m, (2) 100 m, (3) 500 m, (4) 1000 m, (5) 1500 m, (6) 2000 m, (7) 2500 m, and (8) 3000 m



In this paper, we set the height of the thundercloud to be 4000 m and the ground range to be 1000 m. The two-dimensional plane is divided into multiple grids, and the simulation range is 4000 × 1000. To establish and validate the fractal development model of lightning leaders, we need to determine the parameters for each step of the downward leader development, including the step size, the amplitude of the lightning current, the starting position of the lightning leader, and the threshold criteria for transitions. By utilizing the aforementioned formulas, the lightning channel path for a mountain with a height of 316 m and a half-width of 153 m was simulated, as depicted in Fig. 5.

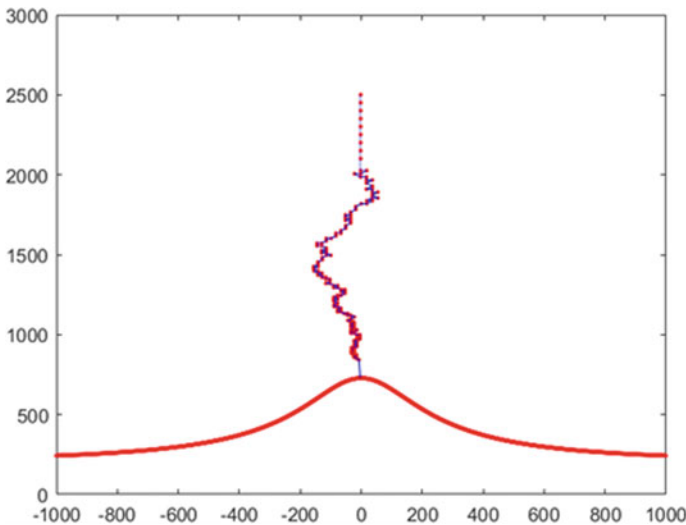


Fig. 5 Simulation results of lightning leader channel

3.2 *Dispersy of Lightning Channels and Distribution of Lightning Strikes*

The comparison between the uniform distribution and the Cooray distribution is shown as follows:

The lightning channel simulated with a uniform distribution exhibits the following characteristics:

(1) Uniform charge distribution:

In the lightning channel, the charge is evenly distributed, meaning that each point in the channel carries the same amount of charge.

(2) Decreasing contribution of the leader head to the development direction:

In the early stages of lightning development, the leader head contributes significantly to the charge, but as the lightning progresses, the uniform charge distribution in the entire channel causes the contribution of the leader head's charge to decrease. The proportion of charge from the leader head gradually decreases, while the proportion of charge from the developed channel increases. Therefore, the contribution of the leader head to the electric field in the next step of development becomes much smaller compared to the already developed channel. As a result, the lightning channel simulated with a uniform distribution exhibits a more concentrated morphology and lower dispersion.

The range and variance of the abscissa for both distributions were calculated. The range of the abscissa for the uniform distribution is 44, with a variance of 113.9373. The range of the abscissa for the Cooray distribution is 123, with a variance of 1067.7205.

In the early stages of lightning development, the Cooray distribution creates high charge density regions in the lightning leader's head. These regions attract surrounding charges, leading to charge accumulation effects, making the electric field generated by the leader's head a decisive factor for the subsequent development. This results in the spatial discontinuity and dispersion of the lightning channel path. Simulating the lightning channel using the Cooray distribution accurately reflects the distribution of charges in real lightning channels, and its morphology is more dispersed compared to a uniform distribution.

Under the same conditions except for the charge distribution, namely uniform distribution and Cooray distribution, 100 simulations of the lightning channel were conducted. The simulated paths are shown in Fig. 6. The distribution and timing of lightning strikes were recorded and compared with the results obtained from finite element simulations, as presented in Table 2.

The lightning channel was modeled with a uniform distribution, and electric field simulation was conducted using both conformal mapping and finite element methods. The finite element method took 540 s to simulate the entire path of a uniform distribution lightning channel. Conversely, the conformal mapping approach considerably reduced the computational time for a single lightning simulation compared to the

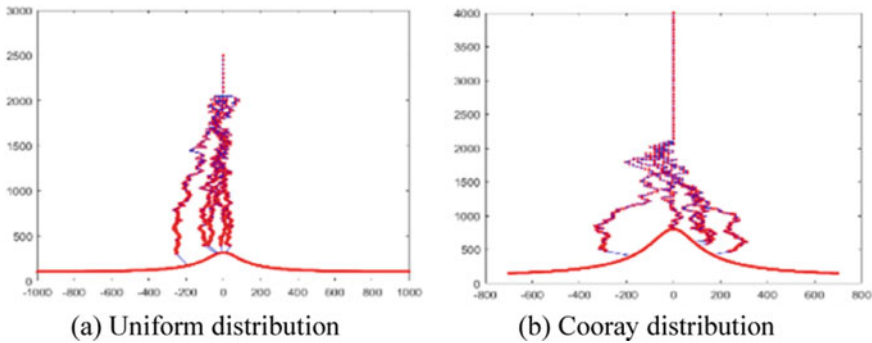


Fig. 6 Lightning leader simulation with two channel charge distributions

Table 2 Lightning distribution and time comparison

	Uniform distribution	Uniform distribution in finite element method	Cooray distribution
Time (s)	3	540	10
Horizontal variance of paths	113	–	1067
Range of lightning strikes (m)	–100 to 100	–	–280 to 380

finite element method. Employing conformal mapping for calculating the electric field in lightning distribution significantly speeds up computations in mountainous regions.

4 Conclusion

In this study, we applied the conformal mapping function to map the electric field of a typical mountainous terrain onto a flat terrain in a two-dimensional plane. The accuracy of the electric field calculation was validated using the finite element method. By combining the Cooray lightning channel charge distribution with the conformal mapping function, we derived the charge distribution pattern of the Cooray lightning channel in mountainous areas. Incorporating fractal theory and the variation of step length in lightning leader development, we simulated the development of lightning leader channels in mountainous terrain. The simulation results showed that the time to lightning strike was reduced to 10 s when using the Cooray distribution lightning channel model. Compared to the uniform distribution, the Cooray distribution lightning simulation exhibited a more dispersed pattern, consistent with the observed development of lightning in practice. The lightning channel simulation

model presented in this study provides an effective approach for the calculation of spatial electric fields and the simulation of lightning channels in mountainous areas.

Acknowledgements This work was funded by National Natural Science Foundation of China (52177161).

References

1. Ahmed NY, Illias HA, Mokhlis H (2023) A protocol for selecting viable transmission line arrester for optimal lightning protection. *Electric Power Syst Res* 221:109489. <https://doi.org/10.1016/j.epsr.2021.109489>
2. Almeida GLS, Visacro S (2023) Modeling the lightning-channel formation based on the bipolar leader theory by an electrostatic-by-step approach allowing representing non-regular ground surfaces for applications related to lightning protection. *Electric Pow Syst Res* 214:108876. <https://doi.org/10.1016/j.epsr.2022.108876>
3. Yao Y, Li J, Li H, et al (2015) Simulation study on improved electrical geometric model based on the development of mountainous lightning pilot. *High Volt Eng* 41(5):1550–1557 (in Chinese)
4. Tao X (2019) Study on the distribution law of ground lightning in mesoscale terrain of mountainous areas. Southwest Jiaotong University (in Chinese)
5. Karnas G, Barański P, Masłowski G (2022) A new method for modeling and parameter identification of positively charged downward lightning leader based on remote lightning electric field signatures recorded in the ELF/MF range and 3D doppler radar scanning data. *Energies* 15(22):8566. <https://doi.org/10.3390/en15228566>
6. Markushin MA, Kolpakov VA, Krichevskii SV (2020) Specific features of the distribution of nonuniform electrostatic field in a system with variable configuration of electrodes that generates high-voltage gas discharge. *Tech Phys* 65(12):1956–1962
7. Cooray V, Rakov V, Theethayi N (2007) The lightning striking distance—revisited. *J Electrostat* 65(5):296–306
8. He H (2011) Study on three-dimensional pre-simulation model for lightning shielding performance of ultra/extra high voltage transmission lines. Huazhong University of Science and Technology (in Chinese)
9. Li R, Du H, Li K et al (2021) Research on calculation method of electric field in three-dimensional terrain. *High Volt App* 57(4):47–54 (in Chinese)

Research on Step Size Distribution in Lightning Path Simulation



Qian Lei, Ruifang Li, Nengxing Guo, Ziyue Guo, Chengzhi Li, Lejia Liu, and Xiaobin Cao

Abstract Lightning path simulation is of great significance for lightning protection design and lightning warning of transmission lines or buildings. Lightning step size is one of the most important parameters in lightning path simulation research. The research of this paper has important theoretical significance. In this paper, the lightning video shot by a high-speed camera is divided into frames, and the lightning and shading changes of each frame are observed to obtain the statistical distribution rule of step size. On the basis of statistical analysis, the lightning step size is further studied theoretically. Firstly, the lightning strike path is divided into several segments, and the corresponding relationship between the step change of each segment and the number of boxes is obtained based on the box dimension method, so as to determine the step size of each segment, and obtain the corresponding theoretical distribution law of step size. On this basis, the statistical distribution law of the step size is used to modify it. The research of this paper lays a foundation for the simulation of lightning strike path.

Keywords Lightning path · Lightning step size · Statistical distribution law · Theory distribution law · Box dimension method

1 Introduction

Research on lightning path simulation is of great significance to lightning protection technology, and lightning leader is an important physical process in lightning research [1]. The research on lightning is mainly applied to the lightning protection and lightning protection of transmission lines. The strike distance [2] proposed by the traditional electric geometric model (EGM) is widely used in the lightning protection design of transmission lines. However, in real line operation, the electric geometric

Q. Lei (✉) · R. Li · N. Guo · Z. Guo · C. Li · L. Liu · X. Cao
School of Electrical Engineering, Southwest Jiaotong University, Chengdu 611756, China
e-mail: 1163790353@qq.com

© Beijing Paiké Culture Commu. Co., Ltd. 2024
X. Dong and L. Cai (eds.), *The Proceedings of 2023 4th International Symposium on Insulation and Discharge Computation for Power Equipment (IDCOMPU2023)*, Lecture Notes in Electrical Engineering 1100, https://doi.org/10.1007/978-981-99-7393-4_47

model cannot explain some lightning protection. Due to their obvious fractal characteristics, the lightning leader will soon introduce the knowledge of fractal theory to conduct an analysis and research on them, such as Niemeyer et al. Dielectric Breakdown Model DBM (Dielectric Breakdown Model) was introduced to study the characteristics of insulation discharge [3]. Professor He Jinliang et al. applied the lightning fractal model to the lightning strike analysis of power transmission lines [4]. Later, more and more people applied the fractal theory to the simulation of lightning channel.

As one of the important parameters in the fractal model of lightning, the observation of the actual step size of lightning has been started since the 1930s. The size of each step of the positive ascending leader measured by the Empire State Building in literature [5] is 6.2–23 m. Our country in the 1990s is measured in the experiment of thunderstorm or thunder guide each stage is size 12–24 m [6]. However, the average step size of two lightning bolts measured in the artificial mine induction experiment in 2006 was 7.16 and 8.59 m [7]. Although the actual step size has been measured and studied a lot, in the research and simulation of the lightning leader fractal model, there is a lack of setting the leader step size of the simulation and the actual leader step size, that is, the step size of the model does not have the characteristics of real lightning.

On the basis of existing studies, this paper analyzes the high frame rate lightning video based on background difference method and box dimension method, further divides the variation interval of the lightning leader size, and calculates the actual leader step size rule. Then, the lightning image extracted from the video is processed by the box dimension method to obtain the maximum simulation step size conforming to the real fractal dimension of lightning. Finally, the step size setting conforming to the change rule of the real lightning leader step size and suitable for simulation is obtained by contrast correction with the statistical leader step size. It provides more accurate lightning path simulation for lightning protection design.

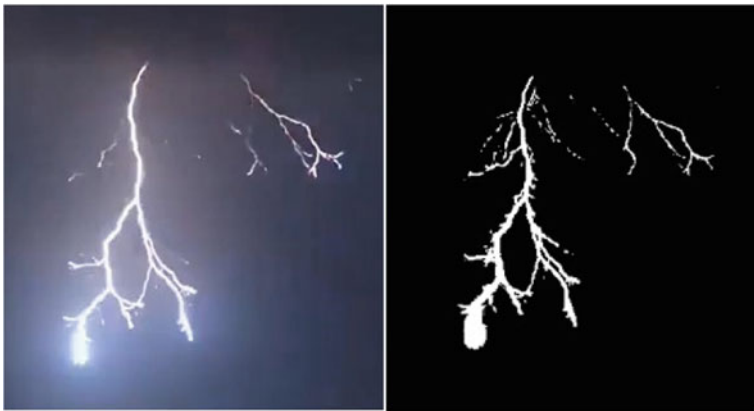
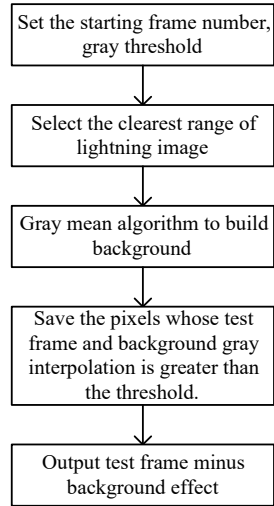
2 Law of Statistical Distribution

2.1 *Picture Processing*

Background difference method is used to extract the lightning path from the lightning strike video shot. The flow chart is as follows (Fig. 1).

Figure 2 shows the image before processing and the lightning leader path diagram after processing.

Fig. 1 Background difference flow chart



(a) Original picture.

(b) Processed path picture.

Fig. 2 Lightning original and processed path picture

2.2 Rule of Step Size

By playing the lightning video shot by a high-speed camera one frame at a time, it can be seen that the alternating size of each step of the lightning leader is the same. When the lightning leader developed to the middle part, each step size gradually became longer, but the development time of each step size did not change.

3 Law of Theoretical Distribution

3.1 Box Dimension Method

Box dimension method is a method for quantifying fractal structures. Its principle is to measure self-similar structures contained in a specific space on a certain scale. The box dimension method is very suitable to analyze the fractal characteristics of lightning because of its strong self-similarity. In the actual fractal development model, the fractal dimension is determined by the following formula:

$$N(\varepsilon) \sim \varepsilon^{-D} \quad (1)$$

Since each division of the new box, the side size ε becomes before the half, so ε constantly decrescent, eventually converge to zero. When ε tending to zero, $\ln k / \ln \varepsilon = 0$. And D is a definite positive number, so the final expression of fractal dimension D is:

$$D = \lim_{\varepsilon \rightarrow 0} -\frac{\ln N(\varepsilon)}{\ln \varepsilon} \quad (2)$$

For a fractal graphics, the fractal dimension D when certain, so take different box ε size and $N(\varepsilon)$, respectively take its log $\ln(\varepsilon)$ and $\ln N(\varepsilon)$, made by the horizontal ordinate scatter plot. Which is in the linear area point corresponding box ε size can be used, at the same time with a straight line using the least square method for fitting, fitting for the slope of the straight line its opposite is the fractal dimension [8].

Through the frame processing and observation of the lightning video shot by high-speed camera, it is preliminarily concluded that the lightning step grows longer and longer from top to bottom, and can be preliminarily divided into three segments. The lightning image was divided into three segments, as shown in Fig. 3a–c, and the box dimension method was used for processing and analysis respectively. In the analysis of the lightning path image extracted by the box dimension method, the maximum box side size conforming to the linear part of the fractal dimension curve is taken as the theoretical step size of lightning.



(a) First segment.

(b) Middle segment.

(c) Tail segment.

Fig. 3 Segmented map of lightning path

3.2 Step Size Analysis

Figure 3a was processed by box dimension method in MATLAB, and fractal dimension fitting diagram and box side size and corresponding box number diagram were obtained respectively, as shown in Figs. 4 and 5.

The point belonging to the maximum linear interval of the fitted fractal dimension curve is found in Fig. 4, and the corresponding point is found in Fig. 5, whose horizontal coordinate is the size of the box side and the development step of the

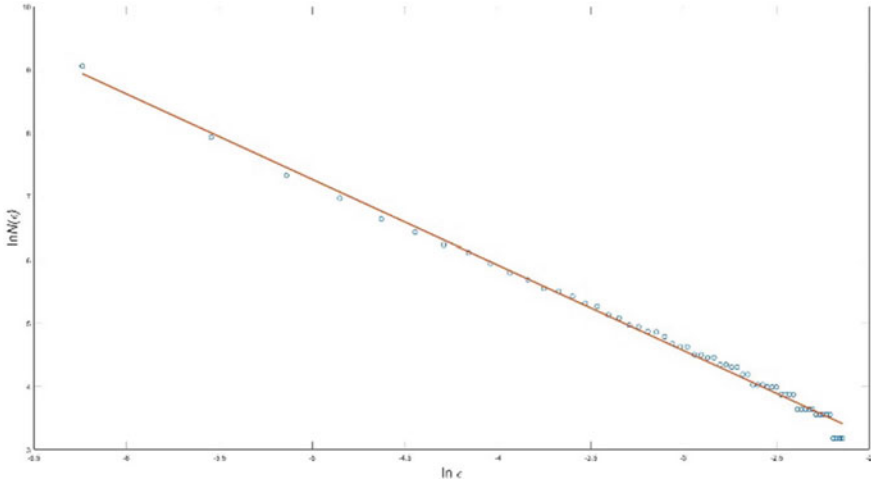


Fig. 4 Fractal dimension fitting diagram of first segment

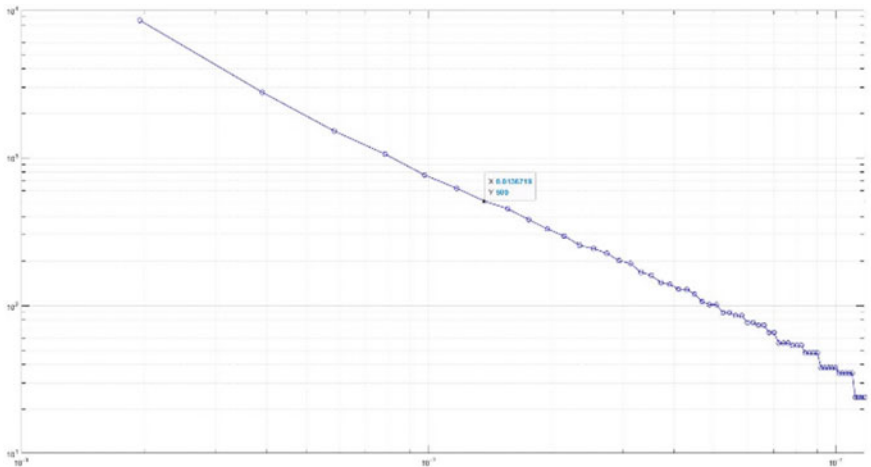


Fig. 5 Box side size and corresponding box number of first segment

Table 1 Comparison of step size of three-stage distribution

Segment	Step size
First	0.0136719
Middle	0.0292969
Tail	0.0371094

Table 2 Comparison of step size of four-stage distribution

Segment	Step size
First	0.013
Second	0.022
Third	0.034
Fourth	0.021

lightning leader path in this segment. The same method was used to obtain the development step size of Fig. 3b, c. And the step size of each segment is shown in Table 1.

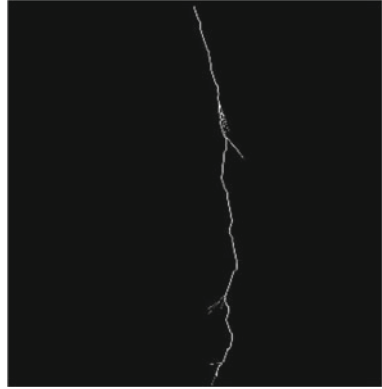
As shown in Fig. 5, the side size of the box increases by 1 pixel from left to right. When the side size is small, the scatter point roughly maintains in the linear area, but when it increases to a certain size, it will produce violent shaking, which is obviously not in the linear area. Moreover, since the step size of the adjacent scatter point only differs by the side size of one pixel, the boundary of the linear interval is relaxed for the artificial definition. In this paper, the side size corresponding to the point with obvious changes is taken as the leading step size of this lightning path. Therefore, after analyzing the latter two segments by the same method, the step size of the three segments of this lightning path is 0.0136719, 0.0292969 and 0.0371094, respectively. The theoretical distribution of lightning lead step size is obtained by the box dimension method. It also shows that the step size is increasing during the process from the initial to the breakdown.

Divide Fig. 2b into four paragraphs. Then use the same method for processing and analysis. The step size of each segment is obtained as shown in Table 2. The general pattern is also longer from top to bottom, but the step size of the last segment decreases because of the presence of the end of the preceding lightning branch in the image of the last segment.

4 Lightning Lead Path Simulation

Through MATLAB programming, the lightning strike path model with variable step size was established. According to the theoretical step size law, the step size of the beginning, middle and tail of the leader was set respectively according to the increasing size and their proportion. The following is a simulation of the lightning strike path (Fig. 6).

Fig. 6 Lightning strike path simulation diagram



Due to the shortest step size, it is difficult for single step size to show the direction of lightning leader development, that is, there are few abrupt directional turns in the front segment. In the middle and back, as the steps get longer and longer, the difference in direction between the two steps becomes more pronounced, and more bending occurs. This phenomenon is consistent with the characteristics of real lightning.

5 Conclusions

Based on background differentiation method, this paper extracts the lightning strike path from the lightning video and obtains a clear lightning strike path. Through the analysis of the lightning path graph by the box dimension method, the law of lightning leader development is obtained. The law is that the step length from the leader head to the breakdown is longer and longer. The lightning path simulation is carried out according to the step size law obtained in this paper, and the simulated lightning path obtained accords with the real lightning characteristics.

Acknowledgements This work was funded by National Natural Science Foundation of China (52177161).

References

1. Ye K, Li CS, Zhang WG et al (2013) Establishment of fractal model for analysis of lightning strike process of transmission lines. In: Proceedings of the 2013 Annual Meeting of the Chinese Society of Electrical Engineering, 492–495
2. Zhang WB, He JL, Gao YM (2002) Over-voltage protection and insulation. Tsinghua University Press

3. Niemeyer L, Pietronero L, Wiesmann HJ (1984) Fractal dimension of dielectric breakdown. *Phys Rev Lett* 52(12)
4. He JL, Zhang XW, Dong L et al (2009) Fractal model of lightning channel for analysis of lightning strike process of transmission lines. *Chinese Sci* 39(11):1818–1823
5. Hagenguth JH, Anderson JG (1952) Lightning to the empire state building-part III [includes discussion]. *Trans Am Inst Elect Eng. Part III: Pow Apparatus Syst* 71(3)
6. Zhang YJ, Liu XS, Xiao QF (1997) Comparative analysis of electrical characteristics of thunderstorms and artificially triggered lightning in northern and southern China. *Plateau Meteorol* 1997(02):2–10
7. Chen SD, Zhang YJ, Yang SJ et al (2009) Analysis of the characteristics of two negative polarity artificially induced lightning with only continuous current. *Chinese J Elect Eng* 29(01):113–119
8. Cao JX, Song CL (2017) The calculation and improvement of fractal dimension. *Info Tech Informat* 2017(10):19–23

Analysis and Optimization of Influencing Factors of DC Sheath Induced Voltage of AC/DC Trench Submarine Cable Based on Electrostatic Complementary Model



Jingying Cao, Jie Chen, Xiao Tan, Kairui Li, Lixiang Wang, Chenjin Xu, and Wei Wang

Abstract Excessive voltage induced on the cable sheath in the AC/DC trench laying submarine cable system may cause sheath breakdown, resulting in paralysis of the submarine cable system and even endangering the safety of personnel. To grasp the law of DC submarine cable induced voltage change effectively, an electrostatic induction complementary model on the basis of the extensive electromagnetic induction model is proposed in the paper, which explores the influencing factors of DC cable sheath sensing voltage and the change map of induced voltage under abnormal working conditions. Taking the 110 kV submarine cable system in a coastal city as an example, the accuracy of the calculation method is verified in the finite element analysis simulation software.

Keywords DC submarine cable · AC/DC trench laying · Electromagnetic induction · Electrostatic induction · Analysis of abnormal operating conditions

1 Introduction

Submarine cables are an important connection equipment between offshore wind farms and onshore power grids. To improve the efficiency of power transmission and transmission resources, the laying method of AC and DC trenches is usually adopted. However, the co-trenching method of AC and DC submarine cable will cause induced

J. Cao · J. Chen · X. Tan

Electric Power Science Research Institute, State Grid Jiangsu Electric Power Co., Ltd, Jiangsu 211106, China

K. Li · L. Wang · C. Xu · W. Wang (✉)

School of Electrical and Automation Engineering, Nanjing Normal University, Jiangsu 210046, China

e-mail: wangw_seu@163.com

© Beijing Paiké Culture Commu. Co., Ltd. 2024

X. Dong and L. Cai (eds.), *The Proceedings of 2023 4th International Symposium on Insulation and Discharge Computation for Power Equipment (IDCOMPU2023)*, Lecture Notes in Electrical Engineering 1100, https://doi.org/10.1007/978-981-99-7393-4_48

499

voltage on the metal sheath of the DC submarine cable in the alternating magnetic field, which will have a certain impact on the equipment, and even produce an over-voltage of tens of kilo-volts in severe cases [1, 2], breaking through the DC cable sheath, thereby paralyzing the submarine cable system. Hence, to effectively protect the safety of equipment and improve transmission efficiency, the relevant calculation methods of induced voltage need to be explored.

At present, the researches on the induced voltage of submarine cable sheath at domestic and foreign mainly focus on calculation methods [3–9], abnormal working conditions [10, 11] and influencing factors [12]. However, the main object of these studies is the AC part of the submarine cable system, and the researches on DC submarine cables mainly focus on the current carrying capacity [13, 14] and abnormal working condition analysis [15, 16]. Regarding the model simulation issue, the application of the EMTP/ATP for overhead cables are modeled and simulated [17], and the PSCAD is employed to simulate the transient voltage of 500 kV XLPE submarine cable [18, 19]. However, the problems of induced voltage is not inferred in the above mentioned researches.

To sum up, there are still loopholes in the calculation method, influencing factors, and protective measures for the protective layer of DC submarine cables. Aiming at the protection problem of submarine cable system, this paper first establishes a comprehensive model of extensive electromagnetic induction and electrostatic induction complementarity for calculating the induced voltage of DC submarine cable sheath. Then, the main influencing factors of the induced voltage amplitude are analyzed, the relevant simulation models are established, the influence of different laying methods on the induced voltage is studied, and the optimization method of the induced voltage amplitude is proposed. Finally, the simulation analysis of the abnormal working state is carried out, and the response method of abnormal change of induced voltage under abnormal normal working conditions is proposed.

2 Modeling and Analysis of DC Sheath Induced Voltage

The induced voltage on the DC cable sheath is usually composed of two parts, one is the induced voltage generated by electromagnetic induction by the conductor in the alternating magnetic field, and the other is the induced voltage generated by the DC cable itself due to electrostatic induction.

2.1 Extensive Model of Electromagnetic Induction

The calculation of the magnetic flux between DC submarine cable D and three-phase AC cable A, B, C can be expressed as:

$$B = \frac{\mu_0 I}{2\pi x} \quad (1)$$

$$\begin{aligned} \varphi_{Di} &= \int B dS = \int_r^{Dis} \frac{\mu_0 \dot{I}}{2\pi x} dx = \int_r^{Dis} 2\pi \times 10^{-7} \frac{\dot{I}_i}{x} dx \\ &= 2 \times 10^{-7} \dot{I}_i \ln \frac{Dis}{r} \end{aligned} \quad (2)$$

where B is the magnetic induction intensity, in T ; μ_0 is the vacuum permeability, and its value is $4\pi \times 10^{-7}$ H/m; \dot{I}_i is the i -phase core current, φ_{Di} refers to the magnetic flux between the DC submarine cable and the i -th phase core current, in Wb/m; Dis is the distance between the i -th phase core and the DC cable, and r is the geometric mean radius of the DC cable.

According to the mutual inductance calculation $M = \psi/I$, the equation for calculating the mutual inductance M between the i -th phase AC cable and the DC cable is as follows:

$$M_{SiD} = 2 \times 10^{-7} \left(\ln \frac{1}{S_i} \right) \quad (3)$$

where S_A, S_B, S_C indicates the distance between the three phases of The distance between the DC submarine cable and the three-phase AC submarine cable.

The inductance calculation can be listed as:

$$L_{SD} = M_{SAD} \dot{I}_A + M_{SBD} \dot{I}_B + M_{SCD} \dot{I}_C \quad (4)$$

The induced voltage per unit length on the DC cable sheath can be expressed as:

$$\dot{U}_{SD} = -j\omega L_{SD} \quad (5)$$

If the AC submarine cable has a three-phase current balance, bringing Eqs. (3) and (4) into Eq. (5), which can be simplified as

$$\begin{aligned} \dot{U}_{SD} &= j \cdot T \left(\ln \frac{1}{S_A} + \ln \frac{1}{S_B} \angle -120^\circ + \ln \frac{1}{S_C} \angle 120^\circ \right) \\ &= \frac{1}{2} \cdot j \cdot T \cdot I_A \cdot \left[\ln \left(\frac{S_B S_C}{S_A^2} \right) + \sqrt{3} j \ln \frac{S_B}{S_C} \right] \end{aligned} \quad (6)$$

$$\left| \dot{U}_{SD} \right| = \frac{1}{2} \cdot T \cdot I_A \cdot \sqrt{\ln^2 \left(\frac{S_B S_C}{S_A^2} \right) + 3 \ln^2 \left(\frac{S_B}{S_C} \right)} \quad (7)$$

where $T = -2 \times 10^{-7} \omega$.

The electromagnetic component of the induced voltage of the DC cable sheath is expressed by Eq. (7), in V/m. It can be seen from Eq. (7) that for AC three-phase balance systems, the electromagnetic component value of the induced voltage on the DC cable sheath is determined by the current amplitude and the AC and DC cable spacing.

2.2 Electrostatic Induction Complementary Model

Due to the presence of electrostatic induction on DC cables, there are mutual currents between the DC cable core and the sheath and between them and seawater, and the DC voltage on the core also generates induced voltage on the sheath. Figure 1 shows the equivalent circuit diagram of a DC submarine cable.

In Fig. 1, R , D and M represent the core, shielding layer and armor layer respectively; i_R, i_D, i_M represent the current at the head of the three-conductor layer, respectively; u_R, u_D, u_M represent the first voltage between the core, shield, armor layer and seawater; u_1, u_2 and u_3 indicate the voltage difference between the wire core and the shielding layer, the shielding layer and the armor layer, and the armored layer and the seawater, respectively; Y_{RD}, Y_{DM} , and Y_{ME} represent the mutual capacitance between the corresponding conductors, respectively; Δu and Δi indicates the amount of voltage and current change between the head and the extremity of the cable, respectively. The submarine cable system can be seen as three circuits, circuit 1 consists of a wire core and a shield, circuit 2 consists of a shield and an armor layer, and circuit 3 consists of an armor layer and seawater, and each has a loop current.

According to the transmission line equation:

$$\begin{cases} \frac{d}{dx}U + ZI = 0 \\ \frac{d}{dx}I + YU = 0 \end{cases} \tag{8}$$

where Z is a unit-length impedance matrix and Y is a unit-length admittance matrix and $Z = R + j\omega L, Y = G + j\omega C$.

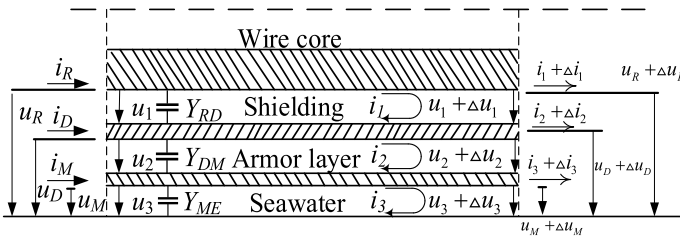


Fig. 1 Circuit diagram of DC submarine cable equivalent

The loop voltage drop frequency domain equation for the axial direction of the coastal cable can be obtained as follows:

$$-\frac{d}{dx} \begin{bmatrix} U_1 \\ U_2 \\ U_3 \end{bmatrix} = \begin{bmatrix} Z_{11} & Z_{12} & 0 \\ Z_{21} & Z_{22} & Z_{23} \\ 0 & Z_{32} & Z_{33} \end{bmatrix} \begin{bmatrix} I_1 \\ I_2 \\ I_3 \end{bmatrix} \tag{9}$$

where Z_{11} , Z_{22} and Z_{33} represent the self-impedance per unit length of the three circuits respectively. The loop self-impedance consists of the intrasurface impedance of the two conductors and the impedance of the time-varying magnetic flux of the insulating medium between the two conductors. Z_{12} , Z_{21} , Z_{23} and Z_{32} indicate the transfer impedance of the shielding layer and the armor layer respectively. $Z_{12} = Z_{21}$, $Z_{23} = Z_{32}$.

In order to study the actual voltage of each conductor layer, using the seawater layer as a reference point, Eq. (7) can be rewritten as follows:

$$\begin{aligned} -\frac{d}{dx} \begin{bmatrix} U_R \\ U_D \\ U_M \end{bmatrix} &= \begin{bmatrix} 1 & 1 & 1 \\ & 1 & 1 \\ 0 & & 1 \end{bmatrix} \begin{bmatrix} Z_{11} & Z_{12} & 0 \\ Z_{21} & Z_{22} & Z_{23} \\ 0 & Z_{32} & Z_{33} \end{bmatrix} \begin{bmatrix} 1 & 0 & 0 \\ 1 & 1 & \\ 1 & 1 & 1 \end{bmatrix} \begin{bmatrix} I_R \\ I_D \\ I_M \end{bmatrix} \\ &= \begin{bmatrix} Z_{RR} & Z_{RD} & Z_{RM} \\ Z_{DR} & Z_{DD} & Z_{DM} \\ Z_{MR} & Z_{MD} & Z_{MM} \end{bmatrix} \begin{bmatrix} I_R \\ I_D \\ I_M \end{bmatrix} = \mathbf{Z}_{ph} \begin{bmatrix} I_R \\ I_D \\ I_M \end{bmatrix} \end{aligned} \tag{10}$$

The various impedances mentioned above can be roughly divided into four categories: the impedance Z_{tf} expressed by time-varying magnetic flux in the insulating medium between concentric cylindrical electrodes; tubular conductor internal and external surface impedance Z_{is} and Z_{os} ; transfer impedance Z_m between the inner and outer surfaces of the tubular conductor; seawater internal impedance Z_w . They can be solved by the following equation:

$$\left\{ \begin{aligned} Z_{tf} &= j\omega \frac{\mu_0}{2\pi} \ln \frac{r}{q} \\ Z_{is} &= \frac{\rho m}{2\pi q D} [I_0(mq_c)K_1(mr_c) + K_0(mq_c) + I_1(mr_c)] \\ Z_{os} &= \frac{\rho m}{2\pi r D} [I_0(mr_c)K_1(mq_c) + K_0(mr_c) + I_1(mq_c)] \\ Z_m &= \frac{\rho}{2\pi q r D} \\ Z_w &= j\omega \frac{\mu_w}{2\pi} [-\ln(\gamma m q_w/2) + \frac{1}{2} - 4\frac{mh}{3}] \\ D &= I_1(mr_c)K_1(mq_c) - I_1(mq_c)K_1(mr_c) \end{aligned} \right. \tag{11}$$

where μ_w is the magnetic permeability of seawater, the value of the relative permeability of seawater equals 1, and the value of μ_w is $4\pi \times 10^{-7}$ H/m; r and q represent the inner diameter and outer diameter of the corresponding insulation layer respectively, r_c and q_c represent the inner diameter and outer diameter of the corresponding conductor respectively, and q_w represent the outer diameter of the insulation layer between the armor layer and the seawater; ρ indicates the resistivity of the corresponding conductor, ρ_w represents the resistivity of seawater, usually the value is 4.54–4.81 Ω /m; m represents the magnetic permeability of the corresponding conductor, $m = \sqrt{j\omega\mu/\rho}$, μ is the permeability in the medium; I, K_0, I_1, K_1 is the first and second type of Bézier’s coefficient of the zero order and the first order; γ is Euler’s constant, the value is 0.577216; h is the buried depth of the cable.

By converting an expression containing a Bessel function in Eq. (11) to an expression containing a hyperbolic function and expanding it into the complex frequency domain, the following simplified equation is obtained:

$$\left\{ \begin{array}{l} Z_{tf}(s) = k_{tf} \cdot s \\ = c_{tf} \cdot s \\ Z_{is}(s) = 0.1k_{is}k_{is}' \cdot \sqrt{s} + 0.25k_{is}^2k_{is}' \cdot s + k_{is}' + a_{is} \\ = c_{is} \cdot \sqrt{s} + c_{is}' \cdot s + c_{is}'' \\ Z_{os}(s) = 0.1k_{os}k_{os}' \cdot \sqrt{s} + 0.25k_{os}^2k_{os}' \cdot s + k_{os}' + a_{os} \\ = c_{os} \cdot \sqrt{s} + c_{os}' \cdot s + c_{os}'' \\ Z_m(s) = k_m' \cdot \frac{1}{1 + 0.15k_m^2s} \\ = c_m \cdot \frac{1}{s + c_m} \\ Z_w(s) = 5k_w'k_w^{\frac{1}{10}} \cdot s^{\frac{21}{20}} - 5k_w'k_w^{-\frac{1}{10}} \cdot s^{\frac{19}{20}} + k_w'' \cdot s + k_w''' \cdot s^{3/2} \\ = c_w \cdot s^{\frac{21}{20}} + c_w' \cdot s^{\frac{19}{20}} + c_w'' \end{array} \right. \tag{12}$$

where the elements are given by Eq. (13):

$$\left\{ \begin{aligned} k_{tf} &= \frac{\mu_0}{2\pi} \ln \frac{r}{q} \\ k_{is} &= |r - q| \sqrt{\frac{\mu}{\rho}} = k_{os} = k_m \\ k'_{is} &= \frac{\sqrt{\mu\rho}}{2\pi q|r - q|} = \frac{q}{r} k'_{os} \\ a_{is} &= -\frac{\rho}{2\pi q(r + q)} = \frac{q}{r} a_{os} \\ k'_m &= \frac{\rho}{\pi(r + q)|r - q|} \\ k'_w &= \frac{\gamma q_w}{2} \sqrt{\frac{\mu_w}{\rho_w}} \\ k''_w &= -\frac{\mu_w}{2\pi} = -2 \times k''_w \\ k'''_w &= -\frac{2\mu_w h}{3} \sqrt{\frac{\mu_w}{\rho_w}} \end{aligned} \right. \tag{13}$$

Converting Eq. (8) into the complex frequency domain yields the complex frequency domain form of the transmission line equation:

$$\begin{cases} \frac{d}{dx} U_{ph}(s) + Z_{ph}(s) I_{ph}(s) = 0 \\ \frac{d}{dx} I_{ph}(s) + Y_{ph}(s) U_{ph}(s) = 0 \end{cases} \tag{14}$$

where $U_{ph}(s) = [U_R(s) U_D(s) U_M(s)]^T$, and the $U_{ph}(s)$ represents the complex frequency domain form of the voltage to ground of the cable guide core, shielding layer and armor layer, $I_{ph}(s) = [I_R(s) I_D(s) I_M(s)]^T$ and the $I_{ph}(s)$ represents the complex frequency domain form of the current passing through the cable guide core, shielding layer, and armor layer.

Bringing Eq. (12) into Eq. (14) yields the complex frequency domain form of the impedance matrix. After combining the same order terms in the impedance matrix, the following impedance matrix expression is obtained:

$$\begin{aligned} \mathbf{Z}_{ph}(s) &= \mathbf{Z}_{ph}^0 + \mathbf{Z}_{ph}^{0.5} \cdot s^{0.5} + \mathbf{Z}_{ph}^1 \cdot s + \mathbf{Z}_{ph}^{1.5} \cdot s^{1.5} \\ &+ \mathbf{Z}_{ph}^{1.05} \cdot s^{1.05} + \mathbf{Z}_{ph}^{0.95} \cdot s^{0.95} + \mathbf{Z}_{ph}^{m1}(s) + \mathbf{Z}_{ph}^{m2}(s) \end{aligned} \tag{15}$$

where \mathbf{Z}_{ph}^n represents a matrix of coefficients of order n of s.

For admittance matrices, the same applies to the complex frequency domain form of the admittance matrix:

$$Y_{ph}(s) = \bar{Y}_{ph} \cdot s$$

$$= \begin{bmatrix} C_{RD} & -C_{RD} & 0 \\ -C_{RD} & C_{RD} + C_{DM} & -C_{DM} \\ 0 & -C_{DM} & C_{DM} + C_{MW} \end{bmatrix} \cdot s \quad (16)$$

where C_{RD} , C_{DM} and C_{MW} indicates the mutual capacitance between the wire core and the shield, the shield and the armor, and the armor layer and seawater, and C can be represented by:

$$C = \frac{2\pi \varepsilon_{in}}{\ln \frac{r_{in}}{q_{in}}} \quad (17)$$

where ε_{in} indicates the dielectric constant of this insulating layer, r_{in} indicates the outer diameter of the insulation, q_{in} indicates the inner diameter of the insulation.

The electrical parameters are brought into Eq. (14), and the differential equation is solved to obtain the induced voltage value U_M generated on the sheath of the DC submarine cable due to electrostatic induction.

In summary, the rms value of the electromagnetic component U_{SD} of the induced voltage of the DC submarine cable is obtained by formula (7), and the electrostatic complementary component U_M of the induced voltage can be obtained through formula (12–17). By superimposing the rms value of the electromagnetic component and the calculated value of the electrostatic complementary component, the calculation formula of the induced voltage of the DC cable sheath is:

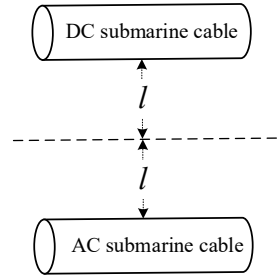
$$U = U_{SD} + U_M \quad (18)$$

It can be seen from Eq. (7) that the influencing factors of the electromagnetic component of the induced voltage mainly include the frequency and amplitude of the current on the AC submarine cable and the distance between the AC and DC submarine cables; the influencing factors of the electrostatic complementary component are mainly the physical characteristics of the DC submarine cable itself, including the resistivity, magnetic permeability, dielectric constant and inner and outer diameter of the material. In practical application scenarios, considering the national standards, economic benefits and other factors, the selection of DC submarine cable can not be greatly optimized. Therefore, the optimization of induced voltage should mainly focuses on the distance between AC and DC submarine cables and the arrangement of AC submarine cables.

3 Optimization of Induced Voltage Influencing Factors

The laying method of AC/DC trench submarine cable is shown in Fig. 2, where l represents the distance between AC and DC submarine cable and the central axis.

Fig. 2 Laying of AC and DC trench submarine cables



In order to explore the influencing factors of the induced voltage of the sheath of DC submarine cable, and determine the optimal laying spacing and arrangement mode, the submarine tunnel section laid with 110 kV AC/DC co-trench was selected as the research object, the current carrying capacity of the submarine cable was 400 A, the length was set to the length of 100 km, the structural parameters were shown in Table 1, and the three-phase arrangement order of AC submarine cable was shown in Fig. 4b, d.

The simulation model in the finite element analysis software is illustrated as Fig. 3 shown, and the field-path coupling co-simulation circuit is built.

Table 1 Structural parameters of submarine cables

Cladding	Material	Outside diameter (mm)	Relative permittivity	Resistivity (ohm*m)
Core conductors	Copper	18	1.0	1.68e-8
Insulation	XLPE	38	2.3	–
Metal cladding	Aluminum alloy	53	1.0	2.63e-8
Corrosion protection layer	XLPE	59	2.3	–
Armor layer	Stainless steel wire	71	1.0	9.09e-7

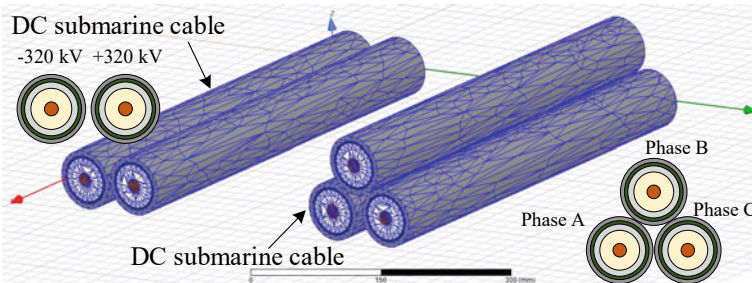


Fig. 3 Finite element simulation model of submarine cable system

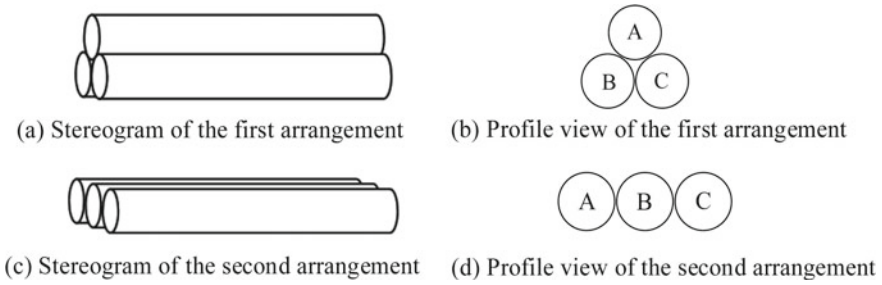


Fig. 4 AC cable arrangement

In actual engineering, AC submarine cables usually have two arrangements, as shown in Fig. 4.

3.1 The First Arrangement of AC Submarine Cables

When the three-phase AC submarine cable is arranged in the first way, the magnetic field distribution of the submarine cable is shown in Fig. 5. By changing the distance l between the submarine cable and the central axis can obtain the change of induced voltage amplitude on the DC cable sheath shown in Fig. 6.

When l is 2.5 m, the induced voltage amplitude is 53.05 V, and when l is 3 m, the induced voltage amplitude is 43.38 V, so when the AC and DC submarine cables are 3 m or more apart, the induced voltage threat is small.

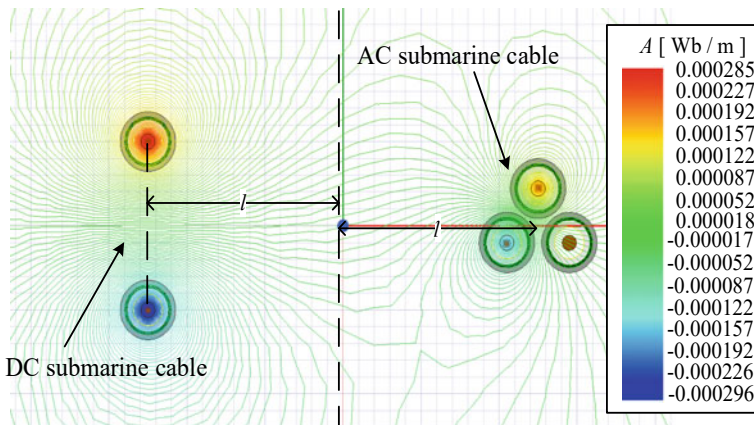
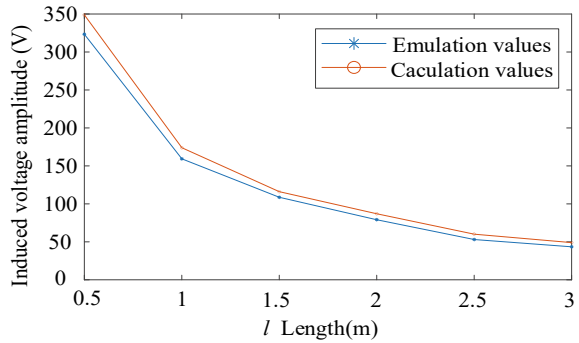


Fig. 5 The magnetic field distribution of the first arrangement

Fig. 6 The changes in the induced voltage in the first arrangement



3.2 The Second Arrangement of AC Submarine Cables

When the three-phase AC submarine cable is arranged in the second arrangement, the magnetic field distribution of the submarine cable is shown in Fig. 7. Figure 8 shows the change of the amplitude of the induced voltage on the DC cable sheath when l is changed.

When l is 5 m, the induced voltage amplitude is 53.8 V. When the value of l reaches 6 m, the induced voltage amplitude is 48.97 V. Therefore, when the AC and DC submarine cables are 6 m or more apart, the induced voltage threat is small.

As the distance increases, the amplitude of the induced voltage decreases more and more slowly, because the size of the induced voltage depends on the intensity of electromagnetic induction, and as the distance increases, the electromagnetic effect becomes weaker, and its fluctuations become smaller. Therefore, as the distance increases, the induced voltage value decreases, and when the distance gets smaller,

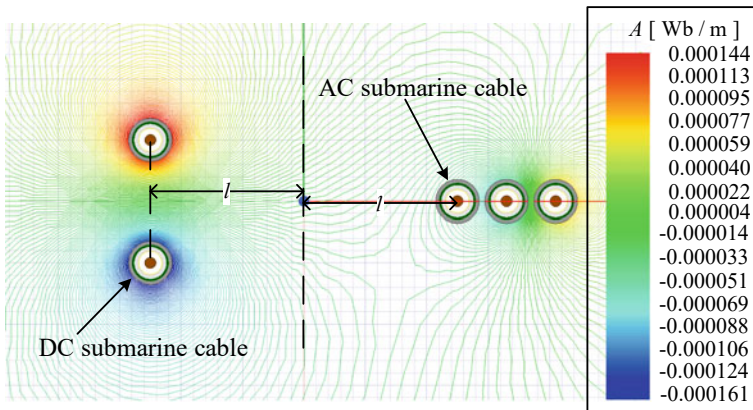
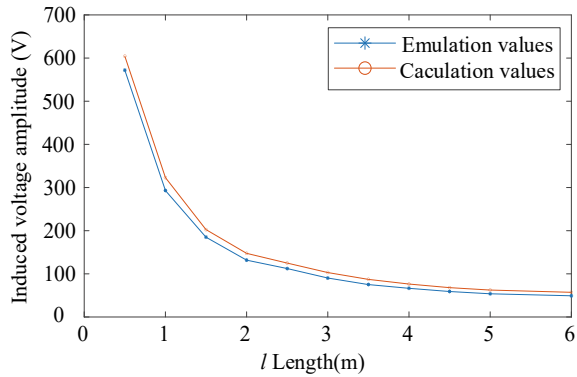


Fig. 7 The magnetic field distribution of the second arrangement

Fig. 8 The changes in the induced voltage in the second arrangement



the induced voltage changes rapidly, and when the distance is far, the induced voltage changes slowly.

And because the center of the three-phase submarine cable is symmetrically arranged, the electromagnetic field generated by it has a better cancellation effect than the “one” shape, so when the three-phase submarine cable is arranged in the shape of the product, the induced voltage of the DC cable sheath is smaller and the change rate is faster.

4 Analysis of Abnormal Operating Conditions

In actual engineering, there may be power failure or harmonic interference in the system, which may distort the induced voltage, produce an over-voltage with a large amplitude, and have a destructive effect on the armor layer. The following is an analysis of two scenarios.

4.1 Power Outage Failure

Power failure fault mainly refers to the failure caused by the occurrence of a power outage in one or more phases of a three-phase AC submarine cable, resulting in a three-phase unbalanced current. Common causes of power outages include lightning, external damage, etc. Figure 9 shows the induced voltage value on the DC cable sheath under normal conditions.

Figure 10 shows the change of induced voltage on the sheath of the DC submarine cable in the event of a single-phase power outage fault, and the amplitude of the induced voltage will rise sharply when a single-phase power outage fault occurs, reaching a peak of 2.98 kV, far exceeding the safety threshold, which threatens the human body and equipment.

Fig. 9 Under normal circumstances, the induced voltage value on the DC cable sheath

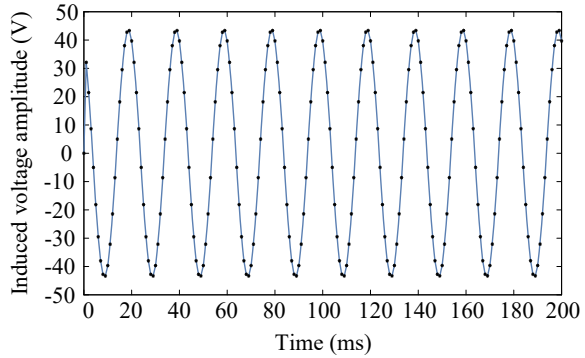


Fig. 10 The value of the induced voltage in the event of a single-phase power failure

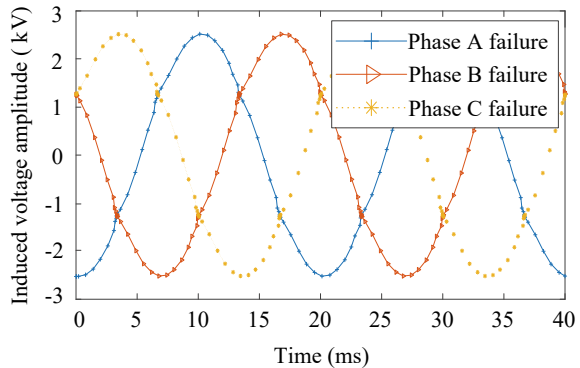
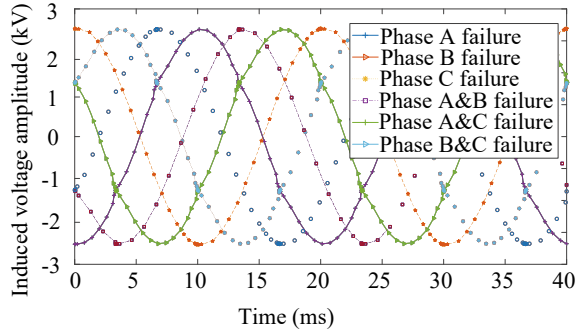


Figure 11 shows the comparison chart of single-phase power outage fault and two-phase power outage fault, and when a single-phase power outage fault occurs and a two-phase power outage fault occurs, the amplitude of the induced voltage on the DC submarine cable sheath is similar and far exceeds the safety threshold. Moreover, the phase difference between the induced voltage amplitude diagram of the A-phase fault and the amplitude diagram of the A&B two-phase fault and the amplitude diagram of the A&C two-phase fault is 1/6 cycle, and the phase relationship of the positive sequence three-phase circuit is satisfied.

4.2 Harmonic Analysis

In the AC/DC trench laying submarine cable system, the AC submarine cable is in a three-phase equilibrium system, and due to the symmetry relationship, the second harmonic has been eliminated, and usually only odd harmonics exist. In this section of the analysis, an example is an example of a submarine cable system with a second arrangement of AC cables and 6 m from the central axis.

Fig. 11 Comparison chart of the effects of single-phase faults and two-phase faults



Firstly, considering the situation that the fundamental wave, third harmonic, fifth harmonic, seventh harmonic and ninth harmonic exist separately, the change of induced voltage value on the DC cable sheath under the separate action of different harmonics is shown in Fig. 12.

Figure 12 is a double-coordinate axis diagram of the amplitude of the induced voltage of the DC cable sheath under the sole action of odd harmonics, in which the third and ninth harmonics use the right coordinate axis, and the amplitude is in kilovolts, and the remaining harmonics use the left coordinate axis in volts. The induced voltage has the same amplitude under the action of fundamental, fifth harmonic and seventh harmonic, and the amplitude of the induced voltage is the same under the action of the third harmonic and the ninth harmonic, and the induced voltage frequency period generated by the five harmonics has a proportional relationship.

When the system is under the action of the third harmonic or the ninth harmonic, the induced voltage amplitude is thousands of times that of several other harmonics. When there is a third harmonic in the line, the phase angle of the three-phase power

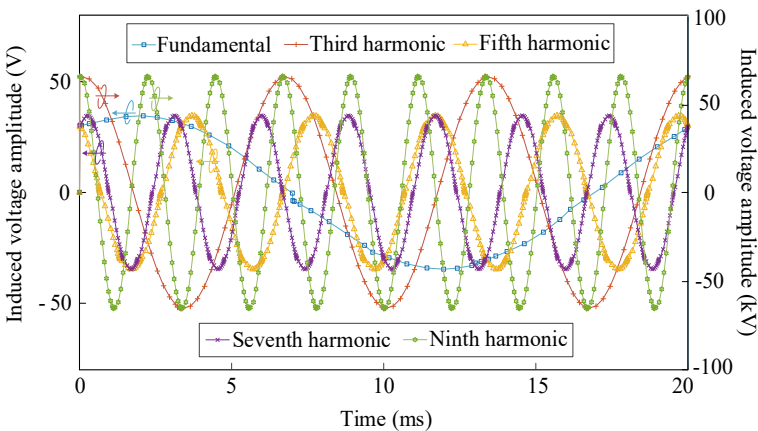


Fig. 12 Odd harmonics exist alone

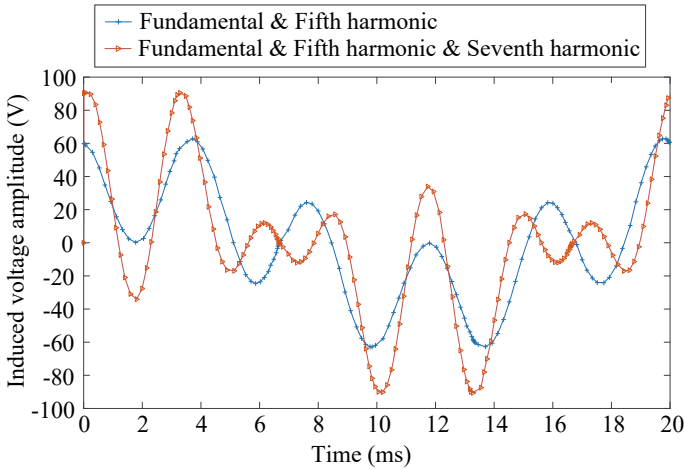


Fig. 13 The change in induced voltage at the third harmonic is not included

supply system becomes 0° , -360° , 360° , and there is no imaginary part for vector cancellation, which will cause the generation of power superposition and cause abnormal over-current. The principle is similar under the action of the ninth harmonic, and the absence of real parts in the system also leads to the generation of superposition states. Therefore, the harmonic vector angle should be adjusted by installing filters and other measures to reduce the damage caused by the third harmonic.

Figure 13 shows a cycle of induced voltage waveform change in a submarine cable system without the third harmonic. As can be seen from Fig. 13, the induced voltage waveform will be distorted, and the amplitude will increase significantly, but it will still be within the controllable range. This is because the waveform of the induced voltage is superimposed by several harmonics, because there is no particularly large voltage, so the waveform changes are more obvious, usually using a filter or adding a grounding point to leak a larger voltage.

5 Conclusion

In this paper, the calculation method of induced voltage on the DC cable sheath is given, the influence of the induced voltage amplitude on the DC cable sheath is studied, and the abnormal working conditions are analyzed, and the following conclusions are obtained:

- (1) The induced voltage is generated by the joint action of electromagnetic induction and electrostatic induction, and the induced voltage amplitude of the DC cable sheath can be calculated more accurately through the calculation model proposed in this paper.

- (2) In the case of the same length and spacing of the submarine cables, the AC cables arranged in the first arrangement generate less induced voltage on the DC cable sheath than the second arrangement.
- (3) For a 110 kV AC/DC trench laying submarine cable system with a length of 100 km, using the first arrangement method for AC submarine cables with an interval of more than 3 m can keep the induced voltage on the protective layer of DC submarine cables within the safety threshold. If using the second arrangement method for AC submarine cables, the interval must be more than 6 m.
- (4) When power failure or harmonic interference occurs, the submarine cable system will generate an induced voltage of up to thousands of volts due to asymmetric current, which will break through the cable sheath and cause serious harm, and it is necessary to install filters to deal with harmonic interference, or add grounding points to leak large voltages.

Acknowledgements This research is supported by Science and Technology Project of State Grid Jiangsu Electric Power Co., Ltd. (J2022024).

References

1. Ruijie D (2022) Analysis of countermeasures for prevention of electric shock injury induced by the construction of power grid transmission lines. *J. Elect. Tech. Econ.* 04:177–179 (in Chinese)
2. Yingpei L, Xiangyu W, Xinming W et al (2022) Fault identification method of outage transmission lines based on induced voltage features. *J North China Elect Pow Univ (Natural Science Edition)* 49(4):14–54 (in Chinese)
3. Xue H, Mahseredjian J, Morales J, Kocar I, Xemard A (2022) An investigation of electromagnetic transients for a mixed transmission system with overhead lines and buried cables. *IEEE Trans Power Deliv* 37(6):4582–4592
4. Lei Q, Hui Y, Lin L et al (2013) Transmission line modelling of inductive coupling of overhead power lines subjected to grounding fault to underground metal pipeline. *J Trans China Electrotech Soc* 28(06):264–270 (in Chinese)
5. Nazarčík T, Benešová Z (2017) Modelling of the transients on the multi-circuit EHV/HV overhead transmission lines. In: 18th International Conference on Computational Problems of Electrical Engineering (CPEE), Kutna Hora, Czech Republic, pp 1–4
6. Weiyuan W, Jinmin C, Yi S et al (2021) Calculation of induced voltage and induced current of double circuit cable-overhead hybrid line. *J Elect Pow Eng Tech* 40(04):89–94 (in Chinese)
7. Yi S, Jinghui L, Yiqing X et al (2021) Calculation of induced voltage and current of UHV double loop GIL. *J Elect Pow Eng Tech* 40(05):171–176 (in Chinese)
8. Jinchao M, Wenfeng H, Xiaokang X et al (2022) Analysis of induced voltage and current of 10 kV bypass flexible cable sheath in distribution network. *J Elect Mat* 4:10–23 (in Chinese)
9. Haifeng Y, Muzhi N (2022) Analysis of induced voltage and circulation of 800kV three-phase sub-box GIS substation shell. *J Elect Tech Econ* 04:95–97 (in Chinese)
10. Fei G, Lei H, Lei Z et al (2020) Research on increasing the segmented length in the high-voltage cable. *J Elect Appl* 39(07):79–85 (in Chinese)
11. IEEE Guide for the Planning, Design, Installation, and Repair of Submarine Power Cable Systems (2005) IEEE Std 1120-2004, pp1–45, 31

12. Wei X, Bojing L, Yuan G et al (2022) Analysis and evaluation of electromagnetic interference of 220 kV submarine cable to submarine pipeline. *J China Offshore Oil Gas* 34(05):197–204 (in Chinese)
13. Wu Q et al (2021) Simulation study on steady-state ampacity of ± 400 kV DC submarine cable under different laying environments. In: 22nd International Symposium on High Voltage Engineering (ISH 2021), pp 60–65
14. Yuan X, Xuotong Z, Yong F et al (2022) Simulation study on steady-state ampacity of +500 kV DC submarine cable under J-tube laying environment. In: Proceedings of the CSEE, 1–11 (in Chinese)
15. Shuji H, Ning C (2022) Sea cable fault analysis and detection practice. *J Ship Eng* 44(S1):14–17 (in Chinese)
16. Tao C, Shouyuan W, Ke Z et al (2020) Research on harmonic overvoltage suppression technology in metal shielding layer of single-core cable. *J Elect Appl* 39(9):55–63 (in Chinese)
17. Yi S, Jinghui L, Xinlei Z et al (2022) Influence of UHV GIL access on transient recovery voltage of circuit breaker. *J Elect Pow Eng Tech* 41(05):240–245 (in Chinese)
18. Shaohua W, Jingwei Z, Ling L et al (2019) Research on transient voltage and insulation coordination of 500 kV XLPE submarine cable line. *J Insulat Mat* 52(12):89–94 (in Chinese)
19. Peng Z, Chen H, Zheng Z, Kai H et al (2020) Calculation and analysis of the fundamental frequency electromagnetic induction of hybrid laying AC and DC cables. *Journal of High Voltage Engineering* 46(02):576–585 (in Chinese)

Research on Typical Defects Electrical Performance of 1100 kV GIS Basin Insulator



Xiangsong Zhan, Chun Xiao, Xixiu Wu, and Biao Zhang

Abstract In order to investigate the electric field distribution characteristics of 1100 kV UHV GIS basin insulator under defect condition, a typical defect model of basin insulator is established in this paper. The internal bubble defect and surface metal particle attachment defect of 1100 kV basin-type insulator were simulated. In the case that the basin-type insulator is attached with metal particle along the surface, the larger the radius of the metal particle is, the more serious the surface electric field distortion at the nearest point is. Meanwhile, the electric field distortion reaches the maximum in the condition of metal particle attachment from the middle to the end of the basin-type insulator. When the 1100 kV basin insulator has an internal bubble defect, except for the position near the central conductor, the core field strength of the bubble in most areas is 4.55×10^6 V/m, which is 1.7 times of the position without bubble defect. The larger the bubble radius inside the basin insulator, the more prominent the influence on the local field strength, and the field strength extreme value is distributed at the boundary between the bubble and the basin insulator material.

Keywords 1100 kV · GIS · Basin insulator · Internal bubble defect · Adhesion of metal particles · Electric field distribution

X. Zhan · C. Xiao · X. Wu (✉) · B. Zhang
Wuhan University of Technology, Wuhan 430070, China
e-mail: wuxixiu@whut.edu.cn

X. Zhan
e-mail: zhanxiangsong@whut.edu.cn

C. Xiao
e-mail: xiaochun@whut.edu.cn

B. Zhang
e-mail: zhangbiao@whut.edu.cn

1 Introduction

As an important part of GIS gas combination electrical apparatus, basin insulator plays important roles such as mechanical support and electrical insulation [1]. At present, most basin insulators used in UHV construction use 126 kV, 252 kV, 550 kV and other voltage levels, and the research on 1100 kV basin insulators is not enough [2–4].

Due to the non-standard preparation process and operation, bubble defects may occur in the curing process of epoxy materials. At the same time, during the installation process of equipment, collision and wear between components may be caused due to the inaccurate connection of equipment, resulting in metal particles attached to the surface of the insulator [5].

At present, there are relatively few researches on 1100 kV basin insulators in China. In reference [6], the stress distribution in the solidification process of 1100 kV basin insulators is simulated. In reference [7], the influence of bubble defects on the stress distribution of a 1100 kV basin insulator was analyzed by establishing a three-dimensional model. In reference [8], fine iron wire was used to simulate surface defects of 1100 kV basin-type insulators and induce flashover, laying a foundation for accurate 10 ns fault location. Most of the studies on basin insulators stay at the voltage level below 1100 kV, and the studies on 1100 kV basin insulators are mainly focused on stress distribution and structure optimization, while the studies on the electric field distribution of typical defects of 1100 kV insulators are slightly insufficient [9–12]. However, there is a relative shortage of basin insulators for ultra-high voltage in foreign countries, and most of the voltage levels are lower than 550 kV [13–15].

In order to research the influence of typical defects of 1100 kV GIS basin insulators on the electric field distribution along the surface and inside the insulator, this paper modeled the internal bubble defects and the adhesion defects of metal particles along the surface of the basin insulators, and used the finite element analysis software to simulate the overall electric field distribution of the above defect models.

2 Modeling and Preprocessing of 1100 kV Basin Insulator

In the process of modeling, in addition to the high-precision restoration of the basin insulator, detailed modeling is also carried out on the surrounding parts, such as shielding cover, center conductor, GIS housing, contacts, contacts, etc. The modeling in this paper refers to the 1100 kV GIS basin insulator production model and the actual size parameters in UHV Nanyang Station, and carries out high-precision restoration of the model [16, 17]. GIS basin insulator and its surrounding parts are shown in Fig. 1.

The specific material properties are shown in Table 1.

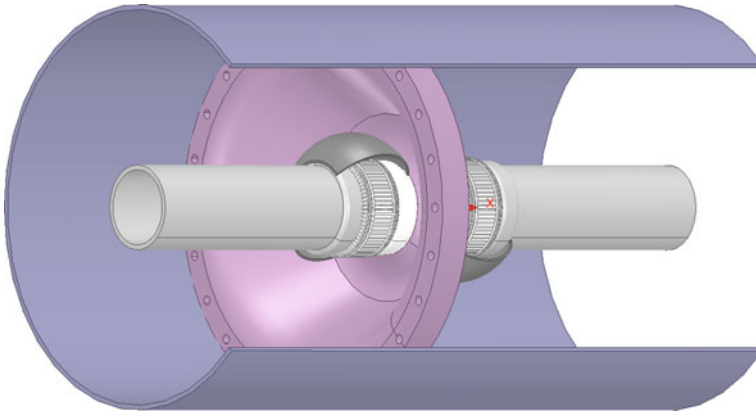


Fig. 1 1100 kV GIS basin insulator model

Table 1 GIS model material parameters

Material	Relative dielectric constant	Conductivity (S/m)
Aluminium alloy 5A02	1	2.00×10^7
Aluminium alloy 6A02	1	2.63×10^7
Red copper	1	5.6×10^7
SF ₆ gas	1.006	0
Epoxy resin	5.2	0

2.1 Defect Modeling of 1100 kV Basin Insulator

Figure 2 shows the defect model of the 1100 kV basin insulator, the bubble defect model on the left, and the metal particle attachment defect model on the right. The blue position is the specific location of the defect.

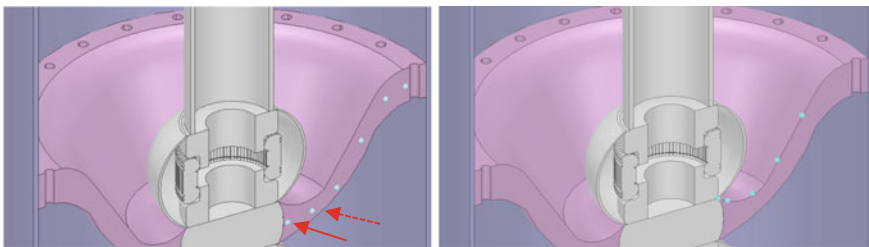


Fig. 2 Schematic diagram of bubble defects inside a basin insulator

2.2 Calculation Principle of 1100 kV Basin Insulator Electric Field

The calculation of the electric field of the basin insulator is to satisfy the Laplace equation in solving region D under the boundary conditions of the first and second kinds. The mathematical expression is as follows:

$$\left\{ \begin{array}{l} D : -\varepsilon \nabla^2 \varphi = -\varepsilon \left(\frac{\partial^2 \varphi}{\partial x^2} + \frac{\partial^2 \varphi}{\partial y^2} + \frac{\partial^2 \varphi}{\partial z^2} \right) = 0 \\ \varphi_1 = \varphi_2 \\ \varepsilon_1 \frac{\partial \varphi_1}{\partial n} = \varepsilon_2 \frac{\partial \varphi_2}{\partial n} \end{array} \right. \quad (1)$$

D is the calculation area of electric field; $\varepsilon_1, \varepsilon_2$ on behalf of the interface between two different dielectric constants of materials. Applying potential φ for boundary conditions; n stands for normal vector perpendicular to the boundary. φ_1 and φ_2 represents the potential at the interface between two different materials. Calculate the electric field distribution of GIS basin insulator and its surrounding parts can be regarded as solving the following mathematical problems.

$$\left\{ \begin{array}{l} D_1 - D_2 = 0 \\ E = \nabla \varphi \\ V_1 = V \\ V_0 = 0 \\ \nabla \cdot E = \rho / (\varepsilon_0 \varepsilon_r) \end{array} \right. \quad (2)$$

ρ represents free charge density; E is electric field intensity; ε_0 and ε_r represent the relative dielectric constant of media and vacuum; D_1 and D_2 are the electrical displacement components perpendicular to the dielectric interface on both sides of the interface. V_1 and V_0 represent central conductor potential and shell potential, respectively.

3 Electric Field Simulation of 1100 kV Basin Insulator

3.1 Simulation of Defect-Free Electric Field of Basin Insulator

In order to compare the electric field distribution of the basin insulator under the condition of defect, the electric field distribution of the basin insulator without defect is simulated (Fig. 3).

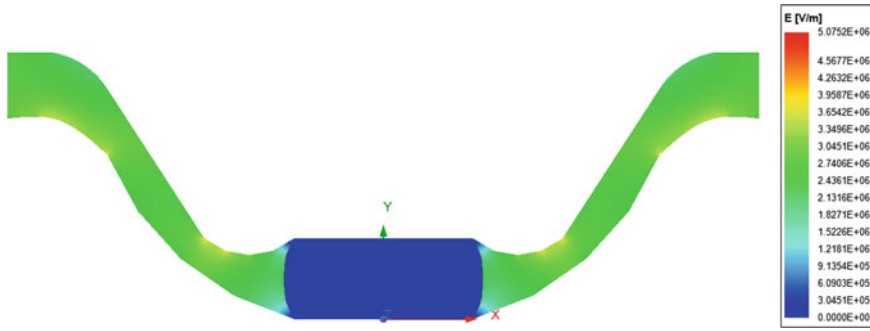


Fig. 3. 1100 kV basin insulator without defect Electric field profile

The overall electrical performance of the basin insulator without defects is relatively stable. The maximum field strength of the whole model is 5.075×10^6 V/m, and the field strength of most areas on the whole insulator is even lower than 3.35×10^6 V/m, and the average field strength is around 2.67×10^6 V/m, far lower than the breakdown field strength.

3.2 Bubble Defect Simulation of Basin Insulator

Figure 2 shows where the solid red arrow points, a bubble with a diameter of $D = 1$ mm is set at the blue dot closest to the conductor rod and simulated. The electric field distribution diagram shown in Fig. 4 is obtained.

By comparing Figs. 3 with 4, it is found that except for the slightly different electric field distribution at the bubble position, the electric field distribution at the other positions is basically the same, and the highest field intensity values of the two are basically the same, the difference is only 0.0001×10^6 V/m, and the bubble area is amplified. The field strength in the bubble area is significantly higher than that of the surrounding basin insulator. The simulation software shows that the surrounding electric field strength is about 2.000×10^6 V/m, the field strength in the center of

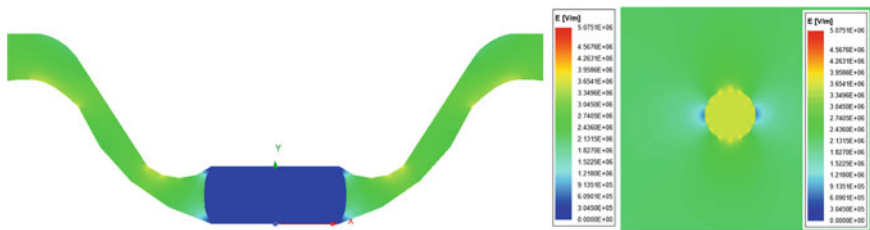


Fig. 4 $D = 1$ mm bubble defect 1100 kV basin insulator Electric field profile

the bubble is 3.623×10^6 V/m, the maximum field strength in the bubble is 4.014×10^6 V/m, and the minimum field strength is 3.181×10^6 V/m.

The overall electric field distribution diagram of the bubble defect diameter of 2 mm, 3 mm and 4 mm and the electric field distribution diagram of the bubble defect are shown in Figs. 5, 6, and 7.

D = 1 mm bubble center field strength size is 3.623×10^6 V/m, D = 2 mm bubble center field strength size is 3.602×10^6 V/m, D = 3 mm bubble center field strength size is 3.613×10^6 V/m, D = 4 mm bubble center field strength size is 3.601×10^6 V/m. It can be seen that the bubble size has little effect on the electric field intensity.

Create bubble defects of different sizes in the position indicated in Fig. 2 (Red dotted arrow). As shown in Fig. 8, when the bubble diameter is 1 mm, the position where the overall electric field strength of the basin insulator reaches the maximum is that of the bubble, and the maximum is 5.671×10^6 V/m, which is obviously

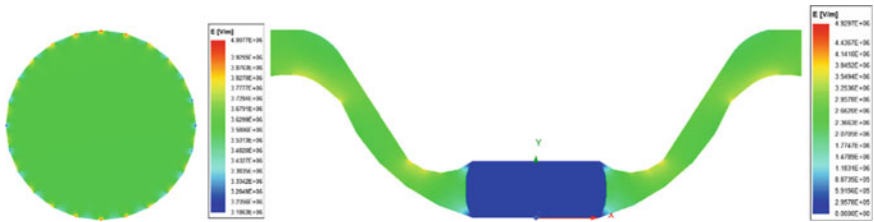


Fig. 5 Bubble defect D = 1100 kV basin at 2 mm, electric field distribution diagram of insulator

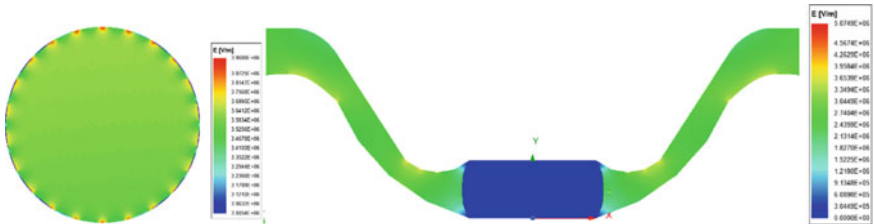


Fig. 6 Bubble defect D = 1100 kV basin at 3 mm electric field distribution diagram of insulator

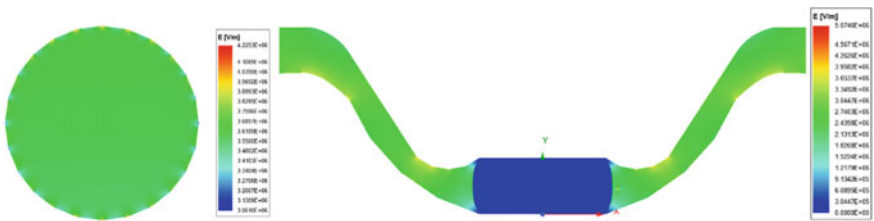


Fig. 7 Bubble defect D = 1100 kV basin at 4mm electric field distribution diagram of insulator

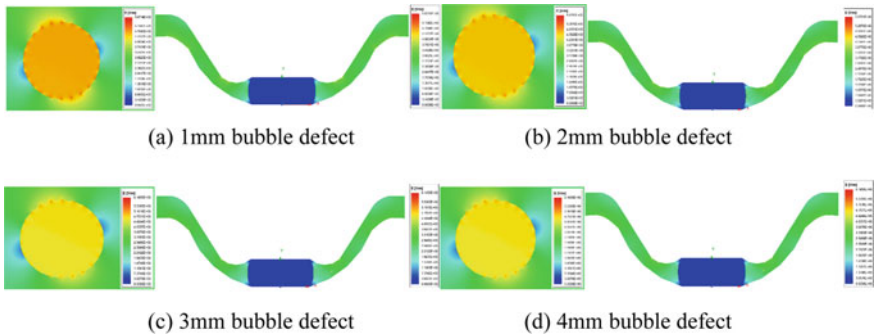


Fig. 8 Bubble defect $D = 1\text{ mm}$ to 4 mm 1100 kV basin insulator electric field distribution

higher than that of the surrounding. The central field strength of the bubble with a diameter of 1 mm can reach $4.656 \times 10^6\text{ V/m}$. The bubble with a diameter of 2 mm can reach $4.655 \times 10^6\text{ V/m}$. The bubble with a diameter of 3 mm can reach $4.655 \times 10^6\text{ V/m}$. The bubble with a diameter of 4 mm can reach $4.668 \times 10^6\text{ V/m}$. The electric field distribution of the basin insulator is the same as that of the bubble with a diameter of 1 mm , and the highest field intensity of the basin insulator exists at the position of the bubble.

As can be seen from Fig. 8, with the increase of bubble diameter, the maximum field strength of the basin insulator also increases, but the field strength at the center of the bubble basically does not change much. Compared with (12,040), the change of bubble diameter at this position has a significant influence on the maximum field strength on the basin insulator. The more significant change is the bubble center field strength. Compared with the original position (17,350), the bubble center field strength at this position (17,350) increases from $3.600 \times 10^6\text{ V/m}$ to around $4.655 \times 10^6\text{ V/m}$, increasing by 29.3%. The remaining positions in Fig. 2 were simulated and verified, and the data in Fig. 9 was obtained. It is concluded that when the 1100 kV basin insulator has internal bubble defects, the center field strength of the bubble in most areas except the position near the central conductor is about $4.55 \times 10^6\text{ V/m}$, which is 1.7 times of the position without bubble defects. The larger the bubble radius inside the basin insulator, the more prominent the influence on the local field strength, and the maximum field strength is distributed at the boundary between the bubble and the epoxy resin material.

3.3 Surface Particle Defect Simulation of Basin Insulator

The metal particles were selected to be placed on the convex surface of the basin insulator. A line segment is generated on the convex edge where the basin insulator contacts the metal particles on the flat surface, and the electric field distribution on the line segment is calculated (Table 2).

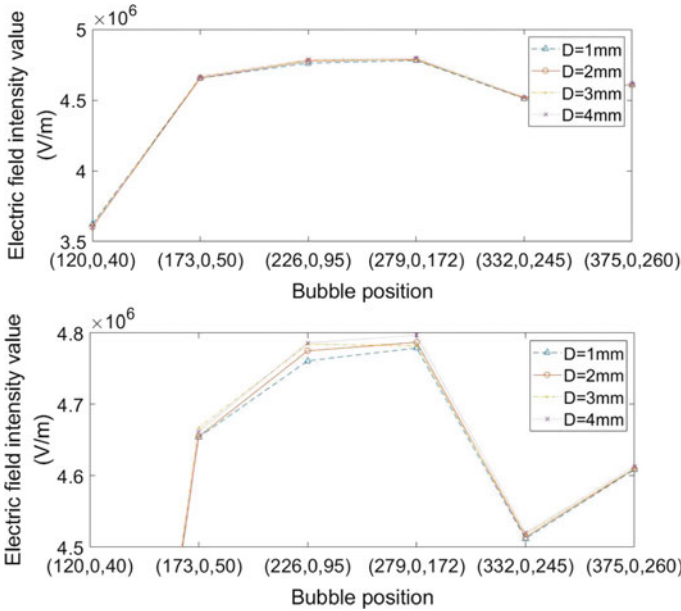


Fig. 9 Electric field intensity diagram under different bubble defects

Table 2 Maximum field intensity around particles with radius of 0.2 mm to 0.5 mm

Radius (mm)	Particle 1 (V/m)	Particle 2 (V/m)	Particle 3 (V/m)	Particle 4 (V/m)	Particle 5 (V/m)
0.2	0.124×10^6	2.81×10^6	5.00×10^6	8.90×10^6	5.98×10^6
0.3	0.135×10^6	2.64×10^6	6.01×10^6	9.68×10^6	5.49×10^6
0.4	0.145×10^6	3.20×10^6	7.01×10^6	14.72×10^6	7.08×10^6
0.5	0.171×10^6	4.18×10^6	9.23×10^6	20.25×10^6	8.85×10^6

4 Conclusion

In this paper, a high precision reduction model is carried out for the 1100 kV GIS basin insulator and its surrounding parts, and the defects of metal particle attachment on the surface of the basin insulator and bubbles inside the insulator are established. The electric field simulation is carried out under the condition that the central conductor rod potential is 1100 kV and the shell potential is 0 V. Finally, the following conclusions are drawn:

- (1) When metal particles are attached along the surface of the basin insulator, the larger the metal particles are, the more serious the surface electric field distortion will be.

- (2) At the same time, the attachment of metal particles between the middle end and the end of the basin insulator has the most serious influence on the electric field distortion, so the attachment of metal particles in this area should be avoided in the process of design and installation.
- (3) In the case of bubble defects, the basin insulator is removed from the position slightly closer to the center. In the case of bubble defects in most other areas, the field strength of the bubble center is around 4.55×10^6 V/m, which is 1.7 times of the position without bubble defects.
- (4) The larger the bubble defect is, the higher the maximum field strength of the basin insulator is, and the highest point is distributed on the boundary surface between the insulator and the bubble.

References

1. Wang C (2022) Miniaturization design of 550kV GIS basin insulator (I)—geometric shape optimization. *Trans China Electrotech Soc* 37(07):1847–1855 (in Chinese)
2. Xu PF, Tian JT, Sun MD, Zhang L, Dong BY, Hou YF, Chen S, Wang N, Lu YH, Dan K, Chen CH (2021) 252 kV three-phase box basin insulator stress test and analysis. *High Volt Elect Appar* 57(10):120–126 (in Chinese)
3. Wang ZB, Shao YY (2019) Dielectric loss measurement method and application of 126 kV GIS basin insulator. *High Volt Elect Appar* 55(10):76–80 (in Chinese)
4. Wu XX, Leng YK, Pang WL, Wu SP, Hui, LLH (2022) Research on electric field deterioration characteristics and fault probability prediction of GIS bus latent fault. *Power Grid Techn*, 1–12 (in Chinese)
5. Wang BX, Tian MX, Feng TN, Ma JQ (2022) Influence of typical defects of GIS basin insulator on its electric field distribution. *High Volt Elect Appar* 58(11):197–204 (in Chinese)
6. Chen CX, Li YF, Hao LC, Yuan DP (2022) Simulation study on stress distribution of insulator curing process in 1100 kV GIS. *Proceedings of the CSEE* 42(13):4992–5001 (in Chinese)
7. Li YF, Zhou J, Wu K (2020) Finite element stress analysis of 1100 kV GIS basin insulator under bubble defect. *Journal of Insulation Materials* 53(07):57–61 (in Chinese)
8. Ding DW, Liu WD, Zhang ZW, He L, Yuan MH, Zhang C (2020) Experimental study on time-frequency characteristics of flashover voltage of 1100 kV GIL insulator based on UWB voltage measurement. *High Volt Elect Appar* 56(02):1–6 (in Chinese)
9. Jia YF, Liu W, Li ZB (2019) Comprehensive optimization of electrical and mechanical properties of 1100 kV basin-type insulator based on finite element simulation and genetic algorithm. *High Volt Techn* 45(12):3844–3853 (in Chinese)
10. Li BB, Yu T, Ke YG, Luo S, Li JL, Zhen C, Zhao HY (2019) Technical characteristics and risk control measures of 1100 kV basin insulator. *China Elect Eng* 7:102–2019 (in Chinese)
11. Liu S, Jiang P, Peng CG, Shao XJ (2016) Breakdown fault analysis of a 1100 kV GIS basin insulator. *Zhejiang Elect Pow* 35(10):36–39 (in Chinese)
12. Chen Y, Cui BY, Wang NH, Wu Y, Cao DX, Cheng P (2016) Structure design of center insert of basin insulator for 1100 kV gas insulated switchgear. *High Volt Techn* 42(2):564–570 (in Chinese)
13. Akbari E, Mirzaie M, Asadpoor MB, Rahimnejad A (2013) Effects of disc insulator type and corona ring on electric field and voltage distribution over 230 kV insulator string by numerical method. *Iranian J Elect Eng* 9(1)
14. Nagaraju A, Reddy NRS, Kiranmayi R (2022) Dielectric withstand capability of functionally graded material disc insulator in single phase - gas insulated busduct. *Mat Today* 66(4)

15. Energy Weekly News (2020) Technology—high voltage research; study results from Wuhan University provide new insights into high voltage research (Dynamics of surface charge and electric field distributions on basin-type insulator in GIS/GIL due to voltage polarity reversal)
16. Tao L, Pei DL, Huang KX, Yu KW, Wang Z, Hou TT (2022) Application of 1000 kV GIL equipment in UHV Nanyang station expansion project. *China Elect Eng* 294(6):36–43 (in Chinese)
17. Luo GH, Zhao SN, Luo XC, Dong CQ, Huang YL (2018) Abnormal analysis of 1000 kV UHV Nanyang station ultrasonic partial discharge detection. *Elect Appl* 37(18):70–152 (in Chinese)

Research on the Thermal Expansion and Contraction Characteristics of UHV AC GIL Expansion Joint



Pengyang Li, Peipei Meng, Xixiu Wu, Hui Hou, Rongtai Wang,
and Yiming Zhang

Abstract As an integral part of the GIL system, GIL expansion joints are closely related to the safe and reliable operation of GIL equipment. The current density and electromagnetic loss distribution of GIL expansion joints under rated operating conditions are calculated, and the eddy current field-temperature field-force field multi-physical field coupling model is used as an excitation to analyze the temperature rise and thermotropic expansion of expansion joints under environmental conditions. The results show that the temperature distribution and axial expansion of the expansion joint under rated conditions are axisymmetric, with a maximum temperature rise of 35.6 °C and a maximum axial expansion of 0.078 mm. conductor heating and solar radiation are the main causes of the expansion joint temperature rise, and the axial thermal strain of the expansion joint is approximately linearly related to the load current and ambient temperature. Increased solar radiation will lead to an increase in temperature difference between the top and bottom of the corrugated tubes and an increase in thermal expansion.

Keywords UHV AC GIL · Expansion joint · Electromagnetic loss · Temperature distribution · Thermal expansion and contraction

P. Li · P. Meng · X. Wu (✉) · H. Hou · R. Wang · Y. Zhang
Wuhan University of Technology, Wuhan 430070, China
e-mail: wuxixiu@whut.edu.cn

P. Li
e-mail: lipengyang@whut.edu.cn

P. Meng
e-mail: mengpeipei@whut.edu.cn

H. Hou
e-mail: houhui@whut.edu.cn

1 Introduction

As an important part of GIL, the main functions of GIL expansion joint are as follows [1, 2]: (1) Length adjustment during installation or assembly; (2) Compensate for thermal expansion and contraction of GIL equipment caused by ambient temperature, thermal effects, etc.; (3) Compensate for equipment displacement from foundation settlement, earthquakes and other factors. Outdoor type GIL will be affected by changes in environmental conditions and its own through-flow heating, resulting in thermal stress on its different units, and then produce expansion and displacement deformation, and when the deformation accumulates to a certain extent, there will be sliding bracket gasket off, holding bolt cracking and other failures.

At present, domestic and foreign scholars' research on the thermal expansion and contraction of GIL expansion joints mainly focuses on loss calculation and temperature distribution, and most of them are field tests, and there are fewer theoretical studies on the thermal expansion and contraction of GIL. In the article [3], the loss analysis and structural improvement of UHV AC GIL expansion joint are carried out. The current density distribution and volume loss density of the expansion joint are calculated. In the literature [4], the temperature distribution of UHV GIL expansion joint was measured and analyzed. Through the type test found that the temperature of the extra-high voltage GIL expansion joint is significantly higher than other unit locations. The article [5] used finite elements to calculate the thermal expansion and contraction of GIL pipes, and analyzed the expansion and contraction as affected by load current. However, the effects of solar radiation and wind speed under ambient conditions were not considered.

In summary, the numerical analysis of thermal expansion and contraction characteristics of GIL expansion joints is carried out to obtain the thermal expansion and contraction characteristics and study the influence law of different factors, which helps to provide a basis for improving the performance of GIL against thermal stress and formulating reasonable measures for unit expansion, deflection and thermal expansion compensation.

2 GIL Expansion Joint Thermal Expansion and Contraction Calculation Model

2.1 Expansion Joint Calculation Model

Figure 1 shows the model of the retest rod-type GIL expansion joint, which includes the main components such as conductor, dunnage, and ignores the small components (Table 1).

Fig. 1 GIL expansion joint calculation model

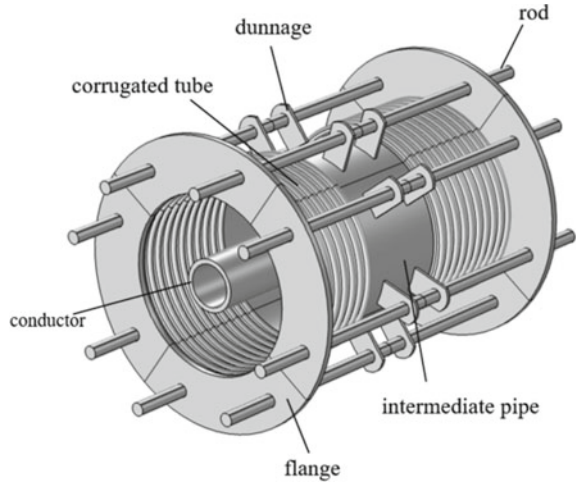


Table 1 Simulation model size parameters

Design project	Design value
Conductor length (mm)	1800
Conductor radius (mm)	80
Corrugated tube length (mm)	1400
Inner diameter of corrugated tubes (mm)	270
Wave number	10 + 10
Single layer wave thickness (mm)	5
Flange thickness (mm)	40
Flange radius (mm)	360
Number of support plates	16
Number of pull rods	8
Rod radius (mm)	20
Length of pull rod (mm)	2000

2.2 Multi-physics Coupling Model

From the Fig. 2, it can be seen that the heat sources of GIL expansion joints thermogenic expansion are mainly load current, ambient temperature, solar radiation.

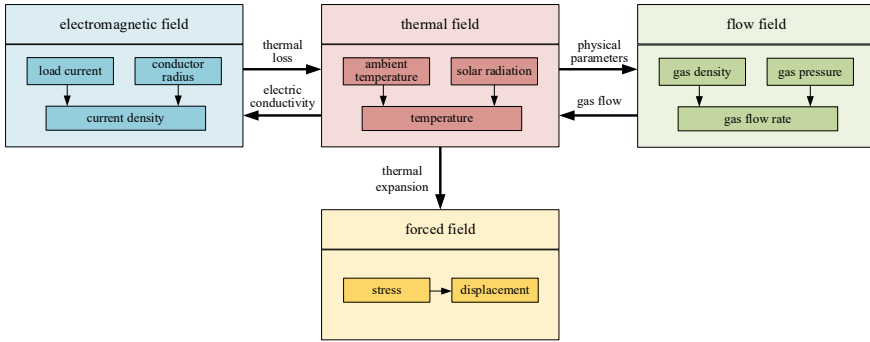


Fig. 2 Multi-physics coupling relationship

2.2.1 Mathematical Model of Electromagnetic Heat

The multi-physical field coupling model of eddy current field-temperature field-force field needs to be established to calculate the loss generated on the expansion joint conductor and corrugated tube and other components [6–9]. When the power-frequency AC current flows through the conductor, quasi-static electromagnetic field can be used to approximate it, and its governing equation is as follows [3, 8]:

$$\nabla \times \mathbf{H} = \mathbf{J} \tag{1}$$

$$\nabla \times \mathbf{E} = -\frac{\partial \mathbf{B}}{\partial t} \tag{2}$$

$$\nabla \cdot \mathbf{B} = 0 \tag{3}$$

where, \mathbf{H} is magnetic field intensity, A/m; \mathbf{J} is current density, A/m²; \mathbf{E} is the electric field intensity, V/m; \mathbf{B} is the magnetic induction intensity, T.

By introducing vector magnetic potential \mathbf{A} , the current density equation can be obtained:

$$\mathbf{J} = \mathbf{J}_s + \mathbf{J}_e = \mathbf{J}_s - j\omega\sigma \mathbf{A} \tag{4}$$

where, \mathbf{J} is current density, A/m²; \mathbf{J}_s is source current density; \mathbf{J}_e is eddy current density; ω is the angular frequency corresponding to the power frequency, rad/s; σ is the conductivity, S/m.

The equation of conductivity changing with temperature is as follows [6]:

$$\sigma(T) = \sigma_{20}/[1 + \alpha_{20}(T - 293.75)] \tag{5}$$

where, σ_{20} is the resistivity of the material at 20 °C, S/m; α_{20} is the resistance temperature coefficient of the material at 20 °C; T is the thermodynamic temperature, K.

For the loss power calculation equation:

$$P_s = \frac{1}{\sigma} \int |J|^2 dS \tag{6}$$

where, σ is electrical conductivity, S/m; J is the total current density, A/m².

2.2.2 Mathematical Model of Thermal Expansion

In the force field, the thermal expansion displacement per unit length of the GIL expansion joint is affected by temperature [7]:

$$\varepsilon^{Th} = \alpha_p \Delta T = \alpha_p (T - T_0) \tag{7}$$

where, α_p is the expansion coefficient; T_0 is the ambient temperature, °C.

According to Newton’s law, the equation of solid motion is as follows:

$$\frac{\partial \sigma_{ij}}{\partial x_j} + f_i = \rho \frac{\partial^2 u_i}{\partial t^2} + \mu \frac{\partial u_i}{\partial t^2} \tag{8}$$

where, σ_{ij} is the stress tensor; ρ is material density; f_i is an external force; u_i is displacement; μ is the damping coefficient.

The global strain tensor equation is as follows:

$$\begin{cases} \varepsilon_{ij} = \frac{1}{2} \left(\frac{\partial u_i}{\partial x_j} + \frac{\partial u_j}{\partial x_i} \right) \\ \varepsilon_{ij} = \varepsilon_{ij}^E + \varepsilon_{ij}^{Th} \end{cases} \tag{9}$$

where, ε_{ij} is the strain tensor; ε_{ij}^E is the elastic strain component; ε_{ij}^{Th} is the component of thermal strain.

3 Distribution of Thermal Expansion and Cold Shrinkage Under Rated Conditions

The boundary conditions under simulated rated conditions are shown in Table 2:

Table 2 Rated operating conditions

Parameter	Parameter value
Voltage class (kV) (alternating current)	1000
Running current (A)	6300
Ambient temperature (°C)	20
Insulation gas pressure (MPa)	0.4
intensity of solar radiation (W/m ²)	100

3.1 Electromagnetic Loss Calculation Results

The current density distribution at the cross section of the GIL expansion joint conductor is shown in Fig. 3. It can be seen from the figure that the current density distribution of the conductor conforms to the skin effect principle, and the maximum current density is near the outer surface of the conductor.

According to the simulation calculation results, the bulk density losses of conductor, corrugated tube, flange and tie rod are 123.33 W, 44.5 W and 32.56 W respectively (Fig. 4).

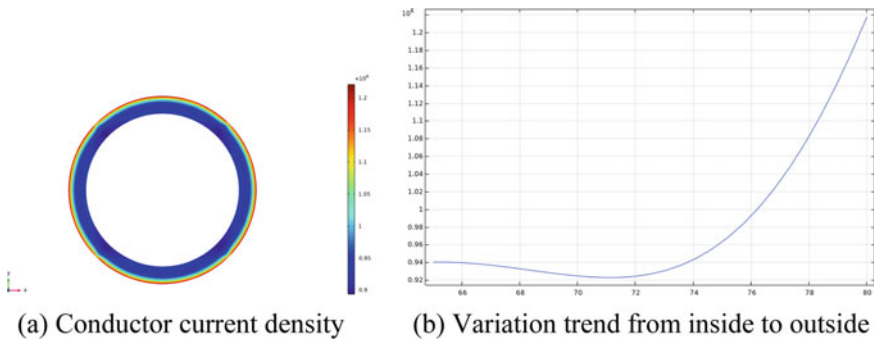


Fig. 3 Current density distribution

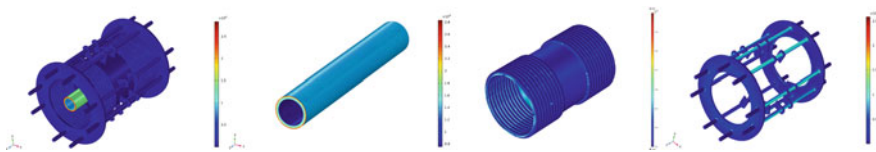


Fig. 4 Distribution of volume density loss at each part of GIL expansion joint

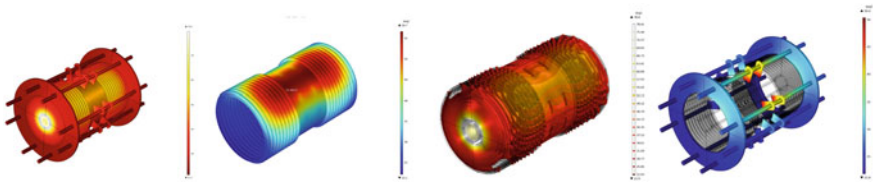


Fig. 5 Distribution of temperature at each part of GIL expansion joint

3.2 Temperature Distribution Calculation Results

Without considering the wind speed, the electromagnetic loss is added to the temperature field model as an excitation to simulate the temperature field distribution characteristics of the GIL expansion joint under environmental conditions. The calculation results are shown in Fig. 5.

The conductor temperature is the highest, with a maximum temperature of 79.9 °C and a maximum temperature difference of no more than 0.2 °C. The highest temperature of corrugated tube is 56.7 °C, and the maximum temperature difference is 34.6 °C. Tie rod temperature distribution is slightly higher in the middle, the highest temperature is 47.8 °C, and the overall temperature difference does not exceed 13.5 °C.

3.3 Stress Distribution Calculation Results

Figure 6 shows the stress distribution characteristics of GIL expansion joint.

The corrugated tube stress is smaller than the conductor stress, with a maximum value of 101 MPa. The stress distribution of corrugated tube is approximately inverted “V” shape, and the thermal stress difference between upper and lower corrugated

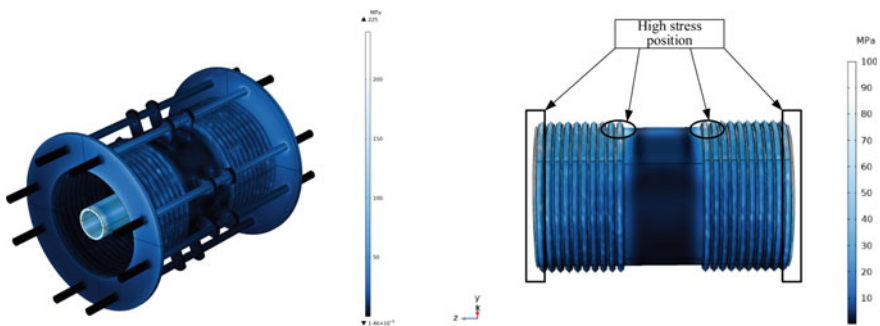


Fig. 6 Stress distribution of GIL expansion joint

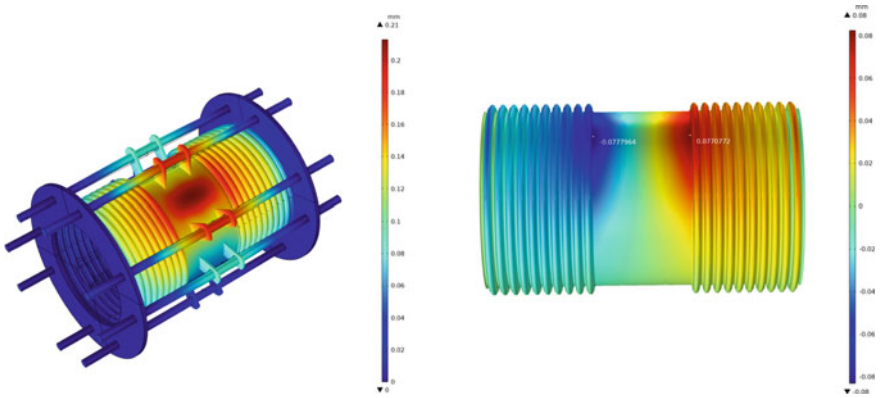


Fig. 7 Displacement distribution of GIL expansion joint

tube is large, because of the uneven distribution of temperature field above and below the shell.

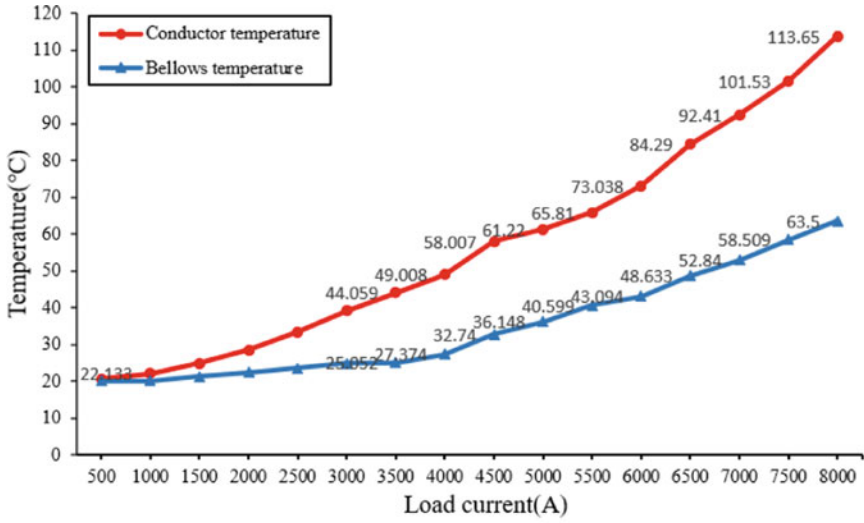
3.4 Expansion Displacement Calculation Results

Under rated conditions, the displacement of the GIL expansion joint is shown in Fig. 7. The overall displacement distribution is approximately axisymmetric, and the maximum displacement occurs above the corrugated tube, which is 0.21 mm. Maximum axial thermal expansion is 0.086mm.

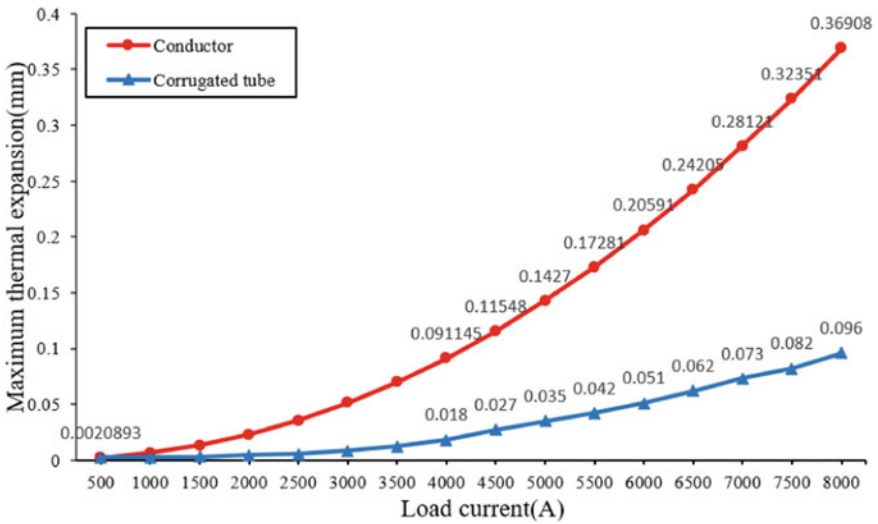
4 Analysis of Influencing Factors on Thermal Expansion and Cold Shrinkage of Corrugated Tube

4.1 Load Current

The main source of heat inside GIL is the conductor’s electromagnetic heat loss. Figure 8a shows how the temperature of conductors, corrugated tube and other components changes with load current under the condition that the ambient temperature is 20 °C, pipeline pressure is 0.7MPa, and there is no wind or light. Figure 8b shows the relationship between thermal expansion of expansion joints and load current under this condition.



(a) Temperature variation



(b) Thermal expansion variation

Fig. 8 Curves of temperature and thermal expansion with load current

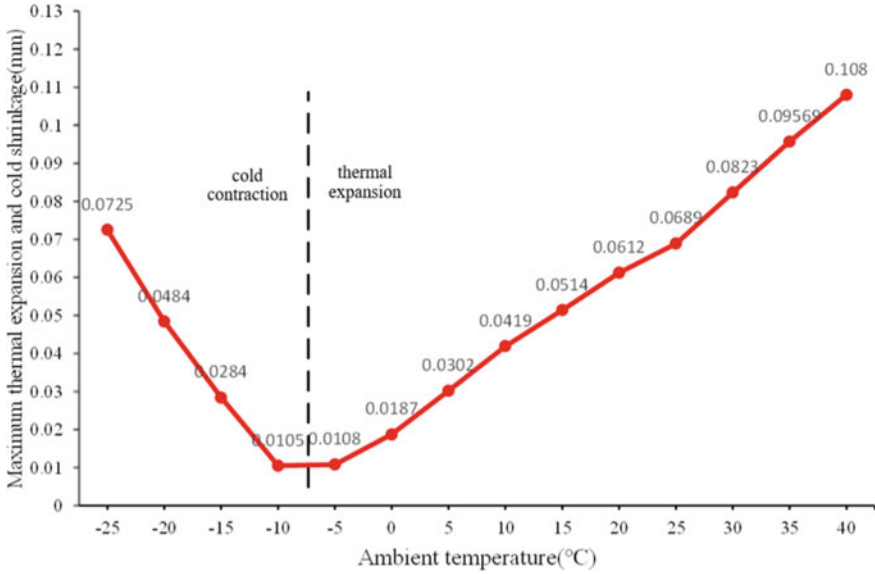


Fig. 9 Curve of thermal expansion and cold contraction with temperature

4.2 Ambient Temperature

The ambient temperature is an external factor affecting the temperature of the GIL expansion joint. The ambient temperature directly affects the thermal expansion and cooling shrinkage of the expansion joint corrugated tube. Figure 9 shows the variation curve of the maximum axial thermal expansion and cooling shrinkage of GIL expansion joint corrugated tube with ambient temperature under the conditions of conductor current of 6300 A, pipeline pressure of 0.7MPa, no wind and no light.

4.3 Radiation Intensity

In addition to the influence of ambient temperature, solar radiation is also one of the main causes of GIL temperature change, and the difference of solar radiation orientation will have a great impact on the temperature difference of GIL expansion joint. Figure 10 shows the relationship between the maximum axial thermal expansion of corrugated tube and solar radiation under the conditions of ambient temperature of 20 °C, conductor current of 6300 A, pipeline pressure of 0.7 MPa and no wind.

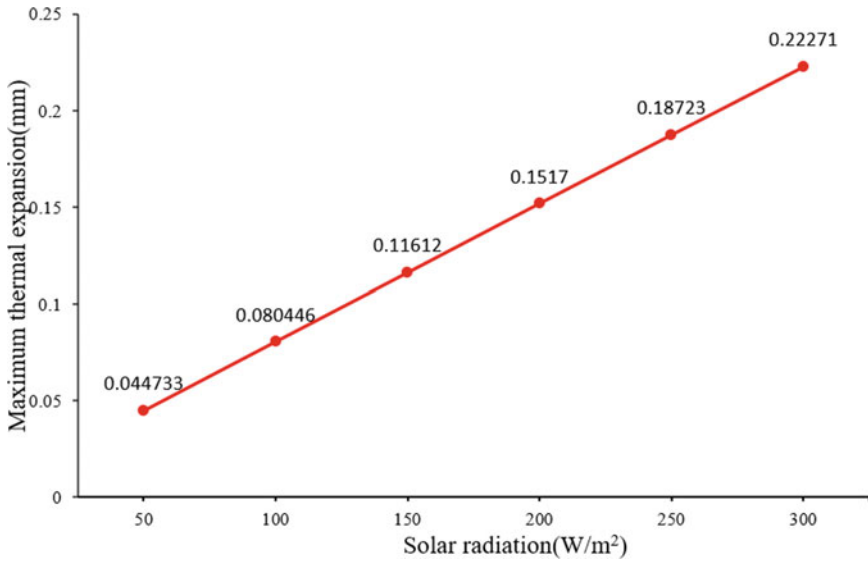


Fig. 10 The relationship between thermal expansion and solar radiation

5 Conclusion

- (1) Under the rated condition, the maximum temperature of the conductor is 79.9 °C, and the maximum temperature of the corrugated tube is 56.7 °C. Due to the influence of solar radiation and thermal convection of SF₆/N₂ mixed gas, the temperature difference between the upper and lower parts of the corrugated tube is large, and the maximum temperature difference is 34.6 °C. The rod is affected by heat conduction, and the maximum temperature is 47.8 °C.
- (2) The stress of conductor and bellows is symmetrically distributed at both ends of the shaft. The conductor stress is greater than the shell thermal stress, and the maximum conductor stress is 225 MPa. The stress distribution of the bellows is uneven, and the maximum value is 101 MPa.
- (3) The overall displacement distribution of the GIL expansion joint is approximately axisymmetric, and the maximum displacement appears above the corrugated tube, which is 0.21 mm. At this time, the maximum axial thermal expansion of the corrugated tube appears above the corrugated tube, which is 0.086 mm.
- (4) Affected by the ambient temperature, when the room temperature is less than -10 °C, the lower the temperature, the larger the cold shrinkage; When the room temperature is higher than -5 °C, the higher the temperature, the greater the thermal expansion. The maximum thermal expansion of the bellows of GIL expansion joint has a linear relationship with radiation intensity, and increases uniformly with the increase of radiation intensity.

References

1. Mao SW, Zhang ZQ, Luo HG (2022) Multi-scale finite element analysis of 550 kV GIS expansion joint. *High Volt App* 58(2):60–66 (in Chinese)
2. Wang C, Shen FH (2022) Design and application of expansion joint for 1100 kV GIS. *Electrotech Elect* 5:62–65 (in Chinese)
3. Liu LL, Tian HD, Wu ZH et al (2018) Loss analysis and structural improvement of UHV AC GIL expansion joint. *High Volt Eng* 44(10):3183–3189 (in Chinese)
4. Liu YP, Fei Y, Chen JB et al (2020) Measurement and analysis of temperature distribution of UHV GIL expansion joints. *High Volt App* 56(12):1–6 (in Chinese)
5. Wang J, Chen C, Li QM et al (2017) Thermal-induced flexible property of gas insulated lines and influencing factors based on thermal mechanical coupling analysis. *High Volt Eng* 43(2):429–437 (in Chinese)
6. Qiao YJ, Liang R, Gao P et al (2020) Heat transfer analysis of different conditions for SF₆/N₂ gas-insulated transmission lines. *IEEE Trans Power Deliv* 99:1
7. Zhang H. Multi-physics coupling field simulation and characteristics of 500 kV GIL [D]. South China University of Technology, (2019). (in Chinese)
8. Pang WL, Wu XX, Wu SP et al (2020) Compact design of 330 kV SF₆/N₂ mixed gas dielectric insulated bus. *High Volt Tech* 46(3):1044–1051 (in Chinese)
9. Niu H, Chen Z, Zhang H et al (2020) Multi-physical coupling field study of 500 kV GIL: simulation, characteristics, and analysis. *IEEE Access* 8:131439–131448

Improve the Toughness of Epoxy Resin Insulating Materials by Compounding Acid Anhydride Curing Agent



Yanning Zhao , Yushun Zhao , Zimin Luo , Xueping Li,
and Shengtao Hu

Abstract Epoxy resin is one excellent insulating material and is widely used in the manufacture of electrical insulation structures, but its toughness is poor. Therefore, toughening has been the first problem to be solved for the development of new epoxy insulating materials. In this paper, the method of compounding acid anhydride curing agent is used to improve the toughness of epoxy resin insulation materials. By compounding methylhexahydrophthalic anhydride (Me-HHPA) with a new special anhydride curing agent, the impact strength, cracking resistance and electrical breakdown strength of epoxy resin curing products are tested. The results show that this new anhydride curing agent can not only improve the mechanical properties and cracking resistance of epoxy resin composites, but also does not affect the electrical insulation properties of epoxy resin composites. Further, the paper also illustrates the mechanism of the effect of this new anhydride curing agent on the toughness of epoxy resin cured products, hoping that the study will provide a reference for the toughening of epoxy insulating materials.

Keywords New special anhydride · Epoxy resin toughness · Anti-cracking ability · Electrical insulation material

1 Introduction

Epoxy resin is an epoxy oligomer that reacts with a curing agent to produce a three-dimensional network of thermosetting plastic, which has excellent bonding, heat resistance, chemical resistance and electrical properties and has been widely used in electronic information, defense construction and other fields, becoming the fourth major material after metal, wood and cement [1]. The liquid epoxy resin can be cured at room temperature or by heating. Despite the many advantages of epoxy resin, it has

Y. Zhao · Y. Zhao (✉) · Z. Luo · X. Li · S. Hu

School of Electrical and Automation Engineering, Hefei University of Technology, Hefei 230009, China

e-mail: yushunzhao@126.com

© Beijing Paiké Culture Commu. Co., Ltd. 2024

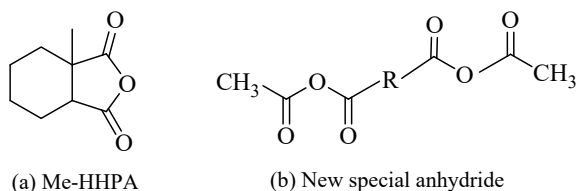
X. Dong and L. Cai (eds.), *The Proceedings of 2023 4th International Symposium on Insulation and Discharge Computation for Power Equipment (IDCOMPU2023)*, Lecture Notes in Electrical Engineering 1100, https://doi.org/10.1007/978-981-99-7393-4_51

539

problems such as poor temperature resistance, brittleness after curing, easy brittle fracture and poor toughness [2–4]. As their applications continue to expand, there are more stringent requirements for their performance. If the toughness of epoxy resin can be improved, it will broaden the application scope of epoxy resin.

There are many studies on the toughening of epoxy resins, which are mainly divided into physical and chemical methods. Chemical methods introduce flexible molecular chains into the main chain by adding reactive substances and thus achieve toughening. The physical method is to modify the epoxy resin by intermixing, alloying and filling, and thus achieve the purpose of toughening [5]. In this paper, we are improving the toughness of epoxy resin insulating materials by compounding with acid anhydride curing agents. Methylhexahydrophthalic anhydride (Me-HHPA), prepared by hydrogenation of methyltetrahydrophthalic anhydride, has a low melting point, is a colorless and transparent liquid at room temperature, and has a long service life [6]. The Me-HHPA/epoxy resin curing system has the advantages of excellent weatherability and leakage trace resistance, and has been widely used [7, 8]. However, the mechanical properties of the complexes obtained after their reaction with epoxy resins are poor, specifically in terms of resistance to mechanical impact. In addition, the cracking resistance of the compound is poor, and cracking is prone to occur when the ambient temperature is too high or too low, which has a serious impact on the insulation properties of the compound. Therefore, the type and content of the anhydride curing agent need to be improved to improve the toughness of the epoxy resin insulation material.

In response to the above problems, the laboratory made a new special anhydride, which has a high melting point, light yellow wax at room temperature, good miscibility with epoxy resin, long trial period of resin curing system, and yellow–brown color of the complex formed by reaction with epoxy resin. Its curing temperature is high and the cured product has good thermal stability. Its mixed with other curing agents, curing epoxy resin system toughness, small shrinkage deformation, high impact strength, high heat resistance index, can withstand severe hot and cold temperature shock. Suitable for large and medium-sized power transformers, mutual inductors, motor components and all kinds of electrical equipment casting insulation. In order to investigate the influence of this anhydride curing agent on the toughness of epoxy resin compound, the epoxy resin compound with different proportions of anhydride compounding curing agent was prepared experimentally. The relationship between different proportions of anhydride compounding curing agents and the toughness of epoxy resin complexes was measured, and the method can substantially improve the toughness of epoxy resin complexes, thus solving the problem of weak impact resistance and weak ability to withstand hot and cold shocks of the cured epoxy resin system.

Fig. 1 Molecular structure of hardener

2 Experimental Materials and Test Methods

2.1 Experimental Materials

Epoxy resin, model DER331 epoxy value of 0.535 mol/100 g, industrial grade, purchased from Dongguan Hongcheng Plastic Material Company; methyl hexahydrophthalic anhydride (Me-HHPA), molecular weight 168.19, purchased from Shanghai Maclean Biochemical Technology Co, The molecular structure is shown in Fig. 1a; A new laboratory-made special anhydride with the molecular structure shown in Fig. 1b; N,N-dimethylbenzylamine (BDMA), molecular weight 135.21, was purchased from Shanghai Aladdin Biochemical Technology Co.

2.2 Epoxy Resin Compound Preparation Process

Put 100 g of epoxy resin DER331 and different compounding ratio of anhydride curing agent in the reaction kettle at 80 °C with heating and stirring to dissolve the new special anhydride solid and mix with epoxy resin evenly, and the formulation of each group of anhydride curing agent is shown in Table 1. Adjust the rotational speed to 300–400 rpm, evacuate to maintain the vacuum degree of 0.1 Mpa to remove the dissolved gas in the system, stir for 1 h at 80 °C, then add the accelerator BDMA and evacuate for 10 min to get a homogeneous casting material, pour into the preheated mold at 80 °C, vacuum degas for 10–20 min, use the curing process 80 °C/4 h + 120 °C/12 h. Natural cooling to room temperature, demold and take out the sample parts.

Table 1 Mass ratio of anhydride curing agent in each group

Programmes	1	2	3	4
DRE331	100	100	100	100
Me-HHPA/New special anhydride	90:10	80:20	70:30	60:40
BDMA	0.6	0.6	0.6	0.6

3 Performance Characterization

3.1 Anti-cracking Index

The cracking resistance of the epoxy resin samples was tested according to the team standard applied by the laboratory. The test apparatus is an elevating alternating temperature chamber with a cooling rate of 0.1–0.3 °C/min. The cracking temperature of the epoxy resin sample is obtained and the cracking resistance index of the sample can be calculated by the following Eq. (1).

$$\tau_{80} = \sum \frac{25 - T_n}{N} \quad (1)$$

T_n is the temperature (°C) of a sample at the time of cracking, and N is the number of samples.

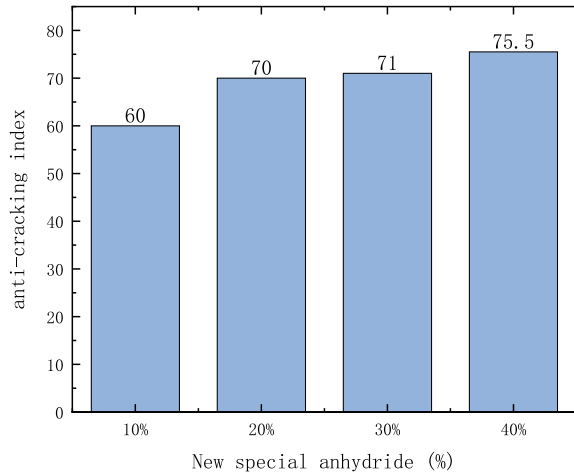
3.2 Impact Strength

According to the test standard of national standard GB/T 2571-1995 “resin casting body impact test method”, the impact strength of the sample was tested by compound impact tester. The test was carried out with a pendulum of 4J energy size, the pendulum angle was 150°, each specimen was tested 4 times, and the measurement results were averaged.

3.3 Electrical Breakdown Strength

According to the test standard of national standard GB/T1408.1-2016 “Test method for electrical strength of insulating materials”, the breakdown strength of the sample under the action of long-time electric field was measured at 100V/s step-up rate. The measurement ambient temperature is 25 °C, the test specimen is a 100mm diameter and 1mm thickness circular piece, the test voltage frequency is 50 Hz, 5 breakdown data are obtained, the test results are averaged and the breakdown strength is calculated using the Weibull distribution. The breakdown strength of each formulation with a breakdown probability of 63.2% was taken to investigate the effect of different anhydride curing agent formulation systems on the breakdown strength of epoxy resin complexes.

Fig. 2 Anti-cracking index of epoxy resin composite with different ratio of anhydride



4 Results and Discussion

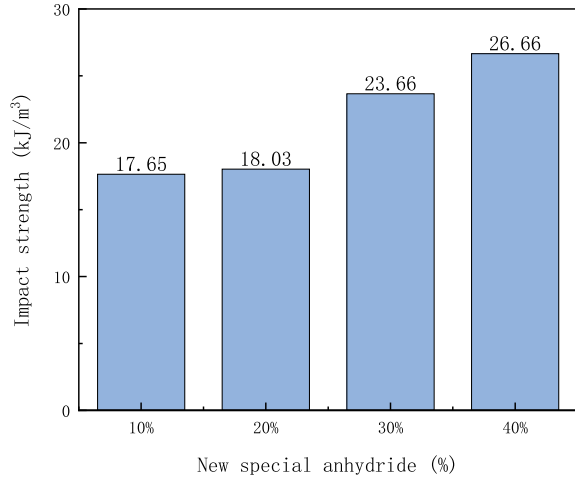
4.1 Anti-cracking Index of Different Acid Anhydride Curing Agent Formulation Systems

From Fig. 2, it can be seen that the addition of different proportions of new special anhydride has a certain influence on the anti-cracking index of epoxy resin compound. When the content of the new special anhydride in the compounding curing agent is 10%, the anti-cracking coefficient of the epoxy resin compound is only 60; when the content of the new special anhydride in the compounding curing agent is 40%, the anti-cracking coefficient of the epoxy resin compound is increased to 75.5. It can be inferred that this anhydride can be added to the epoxy resin as a toughening curing agent, which can well improve the anti-cracking ability of the epoxy resin compound.

4.2 Impact Strength of Different Anhydride Curing Agent Formulation Systems

From Fig. 3, it can be seen that the impact strength of epoxy resin compound is influenced by adding different proportion of new special anhydride. When the content of the new special anhydride in the compounding curing agent was 10%, the impact strength of the epoxy resin compound was only 17.65 kJ/m^3 ; while when the content of the new special anhydride in the compounding curing agent was 40%, the impact strength of the epoxy resin compound was 26.66 kJ/m^3 . It can be inferred that this

Fig. 3 Impact strength of epoxy resin composite with different ratio of anhydride



anhydride can improve the impact strength of the epoxy resin compound when it is added to the epoxy resin as a toughening curing agent.

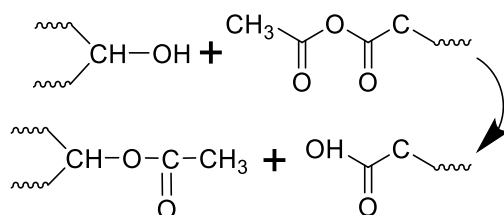
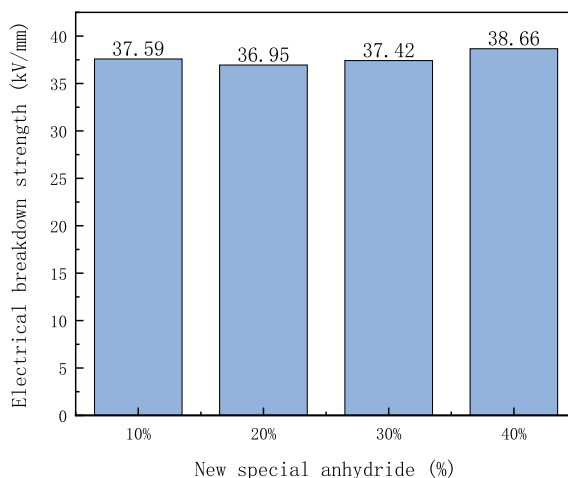
4.3 *Electrical Breakdown Strength of Different Anhydride Curing Agent Formulation Systems*

From Fig. 4, it can be seen that the addition of different proportions of the new special anhydride has little effect on the breakdown strength of the epoxy resin complexes. When the content of the new special anhydride in the compounding curing agent was increased from 10 to 40%, the breakdown strength of the epoxy resin compound was maintained at 36.95–38.66 kV/mm. It can be inferred that the addition of this anhydride to the epoxy resin as a toughening curing agent does not have much effect on the breakdown strength of the epoxy resin compound.

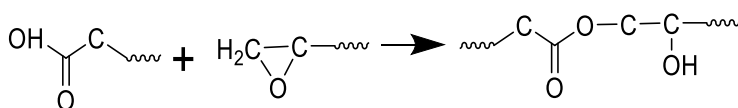
It can be seen that this new laboratory-made special anhydride as a high molecular weight aliphatic anhydride curing agent can improve the toughness of epoxy resin complexes. It mainly shows that it can improve the mechanical properties and cracking resistance of insulation materials. The reaction principle between the new special anhydride and bisphenol A epoxy resin is as follows.

The hydroxyl group in the BPA epoxy resin reacts with the acid anhydride, and the hydroxyl end of the epoxy resin reacts to produce an ester group, and the anhydride reacts to produce a carboxyl group. The reaction formula is as follows:

Fig. 4 Electrical breakdown strength of epoxy resin composites with different ratios of anhydride



The carboxyl group generated in the first step reacts with the epoxy group in the epoxy resin to generate an ester group and a hydroxyl group at the same time, and the reaction formula is as follows. The generated hydroxyl group can react with the anhydride, and the reaction is repeated to form a polymeric network structure.



The molecular structure of the new special anhydride is a chain structure, and the molecular chains are connected by several flexible groups, which are rotatable and can improve the flexibility of the epoxy resin compound [9, 10]. In addition, the main chain does not contain benzene ring groups and other groups that play a role in the rigidity of the material [11, 12]. These characteristics of the molecular structure make this new special anhydride can be used as a toughening anhydride curing agent to improve the mechanical properties and cracking resistance of epoxy resin complexes by compounding with other anhydride curing agents.

5 Conclusion

For the problem of low toughness of epoxy resin anhydride after curing, this paper compounded two curing agents, Me-HHPA and a new special anhydride made in the laboratory. The impact strength, cracking resistance coefficient and electrical breakdown strength of the epoxy resin complexes with different compounding ratios were tested to investigate the effect of the new special anhydride on the toughness of epoxy resin insulation materials, and the conclusions are as follows:

The compounding of Me-HHPA with two curing agents of new special anhydride can improve the impact strength and cracking resistance of epoxy resin composites, and the impact strength and cracking resistance coefficient of the composites will gradually increase with the increase of the ratio of new special anhydride.

The new special anhydride is added to the epoxy resin as a toughening curing agent. While improving the toughness of the epoxy resin composite, it does not affect the electrical insulation performance of the composite, and the breakdown field strength of the composite can be maintained above 36 kV/mm.

The molecular structure of this new special anhydride consists of a single main chain with no side chains. And the main chain is mainly composed of rotatable flexible groups without rigid groups such as benzene rings. These molecular structure characteristics make it possible to improve the toughness of epoxy resin complexes to some extent as an anhydride curing agent.

Acknowledgements This work is supported by Technology Project of Headquarters of State Grid Co., LTD (Item number:5500-202258489A-2-0-JK).

References

1. Zhang TD, Shi ZZ, Wu JX, Zhang CH, Feng Y, Chi QG (2022) Research progress of filled high thermal conductivity epoxy resin composites. *Insul Mater* 55(03):10–22 (in Chinese)
2. Cao JS, Wu SY, Xiang H, Hao PJ, Kuang DL, Liu JF, Shu D, Xing ML (2023) Research progress of rubber toughening epoxy resin. *Spec Rubber Prod* 44(01):58–62 (in Chinese)
3. Li ZQ, Huang PB, Zhou ZP (2022) Thermal properties and toughness of resins modified based on CNTs. *China New Technol New Prod* 11:37–39 (in Chinese)
4. Niu ZW, Cao LL, Li QP (2021) Application and research status of glass fiber reinforced composites. *Plastics Ind* 49(S1):9–17 (in Chinese)
5. Liu DC, Zhang L (2020) Effect of polysulfide rubber on the curing kinetics and mechanical strength of epoxy resins. *Synth Rubber Ind* 43(01):43–47 (in Chinese)
6. Qin YL, Chen LH, Lan FM (2021) Preparation and characterization of wood-plastic transparent materials. *Plast Ind* 49(11):107–112 (in Chinese)
7. Xu TZ, Zhou JA (1992) Modified liquid anhydride. *Insul Mater Newsl* (05):25–26 (in Chinese)
8. Yang T, Cheng Y, Zhang CF, Zhang JY (2014) Effect of diluents on the rheological and mechanical properties of bisphenol F epoxy resin/anhydride system. *J Beijing Univ Chem Technol (Natural Science Edition)* 03:76–81 (in Chinese)
9. Yan K, Shi J, Shi K, Wang M, Li G, Hong Z (2022) Effects of the chemical structure of curing agents on rheological properties and microstructure of WER emulsified asphalt. *Constr Build Mater* 347:128531

10. Okabe T, Oya Y, Tanabe K, Kikugawa G, Yoshioka K (2016) Molecular dynamics simulation of crosslinked epoxy resins: curing and mechanical properties. *Eur Polym J* 80:78–88
11. Li S, Chen D, Yuan Y, Gao C, Cui Y, Wang H, Liu X, Liu M, Wu Z (2020) Influence of flexible molecular structure on the cryogenic mechanical properties of epoxy matrix and carbon fiber/epoxy composite laminate. *Mater Des* 195:109028
12. Xiao Y, Mu X, Chen S, Jiang G, Xu Z, Ma C, Song L, Hu Y (2023) Biomass-derived polyphosphazene towards simultaneously enhancing the flame retardancy and mechanical properties of epoxy resins. *Chemosphere* 311(Part 1):137058

Fault Localization Method for Ring-Shaped DC Microgrids Based on Line Model and Euclidean Distance



Li Xinglong, Feng Bo, Yang Yi, Zhong Jiayong, and Zhao Hongwei

Abstract The rapid and precise localization in DC microgrids is a key technology that needs to be addressed urgently due to their characteristics such as fast-rising current and high amplitude during fault conditions. This paper establishes a mathematical model of the ring-shaped DC microgrid circuit and proposes a novel fault localization method by combining Euclidean distance with an optimization algorithm. Firstly, line models for the normal and ground fault states of the ring DC microgrid are established based on electrical quantities of the microgrid. Secondly, the correlation coefficient of the fault current is calculated using the Euclidean distance measure. Finally, a short-circuit fault localization scheme is established by integrating the Euclidean distance measurement with the genetic algorithm. The simulation results demonstrate that this method can accurately detect the fault location and transition resistance, and is applicable for locating low-resistance and high-resistance short-circuits. The method has low communication requirements, certain anti-interference ability, and satisfies the reliability requirements of protection for DC microgrids.

Keywords Ring-shaped DC microgrid · Mathematical model · Euclidean distance · Short circuit · Fault location

L. Xinglong · F. Bo (✉) · Y. Yi · Z. Hongwei
Chongqing Energy Internet Engineering Technology Research Center, Chongqing University of
Technology, Chongqing 400054, China
e-mail: fengbom@gmail.com

L. Xinglong
e-mail: 15320211987@163.com

Y. Yi
e-mail: yangyi@cqut.edu.cn

Z. Hongwei
e-mail: hongweizhao@vip.sina.com

Z. Jiayong
Electric Power Research Institute State Grid, Chongqing Electric Power Corporation,
Chongqing 401123, China
e-mail: liaozhong10000@163.com

1 Introduction

In recent years, the depletion of fossil fuels and the increasing demand for electricity have led to a rising need for high reliability and quality of electrical energy in power grids. Research has shown that the ring-shaped DC microgrid, which is a common type of structure, has higher efficiency compared to ordinary radial DC microgrid, especially when the distribution lines are short [1]. When distributed power sources or DC bus experience faults, the entire ring system can still maintain normal operating status by rapidly isolating the fault area. Therefore, the ring-shaped DC microgrid is often used in densely populated areas such as comprehensive buildings, factories, and data centers, and also has practical value in distribution systems for ships and spacecraft [1, 2]. Figure 1 shows the schematic of the ring-shaped DC microgrid structure.

If a short circuit fault arises in a DC transmission line, the fault current attains its maximum value in just a few milliseconds due to the combination of high busbar capacitance and low line impedance. Fast fault isolation and precise fault localization are critical for ensuring the normal operation of microgrids and preventing further damage to system equipment [3, 4]. Currently, scholars are mainly conducting research on fault location methods for short circuits in DC microgrids from the following three categories:

The first category is the active fault localization method. It is based on injecting signals into the faulty line through auxiliary equipment and analyzing signal characteristics to achieve fault localization. Reference [2] proposes a power probe unit that detects and locates faults by forming an RLC second-order circuit between the faulty circuit and equipment. Although this method can locate faults in circular microgrid circuits, it requires additional equipment to be added to the circuit, thereby increasing investment costs. To address the fault protection issue in maritime DC microgrids,

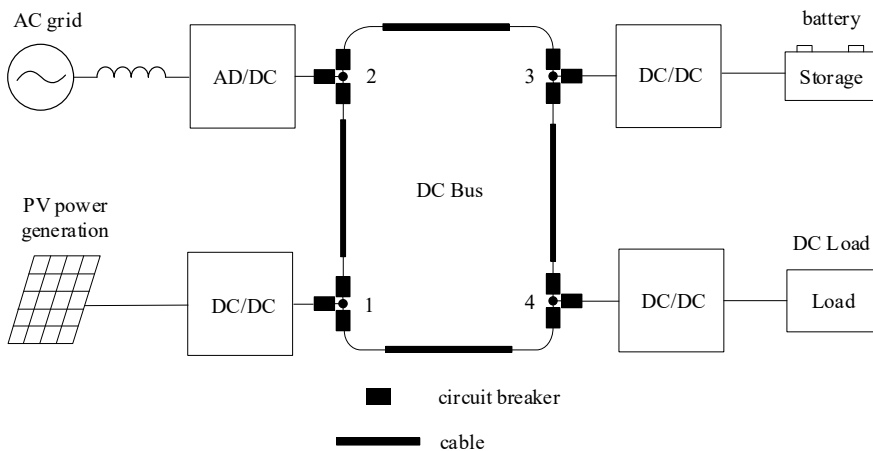


Fig. 1 Structure of ring DC microgrid

a novel power probe unit is proposed in [5], which injects DC signals into cables using an external circuit. This method is effective for detecting low-resistance short-circuit faults without requiring a communication link, but the additional equipment can result in significant cost increases. In [6], a capacitive grounding device was designed to determine the fault location by analyzing the response of the grounding capacitance. However, this technique is associated with significant errors. A novel fault location module composed of inductors and thyristors was designed in [7]. Despite this approach can calculate the fault resistance and location by analyzing the fault response, it still requires a relatively high investment cost.

The second category is the passive fault localization method. Passive fault localization method relies on the acquisition and analysis of electrical measurement values from the system itself. The traveling wave method is a typical passive fault localization method, which has been widely applied to fault protection in flexible DC transmission systems. In references [8, 9], authors proposed a traveling wave scheme for fault diagnosis in DC systems. This scheme locates faults by detecting the traveling wave time, but it requires multiple terminal devices and is not suitable for short line fault protection. Moreover, most scholars choose to utilize current or voltage signals in analyzing and calculating fault protection. Reference [10] proposed a method for fault detection and location, using a current derivative measurement of voltage changes with a limiting reactor. However, this method is incompatible with high-resistance grounding faults. Sliding discrete Fourier transform technology was utilized to achieve fault location in [11], which fundamentally relies on determining the fault position through line resistance and thus has certain limitations. In [12], a proposed parameter estimation method that relies on sampling the peak fault current is utilized to compute the fault location and other relevant parameters. This method requires a high sampling rate to ensure positioning accuracy. Reference [13] employed the Least Squares Method to calculate fault line parameters for the purpose of identifying faulty sections and implementing protection. Reference [14] presented using current oscillation frequency during faults for fault identification in DC microgrids. However, neither of these methods precisely locate faults. The literature [15] introduced a method for identifying low-resistance faults using a series-connected current-limiting inductor device and high-resistance faults using relay ground current. The fault location was achieved through iterative methods. However, this method requires additional current-limiting devices which may have an impact on the operation of the power grid.

As the field of artificial intelligence continues to progress, the third category of methods such as neural networks and image processing techniques have been applied in the field of electrical engineering. A scheme proposed in [1] combines multi-criteria systems with neural networks to achieve fault localization, resulting in an improved fault protection speed compared to the traditional differential protection method. However, it has yet to be validated for cases of high-resistance grounding. Reference [16] introduced an intelligent fault detection method for microgrids that employs wavelet transform and deep neural networks. In this method, the selection of the wavelet family directly affects the accuracy of fault detection and localization. Moreover, the mathematical morphology method has been employed for extracting

features of current signals to detect faults [17]. It can be applied to detect high-resistance short-circuit faults, but fault localization has not been carried out.

To tackle the issues aforementioned, this paper presents a fault localization method based on the Euclidean distance correlation coefficient. It is applicable for high-resistance fault situations. Furthermore, this paper involves the development of a mathematical model for a ring-shaped DC microgrid circuit. The proposed method utilizes local current measurements and avoids the need for additional signal injection, making it suitable for all types of feeder terminations. Finally, the proposed fault localization method is validated through simulation.

2 Ring DC Microgrid Modeling

Assuming a certain ring-shaped DC microgrid has n nodes (directly connected to the rectifier) and b transmission lines (DC lines connecting the nodes). The node voltage matrix U_n for the system can be expressed as:

$$U_n = [u_{n1} \ u_{n2} \ u_{n3} \ \cdots \ u_{nn}]_n^T \quad (1)$$

The output current matrix of the converters I_c can be represented as:

$$I_c = [i_{c1} \ i_{c2} \ i_{c3} \ \cdots \ i_{cn}]_n^T \quad (2)$$

The line current matrix I_0 can be given by:

$$I_0 = [i_{12} \ i_{23} \ i_{34} \ \cdots \ i_{ij} \ \cdots \cdot]_b^T \quad (3)$$

Taking the four-port ring DC microgrid shown in Fig. 2 as an example, analyze the mathematical relationships among various electrical quantities in the DC system. The system has four nodes directly connected to converters, and there are four DC transmission lines in the loop. When the DC system is functioning normally, the voltage matrix of the system U_n nodes can be expressed as follows:

$$U_n = [u_{n1} \ u_{n2} \ u_{n3} \ u_{n4}]_n^T \quad (4)$$

The output current matrix of the converters I_c can be represented as:

$$I_c = [i_{c1} \ i_{c2} \ i_{c3} \ i_{c4}]_n^T \quad (5)$$

Assuming that the clockwise direction of the loop is the positive reference direction for current, the current matrix of the line I_0 can be given by:

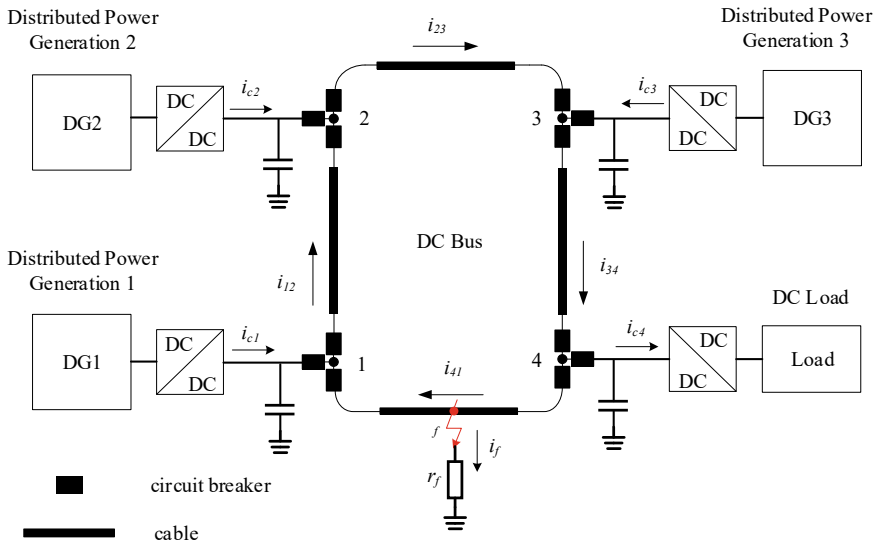


Fig. 2 Structure of the four-port ring DC microgrid

$$I_0 = [i_{12} \ i_{23} \ i_{34} \ i_{41}]^T \tag{6}$$

In existing research, there are mainly two types of models for the converter output current in response to short-circuit faults in DC microgrids. One type ignores input current of the converter [18], while the other type treats the converter as a constant current source [19]. Therefore, distributed power sources and converters can be considered as constant current source inputs.

When the system is operating normally, taking line 1–2 between node 1 and node 2 as an example, the circuit equation can be written according to Kirchoff’s voltage law:

$$l_{12} \cdot \frac{di_{12}}{dt} = (u_{n1} - u_{n2}) - r_{12} \cdot i_{12} \tag{7}$$

In which l_{12} and r_{12} represent the line inductance and resistance of line 1, respectively.

Expanding to each transmission line, the equation for the variation of currents can be represented in matrix form as:

$$L_0 \cdot \frac{dI_0}{dt} = A_0^T \cdot U_n - R_0 \cdot I_0 \tag{8}$$

L_0 is a diagonal matrix with dimensions of $b \times b$ representing the inductance of the DC transmission line. R_0 is also a diagonal matrix with dimensions of $b \times b$ representing the resistance of the transmission line. A_0 is a nodal branch admittance

matrix with dimensions of $n \times b$, where the elements of A_0 are defined as follows:

$$a_{nb} = \begin{cases} 1 \\ -1 \\ 0 \end{cases} \tag{9}$$

When a node is associated with a branch, if the direction of the branch is away from the node, then $a_{nb} = 1$, while if the direction of the branch points towards the node, $a_{nb} = -1$. When the node is not related to any branch, $a_{nb} = 0$.

Similarly, the node voltage change matrix equation can be derived based on Kirchhoff's current law:

$$C_0 \cdot \frac{dU_n}{dt} = I_c - A_0 \cdot I_0 \tag{10}$$

In this equation, C_0 is the diagonal matrix representing the capacitance of the busbars with a dimension of $n \times n$.

In Fig. 2, if there is a short circuit fault on line 4–1, the original four-port network will be equivalent to adding a faulty node between nodes 1 and 4. Both the number of nodes and branches in the network will increase by one. At this point, the voltage matrix of the system nodes, the current matrix of the lines, and the output current matrix of converters are as follows:

$$U_n = [u_{n1} \ u_{n2} \ u_{n3} \ u_{n4} \ u_{nf}]^T \tag{11}$$

$$I_0 = [i_{12} \ i_{23} \ i_{34} \ i_{4f} \ i_{f1}]^T \tag{12}$$

$$I_c = [i_{c1} \ i_{c2} \ i_{c3} \ i_{c4} \ i_f]^T \tag{13}$$

In the Eq. (13),

$$i_f = i_{f1} - i_{4f} \tag{14}$$

$$u_{nf} = r_f \cdot (-i_f) = E \cdot r_f \cdot I_0 \tag{15}$$

E is the coefficient vector, $E = [0001 - 1]$, and r_f represents the short-circuit transition impedance.

In the event of a short circuit fault, the original DC line can be considered as being divided into two separate lines at the fault location. At this stage, the inductance and resistance matrices in the Eq. (8) are adjusted as follows:

$$L = \begin{bmatrix} l_{12} & & & & \\ & l_{23} & & & \\ & & l_{34} & & \\ & & & l_{4f} & \\ & & & & l_{f1} \end{bmatrix}, R = \begin{bmatrix} r_{12} & & & & \\ & r_{23} & & & \\ & & r_{34} & & \\ & & & r_{4f} & \\ & & & & r_{f1} \end{bmatrix} \tag{16}$$

In the Eq. (10), the capacitance matrix is adjusted as:

$$C = \begin{bmatrix} c_1 & & & & \\ & c_2 & & & \\ & & c_3 & & \\ & & & c_4 & \\ & & & & 0 \end{bmatrix} \tag{17}$$

Differential equations for voltage and current are combined as shown below:

$$\begin{cases} L \cdot \frac{dI_0}{dt} = A_0^T \cdot U_n - R \cdot I_0 \\ C \cdot \frac{dU_n}{dt} = I_c - A_0 \cdot I_0 \end{cases} \tag{18}$$

Equation (18) provides a rapid approach to calculate the fault current in a DC microgrid when a short-circuit fault occurs.

3 Fault Localization Scheme

3.1 Calculation of Euclidean Distance

The Euclidean distance is one of the important analysis methods used in discriminant analysis. It is commonly used to describe the true distance between two points in a multi-dimensional space. The purpose of using this method is to analyze the distance between two samples, thereby characterizing the similarity between two samples. The smaller distance, the more related samples are, while the larger distance, the less related samples are [20].

Two groups of sample sequences X, Y are defined as follows:

$$X = (x_1, x_2, \dots, x_n) \tag{19}$$

$$Y = (y_1, y_2, \dots, y_n) \tag{20}$$

The Euclidean distance between two sets of sequences can be defined as:

$$d_E(X, Y) = \left[\sum_{i=1}^n (x_i - y_i)^2 \right]^{1/2} \tag{21}$$

Due to significant differences in the distribution of components across dimensions, it is necessary to standardize each component to eliminate the influence of units. This paper standardizes each component based on its respective mean value. The formula is as follows:

$$d_E(\overset{*}{X}, \overset{*}{Y}) = \left[\sum_{i=1}^n (\overset{*}{x}_i - \overset{*}{y}_i)^2 \right]^{1/2} \tag{22}$$

Within the equation: $\overset{*}{x}_i = x_i/\bar{x}$, \bar{x} is the average value of the sample sequence X ; $\overset{*}{y}_i = y_i/\bar{y}$, \bar{y} is the average value of the sample sequence Y .

If the Euclidean distance between samples consistently approaches zero throughout the entire space, it can be determined that the selected samples have a high degree of similarity and correlation. This also indicates that the sample curves follow a similar trend of change. This article utilizes the Euclidean distance to represent the similarity and amplitude differences in fault current. Practically, there are differences observed between the Euclidean distance of the sampled current and the calculated current. To better represent the current correlation, this article uses the formula (23) to convert the Euclidean distance into a correlation coefficient.

$$r = \frac{1}{1 + \left[\sum_{i=1}^n (\overset{*}{x}_i - \overset{*}{y}_i)^2 \right]^{1/2}} \tag{23}$$

When analyzing electrical currents, Euclidean space can be considered as a two-dimensional space composed of time and current. Therefore, the sampled current sample sequence can be represented as I_{sam} and the calculated current sample sequence can be represented as I_{cal} . The expressions are respectively:

$$I_{sam} = ((i_{sam1}, t_{sam1}), (i_{sam2}, t_{sam2}), \dots, (i_{samk}, t_{samk})) \tag{24}$$

$$I_{cal} = ((i_{cal1}, t_{cal1}), (i_{cal2}, t_{cal2}), \dots, (i_{calk}, t_{calk})) \tag{25}$$

The electrical current correlation coefficient based on the Euclidean distance can be expressed as:

$$r_i = \frac{1}{1 + [(i_{sam}^* - i_{cal}^*)^2 + (t_{sam}^* - t_{cal}^*)^2]^{1/2}} \tag{26}$$

When the time dimension is fixed, the current sequences contain k samples. In this case, the electrical current correlation coefficient can be simplified to:

$$r_i = \frac{1}{1 + |i_{sam}^* - i_{cal}^*|} \tag{27}$$

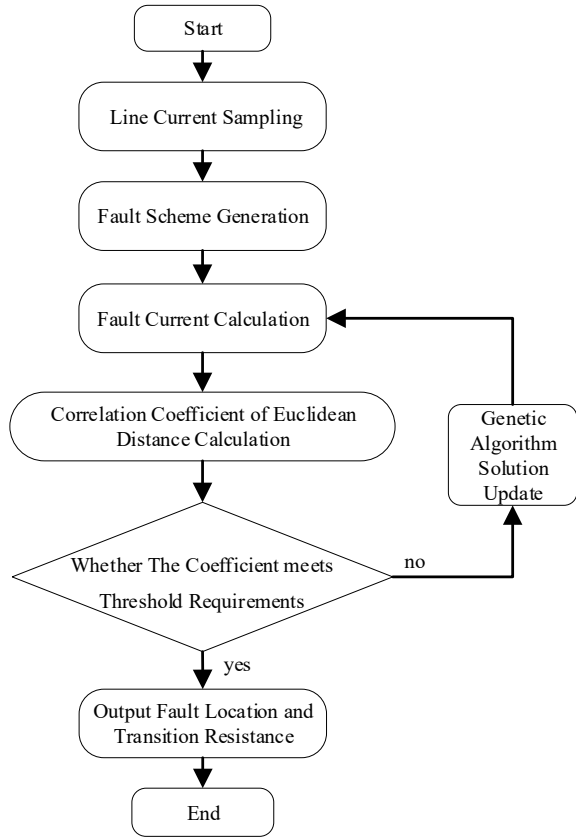
3.2 Fault Localization Method

DC microgrid lines typically have intelligent electronic devices (IEDs) installed at both ends of the line to monitor and protect the system [2]. When a short circuit fault occurs, the system monitors and retrieves information on current and voltage through IED devices. In this part, a fault localization approach is proposed by calculating the Euclidean distance between sampled current and transient calculated current, combined with genetic algorithm analysis.

The fault localization process is illustrated in Fig. 3. The specific implementation steps of the method are as follows:

1. Obtain circuit current: Sample current is obtained through intelligent electronic devices, current sensors, etc.
2. Fault scheme initialization: A large number of combinations of fault resistance and fault location schemes are obtained through randomly generated methods.
3. Calculation of Fault Current: Once the fault schemes are generated, transient fault currents are calculated using the established system mathematical model.
4. Calculation of Euclidean distance and correlation coefficient: The correlation between currents is analyzed by calculating the Euclidean distance between transient current and sampled current.
5. Determine if it meets the threshold: After the occurrence of the fault, the closer the Euclidean distance between the sampled current and the transient calculated current, the more accurate the fault scheme. Therefore, a threshold of k_1 is set for judgment, and when the calculated correlation coefficient is greater than k_1 , the fault scheme is determined. Through extensive simulation validation $k_1 = 0.99$.
6. Genetic algorithm scheme update: When the generated fault scheme does not meet the Euclidean distance correlation coefficient threshold requirement, genetic algorithm is used for scheme optimization to find the optimal scheme.

Fig. 3 Fault localization flowchart



3.3 Data Window Selection and Current Correction

When analyzing currents, the Euclidean space can be considered as a two-dimensional space consisting of time and current. The sampled current and the transient calculated current respectively form two sets of sample sequences. The sample size is determined by the sampling frequency and calculation window. A higher sampling frequency results in more samples and a larger calculation window also leads to more samples. To accurately evaluate the Euclidean distance between the sampled current and the calculated current, the selection of the data window is of great importance.

In this paper, the sliding window method is adopted to slide a fixed-length actual current sampling window on the time axis to ensure alignment between the actual current sampling point and the calculated current point. Due to the discrete nature of sampled current and the influence of noise, it is difficult to accurately determine the time of fault occurrence. However, after the fault occurs and the current rises to its maximum value and then stabilizes, the sampling window will slide and sample

the maximum value of the current. Therefore, the maximum current value can be selected as the reference time for correcting the window current, as shown in Fig. 4.

According to the analysis of simulation data, a data window of $T = 1 \times 10^{-4}$ s is selected in this paper.

When current correction is needed, there are two possible relationships between the actual sampled current and the calculated current:

- When the maximum value of the sampled current I_{s_max} is less than or equal to the maximum value of the calculated current I_{c_max} , the calculated current should be shifted until the maximum value of the sampled current aligns with the calculated current.
- When the maximum value of the sampled current I_{s_max} is greater than or equal to the maximum value of the calculated current I_{c_max} , the calculated current should be shifted until the maximum value of the sampled current aligns with the maximum value of the calculated current on the time axis.

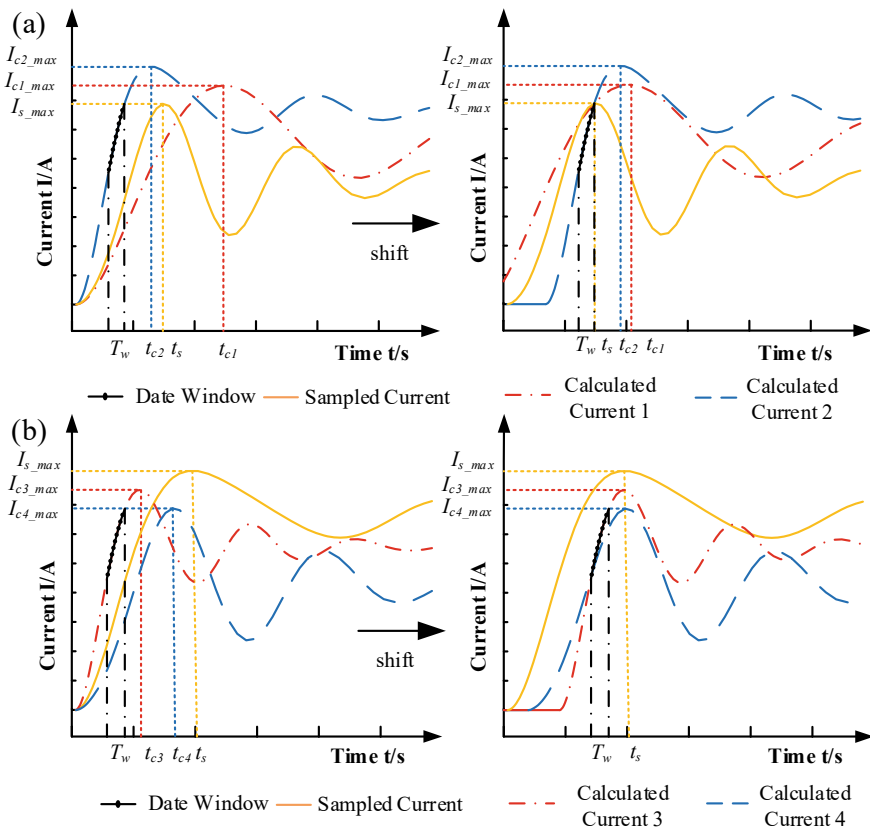


Fig. 4 Current correction a I_{s_max} is less than I_{c_max} , b I_{s_max} is greater than I_{c_max}

4 Simulation Verification

To provide preliminary validation for the proposed fault location scheme, this paper constructed a four-port ring DC microgrid based on the Matlab/Simulink simulation platform, simulating a low-voltage 400 V DC microgrid system. The simulation architecture model and system parameters are provided in the Appendix.

The simulation was set up with a short-circuit fault occurring at $t = 1\text{ s}$ and an initial ground transition resistance of $R_f = 1\ \Omega$. According to the bus voltage waveform shown in Fig. 6, upon the occurrence of a short-circuit fault, the bus voltage quickly drops and then gradually stabilizes after a brief high-frequency oscillation (Fig. 5).

Figure 7 respectively simulate changes in the line current for line 1–2 when a ground fault takes place on line 1–4. As the fault position d increases, the oscillation frequency of the line current I_{21} gradually increases while the current rise rate decreases. When the fault position is fixed, the transition resistance directly influences the amplitude of the line current. Based on these characteristics of current

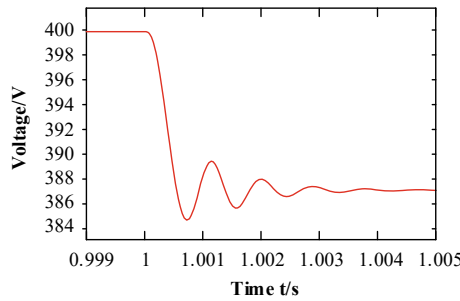


Fig. 5 DC bus voltage

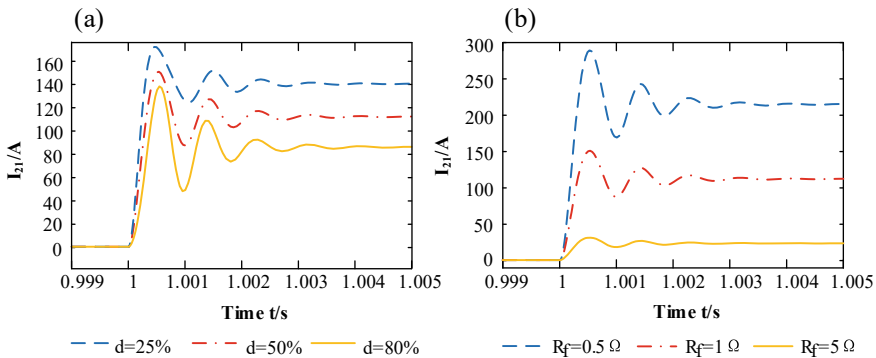


Fig. 6 Current in line 1–2 **a** different fault locations with the same transition resistance, **b** the same fault location with different transition resistances

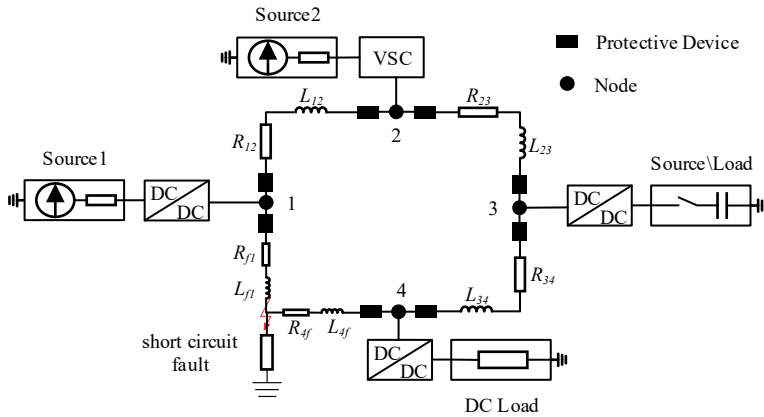


Fig. 7 Simulation structure of the four-port ring DC microgrid

changes, the proposed fault localization algorithm can precisely locate faults and determine the size of transition resistance.

To validate the accuracy of the fault localization approach, this paper defines the errors in fault location and transition resistance as follows:

$$Error_p = \frac{|L_e - L_a|}{L_T} \times 100\%, Error_r = \frac{|R_e - R_a|}{R_T} \times 100\% \quad (28)$$

Here, L_e and L_a represent the detected and actual fault locations, respectively, while L_T is the total length of the fault line. R_e and R_a represent the detected and actual fault resistances, respectively, and R_T is the reference fault resistance, which was set to 10Ω .

Tables 1 and 2 provide the error analysis of fault locations and fault resistances under different conditions.

Table 1 Error analysis for different fault locations with same transition resistances

Fault location (%)	Fault location error			Fault resistance error		
	Maximum error (%)	Minimum error (%)	Average error (%)	Maximum error (%)	Minimum error (%)	Average error (%)
5	3.37	0.23	1.45	5.68	0.02	3.44
10	3.06	0.17	1.28	5.35	0.01	3.19
20	2.79	0.17	0.73	4.77	0.01	2.54
50	1.67	0.06	0.09	3.92	0.00	1.95
70	2.13	0.19	0.48	4.18	0.01	2.01
80	2.88	0.2	1.22	4.75	0.01	2.97
95	3.53	0.2	1.57	5.21	0.01	3.58

Table 2 Error analysis for different transition resistances with same fault locations

Fault resistance (Ω)	Fault location error			Fault resistance error		
	Maximum error (%)	Minimum error (%)	Average error (%)	Maximum error (%)	Minimum error (%)	Average error (%)
0.1	0.16	0.00	0.07	0.19	0.00	0.08
0.5	0.42	0.00	0.12	0.23	0.01	0.10
1	1.27	0.01	0.59	0.46	0.04	0.27
2	2.77	0.09	0.96	1.83	0.08	0.85
5	3.19	0.14	1.75	3.01	0.10	1.56
10	3.74	0.09	2.68	5.42	0.25	2.77

After a short-circuit fault occurs, the transient current in the fault localization algorithm does not exactly match the simulated current. The highest accuracy of fault localization is achieved when the fault position is in the middle of the line. The accuracy of fault localization gradually decreases as the fault position approaches the ends of the line. As the transition resistance of the fault increases, the difficulty of fault localization increases and the accuracy of fault localization decreases. When the transition resistance is at its maximum value of $R_f = 10\Omega$, the fault detection error also reaches its maximum. The average error in the fault location is 2.68%, and the average error in the fault resistance is 2.77%. It can be seen that the proposed method can precisely locate faults and determine the transition resistance.

5 Conclusion

To address the issue of the imprecise fault location in ring DC microgrids when a short circuit fault exists, this article proposes a fault localization scheme based on the Euclidean distance correlation coefficient for grounded short-circuit faults in ring DC microgrids. A system model is established and theoretical analysis and simulation verification are conducted. The following conclusions are obtained:

- By establishing a model of the ring microgrid in a fault state, the transient current resulting from the fault can be computed quickly and accurately.
- The proposed approach can accurately detect the fault location and transition resistance. It is applicable to both low-resistance and high-resistance short-circuit situations, satisfying the reliability requirements of DC microgrids.

Acknowledgements This work was supported by Chongqing Municipal Natural Science Foundation (cstc2020jcyj-msxmX0349), Science and Technology Research Project of Chongqing Municipal Education Commission (KJQN202101147), Science and Technology Research Project of Chongqing Municipal Education Commission (KJQN202101118), Science and Technology

Table 3 Simulated circuit parameters

Transmission line parameters	
Unit resistance R_u	0.121 mΩ/km
Unit inductance L_u	9.7 μh/km
Length of each line l	2 km
Fault location d	1 km
Transition resistance R_f	1Ω

Research Project of Chongqing Municipal Education Commission (KJQN202101119) and Graduate Education High-quality Development Project of Chongqing University of Technology (gzlxc20223066).

Appendix

See Fig. 7 and Table 3.

References

1. Abdali A, Mazlumi K, Noroozian R (2019) High-speed fault detection and location in DC microgrids systems using multi-criterion system and neural network. *Appl Soft Comput J* 79:341–353. <https://doi.org/10.1016/j.asoc.2019.03.051>
2. Park JD, Candelaria J, Ma L, Dunn K (2013) DC ring-bus microgrid fault protection and identification of fault location. *IEEE Trans Power Deliv* 28(4):2574–2584. <https://doi.org/10.1109/TPWRD.2013.2267750>
3. Chen H, Tian XH, Gao CX, Zhen SQ, Yan CX (2019) Research overview on fault location for DC microgrid. *Guangdong Electric Power* 32(7):44–51. <https://doi.org/10.3969/j.issn.1007-290X.2019.007.007> (in Chinese)
4. Bayati N, Baghaee HR, Hajizadeh A, Soltani M (2021) Localized protection of radial DC microgrids with high penetration of constant power loads. *IEEE Syst J* 15(3):4145–4156. <https://doi.org/10.1109/JSYST.2020.2998059>
5. Christopher E, Sumner M, Thomas DWP, Wang X, de Wildt F (2013) Fault location in a zonal DC marine power system using active impedance estimation. *IEEE Trans Ind Appl* 49(2):860–865. <https://doi.org/10.1109/TIA.2013.2243391>
6. Makkieh A, Psaras V, Peña-Alzola R, Tzelepis D, Emhemed AAS, Burt GM (2021) Fault location in DC microgrids based on a multiple capacitive earthing scheme. *IEEE J Emerg Sel Top Power Electron* 9(3):2550–2559. <https://doi.org/10.1109/JESTPE.2020.2995946>
7. Yang Y, Huang C, Xu Q (2020) A fault location method suitable for low-voltage DC line. *IEEE Trans Pow Deliv* 35(1):194–204. <https://doi.org/10.1109/TPWRD.2019.2930622>
8. Wu J, Li H, Wang G, Liang Y (2017) An improved traveling-wave protection scheme for LCC-HVDC transmission lines. *IEEE Trans Power Deliv* 32(1):106–116. <https://doi.org/10.1109/TPWRD.2016.2549565>
9. Azizi S, Sanaye-Pasand M, Abedini M, Hasani A (2014) A traveling-wave-based methodology for wide-area fault location in multiterminal DC systems. *IEEE Trans Power Deliv* 29(6):2552–2560. <https://doi.org/10.1109/TPWRD.2014.2323356>

10. Sneath J, Rajapakse AD (2016) Fault detection and interruption in an earthed HVDC grid using ROCOV and hybrid DC breakers. *IEEE Trans Power Deliv* 31(3):973–981. <https://doi.org/10.1109/TPWRD.2014.2364547>
11. Wakode SA, Ballal MS, Deshmukh RR (2022) Sliding DFT-based fault location scheme for DC microgrid. *IEEE Trans Ind Appl* 58(5):5944–5954. <https://doi.org/10.1109/TIA.2022.3189610>
12. Bayati N, Baghaee HR, Hajizadeh A, Soltani M, Lin Z, Savaghebi M (2022) Local fault location in meshed DC microgrids based on parameter estimation technique. *IEEE Syst J* 16(1):1606–1615. <https://doi.org/10.1109/JSYST.2021.3107905>
13. Mohanty R, Pradhan AK (2018) Protection of smart DC microgrid with ring configuration using parameter estimation approach. *IEEE Trans Smart Grid* 9(6):6328–6337. <https://doi.org/10.1109/TSG.2017.2708743>
14. Mohanty R, Pradhan AK (2019) DC ring bus microgrid protection using the oscillation frequency and transient power. *IEEE Syst J* 13(1):875–884. <https://doi.org/10.1109/JSYST.2018.2837748>
15. Bhargav R, Bhalja BR, Gupta CP (2020) Novel fault detection and localization algorithm for low-voltage DC microgrid. *IEEE Trans Ind Inf* 16(7):4498–4511. <https://doi.org/10.1109/TII.2019.2942426>
16. Yu JJQ, Hou Y, Lam AYS, Li VOK (2019) Intelligent fault detection scheme for microgrids with wavelet-based deep neural networks. *IEEE Trans Smart Grid* 10(2):1694–1703. <https://doi.org/10.1109/TSG.2017.2776310>
17. Bayati N, Baghaee HR, Hajizadeh A, Soltani M, Lin ZY (2020) Mathematical morphology-based local fault detection in DC microgrid clusters. *Electr Power Syst Res* (prepublish) 192:106981. <https://doi.org/10.1016/J.EPSR.2020.106981>
18. Li C, Zhao C, Xu J, Ji Y, Zhang F, An T (2017) A pole-to-pole short-circuit fault current calculation method for DC grids. *IEEE Trans Power Syst* 32(6):4943–4953. <https://doi.org/10.1109/TPWRS.2017.2682110>
19. Satpathi K, Yeap YM, Ukil A, Geddada N (2017) Short-time fourier transform based transient analysis of VSC interfaced point-to-point DC system. *IEEE Trans Ind Electron* 65(5):4080–4091. <https://doi.org/10.1109/TIE.2017.2758745>
20. Deng YP, Yang X, Zhang MX, Pan AQ (2015) Discrimination of magnetizing inrush and short circuit current of converter transformer based on euclidean distance. *Power Syst Technol* 39(9):2671–2676. <https://doi.org/10.13335/j.1000-3673.pst.2015.09.045> (in Chinese)

Mechanical Structure Design and Strength Analysis of 750 kV High Voltage Test Platform



Ming Lei, Xinghui Jiang, and Yonggang Zhao

Abstract In this paper, a vehicle-mounted test platform with a weight of 6500 kg is designed to meet the requirements of 750 kV high-voltage test. In this paper, a three-dimensional model is designed, and a mechanical model is established to carry out theoretical mechanical analysis of the strength of hydraulic support and base support, and conduct mechanical simulation using finite element analysis software to obtain the maximum deformation value and equivalent stress of the test platform. The simulation results show that it can meet the use requirements. At present, the equipment has been successfully applied to the field test of 750 kV high voltage withstand voltage test.

Keywords Structure design · Theoretical mechanical analysis · Mechanical strength check · Finite element simulation

1 Introduction

High voltage insulation is used in many sectors of the national economy, with the largest number of applications in the electric power industry [1]. In order to test the insulation level of electrical equipment and prevent the operation safety accidents of power grid equipment, especially transformers, cables and other major power transmission and transformation facilities, AC voltage test on these equipment is the most effective and direct method to identify the insulation strength of power equipment, is an important content of preventive test [2, 3]. In addition, because the voltage of the AC voltage test is generally higher than the operating voltage, so after the test, the equipment has a larger safety margin, so the AC voltage test is an important means to ensure the safe operation of the power equipment [4–6].

M. Lei · X. Jiang (✉)
Suzhou City University, Suzhou 215104, Jiangsu, China
e-mail: xinghui@szcu.edu.cn

Y. Zhao
HD Electric Co., Ltd., Suzhou, Jiangsu 215104, China

© Beijing Paiké Culture Commu. Co., Ltd. 2024
X. Dong and L. Cai (eds.), *The Proceedings of 2023 4th International Symposium on Insulation and Discharge Computation for Power Equipment (IDCOMPU2023)*, Lecture Notes in Electrical Engineering 1100, https://doi.org/10.1007/978-981-99-7393-4_53



Fig. 1 AC voltage resistance test platform (horizontal). 1. Rain cover, 2. Voltage balancing ring of reactor, 3. Hoop, 4. Reactor, 5. Extended hydraulic support leg, 6. Hydraulic cylinder

The original AC voltage test equipment shows in Fig. 1, it is generally large and heavy, especially the core component: reactor, the weight is generally several tons, the field test relies on crane assembly, but also after complex wiring can be conducted before the experiment. Low efficiency, high labor intensity, easy to connect the wrong line.

The total length of the AC pressure test platform is 9500 mm, the width is 2200 mm, and the transport height is 2600 mm, so the strength of the bottom beam of the whole platform and the structural strength of the bracket are particularly important [7–9]. Because the force of the platform and bracket changes at any time, the dynamic force situation is complex. The structure of 1750 kV voltage test platform is shown in Fig. 2.

2 Theoretical Mechanics Analysis

2.1 Overall Theoretical Check of Horizontal Platform (Static State Without Wind)

The total weight of the equipment on the platform is about 6500 kg, considering the weight of the platform is 3000 kg, the total gravity is 95,000 N, and the area under pressure of the 6 supporting legs is:

$$A = 6 \times \frac{\pi}{4} \times (D^2 - d^2) = 1.5\pi \times (0.08^2 - 0.06^2) = 0.013188 \text{ m}^2$$

The bearing pressure of the supporting legs is:

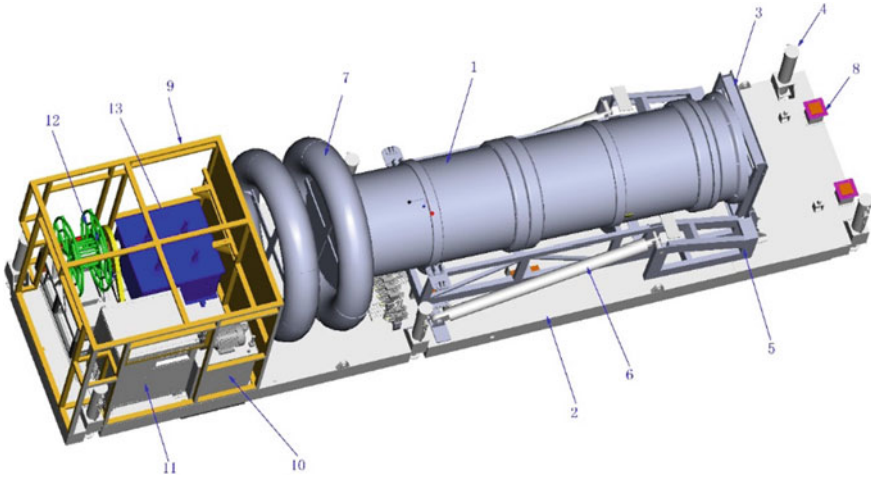


Fig. 2 Schematic diagram of the structure of the pressure resistant platform. 1. Reactor (built-in voltage divider), 2. Bottom frame platform, 3. Reactor bottom frame, 4. Extended hydraulic support leg, 5. Flip bracket, 6. Hydraulic cylinder, 7. Pressure balancing ring, 8. Cushion block, 9. Rain cover, 10. Pump station, 11. Frequency conversion source, 12. Winding coil

$$\sigma = \frac{G}{A} = \frac{95000}{0.013188} = 7.2 \text{ MPa}$$

The full gravity of the model is applied to the hydraulic support leg, only the compressive stress exists, and the shear stress is not calculated.

Conclusion: Six hydraulic support legs can withstand the gravity of the entire platform.

2.2 Check the Flip Mechanism of Horizontal Reactor

Using theoretical mechanics knowledge analysis, the force analysis of the bracket is shown in Fig. 3.

Establish the x-y coordinate system as shown in the figure, and analyze the rotating shaft as follows:

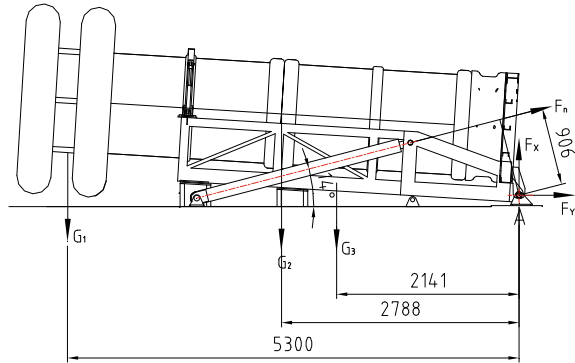
Given $G_1 = 650 \text{ N}$, $G_2 = 40,000 \text{ N}$, $G_3 = 7500 \text{ N}$.

From the statics equilibrium equation:

$$\sum M = 0; 906F_n = 5300G_1 + 2788G_2 + 2141G_3;$$

$$F_n = \frac{G_1 \times 5300 + G_2 \times 2788 + G_3 \times 2141}{906}$$

Fig. 3 Schematic diagram of force analysis of bracket



$$= \frac{650 * 5300 + 40000 * 2788 + 7500 * 2141}{906}$$

$$= 144.6 \text{ kN};$$

$$G_1 + G_2 + G_3 - F_Y - F_N \sin \theta = 0;$$

$$F_n \cos \theta + F_x = 0;$$

Calculated: $F_n = 144.6 \text{ KN}$, take 145 kN ; $F_Y = 13,350 \text{ N}$, $F_X = 141,000 \text{ N}$.

Then the force on the rotating shaft space $F = 141,631 \text{ N}$. Thrust $F = 72.5 \text{ kN}$ for a single hydraulic cylinder.

Known hydraulic cylinder diameter $D_1 = 100 \text{ mm}$, piston rod diameter $d = 80 \text{ mm}$, piston rod stroke 2000 mm , body length 2460 mm . Then push up the equipment required pressure:

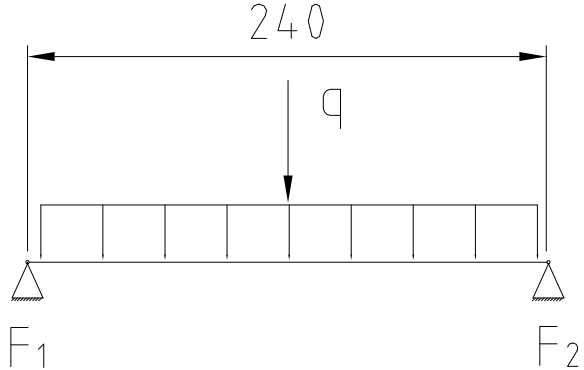
$$P = \frac{F}{S} = \frac{72.5}{\pi 0.05^2} = \frac{72.5}{0.00785} = 9.2 \text{ MPa}$$

The piston rod working condition is stable, can be approximated that only by axial thrust and tension, the maximum stress of the piston rod

$$\sigma = \frac{F \times 10^{-6}}{\frac{\pi}{4} d^2} = \frac{72,500 \times 10^{-6}}{\frac{\pi}{4} 0.008^2} = 144 \text{ MPa}$$

Known piston rod material is 45#, yield strength $\sigma_s = 355 \text{ MPa}$ piston rod meet the strength requirements. Where, F_n represents the total thrust of the hydraulic cylinder; P represents pressure of hydraulic cylinder; F represents single hydraulic cylinder thrust; S represents area of hydraulic push rod; G_1 represents quality of pressure balancing ring; G_2 represents reactor quality; G_3 represents Bracket quality;

Fig. 4 Simplified model of force at the rotating shaft



2.3 Check the Strength of the Rotating Shaft

Given that diameter $D = 60$ mm, length $L = 240$ mm and $F = 141,631$ N, F_1 and F_2 is for support force, a simplified model is established, as shown in Fig. 4.

$$F_1 = F_2 = 141,631/4 = 35,407.75 \text{ N.}$$

$$q = F/L = 141,631/0.24 = 590,129.2 \text{ N/m} = 590.1292 \text{ kN/m.}$$

For a simply supported beam under uniform load, the maximum bending moment is generated at the midpoint section of the beam $M_{\max} = ql_2 \times 0.24/8 = 590.132/8 = 4.25 \text{ kN m}$;

Its maximum normal stress occurs on the upper and lower edges of the beam midpoint section, the maximum stress of a solid shaft beam

$$\sigma_{\max} = \frac{M_{\max}}{W_1} = \frac{4.25 \times 10^3}{\frac{\pi D^3}{32}} = \frac{4.25 \times 10^3}{\pi \times 0.06^3/32} = 200 \text{ MPa}$$

It is known that the rotating shaft material is 45# with yield strength $\sigma_s = 355$ MPa, and the shaft strength meets the requirements.

3 Platform Simulation

1. Finite element analysis

For the long heavy-duty platform, the overall strength and shape variables are the main assessment objects. In order to ensure the safety of the design, the finite element analysis of the main model is carried out in this paper [10–12], and the results are compared with the actual operating conditions. The results show that the simulation results are consistent with the actual maximum deformation.

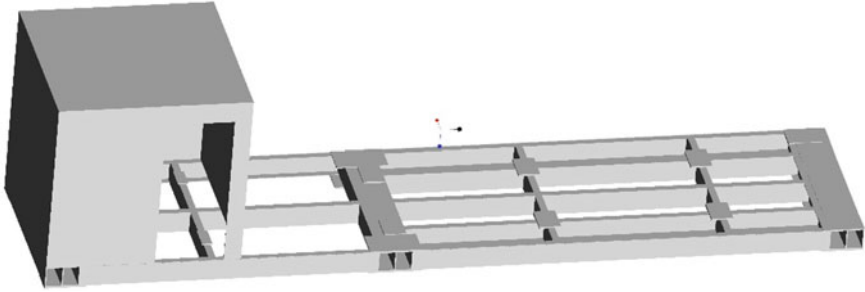


Fig. 5 Simplified model of platform

In this paper, Cero is used to establish a three-dimensional model [13–18], considering the complexity of the platform and the computing of the computer, the simplified model of the platform is shown in Fig. 5.

Material parameters: The base frame is made of 70 Mn, thickness is 7 mm, height is 250 mm, width is 100 mm, yield strength is 450 MPa, tensile strength is 785 MPa, and the boom of the crane is generally made of this material. The front cover shell is made of $60 \times 40 \times 2.5$ square tubes. Considering the complexity of the force on the whole platform, we choose the condition with the maximum force on the platform for analysis, that is, the condition when the platform is lifted off the ground by the legs. Next, we define the constraints. According to the actual working conditions, the contact surface between the three hydraulic leg sleeves and the extension leg is defined as binding. According to the actual contact point between the equipment on the platform and the platform, the downward positive pressure is defined as 50,000 N and 15,000 N, respectively, shown in Fig. 6.

Final analysis results: The overall maximum deformation of the platform is 0.93 mm, and the maximum stress is 32.236 MPa, which is far less than the yield strength of the material itself, as shown in Fig. 7.

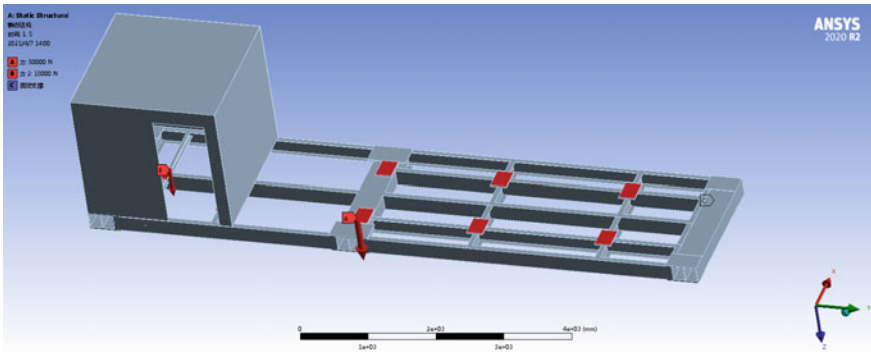
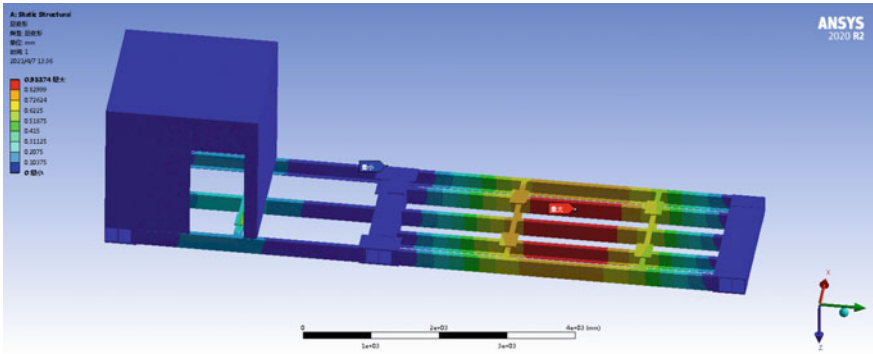
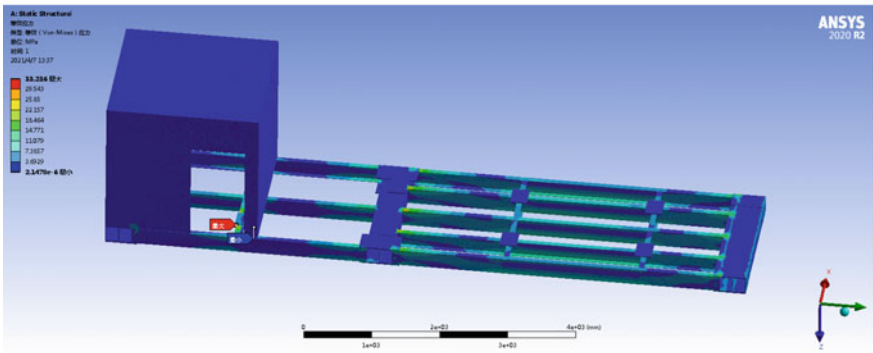


Fig. 6 Add boundary conditions



(a) Total deformation



(b) Equivalent stress

Fig.7 Analysis results

Through the simulation results, it can be judged that the overall design strength of the platform is sufficient and the overall deformation is small.

4 Conclusion

In this paper, PRO/E is used to establish a three-dimensional model, and then theoretical mechanics and material mechanics are used to analyze and check the force of the key components of the platform. Finally, ANSYS is used to analyze the overall stiffness of the platform. Through the above steps, the strength of the main functional parts of the platform, including the platform, the hydraulic cylinder of the support leg and the turning hydraulic cylinder meet the requirements, the thrust of the turning hydraulic cylinder is enough to meet the force required to push up the equipment, and the deformation of the platform under full load meets the design requirements.

The wind resistance can meet the requirements of the field situation, and the test can be carried out safely on the site.

Funding The authors thank the financial support from Suzhou City University to M. Lei via the 2022 Jiangsu Province University Laboratory Research Association Sponsored Research Project (GS220222BZZ36), 2021 Jiangsu Province University Basic Science (Natural Science) Research Project (21KJD460006).

Competing Interests

The authors declare that they have no conflicts of interest to report regarding the present study.

References

1. Meng W, Zhang R, Cai J et al (2022) Analysis of excessive local discharge of a 750kV single-phase shunt reactor. *Transformers* 2022(001):059
2. Chen B, Wu Y, Chen G et al (2022) Application of series parallel resonance in AC voltage withstand test of 750 kV GIS extra-large bus. *Electr Eng* (11):3
3. Zhang M, Wang G, Zhang Y et al (2015) Insulation design and test analysis of ± 1100 kV UHV dry flat-wave reactor. *High Volt Technol* 41(05):386–394
4. Zhao Z (2022) Current situation and technical improvement analysis of high voltage electrical test equipment in substation. *Electr Power Equip Manage* (15):3
5. He X (2022) Current situation of electrical high voltage test equipment and strategy analysis of technical improvement. *Chin Sci Technol J Datab (Full-text Edition) Soc Sci* (2)
6. Zhou J, Gong T, Xiang Y (2022) Research on foundation selection and construction method in confined water area of 750 kV AC transmission line project. *Shanxi Electr Power* (000-003)
7. Wang D, Zhao X, Ma W et al (2022) Analysis and treatment of heating of sleeve cap of 750 kV high voltage reactor. *J Shandong Electr Power College* 25(5):4
8. Zhang M, Liu F, Wang B et al (2022) Seismic response and optimal design method of 750 kV arrester. *High Voltage Electr Apparatus* 58(8):8
9. Feng Z, Zheng X, Chen W et al (2023) Experimental study on 220kV switch contact boom insulation shield. *High Voltage Electr Apparatus* 59(1):5
10. Fu M (2022) Example analysis of 10kV high voltage distribution system and relay protection action. *Mod Build Electr* 13(11):3
11. Feng R, Che C, Zhao L et al (2022) Experimental study on extremely fast transient overvoltage and transient shell ground potential increase in 500 kV ultra-high voltage GIS switching gas chamber. *Inner Mongolia Electric Power Technol* 40(5):8
12. Xiao J, Wang X, Xiao J (2022) Study on external voltage withstand test method of 220kV power transformer directly connected with cable. *Chin Sci Technol J Datab (full-text version) Eng Technol* (8):3
13. Zhu W, Ren A, Xue Z et al (2022) Seismic performance analysis of ± 800 kV dry plain wave reactor. *Sichuan Electric Power Technol* 45(6):7
14. Zhang F, Song A, He K (2023) Research on vibration characteristics of manipulator joint considering clearance coupling effect. *Mach Des Manuf* (1):5
15. Lu Y, Zhao L, Wu Z (2022) Static test comparison and simulation analysis of heavy-duty rotating platform. *J Mach Des* 39(S01):5
16. Zhang X, Wang X, Ren Y (2022) Finite element analysis of frame strength and fatigue of high pressure roller mill. *Mech Eng Autom* 005:000
17. Meng Y, Shi Y, Liao Y et al (2022) Modal analysis and optimization of shear crusher box based on orthogonal test. *Coal Mine Mach* 43(11):4
18. Peng L, Liu Y, Xiao Z, Huang X, Peng A, Wu C (2022) Structure design and strength analysis of light rail car bogie. *Equip Manuf Technol* (1):86–88

Quality Improvement Method for Power Equipment Defect Record



Linghui Liu, Zehui Zhang, Hui Duan, Xiaojuan Qi, Xuliang Wang,
and Qingquan Li

Abstract Text quality directly affects the merits of the text mining effect. On the basis of summarizing the quality problems existing in the defective text of power equipment, we propose a defect text quality improvement method. First, through the analysis of a large number of actual defect text, the problems of missing equipment layering and irregular description of defective content in defective texts are concluded. Then, to address the problem of missing equipment layering, we transform the problem of missing description of defect of power equipment into the problem of missing text structures. And the conversion of defect text to structures is realized through the UIE (Universal Information Extraction) framework. Finally, to address the problem of nonstandard defect description, we establish a library of standard statement for device defect description. We use similarity calculation to find the standard sentence with the most similar semantic and correct it, so as to achieve higher quality for poor quality text. Results show that the corrected text has a large improvement in accuracy on the defect level classification task. We provide an effective method for improving the quality of defect text.

Keywords Power equipment defect record · Text quality improvement · UIE · Similarity calculation

L. Liu · Z. Zhang · H. Duan · X. Qi

State Grid Shandong Electric Power Company Laiwu Power Supply Company, Jinan
Shandong 271100, China

X. Wang (✉) · Q. Li

Shandong Provincial Key Laboratory of UHV Transmission Technology and Equipment,
Shandong University, Jinan Shandong 250061, China

e-mail: wang715586468@163.com

© Beijing Paiké Culture Commu. Co., Ltd. 2024

X. Dong and L. Cai (eds.), *The Proceedings of 2023 4th International Symposium on Insulation and Discharge Computation for Power Equipment (IDCOMPU2023)*, Lecture Notes in Electrical Engineering 1100, https://doi.org/10.1007/978-981-99-7393-4_54

573

1 Introduction

With the deepening of the construction of smart grid, various aspects of the power system have generated massive amounts of multi-source heterogeneous data, with unstructured data represented by text, audio, and images growing fastest. The text describing the defect of power equipment has attracted the attention of technical and management personnel because it contains information most closely related to the safety of equipment and power grid. However, due to the huge amount of data, it is a difficult task to manually analyze these texts and obtain defect pattern and equipment quality information from them. Therefore, using natural language processing (NLP) technology to automatically mine defect text has become a research hotspot [1].

The quality of text directly affects the mining results [2, 3]. Actual power equipment defect text is influenced by the professional quality and recording habits of the recorder, and there are often non-standard issues such as incomplete descriptions and ambiguities. These records with quality issues can lead to certain deviations in the mining results. In order to improve the effect of power equipment defect text mining from the source, and further promote the wider research and application of defect text in the field of power grids. This paper summarizes the problems that may occur in actual defect text, and proposes a method for improving the quality of power equipment defect text based on information extraction technology.

2 Power Equipment Defect Record

In this section, we briefly introduce the format of power equipment defect text, and analyze the quality issues that may occur with actual defect text.

2.1 *The Format of Power Equipment Defect Text*

During the daily operation and maintenance of power equipment, staff have recorded a large number of equipment defect records, which are referred to as defect text. The defect text shall consist of four parts: equipment layering, defect description, defect level, and classification basis. Equipment layer is based on the equipment classification standards of the State Grid Corporation of China, and is divided into four levels according to structure, function, characteristics, etc.: equipment type, components, component type, and location. Defect description is a standard description of defect characteristics, reflecting the specific locations and phenomena where defects occur. Defect classification refers to the classification of defect into emergency, major, and general defect based on the degree of impact on grid operation.

2.2 Common Problems with Power Equipment Defect Text

The actual defect text is influenced by the subjectivity of the recorder, whose integrity and accuracy cannot be guaranteed, and the level of detail varies greatly. The existing problems are summarized as follows:

- (1) In the hierarchical part of the equipment, the recorder abbreviates a certain level of content according to personal habits or mistakenly writes it for some reason, resulting in ambiguous or even incorrect indication of the defect record. For example, “the main transformer on-load switch is leaking oil,” and there are gas relays and pressure relief valves at the positions where the actual transformer on-load switch may leak oil. Therefore, there is a problem of ambiguous reference in this defect record.
- (2) In the classification basis section, there is a problem of only describing defects without providing specific classification basis, and the classification of defect levels is ambiguous. If the indication of the transformer temperature measuring device is incorrect, and the difference between the actual temperature and the transformer temperature is not given, it is impossible to determine whether the transformer defect level is a general defect or a major defect, and it is impossible to determine whether to immediately shut down the transformer.

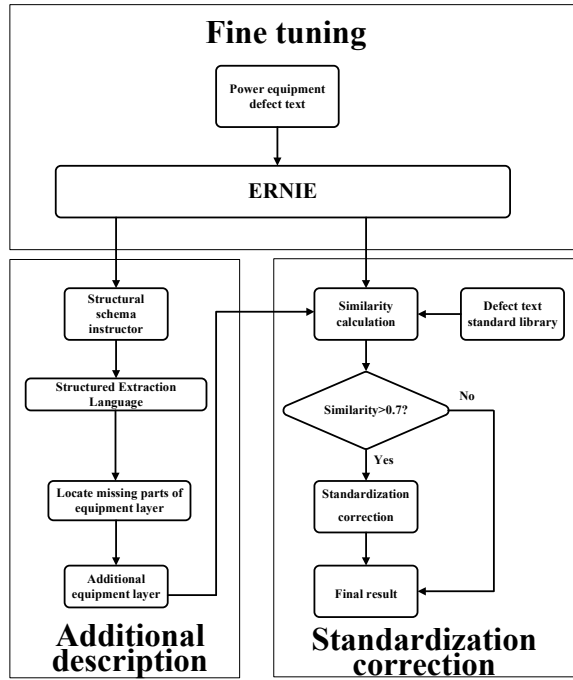
3 Quality Improvement Method for Power Equipment Defect Record

Aiming at the problems existing in actual defective text, this paper proposes a quality improvement method based on information extraction technology. Through information extraction technology, structured information is automatically extracted from unstructured or semi structured defect text. Firstly, entity extraction technology is used to extract each device layer from the defect text, determine which device layer the defect text lacks a specific description, and complete the missing description. Secondly, in the case of nonstandard defect descriptions, a standard statement library for device defect descriptions is established, and similarity calculations are used to find the standard statements with the most similar semantics, which can be corrected to achieve higher quality for poor quality text. The framework of quality improvement method based on information extraction technology is shown in Fig. 1.

3.1 Universal Information Extraction (UIE)

This paper transforms the problem of missing description of power equipment defect text into the problem of missing text structure, and implements the transformation from defect text to structure through the UIE framework. UIE (Universal

Fig. 1 The framework of quality improvement method based on information extraction technology



Information Extraction) is a unified framework for universal information extraction proposed by Yaojie Lu et al. in ACL-2022 [4]. This framework implements unified modeling of tasks such as entity extraction, relationship extraction, event extraction, and emotional analysis, and enables good migration and generalization capabilities between different tasks. Formally, using the predefined structural pattern guide s and text sequence x as inputs, the UIE model generates a structure $SEL(y)$ that contains the required structural information in the text x indicated by the pattern s :

$$y = UIE(s \oplus x) \tag{1}$$

Among $x = \{x_1, \dots, x_n\}$ is a text sequence, $s = \{s_1, \dots, s_n\}$ is a structural pattern guide, and $y = \{y_1, \dots, y_n\}$ is an SEL sequence that can be easily converted into extracted information records. In order to locate the information that needs to be extracted, the structural pattern guide contains two types of token segments: (1) SpotName: the target discovery name in a specific information extraction task, such as “component” and “part” in a power equipment defect text entity extraction task; (2) Special symbols ($[spot]$, $[text]$) will be added before each SpotName and input text sequence. The overall framework of UIE is shown in Fig. 2, and its input form is:

$$s \oplus x = [[spot], \dots, [spot], \dots, [text], x_1, x_2, \dots, x_n] \tag{2}$$

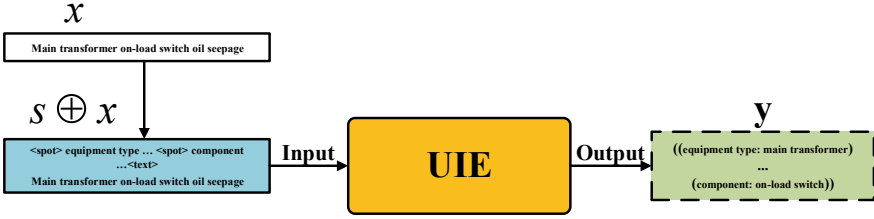


Fig. 2 The overall framework of UIE

Table 1 An example of rejection mechanism

x	Main transformer on-load switch oil seepage
$s \oplus x$	<spot> equipment type ...<spot > component ...<spot> person... <text> Main transformer on-load switch oil seepage
y	((equipment type: main transformer) (component: on-load switch) (person: [Null]))

Training a UIE requires a large scale of datasets, which cannot be met in the electrical field. Therefore, we adopt a “pretraining-fine tuning” mode [5]. Given a pretrained UIE, we can quickly adapt it to the task of extracting text entities from power equipment defect through model fine tuning. Given a tagged power equipment defect text corpus $D_{task} = \{(s, x, y)\}$, we use teacher forced cross entropy loss to fine-tune the UIE:

$$L_{FT} = \sum_{(s,x,y) \in D_{Task}} -\log p(y|x, s; \theta_e, \theta_d) \tag{3}$$

In order to reduce the exposure bias of the autoregressive model in encoding and decoding, we adopted a rejection mechanism [6]. Specifically, given an example (s, x, y) , we first encode $s \oplus x$ normally, and then randomly insert several negative examples into s with probability p . For example, in Table 1, person is the negative point in the mode prompt, that is, there is no person entity in the “Main transformer on load switch oil page”. Therefore, we randomly inject noise during model learning. In this way, the model can reject misleading generation.

After inputting the actual defect text into the UIE, we can locate the missing part of the device layer, and then calculate the device layer missing description by averaging the cosine included angle with the known device layer word vector.

3.2 Similarity Calculation of Defect Text

For cases where the defect description is not standard, we establish a standard library for equipment defect, and use similarity calculation to find the standard sentence with

the most similar semantic, and correct it. So that poor quality text can achieve higher quality.

At present, the common text similarity calculation models include the vector space model (VSM), the knowledge network meaning tree model and the string match model. The latter two models perform well when equipped with complete training corpus. However, due to the professional text language of power grid equipment defects, it is difficult to directly transplant the models trained on the corpus of other fields. Therefore, based on the idea that SIFRank [7] uses cosine distance to calculate the similarity between words and sentences, this paper uses cosine similarity to represent the similarity between the actual defective text and the standard defective text. Input the defect text into the fine-tuned pre-training model ERNIE [8], and the vector representation v_c of each character in the text can be obtained. The vector of the sentence can be expressed as:

$$v_s = \frac{1}{|s|} \sum_{c \in s} \frac{a}{a + f_c} v_c = \frac{1}{|s|} \sum_{c \in s} W(c) \cdot v_c \quad (4)$$

f_c is the probability of a character appearing in a large corpus, and $a \in [10^{-3}, 10^{-4}]$ is the hyperparameter that makes the function smooth.

The similarity between the standard defect text v_{sd} and the actual defect text v_s can be calculated by cosine distance [9]:

$$Sim(v_{sd}, v_s) = \cos(v_{sd}, v_s) = \frac{\vec{v}_{sd} \cdot \vec{v}_s}{\|\vec{v}_{sd}\| \cdot \|\vec{v}_s\|} \quad (5)$$

$Sim(v_{sd}, v_s)$ is between 0 and 1, and the closer it is to 1, the more the actual defect text is related to the standard defect text. When the value of $Sim(v_{sd}, v_s)$ is greater than 0.7, we find the most similar standard defect text as a correction.

4 Experiment

In order to verify the proposed method for quality improvement of defective text based on information extraction technology, this paper conducts experimental analysis on a power equipment inspection and maintenance case recorded by a power grid company.

4.1 Datasets

The text of power equipment defect used in this paper is the equipment inspection and maintenance records recorded by a power grid company for about 20 years. Due to the

Table 2 The data situation of defect texts for different types of devices

Device type	Number of defect texts	Additional description	Standardization correction
Main transformer	1620	1025	322
SF ₆ circuit breaker	472	237	143
Switch cabinet	540	303	21
Drivepipe	723	399	68

long-time span, multiple iterations of the power grid system and the recording habits of the recorder, the original samples need to be pre-processed: The original defect text of power equipment contains data in the form of pictures and tables, which are converted into text data in the form of OCR (optical character recognition) technology and manual review. According to the defect classification standard of State Grid Corporation, the defect text shall include three parts: equipment stratification, defect description and defect grade. Among them, device layer and defect description are the data subjects that need to be mined. The text quality improvement in this paper is mainly aimed at this part.

After preprocessing, a total of 3355 samples were obtained. Table 2 lists the total number of defect texts for different types of devices, the number of text for defect description completion and the number of text for standardization correction. As can be seen from the table, almost all devices have the defect description missing, but the text proportion of standardized correction varies greatly among different devices.

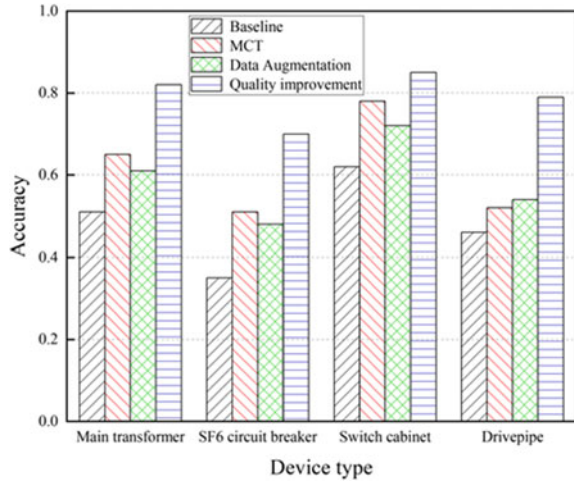
4.2 Example Analysis

This paper evaluates the proposed text quality improvement method through the task of defect text classification, and compares the proposed method with the following methods:

- a. Baseline scheme: original training strategy without quality improvement of training set
- b. Mask the Correct Tokens [10]: Randomly perturb a part of the correct tokens into a special token to predict the correct tokens from the special tokens. We trained the model with standard statements and then corrected the actual defect text
- c. Data enhancement [11, 12]: randomly delete or exchange characters for standard statements, and then use these damaged texts to train the classification model to improve the robustness of the model.

For schemes (2) and (3), we set the probability of replacing characters to 15% and the window size of character exchange to 10. Based on the implementation of LSTM, the classifier needs to specify random seeds manually. The randomness is large, resulting in large fluctuations in the classification results. Therefore, for all

Fig. 3 Performance of equipment defect text classification task corrected by different methods



experiments, we average the results from five different MCT random seeds. The accuracy is used as the evaluation index in this paper. The comparative test results are shown in Fig. 3. It can be seen that compared with other methods, the effect of defect text quality improvement method proposed in this paper is 20–40% higher in the task of defect classification.

5 Conclusion

Taking power equipment defect text as the research object, this paper proposes a text quality improvement method based on information extraction technology. The main contributions are as follows:

- a. Based on the study of the format and content of the actual defect text, the possible problems of the actual defect text are analyzed: the missing of equipment stratification and the inaccurate description of the defect content.
- b. To solve the problem of missing layers of equipment, the missing description of defective text of power equipment is transformed into the missing text structure, and the conversion from defective text to structure is realized through UIE framework. After the actual defect text is input into UIE, the missing part of the device layer can be located, and then the device layer missing description can be obtained by means of the average cosine angle of the known device layer word vector.
- c. In view of the nonstandard description of defects, we establish the standard statement library of equipment defect description. Through similarity calculation, we find out the most semantically similar standard statements and make corrections, so that the poor quality text can obtain higher quality. The example shows

that the accuracy of the modified text is greatly improved in the task of defect classification.

Acknowledgements This work was supported by the Science and Technology Project of the State Grid Shandong Electric Power Company: research on power transformer fault diagnosis technology based on deep learning multi-modal big data analysis (520612220004).

References

1. Rudin C, Waltz D, Anderson RN (2012) Machine learning for the New York City power grid. *IEEE Trans Pattern Anal Mach Intell* 34:328
2. Yang Y, Malaviya C, Fernandez J (2020) Generative data augmentation for commonsense reasoning. arXiv preprint [arXiv:2004.11546](https://arxiv.org/abs/2004.11546)
3. Araci D (2019) Finbert: financial sentiment analysis with pre-trained language models. arXiv preprint [arXiv:1908.10063](https://arxiv.org/abs/1908.10063)
4. Lu Y, Liu Q, Dai D, Xiao X, Lin H, Han X, Sun L, Wu H (2022) Unified structure generation for universal information extraction
5. Gururangan S, Marasović A, Swayamdipta S, Lo K, Beltagy I, Downey D, Smith NA (2020) Don't stop pretraining: adapt language models to domains and tasks. arXiv preprint [arXiv:2004.10964](https://arxiv.org/abs/2004.10964)
6. Zhang RH, Liu Q, Fan AX, Ji H, Zeng D, Cheng F, Kawahara D, Kurohashi S (2020) Minimize exposure bias of seq2seq models in joint entity and relation extraction. arXiv preprint [arXiv:2009.07503](https://arxiv.org/abs/2009.07503)
7. Zhang Q, Wang T, Zhu M, Shen T, Zhao Y, Zhang Y (2022) SIFRANK algorithm for Chinese text keyword extraction based on dependent semantic feature constraints. In: 2022 IEEE 17th conference on industrial electronics and applications (ICIEA), vol 1652. IEEE
8. Sun Y, Wang S, Li Y, Feng S, Tian H, Wu H, Wang H (2020) Ernie 2.0: a continual pre-training framework for language understanding. In: Proceedings of the AAAI conference on artificial intelligence, vol 34, pp 8968
9. Ng N, Cho K, Ghassemi M (2020) SSMB: self-supervised manifold based data augmentation for improving out-of-domain robustness. In: 2020 Conference on empirical methods in natural language processing, EMNLP 2020, vol 1268. Association for Computational Linguistics (ACL)
10. Shen K, Leng Y, Tan X, Tang S, Zhang Y, Liu W, Lin E (2022) Mask the correct tokens: an embarrassingly simple approach for error correction. arXiv preprint [arXiv:2211.13252](https://arxiv.org/abs/2211.13252)
11. Feng SY, Gangal V, Wei J, Chandar S, Vosoughi S, Mitamura T, Hovy E (2021) A survey of data augmentation approaches for NLP
12. Xie Q, Dai Z, Hovy E, Luong T, Le Q (2020) Unsupervised data augmentation for consistency training. *Adv Neural Inf Process Syst* 33:6256

Statistical Analysis of Electrothermal Damage Characteristics of Nanoelectrode Under High Electric Fields



Xinyu Gao, Fei Feng, Guofei Teng, Jun Zhao, Bing Xiao,
and Yonghong Cheng

Abstract The insulation of devices under high electric field is the key to affect the performance and life of devices and equipment. This paper studies the electrothermal damage effect of metal electrodes at the nanoscale. The numerical simulation method based on electrodynamic coupling molecular dynamics and particle simulation is used to simulate the initial process of electrothermal damage of nanoelectrode during vacuum pre-breakdown under the interaction of multiple fields. Based on the correlation and quantitative relationship analysis of 15 multivariate variables of microscopic crystal structure parameters and macroscopic physical properties of different electrode materials, the nonlinear quantitative prediction model of electrothermal damage characteristics of nanoelectrode was obtained, which was in line with the actual physical significance and the goodness of calibration fit was 99.6%. The results can be used to reveal the universal physical mechanism of electrode damage during pre-breakdown.

Keywords High electric fields · Electrothermal damage · Vacuum breakdown · Statistical analysis

1 Introduction

With the rapid progress and development of science and technology, the exploration of the micro world based on micro and nano technology has become the frontier of basic science and equipment manufacturing. Micro-nano processing technology and micro-nano electronic devices have been widely used in the core fields of science and technology equipment of national defense, aerospace and civil products, such as

X. Gao (✉) · F. Feng · G. Teng · J. Zhao
Xi'an Aeronautics Computing Technique Research Institute, AVIC, Xi'an 710065, China
e-mail: gxyood345@163.com

B. Xiao · Y. Cheng
School of Electrical Engineering, Xi'an Jiaotong University, Xi'an 710049, China

© Beijing Paiké Culture Commu. Co., Ltd. 2024
X. Dong and L. Cai (eds.), *The Proceedings of 2023 4th International Symposium on Insulation and Discharge Computation for Power Equipment (IDCOMPU2023)*, Lecture Notes in Electrical Engineering 1100, https://doi.org/10.1007/978-981-99-7393-4_55

chips, large-scale integrated circuits, high-end guidance systems and so on, and are rapidly expanding [1].

The dielectric system composed of dielectric materials determines the structure, performance and life of electrical equipment and electronic devices such as integrated circuit chips, micro and nano electronic devices, switching power supplies, high-power power electronic devices, vacuum electronic devices and field emission devices. A series of classical dielectric theories have been established for a long time to guide the design, development and application of dielectric systems. However, as the characteristic size of the device decreases, the integration of the integrated circuit and the density of the transistor also increase exponentially according to Moore's Law. As the design, production and application of electrical equipment and electronic devices are challenging the limits of micro-scale application of materials and the limits of withstand electric field, the application occasions of dielectric materials are becoming more and more complex, the application scale is getting smaller and smaller, and the strength of withstand electric field is getting higher and higher [2–4]. The classical dielectric theory and macro breakdown theory are no longer applicable at the nano scale.

Therefore, it has become the international academic frontier of electrical engineering to explore the related physical mechanism and mechanism of how the synergistic action of multiple physical fields in vacuum nanoscale leads to the pre-breakdown and breakdown of dielectric system, and how the electrode is damaged after breakdown. The research on the breakdown characteristics and electrothermal damage effect of nanoelectrode under strong electric field can further enrich and improve the existing vacuum breakdown theory, and lay a theoretical foundation for the design, production and application of new generation electrical equipment and future microelectronic devices.

2 Simulation Model

The deformation of nano-metal electrode under strong electric field is usually irregular and random [5–7]. In order to more accurately simulate and analyze the deformation and thermal damage law of nanoelectrode under strong electric field, and ensure the high robustness of the crystal structure change inside the material, only the extensibility and high precision brought by the unstructured flexible mesh of finite element can overcome the dynamic evolution of nanoelectrode under strong electric field and high temperature.

In view of the limitations of existing experiments and simulation studies, common metal electrode materials with different crystal structures were selected as electrode materials for simulation experiments: Face-centered cubic structure metal (FCC): copper (Cu), gold (Au), aluminum (Al); Body centered cubic structure metal: molybdenum (Mo), tungsten (W), vanadium (V); Close-packed cubic structure metal: titanium (Ti), zirconium (Zr), zinc (Zn). The pre-breakdown process and breakdown critical electric fields of metal nanocrystals ($R_0 = 1$ nm, $H_0 = 100$ nm) with different

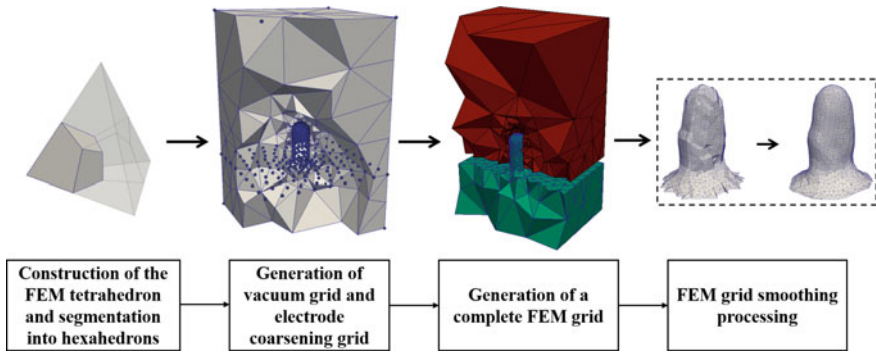


Fig. 1 Schematic diagram of the finite element grid generation

structure and physical properties of electrode materials were statistically analyzed, and then the intrinsic law and physical mechanism of the influence of electrode materials with different crystal structures and physical properties on the electrothermal damage characteristics of nanocrystals under strong electric field were obtained.

The finite element mesh used in this study is solved based on the open-source C++ library Deal. II. All the calculated information will be integrated into the FEMOCS [8, 9] model and interact with the molecular dynamics software PARCAS and LAMMPS. Finally, the purpose of automatically evolving and generating dynamic mesh with the position of atoms and electrode deformation can be realized. Figure 1 shows the schematic diagram of the generation of nano-finite element mesh, which mainly includes extracting surface atoms of nano-electrode, generating vacuum regional mesh, designing electrode coarsened-mesh model, and FEM smoothing processing. The molecular dynamics model of nano-metal electrode used in this paper is based on the nanoneedle electrode prepared in the laboratory and the simulation system [8–10] established by Djurabekova et al. Nano-metal electrodes are constructed by stacking metal atoms with specific crystal orientation.

In the molecular dynamics calculation in this paper, the initial temperature of all atoms at the initial time is set to 300 K, and the time of the entire molecular dynamics simulation calculation is 1–2 ns, and the time step of the simulation calculation $\Delta t = 4.05\text{fs}$. Potential functions for molecular dynamics simulation of different materials mainly include embedded atom potential, Finnis–Sinclair (FS) many-body potential, modified embedded atom method, etc. These potential functions have been successfully verified in molecular dynamics calculations in the fields of multi-physical metal melting, phase transformation, and thermal evaporation [8, 10].

In order to accurately calculate the emission current density, space charge density, Joule heat and heat deposition process caused by Nottingham effect during the breakdown of nanoelectrode under strong electric field, the calculation model for electron emission used in this paper is based on GETELEC (General Tool for Electron Emission Calculations) [11]. It includes the electron emission transition model under strong electric field and high temperature (above the melting point of metal) as well

as the Nottingham thermal calculation model, and takes into account the influence of space charge (SC) effect on electron emission. For specific calculation methods, see literature [12, 13].

The simulation results can be obtained from the empirical formula of external applied electric field E_0 and nanoelectrode atomic evaporation delay t_e in literature [12]:

$$t_e = \tau \cot \left(\frac{\pi}{E_{\max} - E_c} (E_0 - E_c) \right) + t_h, \quad (1)$$

The applied critical field E_c of vacuum breakdown of nanoelectrode was obtained by fitting. In addition, the average atomic evaporation rate of the nanoelectrode can be obtained by extracting the slope of the atomic evaporation number of the nanoelectrode near E_c over time for calculation [12, 13].

3 Correlation Analysis of Multiple Characteristic Variables of Electrothermal Damage Characteristic

The electrothermal damage characteristics during the breakdown of nanoelectrode under strong electric field are closely related to the physical properties of the material structure. In order to comprehensively and systematically reflect the relationship between the multiple variables of physical properties of electrode materials and their electrothermal damage characteristics, 15 different parameters describing the microscopic crystal structure and macroscopic physical properties of electrode materials were selected as independent variables. These include: crystal structure types (CS, FCC: 1, HCP: 2, BCC: 3), lattice constant (a), crystal surface atomic density (ρ_{face}), crystal surface spacing (d_{hkl}), atomic coordination number (Z), liquid average atomic coordination number (Z_l), material melting point (T_m), boiling point (T_b), latent heat of evaporation (h_e), electrical resistivity (ρ), thermal conductivity (κ), work function (Φ). Due to the material resistivity and thermal conductivity with the absolute temperature change so select the following different characteristics for analysis: normal temperature resistivity (ρ_n), liquid resistivity (ρ_l), close to the boiling point of ultra-high temperature resistivity (ρ_{ut}), temperature thermal conductivity (κ_n), liquid thermal conductivity (κ_l). The characteristic dependent variables of electrothermal damage characteristics of nanoelectrode under strong electric field mainly include the applied critical electric field (E_c), average atomic evaporation delay (t_h) and average atomic evaporation rate (r_{evap}) of vacuum breakdown of nanoelectrode. The calculated values of different variables are shown in appendix of Ref. [14].

Due to the strong correlation between many parameters of practical significance, such as crystal structure parameters of materials, melting boiling point and latent heat of evaporation, resistivity and thermal conductivity at different temperatures. Since

the data and information between variables are repeated, direct analysis through 15 parameter variables will not only complicate the model, but also bring large errors due to various collinearity between variables. Therefore, this section mainly analyzes the correlation between 15 multivariate independent variables and dependent variables that affect the electrothermal damage characteristics of the nanoelectrode through SPSS software. By exploring the correlation between various variables, the independent variables are classified and the number of analysis variables is reduced, so as to achieve data reduction and error reduction, so as to more accurately judge and obtain the relationship between the multiple variables of the physical properties of the electrode material structure and the electrothermal damage characteristics.

Firstly, Pearson correlation coefficient (r) in statistics is calculated to measure the degree of correlation between variables. Pearson correlation coefficient between two variables can be obtained by the quotient of covariance cov and standard deviation σ between them:

$$\begin{aligned}
 r &= \frac{cov(X, Y)}{\sigma_X \sigma_Y} = \frac{E(XY) - E(X)E(Y)}{\sqrt{E(X^2) - E^2(X)}\sqrt{E(Y^2) - E^2(Y)}} \\
 &= \frac{\sum_{i=1}^n (X_i - \bar{X})(Y_i - \bar{Y})}{\sqrt{\sum_{i=1}^n (X_i - \bar{X})^2 (Y_i - \bar{Y})^2}}, \tag{2}
 \end{aligned}$$

where E is the expectation of each variable. The Pearson correlation coefficient and its significance among the calculated parameters are shown in Figs. 2 and 3.

It can be seen from the figure that E_c is highly correlated with T_m, T_b, h_e, Z, Z_l , and CS, and the correlation is significant. There was moderate correlation between E_c and $\rho_l, \rho_{ut}, d_{hkl}, E_c$ showed low correlation with a and κ_{nt} but no significant correlation, and basically no correlation with $\rho_{face}, \Phi, \rho_{nt}$ and κ_l . In addition, it can be seen from the correlation between the variables that there is a high degree of collinearity between them, so it is also necessary to reduce the collinear independent variables. Secondly, there may be nonlinear relationship between $a, \rho_{face}, \Phi, \kappa_l$ and E_c , so it is necessary to analyze their principal components and regression models. In addition, ρ_{nt} and κ_{nt} can be reduced because of their low correlation with E_c, t_h and r_{evap} .

4 Nonlinear Relationship of Multivariate Variables Based on Factor Analysis

Based on the basic idea of minimizing information loss, Charles Spearman proposed factor analysis method in 1904. Through the correlation analysis between variables, the original variables were classified. The variables with high correlation were

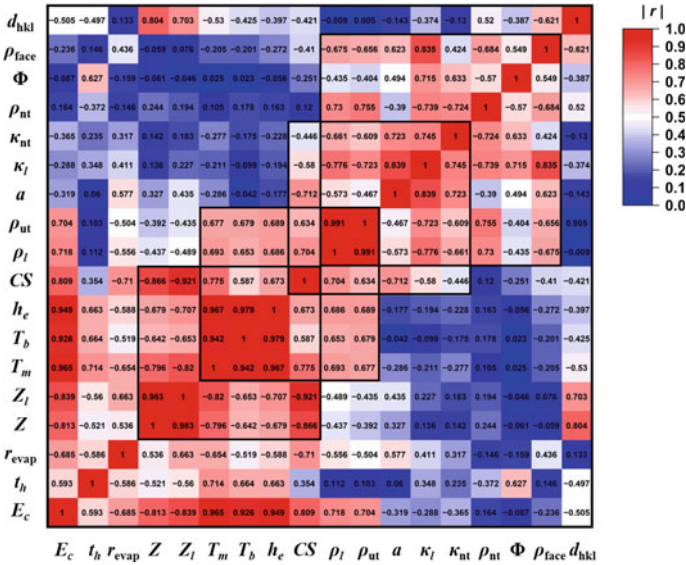


Fig. 2 Pearson correlation coefficient r between multiple variables (Left)

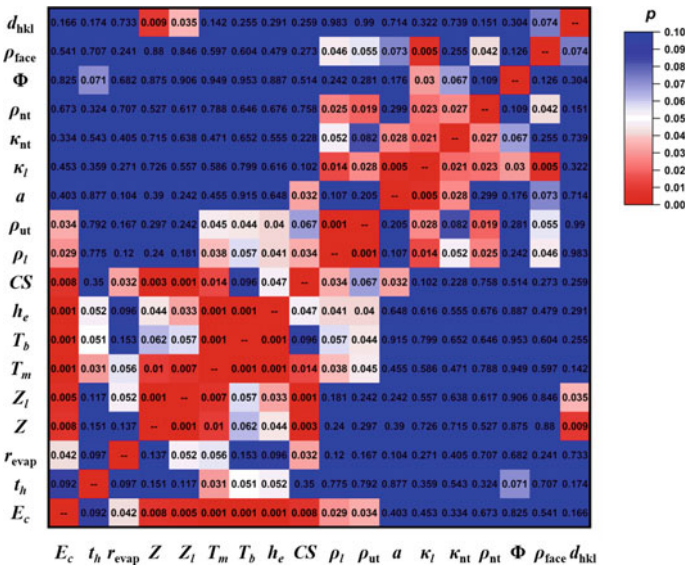


Fig. 3 Significance of Pearson correlation p between multivariate variables (Right)

divided into a group, and then the common factor was used to replace the group of variables. The common factor obtained through factor analysis has clear explanatory property, and the number of variables is far less than the number of original variables, and there is no linear relationship between each factor variable. By introducing the common factor into the regression model, the loss of data information can be greatly reduced under the condition of satisfying the relation of each variable.

For the original variable $X(x_1, x_2, \dots, x_p)$ with P indices and the m -dimensional common factor $F(F_1, F_2, \dots, F_m)$, the factor model is:

$$\begin{aligned}
 X_1 &= a_{11}F_1 + a_{12}F_2 + \dots + a_{1m}F_m + \varepsilon_1 \\
 X_2 &= a_{21}F_1 + a_{22}F_2 + \dots + a_{2m}F_m + \varepsilon_2 \\
 &\vdots \\
 X_p &= a_{p1}F_1 + a_{p2}F_2 + \dots + a_{pm}F_m + \varepsilon_p,
 \end{aligned}
 \tag{3}$$

where, $A = (a_{ij})$ is the factor load matrix; a_{ij} is factor load; ε is a special factor, representing influencing factors other than common factors. By rotating the factor axis, the load of each variable on the factor can be increased, which is more conducive to the parameter interpretation of each common factor. The finally obtained common factor can be expressed as the linear form of all independent variables:

$$F_i = b_{i1}X_1 + b_{i2}X_2 + \dots + b_{in}X_n \quad (i = 1, 2, \dots, m).
 \tag{4}$$

In the case of material boiling point as the principal variable of the regression model, 10 structural physical property variables CS, a , ρ_{face} , d_{hkl} , Z , Z_l , Φ , ρ_l , ρ_{ut} , κ_l with low correlation with T_b were brought into SPSS software for factor analysis. Since the variance of the first five principal components accounted for 98.83% of the variance of all principal components, the number of common factors to be extracted was 5. Finally, the load matrix obtained after factor rotation is shown in Table 1.

Table 1 The factor load matrix after rotation

Factor	1	2	3	4	5
ρ_{ut}	0.962	/	-0.174	-0.136	-0.140
ρ_l	0.922	/	-0.286	-0.171	-0.159
d_{hkl}	/	0.943	-0.131	0.241	-0.174
Z	-0.261	0.762	0.211	0.535	/
ρ_{face}	-0.581	-0.589	0.418	0.238	0.240
a	-0.254	/	0.911	0.209	0.204
κ_l	-0.594	-0.198	0.682	/	0.371
Z_l	-0.139	0.255	0.118	0.932	-0.128
CS	0.450	-0.430	-0.532	-0.546	-0.135
Φ	-0.259	-0.166	0.281	-0.110	0.901

As can be seen from the table, common factors extracted through factor analysis and factor rotation can well explain the respective variables. F_1 can be defined as the resistivity load of the material, F_2 can be defined as the crystal structure load of the material, F_3 can be defined as the thermal conductivity load of the material, F_4 can be defined as the liquid structure load of the material and F_5 is the work function load of the material. According to the factor score function coefficient matrix obtained statistically, the expression of each common factor can be obtained:

$$\begin{aligned}
 F_1 &= 0.599\rho_{\text{ut}} + 0.509\rho_l - 0.041d_{\text{hkl}} - 0.122\rho_{\text{face}} + 0.006Z \\
 &\quad + 0.280a - 0.080\kappa_l + 0.153Z_l - 0.040\text{CS} + 0.193\Phi \\
 F_2 &= -0.045\rho_{\text{ut}} - 0.064\rho_l + 0.544d_{\text{hkl}} - 0.462\rho_{\text{face}} + 0.333Z \\
 &\quad + 0.060a + 0.061\kappa_l - 0.320Z_l - 0.153\text{CS} + 0.101\Phi \\
 F_3 &= 0.299\rho_{\text{ut}} + 0.155\rho_l - 0.002d_{\text{hkl}} - 0.066\rho_{\text{face}} + 0.022Z \\
 &\quad 0.913a + 0.441\kappa_l - 0.293Z_l - 0.237\text{CS} - 0.375\Phi \\
 F_4 &= 0.144\rho_{\text{ut}} + 0.152\rho_l - 0.204d_{\text{hkl}} + 0.383\rho_{\text{face}} + 0.117Z \\
 &\quad - 0.195a - 0.314\kappa_l + 0.978Z_l - 0.147\text{CS} + 0.198\Phi \\
 F_5 &= 0.129\rho_{\text{ut}} + 0.147\rho_l + 0.036d_{\text{hkl}} - 0.020\rho_{\text{face}} + 0.136Z \\
 &\quad - 0.314a - 0.095\kappa_l + 0.166Z_l - 0.029\text{CS} + 1.297\Phi, \tag{5}
 \end{aligned}$$

The common factors $F_1 \sim F_5$ and T_b obtained from factor analysis were taken as independent variables, and the critical electric field (E_c) of the nanoelectrode was taken as dependent variable into SPSS software for linear stepwise regression analysis. When independent variables T_b , F_3 and F_2 were introduced, the calibration goodness of fit R^2_{adj} and partial F statistics reached the highest, and the standard error of the model reached the lowest, in which R^2_{adj} reached 96.9%. Therefore, linear quantitative relationship of common factors based on factor analysis can be obtained:

$$E_c = \hat{E}_c + e_0 = -0.021 + 0.118T_b - 0.053F_3 - 0.027F_2 + e_0, \tag{6}$$

where, e_0 is the residual error under this model. Using Φ and ρ_l as independent variables and e_0 as dependent variables for nonlinear regression, the goodness of fit of the regression model obtained through nonlinear regression analysis by SPSS software reaches 92.3%. Finally, the regression equation obtained is as follows:

$$\hat{e} = 0.036 - 0.198\rho_l^3 + 0.513\rho_l^2 + 0.002\Phi^2 - 0.086\rho_l\Phi, \tag{7}$$

By combining formula (6) and formula (7), the final nonlinear quantitative relationship can be obtained. The goodness of fit R^2 and the corrected goodness of fit R^2_{adj} were calculated to be 99.8% and 99.6%, respectively.

5 Conclusions

This paper mainly studies the influence of physical properties of electrode material structure on its atomic evaporation characteristics. Nine common metal electrode materials with different crystal structures are selected to construct nanoelectrodes for ED-MD-PIC simulation. Based on the correlation and quantitative relationship between 15 independent variables and the dependent variables of electrothermal damage characteristics, a quantitative prediction model was established for the relationship between the characteristic parameters of electrothermal damage characteristics and the microscopic crystal structure and macroscopic physical properties of electrode. Finally, the regression model which accords with the actual physical meaning and the goodness of fit of correction reaches 99.6% is obtained. Among them, the boiling point of nano-electrode materials has the most significant influence on the critical electric field applied outside the vacuum breakdown. The microscopic crystal structure of the materials has a certain correlation with the macroscopic physical properties, which ultimately affects the electric heating damage characteristics under the strong electric field.

References

1. Gu C (2013) *Micro-nano processing and its application in nanomaterials and devices research*. Science Press, Beijing (in Chinese)
2. Muranaka T, Blom T, Leifer K et al (2012) In-situ experiments of vacuum discharge using scanning electron microscopes. IPAC, New Orleans
3. Evans PR, Zhu XH, Baxter P et al (2007) Toward self-assembled ferroelectric random access memories: hard-wired switching capacitor arrays with almost Tb/in. (2) Densities. *Nano Lett* 7(5):1134–1137
4. Bhushan B (2015) Governance, policy, and legislation of nanotechnology: a perspective. *Microsyst Technol Micro Nanosyst Inf Storage Process Syst* 21(5):1137–1155
5. Meng GD, Cheng YH, Dong CY et al (2016) Effect of electrode geometry on the vacuum breakdown behaviors at nanoscale. In: Xi'an: 2016 IEEE international conference on dielectrics (ICD), pp 1159–1162
6. Meng GD, Cheng YH, Dong CY et al (2018) Recent progress in vacuum breakdown at nanoscale: experiment and simulation. In: Greifswald: proceedings of the 2018 28th international symposium on discharges and electrical insulation in vacuum (ISDEIV 2018), pp 15–18
7. Meng GD, Cheng YH, Dong CY et al (2018) Role of thermal properties of cathode materials for the nanoscale breakdown in vacuum. In: Xi'an: 2018 IEEE 2nd international conference on dielectrics (ICD), pp 1–4
8. Kyritsakis A, Veske M, Eimre K et al (2018) Thermal runaway of metal nano-tips during intense electron emission. *J Phys D-Appl Phys* 51(22):225203
9. Veske M, Kyritsakis A, Eimre K et al (2018) Dynamic coupling of a finite element solver to large-scale atomistic simulations. *J Comput Phys* 367:279–294
10. Veske M, Parviainen S, Zadin V et al (2016) Electrodynamics-molecular dynamics simulations of the stability of Cu nanotips under high electric field. *J Phys D-Appl Phys* 49(21):215301
11. Kyritsakis A, Djurabekova F (2017) A general computational method for electron emission and thermal effects in field emitting nanotips. *Comput Mater Sci* 128:15–21

12. Gao X, Kyritsakis A, Veske M et al (2020) Molecular dynamics simulations of thermal evaporation and critical electric field of copper nanotips. *J Phys D-Appl Phys* 53(36):365202
13. Gao X, Nan L, Kyritsakis A et al (2022) Structural evolution and thermal runaway of refractory W and Mo nanotips in the vacuum under high electric field from PIC-ED-MD simulations. *J Phys D Appl Phys* 55:335201
14. Gao X, Nan L, Song Z et al (2023) Atomic structure evolution and linear regression fitting models for pre-breakdown electric field strength of FCC, BCC and HCP metal nano-emitters under high electric field from PIC-ED-MD simulations. *J Phys D Appl Phys* 56:265203

Research on Online Monitoring of Submarine Cable Insulation Based on Two-Terminal Current Method



Huang Tao, Lei Zhicheng, Huang Xuancheng, and Zhou Xuwei

Abstract With the construction of submarine cable projects in full swing, the issue of monitoring the status of submarine cables is a popular research topic today. The insulation of submarine cables is a critical structure in submarine cables, so the online monitoring technology of submarine cable insulation is very important. This paper designs and builds an online monitoring system for submarine cable insulation based on the two-terminal current method, and calculates the dielectric loss factor of submarine cable insulation by simultaneously measuring the current and voltage data at both ends of the cable. The results show that the monitoring system can stabilize the monitoring data under different working conditions, and the data error is only 6% under the influence of 90 ns time synchronization error, which can reflect the overall state of the cable insulation well, but cannot reflect the local insulation deterioration of the cable, and only the serious local defects cause a large change in the results.

Keywords Two-terminal current method · Submarine cables · Insulation · Online monitoring

1 Introduction

The insulation between the cable core and the metal sheath is a very critical part of the cable, and its main function is electrical isolation. The insulation of the cable is mostly made of high resistance materials such as polyethylene, PVC, cross-linked polyethylene, etc. Currently, cross-linked polyethylene material has become the mainstream of cable insulation [1], which can withstand the operating voltage of high-voltage cables during normal operation and can also withstand partial discharges under certain

H. Tao · L. Zhicheng · H. Xuancheng
Jiangsu Frontier Electric Technology Co., Ltd., Nanjing, China
e-mail: qy264257@21cn.com

Z. Xuwei (✉)
School of Electrical Engineering and Automation, Wuhan University, Wuhan, China
e-mail: 1149882508@qq.com

© Beijing Paiké Culture Commu. Co., Ltd. 2024
X. Dong and L. Cai (eds.), *The Proceedings of 2023 4th International Symposium on Insulation and Discharge Computation for Power Equipment (IDCOMPU2023)*, Lecture Notes in Electrical Engineering 1100, https://doi.org/10.1007/978-981-99-7393-4_56

circumstances. The cable insulation needs to have the advantages of high voltage resistance level, long-term structural stability and high temperature resistance [2–4], which is of very major significance for the long-term stable operation of the cable. Therefore, the real-time online monitoring of cable insulation is particularly important [5–7].

So far for the submarine cable insulation online monitoring technology in the continuous development, Europe, America, Japan and other countries have accumulated a lot of experience. At present, the most conventional in industrial production and power systems or regular power outages offline testing, in the operation of the cable for preventive testing will lead to power supply interruptions, and the test voltage is usually higher than the normal operation of the voltage, which may lead to the original insulation of good cable after several preventive tests to develop defects. Because the online monitoring technology of cable insulation is a popular topic of current research [8–10], the real-time mastering of the cable insulation status can predict the fault and take measures in advance to ensure the safe operation of the cable.

In this paper, the two-terminal current method is used to monitor the insulation of submarine cables online, and the current and voltage at both ends of the submarine cable are monitored to calculate the insulation status of the submarine cable. Firstly, the theoretical analysis of the monitoring method is carried out, then the modeling of the submarine cable and the monitoring system is introduced, and finally the influencing factors of the monitoring system and the monitoring effect are analyzed.

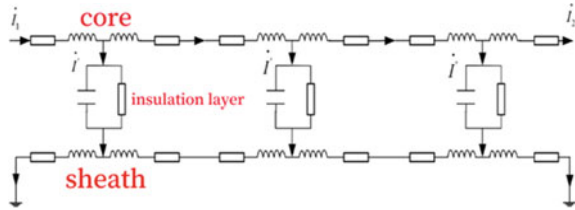
2 Introduction of Two-Terminal Current Method Online Monitoring

The basic idea is that the current and voltage at both ends of the cable are monitored at the same time, and the current and voltage data at both ends are monitored and then the $\tan\delta$ of the cable insulation is obtained through certain calculations, and the $\tan\delta$ of the cable monitored in real time can reflect the real-time insulation status of the cable. The following is a detailed description of this method.

2.1 Insulation Leakage Current Measurement

Submarine cable due to the laying in the sea, can not use the conventional land cable cross interconnection, body transposition and other ways to limit the sheath induction current, submarine cable sheath often take the two ends of the grounding method. The insulation layer of the submarine cable bears the high voltage between the core and the sheath, and the leakage current flows from the core through the insulation layer to the metal sheath and then into the ground. By measuring the grounding

Fig. 1 Leakage current measurement principle diagram



current of the sheath to directly measure the leakage current is not practical, because the grounding current of the sheath is not only leakage current, there is also the existence of induction loop current due to electromagnetic induction. There is also a way to measure the leakage current is by measuring the core current at the first and last ends of the cable, the difference between the core currents at the two ends of the cable is because the core will flow along the line all the way through the insulation layer leakage current, so simply monitor the first end of the current obtained minus the end current, you can get the entire line of the cable through the insulation layer leakage current, that is (Fig. 1):

$$\dot{I} = \dot{I}_1 - \dot{I}_2 \tag{1}$$

2.2 Selection of the Reference Voltage

With the development of offshore wind power to the far shore, the length of the current submarine cable often reaches tens of kilometers, so the problem of voltage drop at the first and last ends of the submarine cable, due to the dielectric loss factor is very small, the selection of the reference voltage has a huge impact on the accuracy of the results, the following analysis of the selection of the reference voltage (Fig. 2).

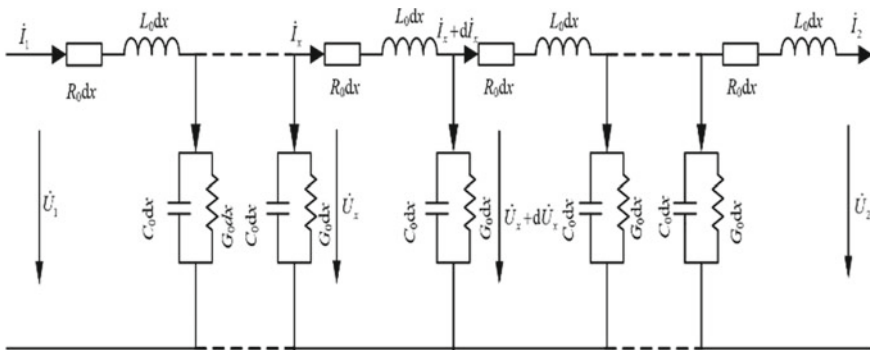


Fig. 2 Single-phase cable AC steady-state circuit diagram

The theoretical derivation of the AC steady-state circuit for single-phase cables, due to the length of the derivation process is not written in the article, the derivation leads to the following conclusions:

$$\frac{\dot{I}_1 - \dot{I}_2}{(\dot{U}_1 + \dot{U}_2)/2} = \frac{-4 \sinh^2(\gamma l)}{Z_c \sinh(2\gamma l)} \quad (2)$$

Observing Eq. 2, the ratio of the difference between the two end currents and half of the sum of the two end voltages is only related to the parameters of the cable itself and the length of the cable, and is not affected by changes in the cable operating current due to load variations.

Based on the above analysis, the sum of the voltages at both ends of the cable is chosen as the reference voltage for good monitoring of the dielectric loss factor of the insulation.

2.3 Calculation of Insulating Layer $\tan\delta$

From the above analysis, it is clear that in order to calculate the insulation $\tan\delta$, the current as well as the voltage data at both ends need to be measured.

The phase difference between the leakage current and the reference voltage is

$$\frac{I \angle \varphi}{U \angle \theta} = \frac{\dot{I}_1 - \dot{I}_2}{(\dot{U}_1 + \dot{U}_2)/2} \quad (3)$$

From this, the dielectric loss factor of the insulation layer can be calculated as:

$$\tan \delta = \tan[90 - (\varphi - \theta)] \quad (4)$$

3 Submarine Cable Modeling and Online Monitoring System Modeling

3.1 Submarine Cable Modeling

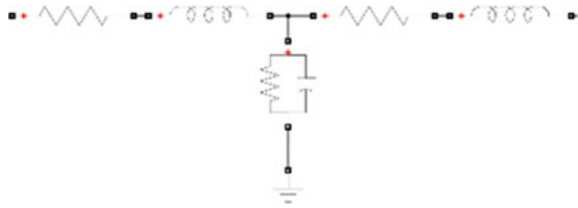
This paper is a study of the dielectric loss factor of the submarine cable insulation, so only the core as well as the insulation is modeled equivalently, and the metal sheath is considered to be directly grounded. A 220 kV submarine cable is modeled and the results of the calculated circuit parameters are shown in Table 1.

A T-shaped equivalent circuit for a 1 km submarine cable is established according to the parameters in Table 1, as shown in Fig. 3.

Table 1 1 km equivalent circuit model parameters

Core equivalent resistance	Core equivalent inductance	Insulation resistance	insulation capacitance
16.4 mΩ	0.107 mH	71.6 MΩ	197 nF

Fig. 3. 1 km equivalent circuit model



Different submarine cable lengths can be combined by connecting multiple 1 km equivalent circuit models in series. For the relationship between submarine cable length and monitoring effect, a 10 km submarine cable model is also established.

3.2 Online Monitoring System Modeling

As shown in Fig. 4, the overall model of the online monitoring system is presented, starting with the submarine cable system and the measurement module. The 220 kV AC power supply model is used, and the packaged submarine cable circuit model is connected to the circuit in series, followed by a load resistor, and the current in the circuit is changed by changing the size of the load resistor to simulate different conditions in the submarine cable system. The current and voltage measurement modules are added to the first and last ends of the submarine cable circuit model, and the current at the first and last ends, and the voltage at the first and last ends, are measured.

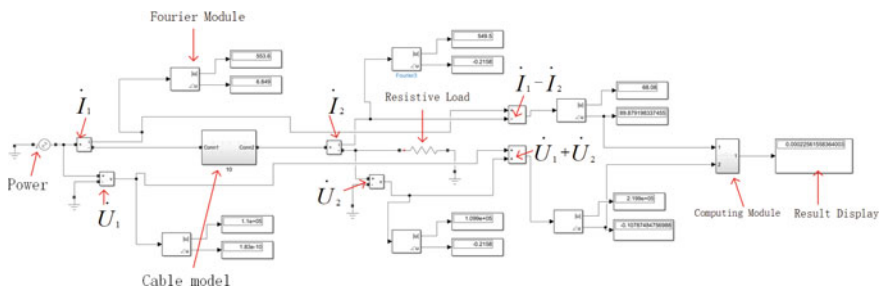


Fig. 4 Overall model of online monitoring system

Since the measured waveforms are the current and voltage at both ends, and the amplitude and phase of the current and voltage are required for calculation, the Fourier module is needed to extract the amplitude and phase of the measured current and voltage waveforms and then provide them to the calculation module.

The first calculations to be performed are the phase subtraction of the current at both ends and the vector addition of the voltage at both ends. Further calculations are then performed on these two results, which are encapsulated in the calculation module, and finally the results of $\tan\delta$ are displayed directly.

The monitoring system model built in this paper integrates the submarine cable system, measurement module, and calculation module, and can directly display the final results of $\tan\delta$.

4 Online Monitoring System Impact Factor Analysis

Calculated by the theoretical formula for $\tan\delta$:

$$\tan \delta = \frac{1}{\omega C R} \quad (5)$$

The calculation result is 2.256×10^{-4} after bringing in the submarine cable parameters in this paper.

4.1 Influence of Reference Voltage Selection

In the first section of this paper, the selection of the reference voltage is explained, and half of the sum of the two terminal voltages is used as the reference voltage in the calculation. In order to verify the effect of this reference voltage selection, the first terminal voltage is also used as the reference voltage for simulation, and the load resistance is set to 200Ω and the current of the control system is at 550 A. The simulation results are shown in Table 2 for the 1 km submarine cable model and the 10 km submarine cable model, respectively.

It can be seen that when the reference voltage is selected as the sum of the voltages at both ends, the simulation results for the submarine cable length of 1 km and 10 km

Table 2 Influence of reference voltage selection

Length of submarine cable (km)	$\tan\delta$ (sum of voltage at both ends) $\times 10^{-4}$	$\tan\delta$ (voltage at first end) $\times 10^{-4}$
1	2.27	3.96
10	2.256	21

Table 3 The effect of different loads on the monitoring effect

Load (Ω)	System current	Tan δ (1 km circuit mode)	Error with theoretical value (%)	Tan δ (10 km circuit mode)	Error with theoretical value (%)
200	1100	2.27	0.62	2.087	7.5
400	550	2.27	0.62	2.256	0
1000	220	2.27	0.62	2.357	5.27
2000	110	2.285	1.06	2.39	5.94
200,000	11	2.28	1.28	2.4	6.38

are very close to the theoretical values, while when the reference voltage is selected as the first end voltage, the simulation results are much different from the theoretical values, and the gap of the 10 km model is larger compared to the error of the 1kkm model. Therefore, the sum of the two end voltages used in this paper as the reference voltage is more effective for monitoring.

4.2 Effect of Different Loads

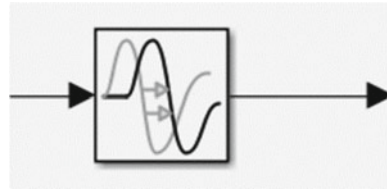
Submarine cable system due to the load changes greatly, especially the offshore delivery system, submarine cable core current can change from a few amps to nearly a thousand amps, the current and voltage at both ends of the cable in real-time changes, in order to explore the impact of different loads on this monitoring system, in the model to change the load resistance and thus change the current in the system, for different loads in the case of simulation, simulation results are shown in Table 3.

As can be seen, when the load changes lead to changes in the system current, the tan δ value obtained from the simulation will vary within a certain range. When the 1 km circuit model is used, the simulated value varies very little and can be kept within 1% error from the theoretical value; when the 10 km circuit model is used, the simulated value varies more than the 1 km circuit model, but both are within 10%, which is an acceptable range.

It can be seen that the model of online monitoring system built in this paper is less affected by different load effects and can monitor credible results under different working conditions.

4.3 Effect of Time Synchronization Error

In the simulation model, the synchronous measurement of current and voltage at both ends can be easily achieved, but in the actual engineering, the time synchronization device will have a certain time error leading to the inconsistency of the measurement

Fig. 5 Time delay module**Table 4** The effect of time error on the monitoring effect

Time delay (ns)	Tan δ (1 km circuit mode)	Error with theoretical value (%)	Tan δ (10 km circuit mode)	Error with theoretical value (%)
15	2.245	1.1	2.23	1.2
30	2.22	2.2	2.21	2.0
45	2.197	3.2	2.187	3.1
60	2.17	4.4	2.16	4.3
75	2.15	5.3	2.14	5.1
90	2.12	6.6	2.12	6.1
200	1.95	14.1	1.95	13.4
500	1.486	34.5	1.493	33.8

time at both ends, and the time error is related by the performance of the time synchronization device. In order to investigate the impact of measurement time error on the monitoring effect at both ends, a time delay (Transport Delay) module is installed before the current and voltage measurement module at the end, as in Fig. 5, which can artificially set a measurement time delay between the end and the first end to model the time error of the time synchronization device in practice.

The simulation results are shown in Table 4 when different time delays are set in the time delay module. The error between the simulation results and the theoretical value is also larger when the time delay is getting larger, and the error between the two circuit models at the same time delay is very close, and the error can reach 6% when the time delay is 90 ns.

5 Effect of Characterization of Cable Insulation Deterioration or Defects in Monitoring Systems

This paper builds the model of online monitoring system of submarine cable insulation based on two-end current method to monitor the state of insulation in submarine cable.

The state of the cable insulation is judged by real-time monitoring of the cable insulation tan δ value. The following equates the cable insulation deterioration or

defects by changing the parameters of cable insulation resistance as well as insulation capacitance.

In the 1 km circuit model to change its insulation resistance to insulation capacitance to simulate the cable insulation degradation or defects, the simulation results are shown in Table 5, the results show that the value is very sensitive to changes in insulation parameters, set the light degradation has changed 60%, set the serious degradation and the occurrence of defects in the results of the change can be more than several times.

Only 1 km of insulation deterioration or defects were set in 10 km of cable to simulate the situation where only some of the insulation deterioration or defects occurred in the submarine cable. The results are shown in Table 6, the partial cable degradation in the whole section of the cable reflects less, set in 1 km in the light degradation reflected in 10 km of the cable only 6% change, but serious degradation as well as the occurrence of defects in the change can still be clearly monitored.

From the results in Tables 5 and 6, it can be seen that the online monitoring system of submarine cable insulation based on the two-end current method adopted in this paper can reflect the overall state of the cable insulation well, but cannot reflect the local insulation deterioration of the cable, and only the local occurrence of serious defects will cause a large change in $\tan\delta$.

Table 5 1 km cable insulation deterioration or defect setting

Insulation condition	Insulation resistance (MΩ)	Insulation capacitance (nF)	Tanδ	Normal changes to insulation (%)
Normal insulation	71.5	197	2.27	0
Mild deterioration	40	220	3.63	60
Severe deterioration	10	250	12.7	460
Defect occurs	1	300	106	4600

Table 6 10 km insulation deterioration or defective setting in 10 km cable

Insulation condition	Insulation resistance (MΩ)	Insulation capacitance (nF)	Tanδ	Normal changes to insulation (%)
Normal insulation	71.5	197	2.256	0
Mild deterioration	40	220	2.391	6
Severe deterioration	10	250	3.51	55
Defect occurs	1	300	17.2	662

6 Conclusion

In this paper, by building a model of submarine cable insulation online monitoring system based on two-terminal current method, the monitoring effect of two-terminal current method for monitoring cable insulation $\tan\delta$ and various influencing factors are studied, and the conclusions are as follows:

- (1) The online monitoring system of submarine cable insulation based on two-terminal current method is less affected by the system load and can be monitored stably under different working conditions.
- (2) There is time error in the measurement of both ends in the actual project, and the error of monitoring can reach 6% when the time error reaches 90 ns.
- (3) This online monitoring system can reflect the overall state of the cable insulation well, but cannot reflect the local insulation deterioration of the cable, and only serious local defects cause a large change in $\tan\delta$.

References

1. Farhangi (2010) The path of the smart grid. *IEEE Power Energy Mag* 8(1):18–28
2. Nakajima, Kashiwagi N, Murata T et al (1989) Development of a hot-line diagnostic method for XLPE cables and the measurement results. *IEEE Trans Power Deliv* 4(2):857–862
3. Oonishi H, Urano F, Mochizuki T et al (1987) Development of new diagnostic method for hot-line XLPE cables with water trees. *IEEE Trans Power Deliv* 2(1):1–7
4. Ahmed NH, Srinivas NN (1997) On-line partial discharge detection in cables. In: *IEEE 1997 annual report conference on electrical insulation and dielectric phenomena*, pp 214–217
5. Liu J, Ouyang B, Xia R (2021) Assessment of the insulation aging state of high voltage XLPE cables. *Electric Power Eng Technol* 40(06):141–149 (in Chinses)
6. Fang J, Peng X, Liu T et al (2020) Development trend and application prospects of big data-based condition monitoring of power apparatus. *Power Syst Prot Control* 48(23):176–186 (in Chinese)
7. Wang T, Bai Y, Lv Z et al (2022) Progress in insulation ageing test and detecting technology of XLPE cable. *Insul Mater* 55(06):6–15 (in Chinses)
8. Zhou X, Xia X, Xia J et al (2021) On-line monitoring of HV transmission cables based on a new criterion established with sheath current. *Electric Power* 54(09):45–54+118 (in Chinses)
9. Li X, An X, Liu J et al (2020) Submarine cable online monitoring technology program research. *Mech Electr Inf* (06):61–62 (in Chinses)
10. Wu W, Lin X (2018) Application and key technologies of submarine cable integrated monitoring. *Electric Power* 51(06):129–135 (in Chinses)

Multi-physical Field Simulation of Permanent Arc Grounding Fault in 110 kV High Voltage Cable



Yisong Wang, Chaoqun Shi, and Yang Xu

Abstract In 110 kV cable systems, most faults are arc grounding faults. Due to the solid grounding of neutral point, short circuit currents can reach tens of thousands of amperes. Arcs of high short circuit currents can cause extremely high energy release into the surrounding environment. This is quite likely to result in a large number of accidents. In the majority of existing studies, the black box model is used to describe the behavior of the permanent arc grounding fault in cable. However, it cannot solve for internal characteristics. In order to solve the above problem, the magneto hydro dynamic (MHD) model was used to study permanent arc grounding faults of high voltage cables. The model was also modified to account for the structure inside the cable. The simulation results show that the maximum temperature inside the arc column can reach 2.2×10^4 K at a short circuit current of 1 kA RMS. When the current is respectively positive and negative peak, the arc voltage can reach 167 V and -155 V. The arc average power is 131 kW. This research paper provides a theoretical basis for the characterization of permanent arc grounding faults and the formulation of relay protection strategies.

Keywords Arc discharge · Grounding fault · AC arc · MHD model · Neutral point solid grounding system

1 Introduction

Over a long time of running, the insulation layer of high voltage power cables develops defects, which manifest as small air gaps. Due to the different resistivities of air and cross-linked polyethylene, the electric potential distribution at their interface is uneven, which leads to a distortion of the electric field [1, 2]. This results in a larger temperature rise at the defect location [3]. Under the combined action of

Y. Wang · C. Shi · Y. Xu (✉)

State Key Laboratory of Electrical Insulation and Power Equipment, Xi'an Jiaotong University, Xi'an 710049, China

e-mail: xuyang@xjtu.edu.cn

© Beijing Paiké Culture Commu. Co., Ltd. 2024

X. Dong and L. Cai (eds.), *The Proceedings of 2023 4th International Symposium on Insulation and Discharge Computation for Power Equipment (IDCOMPU2023)*, Lecture Notes in Electrical Engineering 1100, https://doi.org/10.1007/978-981-99-7393-4_57

603

the electric and thermal fields, the insulation layer of the cable deteriorates rapidly. When the electric field strength becomes greater than the insulation breakdown value at this point, it leads to a breakdown of the defect location, and a strong arc discharge occurs. The above phenomenon is considered as a permanent arc grounding fault. In this case, the cable will get continuously corroded by the high temperature arc, and it is very likely to cause fire or explosion [4]. This has a significant negative impact on people's life and production. Therefore, research on permanent arc grounding faults of high voltage cables is of great significance for safety in energy transmission.

At present, the cable breakdown and discharge at the defective part are generally modeled as a black box. The arc column is equivalent to nonlinear resistor. A differential equation is used to describe the conductivity, and the resistance is obtained by solving the equation. The external characteristics of the arc, such as voltage, current, and impedance, are obtained by iterating according to a specific time step. This type of mathematical model is called the black box model, which can be further classified into the Cassie model, the Mayr model, the improved models based on the two previous models, and other models [5–7]. With advancement in computer technology, the MHD model has been developed to solve the problem that the black box model cannot calculate the physical field inside the arc column. The MHD model comprehensively considers the influence of the electromagnetic, thermal, and flow fields of the arc. The physical fields inside the arc column can be calculated by the finite element method, and the features of the arc under different physical fields can be obtained. The MHD model can simulate the arc discharge relatively completely.

However, solving the complex MHD model requires a large number of calculations. A piece of wire with an air gap [8, 9] or a simple arc generator [10, 11] is generally used to simulate the physical structure of the arc ignition. A real high voltage cable is rarely used for simulation because of its complex structure. Therefore, research on the breakdown and discharge of the real cable is usually carried out through experiments. Air column defects are created in the insulation layer, and a metal wire is used to short-circuit for arc ignition [12]. The fault parameters of the grounding arc are obtained. But these experiments still fail to obtain the internal characteristics of the arc. So far, the multi-physical field simulation of a power cable permanent arc grounding fault has remained a difficult problem to solve.

A multi-physical field simulation of a 110 kV high voltage cable permanent arc grounding fault in the real cable structure was not done in previous research. A simulation model of a real cable was built based on the MHD model. The internal arcing process of a 110 kV high voltage cable was simulated. Then the characteristics of energy release were analyzed. The energy of the arc is mostly in the form of heat, so it can reflect the impact of cable arc grounding fault on the surrounding environment to a certain extent. Finally, we summarized the multi-physical field characteristics of the permanent arc grounding fault. The changes in electric field and thermal fields with time were stated.

2 Simulation Methodology

2.1 110 kV High Voltage Cable Geometry and Materials

The typical cross-section of a 110 kV high voltage cable is shown in Fig. 1. The main structures are the conductor, insulation, metal sheath, outer sheath, and other thinner layers. When a permanent arc grounding fault occurs, the air column defect rapidly develops into a penetrating channel between the conductor and the metal sheath. Under the combined action of the thermal and electric fields, the air inside the channel breaks down and a strong arc discharge is generated.

The geometric dimension and materials of the cable are shown in Table 1. Considering that the semiconductive tape, conductor screen and insulation screen of the cable are thin, they are combined into the insulation layer for simplified modeling. In addition, the corrugated aluminum sheath is assumed to fit the surface of the insulating. Since the arc is always generated between the corrugated aluminum sheath and the conductor, the above simplification does not affect the length of the arc and has little effect on the result. The simplification is done only to reduce the difficulty in meshing and calculations.

As shown in Fig. 2, the defect was a 2 mm diameter air column through the insulation layer. It simulated the damage to the cable during manufacturing, laying or long-term running. The mesh was denser in the defect area in order to obtain higher precision calculation results. The boundary of the air column defect was also refined. This helped strengthen the convergence of the calculation. Then the material properties of each structure were set.

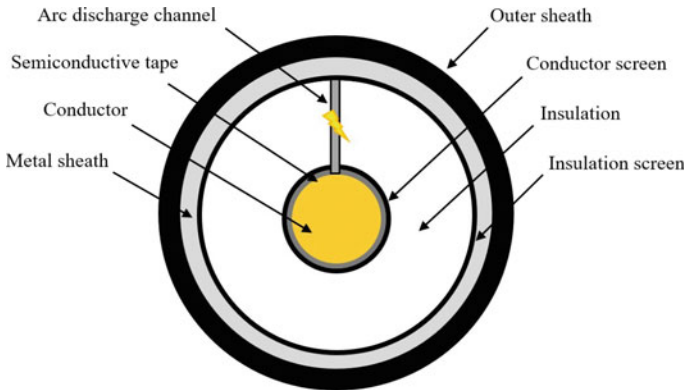


Fig. 1. 110 kV high voltage cable typical cross-section

Table 1 Geometric dimension and materials of 110 kV cable

Structure	Material	Diameter (mm)
Conductor	Copper	30.0
Semiconductive tape	Nylon fiber	30.6
Conductor screen	Polyolefin	33.0
Insulation	XLPE	66.0
Insulation screen	Polyolefin	68.0
Metal sheath	Aluminum	79.0
Outer sheath	PVC	87.0

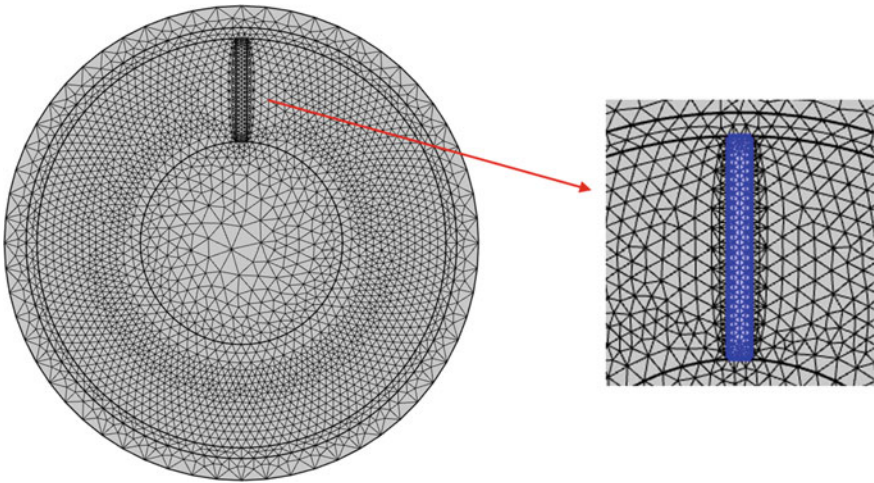


Fig. 2 Cable defect setup and meshing

2.2 Multi-physical Field Modeling

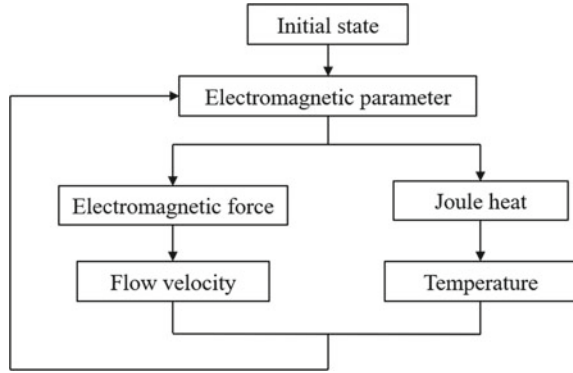
The arc can be described using the MHD model. The relationship between physical fields is shown in Fig. 3. The initial state determines the initial electromagnetic parameters. Over time, the electromagnetic parameters begin to change under the action of the AC power supply. Electromagnetic force and Joule heat change with that and both result in flow velocity and temperature, which eventually act on electromagnetic parameters again.

In the simulation model, the electric field needs to satisfy the current continuity equation, which is expressed as follows:

$$\nabla \cdot \mathbf{J} + \frac{\partial \rho}{\partial t} = 0 \tag{1}$$

where \mathbf{J} is the current density vector, ρ is the electric charge density, and t is time.

Fig. 3 Coupling of multi-physical fields



The magnetic field follows Ampere’s law, and its governing equation is as follows:

$$\nabla \times \mathbf{H} = \mathbf{J} \tag{2}$$

where \mathbf{H} is the magnetic field intensity vector.

When analyzing heat transfer, the following temperature field equation can be used:

$$\rho C_p \frac{\partial T}{\partial t} + \rho C_p \mathbf{u} \cdot \nabla T + \nabla \cdot \mathbf{q} = Q \tag{3}$$

where ρ is the air density, C_p is the heat capacity of air, T is the thermodynamic temperature, \mathbf{u} is the velocity vector of the air, and \mathbf{q} is the heat flux vector of the air.

Heat flux is derived from Fourier’s law:

$$\mathbf{q} = -k \nabla T \tag{4}$$

where k is the thermal conductivity of the material.

3 Results and Discussion

3.1 Arc Current and Voltage Characteristics

Arc voltage and current curves are shown in Fig. 4. At 1 kA RMS short circuit current, the voltage shows an obvious distortion. The slope of the voltage curve increases rapidly near the zero current crossing point at 0, 10 and 20 ms. Approximately between 2 and 8 ms and 12 and 18 ms, the shape of the curve is more like a sine wave. This distortion is caused by the low temperature of the arc near the zero current crossing and the higher temperatures at other times. The conductivity of the arc is

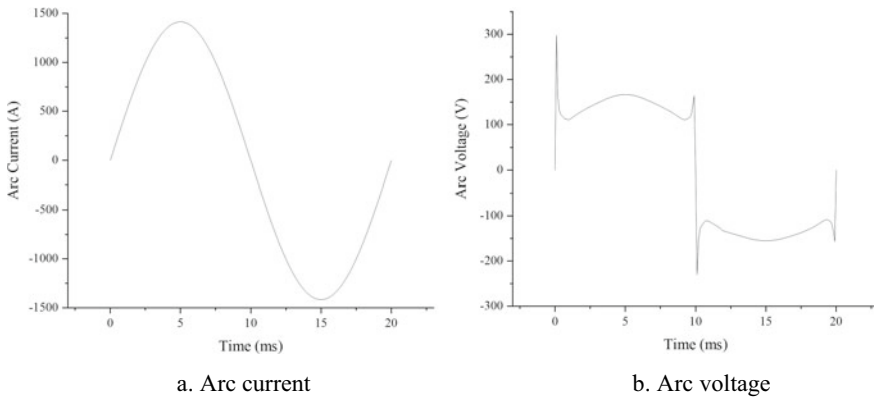


Fig. 4 Arc current and voltage curves for one cycle

higher when the temperature is high, so it can be assumed that the arc behaves as a conductor, and the voltage distortion should be small. On the contrary, the voltage distortion is relatively large. The peak value of the arc voltage reaches 167 V at 5 ms. This means that the resistance is approximately 0.12 Ω .

3.2 Electric Field Distribution

The electric potential distribution of the cable cross-section is shown in Fig. 5. It distorts at the insulation-air column interface. This is due to the difference in electrical conductivity between the two materials. At high temperatures, the conductivity of the arc is higher and results in a more distorted distribution of potential. In the positive and negative half cycles of the current, the electric potential distribution characteristics of the cable cross-section are reversed. The electric potential value of the conductor reaches 167 V and -155 V respectively at the positive and negative peaks of the current.

3.3 Thermal Field Distribution

Temperature distribution is shown in Fig. 6. The temperature shows a trend of first rising and then falling during half cycle. The high temperature areas are near the copper conductor and the corrugated aluminum sheath. The maximum value is approximately 2.2×10^4 K at 5 ms and 2.1×10^4 K at 15 ms. The overall temperature of the arc column is about 1.5×10^4 K at 5 ms and 1.6×10^4 K at 15 ms. Because of heat accumulation, the temperature of arc column during negative half cycle is

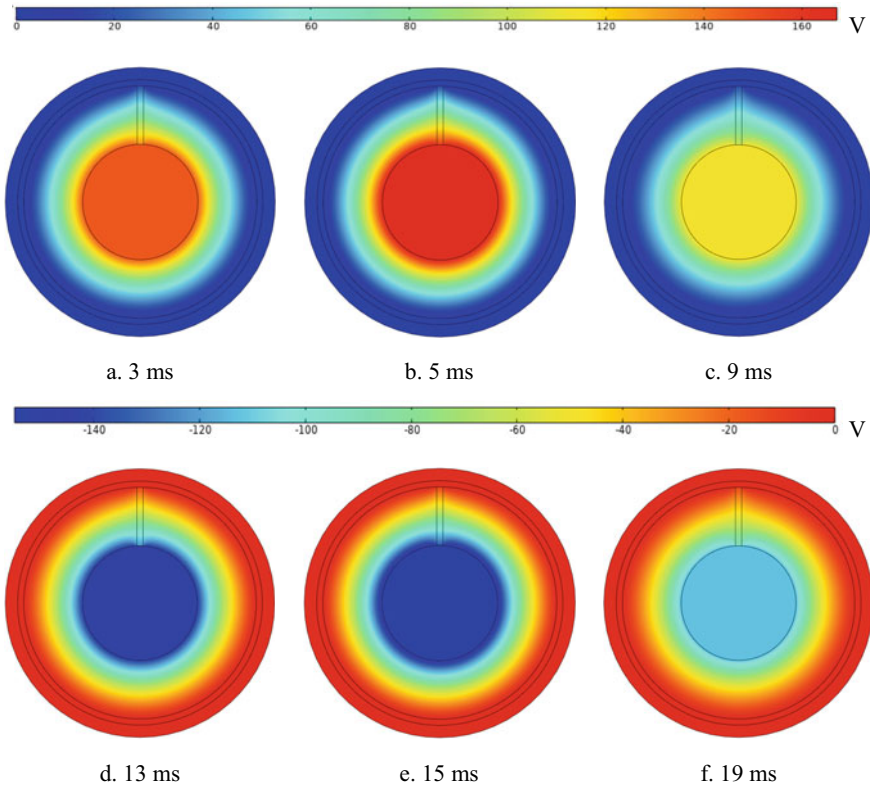


Fig. 5 Electric potential distribution

higher than that in positive half cycle. This also explains why the amplitude of the arc voltage curve during negative half cycle is smaller than the positive half cycle.

3.4 Energy Release Characteristic

The energy release characteristic of the arc is shown in Fig. 7. In one cycle, the arc power curve has two peaks of approximately 238 kW at 5 ms and 219 kW at 15 ms. Through integration, the total energy released by the arc in one cycle is calculated to be 2.62 kJ. The average power of the arc in one cycle is 131 kW.

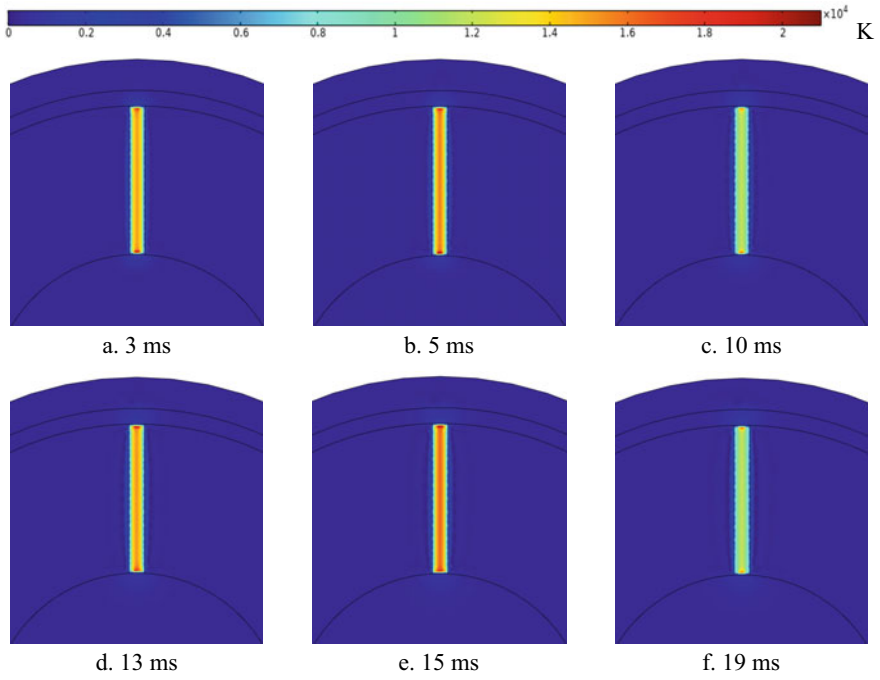
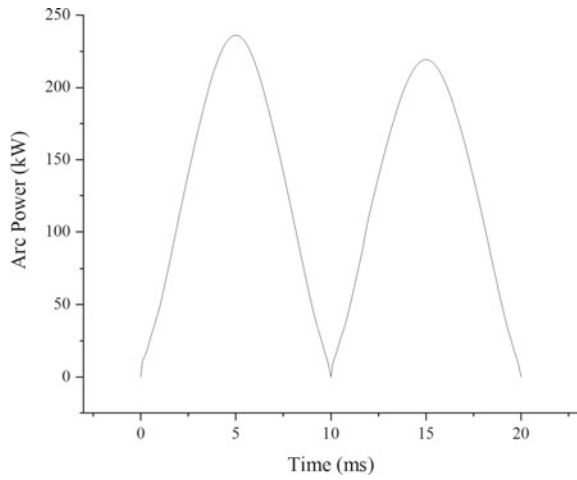


Fig. 6 Temperature distribution

Fig. 7 Arc power curve for one cycle



4 Conclusions

In this paper, the method of multi-physical field simulation method is used to simulate the characteristics of a permanent arc grounding fault of a 110 kV cable during one cycle. The results show that the 110 kV cable can produce an temperature of up to 2.2×10^4 K at 1 kA RMS fault current. This means that the cable has a very high risk of combustion. Electric field distortion occurs at the insulation-air column interface. The arc voltage reaches a maximum value of 167 V. This characterization will be helpful to better analyze the arc discharge conditions of high voltage cable grounding faults and provide a basis for the formulation of relay protection strategies.

References

1. Musa U, Mati AA, Mas'ud AA et al (2021) Finite element modeling of fields distributions in a three-core XLPE cable with multiple cavities. *IEEE PES/IAS Power Africa 2021*:1–4
2. Zhan Y, Hou S, Fu M et al (2022) Electric field simulation analysis of typical defects of 220kV molded joints of polypropylene cable. In: 2022 IEEE 5th international electrical and energy conference (CIEEC), pp 2309–2313
3. Hu X, Zhu H, Chen X (2022) Simulation study on defect electric field of 10kV XLPE cable joint. *J Chongqing Univ Technol (Natural Science)* 36(2):171–178 (in Chinese)
4. CIGRE Working Group B1 of Study Committee 51 (2018) Fire issues for insulated cables insulated in air. CIGRE, Paris, France
5. Yang F, Tang Z, Shen Y et al (2022) Parameter determination method of Cassie-Mayr hybrid arc model based on magnetohydrodynamics plasma theory. *Front Energy Res* 10
6. Wei M, Liu W, Shi F et al (2021) Distortion-controllable arc modeling for high impedance arc fault in the distribution network. *IEEE Trans Power Deliv* 36(1):52–63
7. Wang B, Cui X (2022) Nonlinear modeling analysis and arc high-impedance faults detection in active distribution networks with neutral grounding via Petersen coil. *IEEE Trans Smart Grid* 13(3):1888–1898
8. Zhang Z, Tang X, Huang Q et al (2021) Preemptive medium-low voltage arc flash detection with geometric distribution analysis on magnetic field. *IEEE Trans Ind Appl* 57(3):2129–2137
9. Rong M, Li M, Wu Y et al (2017) 3-D MHD modeling of internal fault arc in a closed container. *IEEE Trans Power Deliv* 32(3):1220–1227
10. Fu G (2018) Research of fault arc simulation based on COMSOL. Shanghai Jiaotong University (in Chinese)
11. Londero RP, Dutra AC, Bender VC et al (2021) Analysis and simulation of direct current electric arcs using the magnetohydrodynamics theory. In: 2021 International conference on electrical, computer and energy technologies (ICECET), pp 1–6
12. Takagi T, Yagi M, Fukushima H et al (2018) Protection against ground faults for a 275-kV hts cable: an experiment. *IEEE Trans Appl Supercond* 28(4):1–4

Review of Operation and Control of the New Energy Storage Isolated Network Systems



Xianqiang He, Weixing Zhao, Fei Cao, QinFeng Ma, Mingshun Liu, Hai Qin, Qingxin Pu, and Yudong Sun

Abstract With the rapid development of distributed power generation technology and microgrid technology, research on the operation and control of new energy storage isolated network systems has received widespread attention. Compared with grid-connected operation, isolated operation can improve the acceptance and application of new energy, increase the flexibility of power grid operation, and solve the problem of difficulty in long-distance transmission in remote areas, which is an important application form and development trend of future new energy. This article reviews the latest progress in the operation and control of new energy storage isolated network systems. The key technologies for the operation and control are analyzed, general methods for the operation and control strategy of are given, and future technology development trends are predicted and discussed.

Keywords New energy isolated network systems · Stability control · Optimal allocation · Energy management · Relay protection

1 Introduction

With the continuous development of the economy, the scale of the power system is constantly expanding, and the demand for energy is increasing. Since traditional fossil fuels such as oil and coal are non-renewable resources and are gradually being depleted [1], countries around the world are planning to adjust and upgrade their energy structures. New energy power generation has become a hot topic of research

X. He · W. Zhao · Q. Ma · M. Liu · H. Qin · Q. Pu
Guizhou Power Grid Co., Ltd., Electric Dispatching and Control Center, Guiyang 550000, China

F. Cao
Beijing Sifang Protection and Automation Engineering Technology Co., Ltd, Beijing 100044, China

Y. Sun (✉)
School of Electrical Engineering and Automation, Wuhan University, Wuhan 430000, China
e-mail: 1638569984@qq.com

© Beijing Paiké Culture Commu. Co., Ltd. 2024
X. Dong and L. Cai (eds.), *The Proceedings of 2023 4th International Symposium on Insulation and Discharge Computation for Power Equipment (IDCOMPU2023)*, Lecture Notes in Electrical Engineering 1100, https://doi.org/10.1007/978-981-99-7393-4_58

[2, 3]. As the capacity of new energy power generation connected to the grid continues to increase, its drawbacks such as volatility and randomness have brought varying degrees of impact on the operation and control. Therefore, it is necessary to allocate certain energy storage systems to smoothen the fluctuations in these new energy sources. The application of energy storage technology can suppress power fluctuations, stabilize output, predict power values, achieve scheduling of new energy power generation, and also achieve spatial–temporal transfer of electrical energy, with fast response speed and feasibility of large-scale application. Compared with grid-connected operation, the islanding operation of new energy storage systems has the characteristics of flexible operation, efficient capacity, and high reliability, and is an important form of application for future energy transformation [4, 5].

In recent years, with the rapid development of distributed power generation technology and microgrid technology, further research and application have been promoted for the operation of new energy storage isolated network systems, and the technology has also been widely valued. Conducting research on the operation and control of new energy storage isolated systems has the following benefits: improving the acceptance and application of new energy, improving the flexibility of power system operation; solving the problem of the difficulty in long-distance transmission of electricity in remote areas, and so on [6]. Therefore, the research on the operation and control of new energy storage isolated network systems is of significance for future energy reform and upgrading. This paper reviews the latest developments in research on the operation and control of new energy storage isolated systems. And it also analyzes the key technologies for the operation and control, predicts and prospects the development trend, providing references for in-depth research and practical application of new energy storage isolated systems.

2 Research on Operation and Control Strategy

2.1 Voltage and Frequency Stability Control

Renewable energy sources in modern power system exhibit fluctuations due to natural randomness, which directly affects the balance of electricity supply and demand and can endanger the voltage and frequency stability of the power system. This is particularly evident in new energy storage isolated network systems. Thus, to ensure the safe and stable operation and the quality of power supply, it is essential to stabilize the voltage and frequency within the new energy storage isolated systems.

Several control methods can stabilize the voltage and frequency in new energy storage isolated network systems. These include master–slave control, peer-to-peer control, and hierarchical control, and so on.

Master–slave control is a common method for small isolated grid systems that divides the power sources into master and slave categories. The master power provides reliable frequency and voltage support to the grid using V/f control. The

other power sources are slave power sources that use P/Q control [7]. A significant advantage of master–slave control is its capability to track changes in distributed power output and load during islanding operation. However, it requires the master power source to have sufficient adjustment capacity and quick response adjustment energy. A method proposed in [8] can reduce the performance requirements of the master power source for master–slave control by coordinating with energy storage devices, expanding the application scenarios of master–slave control.

Peer-to-peer control is another mature control method where all power sources operate under droop control mode, simulating the frequency characteristics of a generator and realizing the coordinated power allocation of each unit. This mode has “plug and play” features for distributed power sources, but it can lead to loop currents affecting the safe operation of the system. Additionally, the control algorithm based on droop control mode in isolated network system is complex, and reactive power cannot be accurately allocated due to the existence of line impedance. Peer-to-peer control sacrifices power quality and is not typically used in actual isolated grid operations due to its drawbacks.

Hierarchical control is a commonly used method that standardizes the operation and function of the power grid during isolated system operation [9]. The hierarchical control divides the control structure into three levels: first-level control, second-level control, and third-level control. The first-level control is consistent with the peer-to-peer control method and adopts droop control, including voltage loops, current loops, and droop control loops [10]. To solve these problems, second-level control restores frequency and voltage to their rated values, as proposed in [11], and improves voltage quality, compensates for unbalanced voltages, and weakens harmonics. Third-level control considers macroeconomic dispatch, power flow control, and energy management issues. The various levels of hierarchical control operate on different time scales, belonging to a multi-time-scale control method. Therefore, the control of each node under hierarchical control is asynchronous and exhibits delay.

2.2 Optimal Allocation of Energy Storage Capacity

It is difficult to effectively connect to the grid because new energy sources are affected by the limitations of local consumption capacity and different standards of design, acceptance, price and operation and maintenance. The development of energy storage is a guarantee for the effective grid connection and large-scale application of new energy sources, so it is very important to optimize the configuration of the capacity new energy storage.

The energy flow of the multi-energy system of wind power, photovoltaic power, hydro power, thermal power and energy storage is shown in Fig. 1. And the arrows represent the direction of energy flow. For the different characteristics of each energy storage system, a suitable strategy is used to optimize the capacity configuration by controlling the start/stop of the DC/DC converter of each energy storage device [12].

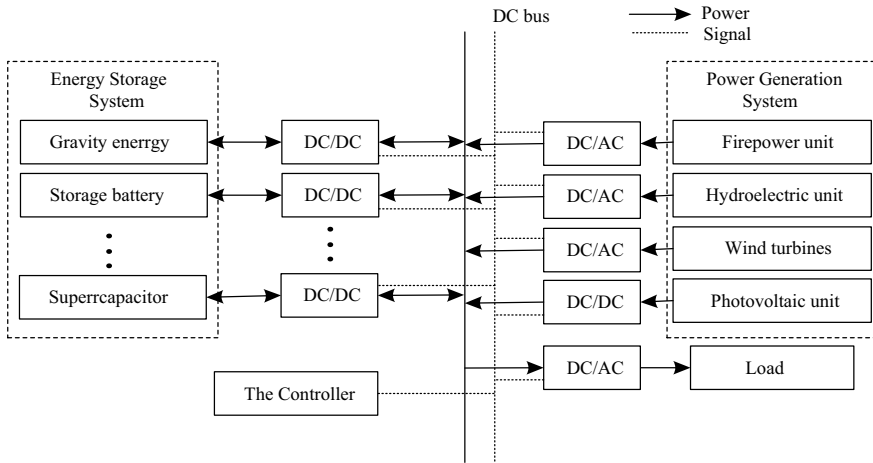


Fig. 1 The energy flow of the multi-energy system

In order to solve the complex nonlinear problem of coordinating the dispatch of multiple energy sources in the optimal allocation of energy storage capacity, [13] proposes a hybrid energy storage capacity optimization allocation strategy based on variable fractional modal decomposition for the optical storage co-generation system. It uses the Euclidean distance method to distinguish the modes, the sliding average method to extract the continuous component signals, and establishes the capacity optimization model of hybrid energy storage system with the minimum annual average allocation cost of the storage system as the objective function and solves it with the improved booster algorithm, which has better economy. Reference [14] has established a single-objective nonlinear programming model based on genetic algorithm with load shortage rate and other indicators as constraints and energy storage device life-cycle cost minimization as the objective function, while its combination of battery and supercapacitor energy storage characteristics enables the optimized system to save economic cost to a large extent.

In order to make the optimization objectives more diversified, Xiao [15] establishes a joint system hierarchical dispatching model with minimum thermal unit operation cost and minimum energy abandonment as the lower-level optimization objectives, and maximum revenue from energy storage system operation and minimum net load fluctuation as the upper-level optimization objectives, based on the deep peaking performance of thermal units. The method, after several iterations, makes full use of the peak-shaving and valley-filling performance of energy storage devices and can give full play to the advantages of each energy source and traditional thermal power for complementary purposes. Reference [16] considers the electric and thermal storage response characteristics and establishes a multivariate hybrid energy storage two-layer capacity optimization model with the minimum equal annual value cost as the objective function. It also considers the coupling and internal dependence between

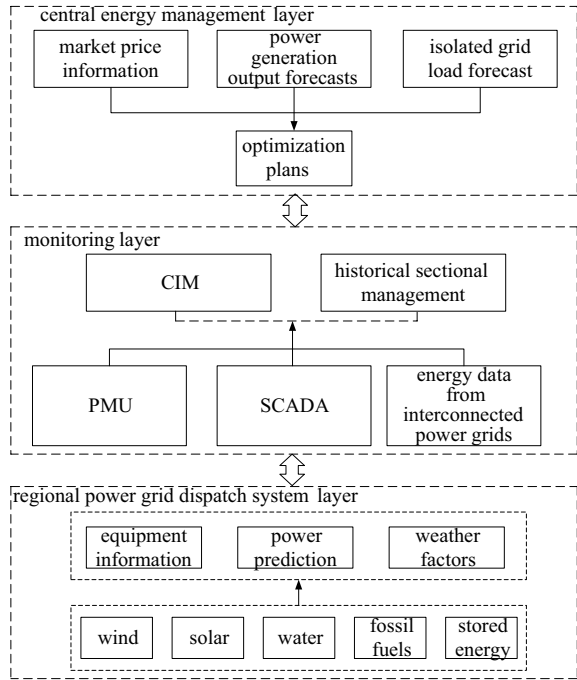
multiple energy sources to achieve the optimization of energy storage power allocation and capacity configuration. In order to consider the capacity allocation of hybrid energy storage system with battery and supercapacitor under multi-objective planning. Reference [17] has proposed a multi-objective capacity optimization allocation model for hybrid energy storage system. It also applies an improved particle swarm algorithm to design the capacity and power of the battery and supercapacitor, which avoids the problems of premature convergence and poor global search capability that traditional particle optimization algorithms tend to produce, and the improved algorithm has strong fast convergence and reliability.

2.3 Energy Management

Large-scale isolated grids typically integrate multiple energy sources such as wind, solar, water, fossil fuels, and electricity, making them nonlinear and complex systems with coupled thermodynamic, chemical, and electrodynamic behaviors. The stochastic variability of renewable energy generation and the time-series coupling characteristics of energy storage operation control pose significant challenges for energy management and optimal operation of isolated grids.

Currently, energy management in new energy storage isolated network systems is mainly divided into two modes: centralized dispatch and decentralized control. In the centralized dispatch mode, as shown in Fig. 2. It consists of a central energy management, monitoring, and regional power grid dispatch system. The central energy management layer, based on market price information, isolated network system load forecast results, and distributed power generation output forecasts, uses certain energy optimization algorithms to develop isolated network energy optimization plans. The monitoring layer uses SCADA and PMU hybrid measurement technology combined with energy management system data from interconnected power grids to synchronously detect the status of grids, ensuring the stability of energy exchange between the isolated system and the interconnected power grid [18]. The system uses the CIM model to process the isolated grid data and combines the historical sectional management module and finally obtain the integrated data. The monitoring layer passes the processed data to the central energy management layer and receives energy optimization plans from the management layer, and then transmits control information to the regional power grid dispatch system layer. The regional power grid dispatch system layer includes wind, solar, water, fossil fuels, and electricity. Renewable energy sources such as wind and solar are greatly affected by weather factors, requiring power prediction combined with weather forecasts, and energy storage systems also require equipment information for prediction [19]. Through this centralized dispatch mode, isolated grid energy can be well managed. In the decentralized control mode, energy management optimization is completed by decentralized power generation device controllers. The controller of the power generation unit works in concert with other devices in the isolated system on the basis of ensuring the efficiency of the use of its own equipment. Compared to the

Fig. 2 Isolated grid energy management structure diagram



decentralized control mode, the centralized dispatch mode is easier to implement and widely used.

Energy management optimization algorithms in new energy storage isolated system can be divided into three main categories: heuristic energy management algorithms, model predictive control (MPC) algorithms, and reinforcement learning algorithms. Heuristic energy management algorithms can provide optimal feasible solutions within a certain time and space range [20]. Reference [21] proposed an energy management technology based on a composite particle swarm optimization algorithm, which predicts changes in load demand, and establishes a multi-objective optimization mathematical model, minimizing operational costs and environmental management costs. However, such algorithms have long computation times and are prone to getting stuck in local optima, making them unsuitable for complex systems. MPC algorithms solve the open-loop problem in a limited time domain by model prediction, rolling optimization, and feedback correction. Reference [22] used a value-based algorithm and proposed an improved competitive deep Q network algorithm, which uses a multi-parameter action exploration mechanism and an optimized neural network structure to learn environmental information from energy management. Such algorithms can cope with constantly changing isolated grid environments, have better stability and economics, but depend on training data and have long training times, still having room for development.

2.4 Relay Protection

The relay protection of new energy isolated network systems refers to a key technology that ensures the reliable and stable operation of the system by enabling relay protection devices to quickly identify and locate faults and implement fault removal when faults occur.

Currently, the relay protection methods in new energy isolated network systems mainly include traditional protection [23]. Traditional protection includes overcurrent protection, differential protection, and distance protection, which mainly focus on how to extract fault features and highlight traditional protection improvements to adapt to new energy isolated network systems. In contrast, the core of the adaptive protection method is that the protection strategy can be automatically adjusted to suit the appropriate protection settings when the power grid operating mode changes. These protection methods require extremely high transmission requirements for communication networks, extremely rapid fault detection, and are difficult to apply in new energy isolated network systems operation. Right now, researchers both domestically and internationally have used intelligent algorithms to construct protection strategies [24, 25]. The advantage of intelligent algorithms lies in their strong control robustness, making protection strategies flexible to adapt to changes in the structure and status of microgrids. In the future, it should combine intelligent algorithms with traditional protection and configure protection for various components such as PC points, microgrid buses, feeder lines, distributed power sources, and loads, while also addressing the coordination problems between different protection methods.

3 Conclusion

This article summarizes the research progress in the operation and control technology of the new energy isolated network systems. Firstly, it introduces three methods of voltage and frequency stability control and elaborates on the method of configuring different energy storage capacities for different purposes. Secondly, it describes the modes of energy management and describes three optimization algorithms based on power generation and load forecasting data, with the constraint of safe operation and the goal of economic operation. Lastly, it explains traditional protection methods and protection methods combining artificial intelligence algorithms.

Future prospects:

- (1) Single energy storage systems have limitations, as they cannot simultaneously meet the requirements of high energy density, high efficiency, high cycle count, and low cost. Therefore, the future research focus will be on studying new types of energy storage systems that meet the requirements by achieving optimal energy storage capacity configuration.

- (2) Energy management will face more complex control structures in the future. The future research focus will be on achieving coordinated control of all modules of the new energy isolated grid systems, designing multi-objective optimization algorithms, and updating reliable and compatible communication network technologies to build rational energy management systems.
- (3) Future relay protection will have higher self-diagnosis, fault judgment, and self-repair capabilities, enabling real-time monitoring and analysis based on changes in system operation and environmental parameters.

Acknowledgements This work was supported by Guizhou Power Grid Co., Ltd, Electric Dispatching and Control Center (066500KK52210040).

References

1. Nguyen TH, Hosani KA, Moursi MSE et al (2019) An overview of modular multilevel converters in HVDC transmission systems with STATCOM operation during pole-to-pole DC short circuits. *IEEE Trans Power Electron* 34(5):4137–4160
2. Liu W, Wen J, Xie C et al (2015) Multi-objective optimization method for source-load coordination considering wind power integration in power system. *Chin J Electr Eng* 35(5):1079–1088 (in Chinese)
3. Wang X, Chen Z, Bian Z et al (2022) Optimal configuration of wind-solar-storage capacity for intelligent micro-grid based on particle swarm optimization algorithm. *J Compr Smart Energy* 44(6):52–58 (in Chinese)
4. Xie N, Yang P, He H et al (2023) Study on energy storage control strategy during the black start process of wind-solar-storage microgrid and thermal power unit. *Proc CSEE* 43(3):1–9 (in Chinese)
5. Jiang W, Han Y, Xue Z et al (2022) Energy storage principle and its application in multi-energy complementary systems. *J Compr Smart Energy* 44(1):63–71 (in Chinese)
6. Fu C, Liao Y, Fan S et al (2015) Real-time simulation test research on the operation and control of wind-storage-seawater desalination standalone microgrid. *Power Syst Prot Control* 43(14):41–47 (in Chinese)
7. Ming Q, Chu S, Cheng Y et al (2016) Multi-master and slave hybrid coordinated control for microgrid based on improved droop control. *Power Syst Autom* 40(20):69–75 (in Chinese)
8. Zhang F, Mou L, Wang Z et al (2020) Optimizing fault control strategy for master-slave controlled islanded microgrids. *Proc CSEE* 40(4):1241–1248+1414
9. Guerrero JM, Loh PC, Lee TL et al (2012) Advanced control architectures for intelligent microgrids—Part II: Power quality, energy storage, and AC/DC microgrids. *IEEE Trans Industr Electron* 60(4):1263–1270
10. Bidram A, Davoudi A (2012) Hierarchical structure of microgrids control system. *IEEE Trans Smart Grid* 3(4):1963–1976
11. Savaghebi M, Jalilian A, Vasquez JC et al (2012) Secondary control scheme for voltage unbalance compensation in an islanded droop-controlled microgrid. *IEEE Trans Smart Grid* 3(2):797–807
12. Hou H (2021) Capacity optimization and economic benefit analysis of integrated energy system. Ph.D. dissertation, Northeast Electric Power University (in Chinese)
13. Li X, Wang J, Qiu Y, Hou Y, Zhou Q (2022) Optimal sizing of hybrid energy storage system based on VMD. *Acta Energaie Solaris Sinica* 43(2):88–96

14. Yang G, Zhu X, Zhou X, Ding X, Wei N, Ma Y, Wang J (2015) Optimization of wind-solar-storage capacity mix based on genetic algorithm. *Electric Drive* 45(2):50–53
15. Xiao J (2022) Multi-energy capacity optimization configuration analysis of wind, solar, water and fire storage system. *Electr Technol Econ* 22(3):69–71 (in Chinese)
16. Wang S, Xie K, Hu B, Cao M (2019) Optimal sizing of multi-energy storage in microgrid with CCHP system. *Distrib Energy Syst* 4(5):58–66 (in Chinese)
17. Li S, Gao S, Guo C (2018) Multi-objective optimal sizing of hybrid energy storage system. *J Power Supply* 16(4):174–180 (in Chinese)
18. Cui Q, Shu J, Wu Z (2015) Research on the functional structure of microgrid energy management system. *Electr Meas Instrum* 52:118–122
19. Bai Y (2021) Design and application of energy management system for smart microgrid. *Ind Control Comput* 34:146–148 (in Chinese)
20. Jia K, Lin Y, Chen Y et al (2018) Microgrid energy management method based on real-time correction of double ring control of energy storage. *Autom Electric Power Syst* 42:131–138 (in Chinese)
21. Xu K, Wu M, Huo X et al (2018) Energy management strategy of microgrid based on composite particle swarm algorithm. *Electr Meas Instrum* 55:57–61
22. Li H, Shen B, Yang Y et al (2022) Energy management and optimization strategy of microgrid based on improved competitive deep Q-network algorithm. *Autom Electric Power Syst* 46:42–49
23. Buigues G, Dyaksova A, Valverde V et al (2013) Microgrid protection technical challenges and existing techniques. In: *International conference on renewable energies and power quality*, Bilbon, Spain, 20–22 March, pp 1–6
24. Ma Y, Yang P, Wang Y et al (2015) Typical characteristics and key technologies of microgrid. *Autom Electric Power Syst* 39(8):168–175 (in Chinese)
25. Xu H, Miao X (2017) Review of hybrid AC/DC distribution mode and its fault protection. *Power Syst Prot Control* 45:139–146 (in Chinese)

Design and Implementation of Passive Chip Temperature Measurement System for Primary Equipment



Kai Zhu, Fanglei Liu, Yaqing Li, Zhen Zheng, Zhaoyu Qin,
and Zhaofan Wang

Abstract In order to reduce the equipment damage and potential safety failure caused by abnormal temperature rise at critical locations of substation primary equipment, temperature monitoring is the most effective and cost-effective method, a new design scheme of passive temperature measurement system based on wireless radio frequency identification technology is proposed. The system is composed of passive temperature sensor, UHF-RFID identification transmission system (Include high-gain directional circularly polarized antenna and fixed data transmission terminal), and status evaluation software package, and it can implement temperature monitoring, thermal fault identification, and early warning for the entire substation. This paper has given a detailed system implementation, and verified the feasibility of the design scheme according to the specific test situation.

Keywords Primary equipment · Passive temperature sensor · UHF-RFID · Wireless transmission

1 Introduction

The reliability of primary equipment is very important. Defects (such as poor contact performance) or faults will cause abnormal temperature rise of the equipment. If not diagnosed and eliminated in time, the abnormal temperature rise will soon lead to long-term high-temperature operation, seriously damage the insulation, greatly shorten the normal operation life of the equipment, and gradually evolve and deteriorate to form accidents or damage equipment, this will finally affect the normal work of the entire power system. In order to ensure the normal operation of primary equipment and the safety of the power system, grasp the heating law and temperature rise

K. Zhu (✉) · F. Liu · Y. Li · Z. Zheng
State Grid Shanghai Qingpu Electric Power Supply Company, Shanghai 201700, China
e-mail: 13585760018@163.com

Z. Qin · Z. Wang
Hubei University of Technology, Wuhan 430068, China

© Beijing Paiké Culture Commu. Co., Ltd. 2024
X. Dong and L. Cai (eds.), *The Proceedings of 2023 4th International Symposium on Insulation and Discharge Computation for Power Equipment (IDCOMPU2023)*, Lecture Notes in Electrical Engineering 1100, https://doi.org/10.1007/978-981-99-7393-4_59

of primary equipment, analyze various equipment defects and fault situations, and effectively diagnose equipment faults. Therefore, timely and accurate measurement of the temperature at each key point of the equipment is of great significance.

At present, the temperature monitoring methods for the high-voltage end of primary equipment mainly include temperature indicating wax method, infrared temperature measurement method, and optical fiber temperature measurement method [1–4]. When using wax flakes for temperature measurement, operation and maintenance personnel need to regularly visually inspect all temperature indicating wax flakes at the tested positions, record and handle the color and melting of the wax flakes in a timely manner. However, human negligence may result in failure hazards not being recorded. The infrared temperature measurement method is currently the most widely used, but it is susceptible to external factors such as sunlight, surface material of the tested part, and testing distance, resulting in temperature measurement errors. The fiber optic temperature measurement method has high temperature measurement accuracy, but the system itself and installation deployment costs are high, which is not conducive to large-scale promotion and use. Moreover, the surface of the fiber optic is easily contaminated, affecting the external insulation of the equipment [5].

Due to certain technical limitations of the above methods, they cannot meet the current requirements for temperature live detection of key points in the entire substation [6]. Therefore, this paper develops a new passive wireless temperature measurement system for key points of substation primary equipment based on radio frequency identification technology. This system can automatically record and analyze the temperature of key points of the entire station equipment, without the need for power supply or maintenance. Contact temperature measurement is not affected by external factors such as sunlight, and can meet the temperature measurement requirements of key points of the entire substation equipment.

2 Design Scheme

The passive temperature measurement system for key points of primary equipment (hereinafter referred to as “passive temperature measurement system”) adopts the passive temperature measurement method based on RFID, including passive temperature sensor, high-gain directional circularly polarized antenna, fixed data transmission terminal and background management and analysis system, which can be conveniently installed to the high-voltage conductor or key parts of the equipment to collect the temperature of key points of the equipment. By analyzing and collecting the state information such as the temperature of the substation equipment with identification information, early warning can be given, according to the relevant maintenance procedures, the normal, abnormal and serious state of the equipment is judged, and the maintenance cycle and maintenance strategy suggestions are put forward to greatly reduce the potential safety hazards, effectively improve the work efficiency

and maintenance quality, and reduce the maintenance cost, which is applicable to all substations below 220 kV.

2.1 Passive Temperature Sensor

The temperature sensor adopts RFID tag embedded with surface acoustic wave temperature sensor, which is mainly divided into four modules: RF analog front end, digital controller, memory and temperature sensor. Its structure is shown in Fig. 1 [7, 8].

According to the detection principle, saw temperature sensor can be divided into two types: delay type and vibration type. The resonant sensor is used here because its

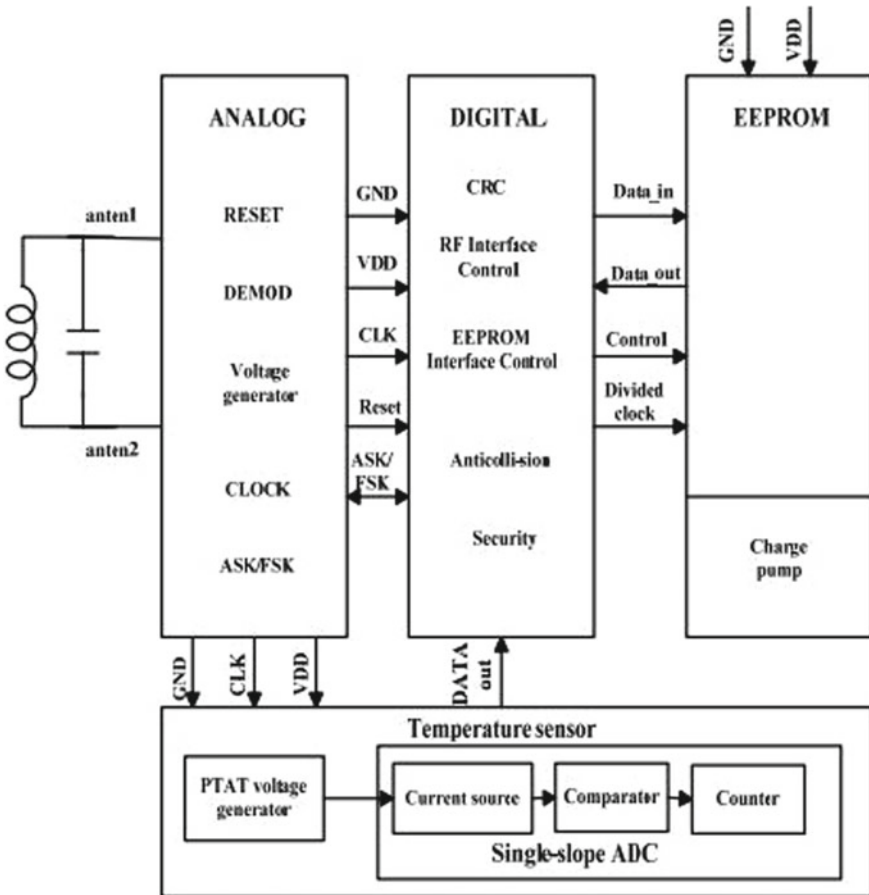


Fig. 1 RFID temperature measurement tag internal structure

quality factor is much higher than that of the delay type device, and the loss is very small, which is more suitable for long-distance passive wireless remote sensing. The distributed passive wireless array sensor can be formed by using multiple passive surface acoustic wave sensors. As long as the interdigital transducers of each surface acoustic wave device in the array sensor have different frequency selection characteristics or different coding (decoding) functions, each sensor element in the array can be excited by the frequency or coding of the transmitted signal, so as to achieve the purpose of identifying (addressing) each sensor element in the array, Meet the design needs.

RFID tag adopts a passive intelligent UHF electronic tag chip, which is used in an application environment with a reading and writing distance of up to 10 m. It has the function of anti-collision algorithm. Within the reading range of the reader antenna, it can read and identify more than 100 electronic tags per second. The temperature chip is designed with 11bits low-power ADC, with a temperature range of $-40\text{ }^{\circ}\text{C}$ to $120\text{ }^{\circ}\text{C}$ and a temperature accuracy of $0.5\text{ }^{\circ}\text{C}$. It supports EPC global class 1 Gen 2 standard protocol (v1.2.0) and ISO 18000-6c ultra high frequency radio frequency identification (UHF-RFID) international standard. The communication frequency is between 860 and 960 MHz. The unique digital architecture is used inside, which can further optimize the structure of the user area. Its internal highly integrated hardware circuit design can well solve the interference of short-range field strength on the chip. At the same time, it uses internationally mature technology to further reduce its power consumption, meet customers' requirements for fast reading and writing of product data, data erasure and security protection of special passwords specified in the user area, and ensure the stability of product labels to meet the design requirements.

2.2 Design of High-Gain Terminal

The fixed terminal is a RF transceiver and signal processing system based on the principle of radar. The circuits used mainly include pulse type, pulse compression type and FM continuous wave type. At present, pulse radar system with amplitude decoding is generally used, and its principal block diagram is shown in Fig. 2. The system shown is universal. It can be applied to the reading and writing of saw tags in various frequency bands below 1000 MHz as long as the local oscillator frequency and a few related components are changed.

The fixed terminal adopts two anti-conflict protocols, free mode and stop mode. In free mode, the sensor sends its own data through different time intervals. The fixed terminal first attempts to read the data of the sensor, but since the sensor also starts to send during the reading process, the fixed terminal finds data conflict through data verification (Manchester decoding and CRC verification), and discards the data. Then the fixed terminal continues to send signals to try to read the data of the sensor, and no data conflict is found through data verification, so the data of the sensor can be read out smoothly. In the stop mode, after the fixed terminal successfully reads the data of the electronic tag, it sends a stop command, and the successfully read

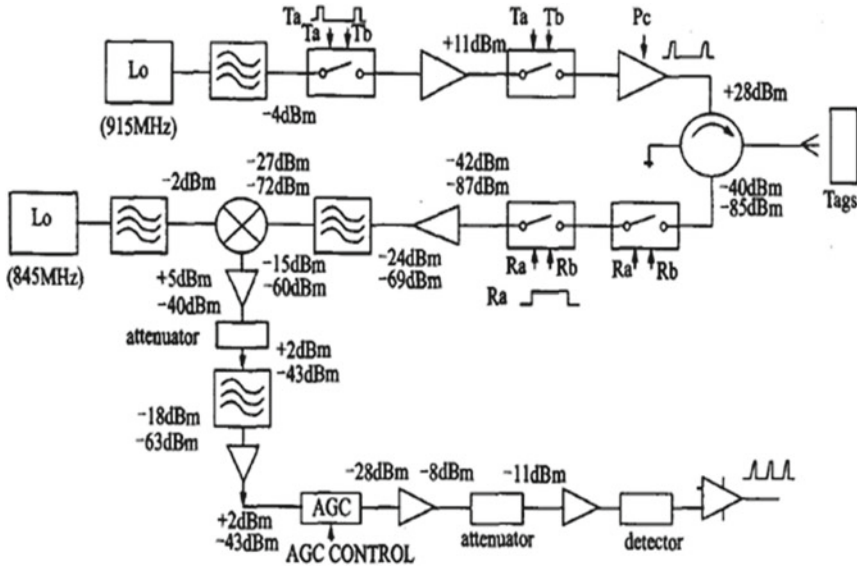


Fig. 2 Schematic diagram of general decoding fixed terminals

sensor stops transmitting its own data and enters the "static" state, so that the tag data can be read more quickly. The schematic diagram of the fixed terminal is as follows (Fig. 3).

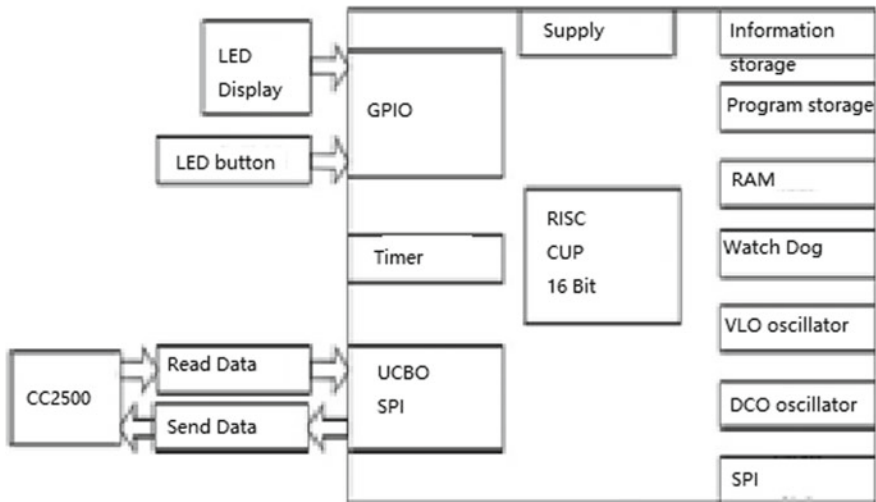


Fig. 3 Schematic diagram of the fixed terminals

The fixed terminal is composed of wireless communication module, LCD module, keyboard input module, wireless communication module, etc. The wireless communication module is used to communicate with the background analysis management system located in the workstation. The management system sends the authorization information to the fixed terminal through the communication interface. The person in charge of the work will associate the patrol inspection personnel with the fixed terminal information and complete the authorization of the patrol inspection personnel by means of wireless communication. In addition to completing the authorization, the wireless communication module can also send temperature measurement data to the background analysis software, and receive equipment warning information and maintenance suggestions.

2.3 RFID Identification Transmission System

The complete RFID identification transmission system should be an application system combining passive sensors and fixed terminals. The monitoring model is shown in Fig. 4.

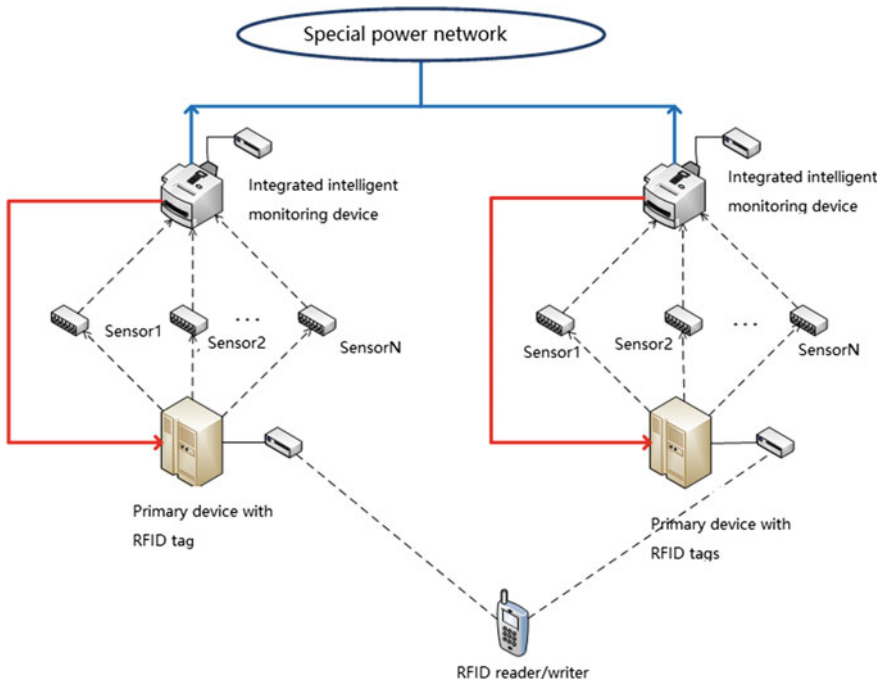


Fig. 4 Software structure diagram of data management

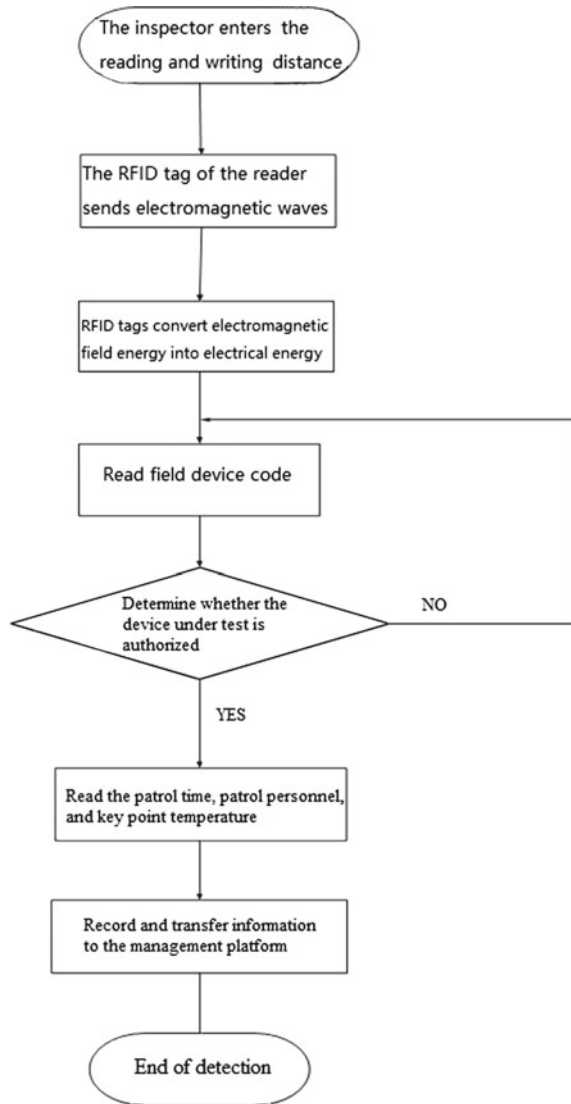
RFID identification transmission system is a set of interface specification system for power equipment identification and data exchange based on extended RFID tags, and applies the rapid identification, information acquisition and positioning technology of RFID and GPS. The system uses two kinds of electronic tag readers and writers: one is the electronic tag reader and writer that maintains the device code, which is used to read the code when maintaining the electronic tag and provide the unique correspondence between the code and the actual position of the device; One is an electronic tag reader built into a fixed terminal, which is used to read the code installed on the device. After reading the code of the field device, it is compared to determine whether the tested device is authorized. At the same time, key information such as test time, tester, key point temperature, etc. are recorded to facilitate tracking management after patrol inspection. The working flow chart of RFID system is as follows (Fig. 5).

The RFID identification and transmission system adopts efficient and low-power communication transmission technology and its acquisition and transmission technology in the strong electromagnetic interference operation environment of the substation. It has the functions of self-identification, environmental perception, self-diagnosis and self-repair, and the power dedicated chip and fixed terminal with the Internet of things interactive interface. It realizes the intelligent acquisition, transmission and processing of information, and meets the design requirements.

2.4 Temperature Measurement System and State Evaluation Software Package

The passive temperature measurement system adopts the method of hierarchical design, which is divided into basic platform, service support, public service, service management and security management. It forms a business development and operation support environment for temperature testing technology at key points of substation primary equipment based on a unified technical architecture, provides basic services and common service functions for various systems, realizes information resource sharing and business collaboration, and combines the historical temperature data of monitoring points, Carry out real-time analysis, and for the monitoring points with gradually increasing temperature changes, early warning can be given before the temperature reaches the upper limit, so as to eliminate the fault in the bud. At the same time, based on the RFID technology of the Internet of things, the temperature measurement data of the primary equipment in the substation are analyzed, and the preventive test data, patrol inspection and live detection data are combined to conduct a comprehensive analysis. Combined with the existing experience, the equipment status is evaluated, and the maintenance suggestions are given.

Fig. 5 Flow diagram of RFID identification system



3 Test Results of Passive Temperature Measurement System

In order to verify the effectiveness of the system, the project team completed the background software development of the passive temperature testing system for key points of primary equipment in the substation, and conducted joint online testing of chips, terminals, and fixed readers. The test chip sensors and read/write terminal are shown in Fig. 6, and the test installation site is shown in Fig. 7.



Fig. 6 Chip sensors and read/write terminal

Fig. 7 Test and installation site of the system



After the experimental test of the passive temperature measurement system, we found that there was a certain error between the measured temperature and the actual temperature. The reasons for the measurement error of the temperature measurement system were analyzed as follows: first, the error of the temperature probe. The better the thermal conductivity of the temperature probe, the faster the response to temperature changes, and the smaller the hysteresis degree; The second is the quantization error of AD conversion circuit. The higher the AD digit is, the smaller the quantization error is; In addition, there are external interference heat sources on the site, including the human body, the heating body around the sensor, and the flowing air, which will affect the measurement. In addition, the surface condition of the key points of the measurement will also bring some measurement deviation. Table 1 shows the measurement results of the temperature rise test of the system.

Table 1 Test results

Test time (min)	Standard temperature (°C)	Measured temperature (°C)
0	0.0	0.0
1	10.0	9.7
2	20.1	19.8
3	28.0	28.5
4	34.2	35.1
5	38.3	38.7
6	42.0	42.1
7	45.3	44.8
8	48.3	48.0
9	50.7	51.1
10	52.2	52.5
11	53.4	53.2

From the test data, the maximum error between the data measured by the passive temperature measurement system and the actual temperature is less than 1 °C, which has good temperature measurement effect and meets the design requirements (Fig. 8).

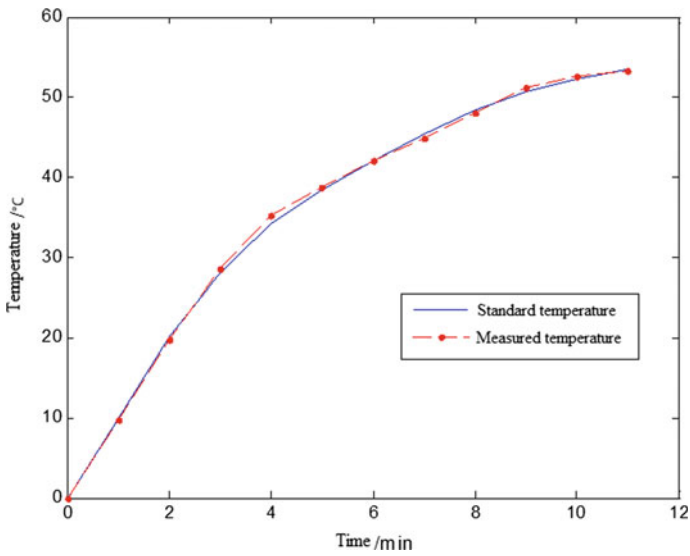


Fig. 8 The experiment results sheet

4 Conclusion

Compared with other temperature measurement methods, the passive temperature measurement system has the advantages of wireless, convenient installation of temperature measurement components, almost any key point can be used, accurate and timely information, and good alarm system. The system can realize the on-line monitoring of the temperature of key parts in the power system. By analyzing and collecting the state information such as the temperature of the substation equipment with identification information, it can realize the early warning. According to the relevant maintenance procedures, it can realize the evaluation of the normal, abnormal and serious state of the equipment, assist the operators to find the equipment abnormalities in time, put forward the maintenance cycle and maintenance strategy suggestions, and change the maintenance mode of the power system, The reliability of power supply system can be improved to a certain extent by enabling operators to grasp the operation of equipment in time.

The system meets the actual on-site operation requirements of the provincial power company, can greatly improve the management level of related professional work, save a lot of manpower and material resources, effectively improve work efficiency and maintenance quality, reduce maintenance costs, and has good social and economic benefits.

Acknowledgements This work was sponsored by the Scientific and Technology Project (B30934220005) of State Grid Shanghai Electric Power Company.

References

1. Qiao K (2013) Application of wireless temperature measurement technology in substation. Hebei Coal (01):56–58 (in Chinese)
2. Wang X (2014) Design of remote wireless temperature measurement system for high voltage switchgear monitoring. Electron Des Eng (03):104–106 (in Chinese)
3. Tai C, Wu B (2018) Research on wireless temperature monitoring system of power equipment. J Electric Power (5):415–417
4. Liu Q (2015) Wireless monitoring of grid equipment temperature. Suzhou University
5. Jin Z, Xu Z, Jin F et al (2007) overview and analysis of temperature measurement methods for high voltage live equipment in China. Power Equip 12:57–61 (in Chinese)
6. Lu X, Wu R, Shen J (2013) Design and application of wireless temperature measurement system for high voltage live equipment. Hebei Electric Power Technol (01):47–49 (in Chinese)
7. Tian W (2013) Analysis and design of CMOS temperature sensor for RFID tag. Huazhong University of science and technology
8. Du Z (2009) Design of a CMOS temperature sensor integrated in RFID tag chip. Huazhong University of science and technology

A Multiphysics Computational Method for Thermal Field of Transformer Winding Using Finite Element Method



Xingxiong Yang, Yanpu Zhao, and Shucan Cheng

Abstract Since the age of the insulation is strongly dependent on the thermal field of transformers, accurate computation of temperature distribution, the hot-spot temperature and reducing the temperature rise are crucial concerns when designing power transformers. With the development of advanced numerical solution techniques, the complicated multiphysical fields including fluid and thermal fields inside power transformers are widely simulated. In this work, the numerical formulations for all the physical fields and the iterative schemes are summarized for computing the thermal rise of transformers. And both oil-directed and oil-natural thermal dissipation modes are simulated using in-house developed code. A parameterized mesh of the transformer is built by calling open source mesh generators for the fast design of transformers, where inlet position parameters are also optimized for illustration of the convenience by utilizing the in-house code. Numerical examples are presented to showcase the results of the in-house developed scripts based on open source software packages. The contribution of this work lies in that it provides a convenient geometric modeling and numerical computation framework for the analysis of complicated multiphysical fields within the same coding framework, instead of having to switch among different packages when using commercial finite element software. The developed in-house scripts can be used also for convenient optimal design of shape parameters of real-world transformer applications.

Keywords Finite element method · Fluid-thermal coupling · Multiphysics computation · Power transformer

X. Yang · Y. Zhao (✉) · S. Cheng
School of Electrical Engineering and Automation, Wuhan University, Wuhan 430072, China
e-mail: yanpu.zhao@whu.edu.cn

© Beijing Paiké Culture Commu. Co., Ltd. 2024
X. Dong and L. Cai (eds.), *The Proceedings of 2023 4th International Symposium on Insulation and Discharge Computation for Power Equipment (IDCOMPU2023)*, Lecture Notes in Electrical Engineering 1100, https://doi.org/10.1007/978-981-99-7393-4_60

635

1 Introduction

An excessive temperature rise in power transformers can hasten insulation aging and reduce its reliability, thus threatens the safety operation of power system. Accurate and fast multiphysics computation that include thermal field can help find the optimal solution to reduce temperature rise, then guide the optimal design of transformer. The temperature rise of transformer is the resultant from multiphysics coupling such as magnetic field, thermal field, and fluid field. Accurate calculation of loss that acted as heat source is crucial for predicting temperature rise. To this end, Wang used Fourier algorithm to calculate the transformer core loss and stray loss under saturated conditions in [1], and studied the effect of the core material's permeability on the distribution of leakage magnetic field. In order to meet the fast and simple requirements of practical engineering application, Olivares-Galván et al. [2] used two temperature method and two frequency method to estimate the percentage of eddy current loss in iron core loss, and conducted experimental verification. In order to calculate transformer loss with higher accuracy, the three-dimensional (3D) effect of structural components is taken into account, and the 3D finite element (FE) method is used to calculate the eddy current losses of the steel and tank [3, 4]. The two-dimensional (2D) FE method is used to calculate the ohmic losses and eddy current losses of converter transformer windings containing higher harmonic currents in [5], the accuracy and efficiency of time domain and frequency domain FE numerical methods were compared.

For fast evaluation of the thermal field, the thermal network method can be used to calculate the temperature rise of the transformer, but the parameters of the model need profound tuning and the versatility is a big bottleneck. In [6], the thermal distribution of dry-type transformer windings is studied, the convective thermal resistance of the thermal network model is modified based on the FE fluid-field simulation results, then the axial temperature distribution and the hot-spot temperature of the winding under typical overload conditions are analyzed. A detail-layered thermal path method of the water-cooled winding is proposed in [7], taking into account the copper loss varying with temperature. The conductive thermal resistance of the double wing fin tube cooling unit is calculated, and the accuracy of the model is verified by 2D FE simulation.

The most accurate and versatile method for finding the thermal distribution is to couple the thermal field with fluid field. Computational Fluid Dynamics (CFD) method has been commonly used to implement fluid-thermal simulations for oil immersed transformer [8–10]. Recently the least square finite element method (LSFEM) and upwind finite element method (UFEM) are proposed in [11] to study the fluid-thermal coupled model of oil-immersed transformers, where indirect coupling iterative algorithm is adopted by calculating the fluid's velocity, temperature, and considers the effect of temperature on material properties and winding loss density accordingly.

In summary, existing methods for studying multiphysical fields of transformer include finite element/finite volume simulation, thermal network method and experimental method. Commercial multiphysics simulation software is widely used for numerical simulation, such as ANSYS, COMSOL Multiphysics, Altair etc. While commercial software provides ease of use and versatility, the openness of its black-box interface is extremely limited for testing numerical algorithms, which also limits users to only at the interface and command line interaction level. Besides, when optimizing equipment structure parameters and embedding new solvers or algorithms, which is also difficult to do with commercial software packages. To meet the needs of wide engineering design applications, this work provides a convenient and fast geometric modeling method and numerical computation framework for thermal rise of transformer windings, it is also really powerful for structure optimization of power equipment.

2 Calculation of Transformer Winding Losses

The heat source in transformers is mainly resulted from eddy current losses, ohmic losses, and circulating current losses of windings. The calculation method of direct-current (DC) resistance loss is relatively simple and mature, and the calculation of eddy current loss and circulating current loss is mainly conducted here. Eddy current losses can be calculated using analytical methods, finite element methods, empirical formulas methods [12]:

$$P_B = \sum_{i=1}^N (P_{ri} + P_{zi}) = \sum_{i=1}^N \left(\frac{1}{12\rho} (\omega a B_{ri})^2 \pi R_i S_i + \frac{1}{12\rho} (\omega b B_{zi})^2 \pi R_i S_i \right) \quad (1)$$

where P_{ri} , P_{zi} are the transverse and longitudinal eddy current losses (W); B_{ri} , B_{zi} are the transverse and longitudinal magnetic flux densities (T) within the i th element; ρ is resistivity ($\Omega \cdot m$); a , b is the geometric parameter (m); R_i is the distance from the center of gravity of the i th element to the center line of the iron core (m); S_i is the area of the i th element (m^2).

$$P_B = P_{Bm} W n_1 L_p / (ml) = \frac{\omega^2 b a^3 l B_m^2 W n_1 L_p}{72 \rho_r} \quad (2)$$

where a , b is the geometric parameter of the conductor (m); B_m is the peak magnetic leakage density (T); L_p is the average turn length of winding; W is the total number of turns, and n_1 is the number of parallel conductors per turn; ρ_r is the temperature dependent resistivity ($\Omega \cdot m$).

Using Eq. (2), the winding eddy current loss coefficient commonly used in engineering can be extracted:

$$k_a = \frac{P_B}{I_N^2 R} \times 100\% = \frac{\omega^2 b a^3 l B_m^2 W n_1 L_p / 72 \rho_r}{\delta^2 b^2 a^2 \rho_r W n_1 L_p} \times 100\% \tag{3}$$

where δ is the current density of the winding (A/mm²).

Considering the operating conditions: $\rho_{75^\circ\text{C}} = 2.135 \times 10^{-8} \Omega \cdot \text{m}$, $f = 50 \text{ Hz}$, the above Eq. (3) can be simplified as follows:

$$k_a = k \left(\frac{a}{\delta} B_m \right)^2 \times 100\% \tag{4}$$

where k is related to ρ_r , according to experience, $\rho_{75^\circ\text{C}}$, $k = 2.99 \rho_{85^\circ\text{C}}$, $k = 2.99$.

Eddy current loss is not uniformly distributed in the winding wires, which is affected by the distribution of the leakage magnetic field. It is difficult to accurately calculate, thus the eddy current loss of the winding can be calculated by first calculating the ohmic loss P_{dc} :

$$\begin{cases} P_{ec} = k_a P_{dc} \\ P_{dc} = \int_V \sigma |J|^2 dV \end{cases} \tag{5}$$

where σ is conductivity(S/m); J is current density(A/m²).

Multiple strands are usually connected in parallel for large capacity transformer windings. Due to the different positions of multiple parallel wires in the leakage magnetic field, the induced leakage potential is also different. The difference in the leakage potential of each wire will generate a circulating current within the parallel conductors, resulting in a circulating current loss [13].

$$P_c = R \sum_{k=1}^N I_k^2 = R \sum_{k=1}^N \left(\frac{E_k - E_{k,av}}{Z} \right)^2 \tag{6}$$

where R is equivalent resistance of the winding (Ω); E_k is the total induced electric potential caused by leakage flux (V), including self-induced leakage potential and mutual induced leakage potential, which is related to wire parameters and the approach of winding transposition; $E_{av,k}$ is the total average induced leakage potential (V).

3 Heat Transfer Process

The flowing fluid transfers the heat generated by the windings to the radiator through vertical and horizontal oil channels, and then diffuses the heat to the external environment through the radiator. Generally, there are two ways to dissipate heat in power transformers: natural convection and forced convection. For the natural convection

mode, the fluid is driven by forces caused by gravity and difference in density distribution. While for the forced convection mode, the oil fluid is driven by a pump. Overall, there are oil-forced air-forced (OFAF), oil-forced water-forced (OFWF) modes etc.

In order to accurately simulate the temperature distribution inside the transformer, it is necessary to consider the interaction of coupled fluid-thermal fields, where the thermal field will change the density and the oil viscosity and the fluid velocity will influence the thermal distribution. The thermal transfer process can be divided into thermal conduction, thermal convection, and thermal radiation [14].

Thermal conduction: The heat generated by solid components such as wires, iron cores, and oil tanks is transferred from the center to the surface through thermal conduction, which is defined by the following:

$$q = -\lambda \nabla T \quad (7)$$

where q is the heat flux density (W/m^2); λ is the thermal conductivity ($\text{W}/(\text{m} \cdot \text{K})$). **Thermal convection:** convective heat transfer occurs between the surface of solid and the oil, which is the main heat dissipation way. The calculation formula can be obtained by using Newton's cooling formula:

$$q = h \nabla T \quad (8)$$

where h is the convective heat transfer coefficient ($\text{W}/(\text{m}^2 \cdot \text{K})$).

Thermal radiation: the heating component such as cores and clamps radiate energy to the surrounding oil through electromagnetic waves. This heat transfer way is called Thermal radiation. In practical calculations, the correction formula of Eq. 9 is often used:

$$q = \frac{\sigma(T_1^4 - T_2^4)}{(1/\varepsilon_1) + ((1 - \varepsilon_2)/\varepsilon_2)(R_1/R_2)} \quad (9)$$

where ε is heat emissivity ($\text{W}/(\text{m}^2 \cdot \text{K})$); $\sigma = 5.67 \times 10^{-8} (\text{W}/(\text{m}^2 \cdot \text{K}^4))$ is a natural constant representing the blackbody radiation coefficient; R is the radius of the radiation surface (m).

Thermal radiation is a common form of heat transfer between high-temperature and low-temperature objects, but its magnitude is usually negligible compared to thermal conduction and thermal convection. Therefore, the control equation for the temperature field of oil-immersed power transformers mainly includes two parts: the solid region and the fluid region. At steady-state, the temperature field in the solid region is dictated by the thermal conduction equation, as shown in Eq. (10). However, the temperature field in the fluid region is related to the fluid velocity. For incompressible Newtonian fluids, the continuity equation and momentum conservation equation are generally used to solve the fluid velocity using Eq. (11), and then the energy conservation equation shown in Eq. (12) is used to solve the temperature

distribution in the fluid region. After solving the fluid and solid temperature fields, the velocity and temperature can be calculated by iterative solution [15].

$$-\nabla \cdot (\lambda \nabla T) = S_T \quad (10)$$

$$\begin{cases} \nabla \cdot \rho \mathbf{U} = 0 \\ \nabla \cdot (\rho \mathbf{U} \times \mathbf{U}) = -\nabla p + \mu(\nabla^2 \mathbf{U}) + \rho \mathbf{g} \end{cases} \quad (11)$$

$$\nabla \cdot (\rho c_p \mathbf{U} T) = \nabla \cdot (\lambda \nabla T) \quad (12)$$

where ρ is density (kg/m^3); c_p is convective heat transfer coefficient ($\text{J}/(\text{kg}\cdot\text{K})$); S_T is the heat source term (W/m^3); $\mathbf{U} = [u, v]$ is the fluid velocity vector (m/s); μ is the viscosity coefficient ($\text{kg}/(\text{m}\cdot\text{s})$); p is the fluid pressure (Pa); g is the acceleration of gravity (m/s^2).

In particular, the right hand side terms of Eq. (11) are respectively pressure, viscous force, and buoyancy, where the buoyancy term is essential in natural convection mode. While the fluid is driven by a pump in forced circulation mode, with a unit flow that is much larger than in natural convection mode, thus the buoyancy term in forced circulation mode is usually ignored. Note that the heat conduction equation in solid domain (11) and the convection–diffusion equation in the fluid domain (12) are coupled at the solid–fluid interface, where the conjugate heat transfer condition [15] and the no-slipping boundary conditions are applied there. For the inlet, the velocity is specified and at the outlet the pressure is set to be 0.

4 Numerical Example

Based on in-house developed finite element software, the fluid-thermal coupling heat transfer process of the oil-immersed transformer winding segment shown in Fig. 1 was analyzed. The temperature field distribution for different oil inlet locations was simulated. The boundary condition of velocity at the transformer inlet is set to $u = 0$, $v = 0.05 \text{ m/s}$, and $T = 320 \text{ K}$. The outlet boundary condition is set as $p = 0$, and the material parameters are shown in Table 1 [11].

As shown in Fig. 2. Due to the buoyancy direction is downward between two washers, while the oil flow direction is upward, there is a difference of $2 \text{ }^\circ\text{C}$ between the highest temperature. The opposite direction leads to a further slowdown in the oil velocity, thus increases the highest temperature.

When the oil inlet continues to move to the left shown in Fig. 3, the temperature rise continues to increase, reaching a highest temperature of $125.34 \text{ }^\circ\text{C}$. When moving to the far left, most of the oil directly flows toward the outlet, cause a significant change in the highest temperature rise. And when the oil almost flows through the left oil channel as shown in Fig. 3d, it also carries a large amount of heat away from

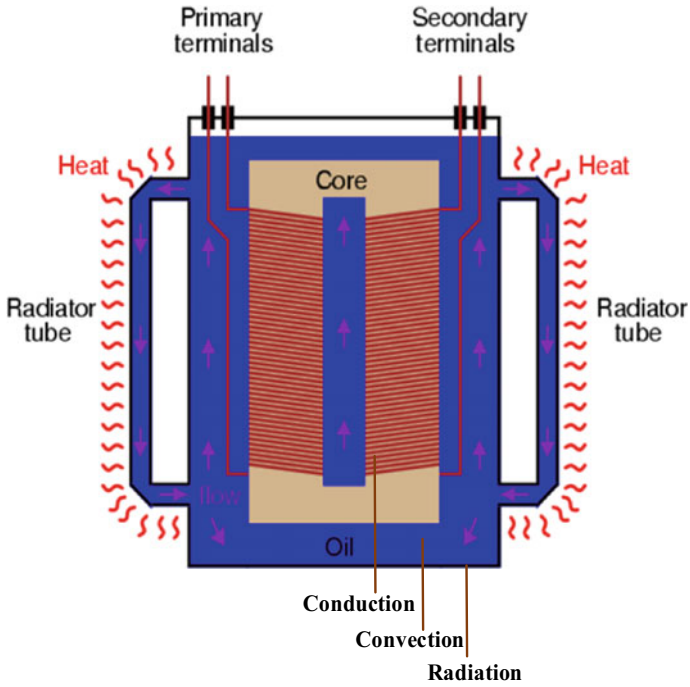


Fig. 1 Heat transfer process of oil-immersed transformer

Table 1 Physical parameters of materials

Materials	Physical parameters	Function fitting
Transformer oil	Viscosity/Pa · s	$0.0846 - 4 \times 10^{-4}T + 5 \times 10^{-7}T^2$
	Specific heat capacity/J · (kg · K) ⁻¹	$807.163 + 3.58T$
	Heat conductivity/W · (m · K) ⁻¹	$0.1509 - 7.101 \times 10^{-5}T$
	Density/kg · m ⁻³	$1098.72 - 0.712T$
Winding	Specific heat capacity/J · (kg · K) ⁻¹	381
	Heat conductivity/W · (m · K) ⁻¹	401
	Density/kg · m ⁻³	8933
Insulation paper	Specific heat capacity/J · (kg · K) ⁻¹	381
	Heat conductivity/W · (m · K) ⁻¹	0.19
	Density/kg · m ⁻³	930

the left winding disc, thus the temperature on the left side of the winding disc also decreases significantly.

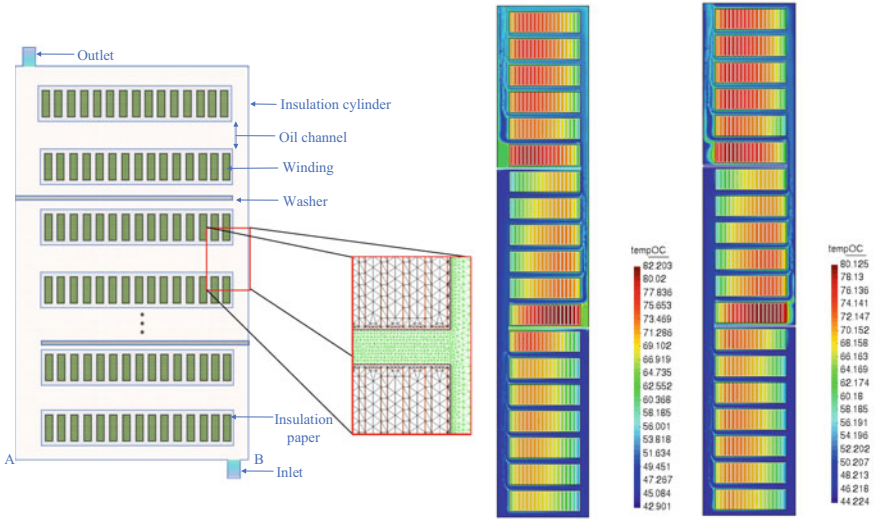


Fig. 2 Left: the winding segment and computational mesh; Middle: temperature field distribution considering buoyancy; Right: temperature field distribution without considering buoyancy

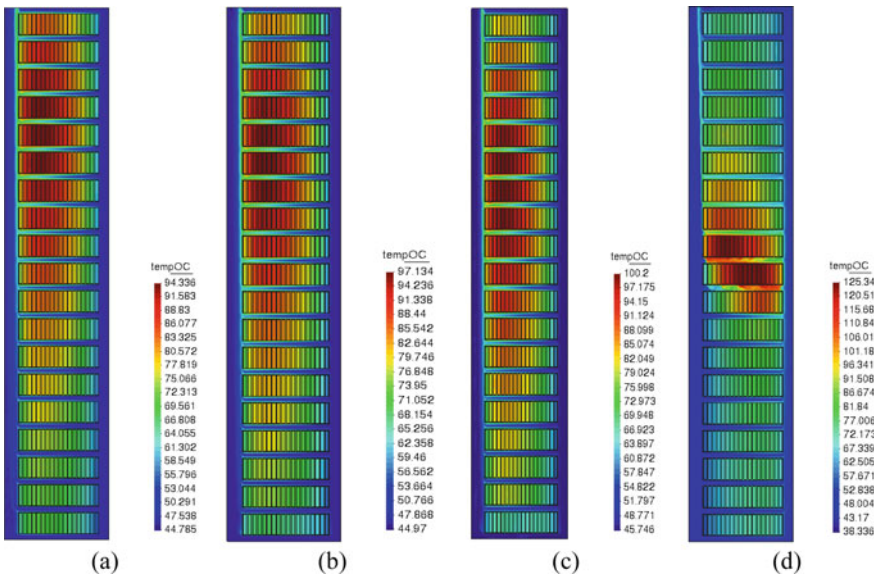


Fig. 3 Temperature field distribution at different oil inlet locations considering buoyancy (no washer). **a–d** the position of the oil outlet remains unchanged, and the oil inlet gradually moves to the left, with distance of 0, 0.3, 0.5, 1(AB) from the initial right position, respectively

5 Conclusion

The multiphysics simulation of coupled fluid-thermal fields in transformer is studied based on in-house developed scripts based on open source software, which provides a convenient method for optimal design of transformers. The proposed method provides a convenient geometric modeling approach and numerical calculation framework. Numerical results based on the developed monolithic code show-case good flexibility and high accuracy for calculating thermal field of transformers. Furthermore, various numerical algorithms can be embedded in this simulation framework to optimize the structure and material parameters of power transformers.

References

1. Wang W, Nysveen A, Magnusson N, Nilssen R (2019) Computation of transformer iron losses under saturation using the Fourier method Part 2: stray loss. In: International conference on the computation of electromagnetic fields (COMPUMAG), Article no. 7200904
2. Olivares-Galván JC, Escarela-Pérez R, Georgilakis PS (2010) Separation of no-load losses for distribution transformers using experimental methods: two frequencies and two temperatures. In: 7th Mediterranean conference and exhibition on power generation, transmission, distribution and energy conversion, Agia Napa, Cyprus
3. Wiak S, Drzymala P, Welfle H (2010) 3D Computer field model of power transformer-magnetic field and power losses computation. In: XIX International conference on electrical machines—ICEM, Rome
4. Wang K, Liu J, Li G (2020) 3-D FEM analysis of loss and temperature distribution in steady state for 550kV oil immersed current transformer. In: 2020 IEEE international conference on high voltage engineering and application (ICHVE), Article no. 8401904
5. Smajic J, Hughes J, Pusch D (2012) Numerical computation of ohmic and eddy-current winding losses of converter transformers including higher harmonics of load current. *IEEE Trans Magn* 48(2):827–830
6. Zhao T, Xuandong L, Ming C (2022) Simulation analysis of dry-type transformer thermal network model considering fluid dynamics. *Trans China Electrotechn Soc* 37(18):4777–4787 (in Chinese)
7. Xiao F, Zhang X, Wang R (2022) A detailed thermal network modeling method of water-cooled epoxy-cast transformer windings with double-wing finned tubes. *Proc CSEE* 42(22):8321–8331 (in Chinese)
8. Vitaly A (2014) Yatsesky: hydrodynamics and heat transfer in cooling channels of oil-filled power transformers with multicoil windings. *Appl Therm Eng* 63:347–353
9. Zhang X, Wang Z, Liu Q (2018) Numerical investigation of oil flow and temperature distributions for ON transformer windings. *Appl Therm Eng* 130:1–9
10. Li YJ, Yan X, Wang C (2019) Eddy current loss effect in foil winding of transformer based on magneto-fluid-thermal simulation. *IEEE Trans Magn* 55(7), Article no. 8401705
11. Liu G, Zheng Z, Yuan D, Lin L (2018): Simulation of fluid-thermal field in oil-immersed transformer winding based on dimensionless least-squares and upwind finite element method. *Energies* 11, Article no. 2357
12. Ye J (2013): Analysis on eddy current loss and thermal field in winding of dry-type transformer. Harbin University of Science and Technology (in Chinese)

13. Sun Y (2011) Calculation and analysis of the eddy current losses and the circulating current losses for 1000 MW hydro-generator. Harbin University of Science and Technology (in Chinese)
14. Xie Y (2017) Study on flow field and temperature field coupling finite element methods in oil-immersed power transformer. North China Electric Power University (in Chinese)
15. Torriano F, Chaaban M, Picher P (2010) Numerical study of parameters affecting the temperature distribution in disc-type transformer winding. *Appl Therm Eng* 30:2034–2044

Field Ionization Degree Influence on Discharge Streamer of Natural Ester Based on Ionization Energy Calculation Under Changing Electric Field



Jingwen Zhang, Junyi Zhang, Wenyu Ye, Hanting Zhang, Hongwei Li, and Jian Hao

Abstract During the development of streamer discharge in transformer oil, field ionization is considered to be the main ionization mechanism that causes liquid dielectric streamer breakdown. With the change of the distortion degree of the space charge to the electric field (EF), the field ionization factor (ionization energy, IE) will also change, further affecting the generation and development of streamers. Therefore, in this paper, the change rule of IE of natural ester with EF is obtained by the DFT (density functional theory) calculation considered solvent effect; Based on hydrodynamic drift–diffusion approximation model, the discharge streamer for natural ester is simulated with field ionization as the source term, and the EF strength and positive ions density in the streamer process are analyzed. DFT results showed that the IE of triglycerides decreased significantly with the increase of EF. Compared with the fixed IE, the development speeds are higher and stop lengths are longer for streamers considering the changing IE in different field strength.

Keywords Streamer discharge · Field ionization · Electric field · Natural ester

1 Introduction

The insulation system of a transformer is crucial for ensuring the safe operation of the power grid. For over 100 years, mineral oil has been commonly used as a liquid insulation in oil-immersed transformers due to its stable performance. However, mineral oil is known to cause severe environmental pollution and is considered a

J. Zhang · J. Zhang · W. Ye · H. Zhang · H. Li · J. Hao (✉)
State Key Laboratory of Power Transmission Equipment Technology, School of Electrical Engineering, Chongqing University, Chongqing 400044, China
e-mail: haojian2016@cqu.edu.cn

J. Zhang
Chongqing Electric Power Research Institute, State Grid Chongqing Electric Power Co., Chongqing, China

© Beijing Paiké Culture Commu. Co., Ltd. 2024
X. Dong and L. Cai (eds.), *The Proceedings of 2023 4th International Symposium on Insulation and Discharge Computation for Power Equipment (IDCOMPU2023)*, Lecture Notes in Electrical Engineering 1100, https://doi.org/10.1007/978-981-99-7393-4_61

nonrenewable energy source with a low rate of bio-degradation. In recent times, there has been a growing preference for using environmentally friendly natural ester (NE) as an ideal substitute for mineral oil. NE offers several advantages, including high biodegradability, ignition point, high flash point, and the ability to delay the aging of oil-paper insulation [1].

During operation, transformers are exposed to lightning impulses. While the lightning breakdown voltages of NE are comparable to mineral oil at small oil gap distances, they are significantly lower than mineral oil when subjected to negative polarity and long oil gaps [2, 3]. Consequently, the lightning impulse data obtained from mineral oil cannot be directly applied to NE [4]. Therefore, it is important to explore the streamer discharge of natural ester oil under the influence of lightning impulse voltages to gain a deeper understanding of the discharge mechanism in NE.

Simulation method for discharge streamer is very important for understanding the physical process of discharge. Based on the research results of the discharge characteristics and process of insulating oil, scholars have established a mathematical and physical model to describe the discharge mechanism of insulating oil. Smalø H. S et al. built the micro-model of ionization energy (IE) of hydrocarbon liquid by using density functional theory (DFT) method, and it was obtained that the change of IE under different electric fields (EF) affected the discharge characteristics of liquid [5]. J. G. Hwang et al. used electro-hydrodynamics equations to study the streamer discharge process of liquid medium, which shows that the charge transfer process can well describe the development process of streamer in the process of space charge generation and dissipation [6]. Therefore, the above simulation is based on the hydrocarbon liquid which has a large difference between the structure of and NE. For NE, the IE is far less than that of hydrocarbon mineral oil [7]. However, the dependence of IE change on EF strength has not been considered in the charge simulation for NE.

Therefore, according to the typical molecular structure of NE, field-dependent model of IE of NE was studied by using DFT calculation. Then the finite element method (FEM) based on electrodynamics is used for streamer simulation by using two different ionization models, field-dependent model and fixed IE value.

2 Methods

2.1 DFT Calculation

The main component of natural fat is triglyceride, which contains three fatty acid branches. Common commercial natural fats usually contain more unsaturated fatty acids. For example, the content of linoleic acid in soybean-based FR3 natural ester reaches 48.1%, while saturated fatty acid only accounts for about 10% [8]. Therefore, trilinolein is selected as the representative component of NE, and the IE of trilinolein under different EF intensities is calculated. The IE of triglycerides is calculated as

formula (1):

$$IE = E^{A+} - E^A \tag{1}$$

where E^{A+} is the energy of cation A^+ ; E^A is the energy of molecule A in isolated state. The quantum chemical calculation software, which is based on density functional theory (DFT), was employed to perform a series of optimizations. Initially, the software was used to optimize the molecular structure in the absence of any external fields (EF). Subsequently, various EFs were applied to the system to carry out additional structure optimizations [9]. In this paper, the quantum chemistry software Gaussian 16 was selected for molecular configuration optimization using the M062X exchange correlation functional and the +6-311G (d, p) basis set [9, 10]. In addition, the solvation effect of molecules is considered in the calculation of energy, and the relative dielectric constant of natural fat is used to simulate the interaction of liquid environment with molecules.

2.2 FEM Simulation

This paper utilizes the FEM to develop streamers and employs the COMSOL Software for simulation purposes. In this paper, three current continuity equations are used to describe the generation, movement and disappearance of electric charge during natural fat discharge, and Poisson’s equation is used to describe the distortion of space charge on EF. The current continuity equation is (2)–(4), the Poisson’s is shown in (5).

$$\frac{\partial \rho_p}{\partial t} + \nabla \cdot (\rho_p \mu_p \vec{E}) = G_E(|\vec{E}|) + \frac{\rho_p \rho_e R_{pe}}{q} + \frac{\rho_p \rho_n R_{pn}}{q} \tag{2}$$

$$\frac{\partial \rho_e}{\partial t} - \nabla \cdot (\rho_e \mu_e \vec{E}) = -G_E(|\vec{E}|) - \frac{\rho_p \rho_e R_{pe}}{q} - \frac{\rho_e}{\tau} \tag{3}$$

$$\frac{\partial \rho_n}{\partial t} - \nabla \cdot (\rho_n \mu_n \vec{E}) = -\frac{\rho_p \rho_e R_{pe}}{q} + \frac{\rho_e}{\tau} \tag{4}$$

$$\nabla \cdot (\epsilon_r \epsilon_0 \vec{E}) = \rho_p + \rho_n + \rho_e \tag{5}$$

where ρ_p , ρ_e and ρ_n represent the charge densities of the electrons, positive and negative ions. $G_E(|\vec{E}|)$ is ionization source term, the production term of electrons and positive ions as described in the Eq. (6).

Field ionization refers to the direct ionization of molecules occurring when subjected to a high electric field. It is widely recognized as the primary mechanism of ionization in liquids. Therefore, only the ionization source term caused by field

ionization was considered in this paper. Other parameters are listed in the Table 1.

$$G_E(\vec{E}) = \frac{q^2 n_i a |\vec{E}|}{h} \exp \left\{ -\frac{\pi^2 m^* a (E_{IO})^2}{qh^2 |\vec{E}|} \right\} \quad (6)$$

where E is the local EF, E_{IO} is the liquid-phase IE, other parameters are fixed values listed in Table I. In order to explore the field dependent characteristics of IE during the development of NE streamers, E_{IO} is defined in two ways in this paper, one is to use the IE without EF as the fixed IE value, and the other is according to the IE field-dependent model calculated by DFT as the IE changing with the field strength.

Positive lightning impulse voltage is applied to the needle-plate electrode. The electrode gap is set to 10 mm, and the radius of curvature of the needle electrode was 40 μm . The positive lightning impulse is given as Eq. (7):

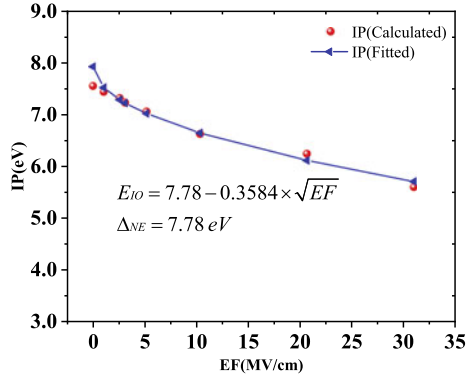
$$V_i = K V_0 \left(e^{-\frac{t}{\tau_1}} - e^{-\frac{t}{\tau_2}} \right) \quad (7)$$

where V_0 is set to +120 kV, K is the compensation factor, τ_1 and τ_2 are the time of wave tail and wave head. The plate electrode is set to have a potential equal to ground potential. The boundary conditions for the charge transport continuity equations at the electrodes are set to “outflow” for the charge species, while the insulating wall boundaries are assigned with no flux.

Table 1 Table of simulation parameters [7]

Symbols	Definition	Value
ε_r	Relative permittivity of oil	3.14
ε_0	Vacuum dielectric constant	$8.854 \times 10^{-12} \text{ F}\cdot\text{m}^{-1}$
μ_p, μ_n	Mobility of the positive and negative ions	$10^{-9} \text{ m}^2\cdot\text{V}^{-1}\cdot\text{s}^{-1}$
μ_e	Mobility of the electrons	$10^{-4} \text{ m}^2\cdot\text{V}^{-1}\cdot\text{s}^{-1}$
R_{pn}	Ion-ion recombination rates	$1.64 \times 10^{-17} \text{ m}^3\cdot\text{s}^{-1}$
R_{pe}	Ion-electron recombination rates	$1.64 \times 10^{-17} \text{ m}^3\cdot\text{s}^{-1}$
τ_a	Electron attachment time	50 ns
ρ_{oil}	Density of NE	$920 \text{ kg}\cdot\text{m}^{-3}$
q	Electron charge	$1.6 \times 10^{-19} \text{ C}$
n_i	Number density of ionizable species	$1 \times 10^{25} \text{ m}^{-3}$
a	Molecular separation distance	$3 \times 10^{-10} \text{ m}$
m^*	Effective electron mass	$9.11 \times 10^{-32} \text{ kg}$
h	Planck's constant	$6.626 \times 10^{-34} \text{ m}^2\cdot\text{kg}\cdot\text{s}^{-1}$

Fig. 1 E_{IO} under the EF



3 Result Analysis

3.1 IE Calculation

Unsaturated triglycerides in esters have low IE, which is close to 7.8 eV without EF. However, the EF strength (EF) can reach more than 108 under the non-uniform EF. And the IE of molecules under the action of EF will change compared with those without EF [9]. Therefore, the IE of triglyceride under different EF intensities is calculated. The IE of triglyceride under the action of changing EF is shown in Fig. 1. It can be seen that with the increase of EF, the IE of triglyceride decreases, is noteworthy in the development of is noteworthy in the development of non-uniform EF streamer under non-uniform EFs. Under the non-uniform EF, the NE molecules at different positions experience different EFs, which means that the NE molecules at the same time have different ionization abilities during the development of streamer. Therefore, the field strength dependence of NE molecules must be considered in the simulation process of streamer. In this paper, the IE (E_{IO}) and EF intensity (EF) are fitted and the formula (8) is obtained.

$$E_{IO} = 7.78 - 0.3584 \times \sqrt{EF} \tag{8}$$

wherein, the unit of E_{IO} for triglyceride is eV, and the EF unit is MV/cm. Formula (8) is substituted into the field ionization source term in the finite element simulation as the IE parameter of the molecule.

3.2 Streamer Morphology

It can be seen from the Fig. 2 that the right streamer develops rapidly. At 50 ns, the right streamer head leaves the needle tip quickly; During the period from 150 to

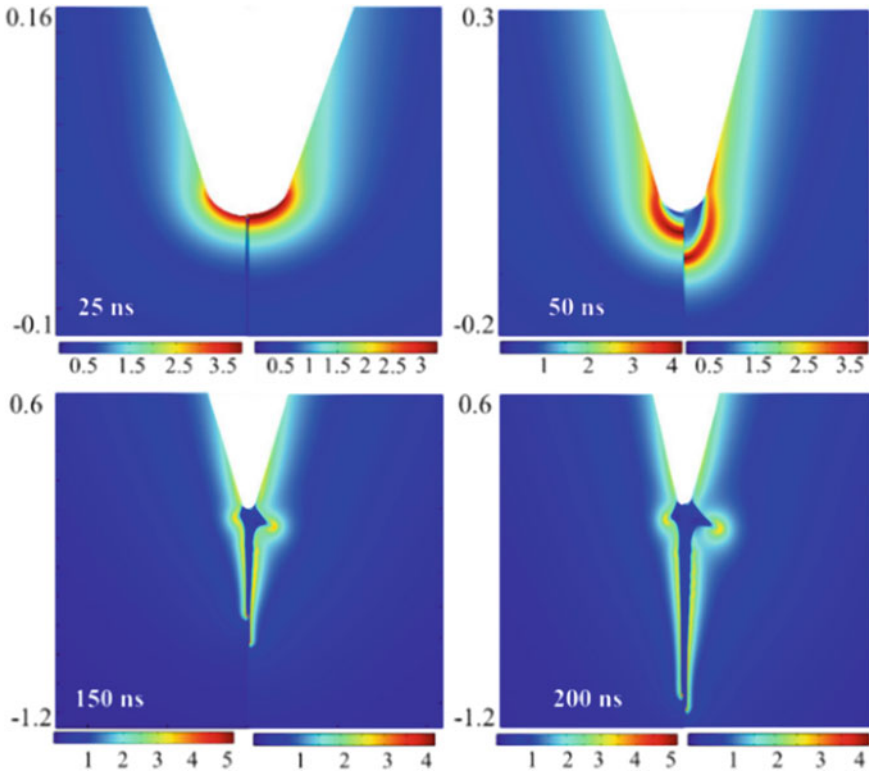


Fig. 2 Streamer electric field comparison with different IE models with different IE models

200 ns, the right streamer developed a relatively obvious branch near the tip of the needle. While for the streamer with fixed IE, the streamer is located at the needle electrode at 50 ns and develops slowly. At 150 ns, there is a weak branch at the electrode that begins to develop, but the branch develops slower than the streamer using the field-dependent ionization model.

3.3 Streamer Electric Field

Figure 3 shows the EF distribution along the electrode axis at different times. In the streamer development model of the two models, there is a peak value of the EF intensity at each time, which corresponds to the position of the streamer head. The EF decreases rapidly after the head position, which corresponds to the EF in the oil outside the streamer.

As shown in Fig. 3a, the field strength of the streamer head using a fixed value as the IE increases first and then decreases, while the EF of the streamer head in Fig. 3b

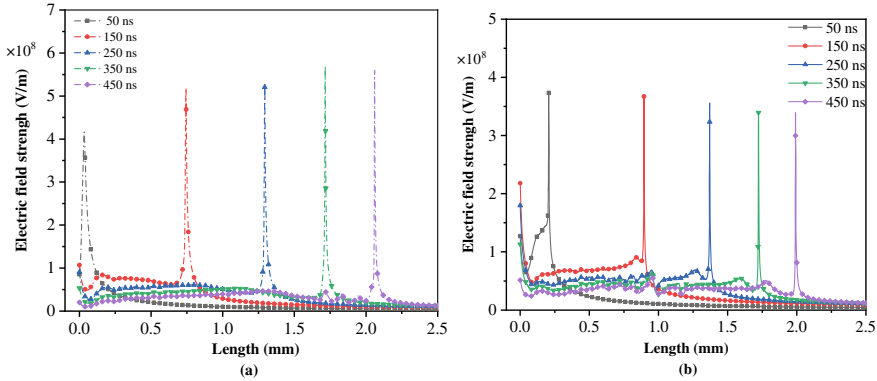


Fig. 3 Streamer electric field along the electrode axis with **a** fixed IE, **b** field-dependent IE model

decreases gradually. This is due to the distortion of the original EF caused by the space EF generated by the positive ions generated by ionization. Because the mobility of electrons is far greater than positive ions, a large number of positive ions remain near the anode and enhance the original EF, which promote the ionization [11]. Therefore, for the streamer with fixed ionization value, the streamer head continuously gathers a large number of positive ions, and the space charge distortion EF strengthens the head EF until the charge accumulation decreases.

The situation is different from IE of the field-dependent model. At 50 ns, compared with the streamer that has not left the anode in Fig. 3a, the head of the streamer in Fig. 3b has been a distance from the anode. The head of the streamer has gathered more positive ions and the distortion effect caused by positive ions reduces the EF within the distance from the electrode to the streamer head. After 150 ns, the decrease of the applied field strength of the anode leads to the decrease of the molecular ionization ability near the ionization region, so the EF distortion ability of positive ions gathered in the streamer head decreases.

3.4 Positive Ions Density Analysis

In this paper, the field-dependent IE model shown in formula (8) and the fixed IE are used to define the field ionization source term for streamer simulation. Because the lower molecular IE means that under the same EF, it is easier with field ionization model to ionize to produce electrons and positive ions than with fixed IE.

As shown in Fig. 4, the head of the streamer has relatively strong ionization, therefore the density of electrons and positive ions produced by ionization in the ionization zone, especially in the head of the streamer, while the density of ions outside the ionization zone is 0. At 50 ns, the ionization ability of (a) with fixed IE is far less than that of (b) with field-dependent IE model, so the positive ion density is

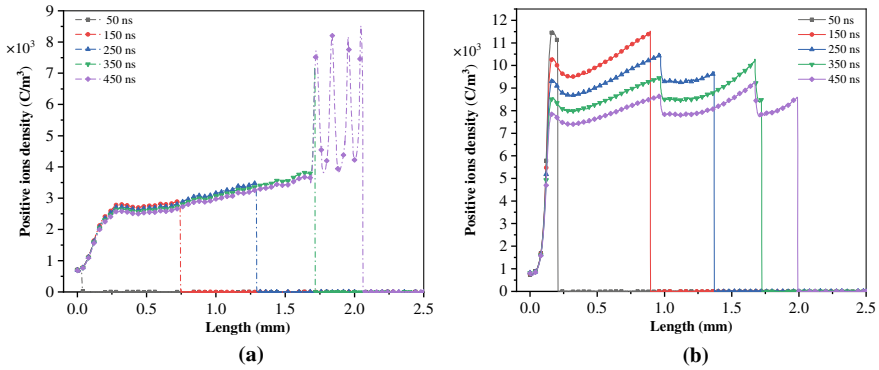


Fig. 4 Positive ions density along the electrode with **a** fixed IE, **b** field-dependent IE model

less than (b). Combined with the analysis of EF and shape, streamer tip field strength in Fig. 4b begins to decrease and the streamer branches at 150 ns reduce the positive ions aggregation of the streamer. Therefore, the positive ion density decreases after 150 ns.

4 Conclusions

The IE of natural ester with changing EF is obtained by calculating the DFT calculation and the simulation of streamer development is performed by finite element method in this paper. The following conclusions are obtained:

The dependence of the IE of NE on the EF strength cannot be ignored. With the enhancement of the EF, the IE continues to decrease. Compared with the case without considering the influence of EF on IE, considering the field intensity dependence of IE makes the streamer develop faster and the branch develop faster. The head of NE streamers is more prone to branching when considering changing IE. As the branching progresses, the strength of the head electric field gradually decreases, along with a gradual reduction in the density of positive ions at the head.

Acknowledgements This work was supported by the Science and Technology Project of State Grid Corporation of China (No. 5500-202327118A-1-1-ZN).

References

1. Mariprasath T, Kirubakaran V (2016) A critical review on the characteristics of alternating liquid dielectrics and feasibility study on Pongamia Pinnata oil as liquid dielectrics. *Renew Sustain Energ Rev* 65:784–799

2. Shen Z, Wang F, Wang Z, Li J (2021) A critical review of plant-based insulating fluids for transformer: 30-year development. *Renew Sustain Energy Rev* 141:110783
3. Liu D, Liu Q, Wang Z (2021) Modelling of second mode positive streamer in cyclohexane by considering optimized electron saturation velocity. *J Phys D Appl Phys* 54(11):115502
4. Zhou J, Li J, He J, Wu G, Wang Q, Li Y, Li Y, Peng H (2018) Study on the propagation characteristic of streamer in long oil gap of natural ester. In: 2018 12th International conference on the properties and applications of dielectric materials (ICPADM)
5. Smalø H, Astrand P-O, Ingebrigtsen S (2010) Calculation of ionization potentials and electron affinities for molecules relevant for streamer initiation and propagation. *IEEE Trans Dielectr Electr Insul* 17(3):733–741
6. Hwang J-WG (2010) Elucidating the mechanisms behind pre-breakdown phenomena in transformer oil systems. Massachusetts Institute of Technology
7. Chen G, Li J, Huang Z, Wang F, Duan Y, Dan L (2020) Simulation of the effect of carrier density fluctuations on initial streamer branching in natural ester during pulsed positive discharges. *IEEE Trans Dielectr Electr Insul* 27(5):1604–1610
8. Das AK, Shill DC, Chatterjee S (2020) Potential of coconut oil as a dielectric liquid in distribution transformers. *IEEE Electr Insul Mag* 36(6):36–46
9. Zhang J, Hao J, Huang Z, Ye W, Xu Q, Liao R (2022) Influence mechanism of molecular structure on the difference of lightning impulse discharge between mineral oil and natural ester using Dft calculation. *IEEE Trans Dielectr Electr Insul*
10. Zheng H, Lv W, Li X, Feng Y, Yang E, Liu C, Wang Z (2022) Electrical properties of insulating liquids based on molecular properties calculated by density functional theory. *IEEE Trans Dielectr Electr Insul* 29(6):2274–2282
11. Xue Q, Timoshkin I, Wilson MP, Given M, MacGregor SJ (2021) Mobility of charge carriers in mineral oil and ester fluids. *High Volt* 6(6):1040–1050

Research on the Energized Ice-Melting for the Ground Wire Optical Cable of ± 800 kV Ultra-High Voltage Direct Current Transmission Line



Wei Li, Xinmin Li, Yanhua Han, Songbo Chen, Lu Zhang,
and Xiaoyue Chen

Abstract In recent years, icing on the ground wire of ultra-high voltage transmission lines has become a major problem threatening the safe and stable operation of transmission lines. In order to effectively solve the problem of ground wire icing on ultra-high voltage transmission lines, this paper proposes a ground wire ice-melting system for ± 800 kV ultra-high voltage DC transmission lines during live operation. Firstly, a twelve-pulse valve group and rectifier transformer are selected as the ice-melting device based on technical and economic considerations, and then the ground wire is insulated and transformed to form a ice-melting circuit with single-point grounding. The parameters such as ice-melting current, ice-melting capacity, and ice-melting time are calculated and verified. Secondly, the temperature rise test under ice-melting current is conducted in the laboratory environment to determine the temperature characteristics and safety of the cable, and finally the parameters of the ice-melting device are determined. The ice-melting system is constructed in a selected section of about 14.45 km on a certain ± 800 kV transmission line, and on-site verification of live ice-melting is conducted under rainy, snowy and icy weather. According to the measurement results of the on-site cable temperature monitoring device, the ice-melting system successfully achieved continuous and adjustable ice-melting current and accurate control of cable temperature rise, which is consistent with the calculated results and achieved the expected goals. The results of this paper can provide reference for the live ice-melting of ground wire/cable of ultra-high voltage DC transmission lines.

W. Li (✉) · X. Li · Y. Han

Power Research Institute of State Grid Shaanxi Electric Power Company Limited, Xi'an 710100, China

e-mail: 175526631@qq.com

S. Chen · L. Zhang

State Grid Shaanxi Electric Power Co., Ltd., Xi'an 710048, China

X. Chen

School of Electrical Engineering and Automation, Wuhan University, Wuhan 430072, China

© Beijing Paiké Culture Commu. Co., Ltd. 2024

X. Dong and L. Cai (eds.), *The Proceedings of 2023 4th International Symposium on Insulation and Discharge Computation for Power Equipment (IDCOMPU2023)*, Lecture Notes in Electrical Engineering 1100, https://doi.org/10.1007/978-981-99-7393-4_62

Keywords Ultra-high voltage direct current transmission lines · Energized grounding ice melting for ground wires · Optical cable · Temperature control · Current control

1 Introduction

Since the beginning of the last century, icing on overhead transmission lines has been one of the main threats to the safe operation of power grids [1, 2]. In recent years, with the global climate change and the increase in extreme weather disasters, the harm of icing on transmission lines has become increasingly severe [3].

Due to their higher altitude, higher wind speed at corresponding positions, and no current passing during normal operation, the ground wires (including optical cables, hereinafter referred to as “ground wires”) of transmission lines are more prone to icing than the conductors. Traditionally, the design value of icing thickness for ground wires is increased by 5 mm compared to that for conductors. However, in recent years, a series of ground wire failures caused by icing on UHV transmission lines have occurred continuously, indicating that the above method is not sufficient to solve the problem of icing on ground wires of UHV transmission lines. For ground wire de-icing, scholars at home and abroad have conducted related research. Bagi [4] studied the de-icing process of overhead ground wires through finite element thermal analysis and laboratory verification. Jiang et al. [5] determined that the de-icing time is closely related to the de-icing current, environmental temperature, wind speed, ice thickness, and type of OPGW, through simulation calculation and artificial climate chamber experiments.

Due to the irreversible damage caused by excessive temperature rise to the fiber optic core, it is necessary to strictly control the temperature rise of the fiber optic cable during ice melting. Additionally, fiber optic cables play an important role in lightning protection and communication, and interruption of fiber optic cables can have a significant negative impact on transmission lines, requiring higher reliability [6–8]. Therefore, it is more difficult to control the temperature rise of fiber optic cables during live ice melting of ultra-high voltage direct current ground wires, and there have been no successful experiences with live ice melting of ultra-high voltage direct current ground wires in China and abroad.

This paper conducts a study on the live ice melting system for ultra-high voltage direct current transmission lines based on the actual situation of a ± 800 kV ultra-high voltage transmission line in Shaanxi. The study covers ice melting scheme selection, ice melting circuit layout, ice melting current, voltage, capacity selection, and fiber optic cable temperature control. Based on the research results, the ice melting system construction was carried out on the ± 800 kV ultra-high voltage transmission line, and ice melting field testing and verification were conducted under icy weather conditions.

2 The Choice of Ice Melting Scheme

In terms of the main body of the DC ice melting device, a large amount of research has been conducted by scholars both domestically and abroad [9, 10]. Based on the previous experiences, this article selects the ice melting scheme. For the ice melting with live ground wire, the safety of the optical cable must be strictly controlled during the process, so it is necessary to control the temperature rise of the optical cable. According to the current research progress on DC ice melting devices, there are mainly four types of DC ice melting devices that can be maturely applied to power grid ice melting, which are as follows:

(1): 12-pulse valve group + rectifier transformer connection scheme; (2): 6-pulse valve group + rectifier transformer connection scheme; (3): Non-control rectifier transformer connection scheme; (4): Full-control rectification scheme.

Scheme (1) has good technical stability, little impact on the station system, mature and extensive engineering application experience, and lower total investment;

Scheme (2) cannot achieve continuous and adjustable ice melting current, and has a high harmonic content;

Scheme (3) has a lower cost, but the ice melting voltage and current cannot be continuously adjusted, and it has poor adaptability to ground wire ice melting, which is not conducive to accurately controlling the heating problem of the optical cable while melting the ice;

Scheme (4) has a high cost and insufficient technological maturity.

Based on the above analysis, this article will adopt scheme (1) (12-pulse + rectifier transformer) as the DC ice melting device scheme for this project, as shown in Fig. 1.

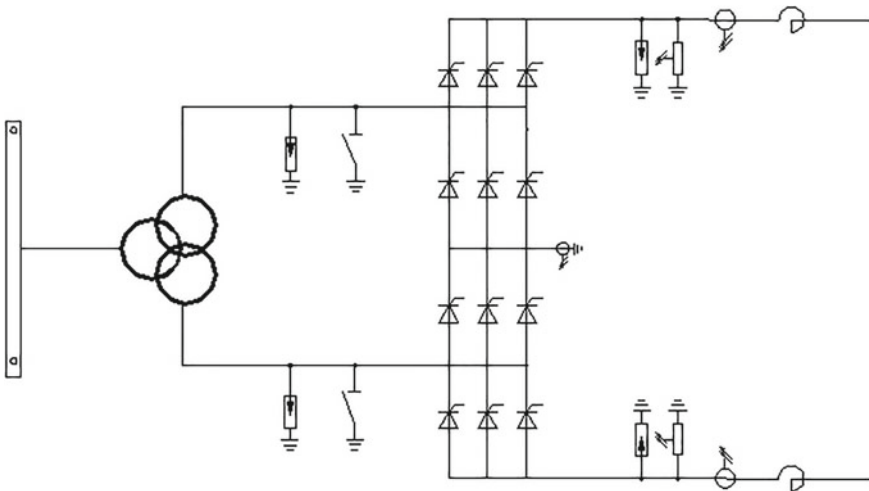


Fig. 1 Schematic diagram of ice-melting device

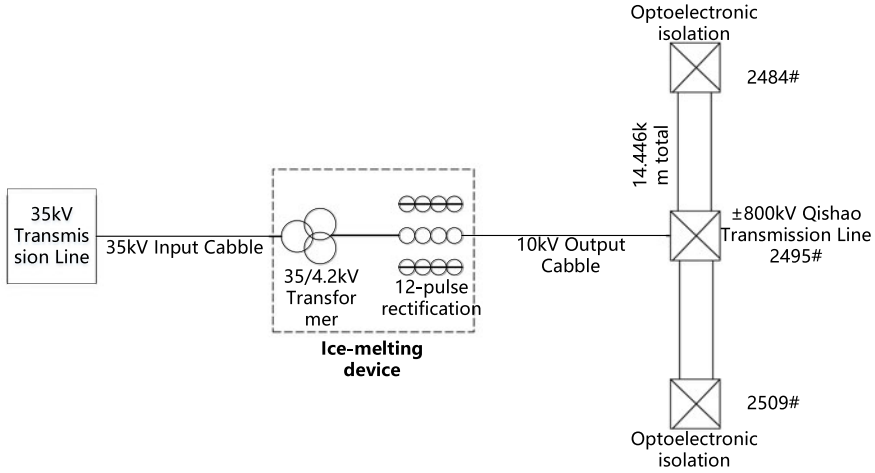


Fig. 2 schematic diagram of ice-melting circuit

3 Ice-Melting Circuit

In order to achieve ground wire icing under live conditions for ultra-high voltage transmission lines, the ground wire needs to be insulated. By installing gap-type insulators on the ± 800 kV transmission line, the ground wire/optical cable and tower are insulated within the section. By leading the ground wire/optical cable down to tower 2495, a icing loop is formed and connected to the DC icing device, realizing DC icing of the ground wire/optical cable within the section. Optical-electricity separation junction boxes are used at towers 2484 and 2509 to achieve metal isolation from the ground wire/optical cable and towers outside the icing section, and to ensure normal transmission of optical fiber signals, as shown in Fig. 2.

To ensure equipment safety and personal safety during icing, the induced voltage of the icing loop after insulation transformation was calculated, and the insulation coordination and protection of the icing device were set according to the calculation results. The icing loop was determined to be wired in a single-point grounded manner at the negative pole.

4 Calculation of Ice Melting Power and Parameters

A certain ± 800 kV transmission line (Shaansi segment), with a length of 14.446 km between towers #2484 and #2509, has a JLB20A-150-19 ground wire and an OPGW-24B1 (ULL)-155 optical cable. According to the temperature conversion formula:

$$R_{20} = R_t / (1 + \alpha(t - 20)) \tag{1}$$

Based on the temperature conversion formula, the DC resistance of the JLB20A-150-19 ground wire is calculated to be 0.539 Ω/km and the DC resistance of the OPGW-24B1(ULL)-155 cable is calculated to be 0.518 Ω/km at 0 °C, with a temperature coefficient α of 0.0036. Therefore, the capacity of the de-icing device should meet the de-icing requirements of the loop formed by the 14.446 km ground wire and OPGW connected end-to-end.

4.1 Minimum Ice-Melting Current

The actual de-icing current of the conductor should be selected between the minimum and maximum de-icing currents based on the de-icing time. If the de-icing current is less than the minimum de-icing current, de-icing will be ineffective, and if the de-icing current is greater than the maximum de-icing current, permanent deformation of the conductor may occur, resulting in increased sag or damage to the mechanical strength of the conductor.

To avoid permanent deformation of the conductor due to overheating, the maximum de-icing current is calculated based on the short-term allowable heating conditions and long-term allowable heating conditions [11]. The recommended environmental temperature for the calculation of the short-term allowable heating conditions is -5 °C, and the simultaneous wind speed is 5 m/s.

According to [12], the minimum de-icing current of the ground wire is:

$$I_{\min} = \sqrt{\left(\frac{\Delta t}{R_{T0} + R_{T1}}\right) / R_0} \tag{2}$$

$$R_{T0} = \frac{\lg(D/d)}{273\lambda_b} \tag{3}$$

For glazed frost:

$$R_{T1} = \frac{1}{0.09D + 0.22 + 0.73(VD)^{2/3}} \tag{4}$$

For hoarfrost:

$$R_{T1} = \frac{1}{0.04D + 0.84(VD)^{3/4}} \tag{5}$$

where:

I_{\min} —minimum ice melting current (A);

Δt —temperature difference between ground wire temperature and ambient temperature ($^{\circ}\text{C}$). When the ambient temperature for ice accretion is -5°C and the temperature for the ground wire not to freeze is 2°C , Δt is 7°C ;

R_{T0} —equivalent ice layer thermal resistance ($^{\circ}\text{C}\cdot\text{cm}/\text{W}$);

R_{T1} —convective and radiative equivalent thermal resistance ($^{\circ}\text{C}\cdot\text{cm}/\text{W}$);

D —outer diameter of the wire or ground wire after ice accretion (cm);

d —outer diameter of the wire or ground wire (cm);

λ_b —ice accretion thermal conductivity [$\text{W}/(^{\circ}\text{C}\cdot\text{cm})$], 0.0227 for glazed frost and 0.0012 for hoarfrost;

V —wind speed during ice melting (m/s), generally taken as 3–5 m/s.

Considering the inconsistency between the actual application of de-icing and the fault conditions on site, Table 1 provides the minimum de-icing currents for different environmental temperatures, wind speeds, and ground wire ice cover thicknesses, which can be used for selecting different operating conditions of the transmission line.

Based on Table 1, it can be observed that the required minimum ice-melting current increases with decreasing environmental temperature, increasing wind speed, and decreasing ice thickness. According to on-site measurements, in the event of a ground wire fault in a ± 800 kV transmission line, the ice covering is of the mixed type, between fog and glaze, and the ice thermal conductivity, convective and radiative equivalent thermal resistance are interpolated linearly. At the same time, it is assumed that the line environment temperature is -5°C (temperature range of -3 to -6°C during the fault), wind speed is 5 m/s (wind speed range of 3.4–5.4 m/s during the fault), and ice thickness is 21.5 mm (measured range of about 20–23 mm during the fault). Based on these values, the minimum ice-melting current is calculated to be approximately 215.10 A.

If the most severe ice type, glaze, is considered for calculation, with an environmental temperature of -5°C and a wind speed of 5 m/s, and assuming ice melting is initiated when the ice thickness exceeds 5 mm, the minimum ice-melting current required is 244.96 A.

4.2 Maximum Ice-Melting Current

According to [12], the maximum ice-melting current for non-full-covered-ice line is:

$$I_{\max} = \sqrt{(W_R + W_F - W_S)/R_m} \quad (6)$$

$$W_R = \pi D_1 E_1 S_1 [(t_m + 273)^4 - (t + 273)^4] \quad (7)$$

$$W_F = 0.57\pi\lambda_f(t_m - t)R_e^{0.485} \quad (8)$$

Table 1 Calculation result of minimum ice-melting current

Environment temperature: °C	Wind speed: m/s	Ice thickness: mm	Minimum ice-melting current: A
-5	5	20	216.16
-5		15	219.71
-5		10	222.90
-5		5	224.22
-10		20	283.01
-10		15	287.67
-10		10	291.84
-10		5	293.57
-15		20	336.85
-15		15	342.39
-15		10	347.36
-15		5	349.42
-5	10	20	234.45
-5		15	242.37
-5		10	252.11
-5		5	263.85
-10		20	306.97
-10		15	317.34
-10		10	330.09
-10		5	345.46
-15		20	365.36
-15		15	377.71
-15		10	392.89
-15		5	411.18
-5	15	20	243.39
-5		15	253.88
-5		10	267.84
-5		5	287.38
-10		20	318.67
-10		15	332.40
-10		10	350.68
-10		5	376.27
-15		20	379.30
-15		15	395.64
-15		10	417.40
-15		5	447.85

$$W_S = \alpha_S J_S D_1 \tag{9}$$

$$\lambda_f = 2.42 \times 10^{-2} + 3.5(t + t_m) \times 10^{-5} \tag{10}$$

$$R_e = \frac{V D_1}{1.32 \times 10^{-5} + 4.8(t + t_m) \times 10^{-8}} \tag{11}$$

where:

I_{max} —Maximum de-icing current (A).

W_R —Radiative heat dissipation power of the conductor or ground wire (W/m).

W_F —Convective heat dissipation power of the conductor or ground wire (W/m).

W_S —Solar radiation absorption power of the conductor or ground wire (W/m).

R_m —Resistance of the conductor or ground wire at allowable temperature (Ω/m).

E_1 —Surface radiative heat dissipation coefficient of the conductor or ground wire, typically taken as 0.9

S_1 —Stefan-Boltzmann constant, equal to 5.67×10^{-8} (W/m²).

D_1 —Outer diameter of the conductor or ground wire (m).

t_m —Allowable temperature of the conductor or ground wire ($^{\circ}C$).

t —Ambient temperature ($^{\circ}C$).

λ_f —Surface air heat transfer coefficient of the conductor or ground wire (W/(m $\cdot^{\circ}C$)).

α_S —Surface absorption coefficient of the conductor or ground wire, typically taken as 0.9

J_S —Sunlight intensity on the conductor or ground wire, usually taken as 900 W/m².

According to the above formula, the maximum de-icing current under different operating conditions can be obtained as shown in Table 2.

Table 2 Calculation result of maximum ice-melting current

Environment temperature: $^{\circ}C$	Wind speed: m/s	Maximum ice-melting current: A
-5	5	611.84
-5	10	718.67
-5	15	790.36
-10	5	629.90
-10	10	739.82
-10	15	813.59
-15	5	647.43
-15	10	760.37
-15	15	836.18

From Table 2, it can be seen that the lower the environmental temperature, the higher the wind speed, and the thinner the ice cover, the larger the allowable maximum de-icing current. Considering the on-site environmental temperature of $-5\text{ }^{\circ}\text{C}$ (when the actual temperature ranges from $-3\text{ }^{\circ}\text{C}$ to $-6\text{ }^{\circ}\text{C}$ during a fault) and wind speed of 5 m/s (corresponding to level 3 wind), the allowable maximum de-icing current is 611.84 A .

4.3 Ice-Melting Time

The ice-melting current should be selected to avoid too short or too long ice-melting time. If the ice-melting time is too short, it may cause the wire to jump off the ice abruptly. Excessive and unbalanced tension may damage the tower. If the ice-melting time is too long, it will result in a long power outage. Therefore, the ice-melting current should be reasonably selected in combination with the ice-melting time.

According to [12], the ice-melting time of the wire can be calculated by the following formula:

$$T_R = \left[10g_0db + \frac{0.045g_0D^2\Delta t}{R_{T0} + R_{T1}} \left(R_{T1} + \frac{0.22R_{T0}}{\ln(D/d)} \right) \right] / \left(I_R^2 R_0 - \frac{\Delta t}{R_{T0} + R_{T1}} \right) \tag{12}$$

where:

T_R is the ice-melting time (h); g_0 is the specific gravity of ice (g/cm^3), which is 0.9 for glazed frost and 0.3 for rime frost; b is the thickness of the ice (cm).

For the $\pm 800\text{ kV}$ transmission line, the relationship between ice-melting time and ice-melting current under 20 mm ice thickness is shown in Table 3.

When selecting the ice-melting current, one should avoid a too short or too long ice-melting speed. The ice-melting time of the ground wire is considered to be no

Table 3 Calculation result of ice-melting time

Ice-melting current: A	Environment temperature: $^{\circ}\text{C}$	Wind speed: m/s	Ice-melting time: h
216.16	-5	5	>10,000
295.76	-5	5	1
358.09	-5	5	0.5
353.313	-10	5	1
411.78	-10	5	0.5
313.17	-5	10	1
375.75	-5	10	0.5
370.59	-10	10	1
424.79	-10	10	0.5

more than 1 h. When the environmental temperature is $-5\text{ }^{\circ}\text{C}$ and the wind speed is 5 m/s, and the mixed-type ice-covering is measured on site for the $\pm 800\text{ kV}$ transmission line, the ice-melting current required for 1 h of ice-melting is about 296 A.

Considering the most severe glaze-type ice-covering, the ice-melting current required for 1 h of ice-melting under 20 mm ice-covering thickness is about 353 A; if ice-melting is initiated from a 5 mm ice-covering thickness, the ice-melting current required for 1 h of ice-melting is about 261 A.

4.4 Ice-Melting Voltage and Capacity

Ice-melting voltage and capacity are calculated by the following formulas:

$$U_R = I_R RL \quad (13)$$

$$P = U_R I_R \quad (14)$$

where:

U_R —ice-melting voltage (kV).

I_R —ice-melting current (A).

RL —resistance per unit length of the ground wire/optical cable in the ice-melting circuit (Ω/km).

L —length of the ice-melting circuit (km).

P —ice-melting power (kW).

The ice-melting voltage should be greater than the voltage drop generated by the ice-melting current in the ice-melting circuit.

Based on the parameters of the ground wire, considering the $\pm 800\text{ kV}$ transmission line (Shaanxi section) #2484–#2509 with a length of 14.446 km and the ground wire model JLB20A-150-19 with a DC resistance of $0.5807\ \Omega/\text{km}$, and the OPGW-24B1(ULL)-155 optical cable model with a DC resistance of $0.5580\ \Omega/\text{km}$, the circuit DC resistance is calculated to be $16.45\ \Omega$. Considering an output of no more than the maximum ice-melting current of 611 A, the ice-melting voltage is 10.05 kV and the required capacity for ice-melting is 6.14 MW.

5 Laboratory Validation of Temperature Control for Optical Cable Ice-Melting

The working temperature range of optical cable is $-40\text{ }^{\circ}\text{C}$ to $+60\text{ }^{\circ}\text{C}$. In order to ensure the safe and stable operation of the communication system, a temperature monitoring device was added during the insulation improvement, which can realize

real-time monitoring of the operating temperature of the optical cable. In addition, a planned unmanned aerial vehicle (UAV) infrared temperature measurement patrol route was set up in the ice-melting section to ensure that the operating temperature of the optical cable during ice-melting does not exceed 40 °C.

To verify the feasibility of DC ice-melting, initial experiments were carried out on ±800 kV transmission lines with an initial OPGW ice thickness of 10 mm. As shown in Fig. 3, when a DC current of 250 A was applied, the OPGW temperature increased significantly. The internal fiber temperature gradually became higher than the surface temperature of the OPGW, and the maximum temperature difference was about 13 °C when the ice was basically melted after 20 min of current flow, as shown in Fig. 3.

Through the OPGW current–temperature characteristic test on the ±800 kV line, the test results show that there is a significant temperature rise on the surface and inside of the OPGW under the recommended ice melting current. As the surface temperature of the OPGW reaches about 20 °C, the ice cover gradually melts, and the highest temperature of the internal optical fiber is about 35 °C, which is far lower than the OPGW’s allowable operating temperature limit (65 °C). The test results show that the OPGW can be melted using the DC ice melting method.

According to the above line parameters and the rated parameters of the ice melting device, the maximum parameters required for the grounding wire/optical cable ice melting operation of the ±800 kV transmission line are calculated in Table 4.

The ice melting current is calculated based on an environmental temperature of – 5 °C and a wind speed of 5 m/s, with a margin for error. As this plan uses a 12-pulse rectifier, the harmonic current is mainly the 11th and 13th, with a relatively small

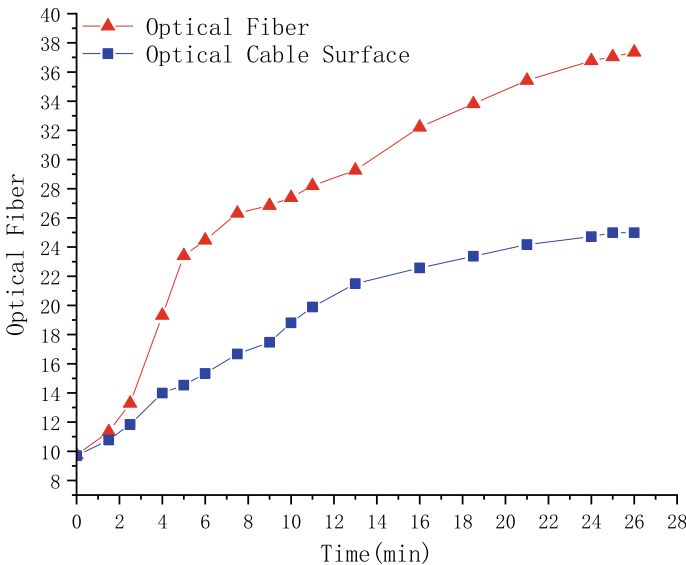


Fig. 3 Temperature rise characteristic of OPGW under ice-covered condition

Table 4 Parameters for ground wires/optical cables ice melting operation of ± 800 kV transmission lines

Voltage level	Line style	Length (km)	Ice-melting current: A	DC output voltage: kV	DC ice-melting capacity: MW
± 800 kV	JLB20A-150-19	14.446	611	10.05	6.14
	OPGW-24B1(ULL)-155	14.446			

proportion of harmonic current, and the ice melting process is short, resulting in a minimal impact on the power quality of the grid, thus no filter equipment is required.

6 Field Validation of Ice-Melting

Based on the research results mentioned earlier, we developed a live-line grounding ice melting device for UHVDC transmission lines and installed temperature sensors on the optical cable to ensure safe operation during ice melting. During rainy, snowy, and icy weather, we conducted on-site verification of the ice melting device during normal operation of the UHVDC transmission line.

The first ice melting operation was initiated at 12:35, and the DC ice melting current rose to 252 A at 12:40 and stopped after 30 min. The second ice melting operation was initiated at 16:36, and the DC ice melting current rose to 260 A and stopped after 75 min. The temperature test results of the optical cable during this period are shown in Fig. 4.

Based on the field verification, the ice melting system can achieve the melting of overhead ground wires and optical cables without affecting the normal operation of the UHVDC transmission line, and the characteristics of ice melting current and temperature rise are consistent with the analysis in the previous sections.

Moreover, this system synchronously measures the temperature rise status of each point in the ice melting circuit through multiple installed optical fiber temperature sensors and feeds back to the control end. The precise control of ice melting temperature is realized through the continuous adjustable output current at the control end, ensuring that the temperature of the optical fiber does not exceed the safety value during the entire ice melting process and ensuring the safe operation of the UHV transmission line. The temperature monitoring situation during one ice melting process is shown in Fig. 5.

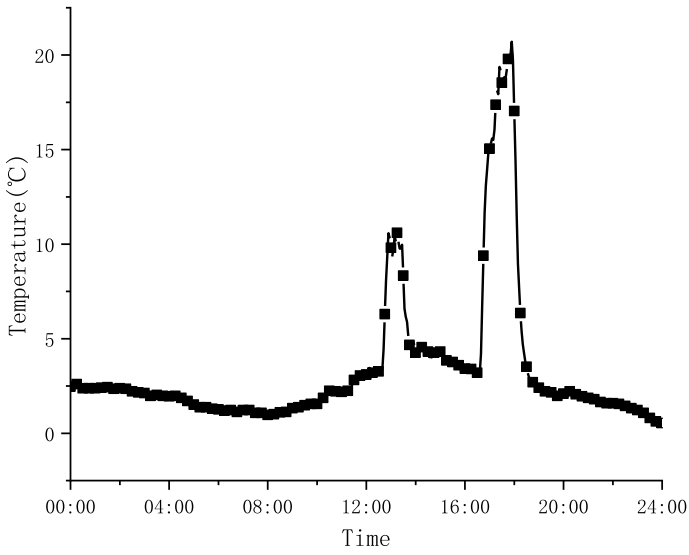


Fig. 4 On-site verification temperature for the optical cable

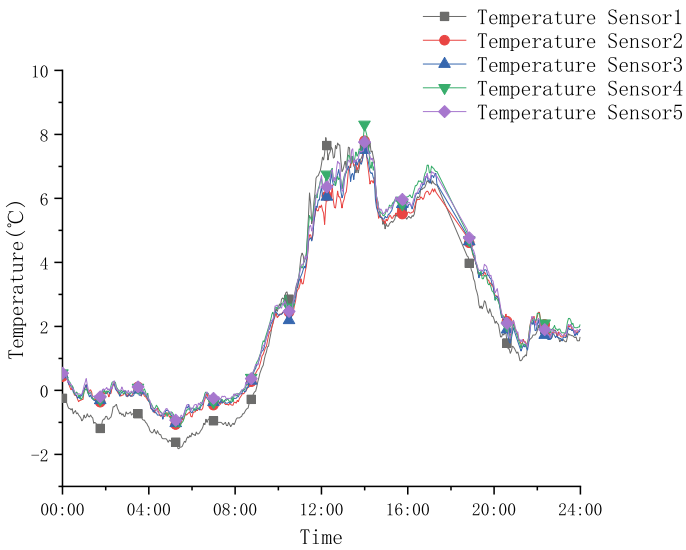


Fig. 5 Multi-point synchronized monitoring of optical fiber temperature

7 Conclusion

This paper presents a solution for on-line de-icing of both overhead ground wires and optical cables on a ± 800 kV transmission line in Shaanxi Province, China. The solution is based on a comprehensive approach that includes the de-icing system design, de-icing loop layout, verification of de-icing current, voltage and capacity calculations, as well as laboratory testing of de-icing temperature. Building on previous research, we developed and field-tested a de-icing system for live operation of overhead ground wires and optical cables on a high voltage DC transmission line, and conducted on-site verification and real-time temperature monitoring in rainy, snowy, and icy weather conditions. The field test results demonstrate that the system can de-ice the ground wires and optical cables during live operation of the transmission line, and that the output current can be continuously adjusted to ensure that the cable temperature remains within a safe range. The experimental results are consistent with the theoretical calculations and simulations. Our research provides a feasible approach and successful case study for on-line de-icing of both ground wires and optical cables on high-voltage DC transmission lines, which can serve as a reference for future work in this area.

Acknowledgements Sincerely gratitude for the project supported by State Grid Corporation of China Scientific and Technological Project “Research on Key Technologies of On-Site Rapid Detection and Performance Improvement of New Grounding Materials” (5500-202232127A-1-1-ZN).

References

1. Yang G, Jiang X, Liao Y, Hu J, Zhang Z (2023) Dynamic simulation study on single conductor torsion-induced icing of transmission lines. Proc CSEE: 1–11[2023–03–30]. <https://doi.org/10.19595/j.cnki.1000-6753.tces.230244>. (In Chinese)
2. Wu H, Han X, Jiang X, Guo S (2023) Analysis of anti-icing properties of expanded-diameter conductor based on droplet impingement freezing efficiency. Proc CSEE, 1–9 [2023–03–30]. <https://doi.org/10.19595/j.cnki.1000-6753.tces.220350> (In Chinese)
3. Zhao Q, Liu Z, Yu P, Chen L, Guan F (2022) Review of transmission line icing and anti-icing technologies. In: Lecture notes in electrical engineering, vol 890. Springer, Singapore. https://doi.org/10.1007/978-981-19-1870-4_129
4. Bagi T (2020) Analytical and experimental investigation of ice melting in power line ground wires. Periodica Polytechn Mech Eng
5. Jiang X, Meng Z, Zhang Z, Hu J, Lei Y (2016) DC ice-melting and temperature variation of optical fibre for ice-covered overhead ground wire. IET Gener Trans Distrib 10(2)
6. Xu F, Li D, Gao P, Zang W, Duan Z, Ou J (2023) Numerical simulation of two-dimensional transmission line icing and analysis of factors that influence icing. J Fluids Struct 118
7. Shang H, Huang Z (2019) OPGW cable icing status monitoring based on BOTDR. AIP Conf Proc 2073(1)
8. Wang M, Wang L, Wu Y, Wang Z, Fang H, Dong J (2022) Analysis and research on icing of OPGW optical cable. In: 2022 International conference on bigdata blockchain and economy management (ICBBEM 2022)

9. Chen L, Li C, Zhou Q, Wang C (2022) A new rectifier bridge series-parallel switching DC ice-melting device. *Electr Power Eng Technol* 41(06):230–238
10. Liao Y, Yang Y, Zhang H, Cheng S (2021) Parameter calculation and harmonic suppression study of 500kV HVDC ice-melting device. *Electr Eng* 03:130–132. <https://doi.org/10.19768/j.cnki.dgjs.2021.03.043>. (In Chinese)
11. GB 50545-2010, Design code for overhead transmission lines of 110 kV–750 kV (In Chinese)
12. DL/T 5511-2016, Technical specification for design of DC ice-melting system (In Chinese)

Analysis of Reactive Oxygen/Nitrogen Species in Cold Atmospheric Plasma Activated Water



Fan Bai and Yumin Xia

Abstract Cold atmospheric plasma (CAP) is generated by excitation of plasma sources with different structures at atmospheric pressure. It has good tolerance to tissues and cells, has shown great benefit and potential in promoting wound healing, resisting bacterial and fungal infections, inducing cell proliferation or apoptosis, and inducing stem cell differentiation. At the micro level, CAP is a non-bound system comprising various free radicals, charged particles, ultraviolet radiation, and excited particles, which is characterized by high safety and strong ionic activity. Free radicals such as reactive oxygen species and reactive nitrogen are the main effector molecules of CAP. In this study, CAP was used to treat deionized water to obtain plasma activated water. The concentrations of several key active oxygen and nitrogen ions in activated water were measured, as well as the variation of ion concentration with the treatment time of the device. The research results can provide valuable references for the research and application of plasma medicine in vivo and in vitro.

Keywords Cold atmospheric plasma · Reactive oxygen species · Reactive nitrogen species

1 Introduction

Plasma is produced by the disintegration of polyatomic gas molecules or by the removal of electrons from the shell of a monatomic gas. It contains molecules, atoms, positive and negative particles, electrons, and ultraviolet light. It is the fourth form of matter different from solids, liquids and gases [1]. Plasma medicine is an emerging biomedical technique and an innovative field combining plasma physics

F. Bai · Y. Xia (✉)

Department of Dermatology, The Second Affiliated Hospital of Xi'an Jiaotong University, Xi'an 710004, China

e-mail: xiayumin1202@163.com

F. Bai

e-mail: baidoudou0523@stu.xjtu.edu.cn

© Beijing Paike Culture Commu. Co., Ltd. 2024

X. Dong and L. Cai (eds.), *The Proceedings of 2023 4th International Symposium on Insulation and Discharge Computation for Power Equipment (IDCOMPU2023)*, Lecture Notes in Electrical Engineering 1100, https://doi.org/10.1007/978-981-99-7393-4_63

and medicine [2]. It has made landmark progress in wound healing, cancer treatment, and skin disease treatment since the 1990s [3–7]. At present, the plasma widely used in medical treatment is called cold atmospheric plasma (CAP) that is under atmospheric pressure, with a normal atmospheric temperature and can be tolerated by human tissues [8].

Studies have shown that the reactive oxygen species (ROS), reactive nitrogen species (RNS) and their derivatives, including ozone (O_3), atomic oxygen (O), superoxide (O_2^-), singlet (1O_2), hydrogen peroxide (H_2O_2), hydroxyl radicals ($\bullet OH$), nitric oxide (NO), nitrogen dioxide (NO_2), nitrate radical (NO_3), and peroxyxynitrite anion ($ONOO^-$) produced by CAP are the main effector molecules for its therapeutic effects [9]. Appropriate levels of free radicals and non-free radicals play an important role in the regulation of biological functions of mammalian cells such as intracellular homeostasis, signal transduction, immunity and metabolism [10]. 1O_2 is a highly reactive molecule that can regulate the process of cell apoptosis and produce cytotoxic molecules. It inactivates certain membrane-associated catalase molecules on some tumor cells. Thus, continuously producing H_2O_2 and peroxyxynitrite [11]. $\bullet OH$, due to its extremely strong oxidizing activity that can destroy cell proteins and membranes, promote lipid peroxidation, and ultimately lead to cell death. H_2O_2 is a long-lived oxidation–reduction substance and a second messenger of signal pathways that can maintain microbial activity and directly cause microbial death. As a member of the RNS, NO is responsible for mediating intracellular signal transduction [12]. However, CAP induced intracellular NO overload can cause apoptosis of A375 and A875 melanoma cells [13] and cytotoxicity test shows that a mixture of H_2O_2 and NO_2^- triggered more cell death than H_2O_2 alone, adding NO_3^- to the H_2O_2/NO_2^- mixture did not change the percentage of live cell activity, which indicated that NO_3^- —has no effect on cell death [14].

Therefore, in this article, we use a CAP device designed and manufactured by the “Plasma Biomedical Research Center of Xi’an Jiaotong University” to generate gaseous and liquid phase active particles. By detecting the content and changes of several key long-lived particles and short-lived particles, we hope to provide a reference basis for medical experiments of plasma in vivo and in vitro.

2 Materials and Methods

2.1 CAP and CAP-Activated Deionized Water

The CAP device used in this study consists of a high-voltage power supply, an oscilloscope, a high-voltage probe, a helium gas cylinder, a flow controller, and a quartz tube; Set the average voltage of the CAP to 8 kV and the average excitation frequency to 9 kHz. Use a high-voltage probe and a digital storage oscilloscope to monitor the physical parameters of the CAP. Use helium gas with a concentration of 99.999% as the working gas and a flow rate of 5 slm.

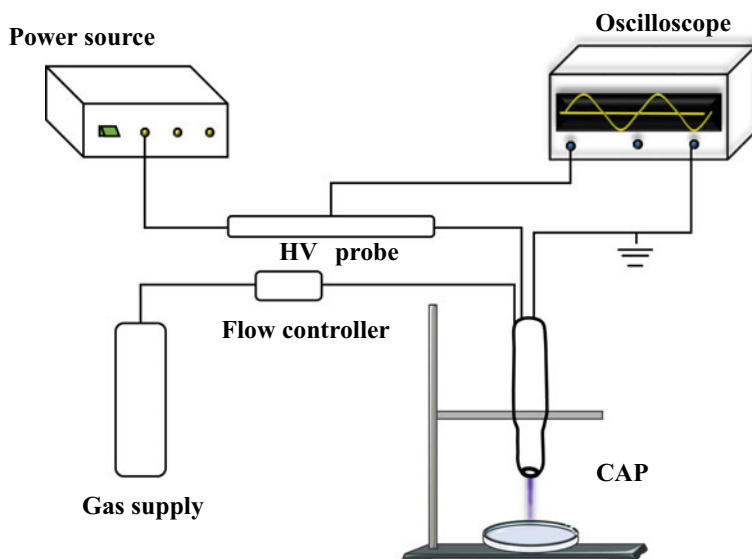


Fig. 1 CAP and CAP-activated deionized water

Start the CAP device in the UV sterilized biosafety cabinet. Place a 6 cm diameter culture dish containing 5 mL of deionized water under the CAP generator, with the probe located approximately 10–15 mm away from the liquid level. After treating deionized water with CAP jet for 5 min, collect the deionized water and store it in a centrifuge tube for later use. The schematic diagram of the cold atmospheric plasma device is shown in Fig. 1.

2.2 $\bullet\text{OH}$, and ONOO- Assays

This study uses an ESR instrument to detect the concentration of short-lived particles in CAP activated water. This is a quantitative method for detecting unpaired electrons, which is based on the spin characteristics of electrons. Electron will spin along its own central axis. In the presence of an external magnetic field, the electron spin energy level will split. At this time, adding a specific electromagnetic wave in the direction perpendicular to the magnetic field, the electromagnetic wave energy is absorbed by the electrons of the low spin energy level and transits to high energy to produce electron paramagnetic resonance phenomenon. The absorbed electromagnetic wave will be expressed in the form of spectral lines. Different free radicals will form different patterns of spectral lines, thus achieving the detection of different free radicals. ESR detection requires that the tested object must be stable, and the active particles we need to measure are all unstable. These active particles have a short lifespan and cannot be detected by ESR. The emergence of spin trapping agents has solved

this problem. Spin trapping agents can combine with short-lived active particles to form relatively stable complexes for detection using ESR. DMPO(5,5-dimethyl-1-pyrroline-N-oxide) captures hydroxyl radical and generates stable DMPO[•]-OH. TEMPONE-H (1-hydroxy-2,2,6,6-Tetra methyl-4-oxo-piperidine) is used to capture superoxide to generate stable TEMPONE[•].

Use TEMPO as a standard to establish a standard curve, use CAP device to treat deionized water, add an appropriate amount of TEMPONE-H and DMPO to the deionized water, and immediately detect it with an ESR instrument. Generally, the instrument displays that the TEMPONE-H curve will have three characteristic peaks, with a ratio of 1:1:1, while DMPO displays four peaks of 1:2:2:1. Finally, use SpinFit software to fit and double integrate the curve; The obtained value is positively correlated with the concentration of short-lived particles in the sample.

2.3 *H₂O₂ and NO Assays*

After CAP treatment of deionized water, the concentration of H₂O₂ was measured using a commercial H₂O₂ assay kit (Beyotime Biotechnology, Shanghai, China). The violet color of the product in the solution was measured at 560 nm. The concentration of NO was inferred from nitrite and nitrate measured at 540 nm absorbance using a commercial Griess detection kit (Beyotime Biotechnology).

3 Results

3.1 *Short-Lived Particles of Reactive Oxygen/Nitrogen Species in CAP Activated Water*

As shown in Fig. 2 5 min after the CAP device processes deionized water, three characteristic peaks appear on the ESR curve of ONOO⁻, with a peak ratio of 1:1:1, indicating an increase in the content of ONOO⁻ in the activated water treated by the CAP device. Compared to the concentration gradient of the standard curve, the content of ONOO⁻ is about 53 μmol.

As shown in Fig. 3, after 5 min of treatment of deionized water by the CAP device, there is no significant characteristic change in the ESR curve of •OH, indicating that the content of •OH in the activated water treated by the CAP device is not detected.

Fig. 2 ESR curve of ONOO⁻ in CAP-activated deionized water

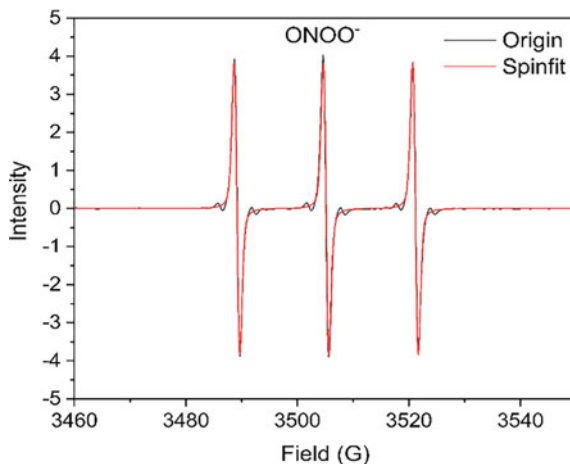
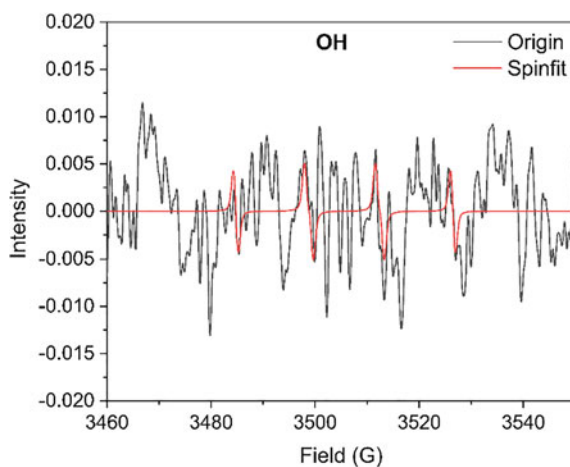


Fig. 3 ESR curve of •OH in CAP-activated deionized water



3.2 Long-Lived Particles of Reactive Oxygen/Nitrogen Species in CAP Activated Water

The concentration of H₂O₂ in activated water was detected to be approximately 58 μmol immediately after CAP treatment for deionization, and remained at a high level within 1 h. After 1 h, the concentration gradually decreased over time, dropping to approximately 38 μmol after 12 h. However, after 48 h, the concentration instead increased to approximately 50 μmol. The results are shown in Fig. 4.

Fig. 4 Concentration changes of H_2O_2 in CAP-activated deionized water

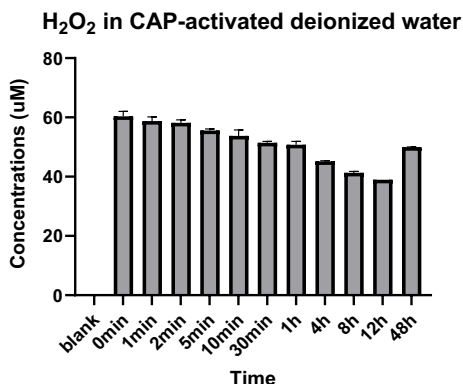
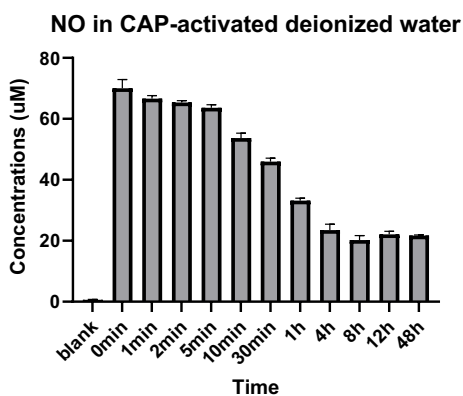


Fig. 5 Concentration changes of NO in CAP-activated deionized water



The concentration of NO in activated water was detected to be approximately $70\mu\text{mol}$ immediately after CAP treatment for deionization. Within 1 h, the concentration rapidly drops to half of the original concentration, about $33\mu\text{mol}$. Subsequently, the concentration gradually decreased over time, reaching approximately $21\mu\text{mol}$ after 48 h. The results are shown in Fig. 5.

4 Conclusion

Immediately after CAP treatment of deionized water for 5 min, the concentration of ONOO- was up to $53\mu\text{mol}$, while $\bullet\text{OH}$ was not detected. Among long-lived particles, the concentration of H_2O_2 can still maintain a high level within 1 h, decreasing by 30% within 12 h, while increasing in a reverse trend within 48 h. As a long-lived particle, the concentration of NO decreases rapidly, decreasing by about 50% within 1 h and dropping to 30% of the original concentration within 48 h.

References

1. Laroussi M, Bekeschus S, Bogaerts A et al (2022) Low temperature plasma for biology, hygiene, and medicine: perspective and roadmap. *IEEE T Radiat Plasma* 6(2):127–157
2. Braný D, Dvorská D, Halašová E et al (2020) Cold atmospheric plasma: a powerful tool for modern medicine. *Int J Mol Sci* 21(8):2932
3. Ulrich C, Kluschke F, Patzelt A et al (2015) Clinical use of cold atmospheric pressure argon plasma in chronic leg ulcers: a pilot study. *J Wound Care* 24(5):196, 198–200, 202–203
4. Stratmann B, Costea TC, Nolte C et al (2020) Effect of cold atmospheric plasma therapy vs standard therapy placebo on wound healing in patients with diabetic foot ulcers: a randomized clinical trial. *JAMA Netw Open* 3(7):e2010411
5. Limanowski R, Yan D, Li L et al (2022) Preclinical cold atmospheric plasma cancer treatment. *Cancers (Basel)* 14(14):3461
6. Zhai S, Xu M, Li Q et al (2021) Successful treatment of vitiligo with cold atmospheric plasma-activated hydrogel. *J Invest Dermatol* 141(11):2710–2719
7. Kim YJ, Lim DJ, Lee MY et al (2021) Prospective, comparative clinical pilot study of cold atmospheric plasma device in the treatment of atopic dermatitis. *Sci Rep* 11(1):14461
8. Vijayarangan V, Delalande A, Dozias S et al (2018) Cold atmospheric plasma parameters investigation for efficient drug delivery in HeLa cells. *IEEE T Radiat Plasma* 2(2):109–115
9. Graves DB (2012) The emerging role of reactive oxygen and nitrogen species in redox biology and some implications for plasma applications to medicine and biology. *J Phys D Appl Phys* 45(26):263001
10. Gao P, Pan W, Li N et al (2019) Fluorescent probes for organelle-targeted bioactive species imaging. *Chem Sci* 10:6035–6071
11. Motaln H, Recek N, Rogelj B (2021) Intracellular responses triggered by cold atmospheric plasma and plasma-activated media in cancer cells. *Molecules* 26(5):1336
12. Zhai S, Kong MG, Xia Y (2022) Cold atmospheric plasma ameliorates skin diseases involving reactive oxygen/nitrogen species-mediated functions. *Front Immunol* 13:868386
13. Xia J, Zeng W, Xia Y et al (2019) Cold atmospheric plasma induces apoptosis of melanoma cells via Sestrin2-mediated nitric oxide synthase signaling. *J Biophotonics* 12(1):e201800046
14. Girard PM, Arbabian A, Fleury M et al (2016) Synergistic effect of H₂O₂ and NO₂ in cell death induced by cold atmospheric He plasma. *Sci Rep* 1:29098

Study on Transient Electric Field Distribution of 40.5 kV Switchgear Vacuum Circuit Breaker Cut-Off Reactor



Wang Huaqing , Huang Daochun, Shuang Mingjing, Bi Jiyu, Li Huipeng, and Qiu Yiqun

Abstract The high frequency electromagnetic wave generated by the interruption of the circuit breaker of the high voltage switchgear may interfere with the performance of the intelligent sensor and even cause damage, endangering the safe and reliable operation of the switchgear. Taking KYN61-40.5 high voltage switchgear as an example, the 3D finite element simulation model of high voltage switchgear was established and its accuracy was verified through the test. Taking cutting off reactor overvoltage in 35 kV system as the example, the distribution of high frequency electric field in typical system of high voltage switchgear is studied. The simulation results show that the maximum internal electric field intensity can reach 2.46 kV/mm during the interruption process. The maximum electric field intensity is located at the top of the breaker truck, the top of the breaker room partition, and near the partition of the bus room and cable room. The research results can provide a reference for the installation of intelligent sensors in switchgear and its electromagnetic compatibility designs.

Keywords High voltage switchgear · Electromagnetic compatibility · High frequency electromagnetic field · Finite element simulation · Vacuum circuit breaker

1 Introduction

High voltage switchgear is one of the important distribution equipment in the power system, playing a crucial role in power transmission and distribution [1]. With the continuous construction of new power systems, the level of intelligence and digitization of grid equipment is also constantly improving. Intelligent sensors such as partial discharge sensors and wireless temperature sensors have been initially applied in high voltage switchgear [2–4]. However, in operating scenarios such as intelligent

W. Huaqing (✉) · H. Daochun · S. Mingjing · B. Jiyu · L. Huipeng · Q. Yiqun
School of Electrical Engineering and Automation, Wuhan University, Wuhan, China
e-mail: 237522104@qq.com

© Beijing Paiké Culture Commu. Co., Ltd. 2024
X. Dong and L. Cai (eds.), *The Proceedings of 2023 4th International Symposium on Insulation and Discharge Computation for Power Equipment (IDCOMPU2023)*, Lecture Notes in Electrical Engineering 1100, https://doi.org/10.1007/978-981-99-7393-4_64

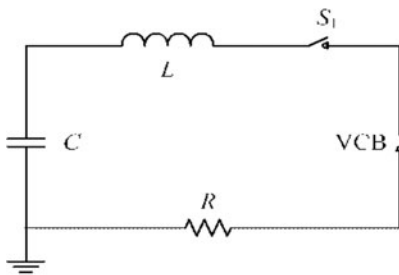
distribution networks and offshore wind farms, due to the random fluctuations in new energy output and user loads, the power grid is frequently subjected to electromagnetic transient shocks. To protect critical equipment, the circuit breakers of high-voltage switchgear need to frequently operate. When a vacuum circuit breaker in the high-voltage switchgear is opened, the high-frequency currents and voltages generated during the restrike arc and current interruption process will radiate electromagnetic waves outward through the busbar. The high-frequency electromagnetic field generated by the opening of the circuit breaker in the switchgear will interfere with the operation of the intelligent sensors in the switchgear, affecting their performance or even causing damage [5]. Therefore, it is necessary to study the distribution of the high-frequency electromagnetic field generated by the circuit breaker in the high-voltage switchgear under typical operating conditions, to select suitable positions for installing intelligent sensors in the switchgear, or to take corresponding protective measures for the intelligent sensors to reduce the electromagnetic interference.

Currently, both domestic and foreign research has been carried out on the measurement and calculation of the transient electromagnetic field inside the high-voltage switchgear and the operation of the circuit breaker. The analysis mainly focuses on the distribution of the electric field on the surface of the insulating material inside the high-voltage switchgear. Reference [6] established a three-dimensional transient electric field finite element simulation model of the switchgear cable chamber and obtained the characteristics of the electric field distribution and concentration area of the switchgear cable chamber under the nominal voltage of 10 kV. Reference [7] established a simulation model of local discharge in the switchgear and analyzed the pulse characteristics of internal discharge and external interference. Reference [8] measured the high-frequency arc discharge faults inside the switchgear using D-Dot sensors and extracted the dominant frequency of 10 MHz through Fourier analysis. Reference [9] established a three-dimensional model of a 12 kV switchgear and simulated the transient electromagnetic field during its operation, concluding that the electric field is mainly concentrated at the top of the surge arrester and the center of the through-wall bushing in the cable chamber. Existing research results show that there is a complex distribution of strong electromagnetic fields inside the switchgear, but the main research objects are the recognition of partial discharge signals inside the switchgear and the impact on insulating materials, and there is little research on the impact of high-frequency electromagnetic fields on internal smart sensors.

This paper addresses the issue of electromagnetic interference caused by high-frequency electromagnetic fields generated by the operation of high-voltage switchgear circuit breakers on intelligent sensors. A three-dimensional finite element simulation model of the KYN61-40.5 type switchgear was established, and a measured electromagnetic disturbance waveform was imported for simulation. The accuracy of the simulation model was verified by comparing it with experimental results. Then, the high-frequency electric field inside the switchgear under the over-voltage condition of the circuit breaker operating in the capacitive current mode was solved, and installation location suggestions for intelligent sensors were proposed.

2 Transient Electric Field Measurement Test of Vacuum Circuit Breaker Interruption

In this paper, the circuit of the vacuum circuit breaker interruption test is established, as shown in Fig. 1a. In Fig. 1a, C is the equivalent capacitance of the current source, L is the inductance of the current source, R is the total resistance of the loop, VCB is the vacuum circuit breaker, the model is ZN85-40.5, the rated voltage is 40.5 kV, the rated current is 1250A, the rated short-circuit breaking current is 31.5kA, and S_1 is the auxiliary closing switch. Tektronix DPO4054 digital oscilloscope was used for measurement, with a bandwidth of 500 MHz and a sampling rate of 5G/s. The electric field was measured by the EM5030 near-field probe of ZhiYong Electronics. Only the electric field in the vertical direction of the probe was measured during measurement. The measuring devices are powered by isolation transformers and placed in galvanized cast iron shielding boxes. The experiment was a single-phase circuit breaker interruption test for phase B, and the typical circuit breaker interference electric field obtained from the measurement is shown in Fig. 1d.



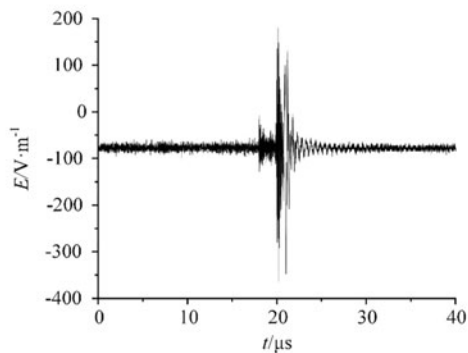
(a) Simplified circuit diagram



(b) Physical arrangement



(c) Electric field probe arrangement



(d) Typical high-frequency electric field waveform

Fig. 1 Schematic diagram of high frequency electric field measurement test for vacuum breaker interruption

Fourier transform was used to analyze the electromagnetic disturbance waveform. The maximum voltage at both ends of the circuit breaker was 649.84 V, and the maximum disturbance current induced by the Roche coil was 780 A. The dominant frequency of disturbance voltage is mainly distributed in the vicinity of 310 kHz, and the frequency of disturbance current on the Roche coil is 4.5 MHz, and some frequency components of 310 kHz and 8 MHz or above are included. The dominant frequency of the disturbance electric field is about 310 kHz, which is consistent with the frequency of the disturbance voltage at both ends of the circuit breaker. However, the dominant frequency will change near the cabinet and many 3.6 MHz or 11.6 MHz components will appear.

3 3D Finite Element Simulation Model of High Voltage Switchgear

3.1 High Voltage Switchgear Model and Simulation Parameter Setting

Because there are many internal components in the high voltage switch cabinet, the simulation model needs to be simplified [10]. The overall structure of the switch cabinet, the structure of the internal compartment, whose model size has a great influence on the distribution of electromagnetic field are precisely modeled. Other components are omitted or modeled using simple geometric.

Based on the above model establishment and simplification principles, the 3D simulation model of high voltage switchgear is shown in Fig. 2, and its material parameters are set in Table 1.

The excitation port is set between the movable and static contacts of the vacuum circuit breaker, and its size is consistent with the maximum opening distance of the vacuum circuit breaker, which is 22 mm. The surface of the metal conductor is assumed to have a finite conducting boundary, with its conductivity and relative permeability parameters consistent with the material parameters. An ideal matching layer is used as a model to absorb the boundary conditions (Perfectly Matched Layer, PML). The measured voltage and current waveforms of the circuit breaker on the primary side are used as the excitation waveform of the dipole antenna, and the high-frequency electric field inside the switchgear is calculated accordingly.

3.2 Comparison of Simulation Results and Test Results

The simulation and test results are shown in Table 2. As can be seen from Table 2, the maximum error between simulation results and test results is 7.15%, which proves the effectiveness of this method for simulation of high-frequency electric field intensity.

Fig. 2 High voltage switchgear 3D model

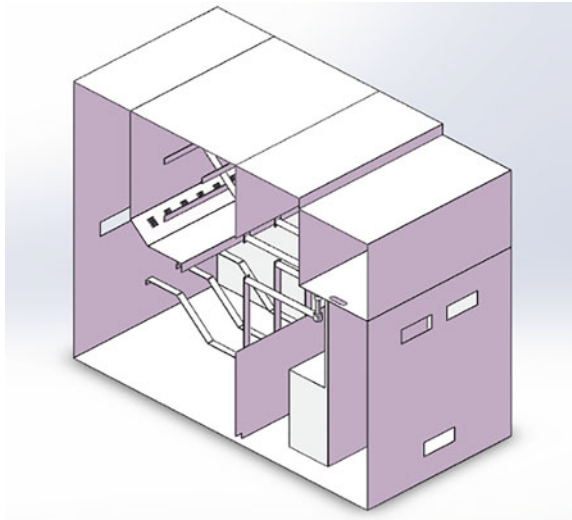


Table 1 High frequency electromagnetic field simulation material parameters of high voltage switchgear

Structural material	Relative dielectric constant	Relative permeability	Conductivity
Air	1.00	1.00	0
Bus	1	0.999991	5.8×10^7 S/m
Cabinet body	1	1	1.1×10^6 S/m

Table 2 Comparison of high frequency electromagnetic field simulation and test results of high voltage switchgear

Electric field measurement position	Test result (V/m)	Simulation result (V/m)	Relative error (%)
Circuit breaker room observation window	640	685.58	7.15
Lower part of bus compartment	224	230.47	2.88
Top of transformer	1170	1224.19	4.6

4 High Frequency Electric Field Distribution in Switchgear Under Typical Breaking Conditions

In this paper, cutting off the overvoltage of the reactor in a 35 kV system is taken as an example to analyze the distribution law of high-frequency electric field inside the high-voltage switchgear [11]. The system diagram is shown in Fig. 3. In Fig. 3, U is the system voltage source, and the effective value of the voltage is set to 20.21 kV

at 35 kV voltage level. L_s is the equivalent inductance of the power supply, C_s is the equivalent ground capacitance of the line from the power outlet to the circuit breaker, Cable is the connecting cable, VCB is the vacuum circuit breaker, and L is the equivalent inductance of the 35 kV shunt reactor. C is the equivalent ground capacitance of the reactor including the connecting cable. The arc time of the circuit breaker is set as 5 ms, and the whole simulation time is 25 ms.

The vacuum circuit breaker model is Helmer model, the reactor inductance value is 360 mH, the connecting cable length is 70 m. The simulated three-phase overvoltage waveform of circuit breaker is shown in Fig. 4. Fourier transform is used to analyze the transient voltage of the circuit breaker. The dominant frequency of the three-phase voltage is 8.7 kHz and contains a small amount of 223.15 kHz component.

Therefore, the circuit breaker transient voltage and current waveform within 10ms-25ms can be imported into the simulation model to obtain the transient electric field distribution inside the switchgear at this time. The electric field distribution at the moment when the three-phase voltage amplitude is the highest is analyzed, and the simulation results are shown in Fig. 5.

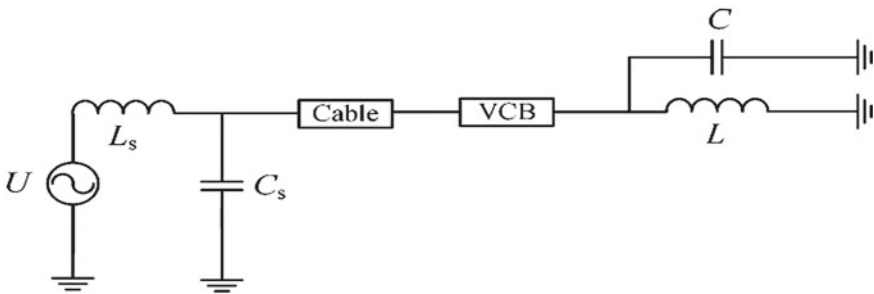


Fig. 3 Simulation model of vacuum circuit breaker cut off the 35 kV shunt reactor

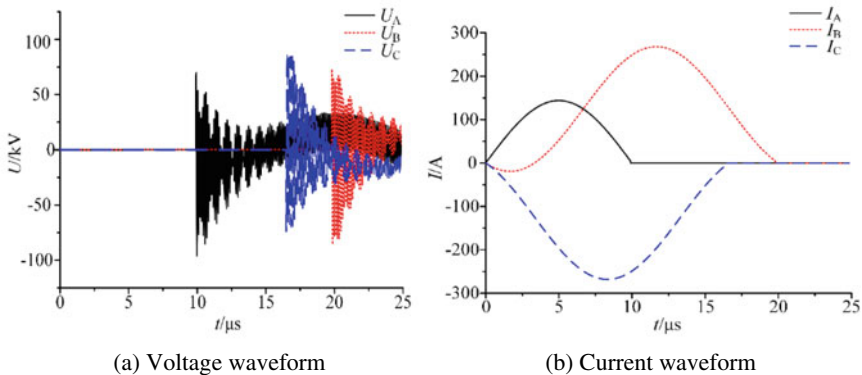


Fig. 4 High voltage circuit breaker three-phase interruption voltage and current waveform

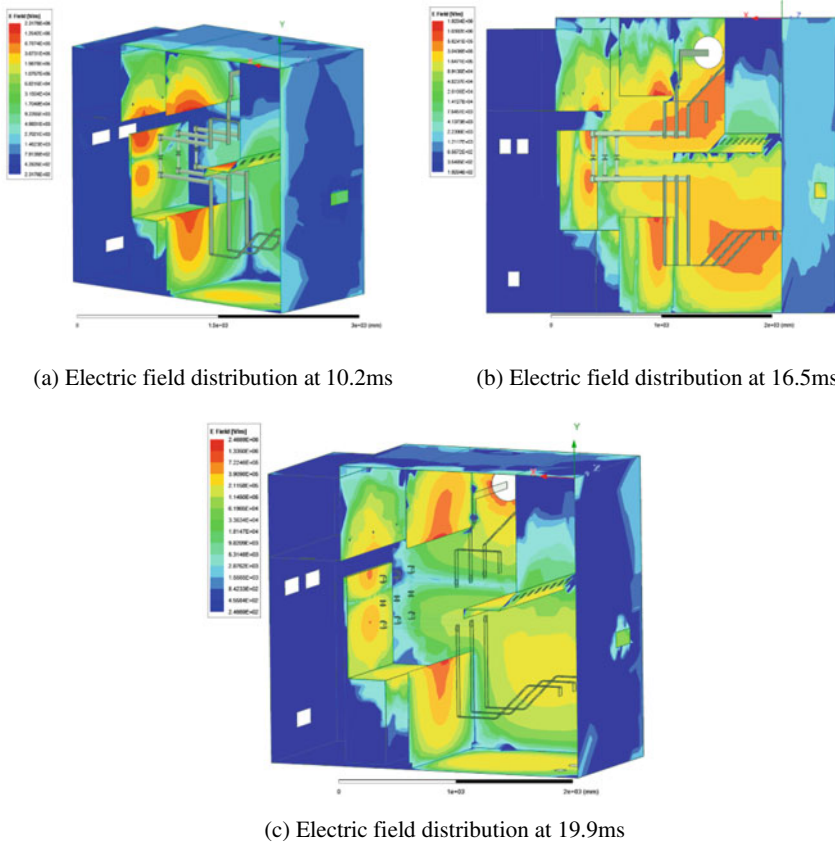


Fig. 5 High-frequency electric field distribution in switchgear at typical time

The simulation results show that when the voltage of phase A reaches its peak value of 96.74 kV, the maximum electric field strength inside the switchgear can reach 2.31 kV/mm, mainly concentrated on the surface of the partition in the circuit breaker room and the top of the circuit breaker trolley near the A-phase position. Due to the distance from the busbar and relatively closed space, the electric field strength inside the instrument room is relatively small, and the field strength range at the position of the transformer is between 0.11 and 0.36 kV/mm. When the voltage of phase B reaches its peak value of 74.02 kV, as the voltage of phase A decreases and phase C is not yet interrupted, the maximum electric field strength inside the switchgear decreases to 1.92 kV/mm, and the location of the concentrated electric field moves closer to the B-phase busbar, and the field strength at other positions also decreases. When the voltage of phase C reaches its peak value of 85.8 kV, due to the high-frequency oscillating voltage between phase A and phase B, the maximum electric field strength inside the switchgear increases to 2.46 kV/mm, and a large area of high-field-strength region is generated on the left sealing plate of the switchgear.

Based on the above simulation results, the high-frequency and high-amplitude overvoltage generated by the vacuum circuit breaker during opening will produce a strong transient electric field inside the high-voltage switchgear. The local maximum field strength has approached the breakdown electric field strength of air, which is 3 kV/mm, posing a serious threat to the safety of smart sensors. The distribution of the electric field is closely related to the position, shape, and voltage of the busbar. When installing and wiring intelligent sensors, they should be kept as far away from the busbar as possible and appropriate shielding measures should be taken.

5 Conclusion

This paper establishes a high-frequency electric field simulation model for a typical 40.5 kV high-voltage switchgear and verifies its accuracy through experiments. Using the overvoltage caused by the vacuum circuit breaker cut off a reactor as an example, the distribution of high-frequency electric fields inside the high-voltage switchgear is studied. The simulation results show that when no breakdown occurs, the maximum internal electric field strength of the KYN61-40.5 switchgear during vacuum circuit breaker switching of a reactor can reach 2.46 kV/mm. The location of the electric field concentration area during the circuit breaker switching process varies with the position of the busbar and the voltage amplitude. The location of the maximum electric field strength is at the top of the circuit breaker carriage, the top of the circuit breaker chamber partition, and near the partition between the busbar chamber and the cable chamber. Therefore, the placement of intelligent sensors should avoid the above locations as much as possible.

References

1. Yong M, Wang L, Wei Y et al (2022) Research on intelligent IoT sensing and key technology of distribution network switchgear. *High Volt Apparatus* 58(7):73–82. <https://doi.org/10.13296/j.1001-1609.hva.2022.07.010>. (in Chinese)
2. He Z, Yang J, Wu Y et al (2023). Investigation on the future AC and DC combined operation form and development trend under energy transition. *Proc CSEE* 43(1):99–114. <https://doi.org/10.13334/j.0258-8013.pcsee.213348> (in Chinese)
3. Liu J, Zhao Z, Ji J, Hu M (2020) Research and application of wireless sensor network technology in power transmission and distribution system. *Intell Converged Netw* 1(2):199–220. <https://doi.org/10.23919/ICN.2020.0016>
4. Dhia SB, Ramdani M, Sicard E (2006) Electromagnetic compatibility of integrated circuits: techniques for low emission and susceptibility. Springer US, pp 293–477
5. Wang HQ, Huang DC, Chen X et al (2022). Research progress in electromagnetic disturbance characteristics and protection due to switching operations of primary and secondary integrated switchgear. *High Volt Eng* 48(1)269–280. <https://doi.org/10.13336/j.1003-6520> (in Chinese)
6. Lin X, Nie Y, Zhu T et al (2020) Research on 3D transient electric field calculation of high-voltage switchgear. *High Volt Apparatus* 56(10):56–62. <https://doi.org/10.13296/j.1001-1609> (in Chinese)

7. Li S, Zhang M, Li D et al (2019) Research on partial discharge transmission and external interference characteristics of high voltage switchgear. *High Volt Apparatus* 55(8):86–95. <https://doi.org/10.13296/j.1001-1609> (in Chinese)
8. Hussain GA, Shafiq M, Lehtonen M et al (2015) Online condition monitoring of MV switchgear using-dot sensor to predict arc-faults. *IEEE Sens J* 15(12):7262–7272.
9. Ji Y, Nie Y, Lin X et al (2020). Research on 3D electric field distribution of 12kV switchgear based on ANSYS. In: 2020 8th International conference on power electronics systems and applications (PESA), Hong Kong, China, pp 1–6
10. Balanis CA (2013) *Advanced engineering electromagnetics*, 2nd edn. Wiley & Sons
11. Sun D, Li Y, Jiang X et al (2022). Research on influence of operation modes on over-voltage of shunt reactor switching by vacuum circuit breaker. *High Volt Apparatus* 58(3):78–85. <https://doi.org/10.13296/j.1001-1609> (in Chinese)

Calculation of the Sensing Performance of SnO₂ Doped with Au Atom on C₄F₇N



Luoyu Li, Jie Yang, Lifeng Zhu, Sipeng Li, Chao Ma, Yang Zhao, Yifan Zhang, and Song Xiao

Abstract C₄F₇N, as a possible environmentally friendly insulating gas used to replace SF₆, has gained much attention due to its low greenhouse effect and good insulating properties. However, considering its incompatibility with sealing materials of power equipment and biotoxicity, it is necessary to detect its leakage in real time to ensure the stable operation of equipment and personal safety of the workers. The existing SnO₂ sensor for C₄F₇N detection has the limitation of high operating temperature, and the doping of metal monomers is expected to improve the adsorption energy and reduce the operating temperature. Therefore, in this paper, the adsorption characteristics of C₄F₇N by SnO₂ doped with Au atom, including adsorption energy, charge transfer and density of states function, were obtained by calculation based on the First-principle. The results show that the doping of Au atoms as catalysts can substantially improve the adsorption energy, providing a theoretical basis for its ability to improve the sensing performance of SnO₂ on C₄F₇N.

Keywords First-principle · Leak detection · Sensing performance · SnO₂ · Au-doped

L. Li · L. Zhu · C. Ma · Y. Zhao
State Grid Zhejiang Lishui Power Supply Company, Liandu District, Lishui 323000, China

J. Yang · S. Li
Lishui Zhengyang Electric Power Design Institute Co., Ltd, Lishui 323050, China

Y. Zhang (✉) · S. Xiao
School of Electrical Engineering and Automation, Wuhan University, Wuhan 430072, China
e-mail: 3237798324@qq.com

S. Xiao
e-mail: xiaosong@whu.edu.cn

1 Introduction

SF_6 is widely used as insulation medium in power systems, but due to its strong greenhouse effect, people began to look for environmentally friendly insulation gases. $\text{C}_4\text{F}_7\text{N}$ deserves wide attention due to its good insulation characteristics and low greenhouse effect [1]. Considering the incompatibility between $\text{C}_4\text{F}_7\text{N}$ and the sealing material in power systems such as Ethylene Propylene Diene Monomer, and the long maintenance cycle of power system devices such as GIS, it means that $\text{C}_4\text{F}_7\text{N}$ leakage may occur [2].

At the same time, $\text{C}_4\text{F}_7\text{N}$ is biotoxic and is classified as a Class IV acute toxicity hazard with an occupational exposure limit of 65 ppm [3]. In summary, $\text{C}_4\text{F}_7\text{N}$ leakage will affect the stable operation of electrical equipment and the health of workers, and we need to develop a reliable and highly sensitive gas detection sensor.

Metal oxide semiconductors (MOS), such as SnO_2 , ZnO , CuO , and WO_3 , have been widely used in gas sensors due to their low cost, ease of integration, and high stability [4]. However, the use of a single metal semiconductor as a sensing material has limitations and is often accompanied by high operating temperatures while meeting the response height [5]. The solution to this problem is mainly to perform doping, such as metal monomers and different metal oxides to form heterojunctions, thus reducing the increase in response height and lowering the operating temperature [6]. According to the study by Tang Ju's team at Wuhan university, when using pure SnO_2 as a sensing material to detect $\text{C}_4\text{F}_7\text{N}$, the response height can reach 60% for 50 ppm at 275 °C [7]. While by doping MXene, the working temperature can be reduced to room temperature, but the response is drastically reduced to 8.8% [8], and due to the presence of functional groups on the surface of MXene, it is not stable enough in air, which will limit its application as sensing material [9]. Yanlei Cui's study showed that by doping Au atoms into SnO_2 , the response to ethanol was increased by a factor of three and the operating temperature could be reduced [10].

Therefore, this paper provides a theoretical basis for the detection of $\text{C}_4\text{F}_7\text{N}$ using SnO_2 doped with Au atom as a sensitive material by simulating the adsorption properties, including adsorption energy, charge transfer amount, density of states function and differential charge density, based on the First-principle, providing a theoretical basis for its ability to improve the sensing performance of SnO_2 on $\text{C}_4\text{F}_7\text{N}$.

2 Calculation Parameter Settings

The calculations in this paper are performed using the Dmol³ module in Materials Studio. All models choose the generalized gradient approximation (GGA) and the Perdew-Berke-Ernzerhof (PBE) generalized function to deal with the exchange interactions between electrons, introduce dispersion-corrected density generalized theory (DFT-D) to correct the van der Waals forces, and use the p-polarized double numeric basis with polarization (DNP) as the basis group function for the linear combination

of atomic orbitals. In addition, a vacuum layer of 20 Å is added to avoid interactions between neighboring units. The energy convergence accuracy is 1.0×10^{-5} Ha, and the maximum force and maximum displacement are set to 0.002 Ha/Å and 0.005 Å. The orbital cutoff radius is set to 4.5 Å. A $6 \times 6 \times 1$ Monkhorst–Pack k-point mesh is used for geometry optimization and a $2 \times 2 \times 1$ Monkhorst–Pack grid is used to calculate the density of states (DOS).

For the doping of Au atom on SnO₂, the binding energy is defined as

$$E_{\text{binding}} = E_{\text{Au-SnO}_2} - E_{\text{Au}} - E_{\text{SnO}_2} \tag{1}$$

in which $E_{\text{Au-SnO}_2}$ is the total energy of Au-doped SnO₂; E_{Au} and E_{SnO_2} is the energy of isolated Au atom and SnO₂, respectively.

The (110) surface of SnO₂ was chosen for the calculation, and a 3×2 supercell was established [7], the optimized geometric model is shown in Fig. 1a. Figure 1b shows the C₄F₇N molecular model, and for the energy change in the adsorption process of the gas occurring on the Au-doped SnO₂ surface, the adsorption energy, is calculated using the following equation,

$$E_{\text{ad}} = E_{\text{Au-SnO}_2 + \text{gas}} - E_{\text{Au-SnO}_2} - E_{\text{gas}} \tag{2}$$

in which $E_{\text{Au-SnO}_2 + \text{gas}}$ is the energy of Au-SnO₂ after gas adsorption; $E_{\text{Au-SnO}_2}$ is the energy of Au-doped SnO₂ and E_{gas} is the energy of the gas molecule.

The calculation of the charge transfer between the gas molecule and the crystal surface is performed using the Mulliken method, which is given by the following equation,

$$\Delta Q = Q_1 - Q_2 \tag{3}$$

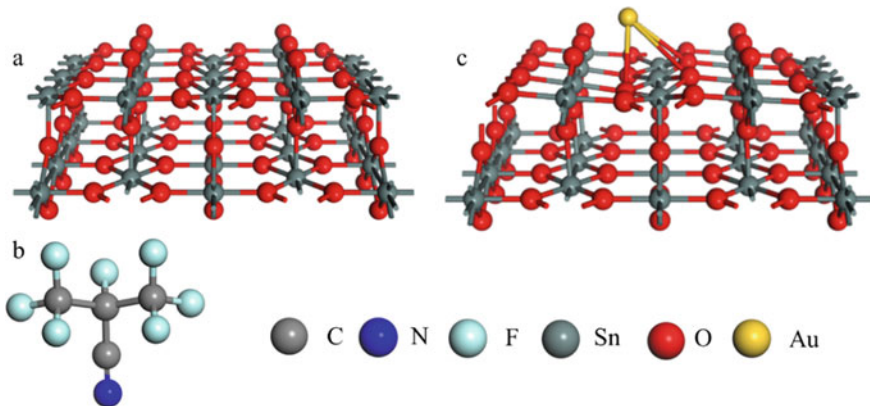


Fig. 1 The model of **a** SnO₂, **b** C₄F₇N, **c** Au-doped SnO₂

in which the value of ΔQ is obtained by subtracting the charge of the gas molecule before and after adsorption. If the result is positive, it indicates that the gas molecules transport electrons to the crystal surface during the adsorption process, and vice versa, it indicates that the gas molecules get electrons from the crystal surface during the adsorption process.

3 Results

3.1 Au-Doped SnO₂ Surface Structure Analysis

Previous studies have shown that the doping of gold atoms in SnO₂ is concentrated in the mass ratio of 0.5–2%, for example, according to Bingxi Feng's study, the response to TEA can be improved nearly five times when doping gold atoms with a mass ratio of 1% [11]. Therefore, we established a doping model of a single gold atom on the surface of SnO₂, as shown in Fig. 1c. The binding energy after doping with Au atom was calculated to be -1.84 eV, and the negative value indicates that it can form a stable binding structure.

To further investigate the interaction between Au atoms and SnO₂ surface, we plotted DOS and partial density of states (PDOS) diagrams as shown in Fig. 2. The DOS diagram shows that the overall energy density of states moves like a lower energy direction after Au doping, but the peak value basically does not change, which indicates that the crystal structure of SnO₂ does not change after doping. The PDOS diagram shows that between -5 and 0 eV, the $6s$ orbitals of Au atoms and the $5p$ orbitals of Sn atoms and the $2p$ orbitals of O atoms are overlapped to some extent, which indicates that the Au atom and the external orbitals of SnO₂ are hybridized. In summary, the two form a stable doping structure.

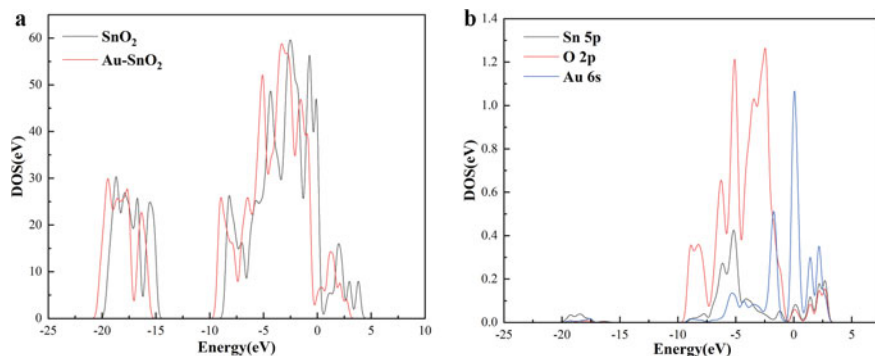


Fig. 2 The a DOS, b PDOS diagram of Au-SnO₂

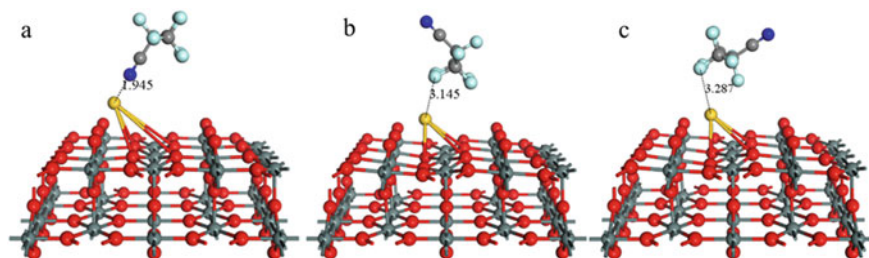


Fig. 3 Three models for the adsorption of C₄F₇N on Au-SnO₂ surface

3.2 Analysis of the Adsorption Structure of C₄F₇N on the Surface of Au-Doped SnO₂

For the surface adsorption of C₄F₇N on SnO₂ doped with Au atom, three adsorption models were developed using C₄F₇N gas in different planes close to the SnO₂ crystal surface as shown in Fig. 3, while the adsorption energy and charge transfer amount are shown in Fig. 4a. By comparing the magnitude of the adsorption energy, it can be seen that the adsorption energy is the largest with the C-N group close to the crystal surface, at -1.71 eV, and the charge transfer amount is 0.18 e. This indicates that compared to the C-F group, the Au-doped SnO₂ is more sensitive to the C-N group, which is the most stable adsorption structure and belongs to chemisorption.

Compared with pure SnO₂, the adsorption energy increased from -1.01 eV [7] to 1.71 eV after doping with Au atom, which is attributed to the catalytic effect brought by Au atom. Observing the adsorption model, it can be seen that the adsorption of C₄F₇N did not destroy the substrate structure of SnO₂, but the distance between the gold atom and the SnO₂ surface changed, compared to the distance between the Au atom and the crystal surface before the adsorption became larger, which also indicates the mediating effect of the Au atom, which changed the interaction process between C₄F₇N and the SnO₂ crystal surface. To further explore the adsorption of C₄F₇N on the surface of doped gold atom, we plotted DOS and PDOS diagrams, as shown in Fig. 4a, b. It can be seen from the DOS diagram that the overall energy density of states shifts to the left after the adsorption of C₄F₇N, and the energy peak at the Fermi energy level changes due to the loss of electrons by C₄F₇N. Further analysis of the PDOS diagram shows that the 2p orbital of the N atom and the 6s orbital of the Au atom and only one crossover exists between -2.5 eV and -5 eV, but there are multiple crossovers with the 5p orbital of the Sn atom and the 2p orbital of the O atom between -10 and 2 eV. These phenomena suggest that the doped Au atom act as catalysts, increasing the interaction between C₄F₇N and SnO₂ surfaces, which leads to an increase in adsorption energy.

Figure 4d shows the differential charge density diagram, red and blue indicate the loss and gain of electrons, respectively, and it can be seen that during the adsorption process, C₄F₇N molecules transport electrons to SnO₂. The occurrence of adsorption

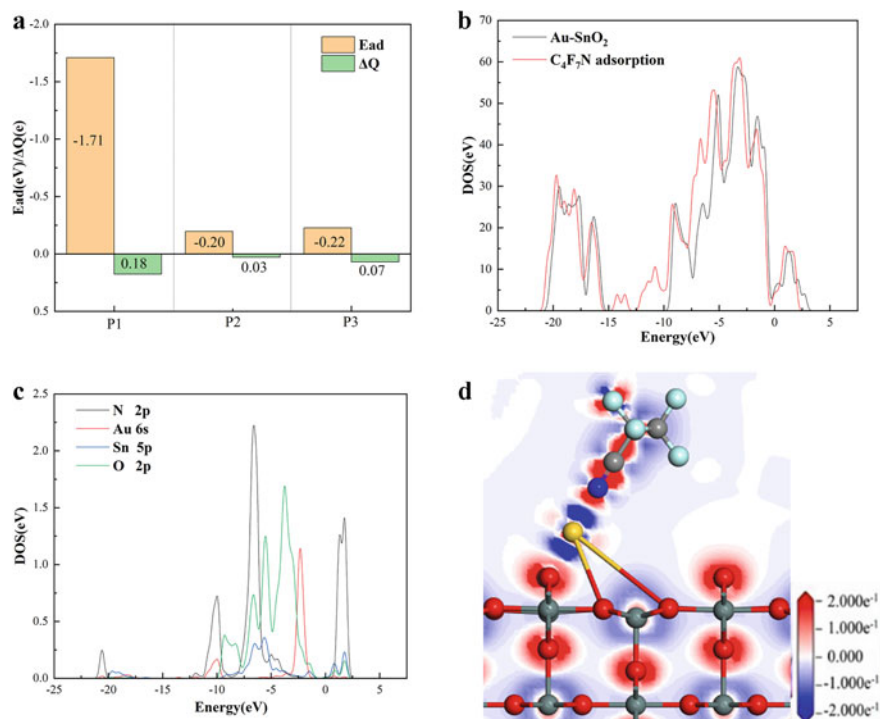


Fig. 4 **a** The adsorption data, **b** DOS, **c** PDOS diagram of $Au-SnO_2$ with C_4F_7N adsorbed, **d** the differential charge density diagram

changes the internal electron distribution of C_4F_7N molecules, and the interaction force between the two is strong and belongs to chemisorption.

4 Conclusions

In this paper, the adsorption properties of SnO_2 doped with Au atom on the environmentally friendly insulating gas C_4F_7N were calculated based on the First-principle, and the conclusions obtained by analyzing its adsorption energy, charge transfer process and density of states diagram are as follows.

- (1) The doping model of Au on the surface of SnO_2 was established, and the binding energy was calculated to be -1.84eV , which can form a stable doping structure.
- (2) For the adsorption of C_4F_7N on the crystal surface, three possible adsorption structures were constructed, and the most stable adsorption structure was found by comparing the magnitude of the adsorption energy.

- (3) The adsorption energy of Au-doped SnO₂ on C₄F₇N is -1.71eV , which is a chemisorption with a charge transfer of 0.18e , and the gas molecules transport electrons to the crystal surface during the adsorption process.
- (4) The doping of Au atom enhances the interaction between SnO₂ and C₄F₇N molecules, which has the potential to be used as a sensitive material to prepare sensors for real-time monitoring of C₄F₇N leakage.

References

1. Li Y, Zhang X, Xiao S, Chen Q, Tang J, Chen D, Wang D (2018) Decomposition properties of C₄F₇N/N₂ gas mixture: an environmentally friendly gas to replace SF₆. *Ind Eng Chem Res* 57(14):5173–5182
2. Zhang X, Wu P, Cheng L, Liang S (2021) Compatibility and Interaction mechanism between EPDM rubber and a SF₆ alternative gas-C₄F₇N/CO₂/O₂. *ACS Omega* 6(20):13293–13299
3. Li Y, Zhang X, Zhang J, Xiao S, Xie B, Chen D, Gao Y, Tang J (2019) Assessment on the toxicity and application risk of C₄F₇N: a new SF₆ alternative gas. *J Hazard Mater* 368(15):653–660
4. Cheng P, Dang F, Wang Y, Gao J, Xu L, Wang C, Lv L, Li X, Zhang B, Liu B (2021) Gas sensor towards n-butanol at low temperature detection: hierarchical flower-like Ni-doped Co₃O₄ based on solvent-dependent synthesis. *Sens Actuators B Chem* 328(1):129028
5. Nakate UT, Yu YT, Park S (2021) High performance acetaldehyde gas sensor based on p-n heterojunction interface of NiO nanosheets and WO₃ nanorods. *Sens Actuators B Chem* 344(1):130264
6. Qu F, Zhang N, Liu D, Zhang S, Talluri B, Zheng Y, Thomas T, Zhao R, Ruan S, Yang M (2020) Engineering Co³⁺ cations in Co₃O₄ multishelled microspheres by Mn doping: the roles of Co³⁺ and oxygen species for sensitive xylene detection. *Sens Actuators B Chem* 308(1):127651
7. Wu P, Li Y, Xiao S, Chen J, Tang J, Chen D, Zhang X (2022) SnO₂ nanoparticles based highly sensitive gas sensor for detection of C₄F₇N: a new eco-friendly gas insulating medium. *J Hazard Mater* 422(15):126882
8. Wu P, Li Y, Xiao S, Chen J, Tang J, Chen D, Zhang X (2022) Room-temperature detection of perfluoroisobutyronitrile with SnO₂/Ti₃C₂T_x gas sensors. *ACS Appl Mater Interf* 14(42):48200–48211
9. Zhou S, Yang X, Pei W, Jiang Z, Zhao J (2021) MXene and MBene as efficient catalysts for energy conversion: roles of surface, edge and interface. *J Phys Energy* 3(1):012002
10. Cui Y, Zhang M, Li X, Wang B, Wang R (2019) Investigation on synthesis and excellent gas-sensing properties of hierarchical Au-loaded SnO₂ nanoflowers. *J Mater Res* 34(17):2944–2954
11. Feng B, Wu Y, Ren Y, Chen Y, Yuan K, Deng Y, Wei J (2022) Self-template synthesis of mesoporous Au-SnO₂ nanospheres for low-temperature detection of triethylamine vapor. *Sens Actuat B Chem* 356(1):131358

A Coordinated Control Method for Active Power Feedforward of Dual PWM Converter



Dapeng Cao and Jie Li

Abstract The dual PWM converter control strategy is mainly divided into direct control and power coordination control. This paper introduces the dual PWM variable frequency speed regulation scheme of active power feedforward control, and adds the compensation amount corresponding to the active power of the inverter to the given value of the active current on the rectifier side, then when the operating state of the asynchronous motor changes, it will not directly change the size of the capacitor voltage on the DC side, but directly change the size of the active current on the rectifier side, thereby reducing the fluctuation of the DC bus voltage, improving the dynamic response performance of the system, and making it possible to reduce the size of the DC bus capacitance. Finally, Matlab/Simulink simulation of the control scheme is carried out to verify its correct feasibility.

Keywords Dual PWM converter · Active power feedforward · Coordinated control

1 Introduction

The traditional general-purpose inverter generally adopts AC-DC-AC structure, and the three-phase input voltage is first obtained by the uncontrollable rectification of the diode, and then stabilized by the filtering of the capacitor on the DC bus side, and finally passed through the inverter output voltage frequency variable alternating current. This type of inverter has a wide range of efficiency, accuracy and speed regulation, and is widely used in the industrial field, but there are also many shortcomings.

First, the use of diode uncontrolled rectification, current harmonic content, the power grid caused great pollution, and the elimination of grid harmonics has become a major topic in the field of power electronics technology, many countries in the

D. Cao (✉) · J. Li

School of Science and Technology, Shanghai Open University, Shanghai 200433, China
e-mail: caodp@sou.edu.cn

© Beijing Paiké Culture Commu. Co., Ltd. 2024

X. Dong and L. Cai (eds.), *The Proceedings of 2023 4th International Symposium on Insulation and Discharge Computation for Power Equipment (IDCOMPU2023)*, Lecture Notes in Electrical Engineering 1100, https://doi.org/10.1007/978-981-99-7393-4_66

697

world, international organizations have specified regulations or standards to limit harmonics. Second, because the energy transmission of the diode rectifier bridge is irreversible, the regenerative electric energy generated when the motor is in the state of regenerative power generation cannot be fed back to the power grid, resulting in a waste of energy, and the reason why the frequency conversion speed regulation system has received widespread attention is based on its significant energy-saving effect. Third, the DC bus voltage fluctuation range obtained after rectification of the uncontrollable diode requires a large electrolytic capacitor for filtering and energy storage, and such a capacitor itself has the disadvantages of high price, large size and short life, so it has a great impact on the cost, miniaturization and reliability of the entire system. The dual PWM converter takes these shortcomings of the traditional general frequency converter as the starting point, adopts PWM controllable rectification technology, and takes the power factor adjustment on the power grid, energy can flow in both directions, and the DC bus voltage stability as the control goal, and will be widely used in new energy technology, wind power generation and solar power generation grid-connected occasions.

The architecture diagram of the dual PWM converter system is shown in Fig. 1.

At present, the control strategy of dual PWM converter is mainly divided into two categories, namely direct control and power coordination control. Direct control is the traditional DC bus voltage feedback control, when the system input and output power imbalance causes the DC bus voltage fluctuation, through the feedback signal of the bus voltage to adjust the input power of the PWM rectifier. Since the response of the DC bus voltage lags behind the change of load power, when the load changes, the DC bus voltage will fluctuate greatly [1–4], and increasing the size of the bus capacitor can solve the fluctuation problem, but simply by increasing the capacitance capacity to stabilize the DC bus voltage has serious drawbacks [5, 6].

Power coordination control includes direct power control [7–9] and power feed-forward control. The direct power control strategy, similar to direct torque control

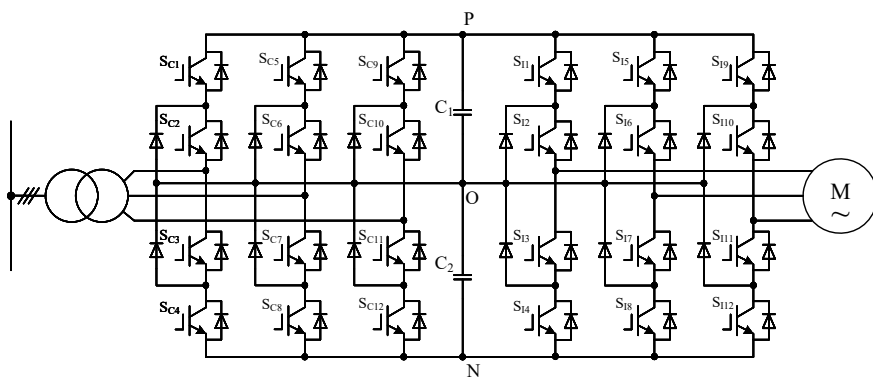


Fig. 1 Structure diagram of a dual PWM converter

(DTC) in variable frequency speed regulation technology, is to compare the difference between instantaneous active power, instantaneous reactive power and a given value in real time, and then generate a PWM modulation signal by looking for a pre-formulated switching state table. This control strategy based on hysteresis control structure eliminates the rotational coordinate transformation unit and the PI regulator of the current inner loop in traditional vector control, simplifies the algorithm, and improves the dynamic response performance of the system. However, this hysteresis-based control method inevitably introduces the problem of unstable switching frequency.

In order to solve the above problems, this chapter introduces the dual PWM frequency conversion speed regulation scheme of active power feedforward control, adding the compensation amount corresponding to the active power of the inverter to the given value of the active current on the rectifier side, then when the operating state of the asynchronous motor changes, it will not directly change the size of the capacitor voltage on the DC side, but directly change the size of the active current on the rectifier side, thereby reducing the fluctuation of the DC bus voltage, improving the dynamic response performance of the system, and making it possible to reduce the size of the DC bus capacitance. Finally, Matlab/Simulink simulation of the control scheme is carried out to verify its correct feasibility.

2 Active Power Feedforward Control Strategy

As an energy storage link, aluminum electrolytic capacitors are generally used in this dual PWM converter system, but in some applications, such as high-power or high-voltage motor drives, aluminum electrolytic capacitors have some disadvantages in terms of size, weight, cost, and stability, the most important of which is stability. Due to continuous gas leakage, the performance of electrolytic capacitors gradually deteriorates as the use time increases. Therefore, capacitance is the main factor limiting the service life of the inverter. People want to reduce the size of the DC capacitor to reduce the cost and the volume of the entire inverter. However, a small capacitance will cause large DC link voltage fluctuations, which will also lead to damage to semiconductor switching devices.

In a traditional DC-link voltage feedback control scheme, the input power of the PWM rectifier is regulated by detecting DC bus voltage fluctuations caused by system input and output power imbalance. Since the response of the DC link voltage lags behind the change in load power, the DC link voltage fluctuates greatly when the load changes.

The active power feedforward control strategy in this chapter combines the output power feedforward control and the DC bus voltage feedback control, and the rectifier control increases the information of the inverter output load change, which can reduce the fluctuation of the bus voltage, so as to reduce the DC capacitance value.

Figure 2 shows the block diagram of the control structure of a dual PWM conversion system with a power feed-forward loop. The block diagram of power feed-forward decoupling is shown in Fig. 3.

Suppose the power supply is a symmetrical (balanced) three-phase voltage:

$$\begin{aligned}
 e_R &= V_m \sin(\omega_e t) \\
 e_S &= V_m \sin(\omega_e t - 2\pi/3) \\
 e_T &= V_m \sin(\omega_e t + 2\pi/3)
 \end{aligned}
 \tag{1}$$

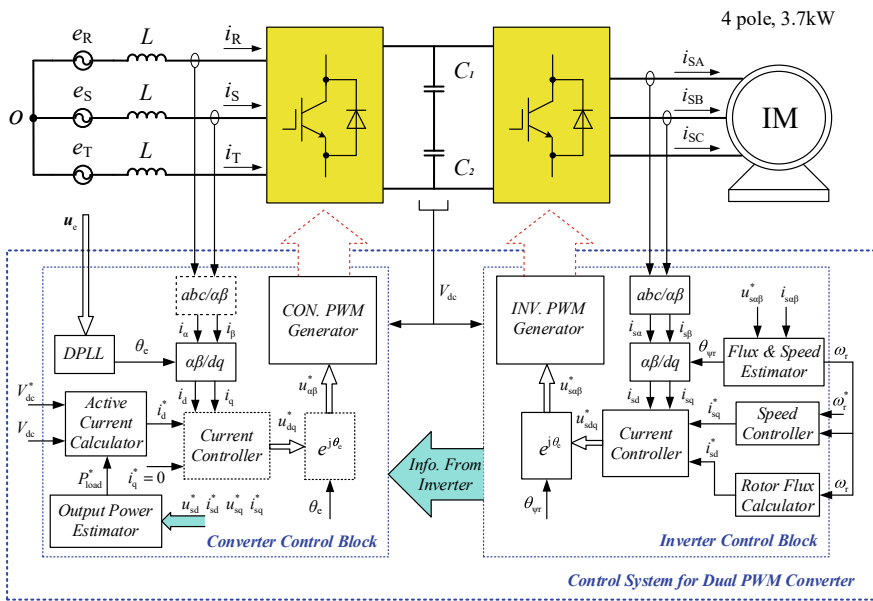


Fig. 2 Block diagram of the control structure of a dual PWM converter system

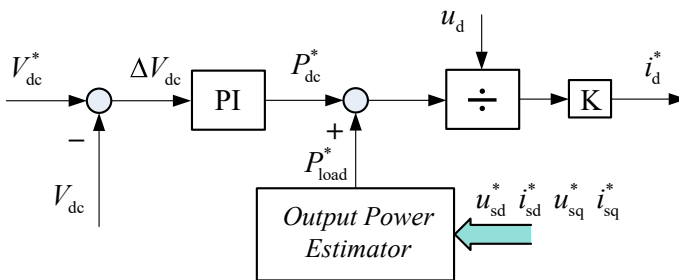


Fig. 3 Block diagram of power feed-forward decoupling structure

Among them, the amplitude of the V_m voltage phase voltage, ω_e represents the angular velocity of the rectifier's synchronous rotation coordinate system.

In the dq rotation coordinate system, the input active and reactive power of the rectifier are:

$$\begin{bmatrix} P_{\text{rec}}^* \\ Q_{\text{rec}}^* \end{bmatrix} = \frac{3}{2} \begin{bmatrix} e_d e_q \\ -e_q e_d \end{bmatrix} \begin{bmatrix} i_d^* \\ i_q^* \end{bmatrix} \quad (2)$$

In the formula, P_{rec}^* and Q_{rec}^* is the input active power and reactive power of the rectifier given values, and the e_d and e_q are the dq components of the three-phase power supply voltage in the synchronous rotation coordinate system. i_d^* and i_q^* is the given values for the dq component of the rectifier input current.

For balanced three-phase systems:

$$\begin{bmatrix} e_d \\ e_q \end{bmatrix} = \begin{bmatrix} V_m \\ 0 \end{bmatrix} \quad (3)$$

So,

$$P_{\text{rec}}^* = \frac{3}{2} e_d i_d^* \quad (4)$$

The output power of the inverter can be expressed as:

$$P_{\text{load}}^* = \frac{3}{2} (u_{\text{sd}}^* i_{\text{sd}}^* + u_{\text{sq}}^* i_{\text{sq}}^*) \quad (5)$$

P_{load}^* is the output power on the inverter side, u_{sd}^* , u_{sq}^* , i_{sd}^* , i_{sq}^* is the given values of dq component on stator voltage and stator current of the inverter side.

The capacitor energy storage on the DC side is:

$$W = \frac{1}{2} C V_{\text{dc}}^2 \quad (6)$$

Which W is the DC bus capacitance energy storage value, C is the DC bus capacitance value, and V_{dc} is the DC bus voltage value.

The changes in the energy storage of the capacitor on the DC side are:

$$P_{\text{cap}}^* = \frac{dW}{dt} = \frac{d}{dt} \left(\frac{1}{2} C V_{\text{dc}}^2 \right) = C V_{\text{dc}} \frac{dV_{\text{dc}}}{dt} \quad (7)$$

Which P_{cap}^* is the DC side power.

Ignore the power loss of the device:

$$P_{\text{cap}}^* = P_{\text{rec}}^* - P_{\text{load}}^* = C V_{\text{dc}} \frac{dV_{\text{dc}}}{dt} = \frac{3}{2} e_d i_d^* - P_{\text{load}}^* \quad (8)$$

It can be seen from Eq. (8) that the power input to the DC side of the control rectifier and the power input to the inverter on the DC side are balanced, which can reduce the fluctuation of the voltage on the DC side, and then reduce the capacitance capacity of the DC side. To do this, the input current on the rectifier side must be able to meet changes in the output power of the system.

For AC-DC-AC converters with uncontrolled rectification of diodes, P_{rec} is uncontrollable, so when the motor operating state changes (e.g. from electric mode to power generation mode), a large P_{cap} will be generated, resulting in large bus voltage fluctuations. However, when PWM is used for controlled rectification, P_{rec} is controllable. If the system can adjust P_{rec} so that $P_{\text{rec}} = P_{\text{inv}}$, P_{cap} is always 0. That means that the DC link voltage can be maintained stable under voltage balance conditions, and the DC bus capacitance can be effectively reduced.

From Eq. (8):

$$i_d^* = \frac{2}{3} \left(\frac{P_{\text{load}}^*}{e_d} + \frac{C V_{\text{dc}}}{e_d} \frac{dV_{\text{dc}}}{Et} \right) \quad (9)$$

It can be seen from Eq. (9) that if the compensation amount corresponding to the active power of the inverter is added to the given value of the active current on the rectifier side, the size of the capacitor voltage on the DC side will not be directly changed when the operating state of the asynchronous motor changes, but the size of the active current on the rectifier side will be directly changed.

3 Simulation Results and Discussion

The rectifier side parameters are: the voltage amplitude of the three-phase voltage source is 220 V, the input inductance $L = 8$ mH, the bus voltage is given as 540 V, and the DC bus capacitance $C = 470$ uF; The inverter side motor parameters are: rated power $P_e = 3.7$ kW, rated current $I_e = 8$ A, rated voltage $V_e = 380$ V, $L_s = 155$ mH, $L_r = 155$ mH, $L_m = 147$ mH, rated speed $n_e = 1500$ r/min (corresponding to the rotor output angular frequency of about 157 rad/s), rated torque $T_e = 23.5$ N·m, pole pair $n_p = 2$, moment of inertia $J = 0.0131$ kg·m², motor friction coefficient $f = 0.002985$. The simulation conditions are: 0–0.12 s is the pre-excitation time of the motor, a given speed at 0.12 s, a sudden rated load at 0.3 s, a sudden reduction in rated load at 0.5 s, and a sudden rated load at 0.7 s.

Figures 4, 5 and 6 is a comparison chart of simulation results based on traditional bus voltage feedback control and power feedforward control. It can be seen that the smaller the power required by the motor load, the smaller the fluctuation of the DC link voltage; When the operating state and mode of the motor change, the

bus voltage controlled by power feed-forward is significantly smoother than the bus voltage controlled by traditional bus voltage feedback.

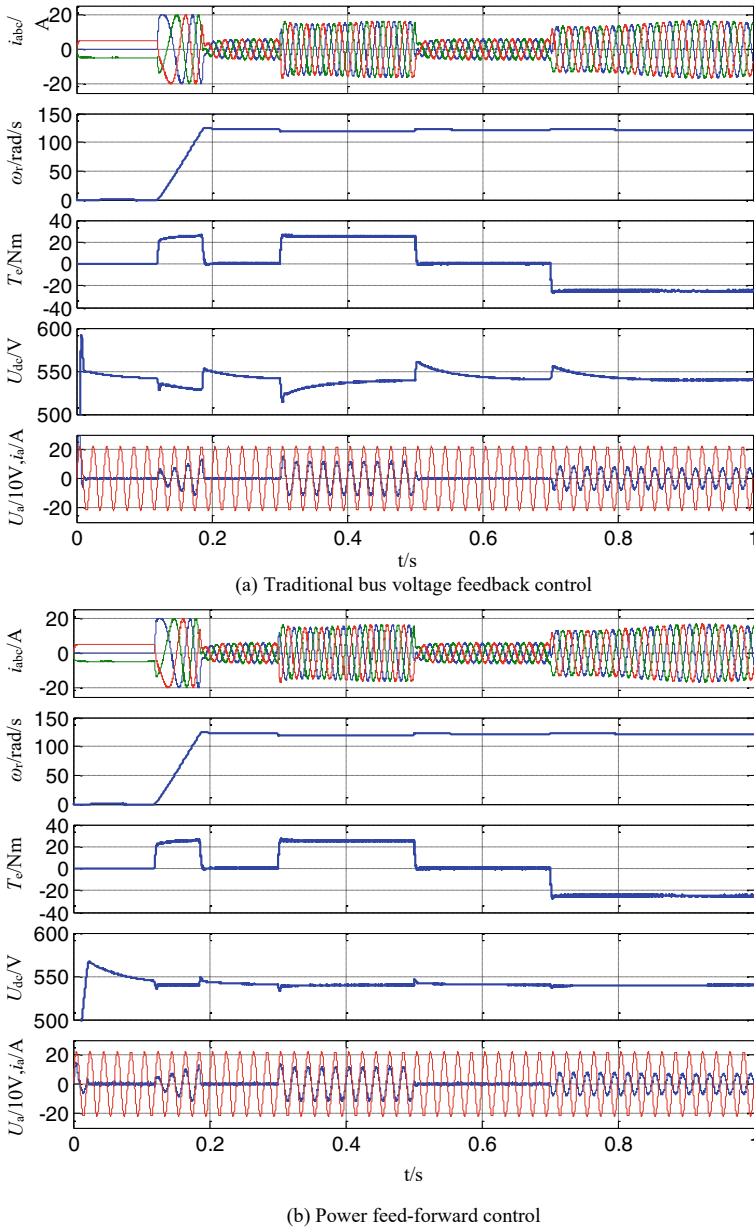
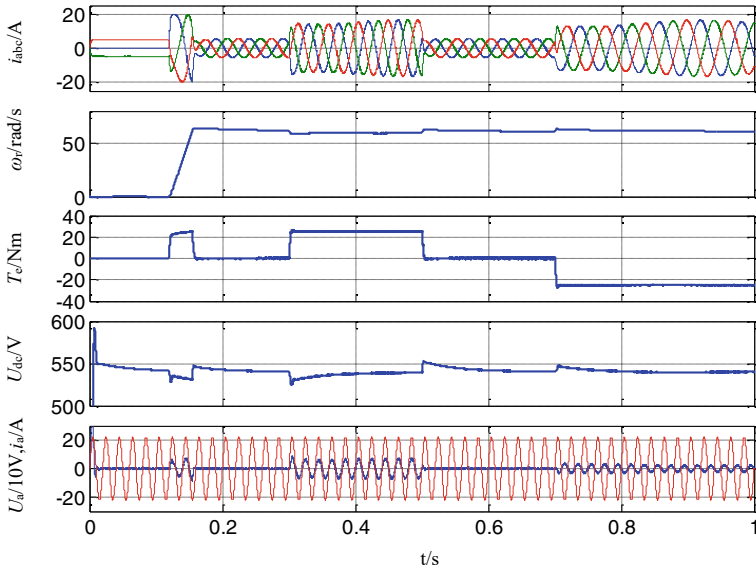
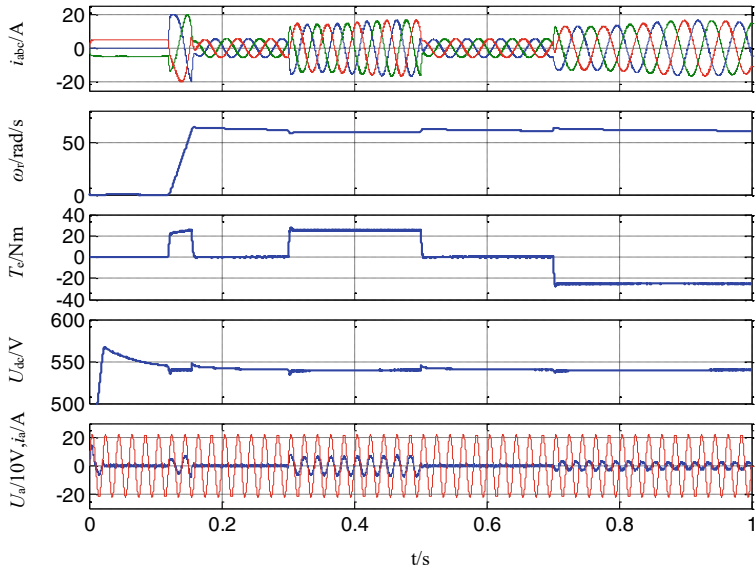


Fig. 4 Comparison of simulation results of two control strategies of dual PWM converter (40 Hz)

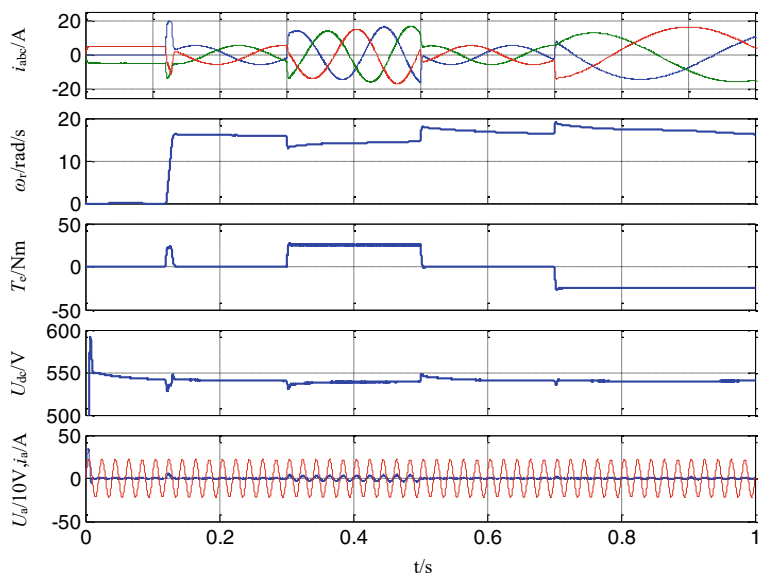


(a) Traditional bus voltage feedback control

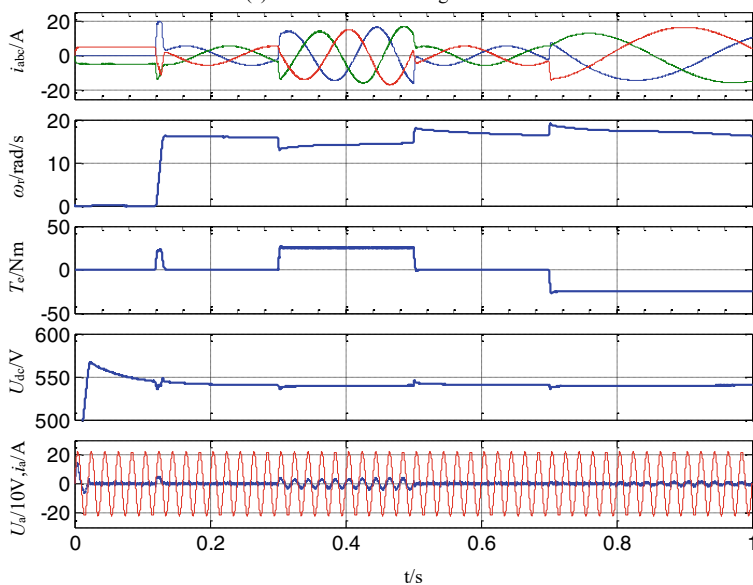


(b) Power feed-forward control

Fig. 5 Comparison of simulation results of two control strategies of dual PWM converter (20 Hz)



(a) Traditional bus voltage feedback control



(b) Power feed-forward control

Fig. 6 Comparison of simulation results of two control strategies of dual PWM converter (5 Hz)

4 Conclusion

In this paper, the conventional dual PWM variable frequency speed regulation system based on bus voltage feedback control is studied, simulated and analyzed. According to the phenomenon of large fluctuations of DC link voltage in its dynamic process, the principle analysis is carried out. On this basis, by adopting the power feed-forward strategy, the fluctuation of DC bus voltage is effectively suppressed, and a good control effect is realized.

4.1 Foundation Items

Project (XK2006) supported by Shanghai Open University scientific research and innovation Foundation.

Project supported by Shanghai Open University research and innovation team Foundation.

References

1. Zhang Y, Zhao Z, Lu T, Li L (2009) Direct power and torque control for three-level NPC based PWM ac/dc/ac converter. In: 6th IEEE international conference on power electronics and motion control, pp 1780–1784
2. Liao JC, Yeh SN (2000) A novel instantaneous power control strategy and analytic model for integrated rectifier/inverter system. *IEEE Trans Power Electron* 15(6):996–1006
3. Antoniewicz P, Jasinski M, Kazmierkowski MP (2005) AC/DC/AC Converter with reduced DC side capacitor value. In: International conference on computer as a tool, pp 1481–1484
4. Hur N, Jung J, Nam K (2001) A fast dynamic DC-link power-balancing scheme for a PWM converter-inverter system. *IEEE Trans Industr Electron* 48(4):794–803
5. Wang F, Jiang J (2006) Research on power balance joint control strategy of dual PWM converter for wind turbine. *Proc CSEE* 26(22):134–139
6. Zhang Y, Zhao Z, Feng B et al (2011) Integrated control strategy of three-level dual PWM inverter. *Proc CSEE* 26(22):25–31
7. Wang W, Yin H, Guan L (2011) Dual PWM variable frequency speed regulation system based on direct power control. *J South China Univ Technol (Natural Science Edition)* 39(3):67–71
8. Wei L, Chen Y, Chen G et al (2011) Integrated control strategy of direct power of doubly-fed induction wind power generation system. *High Volt Eng* 37(7):1818–1824
9. Bian S, Lv X, Xiang H et al (2005) Simulation study on control strategy of AC excitation variable speed constant frequency wind power generation system. *Proc CSEE* 25(16):57–62

Optimal Design of Double-Fracture Disconnect Switchgears Based on BP Neural Network and NSGA-II Algorithm



Xueliang Liu, Jiangang Yin, Jieshuai Ren, Jun Chen, Yaqin Wen,
and Zhao Yuan

Abstract GIS double-fracture disconnect switchgears have high requirements on insulation and stress resistance due to their miniaturized and compact design. How to improve the insulation capacity and stress resistance by optimizing the design of key dimensional parameters within a limited volume is the key point of optimization research. In this paper, the finite element method is used to build simulation models of the electrostatic and stress fields of a double-fracture disconnect switchgear. The key dimensional parameters that have a significant impact on the static electric field and stress field are initially analyzed, and these parameters are parametrically processed. In order to solve the optimization problem of large-scale field models using optimization algorithms, the Box-Behnken experimental design method is used to collect samples and establish a BP neural network model. The global Pareto-optimal solution set under multiple objectives is found by combining the BP neural network model and NSGA-II algorithm, and the global optimal solution is obtained according to different objective weights. Under the optimized dimensional parameters, the maximum electric field strength and the maximum principal stress in critical areas are significantly reduced, achieving an effective improvement in the performance of the double-fracture disconnect switchgear.

Keywords Double-fracture disconnect switchgear · Electrostatic field · Stress field · BP neural network · NSGA-II algorithm

X. Liu · Z. Yuan (✉)

School of Electrical and Electronic Engineering, Huazhong University of Science and Technology, Wuhan 430074, China
e-mail: 971578993@qq.com

J. Yin · J. Ren · J. Chen · Y. Wen

State Grid Hubei Electric Power Co., Ltd., Electric Power Research Institute, Wuhan 430077, China

© Beijing Paiké Culture Commu. Co., Ltd. 2024

X. Dong and L. Cai (eds.), *The Proceedings of 2023 4th International Symposium on Insulation and Discharge Computation for Power Equipment (IDCOMPU2023)*, Lecture Notes in Electrical Engineering 1100, https://doi.org/10.1007/978-981-99-7393-4_67

707

1 Introduction

With the rapid development of China's power grid and the promotion of smart grid construction, GIS equipment has been used in a large number of power grids because of its small footprint, compact structure, high reliability and low maintenance workload. During the 14th Five-Year Plan period, a large number of 110 kV GIS will face the demand for expansion [1]. However, the traditional GIS bus-side disconnect switches have only one disconnecter, which cannot fully meet the demand for non-stopping power expansion and testing, and bring huge difficulties in outage coordination and significantly reduce the reliability level of the power grid structure. The 110 kV three-phase common box type GIS based on double isolation break will avoid extensive outages in 110 kV GIS expansion projects and emergency repair, and meet the increasing demand for GIS non-stopping power expansion and testing [2].

The 110 kV GIS is a three-phase co-box structure, which requires more components to be placed in a limited space compared to the three-phase sub-box structure, so its space is more compact and complex, and the performance requirements for insulation, mechanical stress, temperature rise, etc. are more difficult to design and manufacture, which requires further optimization of the design on the original basis. In order to analyze and verify the performance of GIS equipment, many researchers have used finite element analysis software for simulation modeling analysis [3–9].

2 110 kV Double-Fracture Disconnect Switchgear Model

2.1 Geometric Model

The 110kV double-fracture disconnect switchgear consists of shell, conductive rod, basin insulator, contacts, double-break drive and linkage mechanism and other components. Figure 1 is the three-dimensional model.

2.2 Simulation Model

Electrostatic field simulation results and analysis

According to the assessment requirements of the non-stopping power expansion and lightning withstand voltage test in the type test, a high potential is applied to the static contacts of the double-fracture disconnect switchgear, and a ground potential is applied to the moving contacts, auxiliary ground switch, and enclosure.

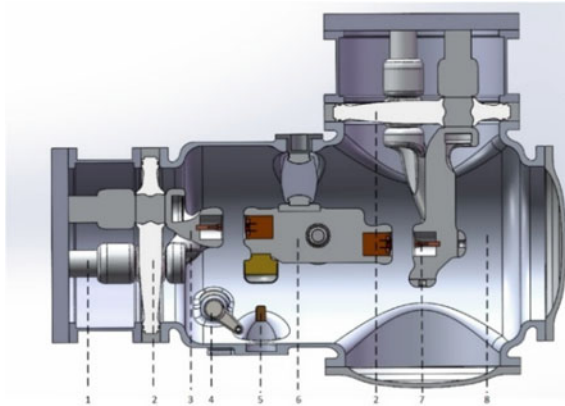


Fig. 1 110 kV double-fracture disconnect switchgear. 1. Conductive rod, 2. Basin insulator, 3. Static side contact, 4. Linkage puller, 5. Auxiliary earth switch, 6. Double break drive mechanism, 7. Busbar static side contact, 8. Shell

Figure 2 is the result of the electrostatic field simulation calculation. It can be seen that the electric field concentration is mainly on the contact surfaces of the static side conductors on both sides. Therefore, the contact size and surface shape will have an impact on the maximum electric field strength and are the main targets for structural optimization.

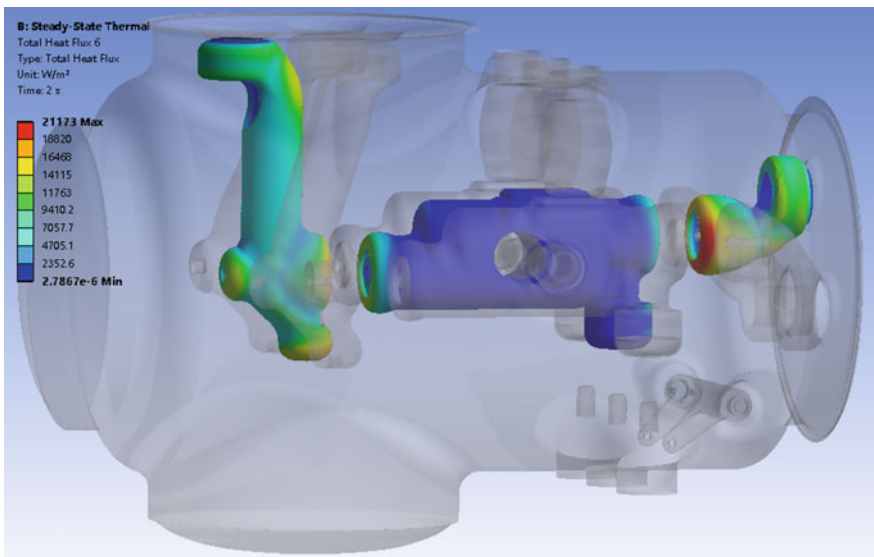


Fig. 2 The electrostatic field simulation result

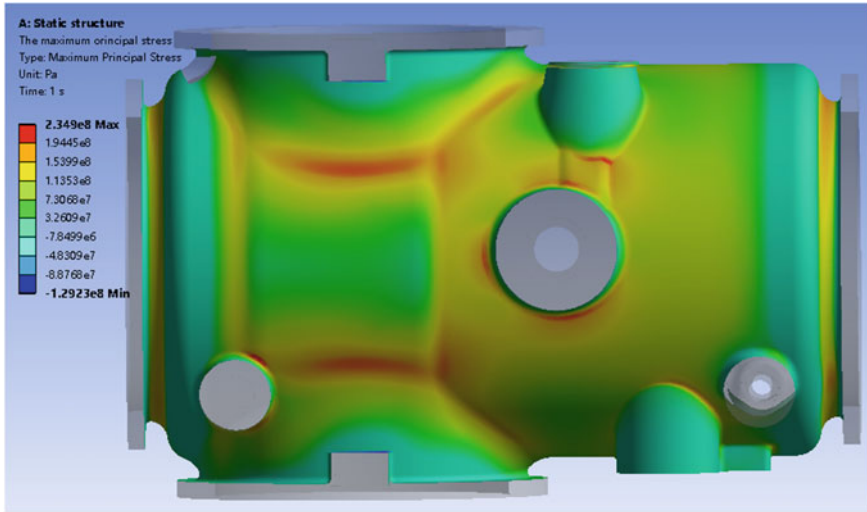


Fig. 3 The stress field simulation result

Stress field simulation results and analysis

The stress field simulation uses static structure module to simulate the shell hydrostatic test with the boundary condition of 3.6 Mpa normal pressure applied to the inner surface of the shell, and the maximum principal stress distribution applied to the shell is obtained by solving, as shown in Fig. 3.

It can be seen that the stress concentration areas are mainly at the intersection of the shell and the cladding. Therefore, in order to optimize the compressive performance of the shell, it is necessary to parameterize and optimize the design for the dimensions of the above key areas.

3 Parameterization and Impact Analysis of Model Key Dimensions

3.1 Effect of Each Dimensional Parameter on the Maximum Electric Field Strength

Excessive electric field strength inside the GIS will pose a significant threat to its insulation performance. In order to analyze the degree of influence of contact dimensional parameters on the maximum electric field strength of the contact surface, the key dimensional parameters are parameterized in this section.

Considering that the high field strength area is mainly distributed on the static side and bus static side conductor contact surface, the shape of the dynamic side conductor

contact surface has little effect on the value and distribution of the maximum field strength, so the static side and bus static side conductor contact surface dimensional parameters are set as the key dimensional parameters, as shown in Table 1, to study the relationship between dimensional parameters and maximum electric field strength.

The contact surface shape is mainly determined by the two radii of curvature and thickness parameters, and the effect of different contact dimensional parameters on the maximum field strength under single factor will be studied below.

In this paper, a number of sample points are taken within the parameter range using the uniform sampling method to analyze the range and law of the maximum field strength of the isolation switch when the single factor is varied.

Among all the parameters, the parameters r_1 , r_2 , d_1 have an obvious linear relationship with the maximum field strength, and the maximum field strength decreases with the increase of the parameters (Figs. 4, 5 and 6).

The static contact radius r_1 is set to 13, 14, 15, 16 mm respectively for electric field simulation to obtain the relationship between the maximum field strength and the static contact radius r_1 .

Table 1 The electrostatic field optimization parameters

Serial number	Dimensional parameters	Parameter range/mm
1	Static side contact radius r_1	13–16
2	Static side contact radius r_2	29–35
3	Static side contact thickness d_1	20–24
4	Busbar static side contact radius r_3	13.5–16.5
5	Busbar static side contact radius r_4	25.2–30.8
6	Busbar static side contact thickness d_2	18–22

Fig. 4 The maximum electric field strength values at different static side contact radii r_1

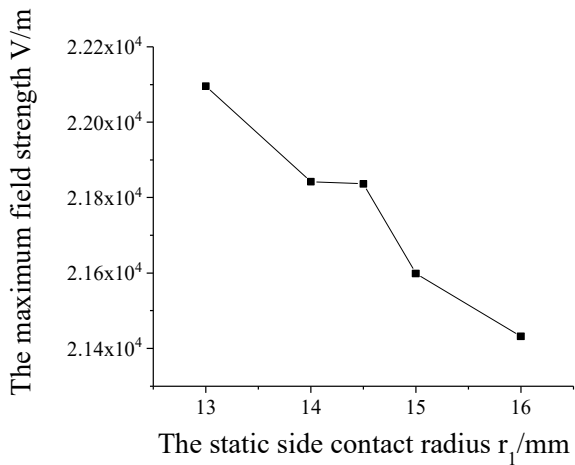


Fig. 5 The maximum electric field strength value at different static side contact thickness d_1

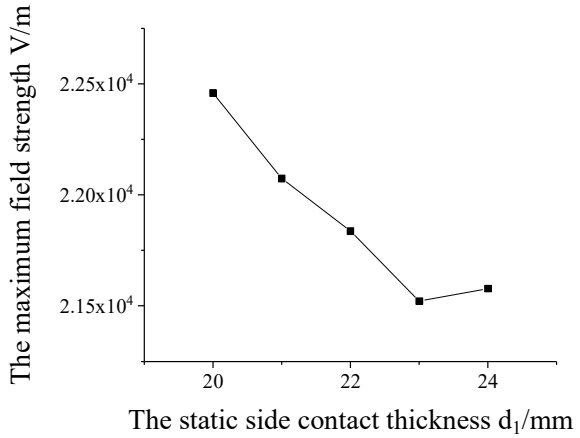
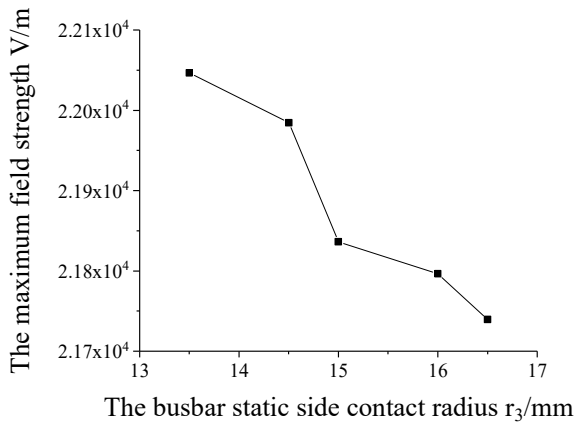


Fig. 6 The maximum field strength at different radii r_3 of the busbar static side contacts



The static-side contact thickness d_1 is set to 20, 21, 22, 23 and 24 mm for electric field simulation to obtain the relationship between the maximum field strength and the static-side contact thickness d_1 .

The busbar static side contact radius r_3 is set to 13.5, 14.5, 15, 16, 16.5 mm for electric field simulation to obtain the relationship between the maximum electric field strength and the busbar static side contact radius r_3 .

The factors such as static side contact radius r_2 , busbar static side contact radius r_4 , and busbar static side contact thickness d_2 have no obvious pattern with the maximum field strength. Table 2 is their results range.

Table 2 The maximum electric field strength variation range for some parameters

Parameters	Parameter range/mm	Maximum electric field strength range V/m
r_2	29–35	21,789–22,037
r_4	25.2–30.8	21,716–22,044
d_2	18–22	21,723–22,077

3.2 Effect of Each Dimensional Parameter on the Maximum Principal Stress

The stress on the shell is related to the applied pressure, shell structure, and shell material. In the case of constant applied pressure and shell material, the distribution of the maximum principal stress should be related to the shell structure size. Therefore, in this paper, the structural dimensions at the stress concentration are parametrized to study the effect of the variation of each factor on the maximum principal stress (Fig. 7, Table 3).

Fig. 7 GIS shell structure.

1. Shell thickening, 2. Rounded corner 54/55, 3. Rounded corner 58, 4. Wrap thickness, 5. Rounded corner 51, 6. Rounded corner 52, 7. Rounded corner 66

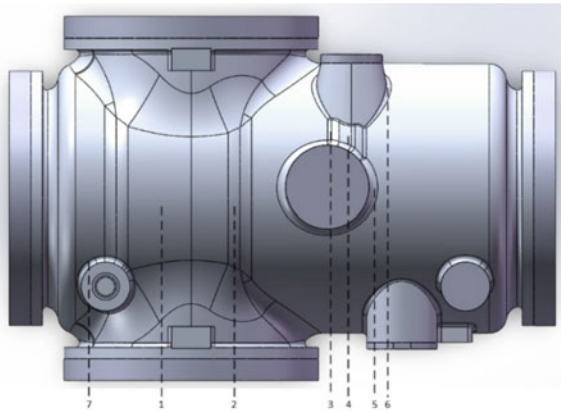


Table 3 The stress field optimization parameters

Serial number	Dimensional parameters	Parameter range/mm
1	The shell thickening D_1	6–10
2	Fillet 54/55 R_1	120–132
3	Fillet 58 R_2	15–25
4	Wrapping thickness D_2	3–6
5	Fillet 51 R_3	14–26
6	Fillet 52 R_4	7–14
7	Fillet 66 R_5	6–14

In the same way as for the electrostatic field treatment, a number of sample points are taken within the parameter range using the uniform sampling method to analyze the range and the law of variation of the maximum principal stress in the shell when the single factor changes.

Among all parameters, the shell thickening D_1 , cladding thickness D_2 , fillet 66 radius R_5 have an obvious linear relationship with the maximum main stress of the shell, and the maximum principal stress of shell gradually decreases with the increase of parameters.

The shell thickening D_1 is set to 6, 7, 8, 9 and 10 mm for stress field simulation, and the relationship between the maximum principal stress of the shell and the shell thickening D_1 is obtained (Figs. 8, 9 and 10).

Fig. 8 The maximum principal stress values for different shell thickening D_1

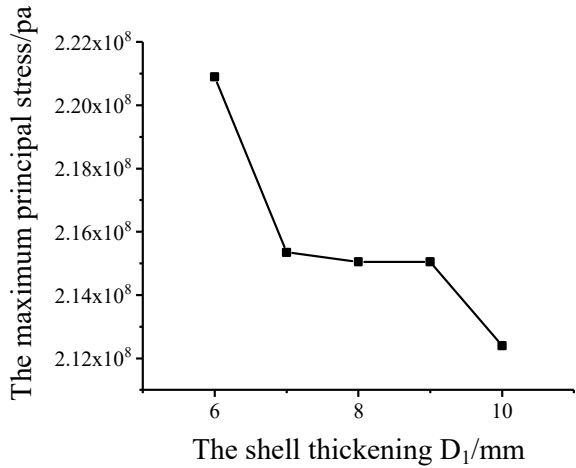


Fig. 9 The maximum principal stress values for different cladding thicknesses D_2

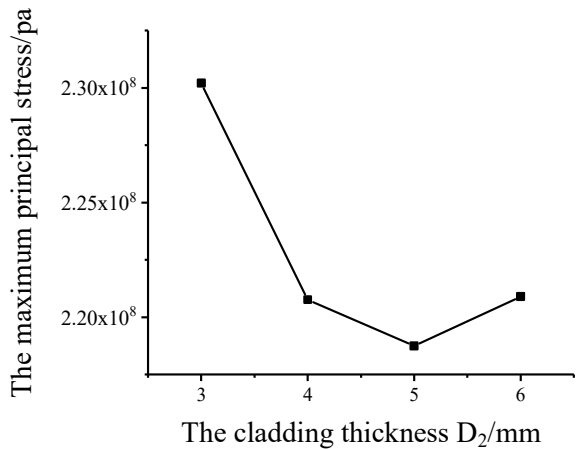
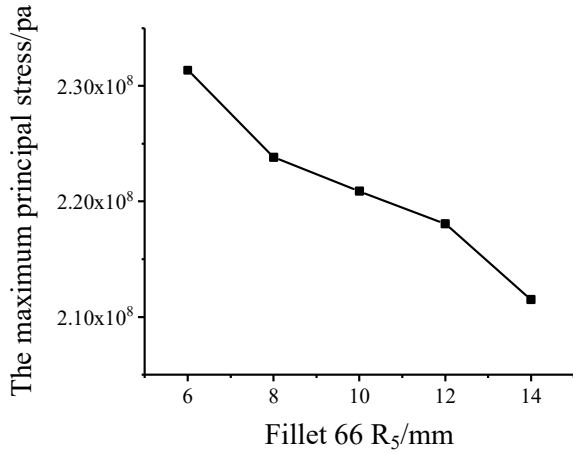


Fig. 10 The maximum principal stress values at different radii of fillet 66 R_5



The cladding thickness D_2 is set to 3, 4, 5 and 6 mm for stress field simulation and the relationship between the maximum principal stress of the shell and the cladding thickness D_2 is obtained.

The radius R_5 of fillet 66 is set to 6, 8, 10, 12 and 14 mm for stress field simulation, and the relationship between the maximum principal stress of the shell and the radius R_5 of fillet 66 is obtained.

And fillet 54/55 R_1 , fillet 58 R_2 , fillet 51 R_3 , fillet 52 R_4 have a large effect on the maximum main stress of the shell but there is no obvious pattern. Table 4 is the range of maximum principal stress variation for these parameters.

Table 4 The range of the maximum principal stress variation for some parameters

Serial number	Dimensional parameters	Parameter range/mm
1	Thickening of the shell D_1	6–10
2	Fillet 54/55 R_1	120–132
3	Fillet 58 R_2	15–25
4	Wrapping thickness D_2	3–6
5	Fillet 51 R_3	14–26
6	Fillet 52 R_4	7–14
7	Fillet 66 R_5	6–14

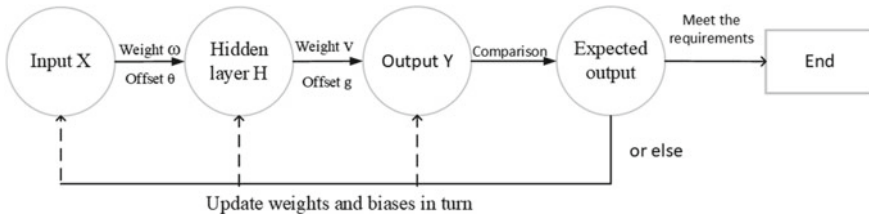


Fig. 11 The BP neural network flow chart

4 BP Neural Network Model Construction

4.1 BP Neural Network Model

Due to the complex structure of the GIS model and too many group elements, it leads to high order of finite element simulation solution, long solution time and high computational cost, and the model needs to be simplified. BP neural network can learn and store a large number of input–output pattern mapping relations without revealing the mathematical equations describing such mapping relations beforehand, and with sufficient sample training, it has better accuracy compared to the function expression fitting, and using BP neural network can greatly improve the computational efficiency under the condition of guaranteeing certain accuracy by downscaling the model [10]. Figure 11 is the workflow diagram of BP neural network.

4.2 Determination of Input and Output

From the above study, it is known that for the electrostatic field, the shape of the static side contacts on both sides has a large influence on the maximum field strength inside the isolation switch, so the dimensional parameters in Table 1 are selected as the input of the BP neural model for the electrostatic field. As shown in Fig. 2 of the electric field distribution of the isolation switch, the maximum field strength is mainly distributed on the static side and busbar static side contact surfaces, so the maximum field strengths E_1 and E_2 on the static side contact and busbar static side contact surfaces are selected as the outputs.

For the stress field, the structure at the shell intersection and the cladding have an effect on the maximum principal stress of the shell, so the dimensional parameters in Table 3 are selected as the input of the BP neural network model of the stress field. From the shell stress distribution Fig. 3, it can be seen that the maximum principal stress is mainly distributed at the shell intersection and cladding, so the maximum principal stresses F_1 and F_2 at these two places are selected as the outputs.

4.3 Experimental Design

After determining the inputs and outputs, it is necessary to design trials to obtain training samples to train the neural network model. Box-Behnken Design is a type of response surface design that can well respond to the relationship between the inputs and outputs at a small operating cost, and also, the Box-Behnken Design ensures that all factors are not set at high levels at the same time, avoiding the appearance of extreme size designs [11, 12]. Therefore, in this paper, the BBD experimental design method is used to collect sample data to construct BP neural network models for electrostatic and stress fields.

4.4 Neural Network Model Error Analysis

After obtaining the sample data, a BP neural network model is built for training and prediction using programming. Several sampling points are sampled for comparison and validation of predicted values and simulation, as shown in Figs. 12 and 13 (Table 5).

It can be seen that the BP neural network prediction error is within the acceptable range, which greatly improves the computational efficiency at the expense of certain accuracy.

Fig. 12 The comparison of the predicted and simulated electrostatic field values

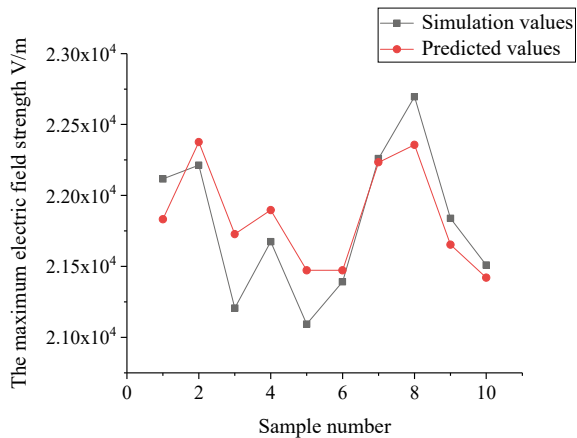


Fig. 13 The comparison of the predicted and simulated stress field values

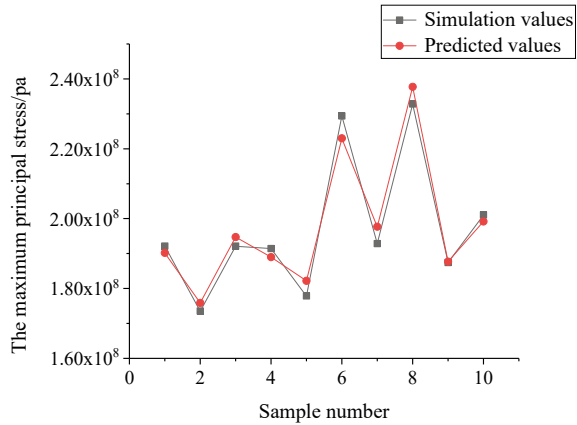


Table 5 The BP neural network model error analysis

BP neural network model	Average percentage error (%)	Correlation coefficient
E ₁	1.12	0.9474
E ₂	0.52	0.9959
F ₁	1.58	0.9813
F ₂	1.05	0.8977

5 NSGA-II Algorithm

5.1 NSGA-II Algorithm Concept

NSGA-II algorithm is a heuristic algorithm based on genetic algorithm and Pareto optimal concept, which can effectively handle multi-objective optimization problems with strong global search capability and operational efficiency.

The GIS structure is complex, with too many dimensional parameters, the influence of parameters may have no obvious regularity, and there are interactions between parameters. Manual modification of parameters based only on existing design experience is not only inefficient but also highly subjective and far from meeting the needs of optimal design. However, the multi-objective optimization problem in this paper can be solved well with the powerful computing power of computer and the global optimization seeking capability of NSGA-II algorithm.

5.2 *Determination of the Objective Function*

The variables and constraints of the electrostatic and stress fields have been determined in Sect. 2. In order to improve the insulation and compressive resistance of the GIS, the main objectives of the optimized design in this paper are: (1) The electrostatic field—the maximum field strength of the static side contacts and the static side contacts of the busbar; (2) The stress field—the maximum principal stress at the intersection of the cladding and the shell.

5.3 *Calculation Process*

(1) the initial populations, which are the preliminary parameters and the objectives, are obtained by utilizing BP neural networks and based on the range of the inputs; (2) the initial population is subjected to non-dominated sorting, and the offspring population is generated by selection, crossover and mutation; (3) the parent and offspring populations are merged into a whole, and after calculating the objective function using BP neural network, the non-dominated sorting is done, the crowding degree is calculated, the new parent individuals are screened, and a new generation of offspring populations is generated after selection, crossover and mutation; (4) the latest offspring population is obtained after iterating repeatedly to the maximum number of generations.

5.4 *Optimization Results and Analysis*

After iterating to a set number of times, the latest population of children, i.e., the Pareto optimal solution family, is obtained. Traditional multi-objective optimization algorithms usually transform multi-objective problems into single-objective problems using a pre-determined weight assignment; However, the NSGA-II algorithm obtains the Pareto optimal solution family based on the Pareto fast non-dominated ordering, and then assigns weights to the desired optimal solution according to the designer's focus on different objectives.

For the electrostatic field, the maximum field strength of the static side contact is usually higher than that of the busbar static side contact, so it is preferred to obtain the parameter solution that makes the field strength of the static side contact smaller during the solution process by giving a higher weight. For the stress field, the maximum principal stress at the intersection of the shell is generally higher than that at the cladding, which should also be given a higher weight. The approximate optimal solution is obtained after the reasonable weight assignment. Figures 14 and 15 show the effect of optimization of the electrostatic and stress fields.

Fig. 14 The comparison chart of before and after electrostatic field optimization

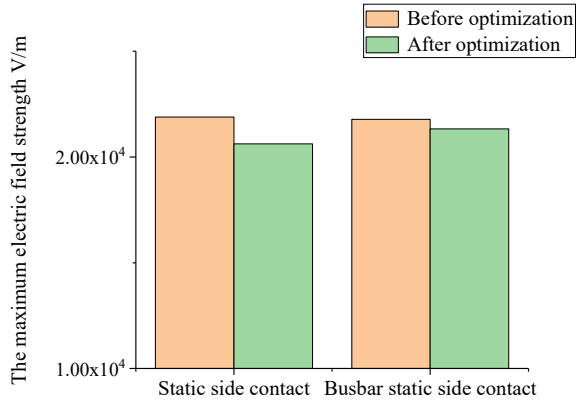
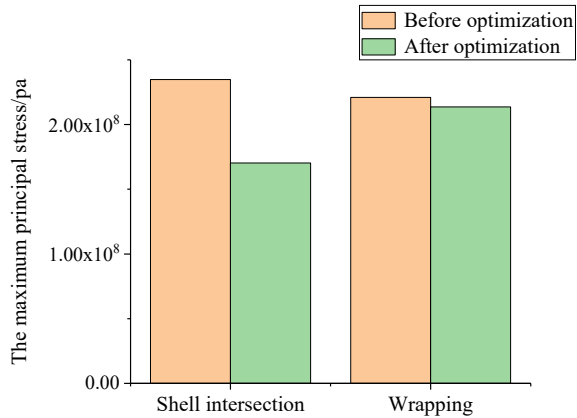


Fig. 15 The comparison of before and after stress field optimization



With the help of the optimization comparison chart, it can be visualized that the field strength and stress of each target are reduced to some extent after optimization, and more significant optimization effects are obtained for the more concerned shell intersection and static side contacts. In general, while taking into account the multi-objective optimization, a greater degree of optimization effect is achieved for the more concerned objectives, and the electrical and voltage resistance of GIS equipment is better improved.

6 Conclusion

In this paper, a model of three-phase common box type GIS double-fracture disconnect switchgear is built, its electrostatic field and stress field are simulated and analyzed, and the key optimization parts are parameterized, the design samples are

constructed according to the Box-Behnken Design principle, the sample data are collected in bulk using the parameterized model, the BP neural network model is constructed to improve the calculation efficiency, and the prediction accuracy of the model is verified by random sampling. The prediction accuracy of the model is verified by random sampling. Finally, the NSGA-II algorithm is used to obtain the approximate optimal solution system for the optimized parameters of electrostatic and stress fields, and the approximate optimal solution is obtained according to the weight assigned to different optimization objectives.

In this paper, based on BP neural network and NSGA-II algorithm, the optimization design of electrostatic and stress field simulation of three-phase common box type GIS double-fracture disconnect switchgear is carried out, which simplifies the complex model and finds the global solution, effectively reduces the electric field strength and stress magnitude of GIS, improves the electric and voltage resistance of GIS equipment, and provides a proven method for miniaturization design.

Acknowledgements This research is supported by technology project managed by the headquarters of State Grid Corporation of China, “Research on non-outage expansion and test technology of three-phase common enclosure GIS (500-202222119A-1-1-ZN)”.

References

1. Yang H, Wang C, Ji H et al (2021) Research on Non-stop overhaul and expansion of GIS. *Shanghai Electr Technol* 014(002):35–39 (in Chinese)
2. Li W, Yang X, Zhang C et al (2019) Simulation and test of double-fracture disconnect switch in GIS. In: 2019 IEEE 3rd international electrical and energy conference (CIEEC). IEEE
3. Yang X, Zhang Changhong, Wang Q et al (2020) Electric field optimization and insulation type test of GIS double-fracture disconnecter based on non-axisymmetric design. *Electr Appl* 39(06):68–75 (in Chinese)
4. Xu JY, Wang F, He RT, Xiao FL (1999) The research on the electric field characteristics and the insulation breakdown property of the disconnecter switchgear inside of three phase in one tank type 110 kV GIS. *Chin J Electr Eng* 09:32–36 (in Chinese)
5. Wang C, Li W-D, Jiang Z-H et al (2021) Compact design for 550 kV GIS insulation system. In: 2021 International conference on electrical materials and power equipment (ICEMPE)
6. Gong R, Wang S, Luo X et al (2010) Simulation and optimization of structure parameters in 550kV disconnectors based on response surface method. *Plos One* 8(11)
7. Liu W, Zhang Y, Song K et al (2012) Finite element analysis and optimization for the high voltage disconnecter self-elastic contact base on ANSYS workbench. *Mater Sci Forum*
8. Huang M, Sheng L (2017) Performance optimization of 110kV disconnecter based on ANSYS workbench. *Electr Eng*
9. Liu Y, Zhou L, Deng W et al (2016) Numerical calculation of electric field and design of grading ring for fixed contact of 550 kV disconnecter. *High Volt Appar*
10. Li X, Xie M, Liu Z, Zhou Z, Zhang C (2022) Optimization technology of composite Insulator shed based on BP neural network model. *High Volt Electron* 58(11):98–105 (in Chinese)

11. Kahhal P, Ghasemi M, Kashfi M, Ghorbani-Menghari H, Kim JH (2022) A multi-objective optimization using response surface model coupled with particle swarm algorithm on FSW process parameters. *Sci Rep* 12(1):2837
12. Sultana N, Hossain SMZ, Mohammed ME et al (2020) Experimental study and parameters optimization of microalgae based heavy metals removal process using a hybrid response surface methodology-crow search algorithm. *Sci Rep* 10(1):15068